Advanced measuring techniques for characterisation of the concrete dynamic tensile response

Bratislav Lukic

Communauté
UNIVERSITÉ Grenoble Alpes

THÈSE

Pour obtenir le grade de

DOCTEUR DE LA COMMUNAUTE UNIVERSITE GRENOBLE ALPES

Spécialité : 2MGE : Matériaux, Mécanique, Génie civil, Electrochimie

Arrêté ministériel : 25 mai 2016

Présentée par

Bratislav LUKIĆ

Thèse dirigée par **Pascal FORQUIN**, Professeur, Université Grenoble Alpes, et
co-encadrée par **Dominique SALETTI**, MCF, Université Grenoble Alpes

préparée au sein du **Laboratoire 3SR**
dans **l'École Doctorale I-MEP2 - Ingénierie - Matériaux, Mécanique, Environnement, Energétique, Procédés, Production**

Mise au point d'une technique de mesure de champs pour la caractérisation du comportement dynamique du béton en traction

Thèse soutenue publiquement le **04/05/2018**,
devant le jury composé de :

M. Julien RETHORE
Directeur de Recherche CNRS, Ecole Centrale de Nantes, Président
M. Michel GREDIAC
Professeur, Université Clermont Auvergne, Rapporteur
M. Stéphane ROUX
Directeur de Recherche CNRS, Ecole Normale Supérieure Paris-Saclay, Rapporteur
M. Michel BORNERT
Ingénieur en chef des Ponts, Eaux et Forêts, ENPC, Examinateur
M. Benjamin ERZAR
Ingénieur de recherche, CEA Gramat, Examinateur
M. Pascal FORQUIN
Professeur, Université Grenoble Alpes, Directeur de thèse
M. Dominique SALETTI
Maître de Conférences, Université Grenoble Alpes, Co-encadrant de thèse

Development of a full-field measuring technique for the characterisation of the dynamic tensile behaviour of concrete

Bratislav Lukić

May 4^{th}, 2018

Mom tati

Acknowledgements

This thesis is a result of a truly unforgettable period of about three years (et des poussières) spent in the Laboratory 3SR in Grenoble. During this time, many people had an (direct and/or indirect) influence on the final outcome, to whom I owe my thanks.

First of all, I want to give my special thanks to my supervisors, Mr. Pascal Forquin and Mr. Dominique Saletti. Thank you Pascal, for introducing me to the academic world and the great field of dynamic behaviour of materials; thank you for showing me the importance of always questioning everything in experimental works; thank you also for your infinite energy and (infectious) enthusiasm throughout this entire time.
Thank you Dominique, for your patience and guidance; thank you for always finding the positive sides of my work (even when it was difficult for me to see any) and thank you for constantly teaching me how to tame a wild thesis. Thank you both, for your continuous support; for giving me plenty of space to deepen my research but also for being there when needed and for always considering my opinion on different topics and issues we had. And finally, thanks for all those great days (and some evenings) spent in the Hopkinson room, where we had a lot of ultra-long laughs and took some great ultra-high speed images.

Next, I would like to express my sincere gratitude to all the members of the jury for encouraging a very pleasant, sometimes challenging but most importantly, fruitful scientific discussion on the day of the defence. It is my honour to specially thank the two reviewers of the manuscript, Mr. Stéphane Roux and Mr. Michel Grédiac, for their constructive feedback as well as detailed comments that were included in their reports, all of which in turn represent invaluable suggestions for further improvements. Also, I sincerely thank Mr. Michel Bornert and Mr. Benjamin Erzar for their interesting reflections on the topic as well as sharing their precious professional know-how. Finally, it is my pleasure to thank Mr. Julien Réthoré for accepting to be the president of the jury and for providing his useful and appreciative comments.

I consider myself very lucky for spending this time in such a great working environment as is the 3SR Lab, where I also had the chance to meet so many extraordinary people. Some have directly influenced this work, therefore I would like to particularly thank Jean-Luc Zinszner for his help at the beginning of this thesis and Federico Schiaffini for being a great set of helping hands in one of the experimental campaigns. Others influenced it indirectly, through brief but powerful scientific discussions, therefore my thanks also go to Eddy and Emanuel. But above all, I am glad that these extraordinary people became my very good friends with whom I now share many nice memories and exciting moments. Thank you Olga and Eleni K. for always being super positive and transferring that to all of us. Thank you Anne, Tjan, Max, Alessandro and Timos for all those (non) scientific discussions that usually occurred after the working hours. A special thanks goes to Eleni and Alexandra for all those short brakes during which we shared our ups and downs and supported one another all the way.

Last but not least, I owe my deepest gratitude to my parents, of whom I am proud and from whom I learned so much. Thank you mom, for all your warm support and for always believing in me during all this time.

Sonja, I cannot put it into words, thank you for everything and you know what all for.

Abstract

In this thesis a photomechanical spalling testing technique has been used in light of identifying concrete failure properties under dynamic tension. The experimental technique uses ultra-high speed imaging, the grid method and the virtual fields method. First, in order to investigate the accuracy and validate the data processing, a method of using simulated experiments has been developed by numerically recreating the entire identification process. In this way, several potential sources of errors have been investigated allowing to place guidelines on how to perform the experiment in a more reliable manner. Second, several ultra-high speed acquisition systems have been used in order to investigate their contribution to a possible measurement refinement. In this case, the trial experiments have been conducted on a material of known characteristics which allowed investigating metrological performance of the cameras on the entire identification chain. Finally, the experimental methodology has been applied to testing several grades of concrete in light of identifying the material constitutive response as well as their fracturing characteristics under dynamic tension. The identified tensile strengths in this work were found to be consistently lower than those obtained from the standard processing of the rear-face velocity profile. Moreover, the values of the identified specific fracture energy were also found to be markedly lower than the ones reported in the literature.

Keywords: Ultra-high speed imaging, The Grid method, The Virtual Fields Method, high strain rate, tensile strength, concrete, simulated photomechanical experiments.

Résumé

Ce travail de thèse a pour objet une méthode expérimentale combinant un essai de traction indirect par écaillage et une mesure de champs à partir d'images obtenues par caméra ultra rapide, ceci à des fins d'identification des propriétés de rupture du béton sous chargement de traction dynamique. Cette méthode fait ici l'objet d'une étude approfondie ainsi que d'une série de développements et d'amélioration. Les images obtenues sont traités par une technique de grille et la méthode des champs virtuels est appliquée pour identifier le comportement local des matériaux quasi-fragiles soumis à de hautes vitesses de déformation (plusieurs 100 s^{-1}). Afin de valider la technique de traitement mais aussi d'étudier l'incertitude de mesure associée, un simulateur de la chaîne de mesure complète a été mis au point. Il a été ainsi possible d'étudier l'influence de différentes sources potentielles d'erreurs qui peuvent être rencontrées dans le protocole expérimental. Cette étude a permis de retenir des recommandations sur les conditions de dépoillement de l'essai afin d'améliorer la fiabilité des mesures obtenues. D'un point de vue expérimental, différentes cameras ultra-rapides ont été utilisées afin d'étudier la qualité des mesures réalisées. Ainsi, plusieurs campagnes d'essais ont été réalisées sur un matériau aux caractéristiques bien identifiées permettant l'étude des performances métrologiques de toute la chaine d'identification, pour chaque modèle de capteur. Enfin, la methode expérimentale a été mise en oeuvre pour étudier le comportement de plusieurs types de béton sous chargement de traction dynamique. L'objectif, ici, est d'identifier leur comportement mécanique ainsi que leurs caractéristiques de rupture sous traction dynamique. En ce qui concerne la résistance à la traction, les valeurs de résistance identifiées dans cette étude sont inférieures, pour chaque cas, à celles obtenues à partir du traitement de la vitesse matérielle mesurée en face arrière de l'échantillon. Pour ce qui est de l'énergie spécifique de rupture, les valeurs obtenues dans ces travaux sont égalements inférieures à celles publiées dans la litérature.

Mots clés: Imagerie d'ultra-haute vitesse, méthode de la grille, méthode des champs virtuels, résistance à la traction, écaillage, béton, simulation numerique.

Contents

List of Figures

Chapter 1

Introduction

1.1 Background

Concrete is one of the most used building materials, thanks to its low density, high compressive strength but also availability of its constituents and straightforward manufacturing. Nevertheless, its range of application in civil engineering has been restricted by its low tensile strength and quasi-brittle response, having these inherent properties usually being considered as concrete weakest characteristics which govern the initiation of the failure process. For this reason, in most engineering codes concrete is usually considered to have only compressive bearing capacity in quasi-static loading conditions while the tensile stresses are transferred to the internal steel reinforcement. This is especially the case when structures are exposed to severe transient dynamic loadings (*e.g.* projectile impacts, blasts or explosions), where the ultimate material response can be highly affected by the complex stress states and high deformation rates that evolve in the material [Li et al., 2005, Wen and Xian, 2015]. For example, during ballistic impacts of a projectile against a concrete target severe damage modes occur and tensile strength as well as the material softening response strongly influence the penetration resistance of the impacted targets [Forquin et al., 2015]. Dynamic loads spread over a range of time intervals depending on the incident situation. Under intense loadings, extremely high strain rates evolve in the medium, leading to both severe and specific damage modes [Forquin, 2017]. One approximative classification of the estimated strain rate intervals which occur during various types of loadings is presented in Figure 1.1 which is based on classifications offten encountered in the literature [Bischoff and Perry, 1991, Meyers, 1994, Daudeville and Malecot, 2011].

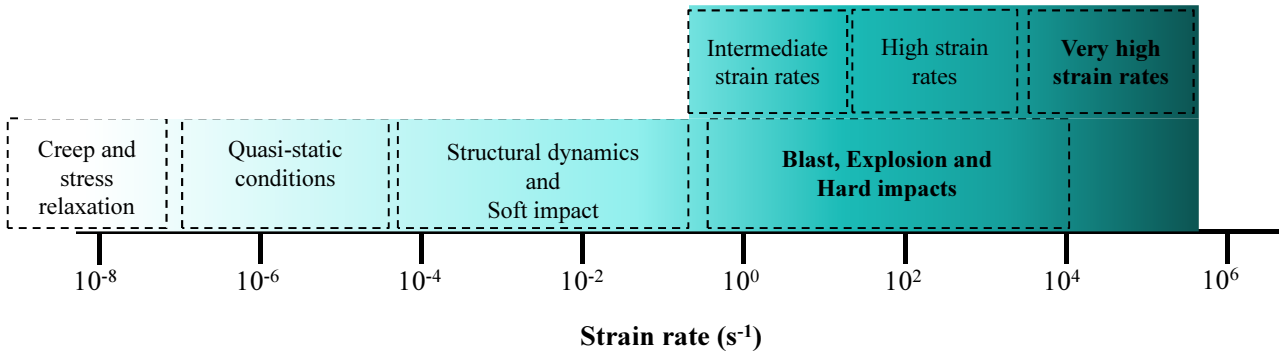

Figure 1.1: General strain rate range for various types of loading situations.

Over the last decades, various studies have been devoted to characterising concrete failure properties under dynamic tension and high strain rates. The reported results show that concrete exhibits a markedly higher tensile resistance under elevated loading rates, revealing the sensitivity of the material properties to strain rate. However, despite decades of research within the area, many phenomena involved in the dynamic tensile response of concrete are not yet fully understood. Some of the main reasons, aside from the fact that various concrete compositions and conditions were considered, are related to the variety of experimental methods that have been used as well as the application of indirect and global measurement methods which make processing of the data for obtaining true material description difficult.

On the other hand, rapid progress in ultra-high speed imaging has allowed material properties to be studied at high

strain rates by applying full-field measurements and inverse identification methods. These fast evolving camera-based measurement methods are currently revolutionising the area of experimental mechanics since they allow not only the visualisation the displacement distribution, but also characterising the complete material constitutive response when subjected to a load. Nevertheless, the sensitivity of these techniques still requires a better understanding, since various extrinsic factors present during an actual experiment make it difficult to separate different sources of errors that can significantly affect the quality of the identified results.

One such measurement method has been suggested for obtaining the information on concrete tensile strength at high strain rates based on the use of a Hopkinson bar and employing ultra-high speed imaging and the virtual fields method to obtain the material response under dynamic tension [Pierron and Forquin, 2012a]. In this work, the aim is to investigate this method from several angles. First one, a focus has been made on exploring the possible refinement of the measurement by testing the metrological performance of some latest ultra-high speed acquisition systems available on the market. A second one was to use a more affordable method of simulating an acquisition of a hypothetical camera applied to the experimental method in question. Apart from validating the processing procedure, this methodology aims to provide general guidelines on which imaging apparatus could be suitable for the test as well as giving guidelines on how to perform the experiment in such a way that the unwanted sources of errors tied to the experimental environment are reduced (as much as possible). Finally, having the procedure as well as the experimental protocol on the data processing well placed and validated, the method can be used to obtain the valuable information on the material dynamic response such as dynamic tensile strength and corresponding strain rate, specific fracture energy at a given fracture opening velocity and complete local stress-strain response. If reliably determined, these information can then be used for deriving possible material models in the framework of fracture dynamics which would enable a better understanding of the involved failure mechanisms as well as engineering guidelines concerning dynamic loading situations.

1.2 Structure of the thesis

This thesis work aims to *explore*, *validate* and *apply* a photomechanical dynamic tensile experiment proposed by [Pierron and Forquin, 2012a] in light of obtaining failure quantities of concrete-like materials in dynamic tension. The experiment in question is the so-called spalling technique relying on the use of a single Hopkinson bar. The method involves the use of an ultra-high speed imaging system to obtain time resolved full-field measurements and the virtual fields method to identify the material response. Pursuing the three emphasised ideas, the thesis is divided into seven chapters and a perspectives section. Their content is the following:

- Chapter 2 presents a literature state of the art which tries to congregate several different aspects into one unity. On one hand, it briefly covers different experimental methods that have been used in previous works to determine the dynamic tensile strength as well as fracture energy of concrete-like materials at high strain rates, providing an overview on the obtained results and discussing along the way the measurement and processing methods used to obtain these information. On the other hand, it reaches towards the domain of ultra-high speed imaging, full-field measurements and material identification, referring to the techniques that will be used in this work.

- Chapter 3 has the aim of putting the photomechanical spalling method to use, testing its application from both experimental and data processing point of view as well as exploring the reliability of the obtained measurements. Several tests conducted on concrete material are presented in order explore all the possibilities of obtaining useful data from the rich information contained in the obtained full-field measurements.

- Chapter 4 presents a methodology of conducting virtual experiments by numerically simulating the entire measurement chain. Its main aim is to provide a validation of the data processing. Additionally, it also numerically explores the sensitivity of the measurement method to various experimental sources of errors, finally

concluding that simulated photomechanical experiments can serve as a good tool for providing guidelines on what can be the best way to conduct the experiment in the first place.

- Chapter 5 proposes a new processing of the obtained data in order to obtain the specific fracture energy from the spalling test. It simply exploits the local content of the information that is being encoded in the measured displacement fields. The numerical tests were also conducted in light of validating the data processing.

- Chapter 6 explores the possibility of the measurement refinement by using two ultra-high speed imaging systems of the latest generation. These systems have been applied on conducting spalling experiments on a material of known characteristics, comparing along the way the results from full-field and point-wise measurements. It also suggests that the spalling test can be considered as a good candidate for testing the metrological performance of such systems when performing full-field kinematic measurements.

- Chapter 7 presents the first application of the method from the point of investigating the effect of concrete composition on the dynamic tensile strength at high strain rates. To this end, three types of concrete compositions were tested and the data obtained from classical data processing are compared to those obtained from the methodology of conducing the photomechanical identification.

- Chapter 8 rounds-up the main parts of the work conducted during this thesis, reflecting back on the observations made regarding the experimental results. Finally, it also gives several suggestions for future work and improvements.

Chapter 2

State of the art

2.1 Experimental techniques

2.1.1 High strain rate dynamic tensile testing

Investigating the dynamic tensile response of concrete has been a great challenge in experimental mechanics for over several decades. The main reasons are linked its intrinsic nature of relatively low tensile strength, high brittleness and low failure strain. In light of studying its behaviour under dynamic tension, various experimental techniques and measurement methods have been devised over the past century. Major experimental techniques that have been used for dynamic tensile testing of concrete material at high strain rates are based on the use of the Split Hopkinson Pressure bar (also known as Kolsky bar) systems or the use of a single Hopkinson bar systems. The former expose the material to direct dynamic tension and the latter to indirect spall tension. Comprehensive review of such techniques can be found in a recently published well-rounded review article [Heard et al., 2018]. Most of these methods will be shortly presented in the following.

2.1.1.1 Dynamic Direct Tension Technique

Direct testing was one of the first approaches used to perform tensile tests at strain rates that differ from quasi-static regime. The earliest ideas were based on the use of a servo-hydraulic machine which can be operated at high speed to apply a high tension rate on the specimen. Several works have used such testing apparatus to reach the values of so-called intermediate strain rates (from 10^{-2} to 1 s^{-1}) such as for example in [Yan and Lin, 2006, Erzar and Forquin, 2011, Wu et al., 2012]. However, the hydraulic machines may not handle well the vibrations caused by wave propagation in typical dynamic tests which can result in oscillating force signal read out from the force sensors. Furthermore, the strain rates which can be achieved with the servo-hydraulic method remain low and can be regarded as insufficient for dynamic characterization of material behaviour. Therefore in the following the accent is on the experimental methods that reach higher strain rates (up-to a few hundred s^{-1}) and are based on some version of the Split Hopkinson Bar (SHB) systems.

The Gravity driven and pre-stressed SHB systems Being introduced as early 1980 [Zielinski, 1980, Zielinski et al., 1981], the Gravity driven SHB set-up is one of the first systems used for the direct dynamic testing of concrete materials at high strain rates reaching up-to 10 s^{-1} (Figure 2.1). It has been installed at the Steven Laboratory at Delft University of Technology (TU Delft) and consists of large diameter aluminium bars, of 74 mm in diameter, in between which a concrete sample ($L = 100$ mm) is placed and glued with polyester resin. The total height of the set-up is 11.5 m which makes it one of the tallest SHB bars of its kind. The direct tensile pulse is generated through an impact of the drop-weight onto the anvil on the lower (incident) bar, which propagates upwards towards the concrete sample and the upper (transmitted) bar. The profile of the incident wave can be controlled through the drop height of the free-fall and the magnitude by the mass of the drop-weight. Soft material (*e.g.* rubber and/or cardboard) can be placed on the contact surface between the anvil and the drop-weight. Changing the thickness of the soft layer aids in controlling the rising time of the tensile pulse which is considered as a way of pulse shaping technique. The stress in the sample is obtained from the measured transmitted wave on the upper bar, whereas the specimen strain and strain rate were deduced from gauge on the sample. One such recently developed gravity SHB system also addresses the design of the pulse shaping through numerical simulations [Levi-Hevroni et al., 2017]. However, when several layers of soft material are applied it was noticed that the drop-weight system was unable to

induce sufficient strain rate in the samples (limit about 2 s^{-1}). To overcome this limitation, a modification based on the use of the pre-stressed cable was introduced in [Reinhardt et al., 1986] which allowed reaching the input force up-to 100 kN.

Later on the principal of the pre-stressed cable was applied to the construction of several horizontal alluminium SHB setups in the DynaMat Laboratory of the University of Applied Sciences of Southern Switzerland (SUPSI) by Cadoni *et al.* [Asprone et al., 2009] (Figure 2.2). The maximum loading capacity of 1 MN can be applied with this set-up by pulling the pre-stressed cable with a hydraulic actuator. The force is released through the rupture of the fragile bolt inducing a tensile pulse of 1200 μs duration with a linear rise tail. Due to this, a classical processing of data registered on wave propagation, by assuming perfect sample equilibrium, is applied to compute the nominal stress, strain and strain rate within the specimen as function of time as follows [Kolsky, 1964]:

$$\sigma(t) = E_b \frac{A_b}{A_s} \varepsilon_T(t) \tag{2.1}$$

$$\varepsilon(t) = -\frac{2C_0}{L} \int_o^t \varepsilon_R(t)dt \tag{2.2}$$

$$\dot{\varepsilon}(t) = -\frac{2C_0}{L} \varepsilon_R(t)dt \tag{2.3}$$

where ε_R and ε_T are the reflected and transmitted wave respectively, E_b is the Young's modulus of the bar, A_b and A_s are the cross-section of the bar and the specimen, L is the length of the sample and C_0 is the sound velocity for the bar material.

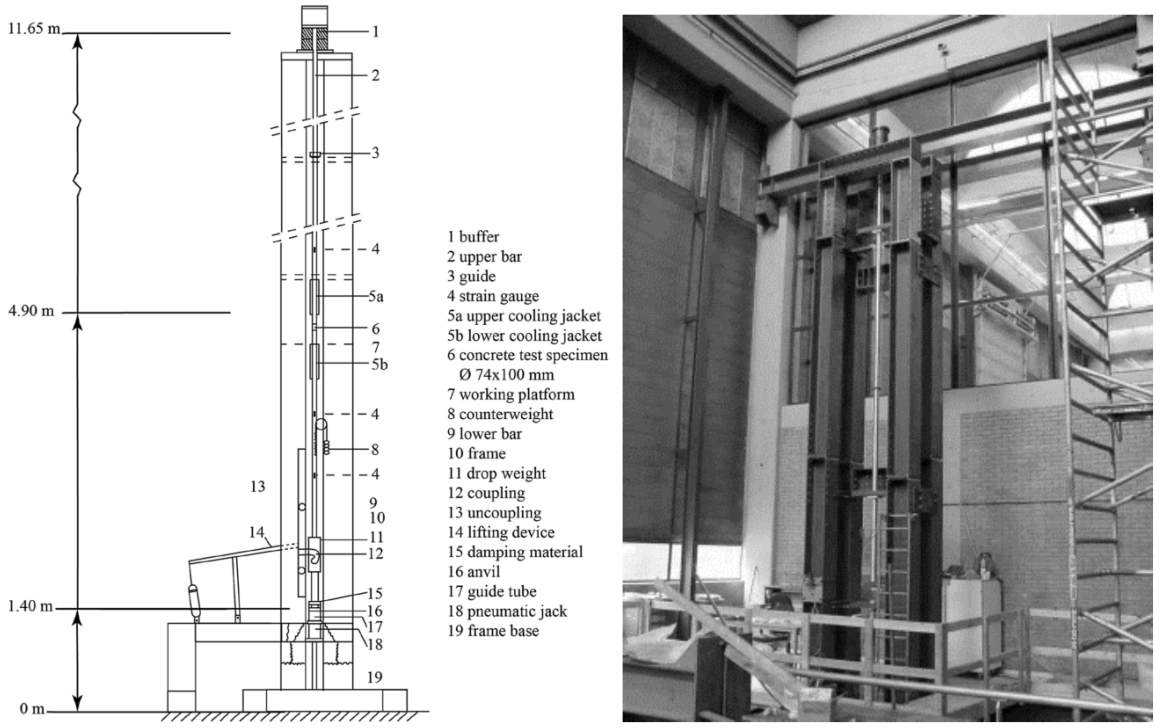

(a) Sketch of the vertical Gravity driven SHB system at TU Delft. (from [Heard et al., 2018])

(b) Image of the Gravity driven SHB system. (from [Vegt, 2016])

Figure 2.1: Overview of the Gravity driven SHB system at Delft University of Technology.

The Hopkinson Bundle Bar (HBB) The SHB set-up with two cylindrical bars (input and output) is considered as a common set-up used for tensile testing in the lower range of strain rates (up-to 10 s^{-1}). However, in order

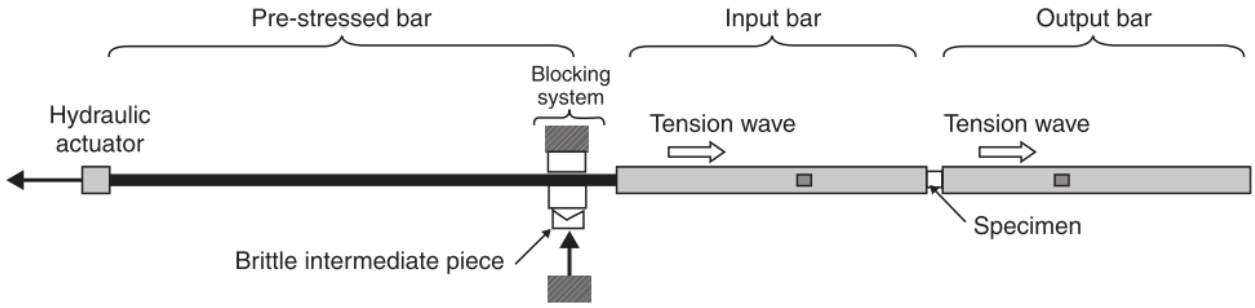

Figure 2.2: Overview of the principal of the pre-stressed SHB bars at SUPSI (bar length ranging from 3 to 15 m and diameter from 20 to 60 mm [Asprone et al., 2009]).

to extend the testing to prismatic samples which geometry was more representative of that often used for characterization of concrete samples proposed in design codes, the idea of using prismatic pre-stressed bars originated. One such system is a specific SHB technique that uses prismatic steel bars of large dimensions, which is usually referred to as the Hopkinson Bar Bundle (HBB) [Albertini and Montagnani, 1994, Labibes et al., 2000, Cadoni et al., 2001b]. It has been developed at the Joint Research Centre at ISPRA specifically for testing large concrete samples (200 x 200 mm^2) with large aggregate size (10 mm in diameter) as reported in [Cadoni et al., 2001a]. The HBB setup is composed of two aluminum alloy Hopkinson bars that are 2 m long which have a square cross-section. The bars are subdivided by electric discharge machine into 25 sub-bars over 1 m which aids the reduction of dispersion effects caused by wave propagation in prismatic bars. Each sub-bar is instrumented by strain gages providing recordings of incident, reflected and transmitted waves (Figure 2.3b). A high strength steal cable of 100 m in length is pre-stretched and is used to generate a direct tensile loading pulse of about 40 ms through a sudden rupture of a ceramic bolt. Based on the same principle as the HBB system, a set-up usually refered to as JRC-MHB was installed in SUPSI using smaller prismatic bars that are of 60 x 60 mm^2 in cross-section [Cadoni et al., 2013].

In all pre-stressed SHB systems, since both amplitude and duration of the incident stress wave are determined by the amplitude of the pretension in the steel cable, it has been difficult to apply any pulse shaping technique. This results in non-constant strain rate over the entire duration of loading which can vary considerably with sample length. Several methods were used to determine the strain rate but often just providing an estimate of a nominal strain rate. Direct tensile testing with SHB systems requires the sample to be glued within the two bars with adhesives that have high tensile strength (at least larger than the tested material). This can induce stress concentrations at the bar specimen contact which may become significant in cases when strong adhesives are used.

2.1.1.2 The Spalling technique

In the last few decades, the spalling test that uses only one Hopkinson (input) bar has been extensively used by many research groups to determine the dynamic tensile strength of concrete-like materials. Compared to the direct tension techniques, the spalling method is an indirect tensile test that combines principles of 1D wave propagation and reflection, and uses the higher compressive strength of concrete to create the spall failure phenomenon due to the dynamic tensile loading (*i.e.* ejection of a spall fragment [Kanel, 2010]). One of the first observation of spall fracture due to wave reflection was in fact reported by Bertram Hopkinson himself [Hopkinson, 1914]. Later, the same experimental principle was used by his assistents, Landon and Quinney [Landon and Quinney, 1923], on long concrete samples who observed multiple spall formation and who noted the difficulty of deducing the mean pressure with the distance of the bar. The spalling principle, due to being relatively simpler and easier to handle compared to SHB systems, was adopted in the groups dealing with dynamic testing of concrete-like materials and has went through several adaptations over the years that will be shortly recalled herein.

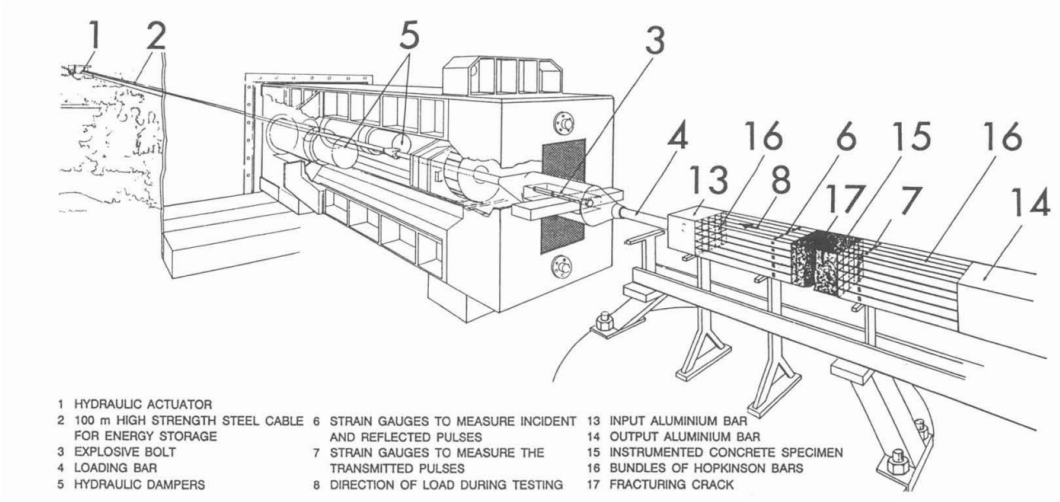

(a) Overview of the first HBB bar introduced in [Albertini and Montagnani, 1994].

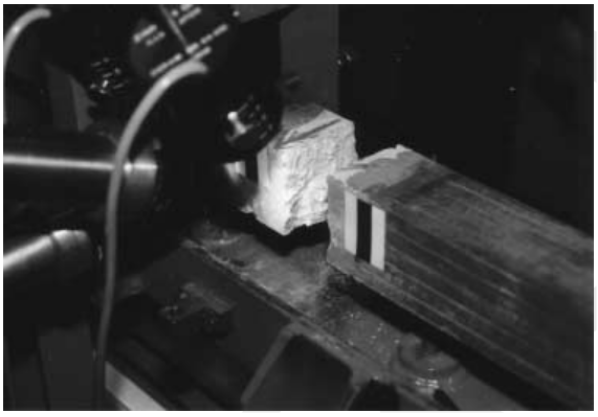

(b) Giant square cross-section concrete sample in a HBB bar.

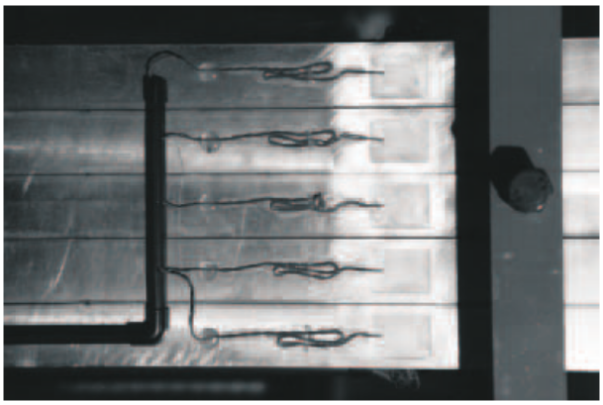

(c) Strain gauge instrumentation on 25 sub-bars of the HBB system.

Figure 2.3: Overview of the Hopkinson Bar Bundle at ISPRA-JRC. (Images taken from [Cadoni et al., 2006, Cadoni et al., 2009])

By the end of 20^{th} century, the data concerning the dynamic tensile strength of concrete was slowly reaching a limit on the reported strain rate of about as high as the SHB systems would work (*i.e.* in the range of 10 s^{-1}). There appeared a clear need to make a step towards higher strain rates (*i.e.* several hundreds s^{-1}); not only to further study the strain rate sensitivity of concrete materials, but also to investigate the already emerging theorise on the multiple fracturing phenomena related to high strain rate loading. Probably the first use of the spalling method that applied intrumented measurements and a projectile to generate the incident pulse was proposed in [Diamaruya et al., 1997]. However, the work did not provide the measurement of the incident load. This led later to the development of one of the first spalling set-ups with instrumented bar installed in 1999 in the Laboratory of Physics and Mechanics of Materials (LPMM) of Metz University [Klepaczko and Brara, 2001] setting a methodology that is still in use today (Figure 2.4). A cylindrical concrete sample is placed in contact with the aluminium input bar on one end, whereas on the other end, an incident compressive pulse is induced that travels through the bar. The method relies on the sample's intentionally unbalanced state, because the tensile wave that induces the desired spall failure is obtained by the reflection of an initially compressive wave from the sample's free-end surface. A gas tank was used to launch the cylindrical projectile against the Hopkinson bar as to generate the compressive wave. The measurement systems employed three strain gauges on the bar that were used to account for wave dispersion effects and shift the recorded wave to the concrete sample. Based on 1D elastic stress wave theory, the stress in the concrete was analytically determined with the d'Alembert's wave equation. An indirect assessment of failure strength and loading rate was performed, corresponding to the maximal reconstructed stress at the same position of the observed position of a macro-crack obtained from post-mortem inspection [Brara et al., 2001].

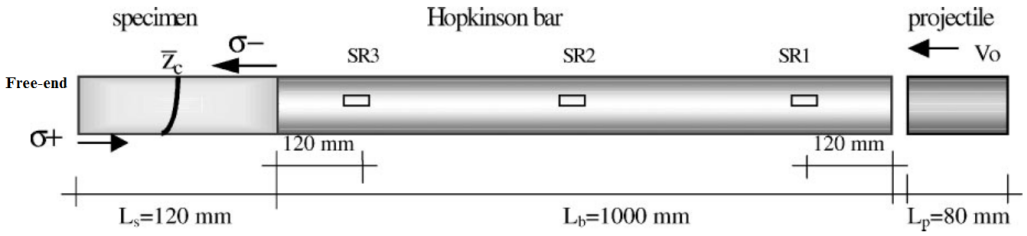

Figure 2.4: Scheme of the mechanical arrangement of the spalling method by Klepaczko *et al.* [Klepaczko and Brara, 2001]. (Bar diameter 40 mm)

Although with clear novelty allowing to reach high strain rates up-to 200 s^{-1} with measurable incident loading, the method lacked the proper measurement technique to reliably determine the sought information: the failure tensile strength and the corresponding strain rate. This drawback was resulting from the fact that no measurement was made on the tested sample and the stress was indirectly reconstructed. In later reported studies, three gauges were placed on the concrete sample with the attempt of directly reconstruct the elastic stress profiles in the sample [Wu et al., 2005]. Subsequently, Weerheijm et al. [Weerheijm and Van Doormaal, 2007] used eight strain gauges and two specialised pressure gauges to better discretise the wave propagating along the sample. However, the inherit heterogeneous nature of concrete material presented an obstacle, which made adequate wave shifting difficult. Clearly, a more reliable measurement method was needed to obtain the sought material tensile strength.

Soon after, Schuler *at al.* [Schuler et al., 2006] proposed to use the method based on the so-called Novikov acoustic approximation [Novikov and Ivanov, 1966] consisting of the measurement of the sample rear face velocity which was initially used to measure tensile strength during shock induced loadings in metals [Antoun et al., 2002]. Assuming linear elastic behaviour up-to peak and instantaneous fracturing, the stress at failure (σ_t) can be related to the

rear-face velocity *pull-back* as:

$$\sigma_t = \frac{1}{2}\rho C_0 v_{pb} \tag{2.4}$$

where ρ is the material density, C_0 is the material wave speed and v_{pb} is the pull-back velocity (Figure 2.5). In the work by Schuler *et al.* the rear face velocity was measured with a small accelerometer glued on the concrete free-end. The work of Erzar *et al.* [Erzar and Forquin, 2010] presented a detailed comparison of the previous methods used to determine the tensile strength of concrete in spall tests, namely the indirectly constructed stress method and the method of the measurement of the pull-back velocity. The inspection was carried on by performing computational simulations with known material peak-stress parameter. The results provided valuable insight that among the proposed methods, the one using the pull-back velocity provides more reliable data of spall strength. Furthermore in the same work, the measurement data and the experimental setup was multiply refined. First, the use of the laser interferometer led to avoiding the use of an accelerometer which could introduce local inertial effects and damage the sample. Second, a more reliable measurement of strain rate at failure was presented using gauges positioned at the anticipated failure location. Finally, a spherical cap-end design was added to the projectile to provide adequate pulse shaping of the incident pulse which proved to be very robust and reproducible (Figure 2.6).

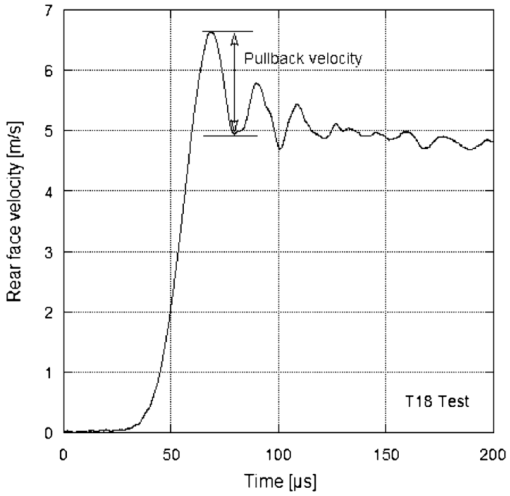

Figure 2.5: Example rear-face pull-back velocity. (Image from [Erzar and Forquin, 2010])

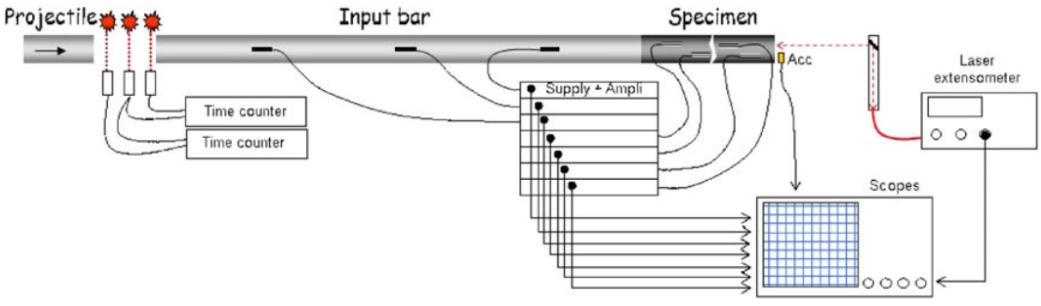

Figure 2.6: The spalling setup used by Erzar and Forquin [Erzar and Forquin, 2010]

Nevertheless, aside the introduced enhancements, the data obtained from one spalling test was limited: it was just one point in ($\dot{\varepsilon}$, σ_t) space which coordinates were indirectly determined assuming several hypotheses on the material behaviour (*i.e.* instantaneous failure, linear elasticity to peak strength). Furthermore, the true material softening response (*i.e.* after the peak tensile strength) was completely out of reach. Recently, a full-field measurement method was proposed using ultra-high speed imaging and the virtual fields method [Pierron and Forquin, 2012b] (Figure 2.7). This ultra-high-speed-full-field-time-resolved displacement measurement method provided a

great step forward, since it demonstrated the potential of having the entire axial stress histories reconstructed along the observed concrete sample throughout the spall test which allowed obtaining a true local stress-strain response (Figure 2.7b). An example is presented in Figure 2.8 which concerns a spalling test performed on a granite material. Thanks to locally identified response the results have reveiled a much smaller Young's modulus in tension than in compression due to the pre-existing crack network within the material [Forquin, 2013]. However, the derived measurements significantly depended on the used ultra-high speed acquisition system. Although it can be considered revolutionizing and (to the opinion of the author of this work) far superior to indirect and point-wise measurement techniques, the use of high speed imaging to perform field measurements and inverse identification introduced a whole new area of possible experimental uncertainties in the test. These have to be well understood before applying such a sophisticated method to perform fine measurements such as stress response of heterogeneous quasi-brittle materials, such as concrete, in dynamic tension.

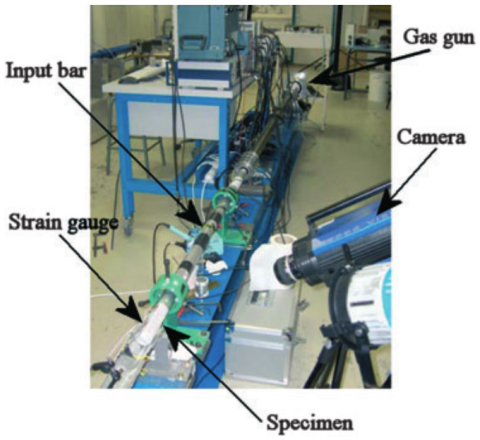

(a) The photographic set-up of a spalling test that uses full-field measurements.

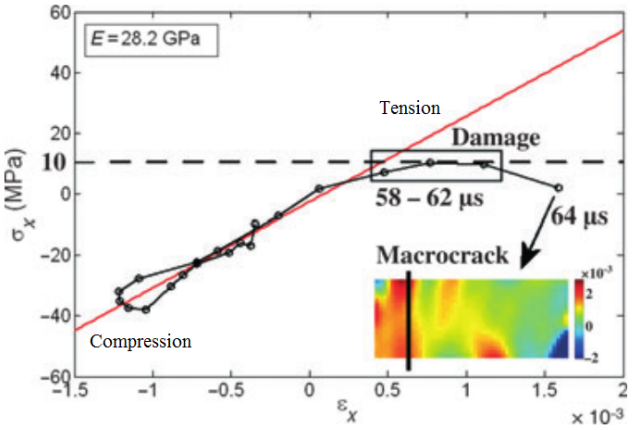

(b) The reconstructed local stress-strain response with the indication of damage in the post-peak regime.

Figure 2.7: The spalling setup used by Pierron and Forquin [Pierron and Forquin, 2012b] that employs full-field measurements.

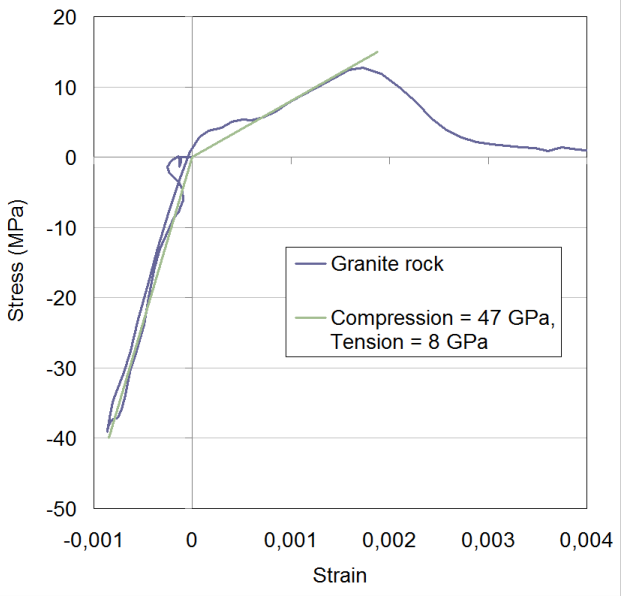

Figure 2.8: The local stress-strain response of a spalling test performed on granite rock with pre-exiting crack network [Forquin, 2013].

2.1.2 Previous works on the Dynamic tensile strength

One comprehensive collection of experimental data regarding the dynamic tensile strength of concrete at various range of strain rates was reported by Malvar and Crawford in 1998 [Malvar and Crawford, 1998]. The data were reported in terms of a Dynamic Increase Factor (DIF) which represents the dynamic tensile strength of one test normalized to a quasi-static tensile strength of the same material. The data have indicated pronounced strain rate sensitivity of concrete in dynamic tension; namely the increase of tensile strength with the increase of the loading rate. This then suggested that, if well understood, the concrete dynamic tensile strength could be exploited during the structural design, leading to better engineering solutions and substantial economical savings. The use of DIF was considered convenient as it allowed providing analytical-empirical formulations that relate the DIF with strain rate, which could be used both as design regulations in engineering codes as well as being directly implemented in numerical computations. One such design regulation which provided the DIF expressions for concrete in both compression and tension loading was introduced by the International Federation for Structural Concrete [CEB, 1993]. Since then, it has become a common practice to also determine the so called DIF empirical curves, often reported for each performed test campaign, and to occasionally present a some sort of alteration of the initially provided expressions. A recent collection of several such expression that link DIF to strain rate can be found in [Lu et al., 2017]. Over the years, the data became mostly restricted to reporting the DIF values of each test and as the number of reported data increased so did the data dispersion, especially at high strain rates [Weerheijm, 2013].

However, the underling fact is that the quasi-static and dynamic strength often do not refer to the same test configuration such as: boundary conditions, specimen shape and size; and most importantly not the same fracturing phenomena which can influence the observed scatter [Régal and Hanus, 2016]. The evaluation of the quasi-static tensile strength is rarely performed in direct tension and often a standardized indirect tests are used, such as splitting tests (*i.e.* Brazilian test) or flexural tests (*e.g.* three-point bending), having the tensile strength indirectly deduced from such results. For example, some works considered the tensile strength in direct tension to be 90% of the splitting strength [Wu et al., 2005, Schuler et al., 2006]. Moreover, some authors assume a tensile strength in direct tension as of 8-10% the compressive strength due to the lack of data on the former, and still report the DIF values (*e.g.* [Zhang et al., 2008]). Such methods can be used to provide estimates of DIF, but however should be taken with caution when an empirical model is derived. The observable wide scatter of the data on the dynamic tensile strength at high strain rates can be augmented by the fact that the normalised strength criterion is used in the data representation and not the intrinsic measure. Additionally, the experimental data is often obtained employing several different testing methods which differ in size and instrumentation, and use different methodologies and assumptions to treat the data.

2.1.2.1 Overview of the literature results – Dynamic tensile strength σ_t

In this section a collection of data from some previous works reported in the literature that directly provide the information on dynamic tensile strength (and not DIF) are gathered and analysed. The data concern dynamic tensile tests performed by using one of the previously described dynamic tensile testing techniques (Section 2.1.1). The accent is on gathering only the data from the works that reported detailed values concerning the deduced dynamic tensile strength and strain rate as a intrinsic measure of one performed test. The plot that presents the reported dynamic tensile strength in function of strain rate from several studies is shown in Figure 2.9. In principle, the results round up the tests performed on several types of concrete compositions. The composition of the tested concrete grades are close to that of an ordinary concrete used in construction works. Although, some variations on mechanical properties as well as maximal aggregate size and tested volume do exist, the main aim is to analyse the data collection from the point of view which concerns the experimental methodology used to obtain these values.

The plot, once again, shows the sensitivity of concrete material to strain rate. However, the scatter of the data

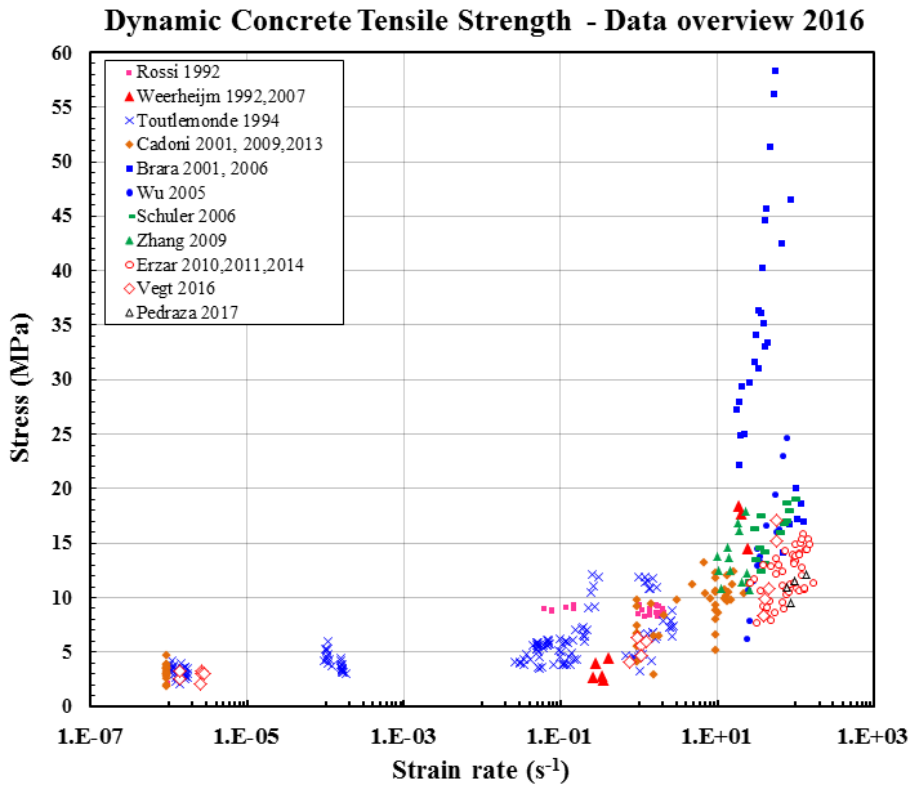

Figure 2.9: Overview of the results reporting dynamic tensile strength at high strain rates.

at high strain rate seems to be more pronounced in some reported studies than others. Among other reasons, such as those that concern the true material effects (*i.e.* cement and granulometric content, mechanical properties, tested volume size and moisture content) the scatter in the results can be induced by the used testing method and, moreover, the methodology adopted for processing the experimental data to derive the tensile strength.

2.1.2.2 Effect of experimental method

The above presented data can be sub-categorized according to the adopted data processing method and experimental technique used (Figure 2.10). The presented data collection consists of two testing techniques, namely those obtained with the SHB bar and the Spalling method. The results reported from the use of the SHB system can be divided into two groups: those which rely the data processing assuming the mechanical equilibrium of the sample [Cadoni et al., 2001a, Cadoni et al., 2009, Cadoni et al., 2013] and those that only treat the results captured in the output bar of the SHB system [Rossi et al., 1992, Weerheijm, 1992, Toutlemonde, 1994, Vegt, 2016]. Concerning the spalling test, the distinction can clearly be made between three groups as:

- First group, considers works where no measurements are made on the concrete sample. The stress in the sample is indirectly reconstructed from the shifted bar wave recordings and the peak stress is obtained through a qualitative measurment of the ejection velocity from capture images. [Brara et al., 2001, Brara and Klepaczko, 2006].

- Second group, contains works that employed strain gauges on the sample to measure the strain rate at failure while the stress in the sample is indirectly reconstructed from the bar measurements similarly to the first group. The calculation of the maximal stress is based either on the observation of the first fracture location or by explicitly enforcing the fracture location by introducing a circular notch [Wu et al., 2005, Weerheijm and Van Doormaal, 2007, Vegt, 2016].

- Third group, relies on the use of the Novikov acoustic approximation and the measurment of the velocity

pull-back in order to deduce the peak tensile strength. The strain rate is either determined from gauge measurements directly placed on the fracture zone [Zhang et al., 2008, Erzar and Forquin, 2010, Erzar and Forquin, 2014, Rey-De-Pedraza et al., 2016] or indirectly from the rise time of the tensile wave [Schuler et al., 2006].

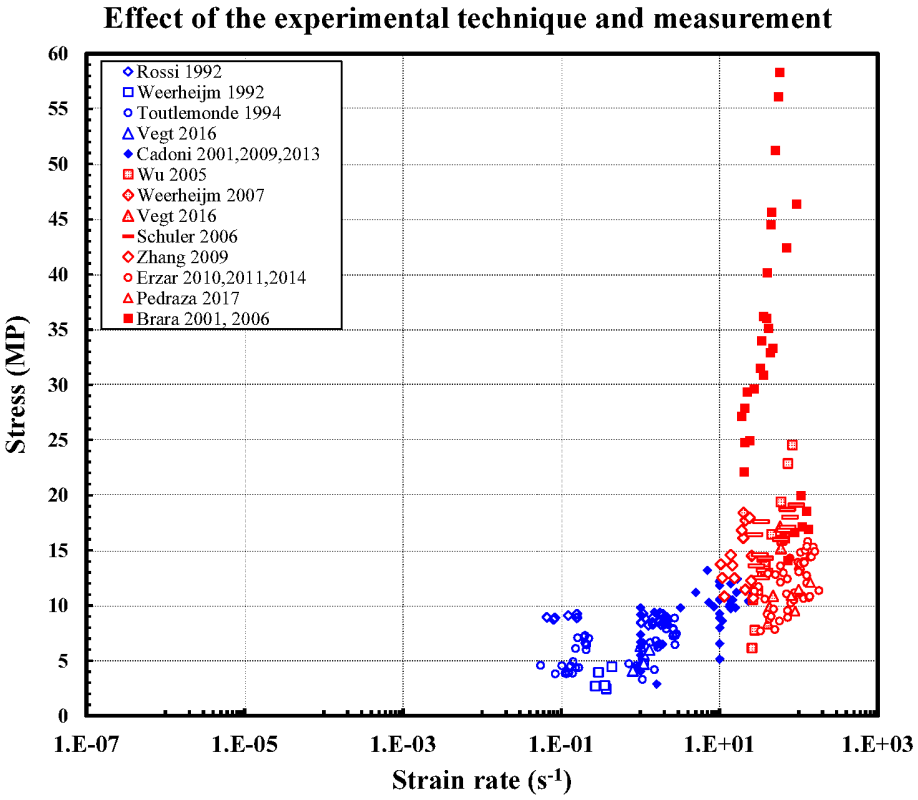

Figure 2.10: Overview of the results reporting dynamic tensile strength at high strain rates classified according to the experimental method used.

From the presented plot several observations can be made. First, regarding the data obtained with the SHB system, the scatter appears to be low for the case of intermediate strain rates (0.1 - 1 s^{-1}) which slightly increases for the data reported at about 10 s^{-1}. This was expected, since this value of strain rate is often considered as a limit up-to which the processing of the SHB data can be performed due to the problem of maintaining the mechanical equilibrium [Zhang and Zhao, 2014]. Nevertheless, within the range of strain rate values covered by SHB techniques, no considerable difference can be observed concerning the method used to process the experimental data. On the other hand, the scatter observed at high strain rates obtained with the spalling method exhibits a considerable data discrepancy. When considered from the point of the processing method used, the data presented in the work of Brara *et al.* where completely non-instrumented samples were used show considerably deviation from the rest of the data. This is due to application of an non-adequate experimental processing relying on the use of the fragment ejection velocity as detailed in Erzar *et al.* [Erzar and Forquin, 2010]. In this work it was computationally shown that this type of processing provides erroneous results since the ejection velocity is deduced from camera time frames in between which the entrapped axial wave travelled multiple round trips in the fragment, dissipating additional energy. In that case the kinetic velocity of the fragment does not represent the particle velocity and cannot be considered as constant. Although this was well established, the erroneous data is even today used to calibrate empirical models regarding the prediction of the dynamic tensile strength [Lu et al., 2017]. Next, as discussed in Erzar *et al.*, the method of measuring the peak tensile stress based on the position of the observed macro-fracture can also provide unreliable results due to fast evolving axial stress within the sample. Since multiple fracturing at high strain rates occurs, it is difficult to conclude which fracture can be considered as the primary one. Finally,

it can be observed that the data processing of the spalling tests which involves the measurement of the velocity pull-back to provide the tensile strength shows a lower data scatter than groups one and two.

From the above presented results it is clear that, aside the material effect, the measurement technique used to determine the dynamic tensile strength plays a crucial role in the accuracy of the obtained data as well as the observed scatter.

2.1.3 Previous works on Dynamic fracture energy

Apart from failure tensile strength under dynamic loading regimes, the information on the material failure quantities such as specific fracture energy and crack opening velocity also play an important role in providing a deeper understanding of the dynamic fracturing phenomena. Such quantities are proved to be essential for deriving well-adapted material models in the framework of dynamic fracture that would enable a better understanding of the involved failure mechanisms. However, the information regarding the specific fracture energy and crack opening velocity have been rarely reported in the literature. The fact that a lot of experimental effort has been focused on just obtaining the ultimate tensile strength at a broad range of strain rates is because the fracturing quantities are extremely difficult to measure under dynamic loading conditions. Still, such quantities are indispensable in modelling the softening behaviour of quasi-brittle materials and therefore, experimental efforts should also be focused on obtaining the fracture energy information.

The specific fracture energy can be defined as the absorbed energy within the damage zone due to the formation and opening of one crack. As such it is the fracture energy per unit area of the fracture surface and represents the area below the stress-crack opening displacement (COD) curve as defined within the framework of the fictitious crack model introduced by Hillerborg [Hillerborg, 1985b] and is a material property [Bazant, 1991]. Unlike quasi-static loading conditions where fracture behaviour of concrete together with fracture models and testing methods are well defined [Bažant, 2001], the technical difficulties associated with dynamic testing of such materials did not permit to establish a universal way of measuring the specific fracture energy without strong assumptions on the material behaviour. Consequently, data present in the literature are scarce and often contradictory. The experimental technique used to obtain these quantities rely on the use of point-wise measurements which provide global information of the tested sample [Brara and Klepaczko, 2007, Schuler et al., 2006, Cadoni et al., 2013, Vegt, 2016]. Moreover, the processing of the acquired data is often based on strong assumptions on the material behaviour. These methods then can be considered to only provide estimates of specific fracture energy since the assumptions such as the linear elastic behaviour of the material are adopted outside the principal fracture zone. Additionally, some methods can overestimate the fracture energy and display large confidence intervals due to the data scattering. Most of the experimental methods devised to characterize the concrete fracture properties at high loading rates are based on various adaptations of the Split Hopkinson Bar (SHB) system and some will be presented in the following accompanied by a collection of results on specific fracture energy reported in the literature.

2.1.3.1 Experimental methods to determine the fracture energy

The Split Hopkinson (SHB) methods The SHB system has been used in a few works to obtain the fracture energy of tested concrete samples at strain rates up-to 10 s^{-1}. In the works reported by Cadoni *et al.* [Cadoni et al., 2013] the Hopkinson Bundle Bar was used (Section 2.1.1.1). Using such set-up, the fracture displacement information was calculated over the entire sample length using specimen elongation information derived from the reflected wave registered on the input bar. The entire post-peak stress response in the sample was obtained as in the processing performed to obtain the tensile strength, using the registered transmitted wave on the output bar and assuming the perfect balance of the sample. Then, both the indirectly obtained stress and displacement records are synchronised and the fracture energy was obtained from a global load-displacement curves for several

concrete samples.

Another method was proposed using the Gravity driven SHB setup (Section 2.1.1.1) in [Weerheijm, 1992, Vegt, 2016]. The measurement systems used on one concrete sample are presented in Figure 2.11a. Relying on uniaxial wave theory, the stress in the sample at the location of the notch is determined by multiplying the strain on the output bar with the bar's Young's modulus and by applying a proper correction for the mismatch of cross-section. The strain data of the output bar is then time shifted to the position of the upper gauge on the sample where the correction of the elastic response is performed. Since the fracture opening is measured with the LVDT's positioned away from the gauge on the sample, a time correction is performed directly on the acquired fracture opening data. Since slight time mismatch is inevitable, manual synchronization is performed to match the initial part of the deformation curves. Finally, a stress-deformation (*i.e.* stress-notch opening) curve is obtained from which the fracture energy is deduced as the integral below the curve while the strain rate is determined from the gauge on the lower bar according to Kolsky's equation [Meyers, 1994].

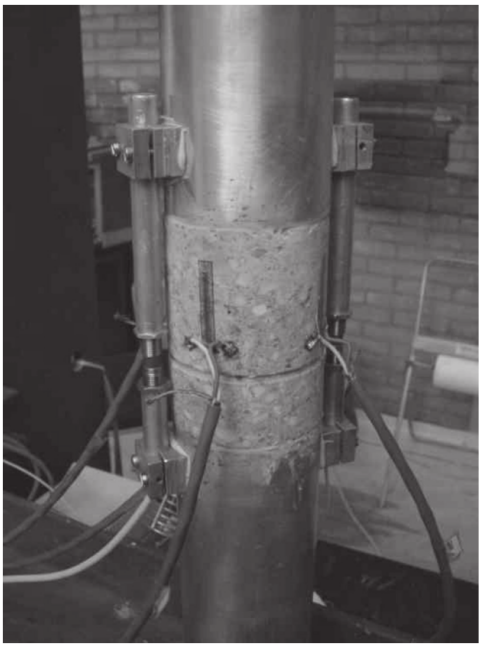

(a) Overview of the concrete sample with a notch placed in the SHB apparatus together with the measurement systems.

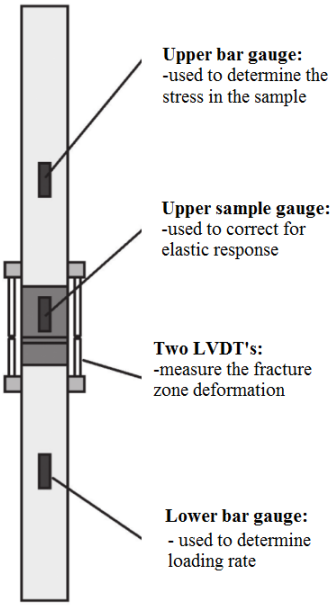

(b) Sketch of the principal instrumentation in the SHB apparatus.

Figure 2.11: Overview of the gravity driven SHB system used to determine concrete fracture energy at TU Delft. (Images taken from [Vegt, 2016])

The Spalling technique method For reaching higher levels of strain rates (up to 200 s^{-1}), the spalling technique (Section 2.1.1.2) that utilizes only the input bar of the SHB device was used in a few works to deduce the values of fracture energy of concrete [Schuler et al., 2006, Brara and Klepaczko, 2007, Millon et al., 2009, Vegt, 2016].

In the method proposed by Schuler *et al.* [Schuler et al., 2006], the specific fracture energy was determined based on the impulse transfer method and the measurement of the specific fracture surface. The total fracture energy was defined through the impulse (I) change and crack opening velocity ($\dot{\delta}$) which can be simplified as:

$$G = \int \frac{\partial I}{\partial t} \dot{\delta} dt = \Delta I \dot{\delta} \tag{2.5}$$

The impulse transfer between the observed spall fragments (ΔI) is obtained from the change of fragment velocities

from the time at which the fracture process starts (t_1) to the time it ends (t_2) (Figure 2.12)a. The initiation time (t_1) at the analysed fracture position (x_i) is obtained by reconstructing the elastic stress field within the sample based on 1D stress wave theory up-to the value of the obtained spall strength deduced from the velocity pull-back. Then, the value of the particle velocity at corresponding time of fracture initiation within the fragments was determined from the same analytical formulation assuming a constant velocity field within each fragment. The time corresponding to the end of the fracturing process (t_2) was considered as the time when the rear face velocity stabilizes and the particle velocities of the fragments were obtained from the use of a high speed camera ($\approx$ 8000 fps) performing manual image analysis. The mass of the fragments is measured in post-mortem analysis. The fracture energy (Equation 2.5) has to be divided by the total fracture surface (A_{frac}) in the spall plane to obtain the specific fracture energy ($G_f = G/A_{frac}$). This represents the drawback of the method due to the presence of multiple fracturing phenomena at elevated strain rates. The method to measure fracture surface proposed by the author was to follow the cracks along the circumference of the sample using microscopy, detecting the cracks with minimal width down to 50 μm (Figure 2.12). However, in order to enforce one fracture plane a notch was introduced and in that case the fracture surface was considered to be the one describing the cross-section at the notch location.

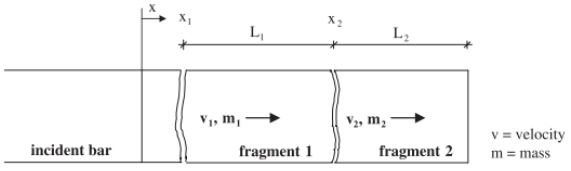

(a) Sketch of a typical fracture image with two fragments used for calculation of impulse change ΔI.

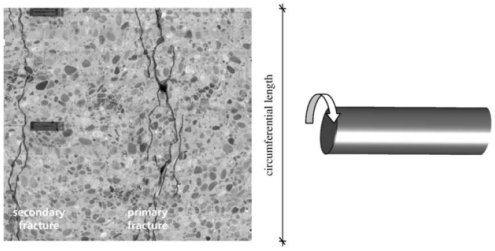

(b) Circumferential crack measurement using post-mortem microscopy to obtain A_{frac}.

Figure 2.12: Overview of the method to determine the fracture energy from spalling tests with impulse transfer method. (Images taken from [Schuler et al., 2006])

Another method for measuring specific fracture energy was proposed by Brara *et al.* [Brara and Klepaczko, 2007]; however in this case the completely non-instrumented concrete samples were employed in a spalling test and only the gauge data at the bar was used. The stress wave registered at the input bar was shifted towards the sample and the stress field in the sample was reconstructed based on 1D wave theory. The failure stress (σ_f) was derived by observing a position of the principal macro-fracture in the post mortem overview. In order to obtain the description of fracture energy multiple strong hypotheses were made. First, the assumption of linear stress increase up-to the critical crack opening (δ_c) that occurs at critical time (t_c) was adopted. Second, the particle velocity at the critical instant is assumed to be equal to the sample extension rate ($\dot{\delta_c} = \delta_c/t_c$) which allows obtaining the critical crack opening as:

$$\delta_c = \frac{\sigma_f t_c}{\rho C_0} \tag{2.6}$$

where ρ is material density and C_0 is the material wave speed. Next, by assuming constant velocity at separation, fragment ejection velocity (v_e) at complete separation (δ_s) could be related as $\delta_s = v_e t_s$. Finally, adopting a linear decrease of stress up-to the moment of complete separation (t_s) which occurs so abruptly that $t_s = 1.1 t_c$ the final approximation of the specific fracture energy was provided:

$$G_f = \frac{1}{2}\sigma_f t_c \Big[\frac{\sigma_f}{\rho C_0} + 1.1 v_e\Big] \tag{2.7}$$

The author measured the critical time of failure (t_c) that was obtained from the distance measurement of first observed fracture from the sample free-end and the ejection velocity (v_e) by visually analysing images obtained

with the multiple CCD acquisition system.

In the work reported by Vegt [Vegt, 2016], fracture energy was determined similarly to a procedure reported in [Weerheijm and Van Doormaal, 2007] using notched spalling samples to enforce the fracture plane. The samples were heavily instrumented with strain gauges at several key positions along the sample axis (Figure 2.13). A newly developed strain gauge of 30 mm in length was placed over the notch allowing to deduce the deformation at the notch position which was corrected for the elastic component. The stress at the notch was reconstructed using the gauges on the sample close to the notch (R9-17 in Figure 2.13) while the gauges away from the notch were used to apply the proper correction of the separation of tensile wave and compressive wave (R5-16 in Figure 2.13) taking into account the wave dispersion and amplitude change. The wave shifting was performed by relying on the 1D wave propagation theory.

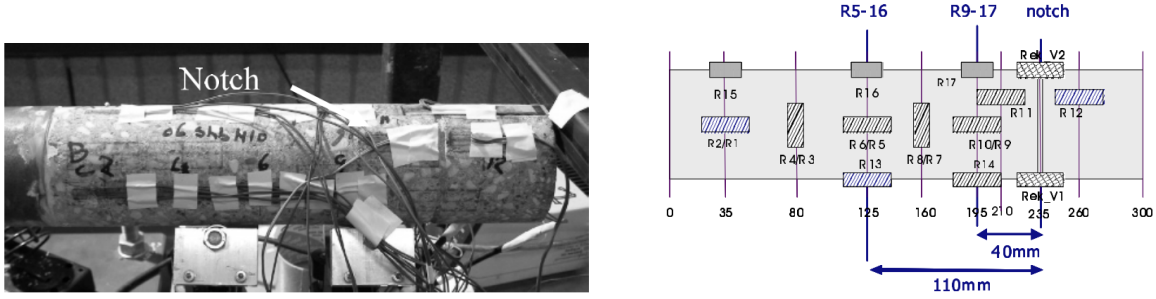

(a) Image of a fully instrumented concrete sample (74 mm in diameter and 300 mm in length).

(b) Detail on the gauge positioning.

Figure 2.13: Overview of instrumented spalling sample used to determin the specific fracture energy in the works reported by Vegt *et al.*. (Images taken from [Weerheijm and Vegt, 2010])

2.1.3.2 Overview of literature results – Dynamic fracture energy G_f

The results regarding the specific fracture energy reported in the literature using the methods described in the previous section are summarized in Figure 2.14. The diagram with the collected data suggests that concrete exhibits apparent strain rate sensitivity with respect to specific fracture energy. Generally, two regions of rate dependency can be distinguished. For intermediate loading rates, a somewhat moderate increase can be observed until a threshold is reached at about 10 s^{-1}, when an abrupt increase in fracture energy is noted. It has to be pointed out that with the increase of strain rate, the scatter of the data substantially increases, which makes the use of experimental data very difficult in view of identifying consistent description of the observed phenomena. What is more, the level of reported energy values need to be taken with precaution due to the fact that different approaches to data processing were used on different concrete compositions.

The energy data presented in Figure 2.14 starts exhibiting scattered values at strain rates of about 10 s^{-1}. Some of the results at these levels of strain rate were obtained with the Hopkinson Bar Bundle [Cadoni et al., 2001b]. Using the assumption of a perfect mechanical balance of the sample and the deformation measurement for the entire specimen length, values of concrete fracture energy were obtained [Cadoni et al., 2013]. However, several numerical works indicated that with the use of SHB systems for direct tensile testing of concrete, applying strain rates of above 10 s^{-1} could yield values of an apparent tensile strength that consists of both true tensile strength and contribution of structural inertia due to material softening [Ožbolt et al., 2013]. At this level of strain rate, multiple cracking starts to occur and several fracture zones can be distinguished which compromise the use of indirect or global measurement systems owing to their assumptions. Both effects of multiple cracking and inertia as well as the fact that the mechanical balance of the sample is not entirely reached could explain the observed

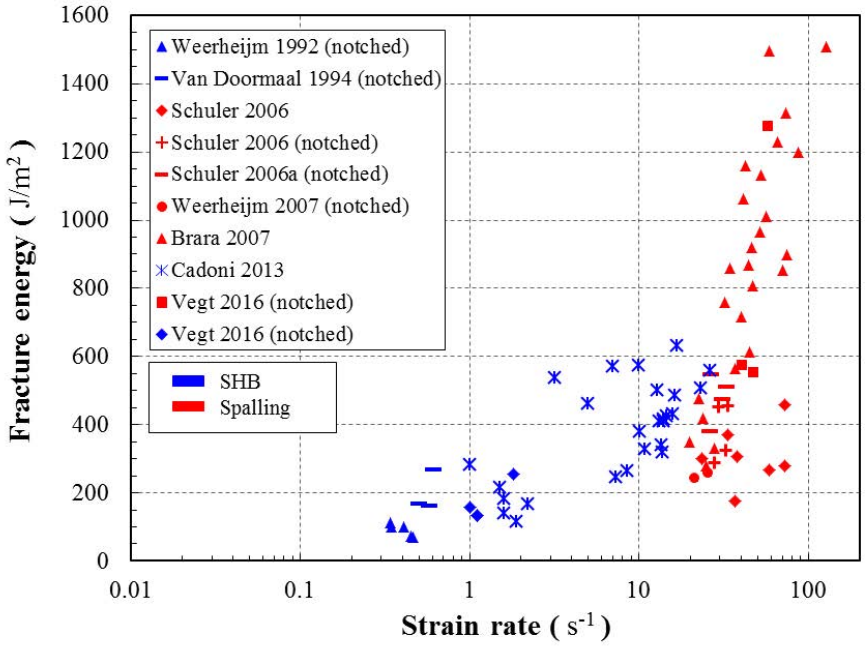

Figure 2.14: Literature overview of experimental results on the specific fracture energy of concrete under intermediate and high loading rates.

scatter. Lately, some works suggested that these measurements are almost impossible to be treated as separate instances since the fracturing information is being encoded in both transmitted and reflected wave at the same time [Volkov et al., 2017]. In order to overcome the problem of multiple fracture formation, notched samples were introduced as to enforce a single fracture plane in several works. This can be considered as a strong drawback since the obtained result can be influenced by the size and shape of the notch. It was reported that the depth and the position of the notch can affect the response of the material due to the reduced specimen strength caused by stress concentration on the notch tip and can further induce a pronounced non-linear response before the peak strength is reached as discussed in [Doormaal et al., 1994]. In addition, the circular notch on the sample outer surface does not prevent multiple fracturing in the core of the sample.

In the part of the diagram (Figure 2.14) at higher loading rates, only few works can be found which use the spalling experimental technique. In the work of Brara *et al.* [Brara and Klepaczko, 2007], the *completely* non-instrumented samples were used as mentioned in the previous section. The reported values of increase up to ten times in specific fracture energy were obtained with strong assumptions on material constitutive response such as linear elastic material behaviour, instantaneous crack formation and the description of stress by the velocity of spall fragments which was later disputed in [Erzar and Forquin, 2010]. As mentioned, the author measured the critical time of failure that was obtained from the distance measurement of first observed fracture from the sample free-end visually analysing images obtained with the multiple CCD acquisition system. On the other hand, it has been shown that simple analysis of camera images without the use of a full-field measurement technique can lead to substantial errors in obtaining the position of the first initiated fracture [Rey-De-Pedraza et al., 2016]. Schuler *et al.* [Schuler et al., 2006] reported values with an increase of about three times the quasi-static fracture energy. However, the multiple crack formation and the accuracy of stress and velocity measurements compromise the calculation of the specific fracture energy. Finally, the assumption of material linear elastic response, used in all the above mentioned works, was argued as quite questionable in some numerical studies dealing with simulation of dynamic tensile fracturing. For example, FE numerical simulation of spalling tests carried with the use of a

rate-sensitive micro plane model showed that concrete samples exhibit a significant amount of micro-damage before localization [Ožbolt et al., 2014]. Another study concentrated on modelling the dynamic crack growth in the framework of linear elastic fracture mechanics (LEFM) and fictitious-failure plane, showed that the critical crack size can be reached at values between 60% and 80% of the tensile strength criterion [Reinhardt and Weerheijm, 1991]. Consequently, the generally observed rate-dependent response of ultimate tensile strength is thought to be mainly governed by the damage initiation and growth at mesoscale of the material, with the failure process being governed by micro-cracking phenomena such as crack nucleation, propagation and obscuration of flaws as well as the ability (or inability) of the material to absorb the energy of fracture into the fracture zone that starts taking place before the peak stress is reached [Weerheijm and Forquin, 2013, Erzar and Forquin, 2014].

2.1.4 Synthesis: Stating the problem

As shown in previous sections, numerous experimental efforts have been aimed at obtaining concrete fracturing properties at high strain rates over the years. However, the collection of the experimental results from various works shows high data dispersion as the testing strain rate increases due to which up-to today there is no general consensus on what are the dominant material effects that influence the sensitivity of concrete in dynamic tension. Apart from the fact that the scatter appears due to difference in concrete mixtures, specimen size and moisture content; the scatter is also induced (or enhanced) by the difference in the used testing set-ups. These experimental methods require the assumptions on the material behaviour in order to provide the information on the stress within the tested sample which is deduced from (indirect) point-wise measurements. Recently, a full-field deformation measurement method has been proposed which allows the local axial stress on the sample surface to be measured without any assumption on the material behaviour. This measurement method presents a great potential since it permits to reconstruct the stress histories in the concrete sample and stress-strain response within close vicinity to the fracture zones. This dynamic photomechanical spalling test uses ultra-high speed imaging, full-field measurements and the virtual fields method to provide such information, which will be introduced in the following sections.

2.2 Ultra-high speed imaging

2.2.1 Introduction

It is said that '*curiosity killed the cat*', but whatsoever it is probably that similar human curiosity which has led the development of high speed imaging over the last century. Since the famous Eadweard Muybridge's shot of Sallie Gardnier at a Gallop in 1878 [Muybridge, 1878], up-to today's light-in-flight Femto-photography [Velten et al., 2013], the ability of capturing events faster than they can be seen by our own eyes allowed observing phenomena that were far too difficult to imagine. Scientific photography differs from everyday photography because of the motivation that stands behind the entire process of acquiring a specific image. For example, two images can be the same but the one considered as the scientific one will carry with it some information. That does not mean that images made for scientific purpose are less interesting, on the contrary, the fact that they carry the underlying information makes their appearance more effective. Hence, what is characteristic for the scientific photograph is in fact that it is a *measurement*.

The principal aim of high speed photography is to capture images of fast-changing events that are too fast to be perceived by the unaided human eye, simply by lowering the acquisition exposure time and supplying sufficient illumination to the imaged scene. The term ultra-high speed imaging is broadly used, covering a large range of acquisition speeds, recording lengths, spatial resolutions, and camera technologies. Owing to continuously expanding technological development, different regions of high-speed imaging have been defined over the years which evolve as the technology progresses. One classification based on the framing rate and the used technology has been provided by Fuller [Fuller, 2013] in which four main groups can be distinguished, arranged from low to high frame rate as follows:

(a) high speed, 50-500 frames per second (fps).

(b) very high speed, 500-100 000 fps.

(c) ultra-high speed, 0.1-10 million fps (Mfps).

(d) super-high speed, above 10 Mfps.

In the following, first a brief historical overview on the development of high speed imaging is provided, maintaining the focus on ultra-high speed imaging with inter-frame below 1 μ s. The interested reader can find more information in a well-rounded review on the historical development of high-speed photographic technology available in [Honour, 2009] and some of the first applications to fracture, impact and high-rate deformation is given in [Field, 1982]. Second, the main UHS camera technologies will be recalled. Finally, basic principles that are required for applying ultra-high speed photography in experimental testing, such as: frame rate, illumination and triggering, will be introduced.

2.2.2 Brief historical overview

From its modest beginnings in 1870s, the aim of high speed photography was to acquire one single shot (one photograph), with a sufficiently small temporal resolution and right exposure, in order to capture a non-blurry subject. One of the early electro-optical devices offering short exposure times, the Kerr cell, relied on the use of high light sensitivity films, that enabled it to reach temporal exposure down to 100 ns. However, the restrictive use to only highly luminous events (*i.e.* detonation and blast) together with the complexity of their application made the Kerr cell difficult to extend to other fields of research. Also, there was a need to acquire a number of time resolved frames (at least two) of a certain event. In that way, temporal information could be extracted and analysed in more detail. Some of the early efforts to address this issue have been made by using a number of aligned Kerr cells. However, aside from the difficulties related to time synchronisation, this configuration also suffered from parallax errors that were introduced due to the use of the multiple independent optical systems. Therefore, the idea of using a single apparatus for capturing multiple frames emerged.

At the beginning of the 20^{th} century, the multiple high speed scientific imaging takes a turn with the introduction of the Cranz-Schardin system (Figure 2.15a) that uses the shadowgraph technique. The shadowgraph is generally produced by having the interest subject (often a projectile) passing between the point light source and a sheet of film. At the correct instant, the light is being fired and the shadow of the projectile with its wake is captured on film. In order to produce multiple recordings, Cranz-Schardin system was based on an integrated multiple sequential spark light source (Figure 2.15b). It introduced the commodity of triggering, using either one synchronised or multiple independent triggers for each spark, that allowed fine temporal tuning depending on the imaged event. This imaging system permitted researchers to make a step forward in understanding the physical mechanisms behind ballistic phenomena. Having the subject movement often in the range of 2 m/s up-to 1 km/s (*e.g.* by employing the two-stage gas gun), ballistics was a perfect environment for applying such photographic methods. Information such as state of the projectile, projectile velocity but also the distribution of the pressure flow in front of the projectile tip could be obtained, more specifically this system allowed also the visualization of shock waves that accompany super sonic bullets (Figure 2.15c). Also, such system was used to study the crack velocity propagation in glass materials (Figure 2.15d), providing valuable insight into the fracturing process of brittle solids [Schardin, 1959]. Many of these images not only brought substantial contribution to the scientific community but also, owing to their aesthetic appearance and visual perception, were often regarded as astonishing works of art [Kleine and Settles, 2008]. There have been several subsequent adaptations of this imaging system according to the application requirements. One such system, able to capture 16 consecutive frames with the acquisition speed up-to 815 kfps was successfully used in the several applications involving dynamic photoelasticity [Riley and Dally, 1969]. Although the upper speed limit of the system was not precisely established, some later versions reported reaching

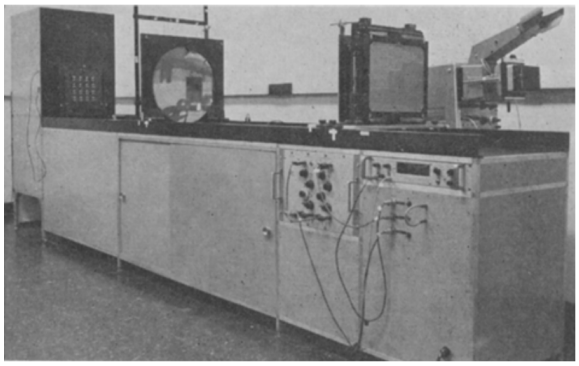

(a) The Cranz-Schardin system. Photograph taken from [Riley and Dally, 1969].

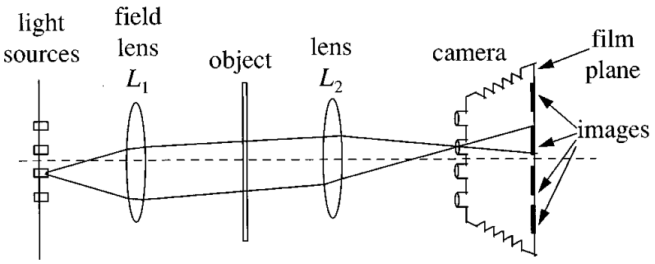

(b) Schematic representation of the Cranz-Schardin principle [Lu and Liu, 1997].

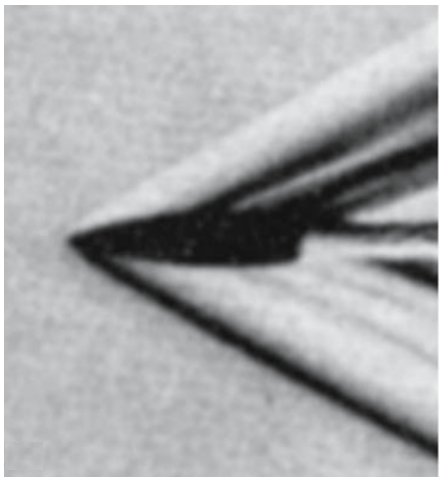

(c) Schardin image of a supersonic bullet [Schardin, 1942]. Photograph taken from [Kleine and Settles, 2008]

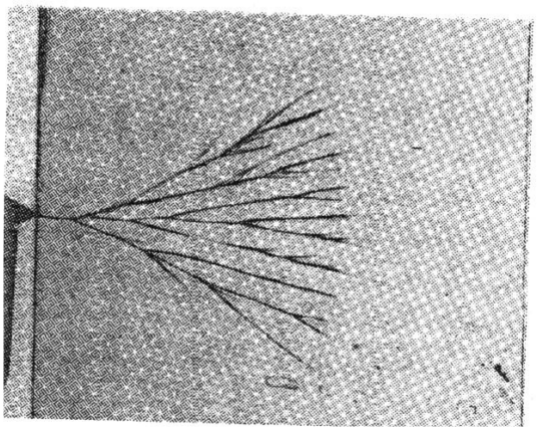

(d) Schardin image of a propagating dynamic crack in glass material. Photograph taken from [Schardin, 1959].

Figure 2.15: Representation and some results of the Cranz-Schardin high speed system.

maximum rate of 1 Mfps [Lu and Liu, 1997]. Despite being considered as a low-cost solution, a restriction due to the size, integrated lightning source as well as with the desire of going faster, drove the motivation away from the Cranz-Schardin system. Even though high speed cinematography was available at that time with the cameras using fast motion of a 16 mm or 35 mm film through the socket, their framing rate was limited by the physical strength of the film to about 500 fps. This limit was increased when continuously rolling cameras were introduced. However, due to problems of image focusing their framing rate was limited to around 100 kfps after which motion blur effects became dominant. Both of the above mentioned technologies did not suffice in acquisition speed for a ballistic application. The idea of using stationary film and moving image systems seemed as a next logic step and has led to what is today referred to as ultra-high speed imaging.

Emerging from the Manhattan project in 1950s, was the ultra-high speed rotating mirror camera, later branded by the Cordin company, which allowed to obtain experimental recording sequences with acquisition speeds up-to 25 Mfps (camera Cordin 119) [Field, 1982]. For applications where even higher frame rates (in range of 10^2 Mfps [Courtney-Pratt, 1957]) where less frames were needed, the image converter cameras were developed. Based on a method of steering the light towards separated photosensitive areas by using the charged plates, these cameras were also known as beam splitters. Both technologies were running parallel to the discovery of electronic flash strobe by Harold E. Edgerton [Edgerton and Killian, 1954], which allowed short and powerful illumination to be supplied to the scene externally. The two techniques, UHS imaging and flash illumination, were coupled in a well-rounded tool used by experimental researchers that provide valuable insight into various fast changing phenomena.

After a few decades, the next great breakthrough in (ultra) high speed imaging came with the development of electronic semiconductor devices in 1970*s* that slowly replaced the photosensitive emulsions. The charge-coupled devices (CCD) allowed complete digitalization of the high speed recordings with getting the final result in matters of several seconds. Passing from mechanical to electronic image formats allow the use of powerful computer software and better extraction of more qualitative data from the acquired images. This influenced the development of three principal high speed CCD sensor camera technologies: rotating mirror - CCD, the intensified CCD (ICCD) and the in situ storage image sensors (ISIS) CCD cameras. Finally, the latest technologies that aim to use the complementary metal-oxide semiconductor (CMOS) sensors by combining the advantages of both CCD and CMOS in ultra-high speed imaging have emerged, having a strong potential of increasing both the read-out speed and the pixel count of each acquired frame.

2.2.3 Ultra-High Speed camera types

In Figure 2.16 an infographic overview of the various HS and UHS cameras currently available on the market is displayed. The horizontal axis represents the maximum frame rate and the vertical axis represents the recording length of each system, while the rectangular area is proportional to the corresponding pixel count of one grabbed frame (lp/mm stands for line-pairs per mm and describes the spatial resolution of a chip). The minimum exposure time of each system is also reported in terms of a pie chart. From the infographic it is clear that the HS systems are characterised by large recording capacities (10^3 to 10^6 frames), whereas for UHS systems the recording length is much lower (about 100 frames). This is mainly induced by the limited read-out speed and the issue related to storage of acquired frames. Several types of systems exist that use CCD technology and different image registration techniques to deal with this limitations: rotating mirrors, beam splitters and in-situ storage devices, which will be shortly presented in the following.

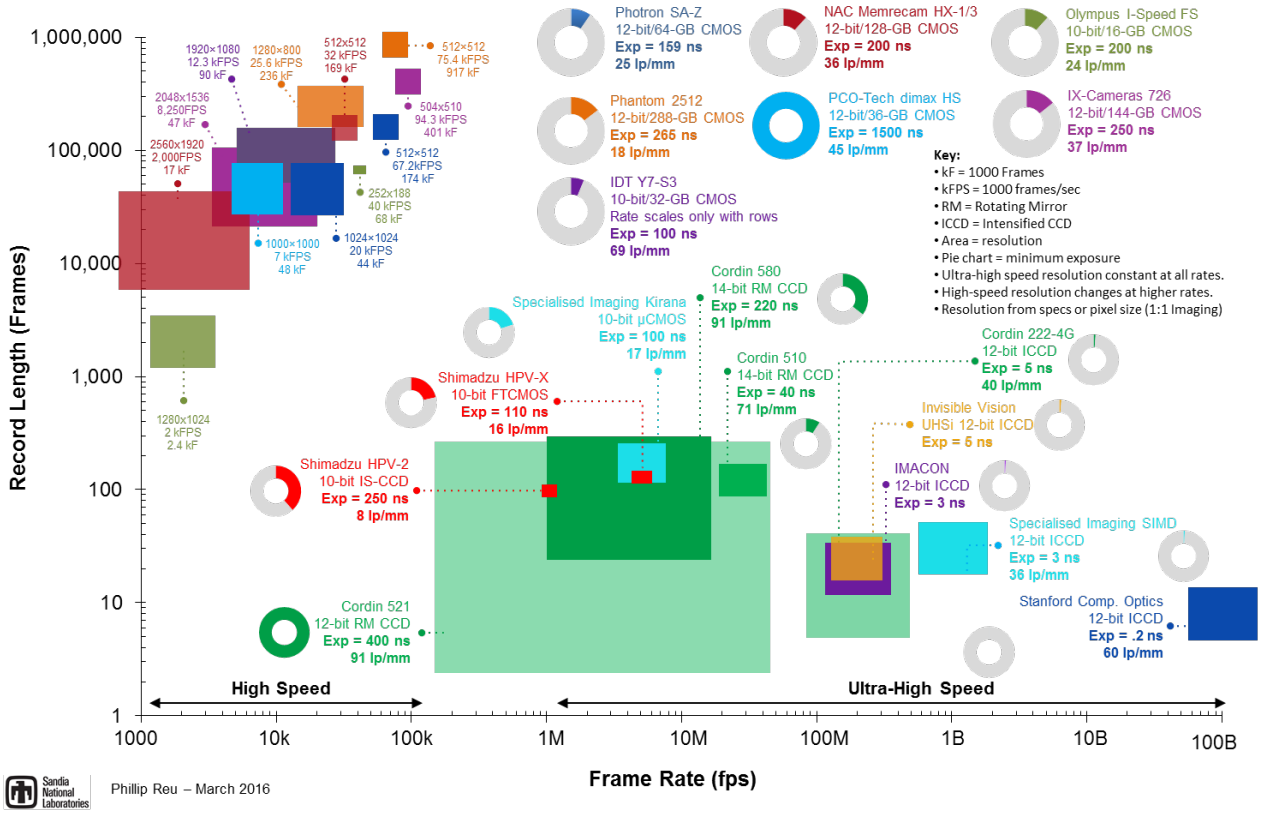

Figure 2.16: Survey of current HS and UHS cameras based on CMOS and CCD technologies from 2016. An updated graphical survey from [Reu and Miller, 2008, Xing et al., 2017b].

2.2.3.1 Rotating mirror

These cameras use a rotating device to move the framed scene from one to another fixed photosensitive element, which are all arranged in a radial fashion (Figure 2.17a). A gas driven turbine is often used to spin the rotating element at high speeds reaching typical frame rates of an order of several Mfps with 2–8 megapixels per captured frame (*e.g.* Cordin 580: 4 Mfps with 3200 x 2400 pix per frame). A high speed shutter is essential to avoid overwriting the consecutively recorded frames. The number of frames of such systems is limited (*e.g.* 78 images with 14-bit depth can be captured with Cordin 580). Aside from the weight and sizes, there are several reported drawback of such systems. From a metrological point, measurement uncertainties can be introduced due to the existing fabrication differences of the spatially separated sensors as mentioned in [Moulart et al., 2011]. A systematic bias can also be introduced in the measured displacement maps which is due to vibrational elements generated by the rotation of the mirror. Morover, the field of view can vary due to possible misalingement of the sensors [Pierron et al., 2011a]. Finally, such systems can suffer from a discrepancy between system reported frame rate and the true frame rate which is induced by delayed camera hardware response [Conneely et al., 2011].

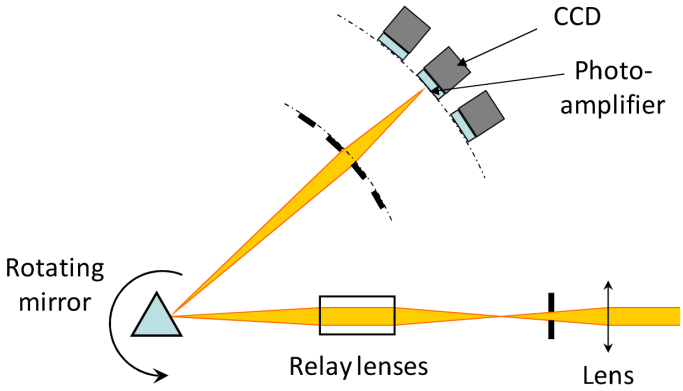

(a) Schema of the principle of imaging with rotating mirror cameras. (Image taken from [Moulart et al., 2011])

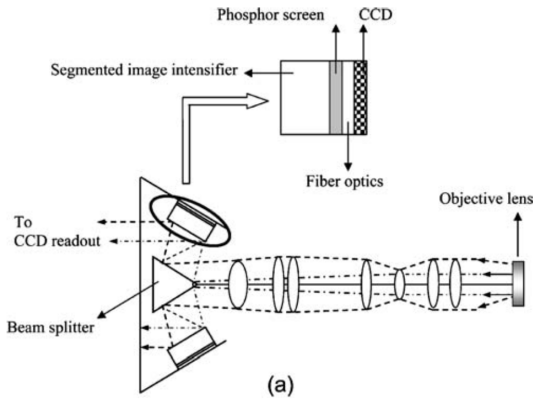

(b) Schema of the principle of imaging with beam splitting cameras. (Image taken from [Tiwari et al., 2007])

Figure 2.17: Two types of multi channel UHS imaging systems.

2.2.3.2 Beam splitters

These cameras use a stationary beam splitter to divide the incident light into multiple rays which are registered by multiple separate channels (Figure 2.17b). Due to splitting of the light, the registered image need to be highly amplified. To achieve this the CCD sensors are intensified by using phosphorus screens turning them into so-called ICCD (intensified CCD). Although having all the components stationary, which avoids any vibration noise as opposed to rotating mirror cameras, the use of image intensifiers introduces noise in the images [Pierron et al., 2011a, Tiwari et al., 2007]. Firstly, since separate sensors are used, the same problem of the varying field of view occurs as in rotating mirror cameras. Secondly, due to the use of image intensifiers a random leakage of signal can be experienced which will affect the reproducibility and accuracy of image based measurements. These drawbacks make these imaging devices difficult to be used for metrological purpose. However, their capacity of reaching up-to 100 Mfps with large pixel count make them unique and adequate for observational inspection of various dynamic phenomena such as observing shock wave caused by dynamic bubble collapse during colission between ink bubble and solid surface [Lauterborn and Kurz, 2018]. As for dynamic fracturing, one type of a beam splitting camera (Imacon 468) was used to provide qualitative information on crack propagation in notched concrete samples using SHPB splitting test as reported in [Lambert and Ross, 2000].

2.2.3.3 In-situ storage cameras

These UHS systems rely on the concept of placing the memory in each pixel domain of the image sensor [Kosonocky et al., 1996]. The principle is that the generated electrons at a photodiode of one pixel are shifted to the input gate and then to an array of CCD elements as in Figure 2.18. Consequently, this principle avoids the problems concerning image distortions introduced by either beam splitter or rotating mirror devices. However, this results in fabrication of large chips with less pixel count when compared to the other two methods. Nevertheless, their advantage is that each image is taken on the same sensor and their use for metrological purposes is favourable. Over the years, several concepts of integrated memory have been developed: those that rely on the use of CCD sensors (*e.g.* the Shimadzu HPV-1 camera), those that use the high sensitive CMOS sensors (*e.g.* the Shimadzu HPV-X2 camera) and those that use hybrid CCD-CMOS technology (*e.g.* the Kirana camera). These three systems have been employed for metrological purposes in the work of this thesis and will be explained in more detail in Sections 3.2, 6.2 and 6.3.

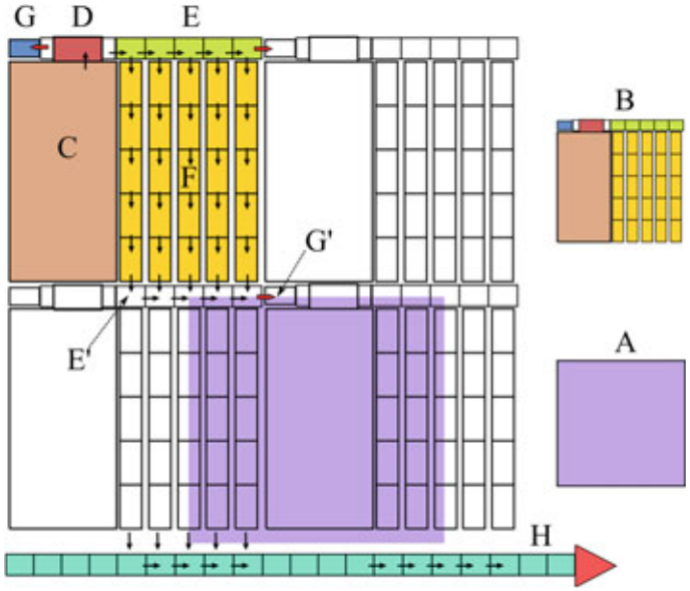

Figure 2.18: Principle of the In-situ UHS cameras as in [Kosonocky et al., 1996]: A–one pixel domain, B–pixel structure, C–photodiode, D–output gate, E–horizontal and F–vertical array of CCD memories, G–drain and H–readout. (Image taken from [Etoh and Nguyen, 2018]).

2.2.4 Basic principles of UHS imaging

Figure 2.19 illustrates principal parameters involved in performing ultra-high speed imaging which will be introduced in the following.

2.2.4.1 Frame rate, interframe time and exposure time

The *frame rate* corresponds to the operating acquisition speed of an imaging device which is expressed as the number of frames per second (fps). The *exposure time* correspond to the time between two subsequently captured frames during which the light integration of the event on the photodiode takes place. As such, it is lower or equal to the *inter-frame time*. The inter-frame time is the time in seconds between two successive frames and is the reciprocal of the frame rate. The exposure time is typically chosen to be shorter than the inter-frame time as to reduce motion blur. In most recent in-situ acquisition systems the exposure time is controllable within the system.

In order to choose the appropriate frame rate for filming a dynamic event it is first necessary to find the relevant time scale. If the observed phenomena is of cyclic nature then the frame rate is directly chosen from the desired

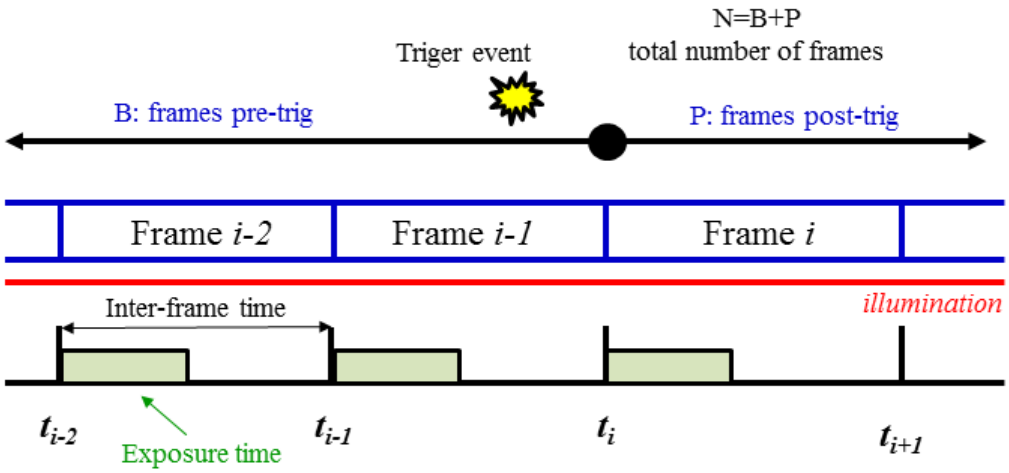

Figure 2.19: Principal parameters involved in performing UHS imaging of an event [Saletti, 2011].

sampling rate (at least two times larger). However, often the events are not of cyclic nature and the relevant time scale can be determined based on the typical velocity and the length scale of the observable event [Versluis, 2013]. The estimate of frame rate can be obtained as:

$$f = \frac{N.v}{l} \tag{2.8}$$

where v is the (particle) velocity of the observable event, l is the length scale and the N is the number of desired sampling frames that discretize the event. As an example, a longitudinal wave in an aluminium bar travels at 4 mm/μs. Assuming the length of the sample $l = 100$ mm and desired number of samples $N = 100$ the estimated frame rate is 4 Mfps. However, this example concerns the assumption of propagating elastic waves and in case when material failure occurs, this should also involve the desired number of frames dedicated to filming the fracturing and post-fracturing stages. Furthermore, when the acquired frames are used to obtain meaningful kinematic information as to perform the identification of the material constitutive response the choice of N plays an important role since it directly influencing the discretization of the sought materiel response.

2.2.4.2 Triggering

In ultra-high speed imaging, triggering is essential for performing a successful recording of a phenomena of interest due to the limited number of frames supplied by the acquisition system that are captured within an extremely short time. There are several triggering methods but most often a signal pulse related to a triggering event is used. Generally a variety of inputs can be used (*e.g.* optical or acoustical) which can be transferred into an electrical trigger pulse. What is important is that the sampling frequency of the triggering event occurs within the chosen inter-frame time. For example, the laser velocity signal at the rear face of a spalling sample. When triggered, two recording regimes can be distinguished. One where the trigger starts the image capture and one for stopping the registration of the images. The latter is possible only if the images are directly stored on chip electronically as in the in-situ imaging sensors. In recent devices, this trigger method has been more in use since the timing can be set in a more flexible way providing both images before the trigger and after. It should be noted that the transportation of trigger signal needs time and can cause a delayed trigger. Some imaging devices can introduce an inevitable delay due to the used technology, for example in rotating mirror cameras some time is needed to accelerate the rotating element up-to the required frame rate. However, the latest in-situ storage devices offer the option of programmable delay triggering that is usually accurate to a few nanoseconds.

2.2.4.3 Illumination

One recorded frame is a result of integration of the amount light hitting the photosensitive part of the sensor. Therefore, the parameters that influence the amount of grey levels registered within one captured frame are: camera dynamic range, shutter speed, sensitivity of the device, exposure time and the illumination source. The light source should be maintained constant between captured frames when full-field measurement techniques are used. In UHS imaging it is important to choose the right illumination device that is corresponding to exposure time and the sensitivity of the equipment. Furthermore, the illumination source should not introduce parasitic effects in the images due to instabilities such as flickering, therefore the source frequency should also be taken into account. With decreasing exposure times more powerful sources can prove to be necessary such as flash units, especially in case where the sensor sensitivity is low in order to reduce the camera noise (*e.g.* Shimadzu HPV-X). In that case the timing of the flash should be also synchronized with the imaging of events considering the rising time of the light source necessary to reach and maintain constant illumination, often requiring a secondary triggering, for example short circuit contact at the surface between the Hopkinson bar and the projectile. The rising time of the flash lights often deteriorates with the increased usage of the flash lamps and needs to be determined beforehand. One way is to frame uniform scene sequences with synchronised triggering between the flash and the UHS camera, then the rising time can be estimated by altering the acquisition speed. In the devices with higher light sensitivity (*e.g.* Shimadzu HPV-X2), constant light sources can be used such as tungsten light sources or light-emitting diodes (LEDs) which facilitate the procedure. However, when constant light sources are used, the lamps have to be focused on a spot as to provide sufficient amount of light which makes framing homogeneously illuminated scenes challenging.

2.3 The Full-Field Measurements

Full-field measurement techniques are non-contact methods which use digital cameras and image processing software to provide quantitative spatial distributions of sought kinematic quantities. A wide variety of such techniques exist [Grédiac and Hild, 2012]. They can generally be classified into interferometric and non-interferometric or white light methods [Chrysochoos and Surrel, 2012]. Some of the commonly used interferometric methods for obtaining in-plane displacement measurement include hologram interferometry [Fällström et al., 1989], speckle interferometry [Jacquot, 2008] and moiré interferometry [Post and Han, 2008]; while non-interferometric techniques include the digital image correlation [Sutton et al., 2009] and the grid method [Surrel, 1994]. The interferometric methods require a coherent light source and in general provide higher sensitivity measurements than interferometric methods. A brief overview of some application of such techniques to high strain rate testing is provided in [Field et al., 2004]. However, these methods due to their sensitivity are often susceptible to disturbances coming from the experimental environment such as vibrations [Grédiac, 2004]. On the other hand, non-interferometric methods allow in general more experimental liberty and thanks to widely available processing tools, have been more used in the experimental mechanics community.

2.3.1 Digital image correlation

Since it was introduced in 1980*s* [Sutton et al., 1983], Digital Image Correlation (DIC) has become one of the most popular full-field optical measurement techniques. It is based on measuring displacement fields by correlating two (or more) digital images acquired before and after the increment of deformation. The correlation is performed by using the sub-sets of the framed surface texture and by relying on the uniqueness of the local encoding of a random signal that acts as an individual sub-set signature. Sufficiently textured materials do not require any preparation while in other cases a random speckle pattern can be applied before image registration, using white and black paint with one of many proposed methods [Dong and Pan, 2017]. A digital image can be considered as a scalar function of the spatial coordinate that gives the gray level at each discrete image point (*i.e.* pixel) of coordinate $\mathbf{x}$. Considering two digital images, which characterize the framed surface before, $f(\mathbf{x})$, and after the deformation, $g(\mathbf{x})$, the relation between them using the conservation of the optical flow [Hild and Roux, 2006] can be expressed

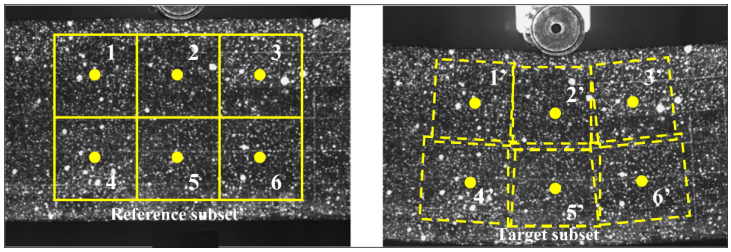

(a) Sub-seta based DIC.

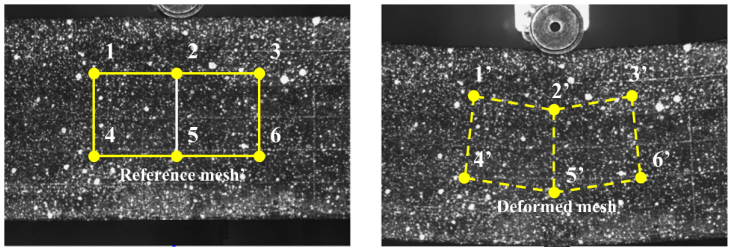

(b) FE based DIC.

Figure 2.20: Schematic representation of the principal difference between local and global DIC algorithms [Pan et al., 2015].

as:

$$f(\mathbf{x}) = g(\mathbf{x} + \mathbf{u}(\mathbf{x})) \tag{2.9}$$

where $\mathbf{u}(\mathbf{x})$ is a displacement field at any pixel. The determination of $\mathbf{u}(\mathbf{x})$ is an *ill-posed* problem which requires some additional hypotheses. A trial function can be introduced on a given sub-domain Ω which minimizes the squared differences with respect to the unknown degrees of freedom as:

$$\mathcal{T} = \int_{\Omega} (f(\mathbf{x}) - g(\mathbf{x} + \mathbf{u}(\mathbf{x}))^2 d\mathbf{x} \tag{2.10}$$

The considered domain Ω can be performed on image sub-sets (*i.e.* zones of interest – ZOI) in case of local approach or on the entire region of interest (ROI) in a global approach [Hild and Roux, 2012]. Over the years many algorithms have been proposed to determine the displacement fields. Often two main groups can be distinguished: subset-based local DIC methods and the finite element (FE) based DIC methods [Pan et al., 2015]. The former relies on a local description of the kinematics by tracking the counterparts of each ZOI individually, while the latter uses the global kinematic description to track all the elements determining the displacement of all nodes at the same time (Figure 2.20). The FE based DIC in principle can capture more complex kinematics in case of heterogeneous deformations [Hild and Roux, 2012, Pan et al., 2015] and has found more applications in the dynamic experimentation [Hild et al., 2018]. In ultra-high speed imaging usually images are of small pixel count and potentially contain high noise levels that can have a significant impact on the overall measurement [Tiwari et al., 2007]. Indeed, the small image definition was found to be a limiting factor when FE based incremental DIC was applied in a spalling tests [Saletti and Forquin, 2015]. A specific strategy in the formulation of FE based DIC, the spatiotemporal regularization [Besnard et al., 2012], has been proposed to deal with these obstacles indicating that positive effect on the reduction of measurement uncertainty when large number of temporal frames are analysed. Therefore in the future, the increase of the spatial size of the images of ultra-high speed cameras coupled with such methods could benefit more from the use of the DIC method.

2.3.2 The Grid method

The grid method is a full-field optical measurement techniques used for obtaining in-plane displacement maps of a test sample that undergoes deformation over time [Surrel, 1994]. Recent advance in acquisition and image processing has influenced growing interest in this technique owing to its easy implementation. The deformation measurements of the sample surface are derived based on determining the phase change between the reference and

the deformed image of the deposited spatial carrier (Figure 2.21). The spatial carrier is characterised with a regular grid pattern (ideally) consisting of black and white lines which are forming a bi-directional pattern (Figure 2.22).

Upon loading, the distortion of a grid occurs that causes locally a modulation of the spatial frequency vector of

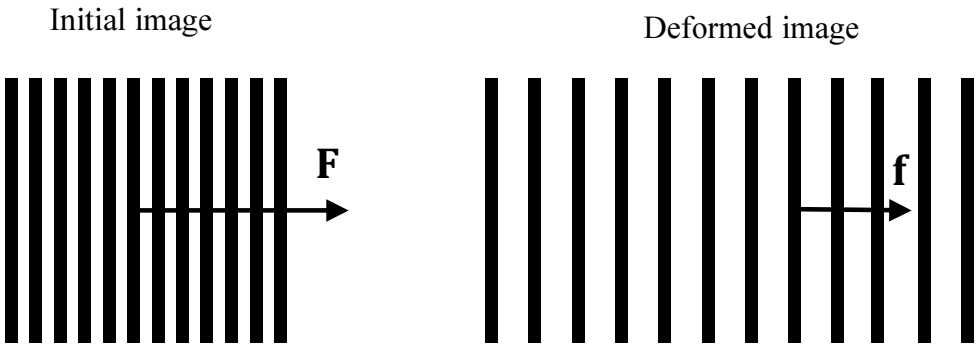

Figure 2.21: Illustration of a positive strain deformation on the spatial frequency vector.

Figure 2.22: Experimental image of a bi-directional grid of 1 mm pitch deposited on a concrete sample captured with the Shimadzu HPV-X2 camera at 1 Mfps and 200 ns exposure having 5 pixel sampling per grid pitch. The image corresponds to a situation of a stationary sample preceding a photomechanical spalling test. Some imperfections of the resulting grid patter caused by depositing procedure are visible.

the initial grid pattern. The intensity of digitalized light at a given pixel position M_0 in a reference state, defined as a material point with a position vector $\mathbf{R}$(x,y) in Cartesian system, can be expressed with a periodical fringe function:

$$I(\mathbf{R}) = I_0(1 + \gamma frng[2\pi \mathbf{F}.\mathbf{R}]) \tag{2.11}$$

where I_0 is the local intensity, γ is the contrast or the visibility of the signal I($\mathbf{R}$), $frng$ is a 2π-periodical continuous function (ideally a cosine). The spatial frequency vector of the grid carrier is defined as $\mathbf{F} = \mathbf{n}/p$, where $\mathbf{n}$ is the unit vector perpendicular to grid lines and p is the grid pitch. The phase of the $frng$ function is defined as $2\pi\mathbf{F}.\mathbf{R}$. After the loading, the material and the grid deform and the ligth intensity at M_0 becomes light intensity at point M'. In that case the variation of the phase from reference to the deformed state, in case a small displacement between the images, is $-2\pi\mathbf{F}.\mathbf{u}(\mathbf{R})$. The displacement field $\mathbf{u}(\mathbf{R})$ consists of the horizontal $u_x(x, y)$ component and the vertical $u_y(x, y)$ component relative to the unloaded condition and are calculated from the corresponding phase variation with respect to vertical lines $\Delta\phi_x$ and to horizontal lines $\Delta\phi_y$ such as:

$$u_x(x, y) = -\frac{p}{2\pi}\Delta\phi_x(x, y) \tag{2.12}$$

$$u_y(x, y) = -\frac{p}{2\pi}\Delta\phi_y(x, y) \tag{2.13}$$

There exist a wide panel of phase extraction methods, each having its specific methodology and metrological performances [Surrel, 2000]. The routine often adopted for treating grid images are based on the Windowed Fourier Transform (WFT) using a triangular convolution window [Surrel, 1996]. Due to the growing interest in this technique, many works in the recent years have been devoted to obtaining reliable measurements of the displacement and strain fields using the grid method, for example in [Badulescu et al., 2009a, Grédiac et al., 2013, Grediac and Sur, 2014, Sur and Grédiac, 2015, Grédiac et al., 2015]. A recent extensive review of the grid method is provided in [Grédiac et al., 2016]. Concerning high strain rate testing, the grid method has been widely used in several works [Moulart et al., 2011, Zhu and Pierron, 2016, Davis et al., 2017, Seghir and Pierron, 2017, Dreuilhe et al., 2018]. This technique provides a good compromise between spatial resolution and measurement resolution [Grédiac et al., 2017], which is an important factor when ultra-high speed imaging is used owing to limited pixel count of currently available acquisition systems. Also, it proves to be suitable for situations where small strains are measured that are accompanied by crack formation phenomena [Avril et al., 2004a]. Consequently, it is chosen as the measurement method in this work since the anticipated failure strain of a concrete sample subjected to dynamic tension is about 0.2 mϵ and the crack opening at failure is around 100 μm.

2.4 Inverse identification strategies based on full-field measurements

Full-field displacement measurements contain rich amount of information which can be subsequently used for material characterization, either in terms of identifying material constitutive parameters (*e.g.* material stiffness) or in terms of inverse characterisation of the entire material response (*e.g.* local stress-strain curve). However, in many situations the quantities that are being measured do not directly provide the sought information on the material behaviour but are rather a consequence induced by the real quantity of interest. Consequently, the problem becomes an inverse one and the sought information needs to be obtained by applying an (inverse) identification method [Avril et al., 2008a]. Such methods are much more advantageous compared to standard testing methods where global quantities are measured or are obtained indirectly. The identification based on full-field data provides greater flexibility since high number or parameters can be retrieved from a few (or even one) test performed with more complex configurations. On the other hand, such methods require suitable computational strategies and adequate computational power to process the experimental data. The increased availability of the latter in the recent years has induced development of a number of such strategies. Among them, some of the most commonly cited in the literature are the Finite Element Model Updating (FEMU), the Constitutive Equation Gap Method (CEGM), the Equilibrium Gap Method (EGM) and the Virtual Fields Method (VFM). These methods, alongside some other prominent techniques, have been documented in [Grédiac and Hild, 2012]. Here, their basic principles will be summarized as follows:

- **FEMU** (Finite Element Model Updating) – is primarily aimed at identifying the material constitutive parameters by minimising the difference between the measured and simulated displacement (or strain) fields obtained with the means of FE computation model. Initial values are predicted and an iterative process is run until the satisfactory result is reached through a minimisation of an appropriate cost function. This method has been subjected to many investigations and was used in identification of linear and non-linear problems (*e.g.* [Lecompte et al., 2007, Cooreman et al., 2007, Mathieu et al., 2014]) and identification of material parameters at high strain rates [Kajberg et al., 2004]. One of the main limitations of the method is that it is based on iterative computations since at each time a complete FE procedure is repeated. Moreover, when dealing with identification of material response under transient loadings explicit solvers are used to well model the phenomena and in that case the accuracy of the identification would also depend on the robustness and efficiency of the numerical model.

- **CEGM** (Constitutive Equation Gap Method) – also know as the constitutive relation error is a measure of the gap between a given numerical stress field and the stress field obtained from experimentally measured

displacement fields using a constitutive model. The material parameters that minimise this gap are considered the correct ones. The method can be extended to include all experimental measurements in the identification where overdetermined data is available and does not specifically require information obtained with the full-field measurements; however, it still requires the assumption of the constitutive model and has been mainly used in problems dealing with elasticity and elasto-plasticity [Geymonat and Pagano, 2003, Latourte et al., 2008].

- **EGM** (Equlibrium Gap Method) – the method was devised for situations where the observable heterogenity with respect to elementry elastic constitutive matrix can be considerd as a scalar field in terms of the local reduction of stiffness [Claire et al., 2004]. In the FE numerical implementation form, the stiffness matrix for each element can be constructed and the scalar contrast results from the minimisation of the residual forces that arise from computing the equilibrium equation using the knowledge on the known (*i.e.* experimentally measured) nodal displacements of each element. This method has been used for the the identification of parameters associated to anisotropic damage laws [Périé et al., 2009].

- **VFM** (the Virtual Fields Method) – introduced in [Grédiac, 1989], the method uses the measured full field kinematic data within the weak form of the equilibrium equation to identify the constitutive material parameters. Introducing an *a priori* chosen and appropriate virtual field which is kinematically admissible, the equilibrium equation can be brought down to a scalar form where the sought parameters can be directly obtained without the need of an iterative procedure. On the other hand, since volume integrals have to be computed, the kinematic fields have to be known within the solid which can be considered as the limitation of the method. However, in practice, the experimental situations often can allow assumptions which reduce the problem to a plane stress (or strain) condition. The method has found various extensions into forms which allow identification in a variety experimental situations [Pierron and Grédiac, 2012]. In the recent years, this method has found extensive applications in the identification of dynamic material response by exploiting the inertial component in the equilibrium equation. This method is therefore selected in the current work and its application to a dynamic spalling test is presented in the following.

2.4.1 The Virtual Fields Method (VFM)

The VFM is an identification strategy that uses the measured full-field kinematic data. The method is based on rewriting the weak form of equilibrium equation for a deformable body using the principle of virtual work as follows:

$$-\int_V \sigma : \varepsilon^* dV + \int_{\partial V} \mathbf{T}.\mathbf{u}^* dS + \int_V \mathbf{f}.\mathbf{u}^* dV = \int_V \rho \mathbf{a}.\mathbf{u}^* dV \tag{2.14}$$

where σ is the Cauchy stress tensor, ε^* is the the virtual strain tensor, $\mathbf{T}$ is the vector of distributed surface load acting on the solid boundary surface ∂V, $\mathbf{u}^*$ is the virtual displacement vector, $\mathbf{f}$ is the vector of body force acting on each point of the volume V, ρ is the mass per unit volume, $\mathbf{a}$ is the acceleration vector; '.' stands for scalar vector product, ':' stands for contracted 2^{nd} order tensor product.

Under quasi-static loading conditions, the right-hand-side term is null and the problem is brought down to choosing as many virtual fields as unknown constitutive parameters that are to be identified. Under dynamic loading conditions, the right-hand-side term can be used as an advantage since the contribution of the inertial component defined through the measured acceleration maps present an image embedded load cell and in that case no external load measurement is needed. One of the first applications of this idea has been applied to determine the stiffness and damping of thin vibrating plates using the inertial forces as a distributed load [Giraudeau and Pierron, 2005, Giraudeau et al., 2006]. The concept was also applied to the identification of the stiffness components of a glass-epoxy laminate at high strain rates using a SHPB setup [Moulart et al., 2011] and to reconstruction of the entire force history measurement from the sample deformation in case of an impact induced three-point bending

test of alluminium bars [Pierron et al., 2011b].

The idea was then extended to uniaxial tensile testing of quasi-brittle materials using the spalling technique [Pierron and Forquin, 2012a, Pierron and Forquin, 2012b, Forquin et al., 2013]. The single Hopkinson bar technique is used to perform a spalling test (Section 2.1.1.2) on a cylindrical sample with a flatten surface on which a grid pattern is deposited (Figure 2.23). In that case, the acceleration field can be directly related to the average axial stress in the cross-section thanks to the uniaxial nature of the spalling test. This original concept has been adopted in this work and is studied in more details through both numerical simulations, that serve for validation purpose, as well as experimental works on several types of concrete materials. The principal formulations of the virtual fields method applied to the spalling test are presented in the following. However, it is also worth mentioning some of the most recent applications that use the same concept of the direct stress measurment as in, for example, the case of ultrasonic excitation of surogate bone [Wang et al., 2013a, Pierron, 2016] and PMMA [Seghir and Pierron, 2017], testing of rubber materials at high strain rates [Yoon and Siviour, 2017], dynamic impact testing of composite materials [Pierron et al., 2014, Zhu and Pierron, 2016], identification of elasto-plastic properties of aluminium under impact loading [Dreuilhe et al., 2018] and visco-plastic properties of copper under dynamic three-point bending [Koohbor et al., 2017] as well as inertial impact testing of very brittle materials such as tungsten carbide [Fletcher et al., 2018].

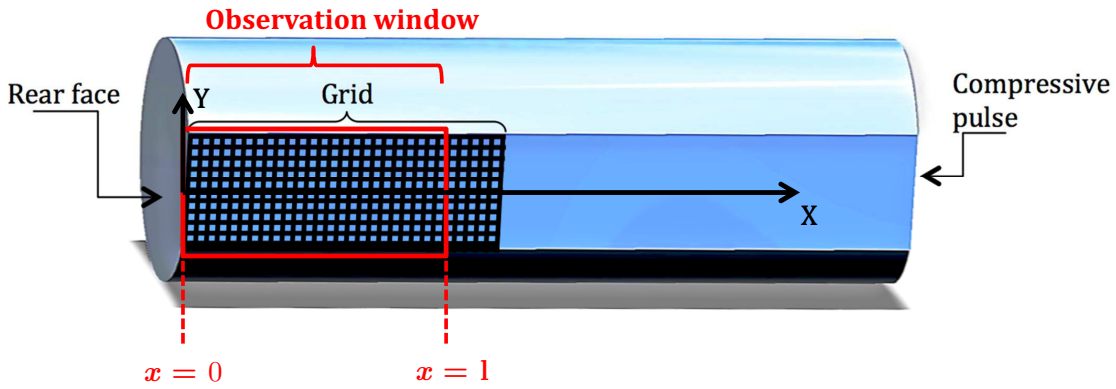

Figure 2.23: Illustration of a grid-instrumented spalling sample.

2.4.2 The VFM for stiffness identification in a spalling test

According to the schematic presentation of the framed spalling sample with the flattened surface shown in Figure 2.23, a virtual displacement field can be defined that depends only on the axial direction as follows:

$$\text{VF1:} \left\{ \begin{array}{l} u_x^* = f(x) \\ u_y^* = 0 \end{array} \right. \quad \left\{ \begin{array}{l} \varepsilon_x^* = f'(x) \\ \varepsilon_y^* = 0 \\ \varepsilon_{xy}^* = 0 \end{array} \right.$$

where $f(x)$ is a continuous and differentiable function of x, with condition $f(x = l) = 0$ which avoids having a contribution of the traction force at the boundary opposite to the free-end ($x = 0$). With the assumption of **uniaxial stress** and incompressible solid, the relation between stress and strain can be written as $\sigma_x = E.\varepsilon_x$ and in that case, introducing these two concepts in Equation 2.14, the principle of virtual work becomes:

$$-E \int_V \varepsilon_x f'(x) dV = \rho \int_V a_x f(x) dV \tag{2.15}$$

next, it is reasonable to assume that the ε_x and a_x depend only on x which makes the volume integral being

transformed into a curve integral as follows:

$$-E\int_0^L \varepsilon_x f'(x)dV = \rho\int_0^L a_x f(x)dV \tag{2.16}$$

where L is the length of the field of view starting from free-end. Finally, since the measured kinematic fields are of discrete nature, a simple expression of global Young's modulus is obtained at each time step of the test by approximating continuous integrals with discrete Riemann sums over the entire field of observation taking all the available measurement points N and M in directions x and y.

First considering the following approximation of internal virtual work:

$$\overline{\varepsilon_x f'(x)} = \frac{1}{NM}\sum_{i=1}^{N,M} \varepsilon_x^i f'(x^i) \tag{2.17}$$

and external virtual work:

$$\overline{a_x f(x)} = \frac{1}{NM}\sum_{i=1}^{N,M} a_x^i f(x^i) \tag{2.18}$$

the global Young's modulus is given by:

$$E = -\rho\frac{\overline{a_x f(x)}}{\overline{\varepsilon_x f'(x)}} \tag{2.19}$$

This very simple expression provides the global material stiffness at each measured time step (*i.e.* capture camera frame). The only thing left to do is to chose the virtual field description which would maximise the two terms in Equation 2.19. One way to ensure this in an easy manner is to define f using the actual measurements as it has been done in [Pierron and Forquin, 2012b]. However, a few other possibilities would also be investigated to evaluate the robustness of the identification, distinguishing between stationary virtual fields (*i.e.* those that do not evolve with the measured displacements) and time altering virtual fields (*i.e.* those that are deduced from the actual measured displacement data).

2.4.3 The VFM with inertial forces – load cell principle [Pierron and Forquin, 2012a]

Another benefit of using the VFM in an uniaxial test case such as spalling is that the inertial nature of the test and its intentional unbalanced state can be taken into advantage. Indeed, by introducing a kinematicaly rigid body like virtual field such as:

$$\text{VF2: } \begin{cases} u_x^* = 1 \\ u_y^* = 0 \end{cases} \quad \begin{cases} \varepsilon_x^* = 0 \\ \varepsilon_y^* = 0 \\ \varepsilon_{xy}^* = 0 \end{cases}$$

the entire internal work is cancelled and again relying on the uniaxial stress condition, the traction force at a given observational distance x can be related to the average stress $\overline{\sigma(x,t)}$ within a cross-section S such as:

$$\int_{\partial V} \mathbf{T}.\mathbf{u}^* dS = S\overline{\sigma(x,t)} \tag{2.20}$$

while the inertial component acts as a volume force in form of a Newton's second law and by considering a $b(x)$ as a length from sample free-end to the observable cross-section at x, this term reads:

$$\int_V \rho\mathbf{a}.\mathbf{u}^* dV = -S\rho b(x)\overline{a_x(x,t)} \tag{2.21}$$

Finally, the averaged stress can be directly reconstructed at any cross-section visualized within the field of view as:

$$\overline{\sigma(x,t)} = -\rho b(x)\overline{a_x(x,t)} \tag{2.22}$$

It should be noted that the minus sign comes from the fact that the compressive load arrives from the right according to the Figure 2.23. The Equation 2.22 is extremely useful since it allows direct stress measurement over the entire field of view captured with an ultra high speed camera. Furthermore, the derivation of this expression does not require any assumption on the material constitutive response and the underlining fact is that the accelerations are used as an local image-embedded load cell. This concept will be used extensively throughout this work building up on its previous application for testing quasi-brittle geomaterials [Forquin et al., 2013, Forquin, 2013]. Similarly to the above demonstrated principle, a shear force and bending moment can be reconstructed using the following two types of rigid body fields:

– translation field

$$\text{VF3: } \begin{cases} u_x^* = 0 \\ u_y^* = 1 \end{cases} \quad \begin{cases} \varepsilon_x^* = 0 \\ \varepsilon_y^* = 0 \\ \varepsilon_{xy}^* = 0 \end{cases}$$

– rotation field:

$$\text{VF4: } \begin{cases} u_x^* = y \\ u_y^* = -x \end{cases} \quad \begin{cases} \varepsilon_x^* = 0 \\ \varepsilon_y^* = 0 \\ \varepsilon_{xy}^* = 0 \end{cases}$$

Such virtual fields were not used in this work, although it is worth mentioning that all the concepts can be combined to acount for linear distribution of axial stress with respect to vertical axis y (*i.e.* linear stress gauge) as shown in [Fletcher et al., 2018].

2.5 Outline of the work

The photomechanical spalling test uses the above introduced techniques to provide measurements which can be directly used to fully characterise a dynamic tensile response of concrete materials at high loading rates. Although a proof of concept on all possible perspectives regarding the use of the method have been made in [Pierron and Forquin, 2012b] it is necessary to perform a throughout experimental application of the method and to compare the obtained results with the results derived from classical point-wise measurements. This is performed in Chapter 3 by conducting several experiments on ordinary concrete.

The use of ultra-high speed photography, full-field measurements and the virtual fields method lead to an increased the complexity of conducting the entire experiment by introducing a whole new area of possible uncertainties. These have to be better understood before the method is used to investigate the material effects influencing concrete strain rate sensitivity in dynamic tension. Virtual photomechanical experiments present a good tool for locating principal sources of errors as well as to provide information on the sensitivity of the used methodology. Simulated experiments also can provide guidelines on how to perform the experiment by reducing the unwanted source of errors to begin with. This is performed in Chapter 4 where the entire chain of measurements has been simulated.

One of the main benefits of the experimental methodology is that it gives access to the post-peak material response in dynamic tension. This then can be used to extract the information on the specific fracture energy of concrete as demonstrated in Chapter 5. Virtual experiments were also conducted in order to validate the procedure.

Finally, after choosing one of the two latest CMOS-based ultra-high speed sensors (Chapter 6), the experimental method is applied to testing two grades of concrete material in order to investigate the effects of concrete composition on its the dynamic tensile properties. This experimental application is presented in Chapter 7.

Chapter 3

Application of Ultra-High Speed Photography and VFM in identification of dynamic tensile material response

In this chapter the data processing of several spalling experiments that were performed with the Shimadzu-HPV1 ultra-high speed camera will be presented. The grid-instrumented sample surface was recorded during the test to extract the time resolved displacement fields which are then processed using the VFM as to finally obtain the material constitutive response. The main aim of the section is to provide a throughout proof of concept regarding the numerous capabilities of the proposed identification procedure accompanied with information regarding the measurement resolution and sensitivity. The experimental campaign has been largely performed in the Laboratory-LEM3 in Metz (Figure 3.1) during the period between March and April 2013 outside the framework of this PhD thesis. Thanks to the simulation procedure that will be presented in Chapter 4, a deeper understanding on the possible sources of errors has been acquired, which makes reprocessing these experiments quite interesting. Furthermore, the better knowledge regarding the data processing allowed an extended analysis of the experiments performed on concrete material. This resulted in obtaining first results regarding the identification of concrete fracturing properties such as material strength and post-peak response.

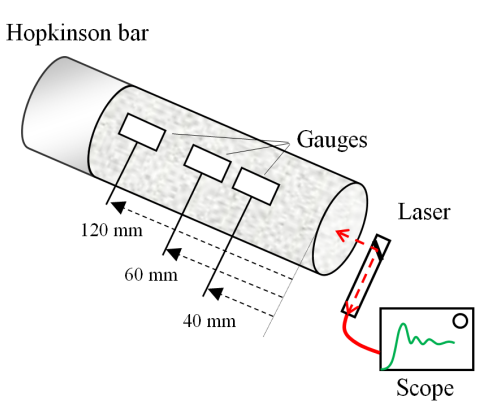

(a) Point-wise instrumentation of the concrete sample used in the spalling test.

(b) Spalling set-up with ultra-high speed camera (The Shimadzu-HPV1).

Figure 3.1: The experimental set-up at LEM3 used to conduct spalling experiments.

3.1 Chapter outline

The structure of this chapter is organised into three principal parts:

- First part 3.2 provides some principal information regarding the metrological performance of the used in-situ storage image sensor, the Shimadzu HPV-1 camera, together with its intrinsic noise structures such as spatial and temporal noise.
- Second part 3.3 summarizes a series of tests conducted on an aluminium alloy in light of identifying an elastic

material response. These tests were performed in order to assess the performance of the entire identification procedure and how it can be affected by real experimental conditions.

- Third part 3.4 contains insightful first results regarding the spalling of concrete material which failure is being recorded with inter-frame time down to 1 μs. Methodology of the experimental processing for obtaining meaningful fracturing quantities is provided. These first results have also put in question some of the traditional processing methods since they indicated a lower tensile strength compared to the one obtained when traditional Novikov processing is used. For this reason, some of the following subsections are also accompanied with, simple yet intriguing, numerical FE works which were conducted with the aim of investigating the validity of the so-called Novikov formula (Equation 3.3).

3.2 On the sensor characteristics and performance of the ISIS-CCD sensor

To overcome the limitations of continuous recording video-systems, a concept of *in-situ* storage in CCD cameras was proposed in order to achieve ultra-high frame rates in excess of 1 μs interframe time [Kosonocky et al., 1996]. The concept consists of placing a memory storage onto the camera sensor in each pixel domain. As such, it allows fast transfer of collected charge from the photodiode into the local memory bank resulting in fast acquisition speed. However, the memory bank occupies certain space of one pixel on the account of a smaller photo sensitive area. With this, several structural ideas arose on how to design one pixel domain in order to achieve high frame rates on one hand, and also provide a sufficient amount of stored data (*i.e.* frames) on the other hand. In the cited work, the 2D organization of the memory bank provided only a 30 recording frames at speed of about 0.5 Mfps. In order to go further in both recording length and speed, a solution based on the so-called slanted *in-situ* CCD imaging sensor was proposed enabeling over a 100 consecutive frames to be grabed with 1 Mfps acquisition speed [Etoh et al., 1999]. It soon reached a wide commercial usage, presenting a great breakthrough in scientific ultra-high speed imaging [Etoh and Nguyen, 2018].

3.2.1 The Shimadzu HPV1 sensor

One representative of the ISIS-CCD type of cameras is the Shimadzu HPV-1 camera. Its detailed characteristics are available in [Kondo et al., 2003]. The HPV1 sensor relies on the in situ storage technology and is equipped with 312x260 pixel domains each containing an on board integrated memory bank providing the 102 consecutive frames in burst mode with interframe time down to 1 μs. The sensor development started in 1999 and was available by 2001, which at the time was considered as first ultra-high speed imaging sensor of its kind to meet most of the users requirements based on distributed inquiry [Etoh et al., 2003]. The basic structure of the Shimadzu HPV-1 sensor is shown in Figure 3.2. It uses a simple CCD structure that is linear and without any bends, allowing for a large number of storage elements and fast gate transfer. In this way the transfer speed is increased without losing much of the transfer charge and subsequently resulting in decreased acquisition noise. However, the linear memory bank extends outside of dedicated pixel into the area of neighbouring pixels, resulting in a low fill factor in the horizontal direction of about 14% and about 76% in vertical one [Rossi et al., 2014] (see Figure 3.2b). For this reason the sensor incorporates slightly slanted photodiod with respect to the optical plane. The successive camera model, advertised as HPV2 or (ISIS-V3), employed the same sensor technology but with the parallel pixel domain structure, using a square diod and slanted CCD grid memory [Etoh et al., 2005].

As shown in Figure 3.2a, the pixel domain is composed of a photodiod and a CCD storage extending linearly downward where a drain and overwriting unit are placed. During the image capturing the charge signals are stored in the linear in situ storage. The overwrite unit allows continuous acquisition of images by draining the old image signals and keeping the latest 102 images. This allows the use of post-triggering option and synchronisation of the

images much easier. Metal shielding covers the storage area of the sensor.

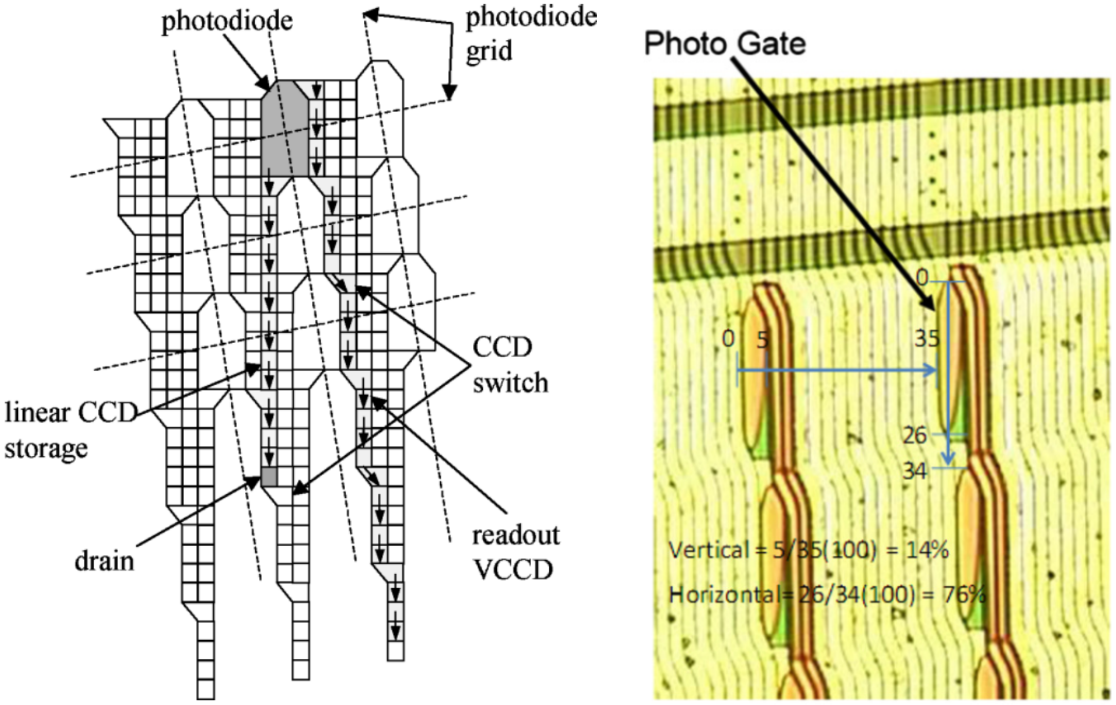

(a) Schematic view of the ISIS architecture used in HPV-1 camera [Etoh et al., 2003].

(b) Microscopic view of the actual pixel domain in the HPV1 sensor [Rossi et al., 2014].

Figure 3.2: The principle representation of the ISIS-CCD camera architecture used in the Shimadzu HPV-1 camera.

3.2.2 Camera acquisition quality

Detail information regarding the camera image quality as well as its metrological performance have been reported in [Rossi et al., 2014]. By performing extensive analysis of blank scene images, in the cited work it was found that when exposed to high illumination, the camera exhibits peculiar image effects. The images contain an increased noise content due to the fact that the saturation effects appear far before the expected limit of 255 grey level count. Therefore, it was suggested as a general rule, to keep the imaged scene at low illumination levels in order to avoid these occurrences. However, even at low illumination levels, additional effects were observed.

First, an increased pixel grey level deviation was noted at maximum frame rate (1 Mfps) that is not usually observed at intermediate frame rates. Second, it was found that small number of pixels deviate from the overall behaviour (about 0.3%), indicating a presence of so-called defective pixels. Next, an effect of pixel unexpected grey level jump was observed when a grid image is framed as opposed to a blank screen. This was contributed to the fact that in case of framing a grid image the high grey level gradient content may cause pixels which are close to saturation to exhibit an unexpected jump. To mitigate the above mentioned effects, it was suggested to keeping the grey level count below about 70. Finally, it was also noted that at maximum frame rate of 1 Mfps significant grey level variation is observed in the first and last 12 frames of the acquisition, while in between only each 12^{th} frame exhibited a certain under exposure (this effect is also presented in Figure 3.3a).

Due to the above mentioned effects certain steps need to be applied before the acquired images are processed with the aim of extracting the measured full-field kinematics. In general, it is advised to time the recording event between 14^{th} and 79^{th} image of the acquisition sequence, since it was that in the given frame range the average standard deviation of pixel grey level is significantly reduced for all acquisition rates. Furthermore, in order to

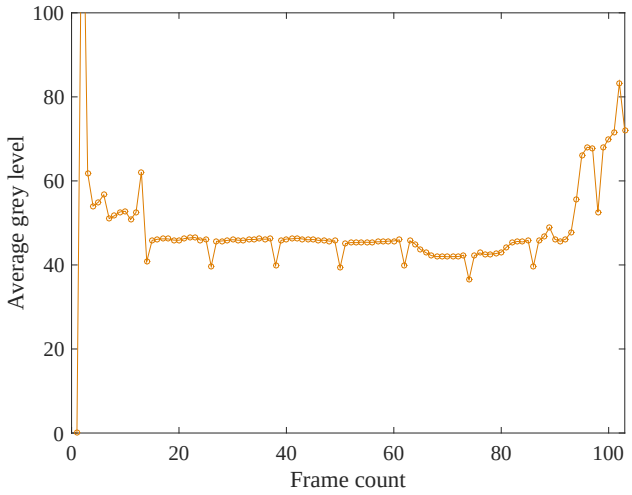

(a) Average frame grey level of a filmed grid instrumented sample surface.

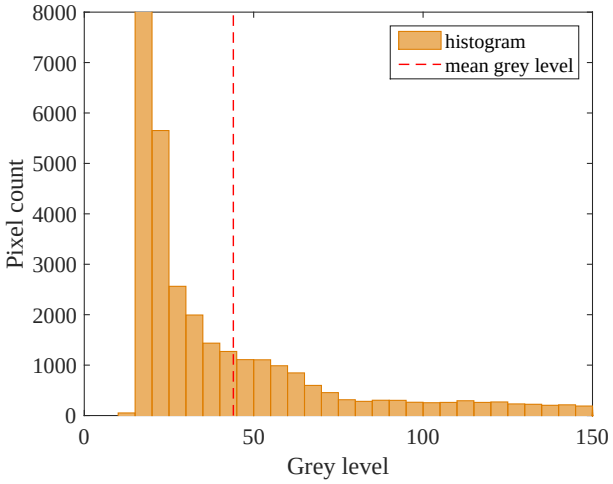

(b) Histogram of an averaged frame from 13th to 90th image of the acquisition sequence.

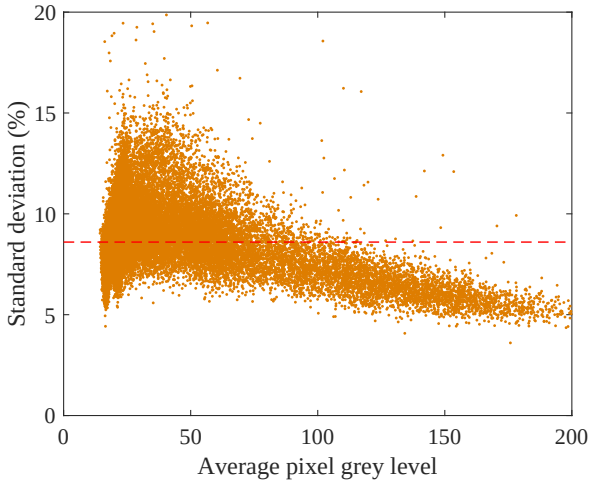

(c) Noise level as a function of mean pixel grey level regarding the corrected image sequence between 14^{th} and 79^{th} image only containing the imaged grid surface.

Figure 3.3: Analysing grey level noise from still sample grid images captured with the Shimadzu-HPV1 camera with 1 Mfps and 1 μs exposure time.

reduce the temporal noise effect, that can propagate from the analysed frame sequence to the measured fields, the frames that exhibit the under exposure with respect to the average sequence illumination can be recreated by averaging two adjacent frames.

An example is presented in Figure 3.3c,d in case of a framed grid image. A surface of a grid instrumented aluminium sample used for a spalling test was recorded with 1 Mfps camera speed and without any movement. As advised, the image illumination was kept in the darker grey level range (see Figure 3.3b). When only the fames between 14^{th} and 79^{th} are considered and the mean image processing is used, the average standard deviation of the pixel grey level content considering only the framed grid surface seems to be around 8% (see Figure 3.3). This value is considerably lower than the valus reported in [Rossi et al., 2014]. For this reason, the above explained measures are taken in all cases of the following image processing situations, considering the 15^{th} image as the reference one.

3.3 Spalling Aluminium – Experimental benchmark

In this section, the aim is to investigate the metrological performance of the given acquisition system and the identification methodology based on the VFM in real experimental conditions by preforming spalling tests on a material of known mechanical behaviour. Processing of a series of spalling experiments conducted with an aluminium sample, instrumented both with strain gauges and 1 mm pitch grid, will be presented. The acquisition system used to film the sample surface is the Shimadzu HPV-1. The test series consists of several spalling experiments carried out over a period between 2013 - 2014. The tests have been performed varying the camera settings. This enabled also the investigation of the possible influence of several testing parameters such as inter-frame time (0.5 - 1 Mfps), lens defocusing and image contrast. Furthermore, the effect of the processing parameters such as the degree of polynomial filtering used to compute acceleration fields, effect of acceleration window size as well as effect of spatial filtering due to the size of the virtual gauge were also investigated. These have been considered regarding a reference test in light of fixing the processing parameters so that they can be used for treating the tests conducted on concrete material. Therefore this section presents a short synthesis of most of the spalling test performed with the Shimadzu-HPV1 applying the grid method, some of which have already been published in [Saletti and Forquin, 2015].

The structure of this section is as follows:

- First, the general testing conditions are introduced
- Next, the general information regarding the displacement uncertainty when filming a 1 mm pitch grid are presented.
- A reference test is chosen to present the results on the identification of the material elastic response, on which, the effect of several processing parameters is investigated.
- The effect of several experimental settings such as: camera frame rate, lens focusing and grid sampling are investigated by performing additional spalling tests.
- Finally, all the identification results are gathered in order to provide an overall accuracy of the proposed identification methodology.

Another underlining idea of this section is to also propose the spalling aluminium as a standardized benchmarking test for application of ultra-high speed full-field measurements and inverse identification procedures. Indeed, in many works concerning the metrological performance of the full-field measurements and inverse identification techniques it has become a standardised procedure to perform a simple tensile test on a material of known characteristics (*e.g.* steel or aluminium) [Avril et al., 2008a]. However, in the dynamic loading regimes there does not exist

a standardized experiment on which a metrological investigation can be performed. The spalling technique that uses only the input bar of the SHPB system presented a good candidate since it favours the sample's unbalanced state. Furthermore, the test is designed so that the sample is subjected first to pure uniaxial compression followed by uniaxial tension, allowing to investigate both types of loading stages even separately. The spalling experiment is also easy to set-up, affordable and is easily instrumented with point-wise measurements that benefit the data analysis and can be used for validation and comparison. For example, strain gauges glued on the tested sample can be used to verify the full-field deformation measurement by comparing the results with a virtual gauge on the same position and of the same size. Since the identification of the material response in the spalling test relies on the measurement of the acceleration data, the laser interferometer (often pointed to the sample free-end) can be used to verify the image embedded load cell at a given cross-section, which is later on used to obtain the material axial stress response. Finally, by reconstructing local or global stress-strain response the identified elastic stiffness or the material Young's modulus can be compared to the known parameters, which is a one straightforward verification procedure that can characterize the entire methodological chain of the identification process.

3.3.1 Specimen and testing conditions

The tested specimen, 140 mm in height and 46 mm in diameter, is instrumented with up-to 3 standard strain gages 10 mm in length placed at 40, 50 and 120 mm from the rear face (Figure 3.1a). The rear face velocity is recorded with a laser interferometer from Polytec with bandwidth of 1.5 Mhz and acquisition set to 2 m/s/V. The tested aluminium alloy has a characteristic 1D wave speed of C = 5090 m/s, a density of 2810 kg/m^3 and expected Young's modulus equal to 72 GPa. The sample was manufactured so that it contains a plane surface with a width equal to its radius on which a grid pattern is glued following the standardized procedure [Piro and Grediac, 2004]. It needs to be mentioned that the grids are transferred and not bonded so local strengthening due to transfer film is avoided. All specimens are equipped with crossed grids of 1 mm pitch, printed with a high definition photo-plotter. The specimen surface was illuminated with a continuous light source which was supplied by a 800 W power lamp. The camera is connected to its accompanying external signal analyser on which the acquired 8 bit images are stored in the tagged image file format (.tif). The number of pixels used to sample each grid period directly influences the quality of the results. The higher the number of pixels per period, the better the sampling quality but due to limited camera pixel count, the smaller the surface under investigation. Therefore, the number of pixels used to sample each grid is dictated by the frame pixel count which for the Shimadzu HPV-1 is 312 (horizontal) and 260 (vertical) pixels. The sampling was mostly kept as 5 pixels per grid period allowing to visualize a sample surface of 60 mm (or 59 mm) in length by framing the grid in such way that the 12^{th} (or 15^{th}) pixel is located on the first point of the grid. In this way there is a certain amount of pixels left so that the samples free-end remains within the boundaries of the framed image at the end of the acquisition. It is also necessary to maintain a constant grid sampling over the framed surface, because non-constant grid pitch can introduce measurement errors since a parasitic pattern appears if it is not exactly an integer [Badulescu et al., 2009a]. It is of utmost importance for the measurement accuracy to adjust the position of the camera in such way that the image of the grid is accurately encoded on the camera sensor, even though it can be often tricky and time consuming.

3.3.2 Displacement measurement uncertainty

Before conducting spalling tests it is necessary to assess the resolution of the measured displacement fields. As already shown in Section 3.2, the measurement resolution as well as measurement noise level strongly depend on the performance of the high-speed camera [Pierron et al., 2011a]. Detailed metrological performance of the Shimadzu HPV-1 camera is provided in [Rossi et al., 2014]. As a general guideline it is suggested that measurement resolution can be tied to the grid pitch sampling and it was mentioned that is about $p/650$ (where p is the grid pitch) [Pierron and Forquin, 2012b]. For a 5pix/pitch/mm sampling it is around 1.5 μm or 0.01 pixels. A much more throughout analysis and an analytical estimation of the displacement resolution of the grid method has been

provided in [Grediac and Sur, 2014] concerning stationary spatial noise components and image settings. However, in high speed photography, temporal noise also plays an important role.

The resolution of the measurement can be regarded as the minimal detectable change in the measured quantity that causes a noteworthy change in the corresponding measurement indication (*e.g.* displacement field) greater than one standard deviation of the measurement noise [Chrysochoos and Surrel, 2012]. As such, the measurement resolution can be expressed through the standard deviation of that expected measured result. In that case, the measured result is regarded as a random quantity which can be characterised by a standard deviation – the *measurement uncertainty*. The displacement uncertainty should be obtained by throughout analysis of the stationary images captured before each test, where a specific displacement resolution can be determined for each individual test according to the given conditions of the experimental environment. However, it is not always the case that the stationary images are being captured at precisely the same imaging conditions. For example, in-situ UHS cameras are continuously recording cameras which are constantly filling and emptying their internal pixel memory bank until a signal (trigger) is received. Consequently, two consecutive sequences are not necessarily captured at perfectly the same image forming conditions (*e.g.* sensor temperature). Also, in practice, the stationary images are not always available for each conducted test.

Another way of providing an estimate of displacement resolution is by analysing consecutive captured frames of an unloaded sample [Avril et al., 2004a]. Calculating the corresponding displacement maps which should be zero in all pixels, the standard deviation of these maps can be taken as measurement noise [Chalal et al., 2006]. Here, this is done by performing the analysis on the first several recorded frames of an actual test sequence before the stress wave arrives to the sample. Assuming that the noise present in the displacement fields has a constant variance across each displacement map, a value of standard deviation can be provided for each displacement map (i) for each of the two directions $\sigma^i_{(X,Y)}$. Since in the first 20 frames of each acquired sequence (owing to pre-set triggering conditions) the sample is in unloaded state (where the expected displacement is equal to zero in ideal conditions), a mean of standard deviation can be obtained providing an average estimate:

$$\sigma^{avg}_{(X,Y)} = \frac{1}{N}\sum_{i=1}^{N}\sigma^i_{(X,Y)} \tag{3.1}$$

where N is the number of frames (here it is the first 20 frames). It is also worth getting the overall absolute mean displacement value for these frames since it can give an insight to a possible systematic error of the measured displacement fields. These values for each test conducted on the aluminium alloy and for each displacement component are summarized in Table 3.1.

From the presented data an average displacement resolution of the axial displacement component for the given grid pixel sampling of 5 pixels per grid pitch seems to be about 4 μm (0.02 pix). Although reasonably low, the measurement resolution is far from being ideal and a smoothing techniques has to be used in order to obtain the strain fields and acceleration fields. Especially in the case where small strains are measured such as when testing concrete material. Later on in Chapter 6, similar analysis will be carried for two more UHS sensors which would provide a first head-to-head comparison between their performance.

3.3.3 Identification of the perfect elastic material response

One experiment is taken from the test series, named Alu6, which is used to present the identification of the elastic response of an aluminium sample subjected to a spalling test. The measurement of Young's modulus, stresses and strains in the sample are presented herein. The test has been carried out with the 1 Mfps acquisition speed, 5 pixels per period sampling and clear lens focusing although, the lightning conditions were kept in slightly darker grey level range. The probability histogram of the framed grid in the reference image is shown in Figure 3.4a.

Test	$\sigma^{eq}_{(X)}$ (μm)	$\lvert\overline{U_X}\rvert$ (μm)	$\sigma^{eq}_{(Y)}$ (μm)	$\lvert\overline{U_Y}\rvert$ (μm)
Alu 06	2.19	0.47	5.49	2.21
Alu 08	7.84	0.29	9.93	2.07
Alu 01	3.26	0.07	7.21	11.73
Alu 02	3.69	0.04	5.45	10.11
Alu 03	3.83	0.47	7.88	7.94
Alu 10	3.22	2.56	4.77	2.93
Grid 02	3.83	0.26	5.63	3.55
Grid 01	3.27	0.11	4.84	2.81
Means	3.89	0.53	6.4	4.99

Table 3.1: Estimates of displacement resolution for the spalling tests performed on the aluminium alloy by performing the analysis on first 20 frames of image sequence.(1 Mfps and 5 pix/pitch/mm sampling)

The reference image taken to compute the displacements through determining the frame by frame phase change was the 15^{th} image of the acquisition sequence. After obtaining the displacement fields, the acceleration data was obtained by numerical derivation of the fitted second degree polynomial (in the lest squares sense) over the time window of 11 μs. The effect of the window size is discussed later within this section. The diffuse approximation algorithm was used to derive the strain fields [Avril et al., 2008b], using a second degree polynomial fit over the spatial window size of 8 points. The choice of virtual fields is one of the key issues in the identification procedure and here was chosen as proposed in [Pierron and Forquin, 2012b] by performing a polynomial fit over averaged axial displacement maps. The 12^{th} order polynomials were used to obtain fields that depend only on axial direction. A zero virtual displacement condition was added to the side opposed to the free-end to cancel the contribution of the virtual traction force at the end of the observation window. Once the acceleration fields, strain fields and virtual fields are obtained, the Equation 2.19 was used to obtain the identification of the global Young's modulus. The term global is used since the acceleration fields and the strain fields as well as their corresponding virtual fields are averaged along the whole field of view. The identified value is presented in Figure 3.4b. It can be observed that, in

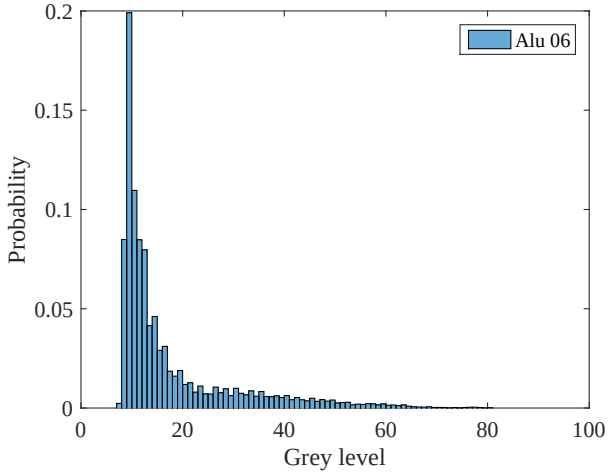

(a) Histogram of the framed grid on the 15^{th} image.

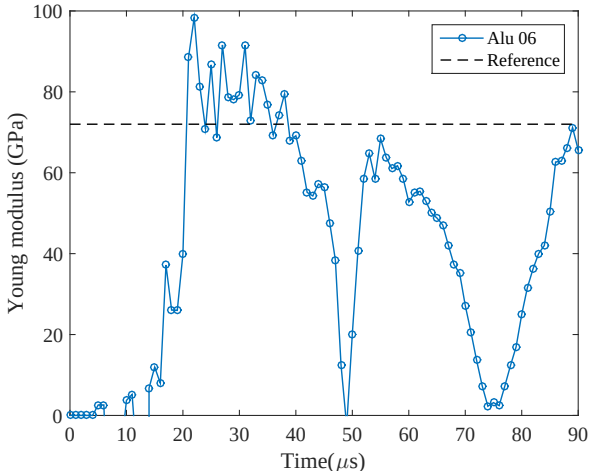

(b) Identified global Young's modulus.

Figure 3.4: Lightning conditions and the identified global Young's modulus from chosen reference test using the Shimadzu HPV-1 – Alu06.

the compressive part of the loading (between 21 μs and 41 μs) the evaluated global Young's modulus of aluminium sample seems to be within the range of the expected value. However, the global Young's modulus varies quite a

lot, from 98.4 GPa to 62.9 MPa, compared to the expected value of Young's modulus that is equal 72 GPa. On the other hand, in the tensile part of loading, the global stiffness seems not to be in the same range as in compression stage with notably lower identified values. Possible sources of this uncertainty will be explored through simulated experiments in Chapter 4.

The results regarding the obtained axial strain and axial stress in the Alu6 experiment are detailed in the Figure 3.5. The axial strain in the cross-section at 40 mm from the free-end measured by a strain gauge is compared to the data of a virtual strain gauge at the same position and of the same size (Figure 3.5a). A good agreement is observed between the strain evolutions obtained from a strain gauge and the virtual strain gauge. The identified axial stress on the same virtual gauge position is plotted as function of time on the Figure 3.5b. Slightly higher level of stress is noted in the tensile loading stage.

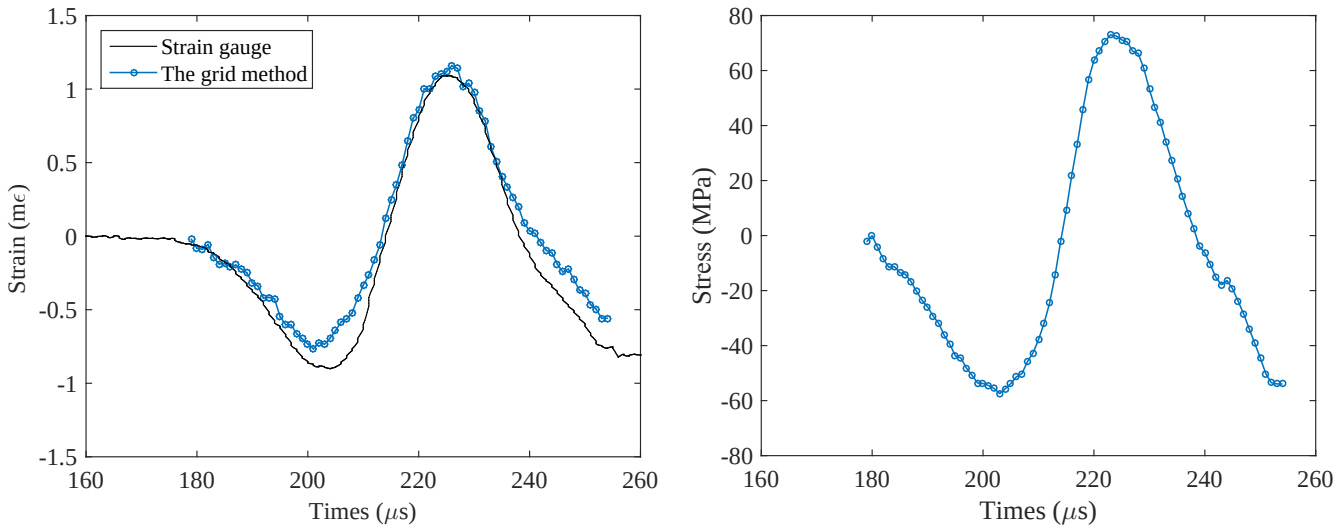

(a) Comparison of strain measurement between the grid method and strain gauge.

(b) Axial stress measurement.

Figure 3.5: Strain and Stress measurement at 40 mm from free surface using the virtual gauge for the test Alu 06 and comparison to strain gauge measurement at the same position (Virtual gauge size 10 mm).

In principle, the average axial stress can be plotted as function of the average axial strain for any of the transversal slices along the longitudinal axis of the specimen visualized by the camera. However, in order to introduce a certain level of spatial smoothing a virtual gauge is introduced, averaging the stress and strain response over several slices. Since the spalling tests provides unidirectional state of stress, then the slope of the reconstructed stress strain curve identifies the material Young's modulus. The reconstructed stress-strain curves for two virtual gauges (L=10 mm) at 30 mm and at 40 mm from free-end are presented in Figure 3.6. The reference line of the expected linear elastic response is also provided. Both curves although exhibiting a generally linear trend are to some extent noisy and certain deviation from the perfect linear elastic response can be noted. The two curves are also slightly offset towards the positive quadrant which can be due to the choice of the reference image and camera triggering. The results obtained by performing a linear regression of the presented curves are given in Table 3.2 with corresponding standard errors of the estimate. The regression has been performed on the entire range of data between 20 μs and 85 μs which correspond to the full compressive and tensile loading stage. For both gauges the estimated Young's modulus from linear regression is within 3% of the expected reference which can be regarded as satisfactory. On the other hand, the standard error of the estimate, which describes the deviation of the expected perfect linear response, is about 10%.

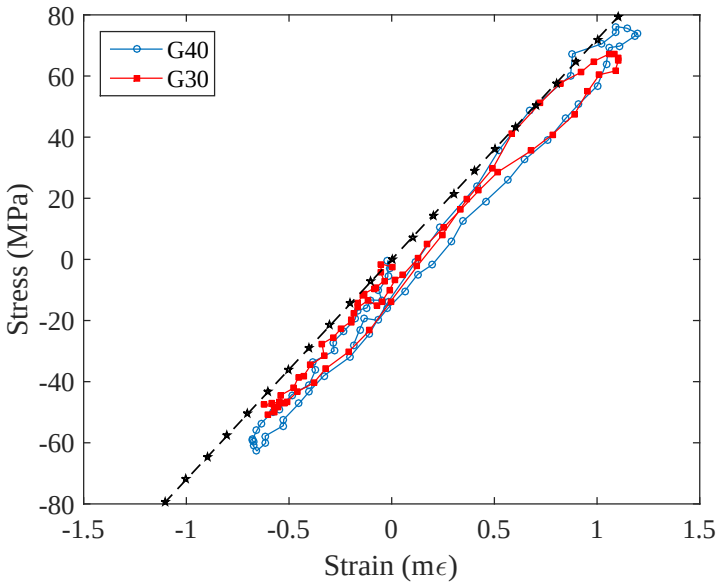

Figure 3.6: Stress-Strain curves at 30mm and 40mm from the sample free surface for the referance test – Alu 06 (Virtual gauge size 10 mm).

Virtual gauge	Young's modulus(GPa)	Standard error(GPa)
G30	68.71	9.62
G40	70.01	7.21

Table 3.2: Identified values of the Young's modulus for the test Alu 06 by performing the linear regression of the stress-strain curves at 30 mm and 40 mm from free surface.

3.3.4 Influence of the processing parameters

The main difficulty in performing reliable identification is that the acceleration field are strongly affected by the noise resulting from double-derivation of the displacement fields. To reduce (as much as possible) the level of noise in the experimental results, a certain amount of signal filtering needs to be used. One of the most common signal filtering approaches is the so-called Savitzky-Golay filter [Savitzky and Golay, 1964]. In the following, the effect of filtering used to derive the axial stress from the acceleration fields is demonstrated. The influence of both the choice of polynomial degree and the window size are investigated monitoring the average axial stress at the virtual gauge at 40 mm from the free-end. The data is also compared to the expected elastic stress response obtained from the real gauge measurement ($\sigma = E.\varepsilon$). The effect of these parameters on the derived axial stress are shown in Figure 3.7. First, the polynomial degree has been changed keeping the same temporal window size (Figure 3.7a). Second, the polynomial degree of the second order was adopted, altering the temporal window size of the applied filter (Figure 3.7b). No notable difference between using the even or odd order of the chosen polynomial degree has been noted. However, when choosing polynomials higher than $2^n d$ degree, the results exibit significant fluctuations. For this reason, the second order polynomial fit was chosen which provides a strong low-pass filtering effect. A similar trend is observed in cases when small window size is chosen. The lower the window size, the lower the effect of the filtering and consequently the more fluctuations are present in the result. According to the reconstructed stress response in Figure 3.7b, the window was chosen to spread over 11 time points (11 μs). This corresponds to 11 consecutive frames of a sequence that already consists of just 92 frames.

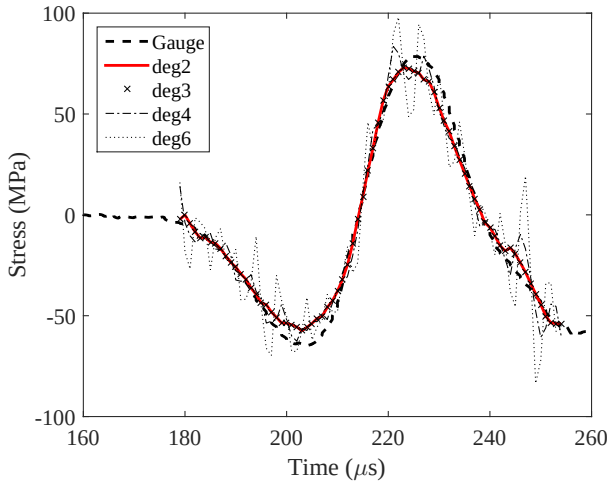

(a) Effect of the order of the polynomial fit (window size is 11 time points).

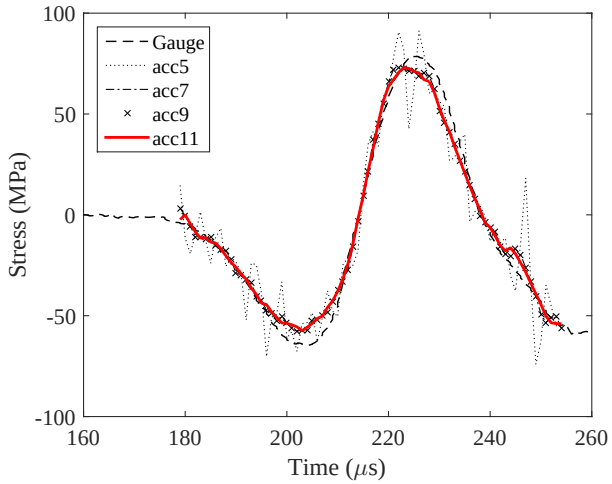

(b) Effect of the temporal window size (2^{nd} order polynomial filter).

Figure 3.7: Influence of signal filtering parameters on the derived axial stress (Virtual gauge size 10 mm).

Another type of smoothing of the identified results is introduced by choosing a size of the virtual gauge, which provides averaging of the data over a certain spatial window length. Although, it is expected that the smoothing of the results by spatial averaging is of a lower impact than the temporal low-pass filtering used to reconstruct the time evolution of the stress response, it is still important to evaluate its effect on the reconstructed stress and strain response. The influence of the length of spatial averaging is investigated for the axial stress and strain at the virtual gauge at 40 mm from free surface. The effect of spatial filtering is evaluated in the Figure 3.8 where it can be concluded that the spatial averaging caused by introducing a virtual gage is of small influence. However, it has to be mentioned that this is the final step before the stress-strain response is reconstructed and until now several other smoothing techniques were used both for computation of acceleration fields and strain fields. In principle,

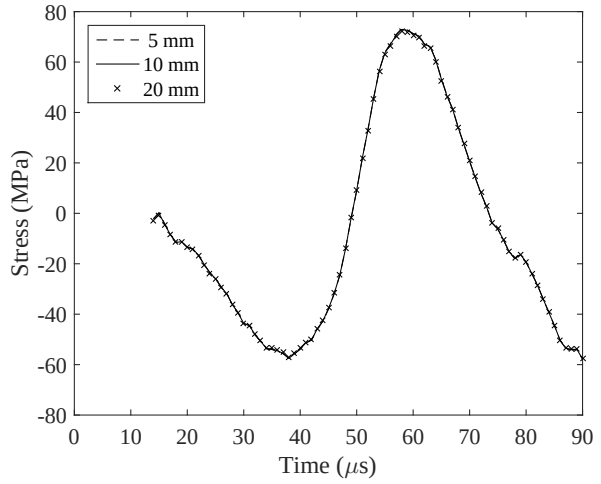

(a) Effect of the virtual gauge size on reconstructed axial Stress.

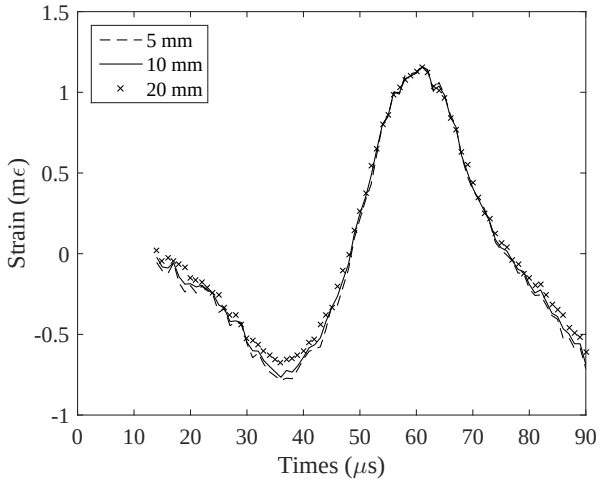

(b) Effect of the virtual gauge size on reconstructed axial Strain.

Figure 3.8: Influence of the length of spatial averaging introduced by the Virtual gauge size. (position at 40 mm from free-end)

the size of the virtual gauge can be of arbitrary choice, however, since the tested aluminium samples were also instrumented with standard 10 mm polyester foil gauge at 30 mm and 40 mm from free end, the size of the virtual gauge used from now on was chosen accordingly.

3.3.5 Various experimental effects on the identification

The intention here is to assess some general aspects of the metrological performance of the identification procedure that can mainly be introduced by the way the grid image is formed within the camera. Indeed, question is to know how noise propagates from the sensor of the camera to displacement maps since the displacements are directly proportional to the phase change. What is more, it is also important to know how these quantities can reflect the overall identification procedure. What often has the meaning of *noise* to an experimentalist is actually the superimposition of actual image noise inherent to any digital acquisition system but also other sources. For example, framed grids generally contain some defects such as subpixel spatial changes in their pitch and/or spatial contrast variability together with some other effects (*e.g.* missing data, non-equispaced grid lines due to lack of ink) which all can locally disturb the phase detection [Badulescu et al., 2009a, Badulescu et al., 2009b]. In order to link the measurement performance to some parameters such as lighting and noise in the images a closed form expression has been provided connecting the variance of noise in the phase to the variance of the noise in the image assuming the non-correlated zero-mean Gaussian noise and Gaussian convolution window for phase detection. The expression for the phase variance ν_ϕ can be expressed through the relation of several image parameters assuming homoscedastic noise [Grediac and Sur, 2014], such as:

$$\nu_\phi = \frac{\nu_{image}\Delta_x\Delta_y}{2\pi\sigma^2\gamma^2 A^2}|d_1| \tag{3.2}$$

Where:

- ν_{image} is the variance of the assumed Gaussian white noise.
- $\Delta_{x,y}$ is the spatial size of the pixel in horizontal and vertical direction.
- σ is the size of the window used to compute the displacements.
- γ is the image contrast (assuming constant contrast of the grid image).

- A is the image lightning (assuming constant lightning over a grid image).
- $|d_1|$ is the first coefficient in the Fourier expansion of the periodic function that describes the grid and is connected to profile of the printed grid lines.

The expression is interesting since it clearly shows that the random error is independent of the magnitude of the measured displacement. Similar conclusion were made for on the sensitivity of measured displacements using digital image correlation technique [Roux and Hild, 2006, Wang et al., 2007]. Several additional interesting indications can be drawn from this expression, which predict how the measurement resolution considered as the variance of the computed phase can be affected by experimental image parameters. For example, the larger the image lighting component A and the more contrasted the grid image, the smaller the measurement uncertainty. Although extremely useful, the expression still does not take into account some often present defects, such as the missing data which can be considered individual for each glued grid. Furthermore, the assumption of the Gaussian noise is a classic one but far from the noise noted in practice when dealing with raw data obtained from UHS digital sensors. Finally, in real experimental conditions it is difficult to decouple these effects since all the image framing parameters are connected and dependent on the set-up.

In the following an experimental attempt for investigating some of these effects is adopted by performing the whole measurement chain under varying recording conditions. In that way, some of these effects can be directly incorporated in the identification of material response. First, the effect of lightning was investigated by changing the light intensity and by keeping a clear lens focusing on the grid plane. Consequently, the framed grid image is close to being a binary one. Second, a slight lens defocusing was used for approximately same lightning conditions. In that case, the grid profile distribution is close to being the sinusoidal grid. Finally, another investigated effect, is the image framing rate which can have an impact on the identified elastic material response.

3.3.5.1 Effect of lightning conditions

In order to investigate the impact of the lightning conditions the reference test (Alu 06) is compared to an experiment conducted at slightly higher light intensity. The test used for comparison is referred to as the Grid 02. This test has already been used in [Saletti and Forquin, 2015] where the aim was to investigate the metrological performance of the grid method and DIC when applied to a spalling test using the Shimadzu HPV-1 camera. The general image lightning conditions of two reference grid images (15^{th} frame) from each of the acquisition sequences is presented in Figure 3.9.

From the presented histogram Figure 3.9a it can be seen that the test Grid 02 was conducted at slightly larger distribution of grey levels due to lighter conditions. However, the overall grey level distribution was maintained below the critical level of 100, above which the sensor exibits peculiar saturation effects [Rossi and Pierron, 2012]. The grid profiles given in Figure 3.9b confirms the brighter lightning conditions of the Grid 02 test but also show the difficulty of framing a perfect grid pattern since some spatial variations are always present. The lens focus was kept on the grid plane in both tests considering a clear focusing. Finally, the average grey level on the entire time sequence given in Figure 3.9c shows that both sequence exhibit the same temporal noise which is an intrinsic characteristic of the imaging sensor used. The test named Grid 02 has been processed according to the parameters fixed in the previous section. What needs to be pointed out is that the test was conducted at a lower strain rate. The stress-strain response reconstructed for virtual gauges (L=10 mm) at 30 mm and 40 mm from the free surface are compared for the two test and presented in Figure 3.10. From the presented curves it is difficult to conclude any significant differences between the two tests although it can be seen that slightly lower deviation from the linear response is noted in the curves for test named Grid 02. The results of the linear regression analysis are given in Table 3.3. The linear regression has been performed on the entire set of data ranging from 20 μs to 85 μs in both cases which correspond closely to the full compressive and tensile loading stage. What can be observed from the regres-

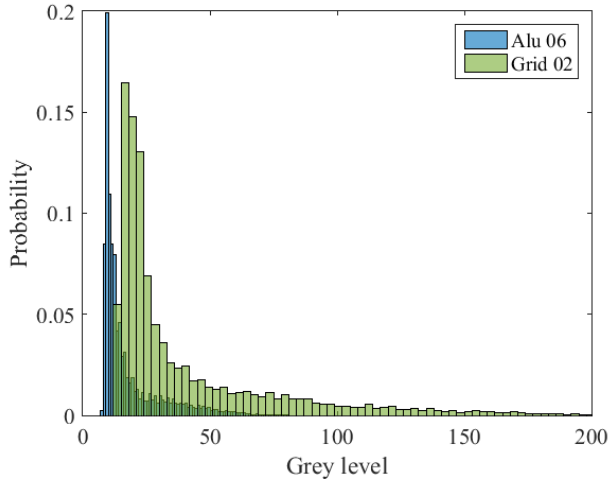

(a) Probability histogram of the reference 15^{th} image of each acquisition sequence.

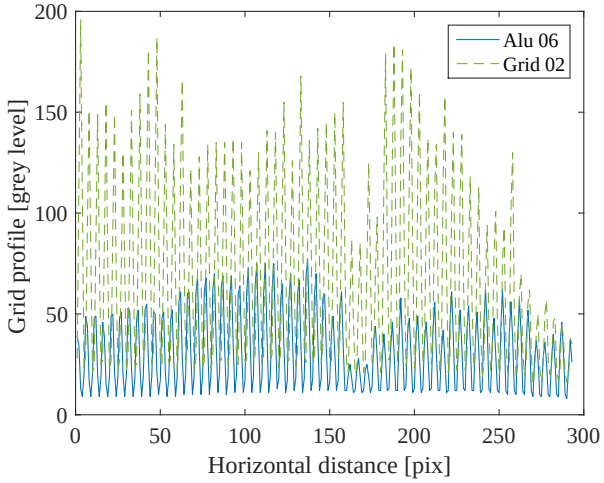

(b) Horizontal grid line profile of the reference 15^{th} image of each acquisition sequence.

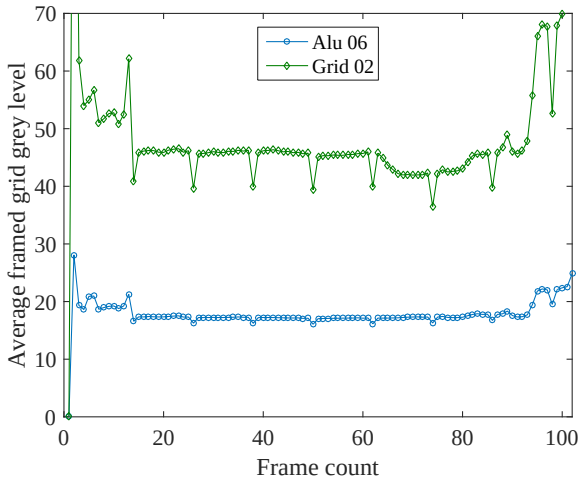

(c) Average frame grey level in the region of interest for two spalling tests.

Figure 3.9: Illumination characteristics of two image sequences used to investigate the effect of lightning conditions by performing spalling tests on aluminium sample.

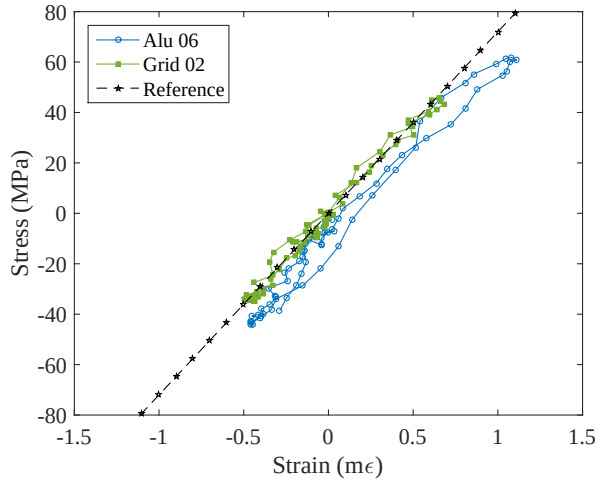

(a) Stress-Strain response of the two tests at 30 mm from free-end.

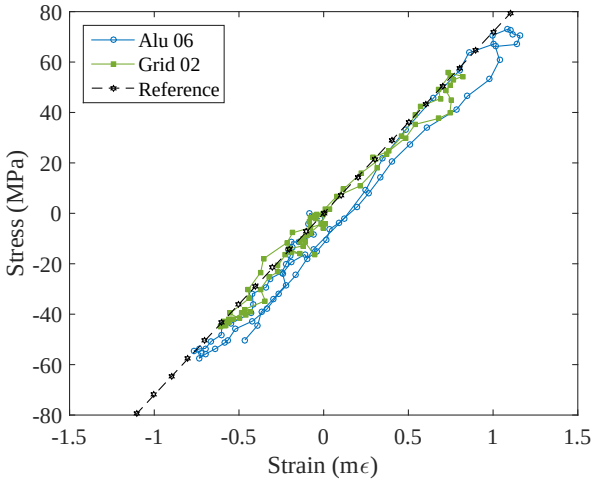

(b) Stress-Strain response of the two tests at 40 mm from free-end.

Figure 3.10: Identified stress-strain curves for the two tests used to investigate the effect of lightning conditions. (Virtual gauge size 10 mm)

sion results is that the standard error of the estimate is lower for the case of Grid 02. Furthermore, it is interesting to notice that both test show systematically lower values in the identified Young's modulus which could be the effect of enforcing the boundary conditions slightly away from it real position. Finally as expected from the Equation 3.2, higher illumination of the imaged grid pattern can be beneficial for the reduction of the measurement error.

Test	Virtual gauge	Young's modulus (GPa)	Standard error (GPa)	Strain rate (s^{-1})
Alu 06	G30	68.71	9.62	110
Grid 02	G30	70.86	0.21	81
Alu 06	G40	70.02	7.2	138.5
Grid 02	G40	70.58	1.92	104

Table 3.3: Identified values of the Young's modulus for the test Alu 06 and Grid 02 (high illumination) by performing the linear regression of the stress-strain curves at 30 mm and 40 mm from free surface (65 points in total).

3.3.5.2 Effect of image sharpness – clear and blurred focusing

Even though high-contrasted grid pattern is desirable regarding a reduction of measurement variance as can be seen in Equation 3.2, errors in local phase shifting algorithm can arise from framing a grid signal that is very close to binary one since high-frequency content caused by a close to bimodal grid distribution can locally introduce fictive distortion to framed grid images [Rossi et al., 2014]. Some positive effects of blurring were already presented in the case of direct extraction of strain measurements [Sur and Grédiac, 2015]

Here, the same principle is explored through real experiments by comparing the reference test (Alu 06) to the one obtained at the same lightning conditions but with slight defocusing of the lens (Alu 08). A portion of the grid profile for the reference image of the two tests is presented in the Figure 3.11b and the probability histogram for the two reference images within the zone of the framed grid is shown in Figure 3.11a. The lighting conditions have been kept the same. Although, the additional lens blurring increases the distribution of grey levels it also reduces the grid

contrast. The data have been processed with the parameters established in previous section. The results regarding the stress-strain response of a virtual gauge at 30 mm and 40 mm from the free surface and are compared in Figure 3.12. The results from the linear regression are presented in Table 3.4. From the presented results it seems difficult to spot benefits of lens blurring, which is contrary to what was expected. This could be because it is difficult to precisely say that the blurred grid image is close to the sinusoidal since only 5 pixels are used to sample the grid pitch. More pixels samples are needed so that the grid profile can be spatially altered to look like a sinusoidal one. Here, due to limited pixel count of the camera sensor the small number of pixels samples had to be used. Therefore, this type of effect is worth reinvestigating once the sensor pixel count allows more pixels to be used for grid sampling.

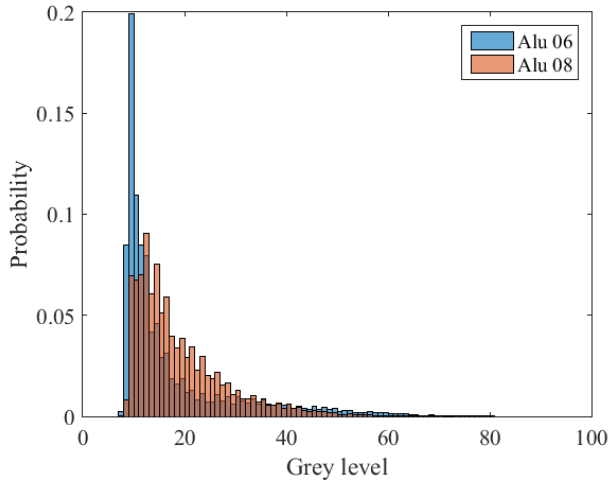

(a) Probability histogram of the reference 15^{th} image of each acquisition sequence.

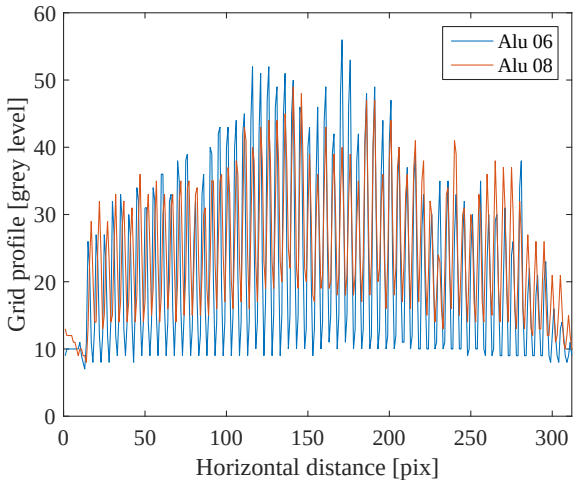

(b) Horizontal grid line profile of the reference 15^{th} image of each acquisition sequence.

Figure 3.11: Illumination characteristics of two image sequences used to investigate the effect of lens blurring. (Alu08 - blurred focus)

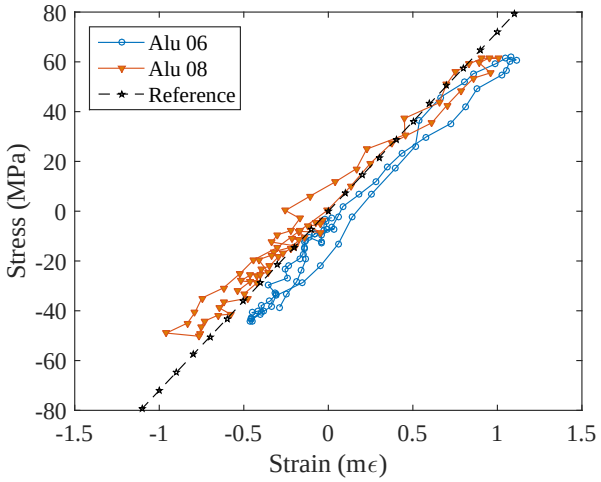

(a) Stress-Strain response of the two tests at 30 mm from free-end.

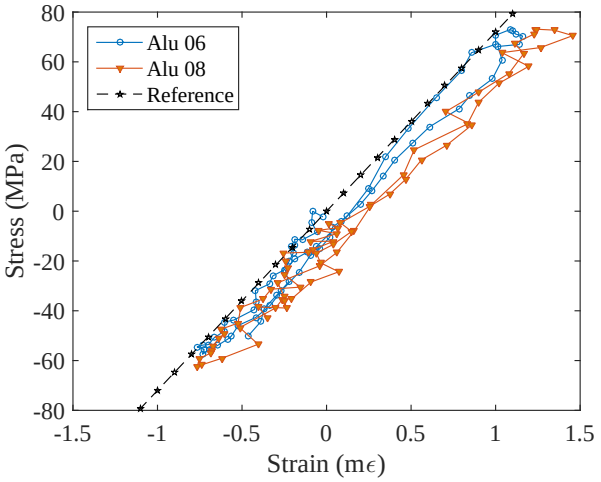

(b) Stress-Strain response of the two tests at 40 mm from free-end.

Figure 3.12: Identified stress-strain curves for the two tests used to investigate the effect of lightning conditions. (Alu 08 - blurred focus, Virtual gauge size 10 mm)

Test	Virtual gauge	Young's modulus (GPa)	Standard error (GPa)	Strain rate (s^{-1})
Alu 06	G30	68.71	9.62	110
Alu 08	G30	62.01	3.22	146
Alu 06	G40	70.02	7.2	138.5
Alu 08	G40	64.12	13.38	154

Table 3.4: Identified values of the Young's modulus for the test Alu 06 and Alu 08 (blurred focus) by performing the linear regression of the stress-strain curves at 30 mm and 40 mm from free surface (65 points in total).

3.3.5.3 Effect of the acquisition frame rate

Temporal resolution plays a significant role in identification of the dynamic response of materials since it directly dictates the time discretization of the captured wave propagation process. Here, a test named Alu 07 was conducted on the same aluminium alloy just at a lower acquisition speed of 0.5 Mfps. In this case, since the displacement data are provided for each 2 μs, the temporal derivation was performed fitting a second order polynomial over a span of 7 time points, while the strains are obtained as in the treatment of the previous tests. The obtained results are provided in Figure 3.13. From the identified global Young's modulus it can be clearly seen that several round trips are captured during the entire acquisition and that only during the first compressive stage the values are close to the reference one while for the rest of the wave propagation and reflection the identified values stay bellow the expected reference (Figure 3.13a). The reconstructed stress-strain for the two virtual gauge positions response is provided in the Figure 3.13b and the corresponding identified results from linear regression are given in Table 3.5. The regression has been performed for two complete round trips of the wave namely between 20 μs and 140 μs. Again, the identified stiffness is well below the expected reference for around 12% indicating that the frame rate of 500k images per second is not sufficient enough for a proper identification of the material elastic response which is same to what was observed in the simulated experiments.

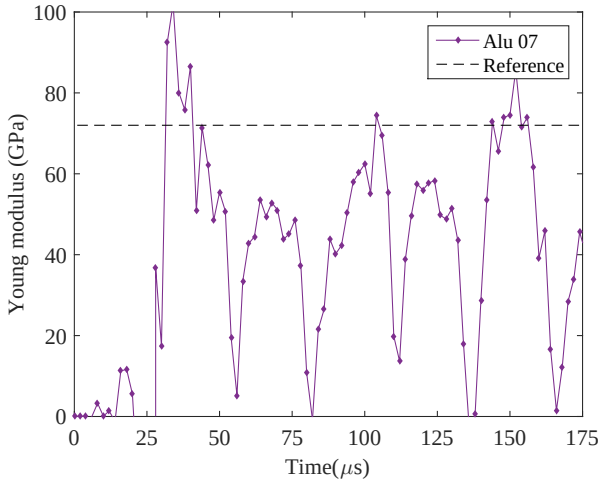

(a) Stress-Strain response of the two tests at 30 mm from free-end.

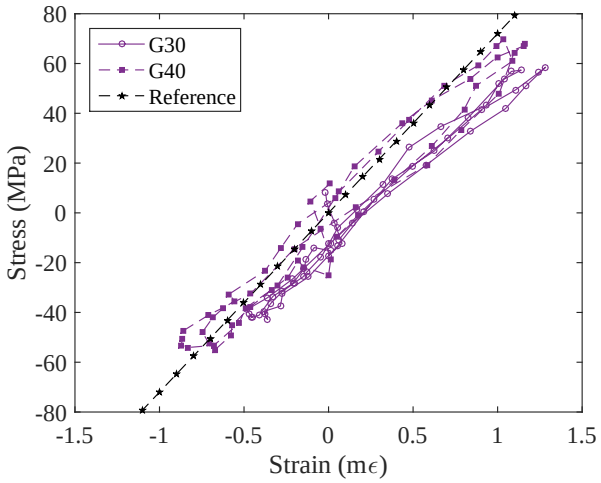

(b) Stress-Strain response of the for the two locations at 30 mm and 40 mm from free-end. (Virtual gauge size 10 mm)

Figure 3.13: Identified global Young's modulu and stress-strain curves for the Alu 07 obtained with 0.5 Mfps acqusition speed.

Test	Virtual gauge	Young's modulus (GPa)	Standard error (GPa)	Strain rate (s^{-1})
Alu 07	G30	60.46	14.91	105
	G40	62.74	3.42	165

Table 3.5: Identified values of the Young's modulus for the test Alu 07 (0.5 Mfps) by performing the linear regression of the stress-strain curves at 30 mm and 40 mm from free surface.

3.3.6 Identification results and errors

It was shown in previous sections that a more reliable and robust way of retrieving the material Young's modulus (as long as the material behaves linearly elastic), is by performing a linear regression of the local reconstructed axial stress-strain response. The cross sectional stress is directly obtained from the measured acceleration fields that are retrieved by recording a grid-instrumented sample surface with an ultra-high speed camera. The stress-strain curves are reconstructed on a portion of data using a so-called virtual gauge. The sizes of the virtual gauges can be arbitrary and it was shown that slight smoothing is induced in the strain data. In the following, this length was chosen to match the length of real strain gauges glued on the aluminium sample. (*i.e.* 1x10 mm^2). An overall synthesis of the linear regression results for two virtual gauge locations of the performed spalling aluminium tests, that have been conducted at 1 Mfps camera recording and with 5 pixels/pitch/mm grid sampling, are gathered in the Table 3.6. Although the data appear quite scattered and consistently lower than the expected reference value, it is interesting to note that for the tests conducted at very high strain rate (*e.g.* test Alu 03) the identified results exhibit a large error while for the test conducted at medium and lower loading rates (*e.g.* Grid 02) the identified results seem to be closer to the expected reference. This just demonstrates the difficulty of conducting a proper identification of material response at high loading rates due to possible uncertainties that could be introduced by the mechanical test itself.

Test	Virtual gauge	Young's modulus(GPa)	Standard error(GPa)	Strain rate (s^{-1})
Alu 06	G30	68.71	9.62	110
	G40	70.02	7.2	138
Alu 08	G30	62.01	3.22	146
	G40	64.12	13.38	154
Alu 01	G30	65.66	4.55	154
	G40	66.52	16.18	123
Alu 02	G30	70.58	2.73	112
	G40	67.93	9.32	146
Alu 03	G30	58.99	5.01	149
	G40	57.72	27.72	272
Alu 10	G30	67.11	5.87	85
	G40	70.94	0.2	81
Grid 02	G30	70.86	0.21	81
	G40	70.58	1.92	104
Grid 01	G30	71.29	4.15	124
	G40	73.03	3.44	108

Table 3.6: Linear regression results for the spalling tests performed on aluminium alloy using the stress-strain curves at 30 mm and 40 mm from free surface (1 Mfps and 5 pix/pitch/mm sampling).

3.4 Spalling of ordinary concrete – Methodology of measuring dynamic tensile strength

In this section, the failure characteristics of ordinary concrete are investigated by performing several spalling tests with the methodology that was described previously. Ultra-high speed photography with high acquisition speed of 1 Mfps and the VFM are used to accurately measure the tensile strength, Young's modulus, strain-rate at failure and stress–strain response of concrete at high strain-rate. The experimental results are presented in the first part. The identified tensile stiffness was observed to be up-to 50% lower than the initial compressive stiffness and the obtained peak stress was about 20% lower than the one obtained by applying the Novikov method. In order to support this claim, numerical simulations were performed and are presented in the second part. The numerical simulations, performed using a damage model, showed that the change of stiffness between compression and tension highly affects the rear-face velocity profile. Additionally, it was numerically observed that the material pre-peak non-linear response can also influence the apparent tensile strength determined with the Novikov formula, since it can introduce the appearance of a secondary velocity pull-back. The overall presented results further suggest that the processing based only on the velocity "pullback" is quite sensitive measurement, since it contains the history of events that preceded the brittle failure, and such can produce an over estimation of the tensile strength in concrete and rock-like materials under Novikov assumptions.

This section consists of an extended and reproduced version of:
*P. Forquin, B. Lukić. On the Processing of Spalling Experiments. Part I: Identification of the Dynamic Tensile Strength of Concrete. Journal of Dynamic Behavior of Materials, **4**:34, (2018) .*

3.4.1 Experimental results

In this section, results of three spalling tests that have been performed on common concrete, using the experimental measurement set-up represented in Figure 3.1 and the procedure described in previous chapter, will be presented. The measured data from both point-wise and full-field measurements are processed and compared, providing that the traditional processing leads to an overestimation of concrete's dynamic tensile strength.

3.4.1.1 Standard measurements

The traditional processing of the spalling test is based on the method that has been previously proposed and validated [Erzar and Forquin, 2010]. The laser interferometer pointed towards the sample free-end provides the measurement of the particle velocity profile throughout the entire test (Table 3.7). Knowing the material density and the material wave speed, the apparent failure strength can be deduced by observing the so called velocity 'pull-back' and employing the Novikov formula [Novikov and Ivanov, 1966]:

$$\sigma_{laser} = \frac{1}{2}\rho C_0 V_{pb} \tag{3.3}$$

The pull-back velocity (V_{pb}) represents the difference between the peak particle speed (corresponding to the point of compression to tension transition) and the velocity at the first rebound. This processing relies on the assumption of unidimensional linear elastic wave propagation until the peak failure stress inside the sample is reached. Three strain gauges glued on the sample surface are located at different distances from the samples free-end as to capture the wave propagation and reflection until the tensile macro failure occurs. The strain gauge close to the contact surface serves to capture the compressive pulse transmitted from the Hopkinson bar to the sample and to acquire the material wave speed. This is obtained by performing a temporal shift of the data captured by the compressive strain gauge to match the velocity profile. One such set of data is presented in Figure 3.14a for one concrete sample, where the gauge data ($E_{dyn}.\varepsilon_{gauge}$) and laser data ($1/2\rho V_{laser}$) are converted into values of axial stress assuming

unidirectional elastic wave propagation.

Sample	Material	Density (kg/m^3)	Projectile speed (m/s)	Wave speed (m/s)
R45	R30A7	2374	11	4250
Tomo1	R30A7	2269	8.18	3810
100w	R30A7	2359	11.24	4250

Table 3.7: Experimental specifications of the three spalling tests conducted on R30A7 concrete.

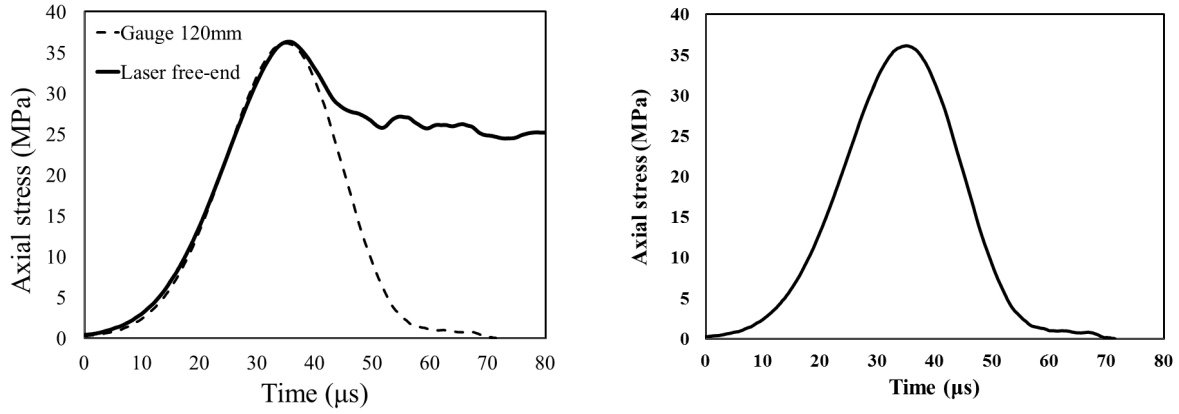

(a) Method for obtaining the material wave speed: shifted compressive pulse to the pulse registered on the free-end (Tomo1).

(b) Incident pulse obtained with the spherical cap-projectile pulse shaping technique (Tomo1).

Figure 3.14: Results from point-wise measurements used in the spalling experiment.

When referring to the mentioned figure it can be observed that the time shifted axial stress curves obtained from the strain gauge measurement and from the rear face velocity overlap quite well up-to the point when the peak stress is reached, after which the two curves are characterised with a different descending slope. The peak corresponds to the point where the transition from compressive to tensile loading stage starts and when the wave reflection starts to exceed in amplitude the incident wave. The observed difference after the peak can be an indication of a different material response in compression and tension, namely due to possible different material stiffness. Furthermore, it can also be an indicator of a presence of a non-linear stress-strain response prior to the peak strength is reached. Both of these hypotheses will be addressed in the following part by processing the full-field experimental measurements and later on discussed in the Section 3.4.2 using FE numerical computations.

3.4.1.2 Full-Field Deformation measurements

As previously mentioned, the temporally resolved in-plane displacements fields are obtained by processing the grey level grid images of sample surface framed with an ultra-high speed camera. Sequences of 102 images are obtained for each test with the camera acquisition speed set to 1 Mfps with the exposure time of 1 μs. The obtained images were processed using the information presented in Table 3.8.

The displacement maps for one tested specimen, Tomo1, are given at the several frames preceding the fracture in Figure 3.15. The displacement map at 70 μs from the beginning of the recording process, clearly shows presence of several displacement discontinuities, namely at around 30 and 40 mm from the free surface. From the presented displacement maps it can be seen that the crack appearing at 30 mm does not appear to fully open by the end of

Camera - Shimadzu HPV-1	
Pixel array size	312x260
Frame rate	1 Mfps
Exposure time	1 μs (1/frame rate)
Field of view	23x60 mm
Number of frame	102
Grid method	
Pitch	1 mm
Sampling	5 Pixels per period (N)
Reference image	15
Displacement	
Window	Triangular
Spatial resolution	9 (2N–1)
Temporal resolution	1 μs
Strain	
Smoothing method	Diffuse approximation, 10 pixel radius
Spatial resolution	10 mm
Temporal resolution	1 μs
Strain rate	
Smoothing method	Second-order polynomial fit over 5 temporal strain points
Temporal resolution	5 μs
Acceleration	
Smoothing method	Second-order polynomial fit over 11 temporal displacement points
Temporal resolution	11 μs

Table 3.8: Imaging measurement performance and processing information.

the test but rather stays closed, likely due to stress relaxation induced by the growth of the macro-crack appearing at 40 mm that ultimately fractures the sample. This can be better observed from the 'Supplementary material: Video 1' (`https://doi.org/10.1007/s40870-017-0135-1`) where the entire evolution of the measured displacement maps can be seen with respect to each recorder frame.

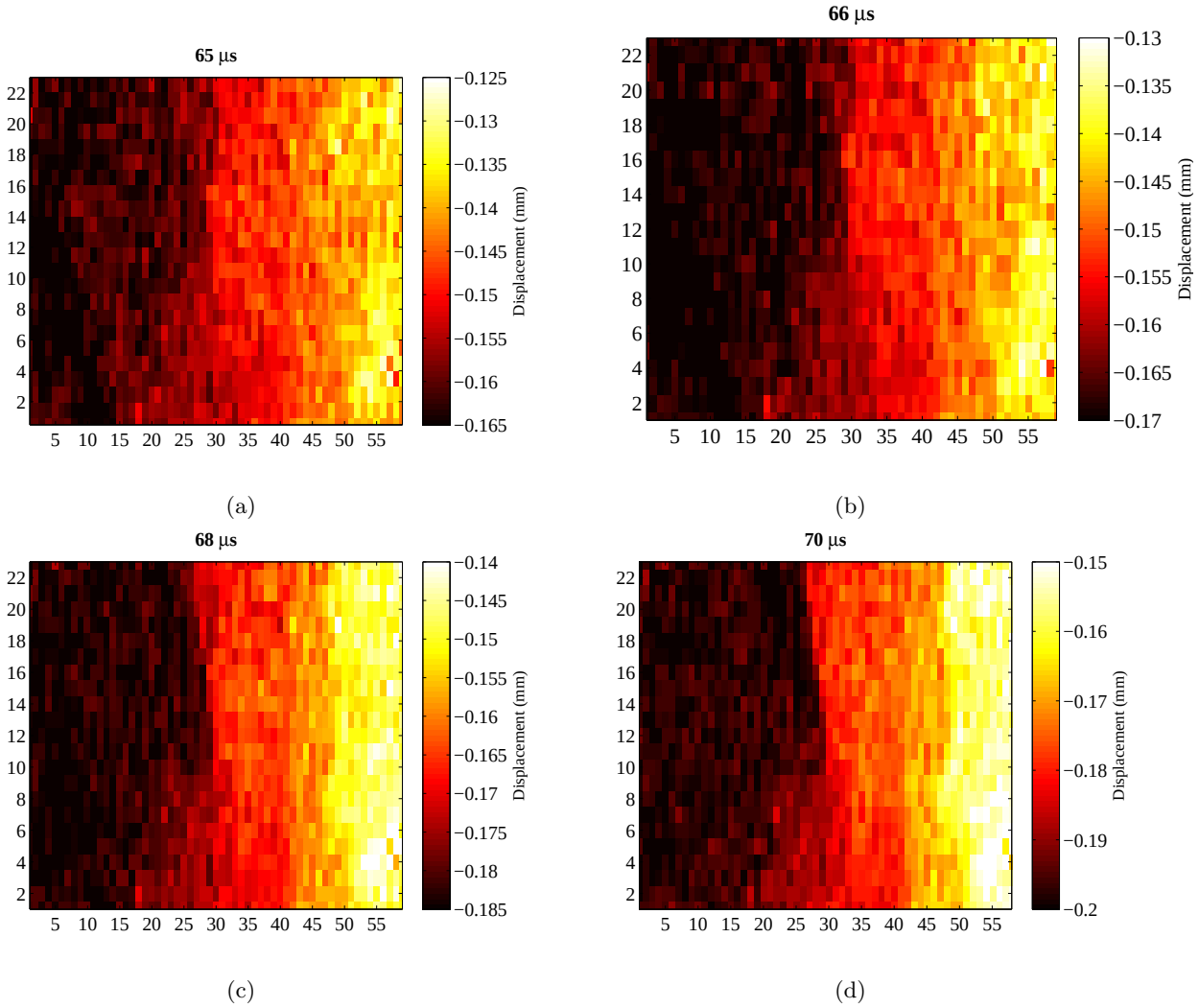

Figure 3.15: Full field displacement maps of the concrete sample surface at different times preceding the macro-fracture clearly show two discontinuities that manifest as displacement jumps at location of 30 and 40 mm (spatial size of presented maps presents horizontal (x) and vertical (y) distribution of measurement points over the sample surface in millimetres where position $x = 0$ corresponds to free-end).

From the obtained displacement fields the strain maps can be derived. The strain fields are derived with the same procedure as used in [Pierron and Forquin, 2012b], namely using the diffuse approximation algorithm [Avril et al., 2008b]. A local fit of the weighted second degree polynomial is performed on a span radius of 10 displacement points. A larger window for strain derivation is used in order to reduce the effect of spatial noise coming from the acquisition system. In complementary to previously shown displacement maps, the Figure 3.16 displays the global axial strain obtained as an average strain evolution on the entire surface visualized with the camera.

The entire evolution of the measured strain maps with the evolution of average axial strain are provided in the 'Supplementary material: Video 2' (`https://doi.org/10.1007/s40870-017-0135-1`). Again, similarly to Video 1, it can be observed that two strain concentrations start to evolve but the strain concentration at 30 mm reduces in magnitude after a certain period, while the one close to 40 mm continues to rise.

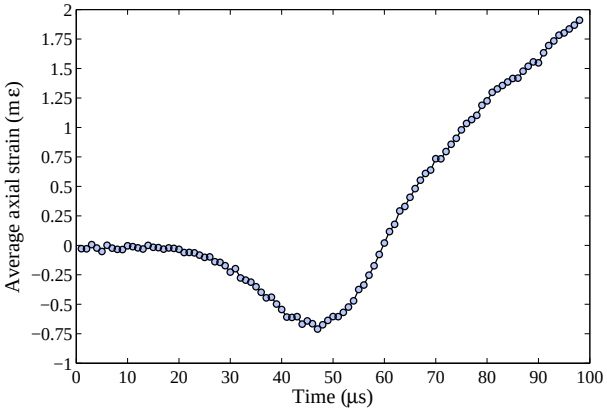

Figure 3.16: Global axial strain obtained as average strain on the entire observation surface of the Tomo1 specimen.

3.4.1.3 Stress and Strain Analysis

It was previously shown in Section 2.4.3 that by introducing a rigid body virtual field in the equation of principle of virtual work and by assuming perfect uniaxial loading conditions, the acting inertia can be utilised as a direct force measurement throughout the spalling test. Then, the average stress in every observed cross section can be calculated as a function of the axial acceleration averaged from sample free-end to the observed location. The great benefit of this method is that the entire fields of information are embedded in the images captured with the ultra-high speed camera, which represent the only necessary measurement to process the entire test. After obtaining the in-plane displacement maps of the sample surface, it is necessary to perform the second degree temporal derivation of the displacement fields in order to obtain the acceleration maps. This is presently performed with applying the temporal Savitzky-Golay filtering of the raw displacement measurements [Savitzky and Golay, 1964]. A second order polynomial fit is performed over a temporal sliding window of 11 images to decrease signal-to-noise ratio and evaluate the derivative in the central point of the moving subset. This type of temporal data processing was adopted from this point onwards for processing all the tested samples presented in this section.

The right column of the Figure 3.17 shows the space-time contour maps of axial stress profiles reconstructed for all longitudinal positions for each concrete sample. Two distinct zones that correspond to the propagation of the compressive and reflected tensile wave can be observed. The compressive stage lasts about 40 μs while the tensile stage is governed by the concrete's tensile strength and seems to last about 15 μs after which the stress values are close to zero. It can also be observed that the stress is much larger during the first stage of the compressive loading than during the second tensile loading stage. Finally, a homogeneous and uniform stress field can be observed during the tensile loading stage. When referring back to the space-time contour maps of axial strain, on the left hand side of Figure 3.17, it is clear that the low stress values in tension are caused by samples' failure that manifests through the presence of several strain localisations. Interestingly, strain localizations can already be observed at 30 mm from the free surface even though after the tests only cracks at 40 mm were visible to the eye in the samples R45 and Tomo1. This is due to the fact that the crack at 30 mm is in fact a closed micro-crack as already mentioned when displacements maps were analysed.

From the illustrated stress and strain maps the local stress–strain curves can be obtained in each cross-section of the tested samples. Those of the highest interest are the locations that correspond to the positions of crack formation where the non-linear material response is expected. The tested samples were also instrumented with strain gauges that are glued at a certain distance from the sample's free-end as shown in Figure 3.1a. The strain gauge generally introduces minor spatial filtering of the deformation data due to their physical size. Therefore, a

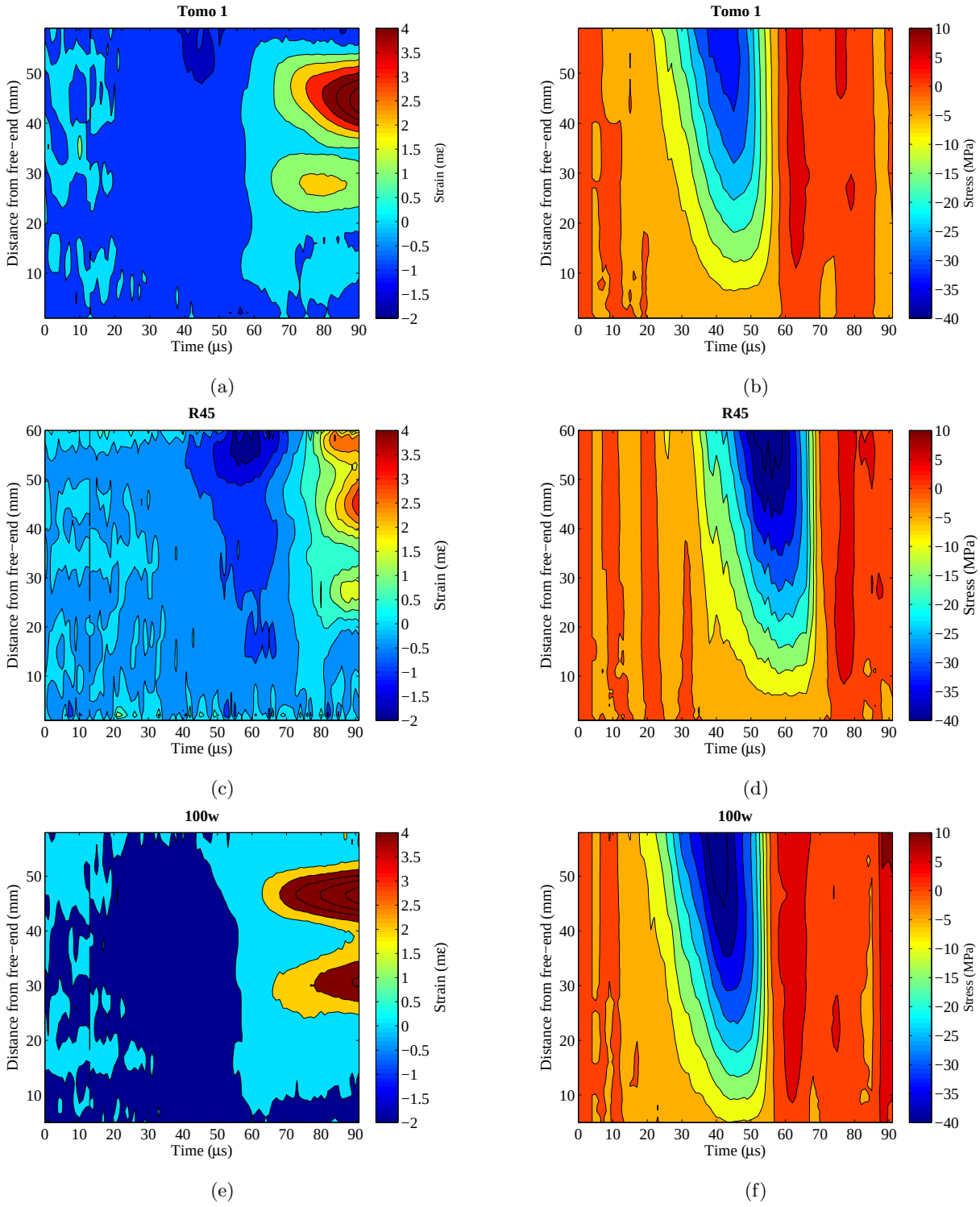

Figure 3.17: Space–time contour maps of stress and strain for three tested concrete samples.

virtual gauge can be chosen to process the stress and strain fields as to provide additional spatial smoothing. The area chosen was of 20 x 1 mm which represents characteristic grid size of conventional polyester foil gauges used in this type of experiment. Figure 3.18 represents the reconstructed stress–strain response of three concrete samples applying a virtual gauge at 30 mm and 40 mm from free-end. In each figure the starting point is marked after which the stress values start to increase.

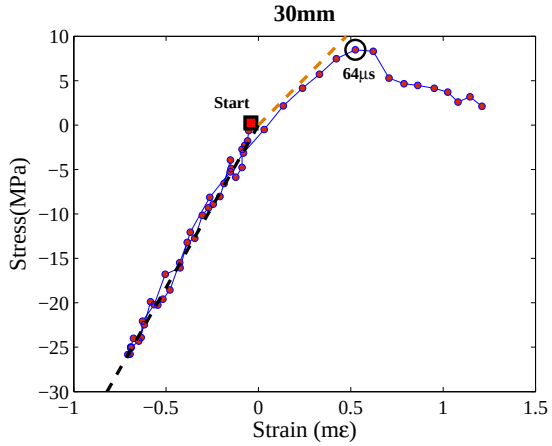

(a) Tomo1: Virtual gauge 30mm

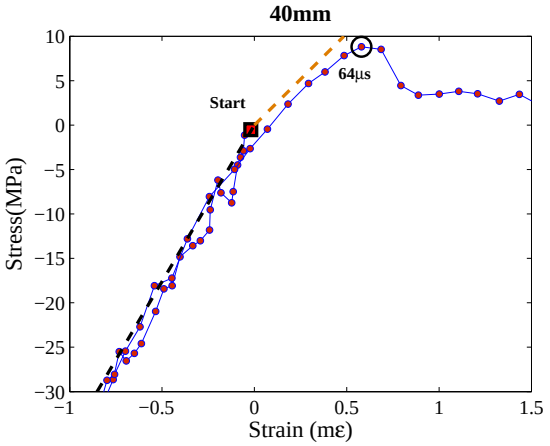

(b) Tomo1: Virtual gauge 40mm

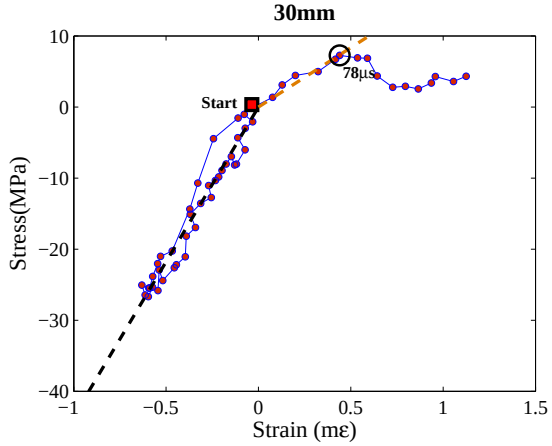

(c) R45: Virtual gauge 30mm

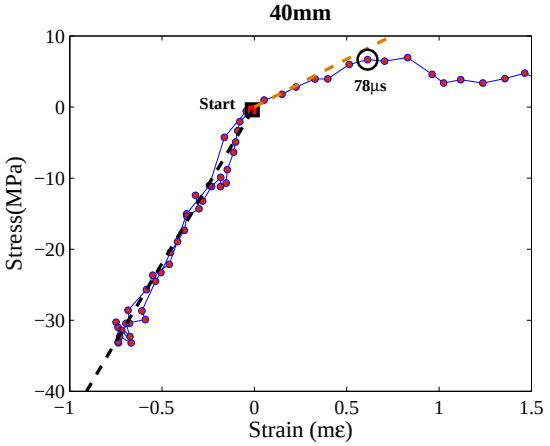

(d) R45: Virtual gauge 40mm

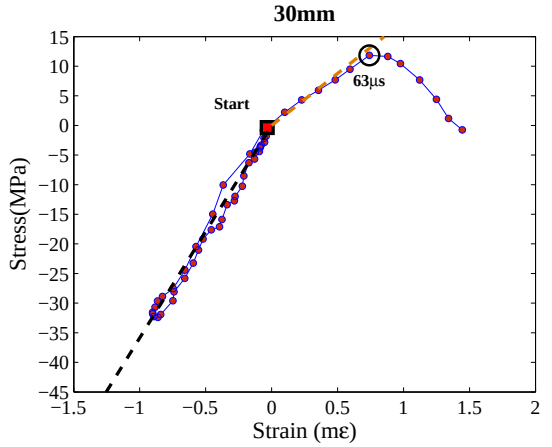

(e) 100w: Virtual gauge 30mm

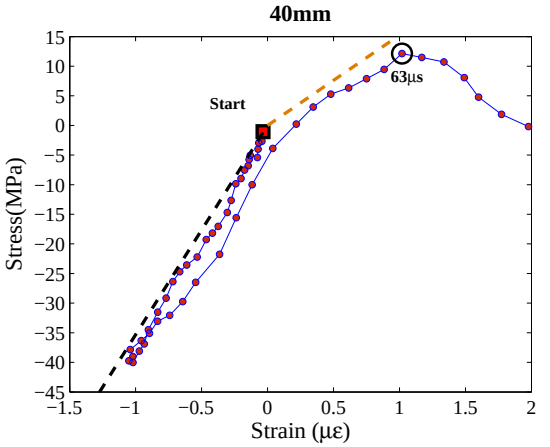

(f) 100w: Virtual gauge 40mm

Figure 3.18: Reconstructed stress–strain curves from virtual gauges for three tested concrete samples at 30 and 40 mm distance from the free-end.

Since the spalling test provides a unidirectional stress state, the slope of the curves describes Young's modulus of

the sample at these locations. It can be observed that the response in all cases is reasonably linear in compression. However, the response of the material is different during the compressive and tensile loading stage, two linear regressions are performed. The first regression line is performed on the set of stress–strain points that construct the compressive stage (about 40 points), neglecting the first several points that correspond to low acceleration levels. The second regression is performed on the tensile part of the curve up-to the point which corresponds to the peak stress (about 7 points). It becomes clear that the slopes of the regression lines differ from compressive to tensile stage pointing towards different material responses. Furthermore, there is an indication of non-linear behaviour few moments prior the peak stress. The curves show that the stress values flatten out after reaching a peak that could be associated with the progressive damage process prior the failure. The obtained values of Young's modulus and the maximal tensile stresses from the presented curves are summarised in Table 3.9. The results obtained from classical measurements and the Novikov processing are summarized in Table 3.10.

Sample	Virtual Gauge position (mm)	Young's modulus-Compression E_c (GPa)	Young's modulus-Tension E_t (GPa)	Dissymmetry factor E_t/E_c (%)	Tensile stress (MPa)	Time to peak (μs)
Tomo1	30	36.61	21.03	57.45	8.48	6
	40	35.22	20.65	58.56	8.82	6
R45	30	43.54	16.72	38.54	7.27	7
	40	44.06	13.47	30.65	6.96	7
100W	30	35.89	17.65	49.11	11.84	6
	40	35.33	15.25	43.21	12.14	7

Table 3.9: Results of identification from the reconstructed stress–strain curves in Figure 3.18.

Interestingly, for all tested samples the maximal stress reached seems to be lower than the values obtained with traditional Novikov processing. The reason for this is that the standard Novikov processing technique for obtaining the ultimate stress relies on the assumption of the propagation of linear-elastic waves up to the failure, while it is clear from the reconstructed stress–strain curves that the response exhibits certain non-linear behaviour far from the macro-crack plane, owing to the progressive growth of cracks. The results clearly show that the Young's modulus in the dynamic tension is 40–70% lower than the Young's modulus identified during the compressive response. This reduction of tensile stiffness could be explained to some extent by the possible presence of initial defaults as it has been observed in previous works on dynamic tensile testing of granite rock material [Saadati et al., 2016]. Second, the reconstructed stress response exhibits non-linear behaviour prior the peak stress which becomes even more pronounced if the size of virtual gauge decreases (Figure 3.19).

Sample	Gauge position (mm)	Strain rate (s^{-1})	Novikov Tensile stress(MPa)
R45	40	60-100	/
Tomo1	40	80-100	10.6
100W	40	120-130	15.1

Table 3.10: Results of identification from the point-wise measurements.

3.4.1.4 Strain rate analysis

Another difficult challenge associated to the characterisation of dynamic tensile response of concrete is to well define both the peak stress and corresponding strain rate in the tested specimens. In fact, both stress and strain rate can considerably vary throughout the spall test. Obtaining accurate values of strain rate at failure is a prerequisite for

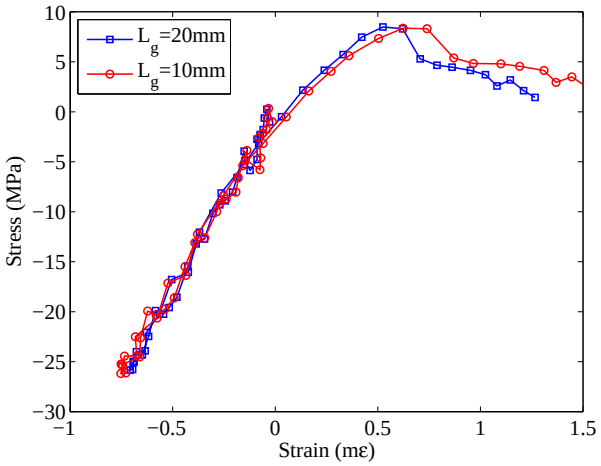

Figure 3.19: Effect of virtual gauge size on the reconstructed stress strain response: position 30 mm in test Tomo1.

well understanding the strength increase with the rise in rates of deformation. One way of controlling the strain rate is to devise experimental techniques that maintain mainly constant evolution of strain rate close to the failure location. In the present work, a pulse shaping technique of so-called spherical cap projectile that was numerically optimised and verified in [Forquin and Erzar, 2009, Erzar and Forquin, 2010] is used. This technique decreases the variation of strain rate and reduces the initial shock effects by increasing the rising time of the loading pulse, resulting in a bell-shaped pulse as shown in Figure 3.14b.

The identification of strain rate at failure, as presented in [Erzar and Forquin, 2010], starts off by obtaining the apparent failure strength of the material from the rear face velocity profile. Next, the fictive stress curves obtained from the strain gauge history (*i.e.* $E_{dyn}.\varepsilon_{gauge}$) are traced up-to the deduced failure stress to obtain the time at failure. It has to be mentioned that the Young's modulus used is the one identified by wave speed analysis (*i.e.* compressive stiffness). Then by simple derivation of the strain data obtained from the gauges glued on the sample surface an interval of strain rate at failure can be obtained. Change of axial stress as a function of strain rate can be reconstructed directly from the full field data. In that case, only one temporal derivation of strain is necessary which is presently performed by deriving a second order polynomial fit over a sliding window of 5 time points. The 20 point virtual gauge processing is introduced to provide additional smoothing to the reconstructed curves that are shown in Figure 3.20 for locations at 30, 40 and 50 mm from the free end.

In the useful part of the plot (positive stress and strain rate) low variations of strain rate close to the point of the macro fracture can be concluded from curves at 30 and 40 mm. The variation of strain rate increases at the location 50 mm when the failure takes place and the axial stress drastically decreases. Another way of obtaining the values of strain rate at peak stress is to analyse the strain rate history at the positions of 30 and 40 mm from the free-end as shown in left side of Figure 3.21. The vertical lines mark the time when the stress in the samples reaches the peak which is obtained from the reconstructed stress-strain curves shown in Figure 3.18. Additionally, measurement data obtained from actual gauges glued at 40 mm from the sample free-end are shown for comparison. It can be seen that the results obtained from the virtual gauge and from real gauge at the same distance coincides well and the small differences can be attributed to the local heterogeneities of the concrete material. Furthermore, space-time maps of strain rate of the tested samples are presented in right-hand side of the Figure 3.21. These maps are simple time gradients of the strain maps already shown in Figure 3.18. What can be seen is that, although exhibiting a certain quasi-homogeneous distribution just before the failure occurs (given the corresponding time), the strain rate values still show some variation in the space domain. These maps serve as an example to illustrate the actual difficulty associated to the spalling test and dynamic testing in general. Strain rate measurements are

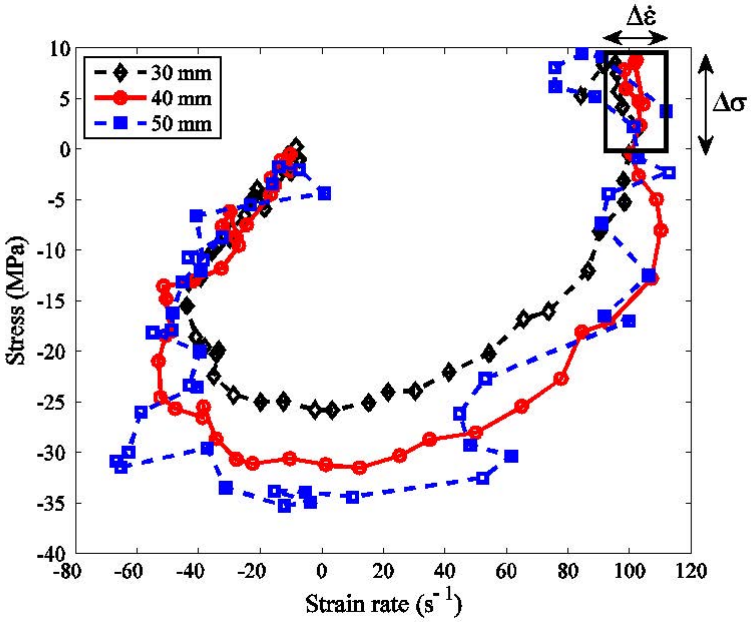

Figure 3.20: Strain-rate as a function of the stress level obtained from full field measurements for the Tomo1 test.

one of the sought information that are needed to describe the material behaviour, however they still are difficult to get. In the following, several proposed methods for estimating the strain rate at failure will be presented and compared.

From the illustrated data the strain rate at stress peak can be estimated. First technique relies on processing only the strain gauge measurements as proposed in [Erzar and Forquin, 2010] (Method 1). The second method (Method 2) utilises the same principle but with the tensile strength obtained from the stress–strain curves reconstructed from full field measurements (using the VFM). In the third method (Method 3), the failure stress and strain rates are provided by only using the virtual gauge measurements. Finally, the time at peak stress can also be used to obtain the strain rate (Method 4). This specific value can be obtained as the intersection of the data from real strain gauge history and the time at failure as on the left side of the Figure 3.21. Here, the Method 4 is used for the sake of general comparison. The data obtained with all four methods are presented in Table 3.11.

The first two methods provide generally lower values of strain rate at the failure location. This is due to the fact that the non-symmetric response of the material is not being taken into account and only the compressive stiffness is being used. The methods three and four, which rely on data extracted from VFM processing, provide higher values of local strain rate, which are considered more realistic as no assumptions have been made on the material behaviour beforehand.

3.4.1.5 Identification of Global Young's Modulus

The procedure to identify the average Young's modulus of quasi-brittle materials subjected to dynamic spalling test is based on the analysis already presented in [Pierron and Forquin, 2012a] and is obtained by dividing the average virtual work associated to internal and external forces (Equation 2.19). The stiffness parameter obtained in this way can also be referred to as the global Young's modulus as it is derived from temporal acceleration and strain maps averaged on the entire framed sample surface. The principle of virtual work is applied taking

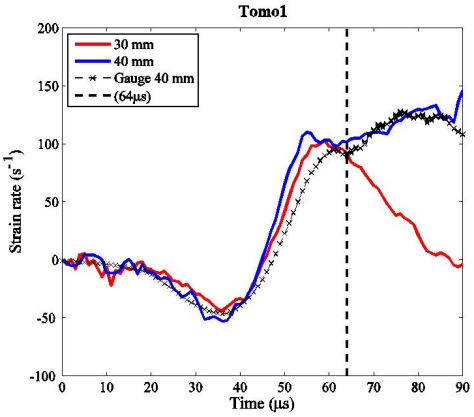

(a) Tomo1: Strain rate gauges

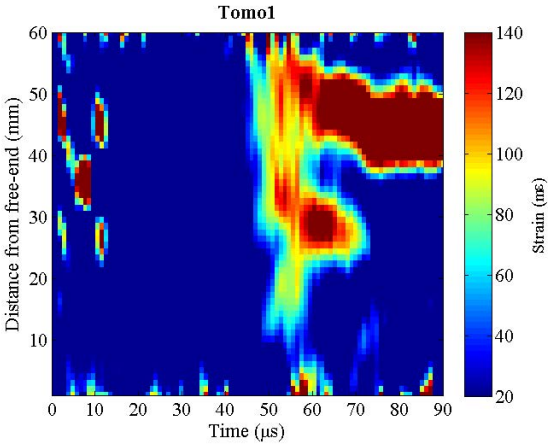

(b) Tomo1: Strain rate map.

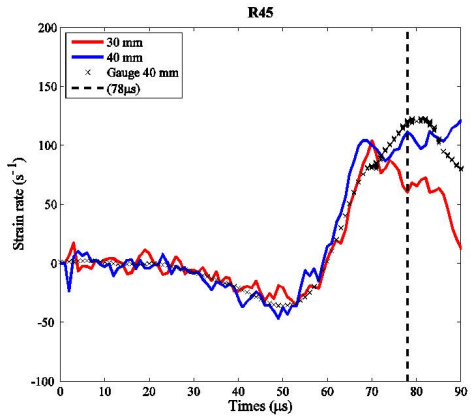

(c) R45: Strain rate gauges

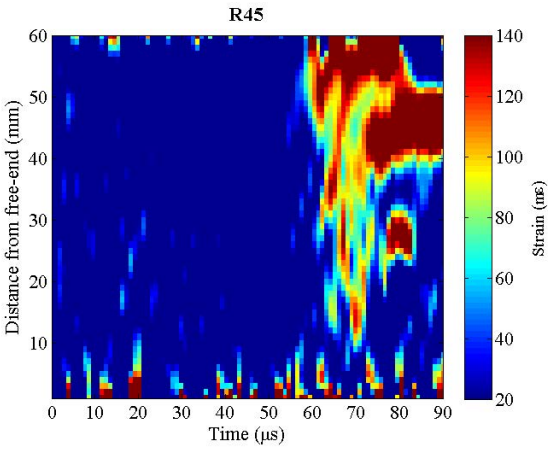

(d) R45: Strain rate map.

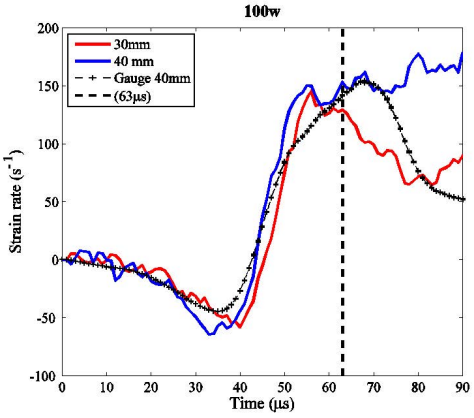

(e) 100w: Strain rate gauges

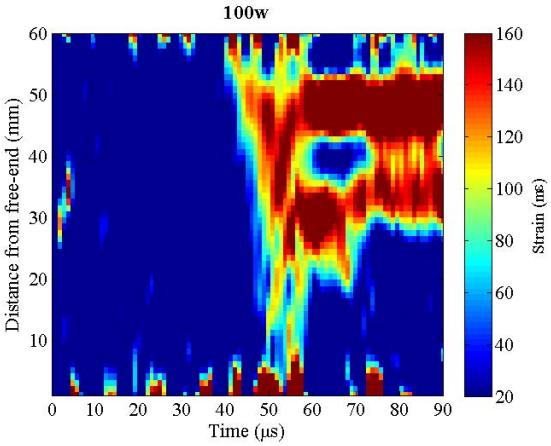

(f) 100w: Strain rate map.

Figure 3.21: *LEFT*: Strain rate history for three tested samples with virtual gauge at 30 and 40 mm and a real gauge at 40 mm (the vertical line represents time at failure from Table 3.9) (Method–4).
RIGHT: Space-time map of strain rate for each tested sample.

Sample		Method–1 ($\sigma_{laser}; \varepsilon_{gauge}$)	Method–2 ($\sigma_{VFM}; \varepsilon_{gauge}$)	Method–3 ($\sigma_{VFM}; \varepsilon_{VFM}$)		Method–4 ($t_{VFM}; \varepsilon_{gauge}$)
Tomo1	Tensile strength	10.6	8.81	8.81	Time to peak	64 μs
	Strain rate	78	94	101		92
R45	Tensile strength	/	6.96	6.96	Time to peak	78 μs
	Strain rate	/	71	111		119
100w	Tensile strength	15.1	12.14	12.14	Time to peak	63 μs
	Strain rate	117	120	153		142

Table 3.11: Results of identification from the reconstructed stress–strain curves in Figure 3.18.

the advantage of the sample non-equilibrium state throughout the experiment assuming perfectly axial loading conditions. This later allows utilising the derived acceleration fields as an alternative 'load cell' and avoiding the need of any other external force measurement. The idea of exploiting the inertial forces as a measurement tool can be used in a wide range of material identification procedures and was firstly proposed and successfully applied for identification of damping properties of thin vibrating plates [Giraudeau et al., 2006]. Later, the concept was extended to identification of material stiffness parameters for intermediate [Moulart et al., 2011] and high strain rate testing of composite materials [Zhu and Pierron, 2016]. Finally, some innovative recent applications have been conducted. One concerns ultrasonic excitation of surrogate bone material that allowed identifying entire maps of Young's modulus [Wang et al., 2013a, Pierron, 2016]. Another concerns coupling ultra-high speed photography and infra-red thermography to characterize the elastic behaviour of PMMA under ultrasonic excitation and various range of temperatures [Seghir and Pierron, 2017].

However, when quasi-brittle materials are in question, the low signal to noise ratio of the measured strain and acceleration values will tend to introduce stiffness identification error. This is specifically the case for concrete, since in the tensile loading stage the failure occurs at low stress levels. Therefore, it is essential to determine whether the sensitivity of the measurement system allows for a valid detection of the stiffness response which is above the measurement noise floor. One way of investigating this is by defining a noise threshold above which the identified material stiffness data could be considered as relevant and not affected by noise. The threshold can be directly obtained by analysing the identification data of one real experiment, as it will be shown in the following. Knowing a crude estimate of the noise floor, confidence intervals can be provided on which material stiffness can be estimated as an average value.

The noise floor above which the identification of the average Young's modulus is possible, can be obtained by analysing the average virtual work associated to internal and external forces as reported in [Pierron and Forquin, 2012a]. Figure 3.22 shows the time history of these two arguments used to identify the global material stiffness parameter for one concrete spall test. The noise limit can be identified by observing the highest fluctuation in both equation terms before the significant part of loading wave has fully propagates inside the material (during the first 20 frames). This allows defining the noise threshold (here adopted as two times the noise level) below which the identified values are considered not significant as the measurement is highly affected by noise structures. Then, an interval can be derived for both loading stages of the test for which the identification of the global material

stiffness is possible and would yield more meaningful results.

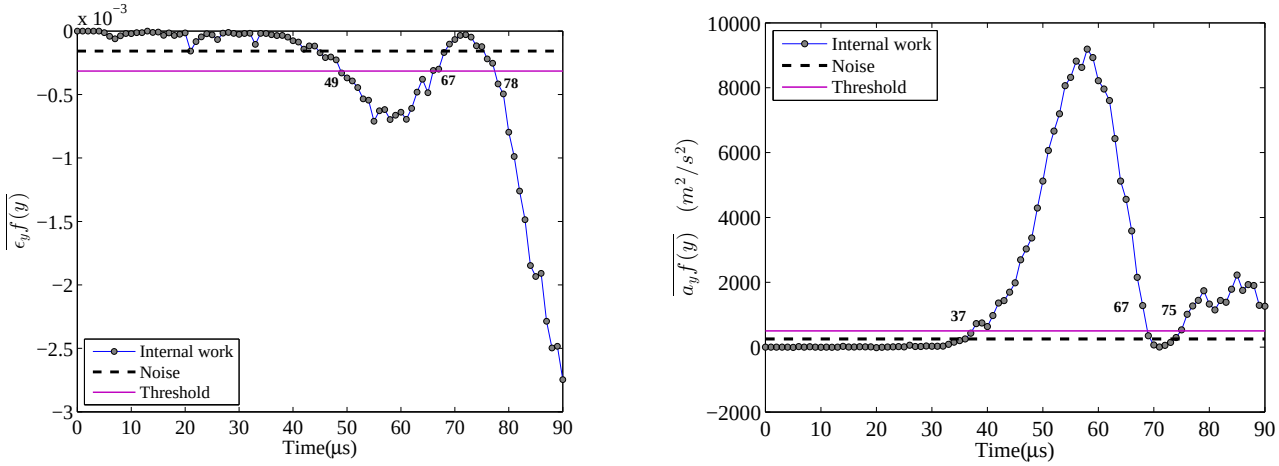

(a) R45: Internal virtual work

(b) R45: External virtual work.

Figure 3.22: Time history of surface average virtual work compliances used to obtain the global Young's modulus in a R45 spalling test.

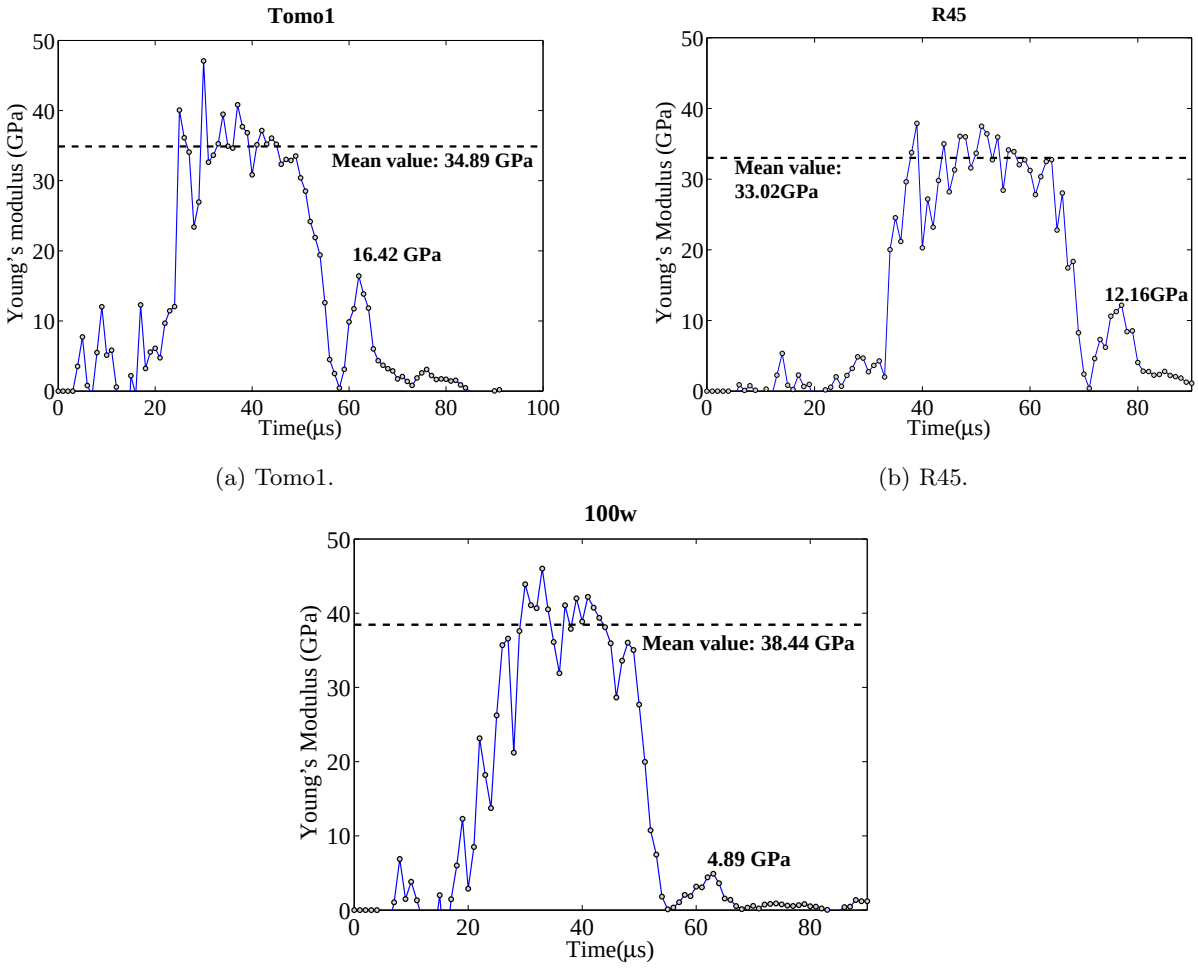

(a) Tomo1.

(b) R45.

(c) 100w.

Figure 3.23: Identified Young's modulus for three concrete samples using virtual fields of 8^{th} order polynomial.

Figure 3.23 shows the temporal identification of the global Young's modulus for performed spalling tests. The

corresponding mean value obtained on dedicated confidence interval in compression for each test is also shown as a dashed line. A more interesting part of the presented results is the second interval which corresponds to tensile loading stage. In all cases, the global Young's modulus values are much lower than in compressive stage. After reaching a local peak, the curves decrease towards zero value by the end of the acquisition. This was attributed to the damage processes that are triggered during the tensile stage, that finally lead to the formation of one or several macro-cracks as discussed in [Pierron and Forquin, 2012b]. On the other hand, the values observed in tension differ from the values obtained by performing linear regression of the local virtual gauge response (Table 3.10).

3.4.1.6 Effect of the choice of virtual fields on stiffness identification

Another reason that prevents the extraction of reliable global stiffness values is that the stability of the identification also depends on the choice of virtual fields. In the Equation 2.19, it is only necessary to choose the adequate virtual fields in order to cancel the virtual traction force on the opposite side of the sample free-end. Furthermore, the choice of virtual fields also provides a certain degree of spatial smoothing to the identified results. One way of validating a good choice of virtual fields is to treat the numerically simulated data [Pierron and Grédiac, 2000]. Here the same procedure will be applied to treat real experimental data since they contain realistic noise structures. According to the uniaxiality of the spalling test, it is fair to assume virtual fields that depend only on the axial direction. Consequently, the virtual field can be described as a vector function which can be evaluated on one 'line' of measurement points and then expanded back in the vertical direction to obtain one field. Then, this can be performed for each frame, to obtain the sequence of time-changing virtual fields. On convenient way of choosing these virtual fields is to obtain them directly from the measured displacement maps by performing a certain type of fit in the least square sense. Polynomial fitting proves to be a sufficiently suitable technique and it has been adopted in previous works [Pierron and Forquin, 2012b]. Another way is to describe one virtual field (note the use of singular) as analytical function that only depends on the sample length without changing in time. These type of fields can be referred to as stationary (or fixed) virtual fields.

To compare the performance of time-changing and stationary virtual fields when treating real experimental data (as opposed to treating synthetic data), several additional types of stationary virtual fields have been chosen, namely:

$$\text{(i)}\quad f_1(x) = (1 - \tfrac{x}{L})$$

$$\text{(ii)}\quad f_2(x) = (1 - \tfrac{x}{L})^2$$

$$\text{(iii)}\quad f_3(x) = \sqrt{(1 - \tfrac{x}{L})}$$

$$\text{(iv)}\quad f_4(x) = \cos(\tfrac{\pi x}{2L})$$

The choice of these simple functions (Figure 3.24a), apart from cancelling the virtual work of the traction force from the opposite side of the free-end ($x = 0$) at the position $x = l$ where l is the recorded length of the sample, also aims at investigating how the material spatial distribution of non-linear behaviour contributes (benefits or not) to the identification. Namely, whether enhancing the response closer to the free-end, where the fracturing occurs, would benefit (or not) the identification. The results of their application in treatment of one spalling test (Tomo1) are shown in Figure 3.24b.

From presented identification it can be seen that stationary virtual fields provide noisier identification of material stiffness compared to the time-evolving polynomial virtual fields. This effect seems more pronounced during the tensile loading stage while for the compressive loading stage some convergence can be noted. This can be simply attributed to the fact that material response rapidly evolves in time, since the complete fracturing can happen in about 20 μs. Therefore the time-changing virtual fields were chosen.

As already mentioned, one way of obtaining time-changing virtual fields is to perform a polynomial fit on the measured displacement data at each frame in a least square sense. This can be achieved by using numerical

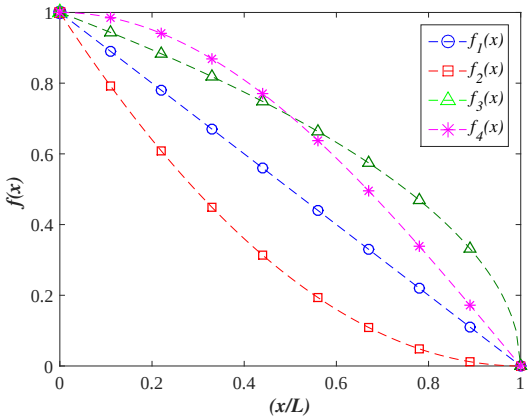

(a) Functions used to expand stationary virtual fields.

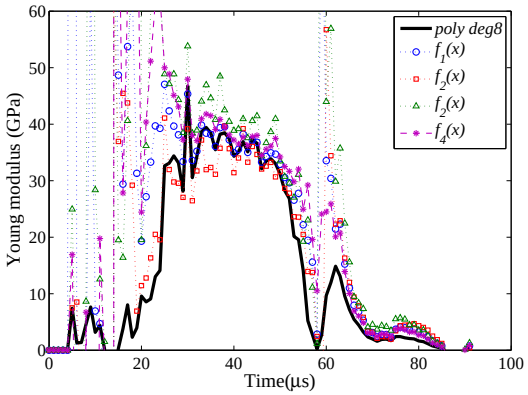

(b) Effect of the choice of virtual fields on the stiffness identification-Tomo1.

Figure 3.24: Functions used for expansion of stationary virtual fields and results on stiffness identification (Tomo1).

functions native for the Matlab environment. The fitting technique produces a certain group of polynomials. In general, on a defined domain $[x_0; x_l]$ (where: x_0 is free-end and x_l is end of observation window), we can distinguish three types of polynomials:

(i) Polynomials of a certain degree, defined on a sub-domain $[x_i - \lfloor a/2 \rfloor; x_i + \lfloor a/2 \rfloor]$ where a is the window size – The Stravinsky-Golay filter.

(ii) Piecewise polynomials defined for each unit sub-domain $[x_i; x_{i+1}]$

(iii) Special piecewise polynomials defined for each unit sub-domain $[x_i; x_{i+1}]$ that satisfy the C^2 continuity – Splines

where the $\lfloor . \rfloor$ represent the Iverson's floor function brackets.

The effect of these three general types of fitting techniques has been investigated. The effect of smoothing the displacement profiles at a given frame is shown on Figure 3.25. One averaged displacement profile (at 66 μs) is presented with corresponding result of fitting cubic polynomials or splines. The corresponding reconstructed virtual field is given in Figure 3.25c and Figure 3.25d. Already from presented maps little difference can be seen between the two fitting techniques which is also noted in the expanded virtual fields. It was noted that both produce the same result on the identified Young's modulus. This is because the displacement themselves are small and not significantly corrupted by spatial noise. A comparison between spline and polynomial fitting of 8^{th} degree to get the virtual fields is presented in Figure 3.25b. Finally, it seems that little effect has been observed between using different types of time-changing virtual fields.

One last fair question that can be asked is whether deriving the virtual fields from averaged displacement fields is in fact the best choice of virtual fields. It is one of the possible choices, which is supported by the uniaxiality of the sample deformation. However, the variations present in the axial displacement maps are caused by camera's complex noise structures which can be regarded in the least sense as random spatial fluctuations. Therefore it is worth investigating the effect of driving 2D maps of virtual fields directly from measured displacements. For this case, the spline fitting technique has been chosen and the maps of virtual fields are derived in a line-by-line manner. The effect of choosing the 2D virtual fields over averaged ones, is shown in Figure 3.26. The identified stiffness values appear lower than the one obtained from wave shifting analysis (3.7) in case for 2D splines. This can be due to possible over-smoothing of the identified results which clearly demonstrates a strong sensitivity of the identified

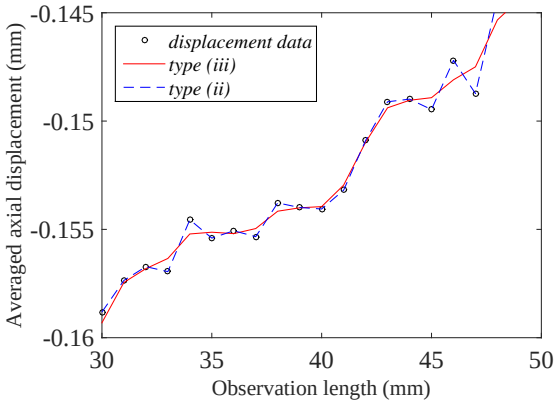

(a) Smoothing of average displacement fields at 66 μs.

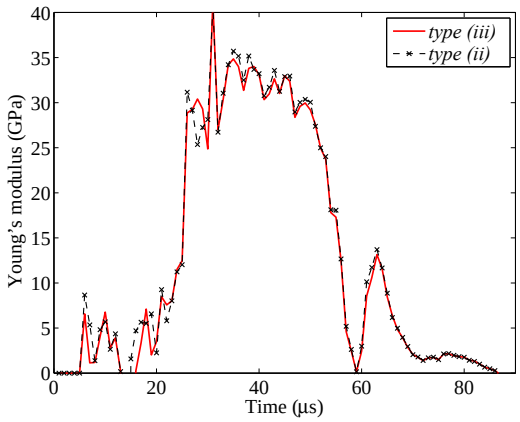

(b) Effect of time-changing virtual fields on the stiffness identification.

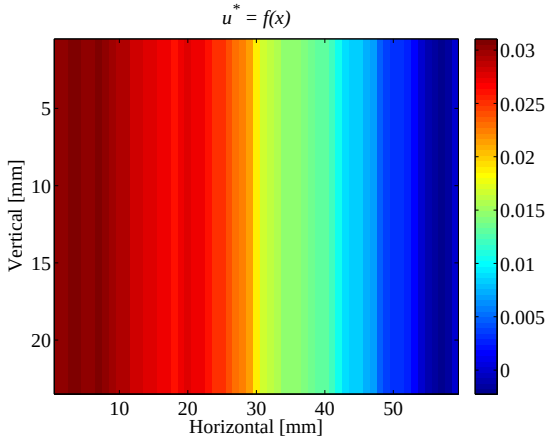

(c) Expanded virtual field at 66 μs using Splines - type (iii).

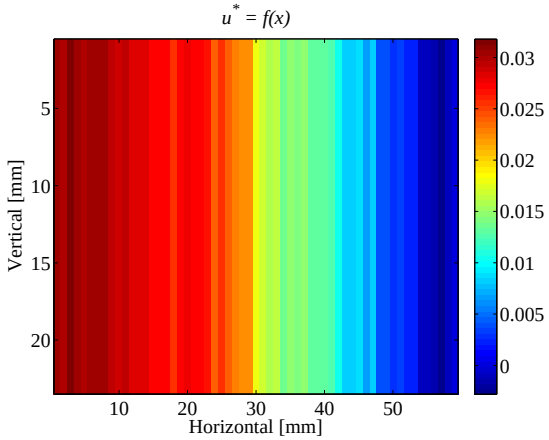

(d) Expanded virtual field at 66 μs using Piecewise polynomials - type (ii).

Figure 3.25: Effect of time-changing virtual fields and introduced smoothing in the stiffness identification (Tomo1).

stiffness values to the choice of virtual fields.

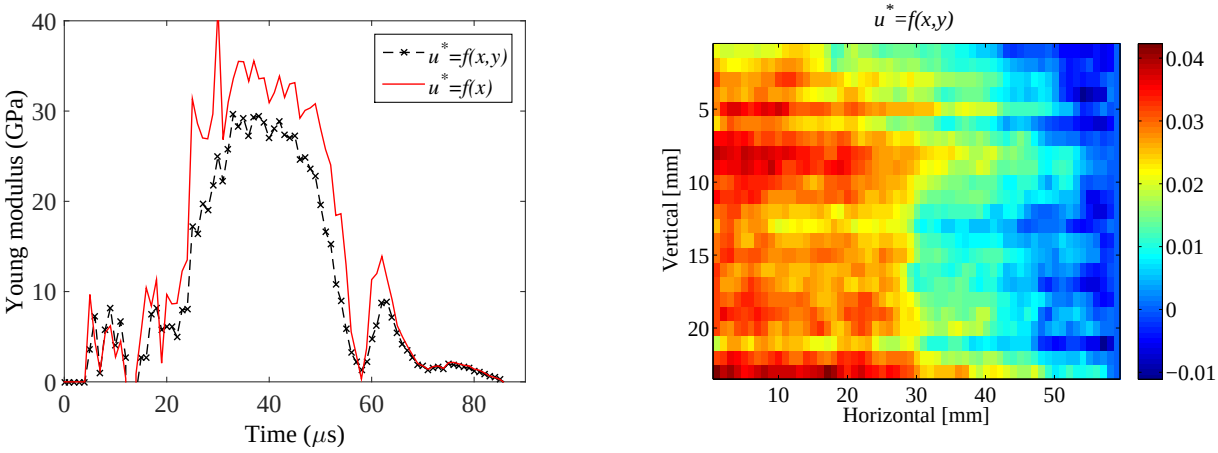

(a) Effect of the space dimension of the time-changing virtual fields on the stiffness identification.

(b) Expanded virtual field at 66 μs using 2D Spline fitting over measured displacement maps.

Figure 3.26: Effect of choosing 2D virtual fields on the stiffness identification. (Tomo1)

The polynomial fit over a range of averaged displacement data was adopted form this point onward. However, it can still be noted that, whatever the choice of virtual fields (presented herein), the method of determining the global Young's modulus prevents the extraction of reliable stiffness values in tension. The same can be noted when polynomials of a certain degree are used. For example, in that case the identification depends on the order of the polynomial used to expand the virtual fields. When the degree is too low and odd, the virtual field cannot well represent the spatially distributions of the actual fields. When higher and odd orders are used they tend to enhance the effect of noise. On the other hand using even orders can 'over-smooth' the already low values of dynamic tensile modulus. An example of using high order even polynomials is provided in Figure 3.27. In conclusion, the methodology of identifying the global Young's modulus according to Equation 2.19 does not allow for a precise identification in dynamic tension due to the sensitivity of the procedure, but rather serves as an indicator that the damage is present in the material.

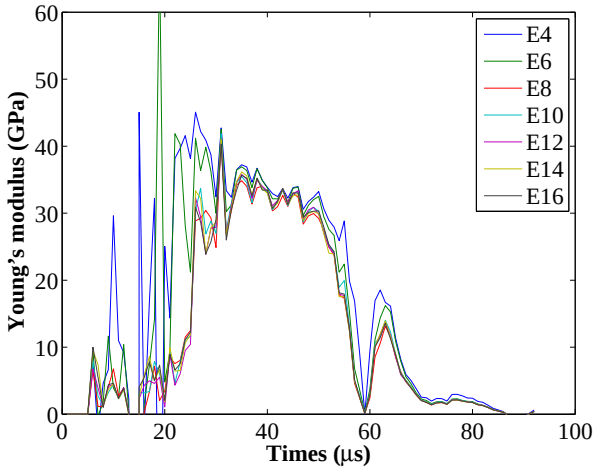

Figure 3.27: Effect of virtual displacement polynomial degree on identified Young's modulus - case of even-order polynomials. (Tomo1)

Nevertheless, the method still provides reasonable identification results during the compressive loading stage that

are closely consistent with the values of Young's modulus obtained from the measurement of unidimensional wave speed using the time shift between strain gauge and laser interferometer ($E_{dyn} = \rho C_0^2$). The results from both methods are summarized in Table 3.12 where the averaged dynamic Young's modulus in compression is obtained as an overall average on corresponding confidence intervals.

Sample	Virtual Fields Method	Wave speed measurement
R45	Mean: 33.02 Std: 3.64	42.88
100w	Mean: 38.44 Std: 4.09	42.61
Tomo1	Mean: 34.89 Std: 3.62	32.94

Table 3.12: Identified dynamic Young's modulus in GPa during the compressive stage of the spalling test by applying virtual fields method and wave speed measurement.

3.4.1.7 Representation of field of Young's modulus

Finally, the previous method only allows the identification of a global stiffness value. The load cell principle provides the ability to obtain local stress and strain for each visualized cross-section of the sample. Then, the analysis of the identified Young's modulus can be carried out on all transverse sections at each time step and and entire map of stiffness can be derived that provides a local description of the Young's modulus at each measurement point. The space-time map of dynamic modulus at each time step and at each measurement point is simply obtained as:

$$\overline{E_{field}(x,t)} = \overline{\sigma(x,t)}./\overline{\varepsilon(x,t)} \tag{3.4}$$

where $\overline{E_{field}(x,t)}$ in this case can be referred to as a field of Young's modulus that describes the local stiffness of the observed sample surface, as a cross sectional average denoted with the over-line symbol. Obviously, at certain time steps when the acceleration is too small and at locations where the strain values are low, the local stiffness values would not be relevant. This is also the case at locations where the strain values go to zero during the transition between the compressive and tensile loading stages. Finally, this procedure is not affected by additional spatial smoothing as it does not depend on the choice of the virtual fields and can indicate possible zones of spatially varying stiffness. The reconstructed stiffness map for one tested sample is reported in Figure 3.28. The map on the right presents a zoom in region of the tensile loading stage with adjusted color bar scale.

The presented map again indicate the two loading stages of the spalling test. Although affected by noise that has propagated from the image acquisition system, it can be seen that the values of Young's modulus are much higher in the compressive stage than in the tensile stage, as expected. Interestingly, the maps also show that the stiffness values are not well identified during the compressive stage in the first 10 mm from the free-end surface after which they start to pick up. The reason for this is that in the zone close to the free-end, where the wave reflection takes place, the strain and stress values are quite low due to wave superposition. This is not taken into account when global Young's modulus is being determined. When maps are zoomed in the zone that corresponds to the time when the tensile wave becomes dominant 3.28b, it becomes clearer that the identification of the dynamic Young's modulus does not reach the same value as in compression. Some zones close to the free edge and in the first several micro seconds of the forming of the tensile wave (60-65 μ s), the tensile stiffness values are in the range of 10 to 25

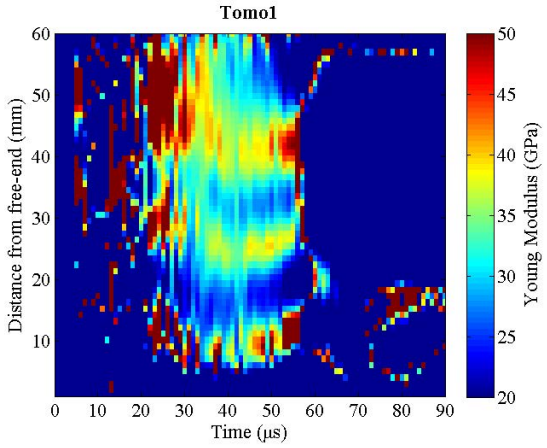

(a) Field of Young's modulus in compression stage.

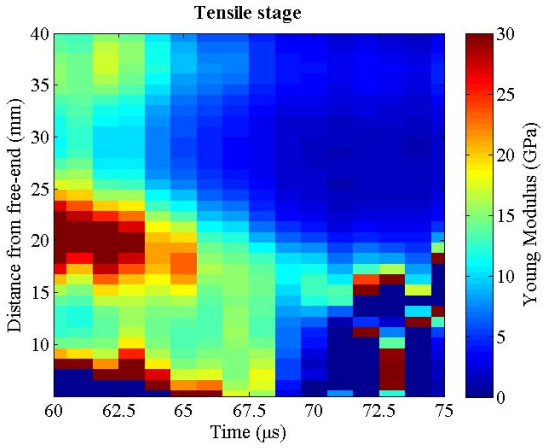

(b) Field of Young's modulus in tensile stage.

Figure 3.28: Space-time map of identified Young's modulus. (Tomo1)

GPa. However, immediately after, they drop and tend towards zero.

Finally, another interesting observation is that stiffness maps exhibit a certain spatial variation in the compressive part, 3.28a. The patterns seem constant in time and therefore the noise cannot be entirely attributed to the temporal camera noise. Being a highly heterogeneous material, one of concrete's constituents are strong siliceous aggregates which cause a local material stiffness variation. Using basic evaluation with simulated experiments and one elastic heterogeneity (Section 4.4.2.2), it was shown that the local stiffness variation can manifest in such way.

3.4.2 Numerical simulations

In the previous section the spalling experiments were treated with both traditional and full-field measurement techniques. The virtual fields method was used to identify the material response from full field displacements using the acceleration maps as an alternative load cell as proposed by [Pierron and Forquin, 2012b]. It was possible to reconstruct the stress–strain curves of each tested sample at any given cross-section visualised with the ultra-high speed camera. The results shown that the value of peak stress obtained from the stress–strain curves was constantly lower than the one obtained with Novikov processing. The identified Young's modulus in dynamic tension was in all cases lower than the stiffness obtained in the compressive stage of the test. Furthermore, the non-linear response prior to the peak stress was observed in reconstructed stress-strain curves. Both of the last two mentioned observations are contradictory to traditional Novikov processing of the spalling tests. In this section, the effect of both change of Young's modulus and pre-peak non-linearity on the Novikov processing of test results is explored through explicit FE numerical simulations using a material damage model.

Firstly, linear elastic up-to peak stress response is modelled, accounting for the difference between tensile and compressive stiffness observed in the experimental results (Figure 3.18). The simulation results show that without changing the failure stress criterion, the rear face velocity is largely affected by the dissymmetric concrete response which can ultimately lead to errors in estimating the apparent tensile strength by using the Novikov data processing. An inverse identification is in this case performed in order to qualitatively fit the numerically rear face velocity profile to the experimental one up-to the first rebound. It was shown that both peak stress and the stiffness dissymmetry response identified by using the VFM and ultra-high speed displacement measurements need to be taken into account in order to have a fairly good agreement between the numerical and experimental velocity curve, since only the change in the dissymmetry factor influences the velocity rebound. Secondly, both the dissymmetric response and the pre-peak non-linear response were considered. In this case the assumption on the Novikov processing are being violated. The pre-peak non-linear response can introduce a second rebound which

is related to material failure while the first rebound is related to peak elastic response. It was shown that the pre-peak non-linear response can cause confusion on which velocity rebound needs to be taken into account when real experiments are processed. Both of the cases and their effect on the traditional processing were discussed, suggesting that the one dimensional linear elastic approximation (The Novikov formula) is not a valid tool for retrieving reliable values of spall strength in concrete-like materials [Sallier and Forquin, 2012].

3.4.2.1 Numerical modelling

The 3D finite element model of a spalling sample was created in order to simulate the mechanical response of concrete under dynamic tension using Abaqus/Explicit software. The model considers concrete material as a homogenized medium to which a constitutive material response is assigned to simulate the mechanical response due to damage. Damage is represented by modelling the material softening response after a peak material strength is reached. A simplified version of the damage model known as the PRM model (Pontiroli, Rouquand and Mazars) [Rouquand et al., 2007] is used to simulate the dynamic spalling tests through a user subroutine VUMAT. This model permits to explicitly impose the level of tensile strength (peak stress in tension). The model incorporates Mazars damage law [Mazars, 1986] and a dissymmetric parameter that can reproduce different linear response of concrete in compression and tension prior the peak stress. Furthermore, by loosening the control on the model parameters, it is also possible to model a pre-peak non-linearity in the stress-strain constitutive tensile response. This allows exploring several cases of material response and their impact on measured rear face velocity. The sample geometry is the same as in the experimental part with a length set to 140 mm and a diameter equal to 45.5 mm. The C3D8R elements (three dimensional elements with reduced integration and eight nodes) were used to generate a mesh of 35140 elements with the average element size of 2 mm. The mesh size was chosen according to the mesh sensitivity study reported in [Sallier and Forquin, 2012]. The loading boundary condition was considered as a distributed pressure pulse with the temporal distribution obtained from an actual experiment. Instead of simulating the entire spalling setup the experimental loading pulse was applied directly on the bar-specimen interface which was shown to be a good approximation from the numerical point [Lu et al., 2013]. Numerical simulation showed that the variation of peak rear face velocity considering all nodes on the free-end is 1.4% of the average peak velocity in linear elastic case. Therefore, the rear face velocity profile was obtained as an average velocity of the entire set of nodes that constitutes the free-end of the numerical sample.

3.4.2.2 The Damage model

Under uniaxial loading condition, where the damage is only considered to take place during the tensile loading, the governing equation of the damage model used in this work is the following:

$$\sigma = E_c \langle \varepsilon \rangle_- + (1 - D_t) E_t \langle \varepsilon \rangle_+$$

where σ is the macroscopic axial stress component in the material, $\langle \varepsilon \rangle_-$ and $\langle \varepsilon \rangle_+$ are the negative part and the positive part of the axial strain in compression and tension respectively, E_c and E_t represent linear elastic material stiffness in compression and tension respectively and D_t is the internal damage variable in tension that is in the domain [0, 1] where value 0 corresponds to perfectly elastic virgin material and 1 to completely damaged state. The damage evolution law is dictated by the amount of ultimate deformation that the material can experience during the loading. In the present case, a simplified version of the model was used to describe the material response subjected to tension while in the compression the material is assumed to behave perfectly linearly elastic. The damage starts if the axial strain in the material surpasses a threshold value defined as ε_0. The damage evolution law for a uniaxial tensile case reads:

$$\begin{cases} \varepsilon < \varepsilon_0 \implies D_t = 0 \\ \varepsilon \geq \varepsilon_0 \implies D_t = 1 - \frac{\varepsilon_0(1-A)}{\varepsilon} - \omega A \exp(-B(\omega\varepsilon - \varepsilon_0)) \end{cases}$$

where the constant A is the characteristic material parameter, $B = 1/\varepsilon_0$ is obtained from the ultimate stress criterion $\varepsilon_0 = \sigma_u/E_t$ where σ_u is the maximal stress limit after which the damage starts taking place and ω is a regularization parameter based on the Hillerborg dissipated energy concept to limit the mesh dependency during strain and damage localization phenomena [Hillerborg et al., 1976]. The regularization method is introduced by modifying the damage evolution law in such way that it ensures a constant dissipated energy per surface unit in a single finite element regardless of the element size (L_{fe}). To this end, a concept of internal characteristic length is introduced (L_c) based on the defined input fracture energy (G_f). Finally, the regularization parameter ω is expressed as follows:

$$\omega = \frac{\varepsilon_0}{\varepsilon} + (1 - \frac{\varepsilon_0}{\varepsilon})\frac{L_{fe}}{L_c} \text{ where } \; L_c = E\frac{G_f}{\sigma_u^2}$$

However, the regularization procedure, when used with small finite elements, can lead to a dissipated energy and velocity profile on the rear face that are sensitive to the mesh size [Sallier and Forquin, 2012]. Indeed, it was shown that for a ratio between the internal characteristic length and the finite element size above 4 the dissipated energy substantially increases. In that case, the simulated free-end velocity profiles are strongly affected after the first rebound due to the development of a quasi–elastoplastic stress–strain behaviour caused by reduced mesh size [Sallier and Forquin, 2012]. An adequate mesh size needs to be chosen as a compromise between the good spatial discretisation of the numerical model on one hand, and the dissipated energy within the system on the other hand. According to the mesh sensitivity study presented in [Sallier and Forquin, 2012] as a general guideline can be adopted $L_c/L_{fe} \leq 4$. In the case when the regularization is not used ($\omega = 1$) the description of the damage law becomes simplified as follows:

$$\begin{cases} \varepsilon < \varepsilon_0 \implies D_t = 0 \\ \varepsilon \geq \varepsilon_0 \implies D_t = 1 - \exp(1 - \varepsilon/\varepsilon_0) \end{cases}$$

The stress evolution of the material response under tension and the corresponding damage evolution law for the case when the regularization is omitted, are presented in Figure 3.29. It is worth mentioning that the applied constitutive law perfectly corresponds to the assumptions made when the spall strength is determined using the Novikov processing. The material behaves linearly elastic up-to point where the ultimate stress is reached after which the response is governed by the damage evolution law.

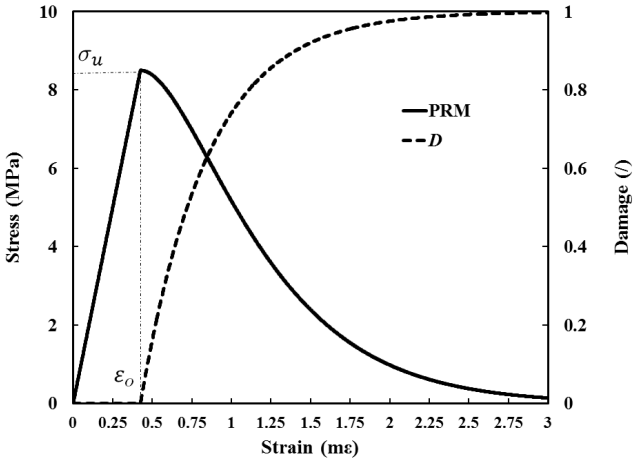

Figure 3.29: The tensile behaviour of the damage model used to simulate the spalling experiments with parameters: $E_c = 35.5$ GPa, $\sigma_u = 8.5$ MPa, $\omega = 1$ and $A = 1$.

3.4.2.3 Numerical results – Effect of dissymmetric response

In this case,the assumption of liner elastic response up-to peak tensile stress is adopted, however, the effect of the dissymetric response between compression and tension is analysed. Since the aim is to investigate the effect of material non-symmetric response on the rear face velocity profile up-to the first rebound, the Hillerborg's regularization technique was omitted by setting the value ω to 1. Figure 3.30 shows the effect of different parameters of the isotropic damage model on the rear face velocity profile in the simulated spalling tests. While the ultimate tensile stress only influences the value of the velocity rebound as expected (Figure 3.30a) a very interesting observation is that the dissymmetrical response, taking into account the different Young's moduli in compression and tension, also has an important effect on the values of the velocity rebound (Figure 3.30b). It is clearly observed that the lower the ratio between the tensile and the compressive stiffness the larger is the value of the velocity pullback (the difference between maximal velocity and the velocity at rebound). This further implies that without taking into account the non-symmetric response of concrete in the spalling experiments, the determined values of the apparent spall strength can be overestimated. Finally, it can be also observed that the deceleration part of the velocity profile (after the peak velocity is reached, that corresponds to the compression to tension loading transition in the sample), is also affected by the dissymmetry factor. This can better explain, in that case, the measured results obtained from the shifted compressive gauge and the laser interferometer in Figure 3.14a. From the figure it can be observed that there is a misalignment of the two reconstructed stress response curves in the deceleration part.

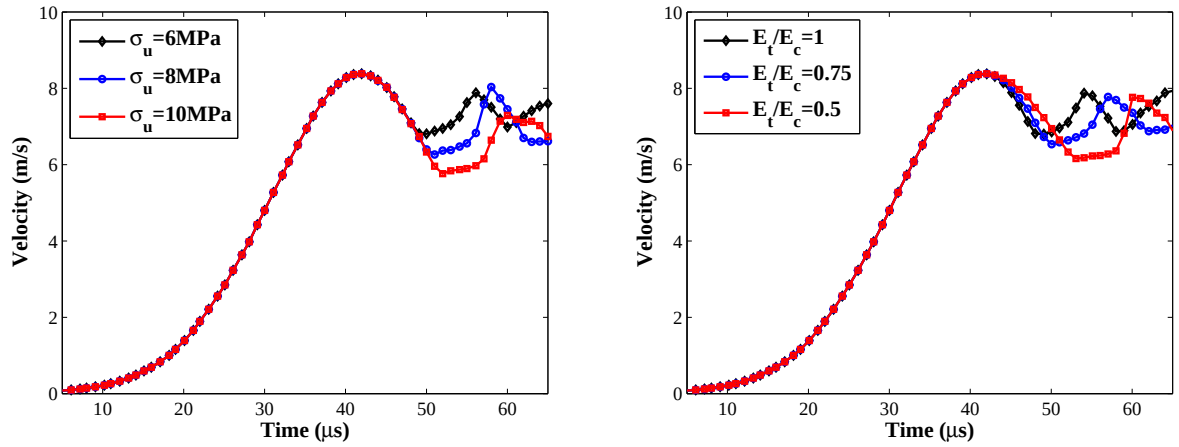

(a) Effect of different ultimate strength with no dissymmetry response ($E_c = 35.5GPa$, $E_t/E_c = 1$, $\rho = 2200kg/m^3$, $\omega = 1$, $A = 1$).

(b) Effect of different dissymmetry factors along with a constant ultimate strength ($E_c = 35.5GPa$, $\sigma_u = 7$, $\rho = 2200kg/m^3$, $\omega = 1$, $A = 1$).

Figure 3.30: Results of the numerically simulated rear face velocity profiles and the effect of model parameters when linear elastic up-top peak assumption is adopted.

It has to be mentioned that the PRM model used in obtaining these results still completely adopts the assumptions made on the material behaviour when experimental results are being processed (linear-elasticity up-to peak). Interestingly, the results presented in Figure 3.30 indicates that if this assumption as well as the assumption of instantaneous failure were valid, the change in ultimate tensile strength would indeed only influence the velocity rebound. However, the experimental results presented in Section 3.4.1 demonstrated non-symmetric response in compressive and tensile stages, which questions the applicability of Novikov processing when concrete-like materials are investigated.

In order to further explore the validity of the material response identified using the full-field measurements and the virtual fields method as well as the reliability of the Novikov processing, an iterative inverse identification is performed based on reproducing the rear face velocity profile. The simulations of the spalling experiments was per-

formed with the PRM numerical model assuming a perfect linear-elastic response in compression while describing a damage response in tension along with a reduction of material stiffness prior the stress peak. The FE computations have been performed using the input data obtained from the experimental measurements (compressive pulse) and the numerical results have been compared to the experimentally measured rear-face velocity profile. The comparison between the numerically simulated and experimentally measured rear face velocity profiles for one concrete sample is depicted in Figure 3.31. The Hillerborg regularisation technique was used for the sake of obtaining the curves with the similar post rebound response. However, it needs to be mentioned that in this case the most important result to be compared to experimental data concerns the simulated velocity rebound.

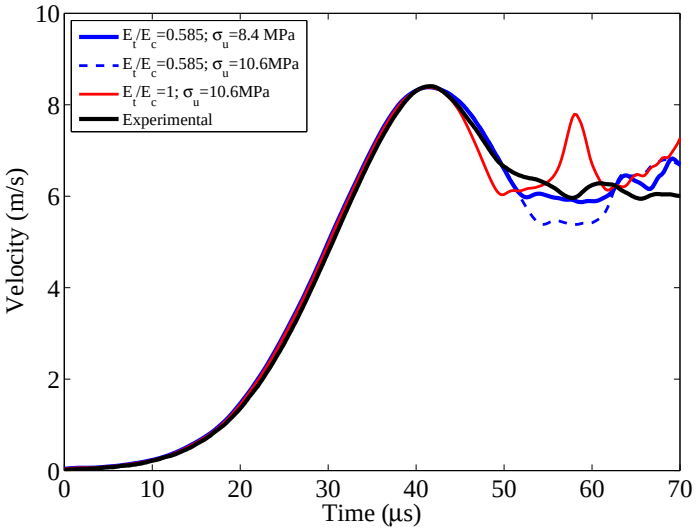

Figure 3.31: Results of the inverse identification of the experimental velocity profile using the PRM model and data obtained from the VFM identification. (Tomo1)

The obtained numerical results demonstrate that both the change of the material stiffness and the ultimate tensile strength influence the rear-face velocity pull-back. In the present case, the non-symmetric response in compression and tension is considered in the numerical simulations through a bi-linear change in material elastic stiffness while strain softening and loss of tensile stiffness is modelled using Mazars' damage law. The experimental specimen analysed in the presented case is labelled as Tomo1 concrete sample. The numerical simulation results in Figure 3.31 have been performed for three distinct numerical test configurations. First one considers only the input parameters obtained utilizing the traditional processing of experimental data, namely the Novikov ultimate tensile stress (σ_u =10.6 MPa) and linear symmetric response in compression and tension ($E_t/E_c = 1$). The second, considers only the data obtained from the virtual fields method processing and full-field measurements, namely a lower ultimate tensile stress (σ_u =8.5 MPa) and a disymmetric material response ($E_t/E_c = 0.585$). Finally, the third numerical test considers the Novikov ultimate stress (σ_u =10.6 MPa) as the damage onset parameter and the non-symmetric response obtained from applying the virtual fields method ($E_t/E_c = 0.585$), making it a combination of the two processing techniques. The parameters of the PRM model used in the above mentioned numerical simulations are given in Table 3.13.

The numerical results (Figure 3.31) indicate that the experimentally tested sample indeed stayed in the domain of linear elasticity in the compressive stage owing to the fact that that all three simulated velocity profiles correspond well to the experimental curve up-to the peak velocity. The more significant part of the curves is after the peak velocity where the wave reflection takes place. In this domain the numerical curves start to display different tendencies. Both numerical velocity profiles for the first and second numerical configuration (see Table 3.13) exhibit the same value of the pullback velocity which is close to the experimental one. However, different ultimate tensile strengths were considered as the input parameters. What seems to be more striking is that if the

Case	Data	Density (kg/m^3)	E (GPa)	ν	σ_u (MPa)	G_f (J/m^2)	L_c (mm)	A, B	E_t/E_c
1	VFM	2290	35.5	0.2	8.5	15	7.37	1, 1	0.585
2	Novikov	2290	35.5	0.2	10.6	15	4.74	1, 1	1
3	Novikov and VFM	2290	35.5	0.2	10.6	15	4.74	1, 1	0.585

Table 3.13: Parameters used in the spalling simulations with the PRM model fulfilling Novikov assumptions.

curve for the second configuration is treated with the Novikov approach, the failure stress obtained would be close to 10.6 MPa while the ultimate failure stress used as an input in the damage model is 8.5 MPa. Additionally, the deceleration part of the velocity curve obtained with the VFM data (second case) somewhat better matches the experimental one after the peak velocity. The small discrepancies between these two curves can be attributed to the fact that the numerical model used is assuming perfect linear elasticity to the peak stress and approximates the non-symmetric response as a bi-linear response (which will be taken into account in the following). Finally, when the third configuration is considered, the simulated velocity rebound largely overestimates the experimental response leading to an error of about 15% in pull-back velocity.

3.4.2.4 Numerical results – Effect of material non-linear response

Owing to its complex microstructure, concrete material behaves in a non-linear way before the failure takes place. It was observed from the experimental results that the material exhibits a non-linear response before the peak strength is reached (Figure 3.18). In order to explore the effect of the non-linear material response on rear-face velocity profile, numerical simulations of the spalling experiments were performed with the PRM numerical model but in this part one of the coefficients describing the Mazars damage model was 'loosened' in order to introduce a non-linear relation in the stress-strain response prior the peak. The considered case was based on:

- Completely violating the Novikov assumptions regarding linear response up-to peak stress.
- Modelling the same peak stress by adjusting the corresponding linear elastic limit and the non-linear response parameter so to see the effect of pre-peak non linearity on rear-face velocity profile.

The Figure 3.32 presents numerical configurations considered and the corresponding results. The parameter B and corresponding elastic limit (σ_{el}) were changed accordingly so to consider three cases of material non-linearity with same peak stress: *weak*, *mild* and *strong*, keeping the peak stress constant. The analytical solution for the constitutive response and the damage variable considering three types of pre-peak non-linearity are given in Figure 3.32a,b. In this way all the assumptions of the Novikov processing are being violated. The result on the simulated rear face velocity for the three cases of non-linearity are presented in Figure 3.32c. From the figure it is clear that the velocity pull-back at the first rebound reduces, which was as expected. However, what is more interesting is how the pre-peak non-linearity influences the post-rebound part of the simulated velocity curve. Moreover, the case referred to as *strong* non-linearity, indicates such change in the post-rebound part of the velocity curve that it makes the first rebound almost *invisible*. It is worth noting that no regularisation was used in these simulations and the parameters of the PRM model used are summarized in Table 3.14. Finally, a qualitative inverse identification was performed using the experimental data as in the previous section. It serves to show that, indeed, the velocity curve contains all possible history of non-linear events that occurred in the material and not only the ones associated to failure. The results of this identification are shown on Figure 3.32d.

3.5 Chapter summary

In this chapter, spalling test that had been conducted having both traditional point-wise and full-field measurements were analysed. An ultra-high speed camera, the Shimadzu-HPV1, has been used to film the surface of grid

Case	Density (kg/m^3)	E (GPa)	ν	σ_u (MPa)	σ_{el} (MPa)	A	B/1000	E_t/E_c
Weak	2290	35.5	0.2	8.5	8.03	1	2.07	0.585
Mild	2290	35.5	0.2	8.5	7.01	1	2.53	0.585
Strong	2290	35.5	0.2	8.5	5.14	1	3.09	0.585

Table 3.14: Parameters used in the spalling simulations with the PRM model violating Novikov assumptions: Second case-study.

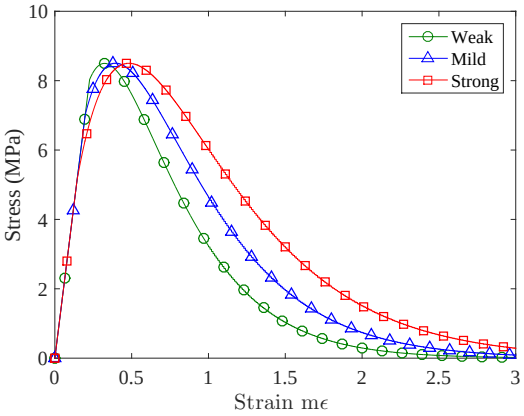

(a) Analytical solution of stress-strain response for three combinations of (B, σ_{el}).

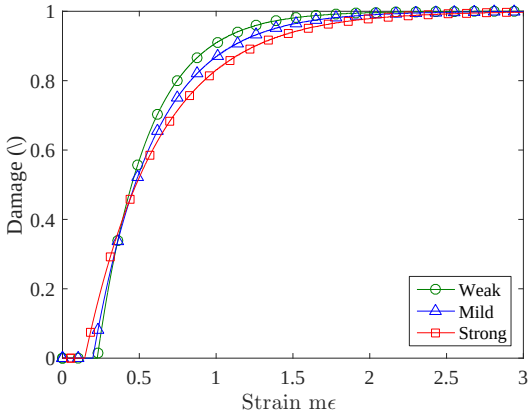

(b) Analytical solution of damage response for three combinations of (B, σ_{el}).

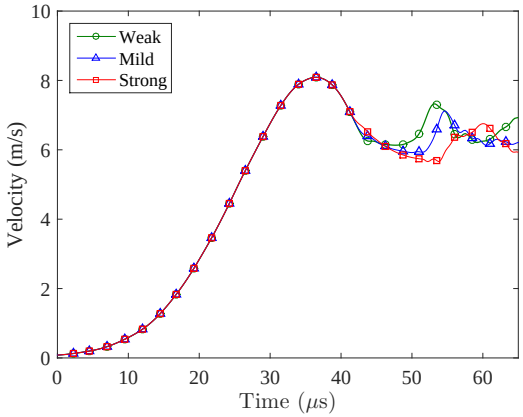

(c) Effect of pre-peak non-linearity on simulated rear-face velocity profile.

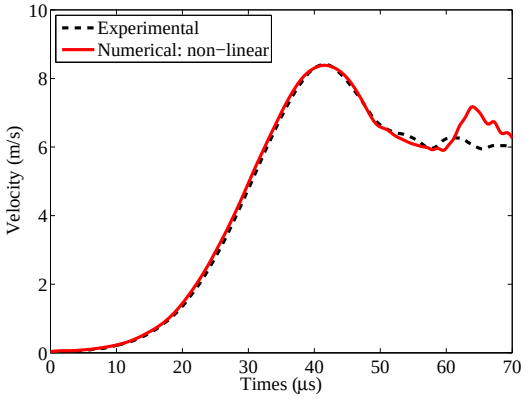

(d) Inverse identification with non-linear pre-peak damage modelling: $E_c = 35.5GPa$, $\nu = 0.2$, $\sigma_{el} = 6.5MPa$, $\sigma_u = 8.3MPa$, $A = 1$, $B/1000 = 2.57$, E_t/E_c=0.7.

Figure 3.32: Effet of pre-peak non-linearity on the numerically simulated rear face velocity profiles. Second case-study: constant peak stress (σ_u). Parameters provided in Table 3.14

instrumented samples with an inter-frame time of 1 μs. The virtual fields method was used to exploit the inertial component of the test to obtain average axial stress history in a cross-section and the evolution of the global Young's modulus in time, without making any previous assumptions on material behaviour. First test series considered a sample made of an aluminium alloy that was loaded within the material linear elastic limit. The comparison between the identified and the expected linear elastic response allowed choosing optimal experimental settings by testing several factors such as the influence of camera frame rate, illumination conditions and lens blurring. Then, several spalling tests performed on concrete material were analysed in regard of identifying the material damage response under dynamic tension. The results showed that the concrete material exhibits non-symmetric response in compression and tension as well as a non linear response prior to the peak tensile strength. These were observed thanks to having the ability of reconstructing entire local stress-strain curves at any visualized sample cross-section. As previously observed in [Forquin et al., 2013], the identified tensile strength from the stress-strain response was found to be lower than the value obtained when the traditional Novikov processing of the rear-face velocity is used. This indicated that, due to the assumption of linear elastic behaviour and the unitary value of material stiffness in compression and tension, the use of the velocity pull-back can lead to erroneous conclusions regarding the tensile strength of quasi-brittle materials.

Numerical simulations have been carried with a damage model in order to further investigate the reliability of the Novikov processing of spalling experiments. The used damage model, aside from modelling the material softening response, allowed to account for the experimentally observed phenomena such as pre-peak non-linearity and non-symmetric stiffness response between compression and tension. Several numerical situations were investigated and the simulation results were compared to the experimental data with respect to the rear face velocity obtained from the laser interferometer. The following was observed:

- The change of ultimate tensile stress in the damage model only leads to the change of the velocity rebound, while the change in the dissymmetry factor of material elastic response influences both the value of the velocity rebound and the deceleration part of the velocity curve.
- In the case when the experimentally identified values of peak tensile stress and the material non-symmetric stiffness response obtained with the VFM processing are used as input parameters, the numerical simulation was able to well reproduce the rear-face velocity profile.
- When pre-peak non-linear response is taken into account it was observed that the rear face velocity exhibits multiple rebounds which can make the data processing difficult since the first rebound is noted necessary tied to the situation when the peak failure stress is reached.

The presented results herein indicate that the rebound velocity does not represent a reliable way of determining the ultimate tensile strength. The reason is mainly due to the fact that the entire damage history, including pre-peak non-symmetric response caused by micro-cracking is embedded in the measured velocity profile. And if this is not taken into account, the simple acoustic approximation and the velocity pull-back seem not to be valid as a spall criterion. On the other hand, the virtual fields method does not rely on any material constitutive assumptions and instead of one measurement provides rich fields of information that can be used for material identification. This technique allows direct identification of the non-symmetric material response and direct measurement of local strains and strain rates on the sample surface. Furthermore, it allows reconstruction of average longitudinal stress profiles using only the acceleration data.

Nevertheless, this photomechanical identification technique, although clearly superior to traditional processing with regards to the amount of information it provides, it strongly depends on the performance on the ultra-high speed acquisitions system as well as all possible noise sources that can propagate from the captured images to the identified results. These different sources of uncertainty should be well understood in order to reduce the unfavourable sources of errors as much as possible and increase the reliability of measured results. Indeed, due to

lack of standards and procedures, it is difficult to well asses the metrological performance of a full field identification method and methodologies that try to model the whole acquisition chain from the imaging through the measurement field to the parameters identification should be adopted to address this issues [Sur and Grédiac, 2017]. The use of simulated photomechanical tests can serve as a good tool for investigating such effects and can represent a small step towards a big picture of generating synthetic image data sets wich can be used to provide guidelines as well as to assess the accuracy of full field identification methods [Reu et al., 2017]. One such methodology for validating the identification technique as well as investigating possible error sources is adopted in the following Chapter 4.

Chapter 4

Simulated photomechanical experiments

Chapter 3 has experimentally demonstrated how acceleration can be used as an alternative load cell to provide a direct stress measurement at high strain rates. Average axial stress can be obtained at any cross-section visualised with an ultra-high speed camera by measuring axial acceleration fields. This principle can be used for the reconstruction of the material stress-strain response, providing direct identification of material stiffness parameters and information on the material limit strength. In this chapter, this concept is explored through numerical simulations. The aim is to reproduce a realistic experimental measurement chain in order to validate the proposed processing method and explore its sensitivity to various external effects. Therefore the chapter is organised into two main parts. The first part focuses on the validation of the processing method. The dynamic response of an elastic material model is simulated using Abaqus/Explicit in order to provide time-resolved kinematic fields that present perfect data for validation. The simulated kinematic fields are extracted from the numerical model and processed using the VFM to identify the material response. The identification procedure is validated by comparing the obtained material elastic stiffness parameter with that of FE simulation. The second part explores the sensitivity of the proposed measurement method. In general, when dealing with full-field measurements, the measured displacement fields are often corrupted with certain non-mechanical content usually referred to as measurement noise. These additional artefacts can cause systematic and/or random identification errors depending on their origin and start to propagate already at image forming. In order to better understand how these effects can impact the identification procedure, a methodology of simulating the entire measurement chain starting from image acquisition to material identification was developed. First, an artificial reference grid image is generated assuming a perfect camera. Then, sequences of deformed images are obtained by numerically deforming the reference image using FE displacement fields, imitating acquisition process of an ultra-high speed camera. Finally, the synthetic images are treated as real experimental ones and identified material response is compared to the expected one. Various external effects can be added to the synthetic images in a controlled manner. The procedure then provides a deeper understanding of the method's sensitivity as well as principal guidelines on how to perform the photomechanical experiment more efficiently, trying to reduce the unfavourable sources of errors.

The following chapter represents an extended and reproduced version of:
B. Lukić, D. Saletti,P. Forquin. Use of simulated experiments for material characterization of brittle materials subjected to high strain rate dynamic tension. Philosophical Transactions of The Royal Society A, ***375****:20160168, (2017).*

4.1 Validation based on simulated elastic measurements

As shown in Section 2.4, both global Young's modulus as well as average axial stress can be obtained from the acceleration measurements using the virtual fields method (VFM). In the following section, the identification of pure elastic material response is demonstrated with numerical simulations considering an isotropic numerical model of an aluminium spalling sample.

4.1.1 3D Numerical model of a spalling test

An explicit three-dimensional FE model of an aluminium spalling sample, assuming linear elastic material behaviour, was generated using the corresponding specimen geometry and loading conditions of a real test. The

numerical model mesh is shown in Figure 4.1a. The mechanical response of this model was simulated using Abaqus/Explicit to produce time-resolved full-field kinematic data. The temporally resolved fields were computed in the region of interest that corresponds to the specimen surface framed in an actual experiment. The FE mesh of the sample model has a length of 120 mm and diameter of 45.5 mm with the flattened surface geometry corresponding to the one used in the actual experiments. The FE kinematic fields were extracted at corresponding nodal positions including the edges of the sample in the region of interest of length 120 mm and width 24 mm. The mesh size was designed to provide the same number of data points that could be obtained experimentally employing a grid method by considering a perfect grid of 1 mm pitch. In order to obtain corresponding numerically simulated fields, the time increment was reduced to 1 ns, whereas the data were stored every 500 ns (200 steps over 100 μs) to simulate a 2 Mfps acquisition rate of a virtual camera allowing to having 500 iterations between every two output step frames. This was chosen on the expense of the increased simulation time because it provides sufficient stability of kinematic fields since any high frequency numerical noise can impact the identification procedure, as it will be shown later on. The FE simulation details are summarized in Table 4.1. The mesh geometry was chosen in order to obtain the field results independent of the mesh size *i.e.* the chosen elements were sufficiently small, so that any further refinement would not result in notably different displacements. The loading boundary condition was considered as a distributed pressure pulse with the temporal distribution obtained from an actual experiment [Saletti and Forquin, 2015]. Rather than simulating the whole experimental set-up, the spalling sample was modelled by directly applying the loading pulse on the bar–specimen interface based on the fact it has been numerically shown that two approaches are fairly similar [Lu et al., 2013]. This is mainly due to the fact that the dispersion effects of the smoothed wave travelling through small diameter bar (45 mm in this case and of 1.2 m in length) are relatively small and can be considered as negligible. This pulse is characterized by an extremely short overall loading time of about 60 μs and an increased rising time of 35 μs. The prolonged rising time is obtained with a specially designed pulse-shaping technique that uses a hemi-spherical projectile to smooth the temporal distribution of the pulse [Erzar and Forquin, 2010]. The amplitude of the pressure pulse used is shown in Figure 4.1b. The material parameters considered are those of an aluminium sample with perfect elastic behaviour. The FE simulation details and the material parameters used are provided in Table 4.2.

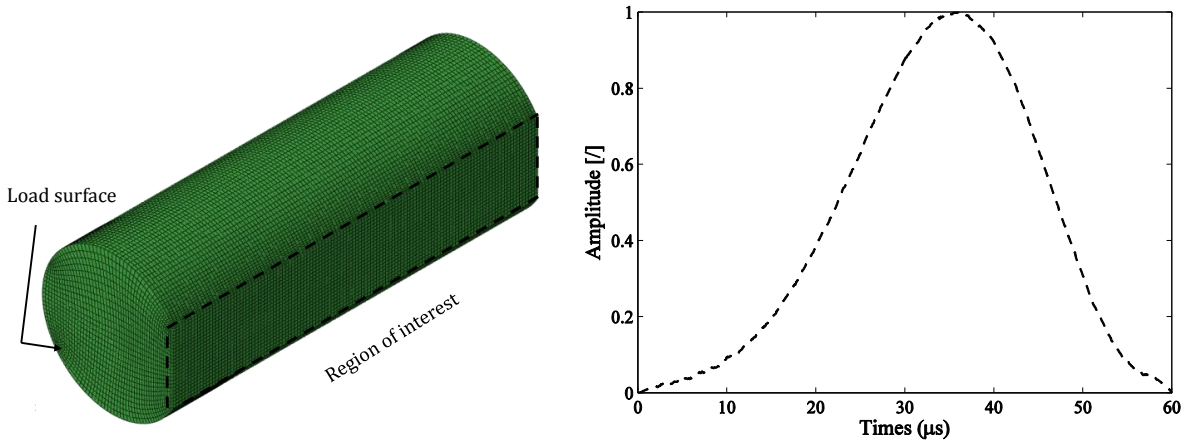

(a) FE mesh of a spalling test with a flattened region of interest.

(b) Amplitude of the experimental loading pulse.

Figure 4.1: 3D Numerical model used to generated perfect-elastic displacement fields.

In the VFM processing the axial stress field is assumed homogeneous in the cross-section which facilitates the derivation of the Equation 2.22. 3D numerical simulations present a good tool to verify if, for the case of a homogeneous elastic response, the stress at the surface is within close range to the averaged stress in the cross section. Also, this allows estimating the eventual gap between axial stress level on the surface and that in the bulk.

Mesh size (mm)	1
Element type	C3D8R (reduced integration)
Inter-frame time (μs)	0.5
Time increment (ns)	1
Total time (μs)	100
Pressure pulse (MPa)	50
Simulated projectile speed (m/s)	7.5

Table 4.1: Details of the numerical simulation used to simulate elastic kinematic fields for numerical validation.

Material density(kg/m^3)	2800
Elastic Young's modulus (GPa)	78
Poisson coefficient	0.3
Plastic limit stress-at zero plastic strain (MPa)	450

Table 4.2: Details of the numerical model and material parameters used to simulate elastic response of aluminium.

Results of one elastic simulation are shown in Figure 4.2 in terms of axial stress, read out for all elements at 40 mm from free end in their centroid integration point. Comparison between the volume average axial stress response obtained in all the elements that constitute the cross-section and the surface is shown on Figure 4.2a. It can be observed that the two plots are very close and they differ for only about 1% at the peak values. The variation of all axial stresses in the cross-section can be represented by tracing the axial stress response for all elements as presented in Figure 4.2b. In this case, the line color thickness can be regarded as the general variation of the axial stress component in a given cross-section. It can be observed that the total variation of the axial stress in the cross-section does not exceed 3%.

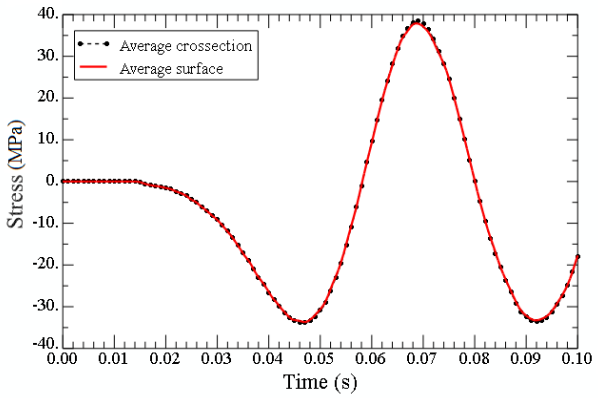

(a) Comparison of average axial stress in the cross-section and on the sample surface.

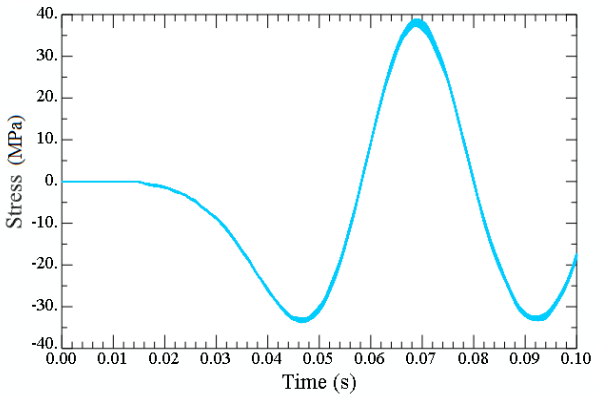

(b) Variation of axial stress in a given cross-section.

Figure 4.2: Evaluation of the axial stress homogeneity conditions at 40 mm from free-end for a isotropic elastic case.

Figure 4.3 presents the extracted full-field displacement, strain, acceleration and strain rate maps at 50 μs after the loading, when high axial acceleration level is noticed. The simulated fields are obtained with 2 Mfps recording speed. It can be seen that the maps are fairly smooth thanks to application of the smooth-step pulse and fixed time increment. Little spatial high frequency content is present in the acceleration fields which could be due to the fact that no additional damping was considered. The spatial patterns of these maps demonstrate the unidirectional loading conditions of a spalling test since the simulation is performed with a 3D numerical model. Finally, it can be seen that the levels of the axial acceleration is quite elevated, reaching values of about 3.5 x 10^5 m/s^2.

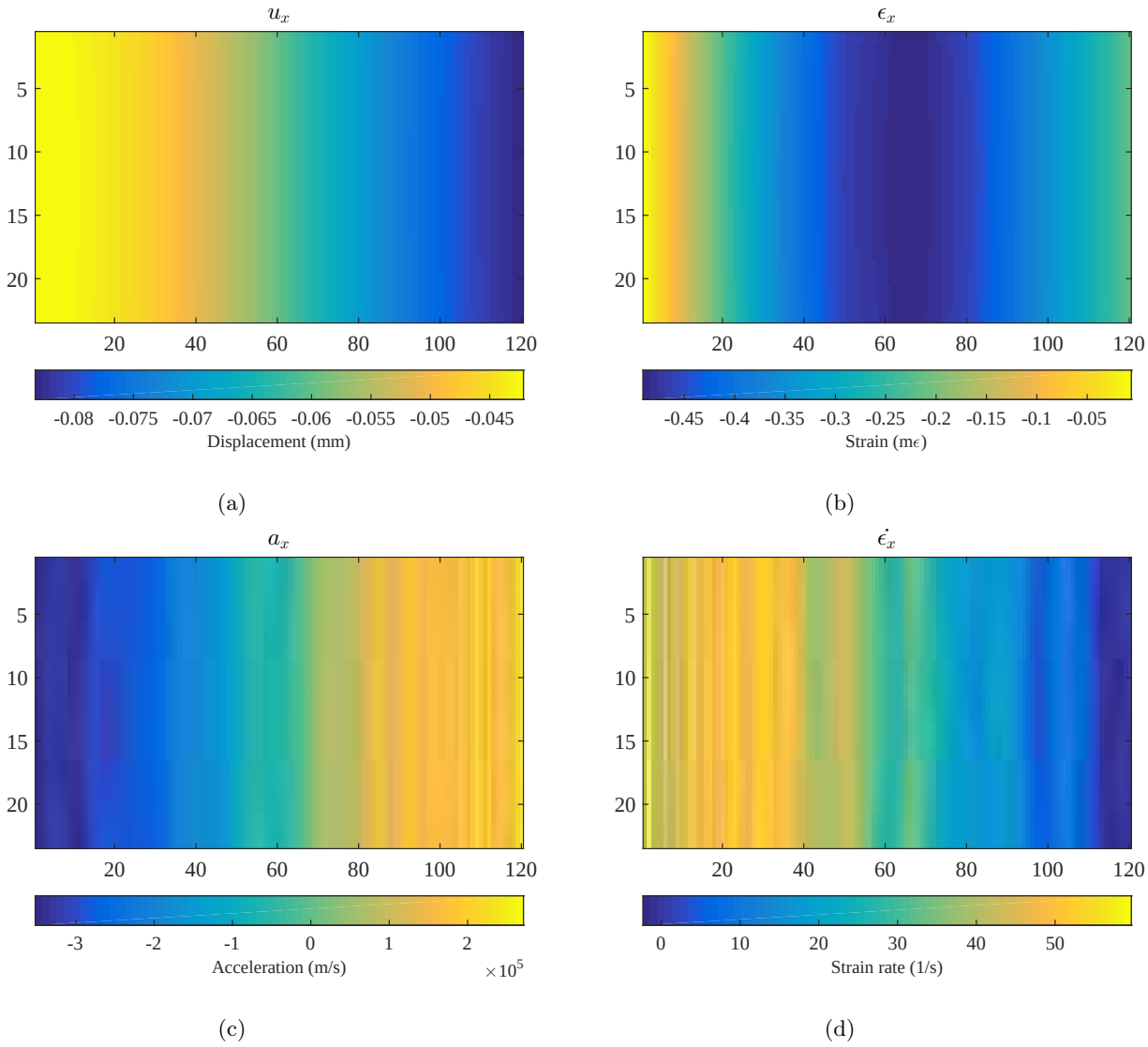

Figure 4.3: Maps of simulated full-field kinematic elastic measurements used for validation at 50 μs (2 Mfps simulated acquisition speed).

4.1.2 Validation of the processing

4.1.2.1 Validation based on acceleration and deformation data

In order to validate the identification procedure based on purely VFM processing, the simulated acceleration and strain fields were extracted from explicit FE computations. The fields of axial acceleration were read out from all the nodes that constitute the sample flatten surface while the axial strains were obtained in the centroid element points, thus needed to be interpolated to nodal positions. The direct treatment of the numerically simulated axial acceleration fields skirts around the derivation procedure of the displacement data. This can be considered as a reliable way to investigate the performance of the identification process. The full field strains and accelerations in axial direction were then processed using the VFM in order to validate the identification of the global Young's modulus (Equation 2.22) and the load cell principle. As mentioned in Section 2.4.2, a choice of virtual fields needs to be performed for the identification of the global stiffness. In the present case the virtual fields are expanded from a 1^{st} degree polynomial (linear) fit to the simulated displacement maps averaged in the vertical direction. The virtual displacement along the contact edge was set to 0 as to cancel out the virtual work contribution of the traction force in the weak form of the dynamic equilibrium equation. Therefore, the virtual fields satisfy the virtual

boundary condition and the condition of kinematic admissibility since they are extracted from real simulated displacement fields. Therefore, it is considered that no additional smoothing is present from the choice of the virtual fields as well. The identified elastic global Young's modulus and reconstructed stress-strain curve averaged on the entire sample surface are shown in Figure 4.4.

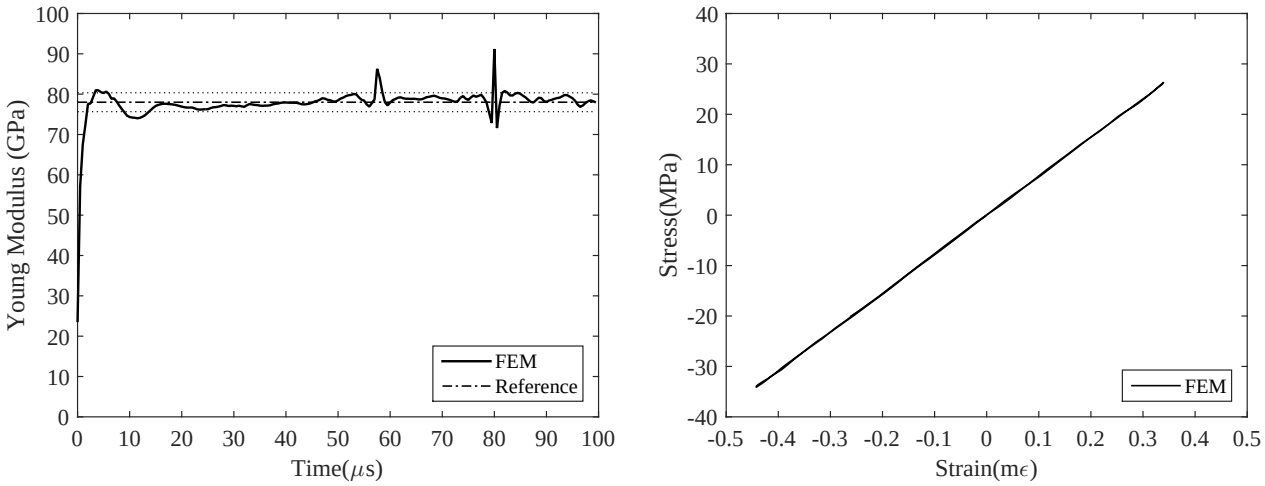

(a) Identified global Young's modulus in case of linear virtual fields (doted lines represent ± 3% of the reference).

(b) Identified stress–strain response averaged on the entire sample surface.

Figure 4.4: Validation of the VFM processing based on simulated acceleration and deformation data.

From the Figure 4.4a it can be observed that the identified values are well within the ± 3% of the reference value with some exemption. Firstly, it can be observed that the evaluated Young's modulus is low for the first several identification points. This is because the values of strains and accelerations are low in the first several time steps of loading stage as the wave has not fully propagated in the material. Next, slight oscillations are present during the first 15 μs. This can be contributed to the fact that the simulation is driven with an amplitude obtained from a real experimental pulse measurement. Finally, slight jumps are noticed at about 58 μs and 81 μs. This time frames correspond to the instances of the reflection of the waves from the free end during which the acceleration values are low and thus some computational instabilities are expected due to performing arithmetic operations with of numbers that are close to zero. Nevertheless, when taking overall mean value without first 15 μs of the loading the mean identified Young's modulus is 78.07 GPa. This already validates the great performance of applying a VFM processing acceleration and strain data even by using virtual fields expanded with a first order polynomial fit. The reconstructed stress-strain response, where the stress and strain fields are averaged over the entire region of interest, is presented in Figure 4.4b exhibits a satisfyingly linear response. The identified Young's modulus in this case, obtained by performing a linear regression of the reconstructed, is 77.36 GPa which is in the range of 0.8% of the reference value.

Sensitivity to noisy deformation data Thanks to computing the internal and external virtual work by introducing the simulated acceleration fields and deformation maps separately into the VFM processing algorithm, it is possible to investigate the sensitivity of the processing method to noise present in one of the simulated measurement data. Different noise sources affect experimental strain measurements that include both external factors (*e.g.* coming from experimental environment) and the noise induced by the measurement systems (*e.g.* camera noise). The superposition of all the noise sources is difficult to model. Generally, it's a common practice to aproximate it by using a statistical random distribution noise [Healey and Kondepudy, 1994], although it is worth mentioning that some other ways of accounting for noise more closely resembles to experimental noise such as Poisson-Gaussian

distributed noise [Reu, 2011b] or extreme value probability noise [Badaloni et al., 2015]. Here, as a first approximation, it will be considered that pure random noise is present in the actual full-field deformation measurements. Whatever its origin, the noise represents a non-mechanical component that impacts the prediction of identified parameters due to the sensitivity of the identification method. In order to validate the sensitivity of the technique used to identify the global Young's modulus, the numerically simulated maps were corrupted with a numerical zero-mean random noise with increasing standard deviation. Assuming for the time being that the acceleration measurements are obtained separately from strain measurements, only numerically simulated strain maps were corrupted frame by frame with non-correlated noise multiplied with a positive value γ, also often referred to as strain uncertainty measurement [Avril et al., 2004b]. The upper level of added noise was 30% of absolute maximum axial strain. In this case, twenty values of γ have been tested, evenly distributed from 10^{-5} to $2\text{x}10^{-4}$. These values are considered to be a usual range of uncertainties of optically measured full-field strain maps [Rastogy, 2000]. For each level of added noise, 20 identifications have been made with 20 different noise copies as to account for the noise randomness nature. The mean evaluated Young's modulus over the entire sequence for all 20 identifications and for different levels of input noise is shown on Figure 4.5. It can be seen that the average value of the identified stiffness parameter does not depend on the magnitude of the input strain noise, which is a similar observation as in [Avril et al., 2004b]. This further suggests that, if for any reason, the acceleration data obtained by optical measurements systems are inexploitable, the strain data can still be used in the identification of global stiffness providing that the acceleration measurements are obtained with a secondary technique (*e.g.* multi probe laser-interferometry).

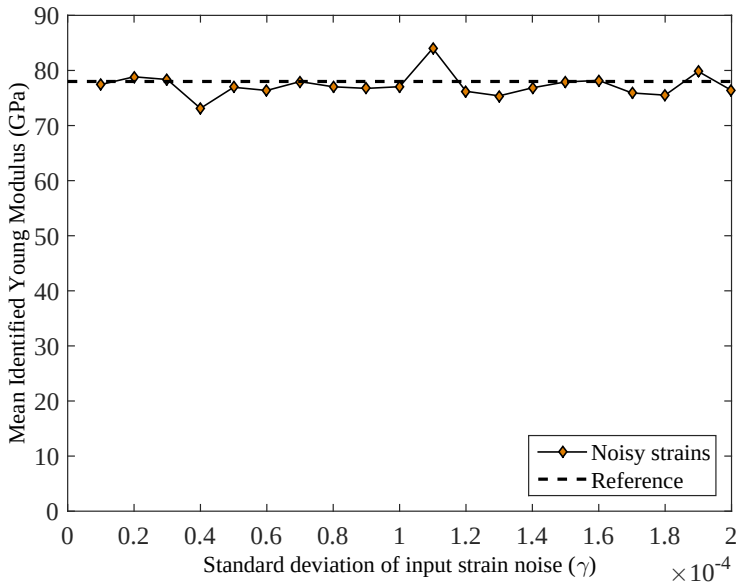

Figure 4.5: Sensitivity of identified stiffness to noisy strain fields: Mean Young's modulus over whole acquisition identified for several standard deviations of input noise.

4.1.2.2 Validation based on displacement data

The main aim of this work is to use ultra-high speed photography in order to apply full field measurement techniques in a spalling experiment. In that way, all the necessary information are photo-mechanically embedded in the recorded image sequences and in principle no additional measurement systems are needed. In that case, the actual measured quantities of an experiment are the displacement maps, obtained via a full-field measurement technique. These displacement maps are then processed by performing the second degree temporal derivation of the displacement fields in order to obtain necessary acceleration maps and spatial derivative to obtain the strain fields. The accelerations data can be derived by employing a temporal sliding window over which a polynomial fitting is performed-SG procedure [Savitzky and Golay, 1964]. In principle, with SG procedure the global Young's

modulus is not identified in the first several points that correspond to the half of the temporal smoothing kernel. Although some solutions to determine weights at all positions exist [Gorry, 1990]. During a spalling experiment, sample is first subjected to an initial compressive loading stage. During this stage, the material behaviour is expected to be linearly elastic and so finally the loss of several initial points does not impair the overall identification process. Therefore, from the above it can be considered that processing the numerically obtained displacement fields provides an identification methodology closer to the actual experimental one.

The simulated elastic displacement fields were extracted at nodal points that constitute the region of interest and would correspond to the experimentally observed sample surface framed by the camera (as in previous case). The selected virtual fields are obtained from a first-degree polynomial fit to the displacement maps averaged in vertical direction (linear fields). Therefore, again it is considered that no additional smoothing is present from the choice of these special virtual fields. The temporal derivation of the displacement fields is presently achieved by employing temporal filtering of the signal using a second-order polynomial over a span of 7 simulated frames. A small-order polynomial fit is applied to decrease signal-to-noise ratio and evaluate the derivation in the centre of the subset. This type of temporal data processing was adopted from this point onward. The strain fields are then derived with the same procedure as when experimental data are treated. A local fit of the weighted second-order polynomial is performed on a span radius of eight displacement points, using a diffuse approximation approach [Avril et al., 2008b, Avril et al., 2012]. The identified elastic Young's modulus and reconstructed stress–strain curve averaged over the entire sample surface obtained with VFM of the simulated displacement data are shown in Figure 4.6.

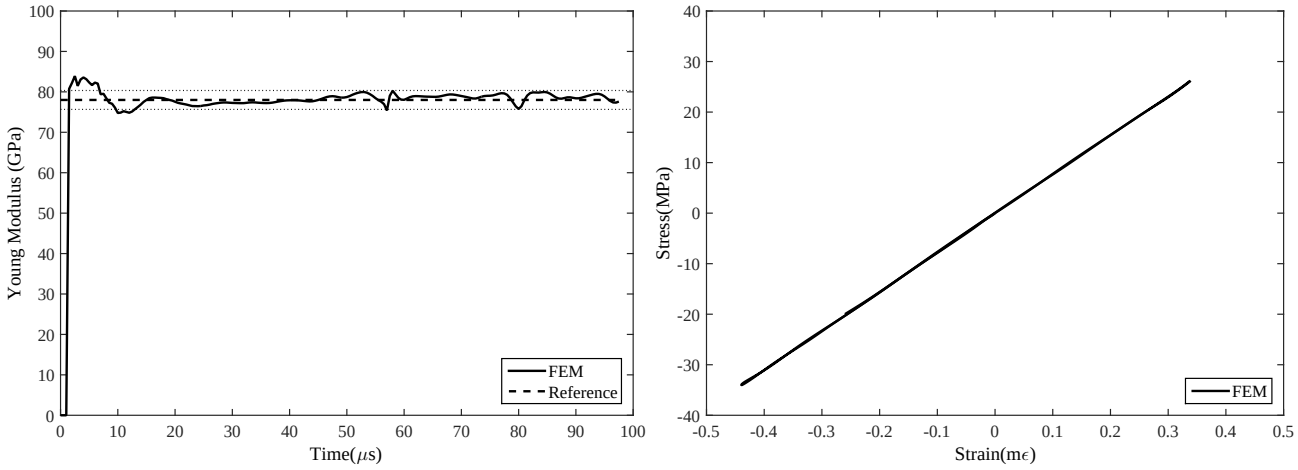

(a) Identified global Young's modulus in case of linear virtual fields (doted lines represent ± 3% of the reference).

(b) Identified stress–strain response averaged on the entire sample surface.

Figure 4.6: Validation of the VFM processing based on simulated displacement data (second-order polynomial reconstruction of acceleration over seven temporal displacement points and eight point strain differentiation).

The mean evaluated Young's modulus is 77.72 GPa which is within 0.3% of the reference value of 78 GPa. This again validates a very good performance of applying the VFM and processing directly the displacement data. Smaller instabilities are observed again at 58 and 81 μs corresponding to times when the reflection of the compressive stress to tensile stress takes place at the sample's free-end surface. The value of Young's modulus obtained by linear regression analysis of the average stress–strain response is 77.28 GPa which again is in the range of 0.8% of the reference value. This further illustrates the benefit of using the load cells for stress reconstruction, in this particular processing situation in which stress–strain curves can be reconstructed without the choice of specific virtual fields rather by simply applying the kinematic rigid virtual field. It has to be pointed out that the experimental benefit of this procedure where the displacement data are directly measured is that no external force measurement

is needed. Figure 4.7 illustrates the reconstructed space–time stress field along the sample throughout the loading where it can be observed that the free-end condition boundary is satisfied. Moreover, this verifies the method of diffuse approximation for strain derivation as well as the method used for reconstruction of acceleration fields when exact displacement fields are processed. Finally, displacement fields obtained experimentally are never exact, and this can introduce an increased numerical noise that is discussed in the following.

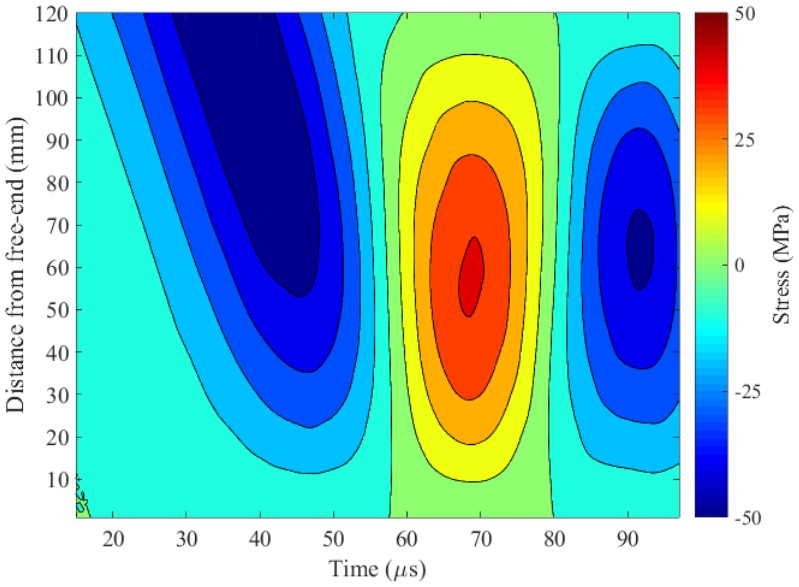

Figure 4.7: Reconstructed stress field when numerically simulated displacement fields are processed with second-order polynomial fit over seven temporal displacement points.

Sensitivity to noisy displacements Different noise sources can arise during the data acquisition process. Additionally, the treatment of experimental measurements (*i.e.* numerical derivation) can also amplify the measurement errors. This means that two identically performed measurements can provide different results. Therefore, it is first necessary to examine the sensitivity of the identification method when the noise is present in both acceleration and strain data which propagated from the measured displacements. This can be investigated by directly corrupting the numerically simulated displacement fields. The displacements are extracted at nodal points that constitute the FE mesh of observed region in the numerical model. The numerically simulated displacement maps are corrupted with noise of an increasing standard deviation. For the simplicity, noise was simulated as a standard random white zero-mean noise, that is added to computed field data. The noise was considered as zero-mean noise in space and was added to the displacement maps frame by frame, multiplied with a positive value γ_d which is also considered as displacement uncertainty measurement. The noise was considered to be uncorrelated, varying at each time step. Only longitudinal displacement field was considered to be affected by noise. One case of noise magnitude will be presented here. The level of added noise was 1% of the final measured axial displacement that is 0.2 mm. The noisy displacement fields were then processed with standard tools. The reconstruction of acceleration field is provided by fitting a second-order polynomial over a temporal window of seven displacement data points, and a linear fit is used to expand the virtual fields, whereas the strain field is obtained with approximate diffusion algorithm on eight points. The identified Young's modulus is shown in Figure 4.9a. What can be observed is that even with low variance of added white noise, the stiffness identification procedure exhibits substantial temporal oscillations. During the first 20 μs, it seems to be impossible to identify the correct value of Young's modulus, whereas during the final 80 μs, the mean identified Young's modulus is 77.91 GPa, but still exhibiting noteworthy temporal fluctuations. Figure 4.8b shows the reconstructed stress–strain response averaged over the entire region of interest. Again, certain oscillations can be observed, although less pronounced than in the identified Young's

modulus. Additionally, a linear response is observed with the stress-strain response, and the value of the Young's modulus obtained from linear regression of the reconstructed stress–strain curve is 77.35 GPa. It was expected that the mean stiffness values identified in both cases are close to the reference since the zero-mean noise was added with the aim to not introducing any offset errors. Finally, it seems that the identification procedure exhibits high sensitivity to noisy displacements. However, this was expected due to the fact that the noise in that case affects both strain and acceleration fields.

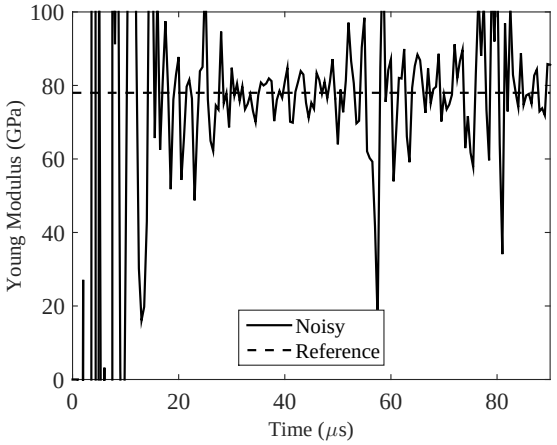

(a) Identified global Young's modulus.

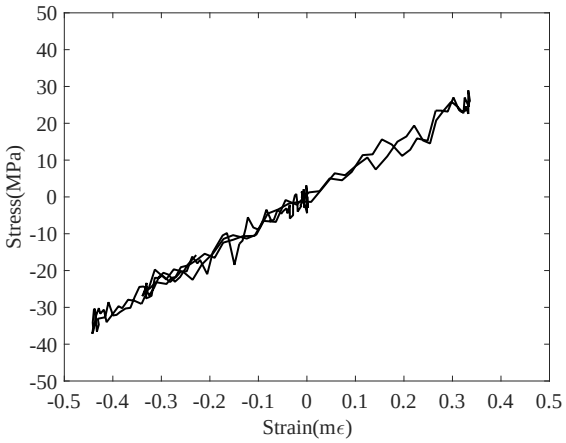

(b) Identified stress–strain response averaged on the entire sample surface.

Figure 4.8: Results of processing displacement field corrupted with zero-mean random noise with standard deviation equal to 1% of final overall displacement ($\gamma_d = 2$ μm).

Effect of the choice of virtual fields The choice of virtual fields may play an importnat role in accurate extraction of the constitutive parameters especially when the measured data is noisy [Pierron and Grédiac, 2000, Avril et al., 2004b, Grédiac et al., 2008]. Methods to select the so-called *optimal virtual fields* that minimize the effect of noisy data have been proposed in the literature, since the choice of virtual fields can help with filtering out some spatial measurement noise [Toussaint et al., 2006, Avril et al., 2008b]. These fields have also been extended for identification of stiffness parameters with dynamic applications to composite and rubber materials [Zhu, 2015, Yoon et al., 2015] and were also extended to non-linear identification problems [Marek et al., 2017]. Furthermore, it has become a common practice to test several options and to verify the choice of virtual fields on simulated data that is corrupted with a controlled magnitude of added noise [Zhang et al., 2016, Yoon and Siviour, 2017]. On the other hand, this type of virtual fields does not deal with the temporal noise component directly in the case time evolving measurements.

One simple way of dealing with time evolving measurements is to deduce virtual fields from the measured displacements by direct fitting of polynomials onto measured displacements. Due to the uniaxial nature of the spalling test it can be assumed that the virtual fields depend only on the axial direction. Furthermore, to introduce additional smoothing that would facilitate the identification, the measured data can be averaged in vertical direction and the fit can be performed on one 'line' of data. Then, the virtual fields can be expanded back from the obtained fitting [Pierron and Forquin, 2012b]. This technique has been adopted generally in treating experimental results by performing a polynomial fit of 8^{th} degree. Here, some additional methods to fit the virtual fields will be examined and compared by processing noise corrupted displacement data obtained with FEM. The simulated elastic displacement fields were obtained with the numerical model described in Section 4.1.1. The noise was assumed to be zero-mean and non-correlated random noise of a standard deviation $\gamma_d = 5.15$ μm that is generated and assigned frame-by-frame to each of the simulated displacement frames. This noise magnitude corresponds to the mean value

of displacement measurement noise in both directions when the Shimadzu HPV-1 camera is used to frame a 1 mm pitch grid glued onto a sample surface (Section 4.1.1). The results regarding the identified global Young's modulus is shown in Figure 4.9b. Although the choice of virtual fields does not play a role in load cell measurement, the identified stress-strain response is presented as well (Figure 4.9b). The processing was carried with similar parameters as those used in the processing of real experimental measurements. Namely, the virtual fields are obtained from 8th degree polynomial expansion. The virtual displacements must be continuous, differentiable and meet the prescribed boundary conditions. Hence, the condition of zero displacement was added to the virtual field maps on the side opposite to free-end as to cancel the contribution of the traction force. The acceleration data was derived by fitting 2^{nd} order polynomial onto a window of 11 points and the strains are derived with 2^{nd} order polynomial fit over 8 time points of axial displacement using the diffuse approach.

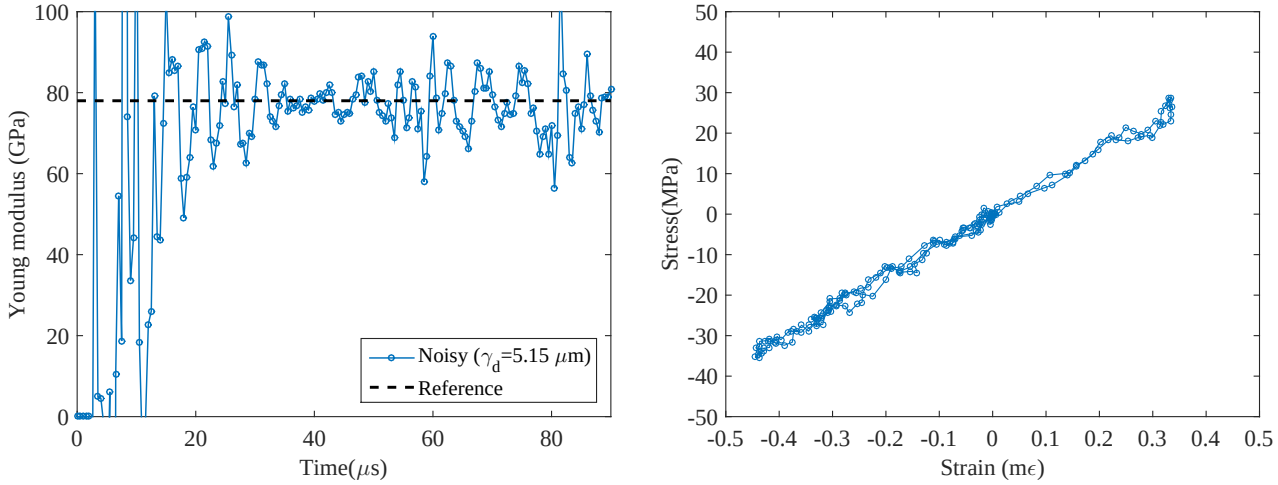

(a) Identified global Young's modulus.

(b) Identified stress–strain response averaged on the entire sample surface.

Figure 4.9: Results of processing noisy displacement field corrupted with zero-mean random noise ($\gamma_d = 5.15\mu m$).

Aside performing a polynomial fit to expand the virtual fields, special polynomials (cubic Splines) can also be used since it is expected that they would provide better low pass filtering of the noise content. Since the noise is present also in the vertical direction, the fit can be performed in two directions and the virtual field maps can be obtained directly. The performance of these three selections of virtual fields on the identification of the global Young's modulus is examined in Figure 4.10. As it can be seen from the plot, the identified result remains noisy in all situations. Hence, it is difficult to pin-point which method provides better performance in this situation.

4.1.2.3 Effect of simulated acquisition speed

Dynamic tensile fracturing of concrete is closely related to the nucleation and propagation of cracks associated with unstable crack growth [Forquin and Hild, 2010]. Additionally, dynamic tensile fracturing increases the crack speed under dynamic loadings to about 0.20–0.30 of the Rayleigh wave speed [Curbach and Eibl, 1990, Forquin, 2012]. This high crack propagation speed of one or several tensile cracks propagating simultaneously, results in a failure process that lasts only a few microseconds. This makes this process difficult to record by obtaining a sufficient number of measurement points that well captures the phenomena. Consequently, the images have to be grabbed at very low inter-frame times which are considered in the range of ultra-high speed imaging [Honour, 2009]. Here the focus is on identification of purely elastic response since the temporal resolution also plays a role in capturing the elastic wave propagation. To demonstrate this, the explicit FE model was used to simulate several recording speeds of a hypothetical camera, simply by changing the data output frequency so as to match the inter-frame time of a real acquisition system. The simulated acquisition speeds were in the range of currently available ultra-high

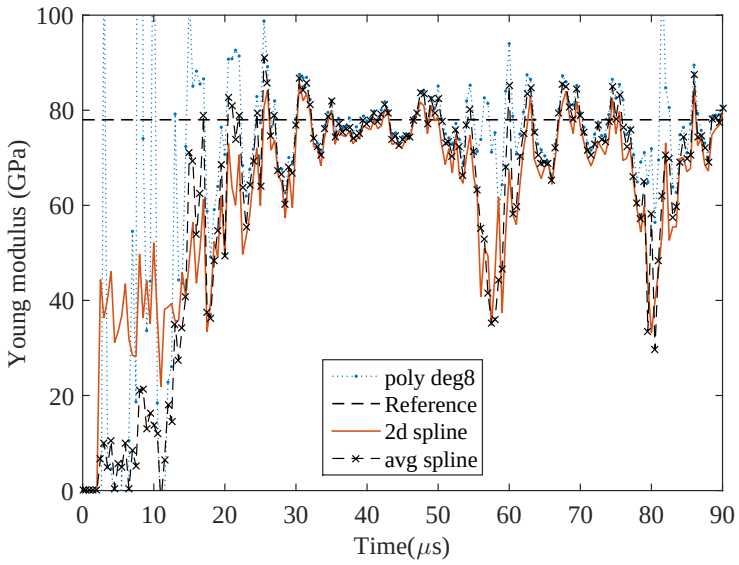

Figure 4.10: Effect of choosing cubic spline fitting for deriving a set of virtual fields in the identification of the global stiffness response.

speed cameras, namely 5 Mfps, 2 Mfps, 1 Mfps, 500 kfps and 100 kfps. The obtained elastic displacement fields were directly implemented in the VFM processor. The identified global Young's modulus and the mean values with corresponding standard deviation are presented in Figure 4.11a,b. The temporal discretization of the axial stress averaged on the entire observation surface is presented in Figure 4.11c. In all cases, a linear curve fit was used to expand the virtual fields and the derivation of a second-order polynomial fit was used to obtain the acceleration fields.

The simulation results indicate that an optimal identification is obtained for a temporal resolution higher than 500 kfps since it provides more reliable values of material stiffness. This is mainly due to the fact that higher the acquisition speed, the larger the number of useful frames are obtained which finally results in a better temporal discretisation of the elastic wave propagation phenomena. Nevertheless, in the case of a spalling test, the highest frame rate is not always considered as the best solution owing to the limitation of the number of images obtained during one shot with a real ultra-high speed camera (180 images with a Kirana model or 128 with an HPV-X2). Extremely high frame rate would drastically decrease the actual measurement time with increasing the triggering difficulty and making impossible to have images for both the compression and tension phases of the test in one recorded sequence. Indeed, it is quite useful to capture the material behaviour in the compressive stage for test validation since the sample is assumed to be loaded elastically in this part of the test. Recording the compressive loading phase enables one to determine the elastic dynamic Young's modulus of the sample along with verifying that no compressive damage is introduced in the sample. Taking into account the usable number of frames from a specific sequence at a given frame rate with the respect of quality of temporal description of the whole test, the measurement time indeed needs to be considered, and it seems to lie between 1 Mfps and 2 Mfps. Therefore, in this study, the simulated acquisition speed of 2 Mfps was mostly used, which appears to be most optimal for this type of experiment.

4.2 Simulation of the entire measurement chain

4.2.1 Introduction

Identification strategies based on the use of full-field measurements are more and more used within the experimental mechanics community and are also slowly transcending into industrial applications. Performing full-field measure-

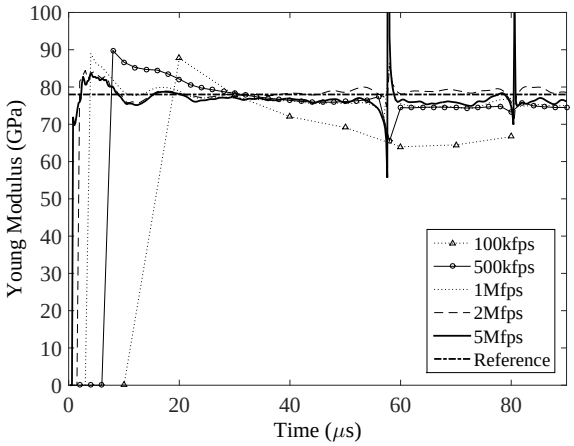

(a) Identified global Young's modulus.

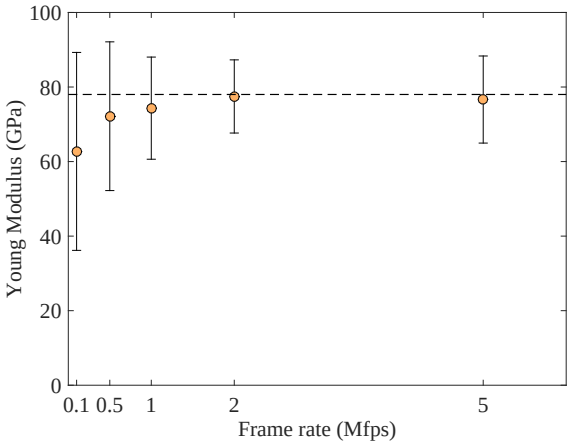

(b) Identified stress–strain response averaged on the entire sample surface.

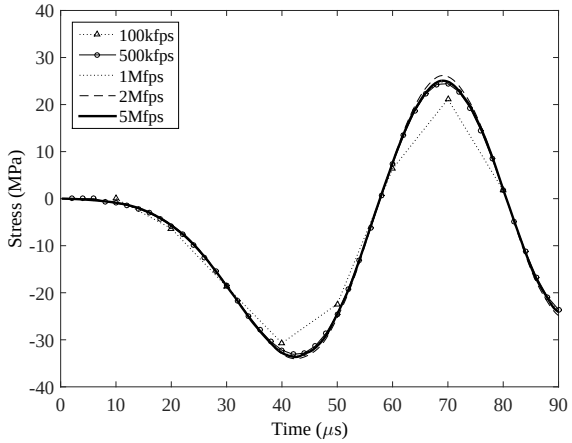

(c) Identified stress response averaged on the entire sample surface.

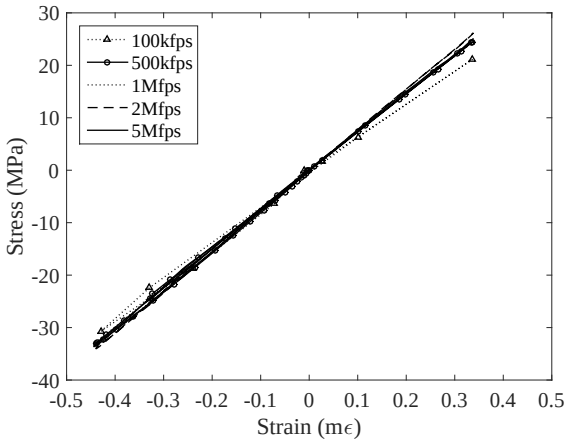

(d) Identified stress-strain response averaged on the entire sample surface.

Figure 4.11: Effect of simulated camera frame rate on the identification of material elastic stiffness.

ments adds on one more extra step in the entire identification methodology and as such can introduce new sources of measurement uncertainties. These can vary from the uncertainties that are induced by the experimental set-up up-to the measurement uncertainness due to complex optical measurement systems (e.g noise of an UHS camera). Therefore, supplementary steps need to be taken as to first understand the uncertainties of these measurement methods and how errors can propagate to the identification results. Analysis of synthetic images generated through performing either controlled shift of a reference image by a fixed displacement value or constantly evolving displacement, is a widely adopted method to examine and benchmark the accuracy of the used full field technique (as in *e.g.* [Schreier and Sutton, 2002, Bornert et al., 2009, Roux et al., 2009, Reu, 2011b, Badulescu et al., 2013]). Although extremely useful for investigating the metrological accuracy of specific methods, these images often do not take the entire measurement chain involved in the real experimental environment. Furthermore, the material response that is embedded in the images is often limited to an elastic behaviour or a rigid body displacement. Synthetic image generation based on FE formulation can present one such method of simulating entire identification chain with virtually any kind of material response, where the *a priori* known material behaviour is directly embedded in the images [Lava et al., 2009, Lava et al., 2010]. Then, various experimental effects can be taken into account and investigated, providing suggestions on how to perform experiments with full-field measurements by minimising possible sources of errors [Badaloni et al., 2015]. One such image generator has been developed in [Balcaen et al., 2017b] and employed for investigating various errors that can arise during stereo-DIC calibration [Balcaen et al., 2017a] or more specificity due to camera rotation induced by experimental vibrations [Balcaen et al., 2018] or out-of-the-plane motion [Yasmeen et al., 2018]. Furthermore, with full-field measurements, experimental set-ups become more complex and optimisation and design based just on FE simulations becomes insufficient. Simulating an entire identification chain based on FE formulations can also provide good way of designing an photomechanical test which can maximise the identification of the sought material quantities [Gu and Pierron, 2016, Wang et al., 2016]. All of the above cited works mainly use the simulated imaging for investigating error propagation in the identification of elastic material response under quasi static loaded conditions, relying mainly on the generation of one (or a few) deformed images.

In the following, a synthetic image simulator based on explicit FE formulations able to generate a sequence of images of a deforming sample in a spalling test will be presented. A numerical procedure was developed to simulate the entire chain of measurement, starting from the generation of synthetic grid image sequence up-to the identification of the material dynamic response. The spalling experiment uses the grid method and ultra-high speed photography to get the displacement data and the VFM to identify the material response. A flow chart outlining the simulation steps is provided in Figure 4.12. It illustrates how various experimental factors can be accounted for, that occur during the experimental procedure. First, an explicit three-dimensional FE model of a spalling sample with the corresponding specimen geometry and loading conditions of a real test (as described in Section 4.1.1) is used to produce the time resolved displacement maps. The displacement fields were computed in the region of interest that corresponds to the specimen surface framed by the camera in an actual experiment. Next, a reference grid image is generated and sequences of deformed synthetic grid images are obtained by imposing the corresponding displacement fields on the reference image. The material parameters input in the FE simulations serve as a good reference to evaluate the performance of the experimental processing. Therefore, these synthetic images can be processed as real ones and the identification error can be evaluated by simply comparing the identified stiffness parameters with the reference values. This methodology proves to be useful in evaluating the performance of the experimental processing and providing suggestions on how to perform experiments in a better way.

The procedure used for image deformation represents a critical stage in the simulation process due to the fact that no numerical method is completely error-free and in particular FE displacement fields have to be interpolated onto imaginary pixel positions as discussed in [Reu, 2011b, Rossi and Pierron, 2012]. This step can introduce numerical errors that additionally influence the error of the material parameters extracted with the identification procedure

and as such cannot be completely avoided especially in an ultimate error calculation regime [Bornert et al., 2012]. However, although these systematic errors exist (because of the interpolation) they are often much smaller than the uncertainty of the sought measurement and the identified material parameter. Here, sequences of deformed images were obtained starting from a reference grid image simulating an acquisition of an ultra-high speed camera. The reference grid image is obtained from an analytical description of a periodical grey-level function using a pixel super-sampling technique and down sampled to the desired resolution. This technique can help to reduce interpolation errors [Wang et al., 2016]. Then, interpolated displacement fields are used to deform the reference image using a cubic spline interpolation function with an image projection algorithm. Finally, the synthetic image sequences obtained from the simulation are treated as experimental images to obtain the acceleration data and material stiffness parameters which are compared to their reference values.

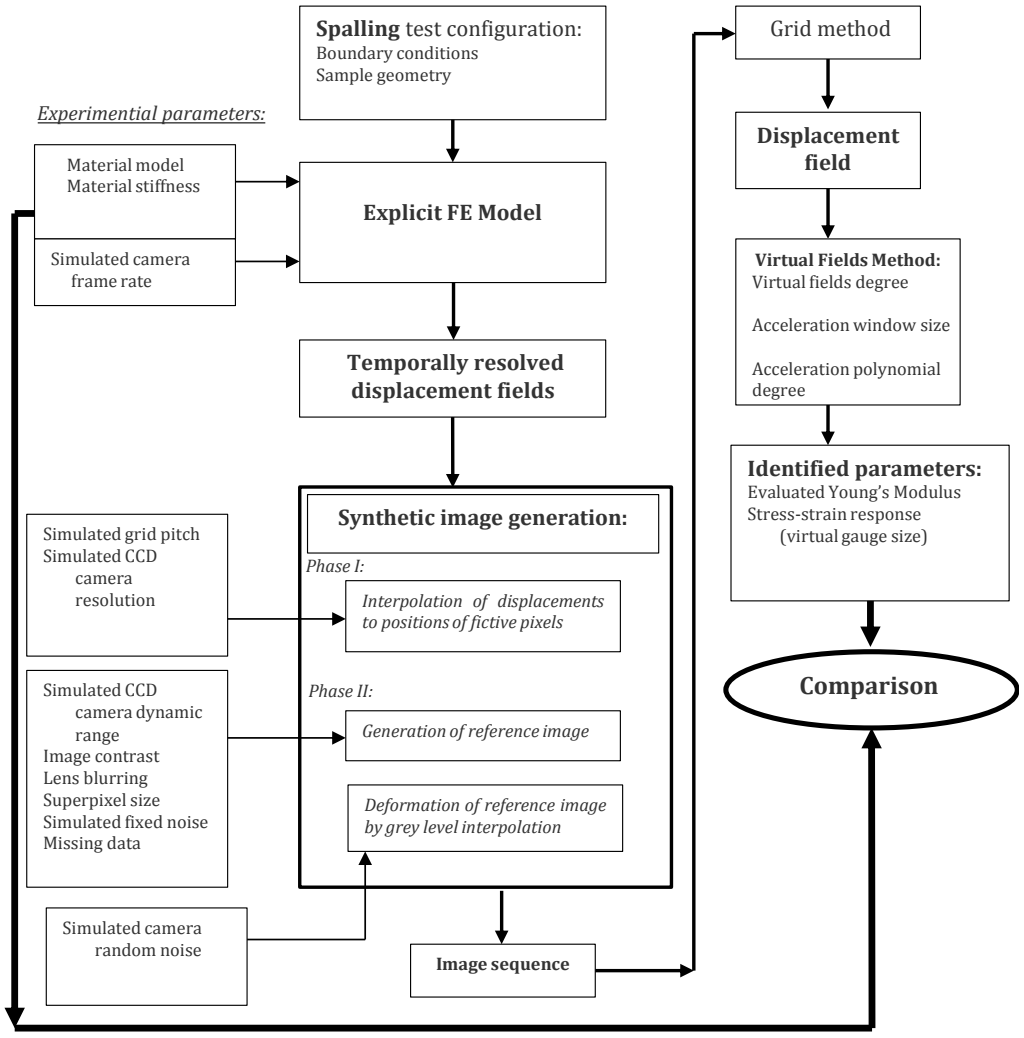

Figure 4.12: Flow chart of the spalling identification simulator.

4.2.2 Generation of a synthetic grid image

In order to create deformed images, one needs to start with a reference image. While generation of a synthetic speckle image used in digital image correlation requires a state-of-the-art knowledge (e.g [Bomarito et al., 2017, Crammond et al., 2013, Lecompte et al., 2006, Orteu et al., 2006]) since it can dictate the method's accuracy, creating a synthetic gridded pattern is a fairly straight forward task that is derived from its analytical description. In a photographical experimental setup that involves framing a grid pattern, it is possible to perfectly align the

imaged grid with the pixel grid of the camera, then a grid image can be modeled as a 2-d pseudo-periodic function [Badulescu et al., 2009a, Badulescu et al., 2013, Sur and Grédiac, 2015, Sur et al., 2016]. Indeed, a pseudo-periodical function better describes a realistic grid pattern which can contain defects caused by, for example, limitations in printing technology [Badulescu et al., 2009b] and/or camera noise [Grédiac et al., 2016]. However, in this work a perfect sinusoidal description of a grid was considered in order to facilitate the investigation of the applied method. The synthetic grid images were recreated by following the procedure proposed in [Rossi and Pierron, 2012]. The analytical description of a periodical black and white line profile which can be defined as a continuous function of grey level intensity variation $I(\mathbf{R})$ on the imaged material point whose position is described by the vector $\mathbf{R}(x, y)$ that is expressed in global coordinate system. The dynamic range of a camera is simulated by considering that the white parts of the grid pattern are close to the saturation limit. Then, a reference image of a grid, before the sample experiences deformation, can be described with the following two-dimensional periodical function:

$$I(\mathbf{R}) = \lfloor I_0[1 + \gamma(cos(2\pi x.\omega) + cos(2\pi y.\omega) - |cos(2\pi x.\omega) - cos(2\pi y.\omega)|)]\rfloor \tag{4.1}$$

where $I_0 > 0$ is the average field illumination that can be varied in order to simulate camera dynamic range, in other words $I_0 = 2^n$ where n characterizes the image bit depth (e.g 8, 10, 16 etc.); $\gamma \in [0, 1]$ is the image contrast that controls the visibility of the oscillatory pattern; ω is the spatial frequency of the periodical grid pattern (*i.e.* $\omega = 1/p$ where p is the pitch of the grid in pixels); $\lfloor \bullet \rfloor$ represent the Iverson's floor function[1] brackets and $| \bullet |$ denotes the absolute value.

In a CCD camera, an image is captured by registering the amount of light that is projected through a camera lens onto a photosensitive pixel region embedded on the camera sensor, where it is then transferred and stored as electrical charge. Therefore, every pixel of the recorded image corresponds to a specific domain on the CCD sensor of the camera. Considering a pixel as a material point M, a physical surface A_M can be defined as the portion of the image captured by that pixel in a finite domain of the CCD sensor. Then, the integer value stored in M is then taken as the average light intensity inside the surface A_M. This surface represents the photosensitive part of the pixel and can be varied in order to take into account non-uniform camera fill factor. In this work, only 100% fill factor is considered. Assuming that all the light intensity which reaches the sensor is captured (*i.e.* no light scattering), the digital value of a one pixel can be computed as:

$$P(M) = \Big\lfloor \frac{1}{A_M} \int_{A_M} I(\mathbf{R}) dS \Big\rfloor \tag{4.2}$$

The super-sampling technique evaluates the analytical function $I(\mathbf{R})$ on the surface A_M inside one simulated pixel, assuming that the domain can be discretised into a sufficient number of points. Then the image quantization on a pixel level can be approximated as:

$$P(M) \approx \Big\lfloor \frac{1}{N_x N_y} \sum_{i=1}^{N_x} \sum_{j=1}^{N_y} I_{i,j}(\mathbf{R}) \Big\rfloor \tag{4.3}$$

where N_x and N_y represent the number of super-sample points with respect to two axis. The generation process of the reference grid image through the proposed image quantization, starting from the analytical description is shown in Figure 4.13.

After obtaining the reference image, a sequence of deformed images is generated by projecting the reference image over a mesh of imaginary pixels previously deformed with FE displacements. This procedure requires several interpolation steps so that the simulated material response can be embedded into fictive pixel positions through their grey level change. The procedure adopted for image deformation is a crucial part in the simulation process as it will undoubtedly introduce systematic errors. These errors can be mainly attributed to the algorithm used to interpolate the grey-level values on a subpixel level that can cause identification errors [Reu, 2011b]. These will be

[1] Note that the floor function is used rather then nearest integer function in order to avoid over-saturation values [Kim, 2008]

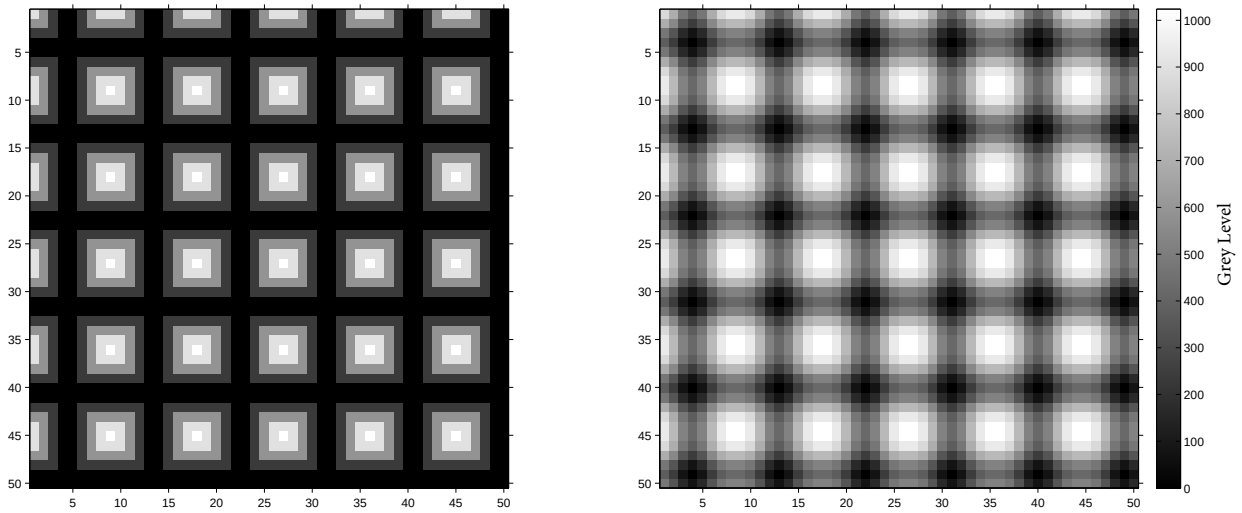

Figure 4.13: Simulated image quantization of the reference synthetic grid image with 1 mm pitch, obtained with 10x10 pix super-samples (N=9 pix/period)–*Left*: Analytical function; *Right*: Synthetic grid.

further discussed in Section 4.2.3. In principle, two interpolation procedures are needed before image deformation, one to obtain the displacement maps on a regular mesh-grid and second to interpolate the obtained displacement maps onto fictive pixel positions. Here, the first step is avoided by already generating a regular mesh of finite elements in the numerical model which corresponds to the grid pitch of the desired synthetic grid image (e.g $p = 1$ mm). A first step is to interpolate the displacement maps onto the mesh-grid which represents position of fictive pixels $U(u_i, v_j)$, given a fixed grid pitch pixel sampling. Already here, some interpolation problems can be experienced at the edges which can be approximated by extrapolating the fictive mesh for one row of fictive pixels and then cutting it back down to the desired frame size. After down-sampling the expanded image, a reference grid image $P(i, j)$ is obtained where i, j correspond to fictive pixel coordinates. Finally, the reference image is interpolated at each simulated frame at new pixel locations $P'(i + u_i, j + u_j)$ providing a sequence of deformed images. It is necessary to mention here that the choice of the super-samples can be beneficial for reducing the systematic errors caused by interpolation. Furthermore, as indicated in [Rossi et al., 2015], deforming directly the super-sample image can further aid in error reduction. But both these steps can also increase the time needed to generate one sequence. For example, considering that a surface of 45x120 mm with 1 mm pitch grid is framed with 9 pixels per period for an image sequence consisting of 180 frames with 16 bit dynamic encoding: using 5x5 pix super-samples and deforming the down-sampled grid, the sequence will be generated within 120s, on the other hand using the 10x10 super-samples the sequence will be generated within 1980s (standard laptop machine: Intel i7-3630 QM 2.40GHz, not parallelized). However, it is advised to use larger super-samples in order to reduce the unwanted bias. This overall numerical simulation procedure allows the investigation of many different sources of errors individually and how they can propagate through the identification chain.

4.2.3 Limitations of the present simulation method

Before proceeding to the application of the proposed simulation algorithm for virtually reproducing dynamic photomechanical spalling tests, some limitations of the current simulator that uses image projection technique need to be firmly stated.

The first limitation is that in the current simulation procedure the FE mesh is required to be a equispaced structured mesh of quadratic 4-node elements whose distance is equal (or proportional) to the pitch of the desired grid pattern that is to be simulated. Second, since the spalling test relies on the propagation of a uniaxial stress wave, it is fair to choose the global coordinate system so that its unitary vectors are same as for a local coordinate system

of any non-deformed finite element constituting the observed sample surface. Assuming that only uniaxial deformation occurs within small displacements theory, the fictive pixel positions in the global coordinate system can be obtained by directly mapping (*i.e.* interpolating) them from the global coordinates that are read out from the FE model for each node and at each simulated frame. This presently limits the simulation procedure to only this type of loading conditions and mesh structure. In principle, for a more general case, a mapping between local and global coordinates should be used as described in [Balcaen et al., 2017a], which is considered as future perspective. Next, the deformed images are created by a simple projection of the reference image onto the subsequently deformed mesh-grid of fictive pixel positions using cubic spline interpolants. This will inevitably introduce systematic errors due to the interpolation of grey level values onto non-integer positions. It is worth mentioning that the same procedure has been used by some authors [Wang et al., 2016, Gu and Pierron, 2016, Seghir and Pierron, 2017]. One way of ensuring that minimal errors are introduced, is to generate a super-sample image, since it can improve the accuracy of the simulation method [Wang et al., 2015]. The super-sample image then also can account for the fictive size of a photosensitive pixel area on which an average of grey level values is computed. This procedure is the procedure employed in this work always assuming a 100% fill-factor of the virtual camera. The errors can be further reduced by directly deforming the super-sample image, however in this work the down sampled images are deformed in order to reduce the computation time since the set of scripts within the procedure are not-optimized. On the other hand, another more reliable way to reduce interpolation errors, is to ensure that each pixel remains within the deformed finite element mesh by performing a check based back- and forth- inverse mapping from global to local system which in turn could cancel the introduced interpolation errors [Balcaen et al., 2017b] and can be combined with the super-sampling method. This is also a perspective for future work since it would allow much more reliable generation of images.

Although the above mentioned shortcomings do exist, it is necessary to say that in this work the images are generated with the aim to primarily validate the identification method and investigate a possible impact of various error sources individually, but it is however not the purpose (yet) to generate absolute ground-truth images. Furthermore, it will be shown that (most) errors which occur in real experimental conditions can be (often) of one order magnitude higher than those that can be introduced by the numerical procedure of image deformation itself.

4.2.4 Accuracy of the simulation procedure

Following the statements made previously, it is essential to investigate errors that will be introduced by the procedure defining the simulation algorithm and as such will affect its accuracy on the identification of sought material parameters. As a first benchmark, an elastic spalling experiment is simulated considering an aluminium sample. The explicit numerical simulations are carried out with the 3D model of a spall sample presented in 4.1.1. The material parameters are given in Table 4.2. Then, an ideal (almost-sinusoidal) reference grid image is generated which assumes perfect imaging conditions (ideal camera with no noise, even lighting, the entire sample in field of view). The parameters used for these photographical settings are given in Table 4.3. Then, a sequence of 200 images is generated using the interpolation of the reference image onto subsequently deformed mesh-grid using cubic-spline interpolation. The generated sequence is treated using the grid method with a triangular convolution kernel of 2N-1 size (where N is number of pixel per period). No smoothing, nor masking, of the zones of poor contrast is used. The displacement maps were then obtained by computing the phase change between the reference image (here taken as img-000.tif) and the deformed images.

The first estimate of the accuracy can be investigated by computing the mean difference of the measured and imposed axial displacements for each simulated frame, which is shown in Figure 4.14 and represents the evolution of the mean absolute error obtained as:

$$\overline{\epsilon}^{abs} = M[U^{FE}(x,y) - U^{G}(x,y)] \tag{4.4}$$

where the $\overline{\epsilon}^{abs}$ is the absolute error of one simulated frame, $M[\bullet]$ denotes the mean operator, and $U^{FE}(x,y)$ and

Parameter	Value
Grid pitch	1 mm
Pixel sampling	9 pix
Camera pixel count	1089x216 pix
Frame rate	2 Mfps
Dynamic range	16 bit
Super-sample	10x10 pix
FFT blur	1 pix
Illumination	54%
Interpolation	cubic-Spline

Table 4.3: Settings of the perfect photographical conditions for accuracy evaluation.

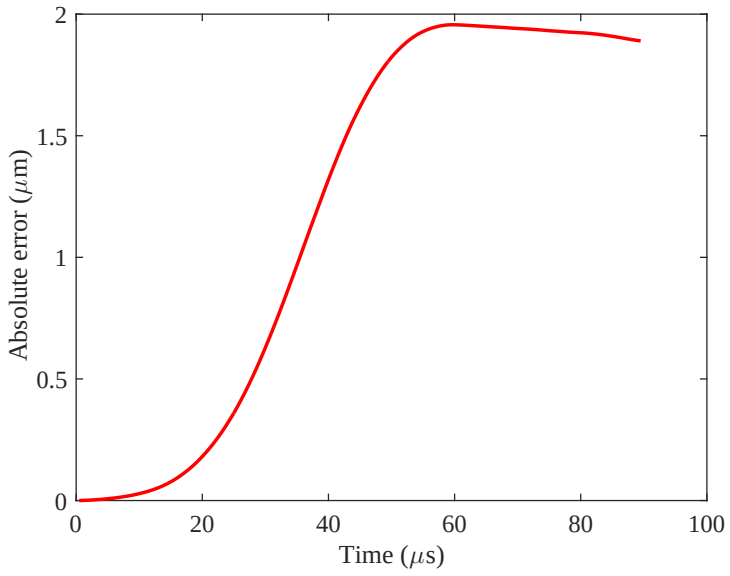

Figure 4.14: Mean difference of the measured and imposed axial displacement obtained by treating perfect grid images from the simulator. (Settings in Table 4.3)

$U^G(x,y)$ denote the axial displacement map from FE computations and that obtained using the grid method from simulated images. From the Figure 4.14, it can be seen that the systematic error propagates through the system, from one frame to the next one. It reaches a maximal value of 2 μm at about 60 μs. Although this time interval corresponds to approximately the time the tensile wave needs to emerge, which is of measurement interest, the error can be adopted as reasonably small. In order to compute the relative error, attention needs to be made in the first several 20 μs due to possible presence of infinite values which come from the point-by-point division of the measured and imposed displacement fields, where the local values can be equal to (or quite close to) null. For this reason, first the relative error for the axial displacement component can be computed over each frame. Then the systematic error introduced by the simulator can be taken as the median value in space and time [Seghir and Pierron, 2017], since it is less sensitive to outliers. The defined systematic error is then computed as:

$$\overline{\epsilon}^{sys} = M\Big[\frac{U^{FE}(x,y) - U^G(x,y)}{U^{FE}(x,y)}\Big] \tag{4.5}$$

where the $\overline{\epsilon}^{sys}$ is the relative error of one simulated frame, $M[\bullet]$ denotes the mean operator, and $U^{FE}(x,y)$ and $U^G(x,y)$ denote the axial displacement map from FE computations and that obtained using the grid method from simulated images. Having computed the mean relative error, a median relative error can be obtained considering frames starting from 20 μs. This error can vary depending on which interpolation technique is used. Several tests were performed with various interpolation methods that are native for the Matlab® environment and implemented through the `interp2` function, the obtained results are presented in the Table 4.4.

Interpolation	$\overline{\epsilon}^{sys}$ (%)
Linear	1.71
Cubic	1.70
Cubic-Spline	2.16

Table 4.4: Overall mean relative error made on the axial displacement from simulated images based on the interpolation technique used to deform the images. (considered frames after 20 μm)

Although it can be observed that in principle smaller error is introduced with linear (or cubic) interpolation method, finally the cubic-spline was chosen since it was observed that linear and cubic interpolation exhibit instabilities when wave reflection takes place and when the acceleration drops (Section 4.3.1). Finally, the results obtained on the relative error to some extent verify the correct working of the image generation since the obtained errors appear to be much smaller than what one usually gets in a real experiment.

4.2.5 Validation of the simulated identification chain

In order to verify the process of generating deformed image sequences, the whole process of identification was applied on a image data set assuming perfect photographical conditions and simulating a case of an acquisition at 2 Mfps with a 16 bit dynamic range. The identified results with respect to the global Young's modulus and the reconstructed stress-strain response are presented in Figure 4.15. The mean evaluated Young's modulus is 77.79 GPa which is within 0.3% of the reference value of 78 GPa. The stiffness value obtained performing the linear regression of the reconstructed stress-strain curve is 77.42 GPa with a standard error of 0.087 GPa. This can be considered as the ground validation of the simulated image deformation process.

Although the accuracy of the image simulator is roughly below 1% (which can be considered acceptable), here it should be noted that that the identified values from linear regression are systematically lower than the reference value. One reason for this can be the approximation performed in image generation procedure regarding the

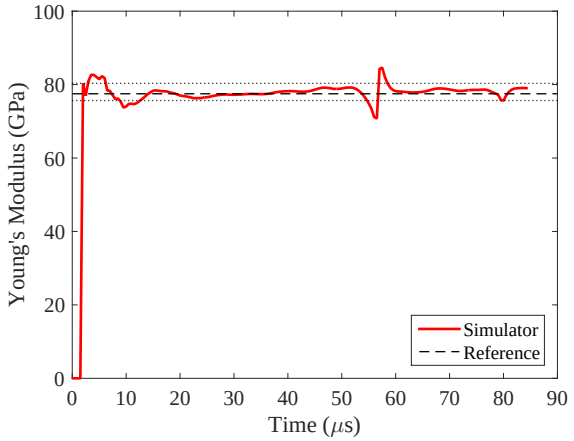

(a) Identified global Young's modulus.

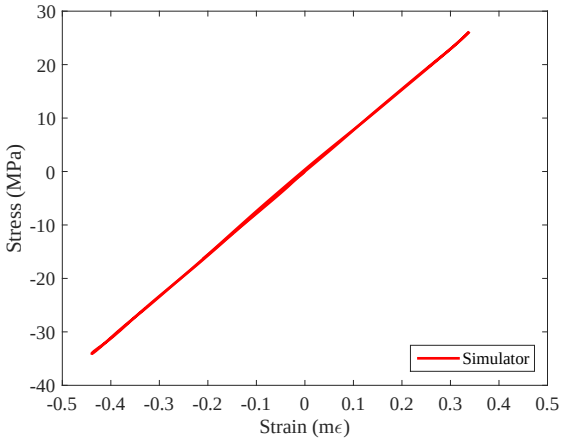

(b) Identified stress–strain response averaged on the entire sample surface.

Figure 4.15: Results of processing synthetic grid image sequence assuming ideal photo-graphical settings.

edge treatment. As mentioned previously, a slightly larger (for one row of super-sized pixel) image is generated compared to the desired super-sampled one. Then, this image is physically cropped down to the desired pixel count of the simulated super-sampled image which is then down-sampled. Another reason can be the use of diffuse approximation approach for derivation of strain date which does not allow the values to be evaluated precisely on the free-end. Both of these shortcomings result in the fact that the true boundary condition of the free-end is not absolutely positioned at the end of the simulated sample edge, but rather slightly within the sample.

4.3 Numerical effects in the proposed synthetic image generation procedure

The approximations under which the synthetic deformed images are generated can result in the evaluation of the errors which are not necessarily representative of the identification methodology in question [Bornert et al., 2012]. It is therefore important to create images which can reproduce the real physical process and not introduce (or as least as possible) unwanted numerical bias.

In the currently proposed simulator, the approximations due to the quantization which occurs at the pixel level as well as image interpolation method used to obtain the grey level values at deformed pixel positions, influence the phase detection and consequently can introduce a unwanted bias that can affect measurement precision. Furthermore, the accuracy of the simulated displacement data that are obtained with explicit FE simulations also directly affects the temporal measurement accuracy since vibrations can be experienced. To have an idea of such effects simulations of the entire identification have been conducted considering several possible sources of numerical errors such as: stability of the simulated displacements, interpolation function used to deform the images and the number of re-sampling points inside one dedicated pixel points used to simulate quantization over one photosensitive area of a pixel.

4.3.1 Effect of interpolation method for image deformation

The choice of the interpolation functions directly affects the systematic errors that are introduced in the synthetic images through the generation of deformed images based on FE displacement fields. In Section 4.2.4 it was observed that a relative error between the displacements obtained from the synthetic data sets and the ones imported from FE simulation is smaller for the case of linear interpolation. Here, this is explored by performing a full ma-

terial identification from the synthetic images by treating them with standard procedure. Two sets of images are considered, obtained by the projection of the same reference grid image (Table 4.3) onto the deformed mesh-grid using linear and cubic spline interpolation method. The elastic displacement fields were extracted from an explicit FE simulation described in Section 4.1.1. Then, these images are treated using the same processing parameters (Table 4.5). The reconstructed stress-strain curves obtained for the two cases of synthetic image sets are presented in Figure 4.16. The material identification of the global stiffness and the axial stress response is obtained by using the VFM. Finally, having access to all these information, a directly identified stress-strain response can be reconstructed at any sample cross-section. From the results, it was observed that in case of linear interpolation the identified response deviates from the expected elastic response when the wave reflection takes place. This occurrence could be caused by the fact that the acceleration levels drastically decrease at a given moment and can be tied to the issue of interpolation of very small numbers. Similar result was observed for the case of cubic interpolation method. On the other hand, such instabilities are not observed with the cubic-spline interpolation method. For this reason, the cubic-spline interpolation was chosen to deform the synthetic image data sets in this work although investigation related to the order of the spline used, remains a perspective.

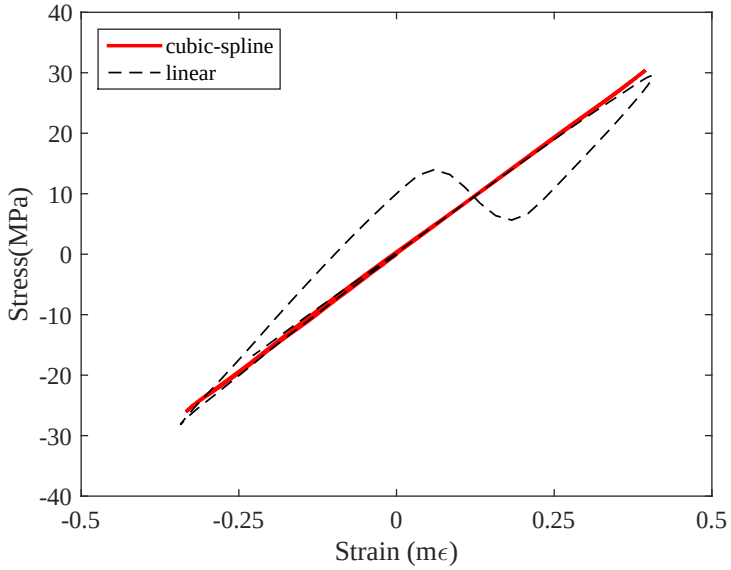

Figure 4.16: Reconstructed stress-strain response at 40 mm from sample free-end (Virtual gauge size 20 points) from two synthetic images sets obtained with *linear* and *cubic-spline* interpolation procedure.

Strains	
derivation method	Diffuse approximation
radius	8 pixels
polynomial order	2
Accelerations	
smoothing method	Savitzky-Golay filter
polynomial order	2
time points	9

Table 4.5: Overall mean relative error made on the axial displacement from simulated images based on the interpolation technique used to deform the images. (considered frames after 20 μm)

4.3.2 Effect of numerical noise on the generation of synthetic images

The simulated displacement fields obtained from a simulation of a spalling experiment that are later on used to generate the deformed images are obtained from conducting an Explicit FE analysis of the problem. In such analysis the equilibrium is not strictly imposed but it is rather the smallness of the time increment that ensures the convergence towards the correct result. Abaqus/Explicit provides the option of the automatic calculation of the time increment and the user defined time increment. In the automatic option the increment is obtained based on two criteria. One is the propagation of the wave through the smallest finite element, calculated element-by-element. Second is based on the highest global mode frequency of the system. With the automatic option the initial guess always starts with element-by-element estimation method. However, this means that the time increment is not necessarily constant through the entire simulation time. This will introduce slight high-frequency numerical noise in the simulated results regarding nodal displacements. It is worth pointing out that such numerical high-frequency content present in the simulated displacement fields will deteriorate the material identification procedure and image generation procedure since the effect of the noise effect will be enhanced due to the second order numerical derivation of displacement fields in order to obtain the desired acceleration fields. For this reason it is imperative that the numerical increment is fixed and chosen to be small enough in order to ensure the stability of the computed displacement fields.

As an example a demonstration will follow. In this work, the numerical model of a spalling test presented in 4.1.1 is used to provide the simulated displacement fields. In case of the elastic material model, the initial time increment chosen by the automatic procedure is $3.228\text{x}10^{-8}$ s, if proceeded, the increment can slightly change throughout the simulated steps causing fluctuations within the simulated displacements. An example when such displacement fields are used to generate synthetic images (properties in Table 4.5) and then treated as to perform the identification of the global Young's modulus, is provided in Figure 4.17. Imposing a fixed increment can solve such problem at the expense of the increased computation time. However, it is imperative to have exact (or as close as possible) simulated displacement fields in order to increase the accuracy of the image simulator and not introduce numerical error in time evolution. For this reason a study on stability of the result was performed and in all the numerical simulations the fixed time increment was enforced to be $1\text{x}10^{-9}$ s. An example of the identified global Young's modulus in that case is presented in the same plot. Although the noise is numerical in nature, once again demonstrates the sensitivity of the identification procedure to any temporal high-frequency noise content in the displacement fields.

4.3.3 Effect of the quantization error in simulated images

The approximation made due to the numerical integration regarding quantization of one pixel will influence the measurement precision of the simulation process [Rossi and Pierron, 2012, Wang et al., 2016]. An example is shown in [Rossi and Pierron, 2012] where synthetic images with uniform axial stretch were generated. High spatial frequency errors were observed in the strain maps obtained from such data sets especially for the case of low resampling points. It was noted that the quantization error is reduced for larger number of resampling points which was later confirmed in [Wang et al., 2016]. In order to demonstrate this effect and how quantization errors propagate within the present method for deforming images, several data sets were generated and a full identification of the elastic material response is performed. Two dynamic ranges were considered, namely 10-bit and 16-bit and three values of sampling points: 1 point, 5 points and 10 points. In all cases grid was sampled with 9 pixels and a slight FFT blur of 1 pixel was added to smooth the spatial frequency of generated reference grid image. The results regarding the identified mean value of global Young's modulus and its standard deviation calculated after the first 20 μs from the loading are given in Table 4.6. It was noted that for larger number of resampling points the deviation of the identified global Young's modulus decreases, confirming that the super-sampling technique can be beneficial for reducing numerical errors within the simulation procedure.

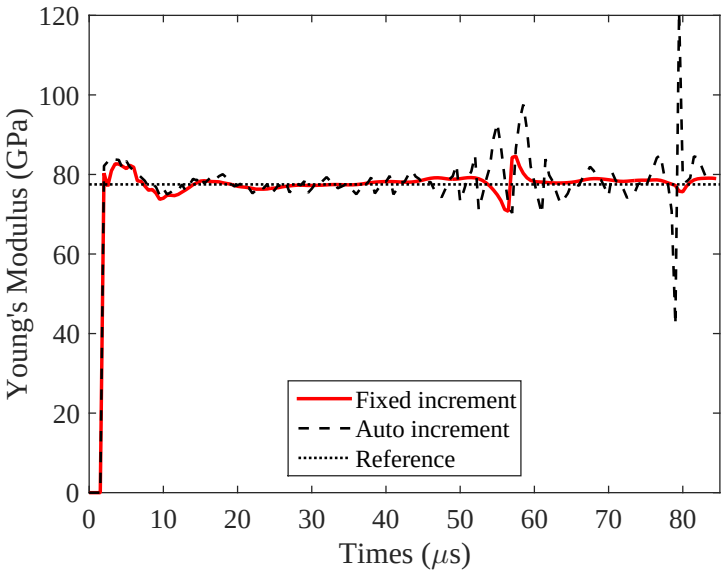

Figure 4.17: Effect of numerical high frequency noise on the identification results obtained from synthetic images (acquisition speed 2 Mfps).

Dynamic range	[GPa]	1x1	5x5	10x10
10 bit	mean	75.679	77.980	77.847
	std	10.617	6.567	7.828
16 bit	mean	77.142	77.951	77.989
	std	3.875	1.699	1.663

Table 4.6: Effect of choice of supersamples on the mean identified global Young's modulus. (considered frames after 20 μm)

4.4 Various effects on the identification of elastic response

The photomechanical spalling test involves various measurement and identification stages and as such presents a complicated procedure that depends on various settings such as: camera settings, image quality and sample conditions. In that case it is difficult to understand how certain errors would propagate to the identified result. The simulator presents a good way to investigate such effects separately and to provide information on what would be their impact on the final result.

4.4.1 Influence of image quality

4.4.1.1 Effect of camera dynamic range

The intensity pattern captured by an ultra-high speed sensor directly encodes the measured physical quantity through its intensity variation. The range of the integer values that can be used up to pixel saturation to describe the amount of detectable light and, therefore, describe the intensity variation, depends on the dynamic range of the camera. Assuming perfect lighting conditions, the dynamic range directly governs the amount of information that can be encoded in one image. Even though there are a number of uncertainties that influence the phase detection, one of the main causes is when the periodicity of the signal that encodes the measured physical quantity is not sinusoidal. An example case is when the fringe profile exhibits a rather triangular shape [Surrel, 2000]. This could be also considered as an insufficient value of grey levels captured by the data acquisition system used to describe

the desired signal intensity, which can then produce patterns that do not have exactly a sinusoidal profile and consequently influences the detection of a phase change in the profile.

In the present work, the synthetic grid image is generated from a continuous light intensity function (Equation 4.1) that describes the light distribution which is digitized in grey levels to simulate the encoding process of an UHS CCD sensor. The light intensity of one simulated pixel is obtained by integrating the values over a small size that represents the pixel area, which is finally rounded up to the closest lower grey level count. Consequently, a small error is introduced that decreases the dynamics of the CCD sensor [Badulescu et al., 2009a]. In order to investigate the impact of the simulated camera dynamic range on the quality of measured displacement as well as on identification of material parameters using the VFM processor, several theoretical dynamic ranges were simulated during the generation of the reference image, namely 8-bit (256 grey levels), 10-bit (1024 grey levels), 12-bit (4096 grey levels) and 16-bit (65 536 grey levels). A matrix of 10x10 sampling points is used to compute the pixel grey level. Additionally, a slight FFT blurring was applied to the images to simulate lens defocusing. The effect of camera dynamic range on the identified global elastic Young's modulus as well as the reconstructed stress–strain response during a simulated spalling experiment is depicted in Figure 4.18. High fluctuations in the identified Young's modulus were observed for the first 10 μs while more stable results were exhibited after this time point. The results for the mean identified Young's modulus as well as its standard deviation obtained after the first 10 μm are presented in Table 4.7.

The plots in Figure 4.18 indicate that simulations with the lower dynamic range can increase the variation in the identification of the elastic stiffness parameter. This later could imply that a capacity of 255 grey levels is just not sufficient. However, a linear regression analysis still provides more reasonable results. An improved identification is achieved with higher dynamic ranges. Finally, it seems that the encoding of 10 bits can be considered as adequate for a proper reconstruction of the acceleration fields. This is an apparent characteristic of most ultra-high speed cameras currently available. Nevertheless, the prospect of increasing the performance of future ultra-high speed cameras with respect to their dynamic range would certainly bring benefit to their metrological application and significantly improve the process of obtaining the identified material parameter values.

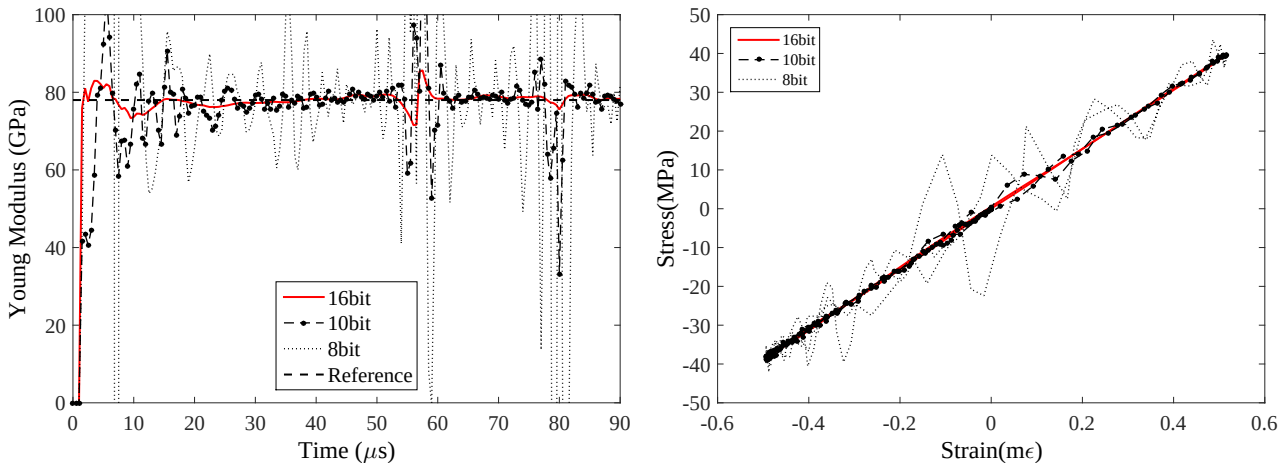

(a) Identified global Young's modulus.

(b) Identified stress–strain response averaged on the entire sample surface.

Figure 4.18: Effect of camera dynamic range on the identified elastic material response in a simulated spalling experiment (2 Mfps, 9 pixel/period/mm).

Young's modulus (GPa)	8bit	10bit	12bit	16bit
Global stiffness				
mean	78.91	77.85	78.00	77.99
std.	44.11	7.83	2.05	1.66
liner regression	77.39	77.40	77.38	77.39

Table 4.7: The effect of simulated camera dynamic range on evaluated Young's modulus and the standard deviation.

4.4.1.2 Effect of image blur

One type of the errors that can occur in local phase shifting algorithm can arise from framing a grid signal close to binary one, black lines on a white background. Even though a high-contrasted grid pattern is desirable regarding a reduction of spatial noise, the high-frequency content caused by a close-to bimodal grid distribution can locally introduce fictive distortion to framed grid images [Pierron and Forquin, 2012b]. A positive effect of blurring was already experimentally sugested in the case of direct extraction of strain measurements [Badulescu et al., 2009a]. Blurring can be even more beneficial for cameras with low dynamic range and fill factor, since it can increase the distribution of grey levels by inducing a quasi-sinusoidal grid image to be formed. This can be done by defocusing the camera lens. However, it can also cause the contrast of the images to decrease which can in turn influence the noise level introduced by the camera to increase [Grédiac et al., 2016].

Here, the beneficial effect of slight optical blurring of the grid image is investigated on noise free image sequence. As a first scenario, this can be demonstrated by simply recreating a deformed sequence of bimodal grid images and comparing the identification results with the results obtained for the same image sequence but with applied fast Fourier transform (FFT) blur. In this case the 10 bit dynamic range is considered. The profile of a bimodal grid before and after applying the filtering are presented in Figure 4.19 and the identification results in terms of a global Young's modulus and reconstructed stress-strain response are depicted in Figure 4.20.

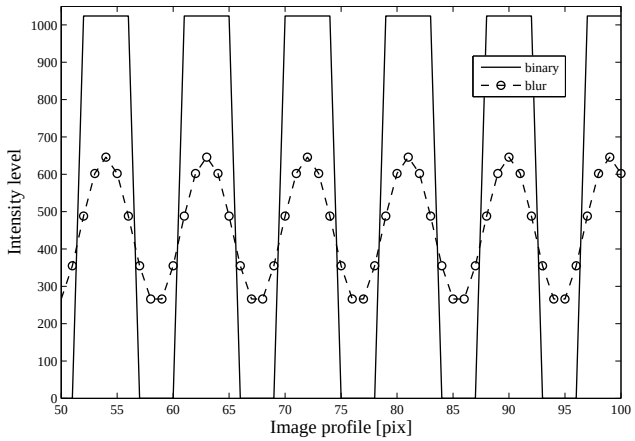

Figure 4.19: Effect of applying a FFT blur on a bimodal grid pattern.

Indeed, it can be observed that when a binary grid is considered, owing to high harmonics present in the images the phase detection algorithm seems disrupted. Although the results from bi-modal images can be over-exaggerated due to the existing interpolation error introduced in the images (which was not considered in [Lukić et al., 2017]); when slight blurring is added, the phase identification is retrieved and the identification results seem more reasonable. Finally, to confirm this effect, regular image sequences were generated using the super-sampling technique, assuming that the white pixels lie on the saturation limit. Then, these sequences were treated with and without added blur and the results on the mean identified Young's modulus are given in Table 4.8. The results indicate positive effect of blur which reduces the standard deviation of the identified values. This then confirms that a slight

lens defocusing during an experimental acquisition can be beneficial.

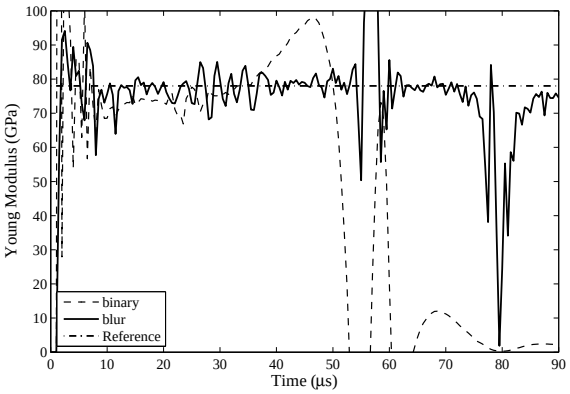

(a) Identified global Young's modulus.

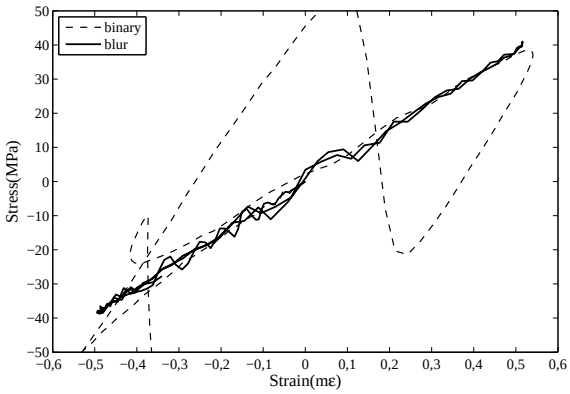

(b) Identified stress–strain response averaged on the entire sample surface.

Figure 4.20: Effect of FFT blur on the identification from bi-modal synthetic grid images. (FFT blur 1 pix)

Dynamic range	[GPa]	no blur	blurred
10 bit	mean	71.578	77.847
	std	14.781	7.828
16 bit	mean	71.111	77.951
	std	13.488	1.699

Table 4.8: Effect of image blur on the mean identified global Young's modulus and the standard deviation. (FFT blur 1 pix)

4.4.1.3 Effect of grid pattern

Owing to uniaxial nature of the spalling test, it can be reasonable to consider only unidirectional spatial carrier which will provide only axial displacement measurements. However, a question arises whether the unidirectional description of the grid pattern could be slightly disrupted by the fact that the deformation also occurs in the orthogonal direction due to the Poisson effect. In order to qualitatively investigate this point, two synthetic reference grids were considered assuming perfect grid periodicity with unidirectional and bidirectional line distribution as shown in Figure 4.21.

In both cases the deformed images were obtained by projecting the reference image onto the meshgrid which is subsequently deformed considering both the axial and vertical displacement maps obtained from the FE simulations. Although, the mean value of the displacement field in vertical direction is zero, the maps are symmetrically distributed due to the presence of the rectangular flatten surface. It is necessary to mention here that this is the advantage of conducting 3D numerical simulations since such fine effects can be captured. A time averaged map over all simulated frames of vertical displacement obtained from a simulated spalling experiment is presented in Figure 4.22 which clearly indicates that these displacements are of a microscopic order which is below the measurement resolution of any UHS camera used in this work. The identification results indicated no notable effect in the identified axial stress response, as expected, and a slight effect on the peak axial strain response during the tensile loading phase. Higher value of average axial strain at the peak of tensile loading was observed in the case of unidirectional grid images that is around 2.5% higher than from simulated FE data (Figure 4.23). This is considered acceptable, finally suggesting that both unidirectional or bidirectional grids can be used in the real experiment.

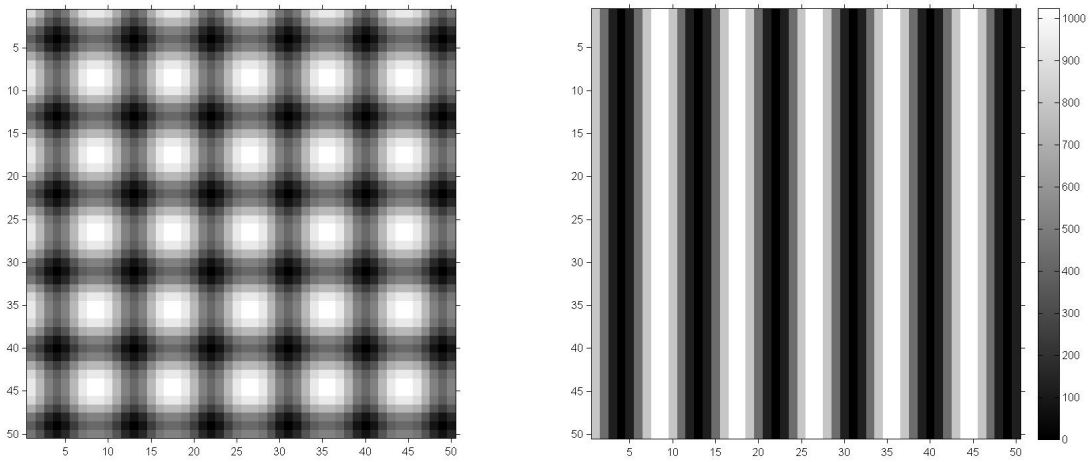

Figure 4.21: Synthetic bidirectional and unidirectional grids used to verify the image deformation chain and determination of axial strain measurement result.

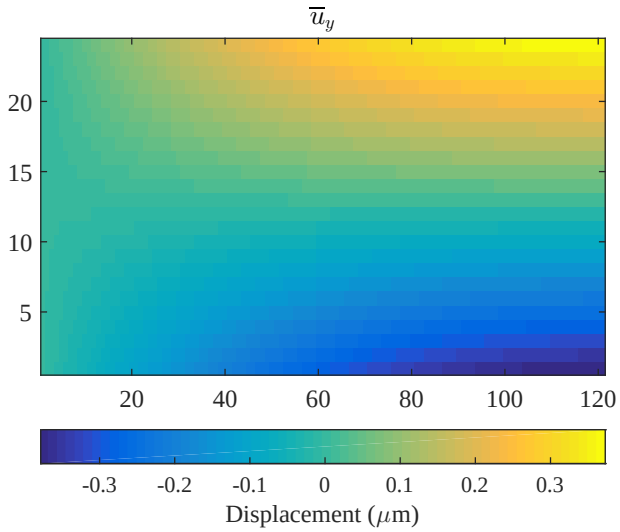

Figure 4.22: Average map of elastic vertical displacement from a simulated spalling test using 3D Numerical model (Section 4.1.1).

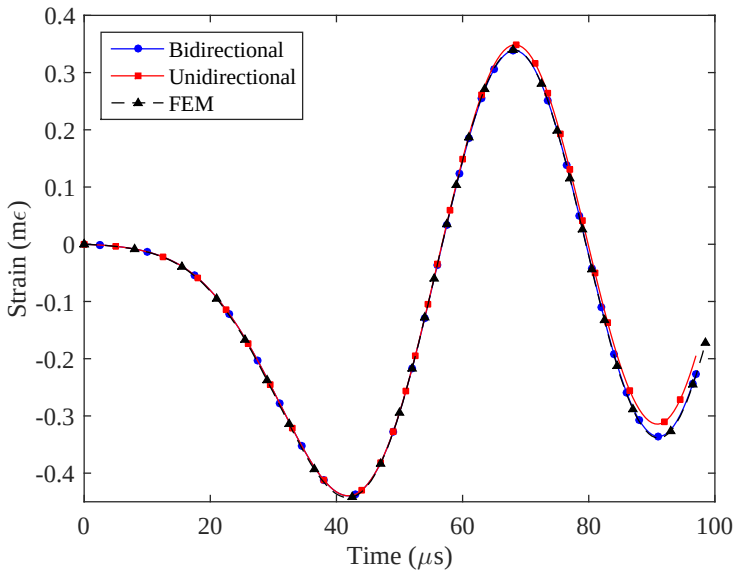

Figure 4.23: Average axial strain from simulated unidirectional and bidirectional grid images.

4.4.1.4 Effect of the grid sampling

The number of pixels used to sample the grid beating period is a parameter that directly influences the identification results. Increasing the number of pixels per period will improve sampling of the grid and thus allow more information to be locally registered in captured frames. Increasing the number of pixels per period used for signal encoding can reduce the standard deviation of the measured quantity [Badulescu et al., 2009b]. On the other hand, the higher the number of pixels per period the smaller is the observed surface of the sample owing to limited camera pixel count and therefore the higher is the sensitivity to mechanical micro-vibrations that may be caused during the experiment [Sur and Grédiac, 2015]. Number of sampling points is a user-dependent parameter that needs to be tuned according to each experimental investigation. Therefore, a compromise between observation window size and measurement resolution must be determined. In theory, if only the first harmonics of the perfect fringe function are used to describe the light intensity of a point, the minimal number of sampling points necessary to obtain the sought unknowns is three pixels. However, as already discussed, the framed grid is never a perfect periodical function, and the minimum value usually used in practice is five sampling points and higher. In the following case, this effect is investigated by taking into account several grid sampling resolutions starting from five pixels per period. In each case, the resolution of the simulated camera was adjusted to obtain the same number of measurement points which enables performing reliable comparison between different situations. The simulated camera dynamic range was defined to be 10 bits with an interframe time of 500 ns. The results describing the effect of grid pixel sampling on the identified mean stiffness as well is presented in Figure 4.24. All in all, it seems that a sampling of 7 pixels per grid period and above seems as an adequate choice to be considered when real experiments are carried.

Figure 4.24 indicates the benefit of increased number of points used to sample the framed grid. A smaller number of sampling points increases the standard variation as well as the absolute error in the mean identified Young's modulus. However, the reconstructed stress–strain response seems less affected by this effect although some instabilities are noted. Finally, the benefit of sampling the grid image with 7 pixels in this case can be considered as fair.

4.4.1.5 Effect of spot lightning

When dealing with ultra-high speed photography and acquisition speeds beyond 1 μs, the amount of light captured in the imaged scene depends on both the exposure time and intensity of the used source. It is one of the difficulties often encountered in high-speed photography which can be the limiting factor in the quality of the data acquired.

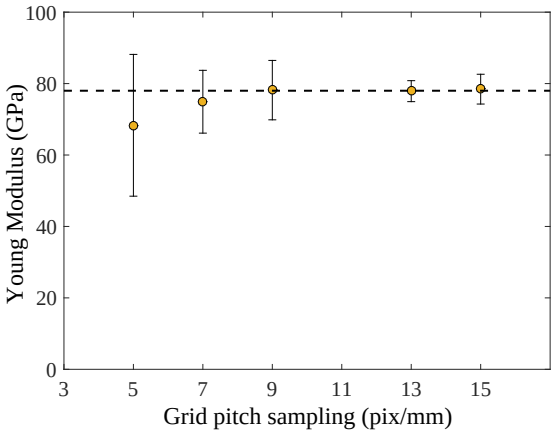

(a) Identified global Young's modulus.

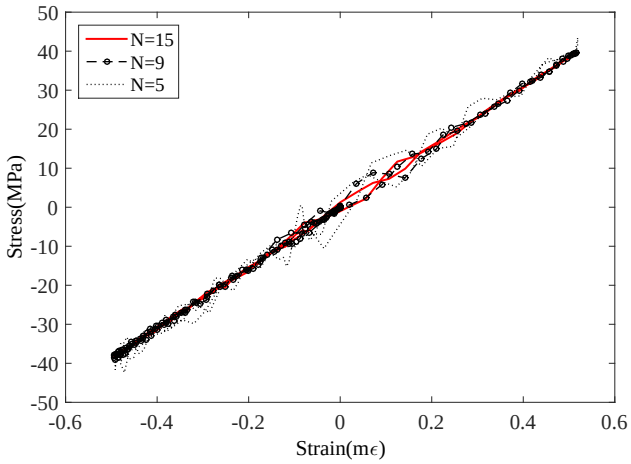

(b) Identified stress–strain response averaged on the entire sample surface.

Figure 4.24: Effect of grid sampling on identification of elastic Young'smodulus and reconstruction of stress–strain response for simulated grid of 10 bits.

When dealing with grid measurements, due to the necessity of fine picture adjustments, it is often resorted towards using continuous lightning source rather than an instantaneous source such as flash. In that case, high-power lightning supply needs to be used to provide sufficient lightning which often needs to be focused on a spot in order to provide better illumination of the scene and to increase the power density [Rossi and Pierron, 2012]. However, this then induces non uniform lightning conditions over the imaged grid and as such could affect the measured results. For example, it was sugested that a spot illumination does not affect the mean identified elastic results, however, can increase the standard deviation of the result [Badaloni et al., 2015]. In order to investigate this effect, the spatial variation of illumination is considered by multiplying the reference and subsequently deformed images with a illumination mask in order to obtain the modified images. Although more realistic illumination models exist which take into account the diffuse, specular and attenuation components of real lightning conditions [Balcaen et al., 2017b]; this quite simple method allows testing various types of illumination gradients and intensities [Badaloni et al., 2015]. Here, in order to simulate a perfect spot focus a mask of the same dimensions as the image was chosen. The lightning distribution is obtained by a convolution of a two Gaussian distributions along the vertical and horizontal image axis. The amplitude of the spot is defined through the percentage of the mean image grey level. A test was carried with spot illumination being 60% of the image average grey level. The reference grid image is generated taking 10x10 super samples and considering 16 bit dynamic range. Slight blur was added to the image and the average image grey level is 54% of the dynamic range (35200 grey levels). The resulting reference image with a simulated spot lighting of 60% is presented in Figure 4.25. It is obvious that a certain amount of pixels within the image center is saturated. The full identification was performed treating the spot sequence with standard tools. The mean identified global Young's modulus and its standard deviation are given in Table 4.9. Finally it can be observed that no notable difference is present within the identified values of stiffness. To some extent this was expected since the spot lightning should not disrupt the phase detection within the grid method as long as within one analysis window the lightning be considered constant as stated in [Sur and Grédiac, 2014] and which is the case here.

4.4.1.6 Effect of image white noise

Noise is almost inevitably present in the images acquired with a CCD sensor and its sources are various. For instance, the light intensity values registered by an CCD imager can be corrupted by the photon noise, dark current noise, readout, and digitization noise [Holst, 1998]. In ultra-high speed cameras, the noise present from one frame to another largely depends on the architecture of the sensor and the way how information is being stored and read

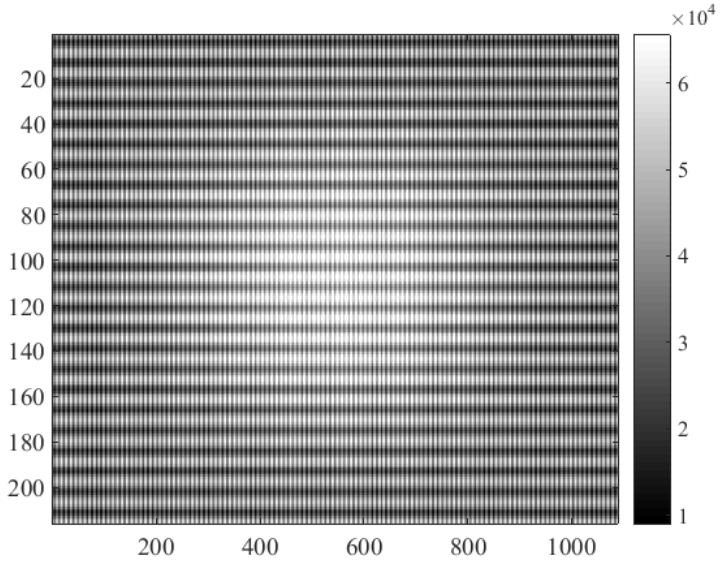

Figure 4.25: Example of a synthetic image with a spot lightning.

Illumination		[GPa]
no-Spot	mean	77.951
	std	1.699
Spot 60%	mean	78.019
	std	1.462

Table 4.9: Effect of 60% spot lightning and non uniform grid illumination.

out from the pixel memory [Pierron et al., 2011a]. This noise then propagates through the identification chain and increases the uncertainty of the identified material response.

Here, the sensitivity of the identification procedure is investigated by adding grey level noise to the simulated images. The supposed camera noise is modelled as non-correlated zero mean white noise assigning a certain standard deviation of grey level at a pixel point [Healey and Kondepudy, 1994]. Firstly, at each simulated image frame, a random set of pixels has been chosen assigning them a grey level standard deviation γ. The process is repeated for several levels of grey level noise which was chosen as a percentage of the mean image illumination (mean sequence grey level). The synthetic images analysed here are generated with 10 bit dynamic range since it is an apparent characteristic of most ultra-high speed cameras currently available (*i.e.* Kirana camera). The grid sampling was taken as 9 pixels and slight blur was added to smooth the grid profile resulting in images with mean grey level of 550 counts. Images were treated with standard procedure using the parameters given in Table 4.12. The virtual fields were expanded from polynomial fit of 8^{th} degree. Figure 4.26 presents error bar plot of the mean identified Young's modulus. It can be observed that the increased standard deviation of the added white noise increases the uncertainty of the identified stiffness while the mean value stays almost unchanged and close to the reference. This result was expected, since same observations are made and analytically derived when only the uncertainty of displacement measurement is analysed [Grediac and Sur, 2014], where it is shown that noise standard deviation directly relates to the metrological performance of phase extraction. Here it is interesting to note that random noise propagates through the entire identification procedure with a similar principle.

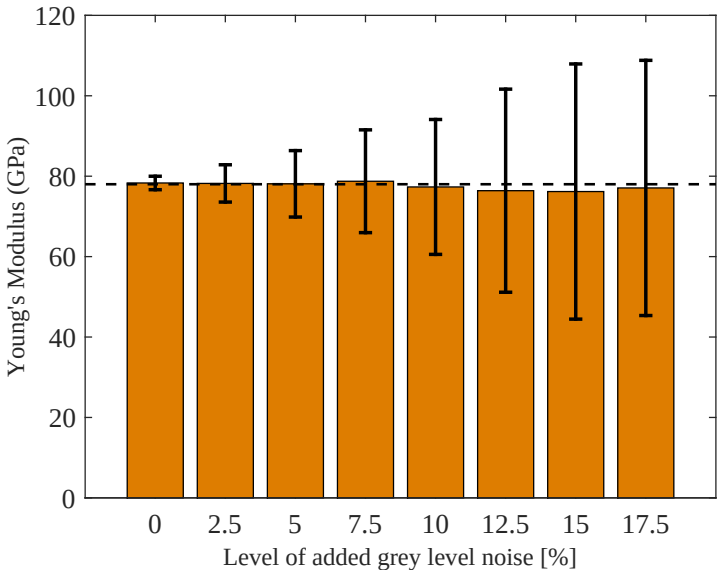

Figure 4.26: Effect of frame alternating zero-mean random grey level noise on the mean identified stiffness.

4.4.1.7 Effect of temporal random noise

The procedure applied above was used in some works to describe the noise intensity of an UHS camera (*i.e.* Shimadzu HPV-X) [Seghir and Pierron, 2017]. However, it is arguable whether spatially random non-correlated frame-to-frame noise can be considered as a representation of that of an UHS camera. In fact in an UHS camera, often all pixel exhibit a certain standard deviation of grey levels with respect to their own mean grey level value. An example regarding the Shimadzu HPV-X2 is shown in Section 6.3.1.3 where all pixels exhibit a standard deviation of approximately 9% of their mean grey level value. The same value regarding Shimadzu HPV-X was reported to be 3.5% [Seghir and Pierron, 2017]. Therefore, adding such standard deviation to the entire signal of each pixel can be considered as a better representation of the grey level noise since it also considers the temporal grey level fluctuation. First, an ideal synthetic image sequence is generated without any added noise content. Then, each pixel is considered as a separate signal to which a random noise component is added with a standard deviation γ_t which is defined as a percentage of the mean pixel grey level value. In that way, a realistic noise level can be added to the simulated images which is extracted from filming a blank scene with an UHS camera. Two noise levels are considered: a first one which is 3.5% and is characteristic of the Shimadzu HPV-X [Seghir and Pierron, 2017] and a second one which is 9% and is characteristic for a Shimadzu HPV-X2 (Section 6.3.1.3). Then these two image sequences are treated with a set of processing parameters (Table 6.2) which involve significant smoothing (*i.e.* acceleration kernel of 15 time points). The reconstructed stress-strain response for the two cases of processing parameters are presented in Figure 4.27. Although the modelled random temporal noise can be considered as strong approximation, an obvious sensitivity of the modelled noise can be observed. All the results regarding the identified mean global Young's modulus are reported in Table 4.10. It can be seen that for this method, larger noise content influences both the systematic and random errors to arise. Smoothing with a larger acceleration kernel can help with the reduction of random errors on the expense in the increase of the systematic errors, and one needs to accept this trade-off. For this reason, linear regression performed directly on the reconstructed stress-strain response provides more robust estimation of the elastic stiffness. Finally, such procedure allows tuning the processing parameters in regard to the noise level which can be evaluated from a stationary image sequence in a fairly simple way.

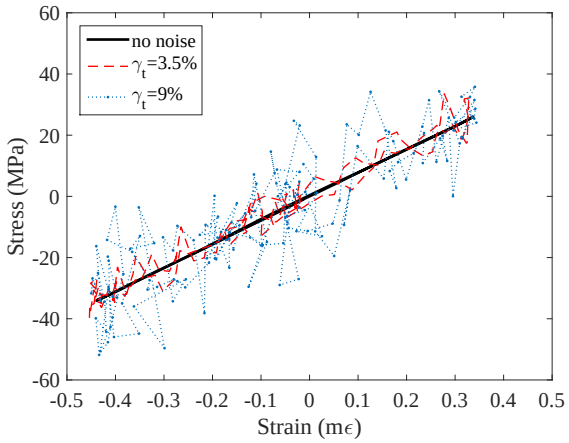

(a) Reconstructed elastic response considering standard set of processing parameters (acceleration kernel 7 points).

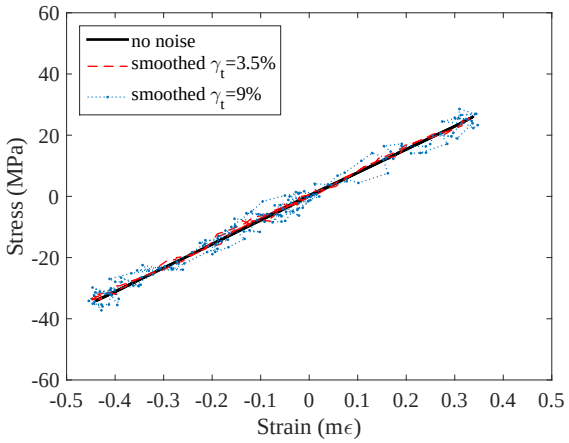

(b) Reconstructed elastic response considering set of processing parameters used in real experimental treatment (acceleration kernel 15 points).

Figure 4.27: Effect of temporal random grey level noise on the reconstruction of stress–strain response.

Noise level		Acc. kernel 7 points		Acc. kernel 15 points
no noise	mean	77.95		
	std	1.69		
$\gamma_t = 3.5\%$ (HPV-X)	mean	76.94	mean	69.56
	std	42.56	std	14.35
$\gamma_t = 9\%$ (HPV-X2)	mean	61.74	mean	51.87
	std	63.21	std	20.41

Table 4.10: Effect acceleration smoothing on the identified material elastic stiffness.

4.4.2 Influence of sample conditions

4.4.2.1 Effect of carrier tilt

When conducting a photomechanical dynamic test there are several types of error sources that can be encountered. One type, often overlooked, corresponds to the methodology of preparing the experimental set-up. In this case, it could be considered that from the beginning, an error is introduced that is systematic in nature (when compared to camera noise for example).

The spalling experiment is by definition a dynamic uniaxial test relying on propagation of axial stress wave. Therefore the desired measurement is the axial displacement component along the sample's length which in principle coincides with the measured horizontal displacement. Nevertheless, there are situations where the actual measured horizontal displacement components do not coincide with the sought axial displacements such as when the grid spatial carrier is not perfectly aligned with the sample axis. Indeed, gluing the grid requires a specialised procedure [Piro and Grediac, 2004], which implies that a certain stationary load needs to be applied over the deposited substrate on the sample surface during the curing stage. In principle such a procedure allows draining excessive glue and ensures a flat bond between the surface and the spatial carrier. However, due to possible imperfections of the surface on which the grid is to be deposited and due to initially viscous nature of the glue, during the curing stage the pressurised substrate can move out of position. In that case the axis of the grid do not coincide with the axis of the sample and errors can be introduced even if all the other calibration conditions are met (*i.e.* grid pixel sampling). In principle, such situation can be corrected by simply performing vector addition of the two displacement components. However, it is often the case that the camera noise magnitude can camouflage this secondary displacement component and as such it is not measurable.

In order to inspect to which extent such errors could have an impact, a scenario is considered where the horizontal axis of a grid and the sample form a rotational angle α (Figure 4.28). The numerically simulated displacement fields are then decomposed into components that correspond to the fictive grid orientation. Assuming that the virtual camera is placed in such way that it matches the grid orientation correctly (the axis of the camera coincides with the grid) then these decomposed displacement components (*i.e.* rotated) can be used within the simulator to recreate synthetic image sequence. Although, it is clear that the material stiffness is preserved and no error is introduced in the determined Young's modulus, an error would occur during the determination of the peak axial stress (Figure 4.29b). Figure 4.29a shows a relative error of peak elastic tensile stress regarding a situation where there is no tilt and subsequently evaluated peak stress in tilted situations. As one could expect, the error is small and even for a large grid tilt since the principal displacement component is governed with a cosine function. For example the relative error of 2 MPa is observed for a tilt of $\alpha = 20°$. Nevertheless, this presents one step towards examining other possible tilt effects which could cause more severe errors such as: camera tilt which would result in non-equal grid/pixel sampling or sample tilt due to defects of parallelism which would violate the axial stress state assumption. Both latter situations remain a perspective of this work.

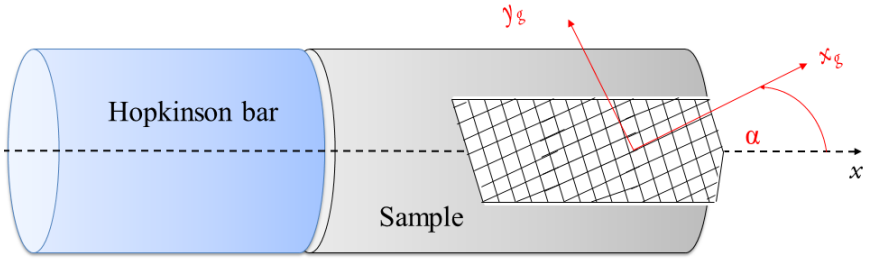

Figure 4.28: Illustration of a tilted grid pattern.

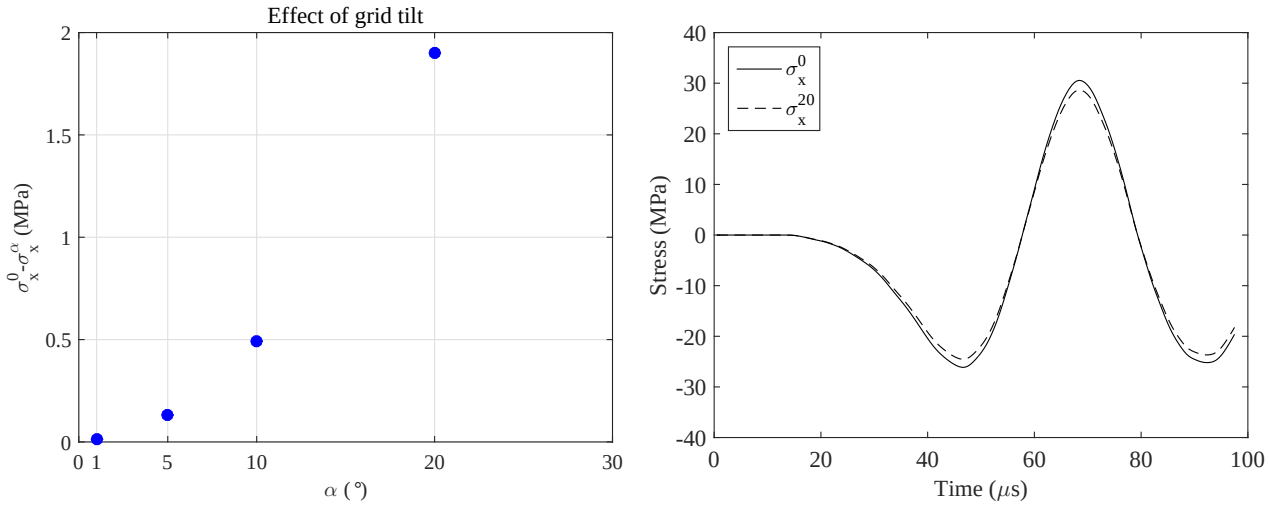

(a) Relative error of the peak tensile stress with respect to rotation angle.

(b) Identified 'axial' stress response for case of tilted and not-tilted grid.

Figure 4.29: Effect of grid rotation angle on identification of peak elastic stress.

4.4.2.2 Effect of the spatially varying material stiffness

The uniaxial tensile response of concrete is also governed by its heterogeneous nature. When characterized from a global standpoint, the tensile strength should be determined on specimen that are large enough in order to account for the material heterogeneous nature. Some design codes suggest that the minimum dimension of the cross-section should be at least three times the maximum aggregate size. In experimental testing, the same principle is often applied when point-wise measurements are taken. For example a strain gauge glued on the sample surface is often arguably considered large enough (with a length of about three times the largest aggregate) so it provides information that are representative of a global material response. In that case, one simply has to hope that the measurements obtained are not being disrupted by a local morphological content of the examined specimen.

On the other hand, full-field measurements do not rely on such assumptions and can provide insight on the influence of heterogeneities on the sought global response, since they often contain a sufficient amount of locally measured information. This insight can be obtained by analysing the derived deformation fields [Considine et al., 2016]. On the other hand, the identification of the material response that contains spatially varying stiffness is challenging especially since it has to be taken into account when performing the inverse identification. Some works dealing with quasi-static tensile tests have shown that when specific formulation of the VFM based on examining local equilibrium is used, a smoothly varying hetorogeneous stiffness can be identified without the *a priori* knowledge of its position [Considine et al., 2017]. In dynamic conditions one could use the load cell principle and the acceleration measurements; however, the assumption of stress homogeneity within the cross-section presents a limit and therefore any captured heterogeneity would not be identified in its entity but would still have an impact on the identified 'apparent' material stiffness by locally disturbing the measurement. Here, we explore such impact and whether it can be captured with the proposed identification methodology by performing FE simulations.

Two simple 2D FE numerical simulations were performed within the domain of elastic material response considering a discontinuous material stiffness. The first case considers a layered material, that it is not characteristic of concrete but satisfies the condition of the stress uniformity within a cross-section. Second case assumes a 20 mm quasi-spherical inclusion (one could imagine a large aggregate). The center of inclusions in both cases is in the sample mid length. The FE mesh for this two cases are shown in Figure 4.30. The numerical models of 45x120 mm dimensions are discretizated with structured 1 mm mesh of CPS4R elements (4 node bi-linear plane stress element with reduced integration). The idea is to perform a full identification chain starting with synthetic

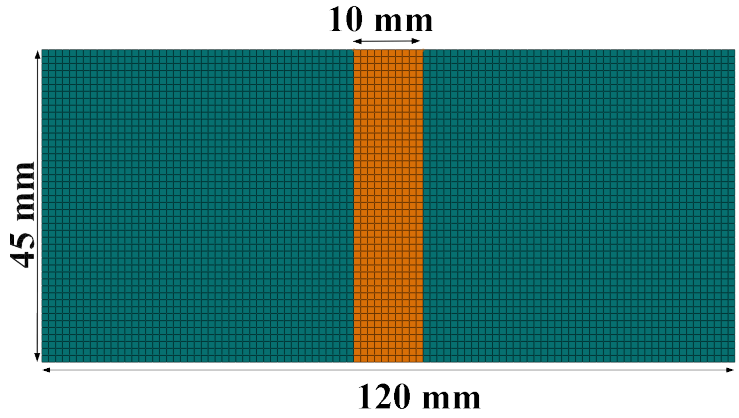

(a) Mesh with layered inclusion with varying stiffness.

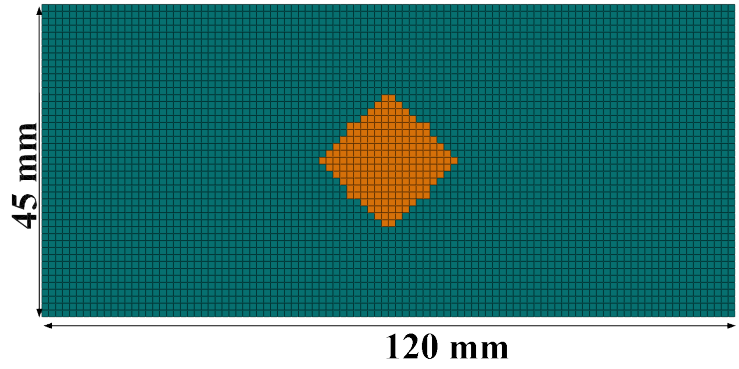

(b) Mesh with quasi-spherical inclusion with varying stiffness.

Figure 4.30: FE mesh used to simulate spatially varying elastic stiffness in a spalling model.

images. Explicit simulations were carried to simulate 100 μs of wave propagation induced by an axial loading pulse (Figure 4.1b) fixing the increment to 1 *ns*. Both the matrix and the inclusion domains were considered purely elastic and the material parameters are given in Table 4.11. The simulated displacement fields considering 2 Mfps acquisition speed were obtained and used to generate sequence of grid images of ideal characteristics as defined in Table 4.3. The images were then treated with standard procedure (Table 4.12). Here, it needs to be mentioned that the spatial density change was not considered when the synthetic displacement data obtained from the images were treated, since in that case, one would have to know the position (and characteristics) of an inclusion. The underpinning idea is to investigate how an inclusion which position is not known, would impact the stiffness measurement when the standard processing is applied. This is in fact what occurs when treating real experimental data.

	Matrix	Inclusion
Material density (kg/m^3)	2249	2700
Elastic Young's modulus (GPa)	35.5	70
Poisson coefficient	0.2	0.2

Table 4.11: Elastic parameters used to simulate a matrix and inclusion.

Grid method	
Window	Triangular (2N-1)
Pitch	1 mm
Sampling	9 pixels
Strain	
Differentiation method	Diffuse approximation
Window span	8 space points
Polynomial	2^{nd}
Strain rate	
Differentiation method	Savitzky-Golay fit
Window span	5 time points
Polynomial	2^{nd}
Acceleration	
Differentiation method	Savitzky-Golay fit
Window span	7 time points
Polynomial order	2^{nd}

Table 4.12: Processing parameters used to treat the synthetic grid images.

Having access to both strain and stress values for all vertical positions (cross-sectional slices) the identification of local stiffness can be carried by analysing all the points for all sections and at all time steps, hence obtaining a so-called space time map of material stiffness [Pierron, 2016]. The modulus can be then simply computed at each data point as:

$$E_{field}(x,t) = \sigma_x(x,t)/\varepsilon_x(x,t) \tag{4.6}$$

The results regarding the identified stiffness maps obtained by processing the synthetic images with the embedded information of spatially varying material stiffness are presented in Figure 4.31. A result from a simulation without any inclusion is also shown for the sake of comparison. As expected, it can be clearly seen that the spatial variation of the stiffness can be locally detected with respect to horizontal position within the sample, since the space-time maps clearly exhibit a change at those locations. However, it is also expected that due to the assumption of the uniform stress state within the one transversal slice (*i.e.* cross-section), constant density and averaging of fields in

vertical direction, the local values will not be correctly evaluated. This can be more closely observed by tracing the identified stiffness values along the sample axis by introducing a virtual time gauge. Figure 4.32 shows results of the identified stiffness along the sample axis averaged between 30 μs and 50 μs where the sample is in compressive loading stage. In the case of layered material, the stiffness is fairly close to the expected values which is not surprising since the densities for two material constituents are quite close. On the other hand, as expected, for the case of quasi-spherical inclusion the stiffness is not identified properly due to field averaging; however, the spatial size can be approximately detected since the change in stiffness occurs between 40 and 60 mm.

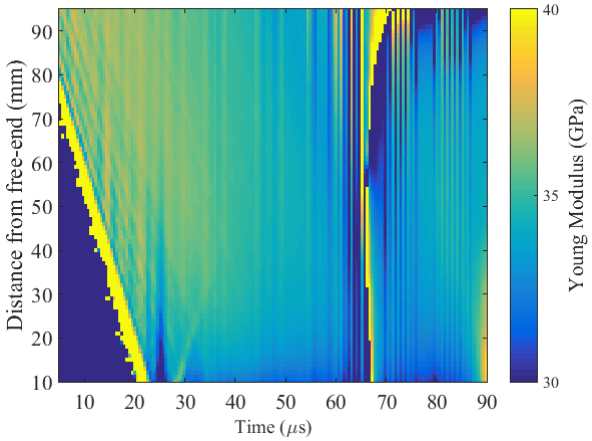

(a) No heterogeneity.

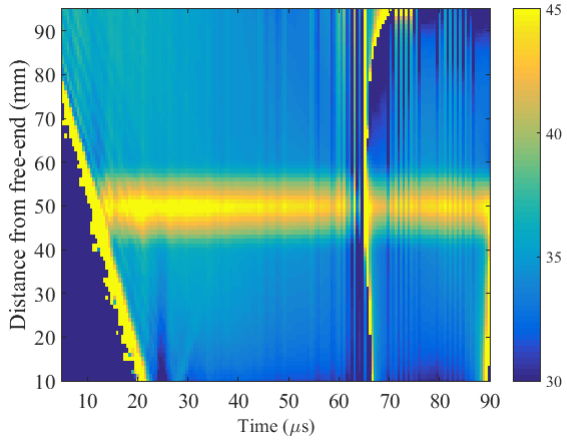

(b) Quasi-spherical inclusion.

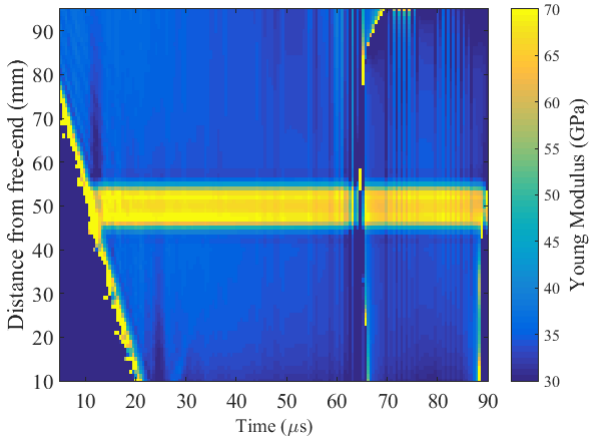

(c) Layered inclusion.

Figure 4.31: Space-time maps of stiffness obtained from simulated images with embedded inclusions and varying stiffness. (Note the change in color bar scale)

The presented results, on one hand, serve as a tool for possible explanation of the stiffness spatial variability which was observed in some of the experimental results (*e.g.* Section 3.4.1.7). Indeed such variability of stiffness could be the cause of the presence of strong siliceous aggregates on the sample surface. On the other hand, they also present a possible perspective regarding detection of heterogeneous stiffness of tested materials under dynamic loading conditions.

4.4.2.3 Effect of missing data at the free-end

In real experimental conditions another source of errors that can occur is due to missing data at the sample free-end. Indeed, when dealing with the grid method it is difficult to measure displacements exactly at the free end due to glueing of the grid and finite size of the convolution window, so it often occurs that this data is lost. In that case,

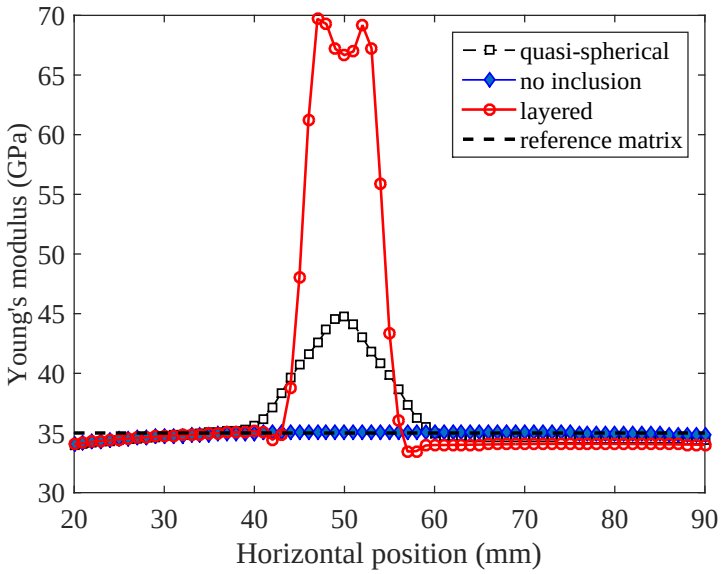

Figure 4.32: Identified stiffness along the sample length between 30 μs and 50 μs.

a situation of missing boundary conditions is experienced and the zero-stress condition is enforced slightly within the sample (away from free-end). In those situations an error is inevitably introduced that affects the identification procedure [Rossi and Pierron, 2012]. When using digital image correlation, same problems are experienced due to the chosen size of the correlation facet [Rossi et al., 2015] and some works suggested test optimisation in to order achieve minimum sensitivity to mising edge data [Wang et al., 2013b].

In this work, the VFM processing requires the measurement of displacement (i.e acceleration) fields up-to free-end so that the stress description (*i.e.* force integral) can be valid. In order to asses the impact of this type of error, the numerically resolved displacement fields extracted from the 3D numerical simulation (Section 4.1.1) were directly treated, from which rows of displacement data at the free-end were forcefully removed. Figure 4.33 illustrates the identified Young's modulus performed by linear regression of the stress-strain response for several considered cases. As illustrated, a dependency on the 'apparent' stiffness (*i.e.* slope of the curves) on the missing data can be noted. Already, if one row of data is missing, a systematic error of 4% is introduced which increases as the missing data increases (Table 4.13). This error is introduced due to the underestimation of the inertial component that acts as indirect force measurement (Figure 4.34). It is worth mentioning that commonly experienced situations in real experiments concern missing data of 1-2 mm from the free-end. An often adopted solution to this issue concerns recreating the missing data by padding procedure [Wang et al., 2016] or by spline extrapolation [Seghir and Pierron, 2017]. In order to instigate if the padding procedure would provide meaningful correction that can be used in experimental situations, the cases of missing data were corrected by the padding. The results obtained are presented in Table 4.14. Although it is a very approximative procedure, the padding technique drastically reduces the error. This in fact suggests that it is not the acceleration levels close to the edge, but it is rather the sample mass which has more influence on the force integral. UHS cameras often have limiting pixel count which results in a risk of not having the dynamic fracture captured within the recorded frames. These results suggest it is maybe not completely necessary to film upto the free edge, but to focus the field of view slightly towards the probable crack location, as long as the displacement data are extended to the true sample edge. Experimental tests should be carried to test this suggestion.

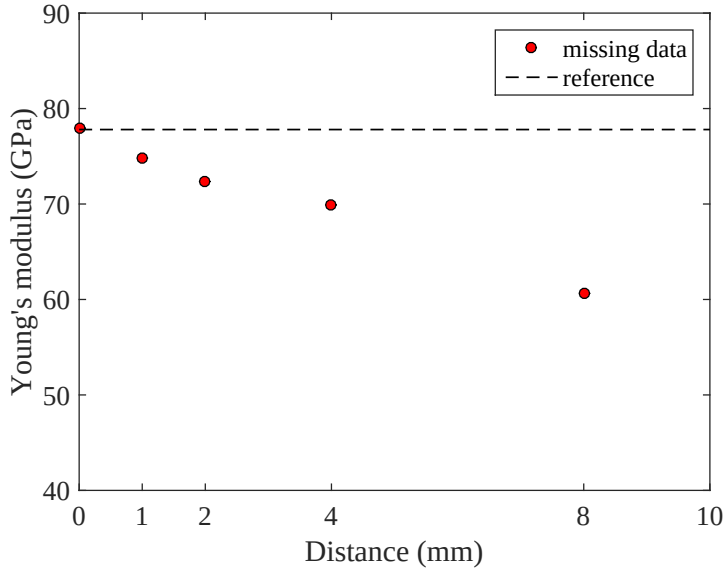

Figure 4.33: Effect of missing data from the sample free-end.

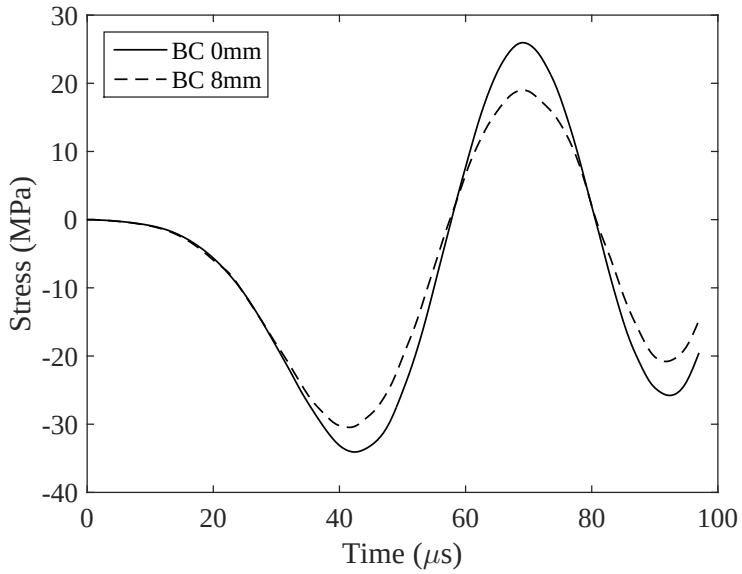

Figure 4.34: Effect of missing data from the sample free-end on mean axial stress measurement.

Distance from edge	Error [%]
0	0.067
1	4.103
2	7.251
4	10.345
8	22.217

Table 4.13: Error with respect to the reference Young's modulus introduced by missing data at the edge.

Distance from edge	Error-no correction [%]	Error-padding [%]
1	4.103	0.89
2	7.251	0.85
4	10.345	0.71
8	22.217	0.6

Table 4.14: Effect of the correction of the missing data at the edge on the error reduction by using padding procedure.

4.5 Dynamic damage measurement

Considered from a mechanical standpoint, damage is a gradual degradation of material due to the applied external load. As such, within the framework of continuum damage mechanics, it can be described through an internal field variable. Although the theoretical aspect of damage has been around for more than half a century, measuring the damaged state (in terms of stiffness loss) of quasi-brittle materials such as concrete presents a challenge even today. Techniques for measuring and identifying damage states from a global approach have been suggested for quasi-static loading regimes, one of which most commonly used for concrete is based on the state coupling of elasticity and damage where the degradation of material elastic stiffness can be used to identify damage [Lemaitre, 1996]. At the beginning, these measurements were performed with point-wise tools that had to assume uniform development of damage. Later, the development of optical techniques loosened such assumptions allowing a step further in the visualization of damaged states and identification based on the use of inverse techniques and field measurements. The equilibrium gap method allows identifying damage by minimising the relative stiffness within the element local equilibrium using directly measured displacement [Claire et al., 2004]. The virtual fields method provides a more direct route to identify damage by chosing appropriate virtual fields [Chalal et al., 2004]. Recent advancements in 3D optical and in situ measurement techniques have made a step forward in visualization of damaged state and direct local extraction of damage parameters within sample bulk [Hild et al., 2015].

In dynamic loading regimes the ultra high speed photography, in that case, presents the diagnostics tool of choice. The spalling experiment on the other hand favours the non-equilibrium stress state and with the aid of the VFM and the load cell principle allows the use of acceleration fields as direct stress measurement. In that case, since the local constitutive response can be reconstructed without an *a priori* assumption, the information regarding damage can be directly derived from the obtained measurements.

In the following this is explored through numerical simulations. First the case of a bi-linear response is considered in order to explore a possibility of using the identified global stiffness as an indicator of a non-symmetric response between compression and tension. Second, a damage model is used to simulate the displacement fields with explicit finite element computations. Then the entire chain of measurements is simulated as in previous sections considering perfect photographic conditions and the grid method. Although the damage law is known, the displacement data are treated without any assumption on the material behaviour and the VFM is used to reconstruct a local stress-strain response that is compared to that of the FE model. This work is aimed to contribute to the use of the VFM as a dynamic measurement tool adapted to the processing of full-field measurement to analyse and identify damage in quasi-brittle materials.

4.5.1 Identification of bi-linear response

Concrete as a geomaterial has a pronounced micro-structure that apart from other heterogeneities (*i.e.* aggregates) consists of voids and micro-cracks mainly present at micro scale. Some of these defaults already develop during hydration of cement paste inducing a distributed development of micro cracks. Owing to these characteristics,

the response of concrete material in dynamic loading conditions is largely affected by its micro-structural content. Upon loading, microscale defects cause concentration of microstresses that lead to physical loss of material (i.e bond breakage and decohesion) on a mesoscale [2] this processes reflect trough the change of material stiffness. Owing to such characteristics, during compressive loading the closure of the pre-existing micro-defects can occur, which then manifests through increased stiffness response; on the other hand, during the tensile loading stage, the pre-existing micro-defects will start to open in a defuse manner which takes place before the ultimate strength response is reached.

Therefore, a first step towards using the proposed methodology for performing dynamic damage measurements of concrete-like materials is to confirm that it is capable of faithfully capturing a possible non-symmetric response of material in compression and tension. To this end, a bi-linear elastic material response is modelled with the means of explicit FE simulations using the previously described 3D numerical model (Section 4.1.1). The material response is modelled assuming a perfectly elastic description in compression and tension in which a dissimmetry parameter is introduced as a ratio of the two Young's moduli (E_t/E_c). The stiffness parameters considered are in the range of that characteristic for an ordinary concrete and are provided in Table 4.15. Then, the same methodology of recreating the entire measurement chain is employed considering perfect synthetic image acquisition (Table 4.3) and are treated with standard set of processing parameters (Table 4.12). The identification results are presented in Figure 4.35. As it could have been expected, the method provides reasonable results. Regarding identified global elastic Young's modulus in both compression and tension with an average error about 1%. A space time map of stiffness obtained directly from the stress and strain measurements is presented in Figure 4.36. However, it is worth noting that idealistic conditions are assumed and that in real experiments numerous sources of errors can affect the accuracy of the identified results.

Density (kg/ m^3)	E_c (GPa)	ν	E_t (GPa)	E_t / E_c
2200	40	0.2	20	0.5

Table 4.15: Numerical parameters of used to incorporate a bi-linear elastic response in a simulated spalling experiment.

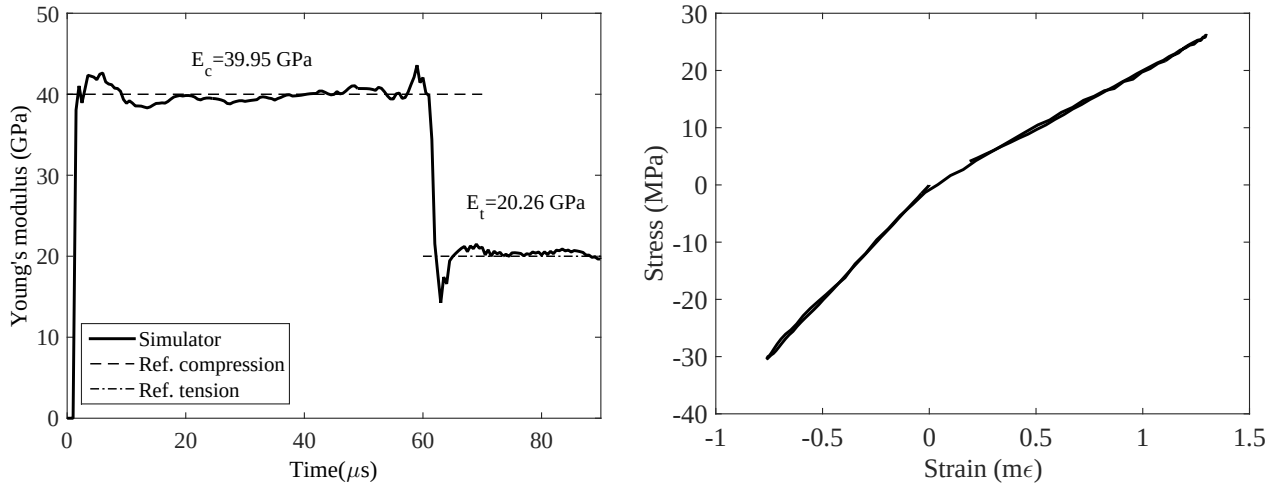

(a) Identified global Young's modulus.

(b) Reconstructed average stress-strain response.

Figure 4.35: Identification of bi-linear material response.

[2] Here mesoscale is considered as a scale at which damage mechanisems can be expressed through constitutive equations [Lemaitre, 1996], for concrete is around $100mm^3$ and as such it is commonly observable in laboratory experiments.

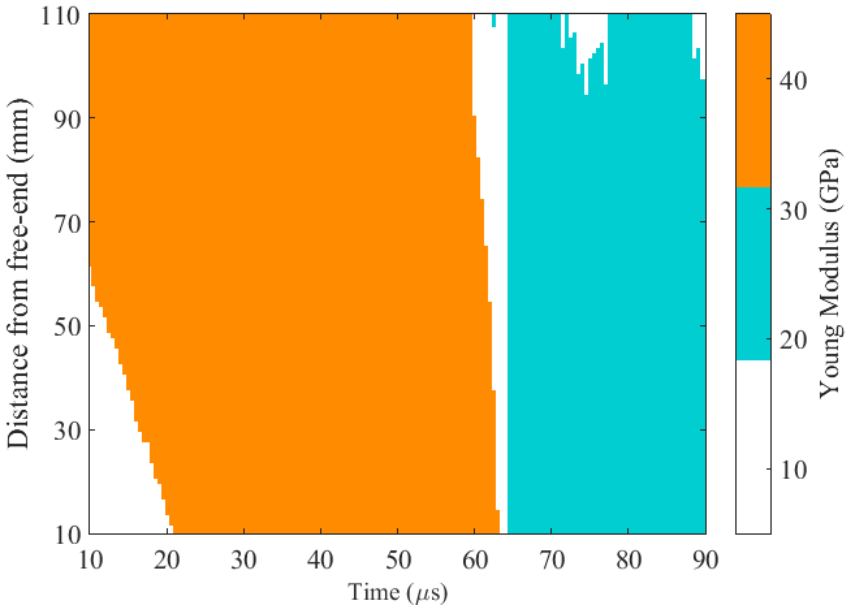

Figure 4.36: Identified space time map of stiffness in case of a bi-linear response in tension and compression.

4.5.2 Identification of damage response

The dynamic damage response of concrete was simulated with a damage model considering only the case of uniaxial damage under tensile loading, while in compression the material is assumed to behave perfectly elastic. The constitutive model used to embed the damage information into the synthetic images is the so-called Mazars' (Section 3.4.2.2). The model was used without the Hillerborg regularization scheme. A non-symmetric elastic response is also considered through a dissymmetry parameter. The parameters of the numerical model are given in Table 4.16. 3D numerical simulations were performed as to obtain temporally resolved displacement fields that are extracted from the region of interest. The damage model is used within its local description, since any kind of regularization that introduces an internal length would produce a quasi-homogeneous displacement fields which would not be adequate for synthetic image generation. On the other hand, for that reason, mesh sensitivity and localisation persist which can be observed in the spurious damage field presented in Figure 4.40. Nevertheless, the simulated displacement fields can still be used to embed some damage information into synthetic images which can be then compared to the results of the FEM model. The synthetic images of ideal characteristics (Table 4.3) were then generated with the procedure developed in this work. It was noticed that due to the mentioned localization phenomena the derivation of strains presents one of the critical steps and that the use of a diffuse approximation with 2^{nd} order can over smooth the zones with high strain concentration. For this reason 3^{rd} order polynomials were used over a span of 3 displacement points. The identified global Young's modulus using 8^{th} order virtual fields is depicted in Figure 4.38. While in the compressive loading stage the reference value of material stiffness of 40 GPa is identified within the confidence interval of $\pm 3\%$ due to presence of damage in the sample the value of stiffness decreases in tension reaching a peak value of about 5% lower than the expected reference. This verifies that the identified global Young's modulus can be used to confirm the presence of damage within the sample; however more reliable values of material stiffness can be extracted from reconstructed material stress-strain response. Owing to localisation phenomena, the averaged stress-strain response at a given distance within a finite virtual gauge also includes some local effects and increase the variability of the identified result so it diverges from its analytical description. The reconstructed stress response at 40 mm distance from the free-end obtained from the simulator and the FE model are shown in Figure 4.39a and the reconstructed stress-strain response in Figure 4.39. Interestingly the data from the simulator show a fairly good qualitative agreement with the results from FE simulation. The peak stress at the 40 mm distance is identified within 3.5% accuracy ($\sigma_u^{FE} = 7.96MPa$ and $\sigma_u^{img} = 7.62MPa$).

Although this result presents just a proof of concept and more thorough investigation is needed, it demonstrates that it is possible to identify a non-linear and damage law just based on the measurement of accelerations fields.

Density (kg/m^3)	E (GPa)	ν	σ_u (MPa)	E_t	E_t/E_c
2290	40	0.2	8	20	0.5

Table 4.16: Parameters used in the spalling simulations with the local damage model.

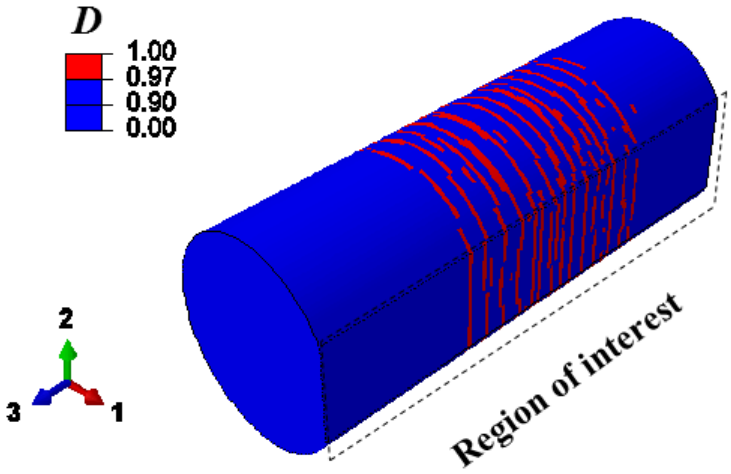

Figure 4.37: Damage field of a simulated spalling test considering a local damage model.

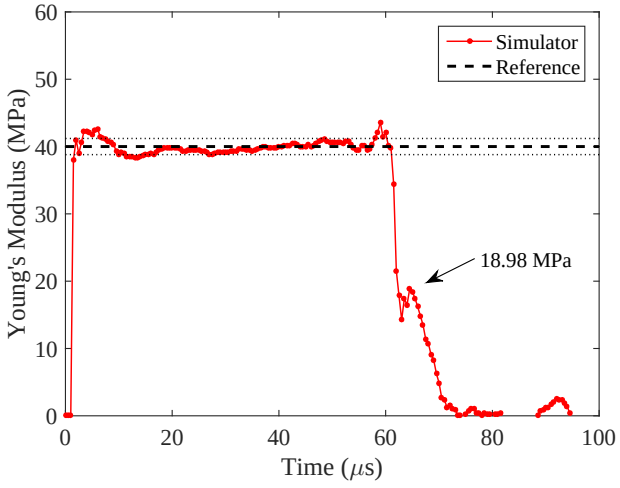

Figure 4.38: Identified global Young's modulus in case of material uniaxial damage response.

4.5.3 Effect of the trigger image position

When dealing with ultra-high speed photography of fast changing phenomena, triggering a high-speed recording has to be done at a microsecond scale and is essential for capturing the examined event in a given temporal region of interest [Field, 1982]. Various techniques for triggering an ultra-high speed acquisition system exist [Versluis, 2013]. Nowadays, most of the UHS imaging systems come with adapted image readout and software trigger control technology. When images are captured and saved on a chip, such features allow more flexible options such as

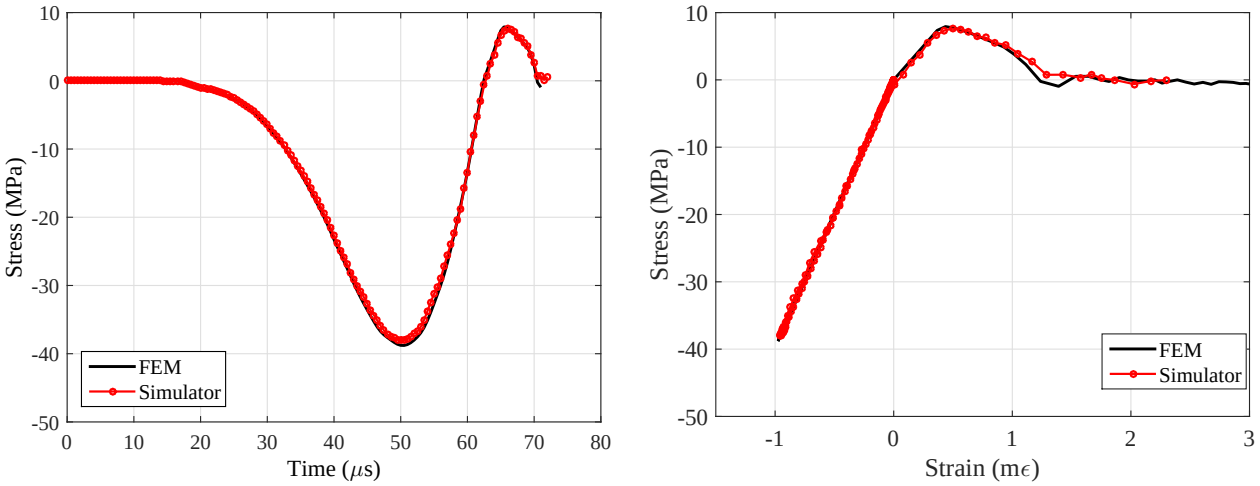

(a) Axial stress response at 40 mm from free end.

(b) Reconstructed stress-strain response at 40 mm from free end.

Figure 4.39: Identification of a damage response from simulated experiments (qualitative comparison with FEM results).

post-trig or pre-trig image acquisition providing a programmable number of frames before or after the triggering signal is received. Therefore with a proper timing, the triggering signal can be obtained away from the imaged zone. In a spalling experiment this is often done by using the laser interferometer pointed towards the sample free end and setting the post-trig frame based on the delayed time obtained from the calculation of the anticipated stress wave velocity that propagates within the sample. When performing full-field measurements, it is a common practice that the first image (or several images) of the camera recording are captured before the event starts taking place so that the reference image can be taken as the one corresponding to the sample dormant state. Therefore, the amount of frames requested is usually equal (or larger) than the duration of the compressive loading stage. However, ultra-high speed imaging systems have a limited number of frames available for the recording and it is possible that not the entire event of interest (*i.e.* the tensile loading stage) is captured. Therefore, a question arises if a delayed triggering can be used instead, to expand the recording in the tensile stage on the expense of missing the initial part of the compressive stage.

Here, this question can be investigated thanks to the numerical procedure of simulation the entire photomechanical spalling experiment which also considers the material softening response. The set of synthetic image generated previously were used to study the possible consequence of late triggering which occurs at 35 μs after the beginning of the loading spreads out the sample. Since only the recording speed of 2 Mfps was considered this corresponds to the 70^{th} frame of the synthetic image sequence. Two cases are considered: (1) the case where late triggering occurs and the reference image is the first of the recorded sequence and (2) where late triggering occurs but the reference image is a stationary one. The second case would correspond to a situation where a stationary sequence is taken before the event. The comparison of these two types of triggering were simulated and compared to the reference case and the results are presented in Figure 4.40. As one could expect, only a time shift (or jump) of the reconstructed stress strain response occurs while no change can be observed on the stress (or strain) level. In case when a stationary image is used as reference, the delayed triggering data synchronises with the case of ideal triggering conditions. On the other hand, when the delayed triggering is performed and the first image of the delayed sequence is used as reference, a shift towards the first quadrant is noted, which if there exists lack of data would be difficult to precisely correct. Hence it can be concluded that in case of missing reference image, a stationary image sequence taken before the test can be used as reference (assuming that no movement is experienced in between two sequences). This simple yet useful result could suggest a possible delayed triggering at the expense of missing

the beginning of the compressive loading stage in order to extend more the recording of the tensile loading stage rather than getting settled with a lower acquisition speed.

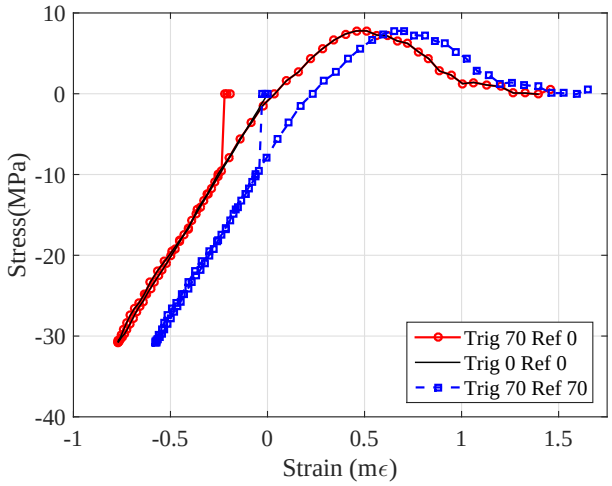

Figure 4.40: Simualted late triggering in a spalling test considering a material softening response.

4.6 Chapter summary

In this chapter, the identification method based on the use of VFM was investigated through numerically simulated experiments. Explicit FE simulations of a spalling test with a representative geometry and boundary conditions were carried to provide time resolved kinematic fields on the sample surface. These were then used in order to validate the VFM identification procedure. In case when a simple isotropic elastic material model was considered, the identified values of stiffness were within 0.5% confidence interval in case of noise-free data, which validated a good performance of the identification procedure. However, strong sensitivity to temporal noise present in the displacement fields was noted.

In order to further investigate and evaluate possible experimental uncertainties that can pollute the displacement data and that can be experienced during a dynamic photomechanical spalling test, a methodology for simulating the entire experimental chain of measurements was applied. The analysis relies on the simulation of the entire chain of measurements starting from the image acquisition of a hypothetical ultra-high speed camera to the identification of the material constitutive response. The generation of synthetic grid image sequences that encode the simulated FE kinematic information through image interpolation techniques was performed with an image simulator developed in this work. These synthetic sequences can then be treated with standard tools and used to investigate various potential sources of errors separately and in a controlled manner. The influence of several user-dependent parameters were investigated by treating the synthetic images as real experimental ones and comparing the identified parameters with their initially defined reference values within the FE model. These included effects such as acquisition speed, blurring, image quality, illumination and sample conditions. The results provided a deeper understanding of how the initial experimental conditions can affect the desired measurement. Furthermore, it provided guidelines on how to perform experiments more efficiently by reducing undesirable user-influenced sources of errors along with designing optimal experimental system configurations.

In the last part, the work investigates the use the VFM used to identify material parameters associated to tensile damage due to spalling. An isotropic damage model was used to simulate damage response of concrete and displacement fields obtained from explicit FE model were used to deform an ideal reference grid image. The damage model considers non-symmetric material response between compression and tension and allows modelling material

softening response in the framework of continuum damage mechanics. The compression was performed between the simulated constitutive response and the one identified from the synthetic image data sets. First results showed a fairly good agreement with respect to peak tensile stress as well as in the softening regime which confirmed the perspective of using the VFM processing in light of identifying a damage response in dynamic tension. Of particular interest regarding dynamic fracturing of concrete material are the specific fracture energy and fracture opening velocity which will be investigated experimentally and numerically in Chapter 5.

Finally, all the simulation procedures used in this chapter validated that the VFM processing and the acceleration data can be successfully used to identify material constitutive response without any need of external measurement nor assumption on material behaviour. Furthermore, this work allowed also some limits to be placed on what type of acquisition system can or cannot be used in this specific experimental configuration. An example is that an optimal UHS camera should have an acquisition speed of 2 Mfps. For this reason, two other types of acquisition systems of new generation cameras which incorporate latest technological developments based on UHS CMOS sensors were applied to spalling tests in Chapter 6.

As a perspective, this work (from the author's point of view) can present a small step towards one very big idea, which can be entitled: *Towards simulated photomechanical experimentation: evaluating experimental uncertainties and errors*, all in light of working towards future creation of standardized guidelines of performing reliable experimental identification in dynamic testing.

Chapter 5

Methodology for measuring Dynamic Fracture Energy G_f

In the following chapter a new methodology for directly determining the specific fracture energy under dynamic tensile loading will be presented. The method allows to extract the fracturing information for each observed fracture zone involved in the dynamic cracking process, which is recoded with an ultra-high speed camera. Thanks to using the Grid method that provides direct full-field kinematic measurements, it is possible to identify the fracture opening displacement (FOD) and the fracture opening velocity of any principal (open) and secondary (closed) fracture at each measurement instance, which may or may not lead to complete physical failure of the sample. Relying on the image-embedded load cell principle (Section 2.4.3), the local Stress-FOD curves can be obtained for each observed fracture zone.

Explicit numerical simulations showed that the present method can reliably predict the specific fracture energy which is needed to open one macro-fracture, contrary to some methods that can be found in the literature. The main reason for this is that these methods use indirect measurement techniques that can lead to an overestimate of specific fracture energy due to the stringent assumption of linear elasticity up-to the peak axial stress.

Finally, the sensitivity and accuracy of the proposed method is investigated through simulating the entire chain of measurements using the procedure presented in Chapter 4. Extended finite element modelling is used to simulate the growth of a single crack in a concrete sample through implicit 2D numerical simulations. First, the displacement fields were directly input in the VFM processor to further validate the processing method. Then, numerical displacement fields are used to embed the fracturing information into sequences of synthetically deformed grid images that are then analysed using the standard tools. The sensitivity of the method was investigated assuming several types of camera noise structures (i.e random spatial and temporal noise) that were added to the synthetic image data, confirming that the simulation of the entire chain of measurements is a useful tool for testing and evaluating the performance of photomechanical tests.

The following chapter consists of a reproduced version of:
B. Lukić, D. Saletti, P. Forquin. On the Processing of Spalling Experiments. Part II: Identification of concrete Fracture Energy in dynamic tension. Journal of Dynamic Behavior of Materials, 4:56, (2018).

and an extended version of:
B. Lukić, D. Saletti, P. Forquin. Evaluation of a full-field measurement method used to identify the dynamic fracture energy of concrete based on simulated experiments. PhotoMechanics, Toulouse, France, (2018).

5.1 Chapter outline

The structure of this chapter is organised into three principal parts:

- First part 5.2 explains the methodology proposed to determine the specific fracture energy from each visualized dynamic crack.
- Second part 5.3 presents a simple yet effective strategy of validating the proposed data processing for deter-

mining the G_f. It consists of performing explicit numerical simulations of a spalling test adopting a damage model within the continuum mechanics description and assuming a homogenised material domain.

- Third part 5.4 presents a method of further validating the proposed experimental data processing by simulating entire chain of measurements. The displacement discontinuity information due to presence of one crack is simulated using XFEM and then this information is embedded into synthetic images that are then treated using the standard tools. Assuming certain type of random noise component (spatial or temporal), the method also allows investigating the noise sensitivity of the method.

5.2 Experimental method for obtaining G_f

Under quasi-static tensile loading, concrete exhibits one failure macro-crack that propagates along a direction perpendicular to the maximal principal stress. Then within the cohesive crack theory, the complete tensile failure of concrete can be represented by the Stress-COD (crack opening displacement) relation around the macro-crack where the energy exchange between the crack and the surrounding material takes place [Hillerborg et al., 1976, Hillerborg, 1985c, Bažant and Oh, 1983]. The specific fracture energy can then be defined as the integral of the entire curve of the load (needed to propagate a crack for a unit length) and the crack-opening displacement, per unit crack surface. Consequently, in order to characterize the specific fracture energy needed to completely open one fracture, information such as peak tensile stress and the softening behaviour until failure at the location of the macro-crack are necessary. However, in dynamic loading conditions, it becomes difficult to follow the formation of one distinct macro-crack. Under such loadings, the multiple cracking evolves within the core of the target [Hild et al., 2003, Forquin and Erzar, 2009, Hild, 2015] owing to the limited material crack speed, making the weakest link hypothesis is no longer valid [Forquin and Hild, 2010]. It can be therefore considered that what is actually observed during the spalling test is rather the opening of one fracture zone throughout the sample cross-section [Weerheijm and Vegt, 2010, Vegt and Weerheijm, 2015] rather than inception of one macro-crack. For this reason the term "Fracture Opening Displacement" (FOD) is introduced and from this point onward used to allude to the opening of one fracture zone that is recorded during one spalling test.

The difficulty of measuring the dissipated energy related to the growth of one dynamic fracture zone in a spalling test is principally twofold. Firstly, the local Stress-FOD description has to be obtained in the vicinity of each individual fracture zone, being close enough so that the measurement is not affected by adjacent fracturing processes. Full-field measurements coupled with the high speed photography are a perfect candidate, due to having a great advantage over indirect point-wise measurements since they yield abundance of discrete information over a portion of the sample. Secondly, and even more challenging, is to obtain the local stress measurement for each observed fracture zone. This is precisely where the virtual fields method exhibits its significance. It allows exploiting the measured acceleration data as an image-embedded load cell (Section 2.4.3) providing the measurement of the averaged axial stress in each visualized cross-section of the sample. What is more, no assumption on the material behaviour are being made, allowing for the direct identification of the material softening response. Although, it has to be mentioned that within the definition of the 'load cell' description, the continuous integral of acceleration forces needs to be approximated over the discrete number of available measurement points using the Riemann sum. Consequently the question regarding the validity of the VFM in the accurate identification of the material post peak response arises. This will be investigated within the framework of modelling one distinct geometric discontinuity using XFEM modelling in Section 5.4.

In the following, the methodology of obtaining specific fracture energy for each fracture zone in the spalling test will be described. The procedure relies on obtaining the local Stress-FOD curve per each visualized fracture zone that consists of several steps within the image data processing:

- Step 1: First, it is necessary to identify the position of the possible tensile fractures by looking at the obtained axial displacement maps. In order to do this, the first step is to perform a qualitatively inspection the last

recorded map of axial displacement, when the complete separation of the spall fragments takes place and to locate the zones where the values of displacements exhibit noticeable changes within a few millimetres of the sample's length. These lications can be then referred to as the displacement discontinuity zones of interest.

- Step 2: Then, it is necessary to analyse the nature of the observed displacement discontinuities by tracing the temporal evolution of the differential displacement around the fracture zone. For this reason, virtual *differential displacement gauges* are introduced which provide the difference in averaged axial displacement from two sides of the observed discontinuity.

- Step 3: Next, it is necessary to perform the correction for the elastic deformation response. The proper correction is only possible if the local tensile stress-strain response prior the stress peak can be obtained on the same set of the measurement points used to analyse the visualized fracture. Using the local values of stiffness in both compression and tension obtained at the same position of the introduced *differential displacement gauges*, a correction can be performed for the elastic response. Furthermore, it has been concluded in Section 3.4.1 that Young's modulus in tension is lower compared to the one in compression, which underlines the necessity of measuring both local stiffness components.

- Step 4: The last step is the reconstruction and integration of the Stress-FOD curves in order to determine the specific fracture energy per one formed macro-crack. It is interesting to mention that, compared to momentum transfer method [Schuler et al., 2006], the measurement of the fractured surface is not an imperative. On the other hand, it is necessary to define the fracture zone around the visualized crack, where the *differential displacement gauges* will be positioned.

- Step 5: Finally by performing the differentiation of the fracture opening displacement obtained from the corrected *differential displacement gauges* the fracture opening velocity (FOV) can be derived. The above-mentioned steps for reconstructing the Stress-FOD response and deriving the specific fracture energy will be detailed in the following.

5.2.1 Visualization and analysis of dynamic tensile fracturing

The first step in the present dynamic fracturing analysis is the identification of the discontinuities in the displacement fields. Under dynamic conditions, as it can be seen from stress-strain curves presented in Figure 3.18, the complete tensile failure occurs within 20 μs, while the time from zero stress to the peak tensile stress takes around 7 μs (Table 3.9). Therefore the images have to be grabbed at very high frame rates as to obtain sufficient number of temporal points to properly discretize the identification of the material response. In this work the Shimadzu HPV-1 camera was used with the interframe time of 1 μs, other settings are presented in Table 3.8. The displacement maps analysed are those from the experimental tests presented in Section 3.4.1. When performing full-field measurements the measurement resolution as well as measurement uncertainty level depends on the performance of the high speed camera [Pierron et al., 2011a]. Some information on the metrological performance of the Shimadzu HPV-1 system have been recalled in Section 3.2 and are presented in more detail in [Rossi et al., 2014]. This value has been obtained on the first 20 frames captured by the camera before the stress wave reached the sample. The measurement resolution is directly defined as standard deviation of the average axial displacement during the first 20 frames as no displacement is assumed to take place during this sequence (Section 3.3.2).

The Figure 5.1 contains two axial displacement maps obtained from two spalling tests (named Tomo1 and 100w) at 92 μs after the camera triggering and when the complete damage took place. These maps can be used to qualitatively observe the displacement discontinuities that occurred due to the formation of spall fragments (Step1). It can be seen that both maps exhibit two localized zones, one at about 46 mm from the free-surface and the second one at about 30 mm from free-end. These fracture zones do not appear to be perfectly planar but rather slanted. An interesting observation to note is, by looking at the color-plots, that the test labelled 100w (Figure

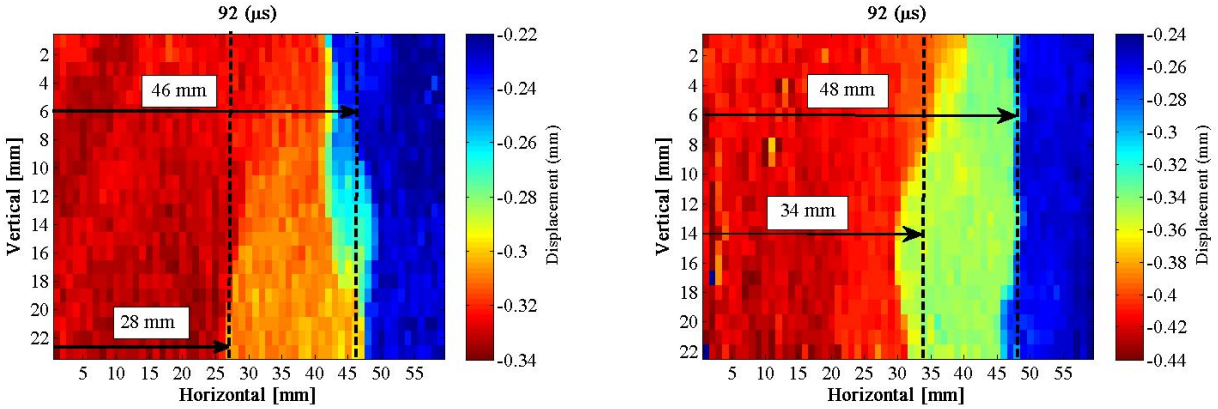

(a) Last recorded displacement map of the Tomo1 experiment.

(b) Last recorded displacement map of the 100w experiment.

Figure 5.1: Final axial displacement maps captured by the end of the test when the full separation of spall fragments took place. (Horizontal axis shows distance in mm from sample's free-end)

5.1b) clearly exhibits two distinct fractures while the test Tomo1 (Figure 5.1a) exhibits a somewhat less pronounced displacement discontinuity closer to the free-end.

In order to better analyse the identified discontinuities the so-called *differential displacement gauges* are introduced which allow to follow the fracture formation in time. The gauges are located on both sides of the discontinuity for which the mean axial displacement on the predefined area is obtained. Then the fracture opening displacement is obtained as the difference in mean displacement from both sides of the fracture. However, before defining the size and the location of the displacement gauges, it is necessary to define the fracture zone. The fracture zone can be regarded as the area of the material that surrounds one macro-crack, which is involved in an active energy exchange during the fracture process [Vegt and Weerheijm, 2015]. Therefore, the fracture zone contains one macro-crack, formed through branching and coalescence of multiple individually formed micro-cracks and the surrounding fractured material in its vicinity [Weerheijm and Vegt, 2011]. One way of determining the size of the fracture zone is to observe the displacement fields. When the axial displacement field from one side of the fracture exhibits uniform values within the reach of elastic strain, it can be considered that that zone is not damaged and is not involved in the fracturing process so it can be regarded as the physical edge of the fracture. This criterion was used in order to choose the position of the differential displacement gauges. Closely observing the displacement fields, it was deduced that the fracture zone is varying between 4 mm and 8 mm in width around the macro-crack which is in the range of the reported values in [Vegt and Weerheijm, 2016] where it was also noted that the width of the fracture zone increases with the increased loading rate. The positions of the displacement gauges chosen for the fracture zone observed at 46 mm from the free end are presented in Figure 5.2a,b in dashed lines. The averaging window size chosen for both of the individual gauges is 3 x 22 mm. This is one of the advantages of the presented method, as the local values of displacement around the fracture zone can be directly measured within proximity of a few millimetres. The results regarding the fracture zone opening for each of the observed axial displacement discontinuities in both of the above mentioned spalling tests are presented in the Figure 5.2c,d choosing the same size of the displacement in all cases. Furthermore, in Figure 5.2e,f the corresponding stress evolution, obtained on the same location as the differential displacement gauges used to obtain the fracture opening, are presented.

The obtained results regarding the differential displacement for two spall tests are depicted in Figure 5.2c,d. The plots clearly demonstrate that the fractures open in the tensile loading stage since in compression stage, the response is in the range of elastic material limit (less than 15 μm). A very interesting observation can be made on the results of the test named as Tomo1 (left-hand side column of the Figure 5.2). The differential displace-

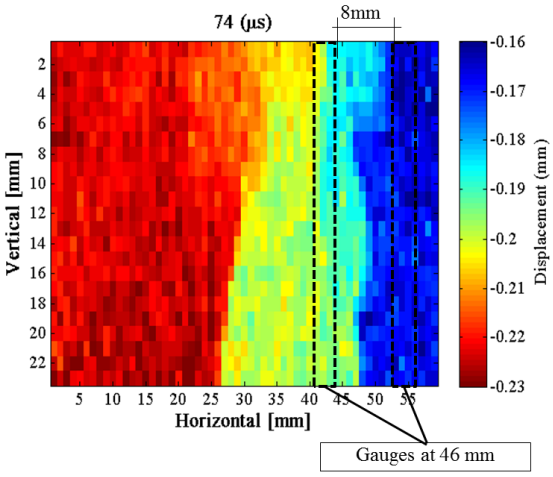

(a)

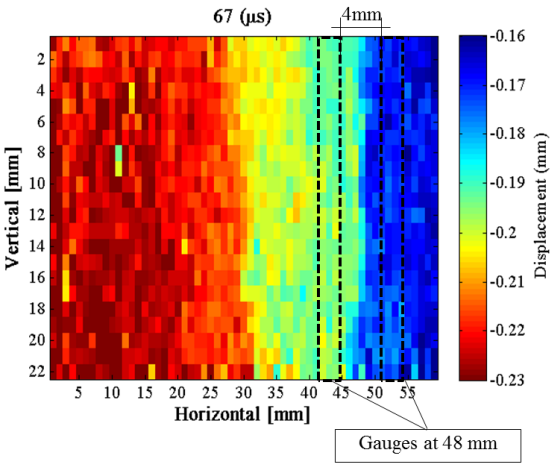

(b)

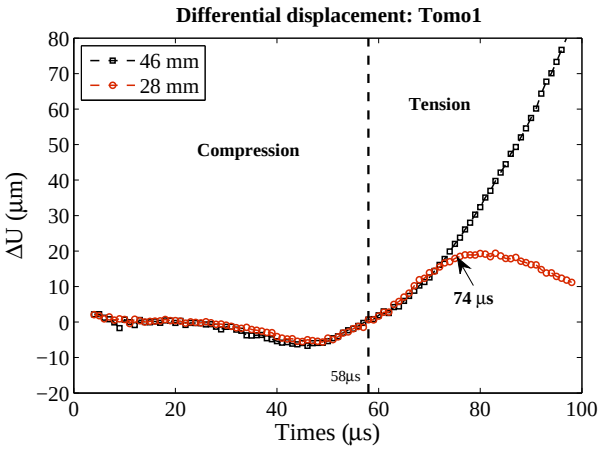

(c)

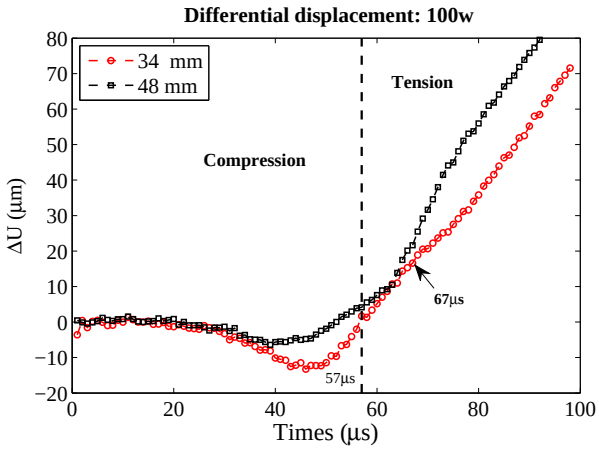

(d)

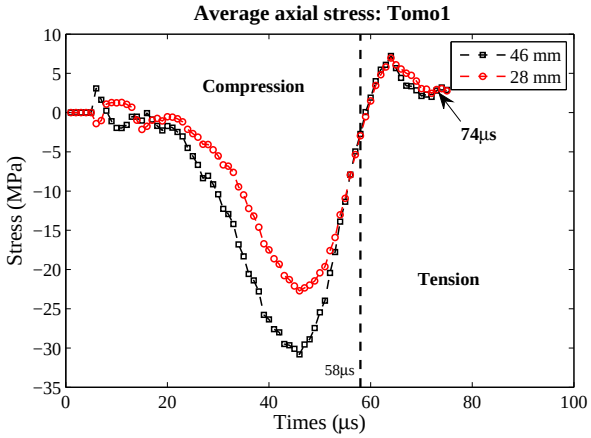

(e)

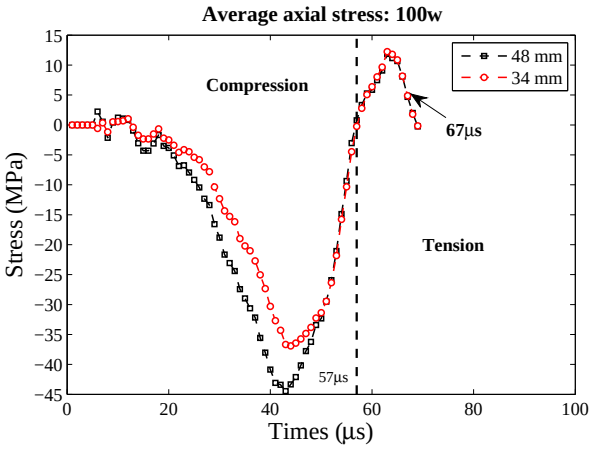

(f)

Figure 5.2: Maps of axial displacement corresponding to time when tensile stress is close to zero and position of principal displacement gauges: (a) and (b) (zero horizontal coordinate corresponds to the sample's free-end); Evolution of crack opening for both displacement discontinuities observed in displacement maps by computing the differential displacement: (c) and (d); Corresponding evolution of axial stress on the same location of differential displacement gauge: (e) and (f).

ments for two distinct discontinuities observed in the displacement maps (at 46 mm and 28 mm from free-end) are plotted in Figure 5.2c. What can be also observed is that the evolution of the two fractures seems to follow the same trend at the beginning of the tensile stage, up-to a point where one fracture becomes the dominant one and continues to propagate, while the other one opens until the peak displacement is reached and then closes (the differential displacement decreases). This could be seen as a form of the obscuration phenomenon [Denoual and Hild, 2000, Hild et al., 2003] resulting from the stress relaxation caused by the dominant macro-crack, only in the present case both cracks are triggered. Hence, it can be concluded that the fracture zone at 46 mm results in the formation of a principal macro-crack that leads to the sample physical fracturing while the crack at 28 mm results in a secondary macro-crack whose opening displacement decreases and tends towards complete closure (here *closed* means that it is not physically separating the specimen into individual parts). The temporal discretization as well as the resolution of the current measurement system simply does not allow any conclusions to be drawn on which is the macro-crack that first initiates; however, this example confirms the evidence of multiple cracking and possibly the obscuration phenomena as mentioned in [Erzar and Forquin, 2010, Erzar and Forquin, 2014]. Furthermore, this could compromise the measurement of the width of the fracture zone and quantification of damage by the means of the post-mortem observation as in [Brara and Klepaczko, 2007], since it is clear that not all the cracks which are formed under dynamic tensile loading are completely open fractures but can also be closed cracks. Although, they do dissipate a certain amount of fracture energy. The evidence of multiple-closed-cracking can be further investigated by the so-called post-tensile spall experiments. The sample is first exposed to low velocity spalling to induce damage without leading to global sample failure [Erzar and Forquin, 2014]. Hence, some amount of fracture energy is dissipated but not enough to result in a macro-crack.

5.2.2 Correction of the differential displacement

During the first stage of the spalling test, the concrete sample is exposed to uniaxial compression under which the material behaves elastically. All of this information is embedded in the deformation response obtained with the differential displacement gauges which need to be corrected for the elastic component in order to obtain reliable values of specific fracture energy. However, this is only possible when the real local elastic response of the material is known. It was shown previously that Young's modulus in the tensile stage is around 50% lower than the compressive stiffness. This difference can slightly vary depending on the position of the virtual gauge due to the sample heterogeneous nature. Therefore, it is necessary to have access to the local stress-strain response at the same position of the differential displacement gauge used to analyse one fracture zone. This allows to account for the realistic elastic response in both compression and tension that is registered by the differential displacement gauges. The local stress-strain response is obtained at the same location and is given in Figure 5.3b. The local compressive and tensile stiffness parameters are reported in Table 5.1. They are recovered by performing linear regression on the entire set of data points in the compression stage and on the ascending data points in the tension stage. When local elastic stiffness parameters are known then the differential displacement curve can be corrected for the elastic part of the material response, both in compression and tension. The equation used to perform this elastic correction is provided as follows:

$$FOD = (\overline{U}_x^{G_1} - \overline{U}_x^{G_2}) - \frac{\overline{x_1\langle\sigma(x,t)\rangle^{x_2}}}{E(t)}(x_2 - x_1) \tag{5.1}$$

where $\overline{U}_x^{G_i}$, $i = 1, 2$, is the average axial differential displacement obtained as mean difference at each of the two sides of the observed fracture zone utilizing the differential displacement gauge (G_1 and G_2). The $\overline{x_1\langle\sigma(x,t)\rangle^{x_2}}$ represents the average axial stress component obtained as a mean value over the sample portion from x_1 to x_2 (see Figure 5.3a) and $E(t)$ represents the identified local stiffness value used to account for the elastic material response of the material in compression and tension. The correction is performed taking into account the mean distance between the virtual gauges used to calculate the differential displacement and both compression and tension material

stiffness. The effect of this correction on differential displacement curve taking into account both local compressive and tensile stiffness is presented in Figure 5.4. It can be observed that the error is introduced when the elastic response of the sample is not subtracted from the differential displacement measurement.

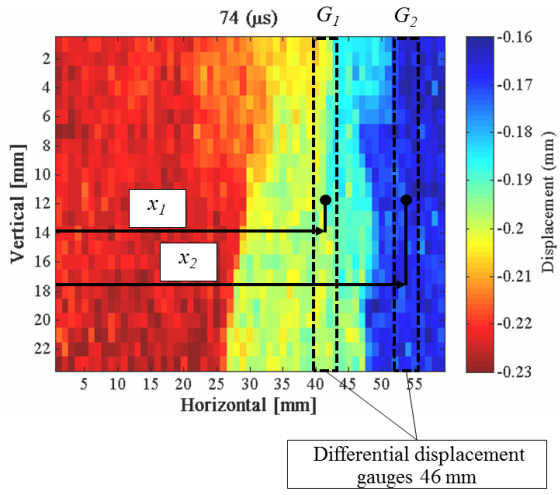

(a) Positioning of the virtual gauges around one distinctly observed fracture zone.

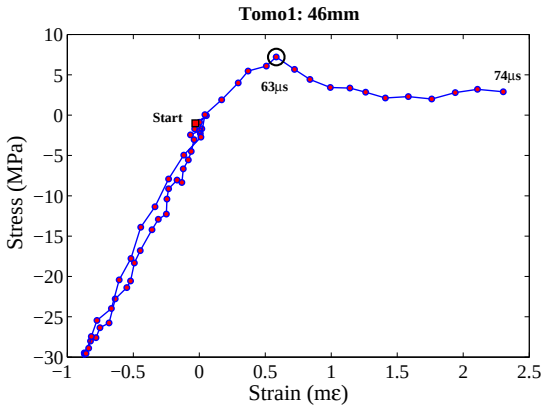

(b) Characteristic local stress-strain curve obtained over the same area around the macro-crack as the corresponding deformation gauges (G_1 and G_2) used to obtain the crack opening displacement.(strains are obtained using diffuse approximation over 8 points and 2^{nd} order polynomial fit)

Figure 5.3: Demonstration of the virtual gauges used to extract the specific fracture energy around one visualized dynamic fracture zone. (Tomo1)

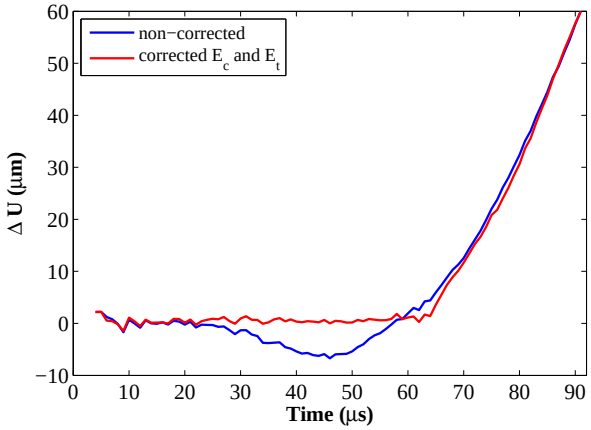

Figure 5.4: Effect of the local correction of the non-symmetric elastic response of the material on the fracture opening displacement. (Tomo 1: Crack 46 mm from free-end)

5.2.3 Experimental results

When the measurement of differential displacement is corrected, the local stress-fracture opening displacement curves (Stress-FOD) can be reconstructed. Thanks to full-field measurements and the VFM, it is possible to obtain the local Stress-FOD response for each observed macro-crack that constitutes the fracture zone at any time recorded by the camera. This can be considered as the sheer novelty of the presented technique compared to methods used in previous studies [Brara and Klepaczko, 2007, Schuler et al., 2006]. The reconstructed Stress-FOD response for two distinct macro-fractures observed in two spalling tests (Tomo1 and 100w) are plotted in Figure 5.5.

Test	Crack position from free-end	E_c (GPa)	E_t (GPa)
Tomo1	28mm	30.31	15.83
	46mm	32.12	16.81
100w	34mm	35.42	14.44
	48mm	34.27	11.86

Table 5.1: Identified local values of elastic stiffness in compression and tension for two spalling tests at the location of the observed macro-cracks.

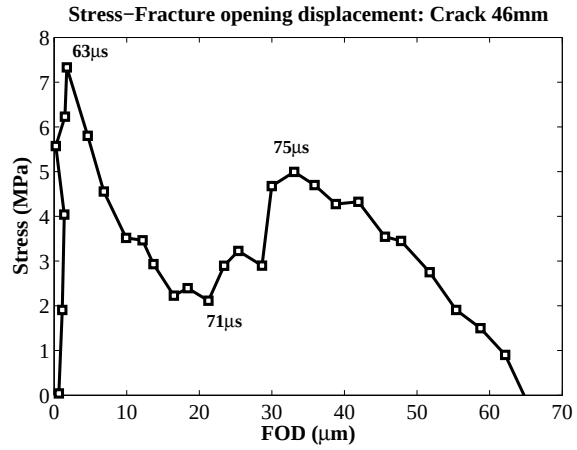

(a) Tomo1: Open fracture.

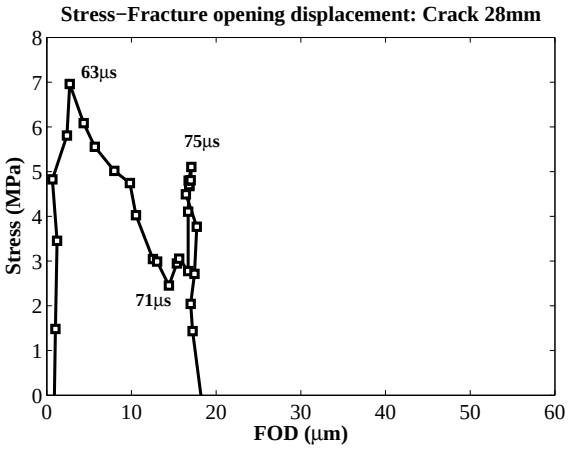

(b) Tomo1: Closed fracture.

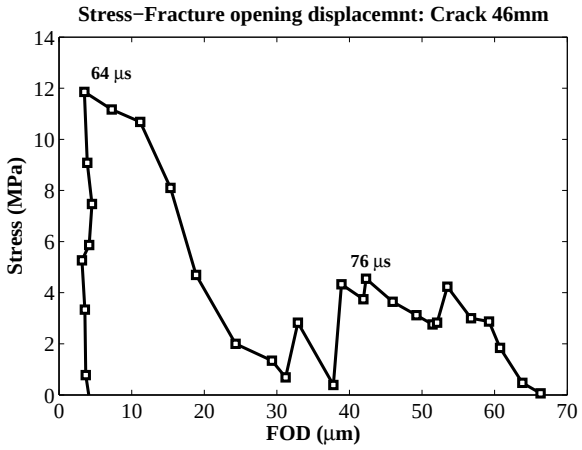

(c) 100w: Open principal fracture.

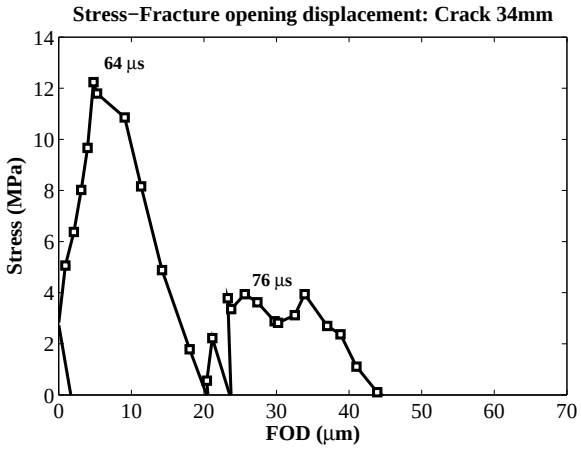

(d) 100w: Open secondary fracture.

Figure 5.5: Local Stress-Fracture Opening Displacement curves obtained in the vicinity of spall fractures from two tests captured by the means of ultra-high speed photography and the virtual fields method (VFM).

From the presented experimental curves some interesting observation can be made at first hand. Firstly, from the curves presented in Figure 5.5 and values summarized for both tests in Table 5.2, it can be observed that the full fracture opening which ultimately leads to the sample physical failure by a macro-crack is about 70 μm. Even though that the lack of experimental data does not permit drawing out any firm conclusions, it seems that the complete opening displacement which leads to the sample failure is several times smaller than reported by some other authors [Vegt and Weerheijm, 2015]. Secondly, another compelling observation can be made by comparing the two curves in Figure 5.5a,b. As mentioned previously, the presented Stress-FOD curves are obtained from local measurements in the vicinity of two fractures observed in the displacement maps of one spall test (Figure 5.2a,b). From the qualitative analysis of the displacement evolution (see Figure 5.2c) it was suggested that the fracture at a distance of 28 mm from free sample surface represents a closed fracture, while the one at 46 mm is considered as the principal fracture which leads to the separation and formation of spall fragments. Here, thanks to fully reconstructed Stress-FOD curves, close observation of the fracturing process at these two locations can be made by following fracture response in time. From Figure 5.5a,b it can be seen that in both cases the tensile stress peak is reached at the same instant and the post-peak response seems to follow the same trend up to the time corresponding to 75 μs after the camera triggering. After this point, it can be noted that the fracture at 46 mm starts to evolve into the principal macro-crack as it continues to propagate and dissipate energy, while the fracture at 28 mm stops. It is also worth mentioning that this point is exactly one time step after the stress-strain response obtained from a virtual gauge at 46 mm exhibits values of axial stress close to zero (Figure 5.3b). This observation could be explained by the obscuration phenomena and stress relaxation due to fracturing. Multiple-fractures occur under dynamic conditions due to the limited crack propagation speed, which are all initiated at approximately the same time on a micro level but one fracture can eventually obscure the others during the propagation process [Forquin and Hild, 2010, Erzar and Forquin, 2014]. It can be regarded as the *Palio di Siena* horse race, where all contestants start at the same time but not everyone makes it to the end. Moreover, both softening curves seem to have two branches containing a distinctive *bump* which can also be observed at 75 μs in both Stress-FOD curves.

Test	Crack position from free-end	G_f (J/m^2)	Complete crack opening displacement (μm)
Tomo1	28mm	66.84	18
	46mm	208.12	64
100w	34mm	161.05	46
	48mm	264.32	68

Table 5.2: Values of specific fracture energy dissipated per one observed macro-fracture in two spalling tests reported.

It is also interesting to analyse the same experiments presented herein with a different approach of obtaining the specific fracture energy. Two methods are usually cited in the literature: the ejection velocity method [Brara and Klepaczko, 2007] and the momentum transfer method [Schuler et al., 2006]. Since the measurement of the mass spall fragments and fracture surface are an imperative of applying the second technique (which are not available for the two analysed tests), here only the ejection velocity method will be considered. What is important to mention is that the method proposed by Brara *et al.* incorporates several assumptions on the fracturing phenomena and assumptions of the material behaviour. First, it is assumed that the stress evolves linearly in time upto a limit when failure occurs. Next, it is also assumed that the spall fragment mass velocity can be related with the failure stress. Finally, assuming that the ejection velocity is constant during the separation and that a bi-linear fracture separation takes place, the approximation of the fracture energy formulation was provided (Equation 2.7). The data necessary to perform the calculation of the specific fracture energy [Brara and Klepaczko, 2007] for the two

tests presented herein are given in Table 5.3. Material parameters are given in Table 3.7. From the presented data is becomes obvious that there is a large discrepancy between the method proposed in this work and the method proposed by Brara *et al.* regarding the measurements of specific fracture energy. Apart from the other adopted simplifications, this difference can be also due to the fact that the velocity at separation is measured after several round trips of the wave trapped in the fragment. Moreover the velocity in the fragment is not necessarily homogeneous, since multiple events take place during fracturing which last about 20 μs Figure (5.6).

Test	Crack position from free-end	Critical time t_c (μs)	Time to complete failure t_s (μs)	Fragment velocity at failure (m/s)	Fracture energy (J/m^2)
Tomo1	46 mm	6	22	5.786	587.7
100w	34 mm	7	23	7.453	1039.4

Table 5.3: Values of specific fracture energy calculated according to Brara *et al.* [Brara and Klepaczko, 2007] (Equation 2.7).

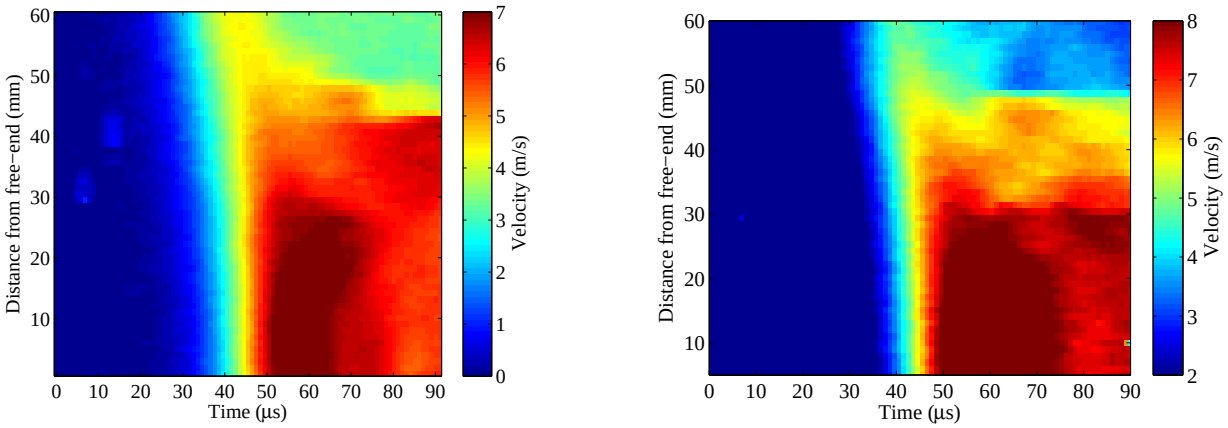

(a) Tomo1

(b) 100w

Figure 5.6: Time space maps of axial velocity for the two tested samples.

5.2.4 Comparison with data from the literature

The specific fracture energy is a characteristic material parameter that governs the crack opening in concrete material. Therefore, it is related to both the fracture opening displacement (FOD) and also to the fracture opening velocity (FOV). Knowing the history of the fracture opening displacement, the fracture opening velocity can be obtained by performing a numerical time differentiation of the FOD signal. In the present work, a moving window of seven temporal data points is used to derive the crack opening speed from the FOD data. Strong filtering is used in order to reduce the effect of noise which is enhanced due to the numerical differentiation procedure. This noise propagated from the ultra-high speed camera to the measurement, and as such cannot be avoided at this stage. This can be regarded as a limitation of the proposed technique, as it completely depends on the acquisition system. However, the future development of new generation of ultra-high speed imaging sensors which have more temporal stability in image forming will provide refinement of the measurement of both speed and acceleration recordings. Figure 5.7 shows two characteristic fracture opening speeds for two spall tests obtained by differentiating the corresponding fracture opening displacements.

Having access to the data regarding the specific fracture energy and fracture opening velocity it is interesting to compare them with the models proposed in the design regulations as well as data that can be found in the litera-

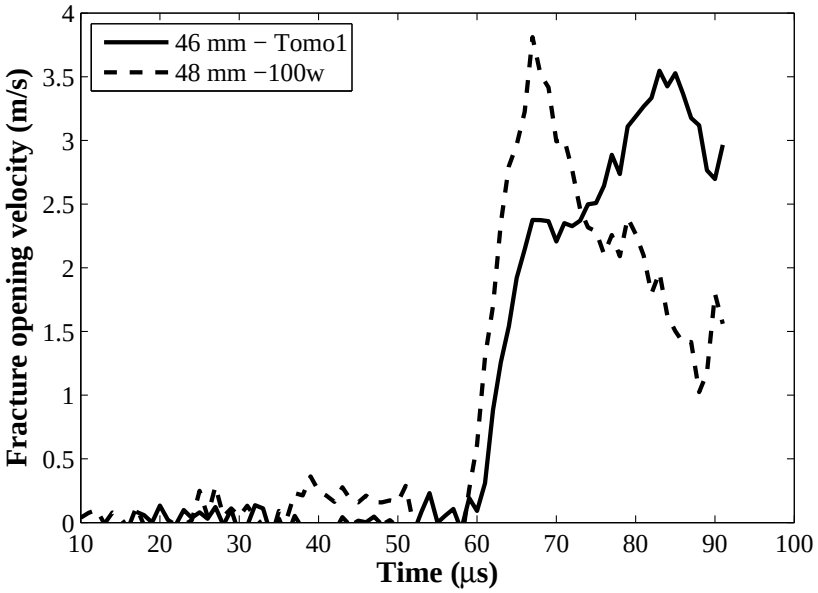

Figure 5.7: Fracture opening velocity for two spalling tests.

ture. Relationship between dynamic fracture energy and the crack opening speed was first given by CEB (Comité Euro-International du Béton, 1988) in a preliminary synthesis report [CEB (Comité Euro-International du Béton), 1988] (Equation 3.19 in the cited document) and is expressed as:

$$G_d/G_s = (\dot{\delta}/\dot{\delta_0})^{0.045} \tag{5.2}$$

Where G_d and G_s are denoted as dynamic and quasi-static fracture energy respectively, $\dot{\delta}$ represents the crack opening speed and $\dot{\delta_0}$ is 10^{-3} mm/s scale parameter. Later on, in the final published version of the design code – CEB-FIP Model Code 1990 [CEB, 1993] this relation was retracted from code section 2.1.5.3.2. (page 50 in the cited document) with the explanation:

- *The information available regarding the effects of stress or strain rate on fracture energy is too incomplete to be included in the model.*

making this work even more interesting to evaluate and verify since there is a clear need for a standardized experimental measurement that can provide reliable results concerning concrete fracturing characteristics.

Regarding the data on specific fracture energy in the literature, the only method able to provide this information on material fracturing is the one proposed by Schuler et al. [Schuler and Hansson, 2006, Schuler et al., 2006]. The data from the cited works as well as two prediction curves from the model proposed by CEB are compared to the experimental values from this work, including both fractures observed in each test, are all presented in Figure 5.8. The results obtained by analysing the fracture zones observed in both tests at the distance of around 40 mm (namely 46 mm in Tomo1 and 48 mm in 100w tests) are in the figure referred to as crack 1 while the ones closer to the free edge refers as crack 2. From the presented collection of data, it is interesting to note that the experimental values obtained herein are in the same range with respect to crack opening speed (in this work also called fracture opening velocity - FOV). However, the values of specific fracture energy are markedly lower than the results present in the literature. This can be regarded as a result of the more realistic measurement of specific fracture energy as it is obtained with no assumptions on the material behaviour in the stage of data processing. The

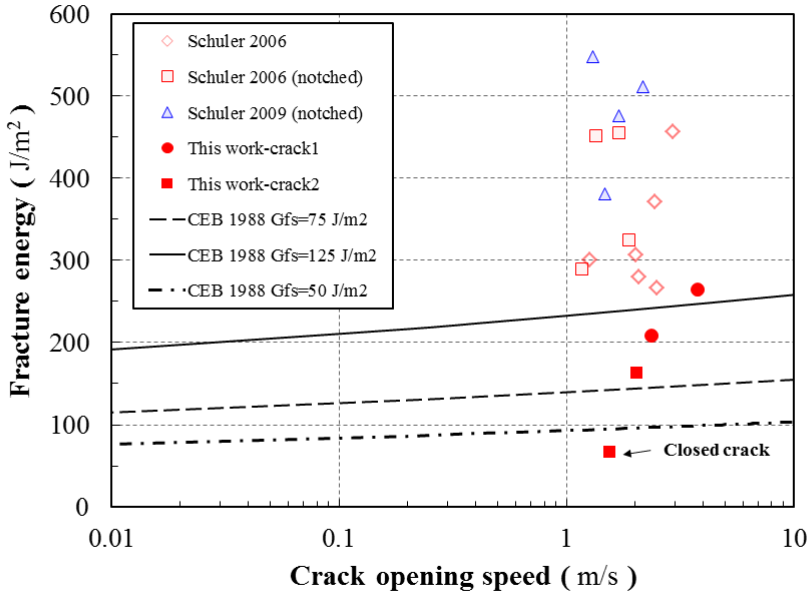

Figure 5.8: Comparison of the obtained experimental values of specific fracture energy for each observed macro-fracture with the data available in the literature.

obtained measurements are refined thanks to the obtained fields of local information through the use of ultra-high speed imaging and full-field measurements. For the sake of comparison, what is also interesting is that the value of specific fracture energy obtained in this work for what is observed as a closed crack, is smaller compared to the values reported in the literature for quasi-static loading conditions when RILEM testing recommendations are applied to what is defined as a common concrete (Table 5.4) [Hillerborg, 1985a, Wittmann et al., 1987, Cifuentes et al., 2013]. While on the other hand, the specific fracture energy for opened – principal cracks is markedly higher. Nevertheless, more experimental efforts have to be aimed at obtaining reliable set of new data in both quasi-static and dynamic loading conditions before any firm conclusions are drawn.

Author	G_f $[J/m^2]$
Quasi-static	
Hillerborg 1985	113
Wittmann *et al.* 1987	112.5
Cifuentes *et al.* 2013	124
Dynamic	
This work: *Open fracture*	211.3
This work: *Closed fracture*	66.8

Table 5.4: Values of dynamic specific fracture energy obtained in this work and some literature results regarding the specific fracture energy of ordinary concrete in quasi-static conditions.

5.3 Validation with numerical simulation

In this subsection, the proposed experimental data processing of a spalling test, that is used to determine the specific fracture energy around one distinct dynamic fracture, will be explored with the support of explicit FE numerical simulations (Abaqus/Explicit). Since the experimental processing method relies on the use of full field displacement maps and the VFM which provides the axial stress in each cross-section of the visualized sample surface, the numerical simulations are carried so that both the axial stresses in the element volumes as well as the nodal displacements around one predetermined localization zone are obtained as temporally discretized output information. A damage model is used to simulate the formation of a localized deformation zone in the dynamic spalling tests through a user-defined subroutine (VUMAT) (Section 3.4.2.2). The current methodology of modelling one localization zone, apart from its simplicity, enables the fracture energy to be easily calculated knowing the constitutive model parameters. Then the analytically computed value of specific fracture energy given to the numerical model can be compared to the value obtained by processing the simulated displacement data in the vicinity of the localization zone. The fracturing process is simulated having one pre-inserted localization zone that is supposed to represent one macro-fracture. This is performed by assigning the constitutive damage model only to one row of finite elements that compose the area of the chosen localization zone while the rest of the elements in the model were kept with the homogeneous elastic material description. Comparison starts by performing the same data processing to get the numerically simulated Stress-FOD curves. First, displacements around the localization zone are processed by introducing the differential displacement gauge as in Section 5.2. Then the appropriate correction is applied to obtain what was referred to as the fracture opening displacement and finally the Stress-FOV curves are being reconstructed and integrated so that the numerical fracture energy can be evaluated. Then this result is compared to the analytical solution that results directly from the used constitutive softening law. Furthermore, on the same numerical sample it is possible to compute the temporal description of the nodal velocities so that the moment transfer method [Schuler et al., 2006] can also be compared to the values of the analytical solution. Thus, the main aim of the numerical computations presented herein is to address the reliability of the two data processing techniques by treating numerically simulated displacements at nodes in the same way as in the experimental processing of displacement maps assuming that the non-corrupted stress measurement is available.

5.3.1 Numerical modelling

The local numerical softening model used to describe the localization zone incorporates the so-called Mazars' damage law [Mazars, 1986] which also includes the dissymmetric parameter that can reproduce different response of concrete in tension and compression and was used in Section 3.4.2. As it is always the case in FE analysis when a local material description is used, numerical localization will inevitably occur when softening is involved, leading to mesh sensitive results especially when explicit solver is used [Sluys, 1992]. On the other hand, even though it can well reproduce the fracturing process in numerical simulations of a spalling test, the regularization procedure can lead to an important increase of fracture energy in the system and non-realistic rear face velocity profiles [Sallier and Forquin, 2012]. Here the accent is on simulating one numerical fracture zone by assigning the proposed constitutive law directly to the predetermined rows of finite elements chosen to represent one localization zone; hence, the regularization technique was omitted in all simulations by setting the value ω was set to 1. The analytical value of fracture energy given to the numerical model can be simply calculated applying the theory of fictitious crack, as the area under the analytical stress-strain curve multiplied with the length of the localization zone l_c [Hillerborg et al., 1976, Hillerborg, 1991]. Hence the analytical expression of the specific fracture energy can be written as:

$$G_f = l_c \int_{\varepsilon_0}^{+\infty} \sigma(\varepsilon) d\varepsilon \tag{5.3}$$

where G_f is the fracture energy per unit area, $\sigma(\varepsilon)$ represents the constitutive equation used to describe the

homogenized material softening behaviour and the ε_0 represents the deformation at peak stress considered as onset of damage. Due to the mesh sensitivity which is characteristic for local damage models used in FE modeling, the element size had to be adapted to the desired value of the dissipated specific fracture energy. The size and the width of the localization zone were imposed so that the value of the dissipated fracture energy is of the same order as the experimentally observed data (Table 5.2). Also, the size was adapted to account for a proper geometrical discretization of the numerical model. Since the geometrical discretization was a limiting factor, it was chosen to use two adjacent rows of elements to model the localization zone by verifying that each row of elements dissipates closely one half of the total fracture energy given to the model. In that way, the constitutive damage model is assigned to two adjacent rows of elements while the rest of the model was kept perfectly elastic. The softening response is enforced in the elements belonging to this localization cross-section. A FE mesh of 8 mm size was used resulting in the generation of 648 linear brick elements with reduced integration scheme (C3D8R) and a localization zone of 16mm which is also know as crack band method [Bažant and Oh, 1983]. There exists evidence that the finite element codes based on the crack band model cannot correctly simulate the brittle failure of concrete structures when complex failures occur [Rots and De Brost, 1989, Ozbolt and Eligehausen, 1991] since mesh-shape sensitivity of the crack band model seems to be too large. However, it is generally suggested that this model is applicable only if the cracking is parallel to the mesh lines and the crack pattern is to be known in advance [Bažant et al., 1994], which is the case here. Furthermore, the mesh localization is, in fact, desirable. Rather than simulating the whole experimental set-up, the spalling sample was modelled by directly applying the experimental loading pulse on the bar–specimen interface. The total simulated time was set to 100 discretized with the time-step of 0.5 μs (200 output frames) and enforcing a fixed time increment of 1 ns that ensured 500 iterations per one output. The numerical spalling sample together with the localization zone, set at 40 mm from free-end and spanning over two rows of elements simulating a crack band of $l_c = 16$ mm, are presented in Figure 5.9a. The parameters chosen for the numerical simulation of the localization zone are the same ones identified from the experimental results and are given in Table 5.5 while the rest of material was chosen to be elastic with non-symmetric Young's modulus in compression and tension. The comparison between the numerical axial stress and strain response obtained as volume average on all elements constituting the localization zone and the analytical solution of the constitutive damage model are presented in Figure 5.9b. In order to avoid numerical discrepancies in analytically and numerically obtained fracture energy that can arise from the 3D propagation of stress waves, the value of the Poisson ratio was set to zero. It is again worth mentioning that the aim of the numerical simulations is not to effectively reproduce the experimental results with all the supporting physics but rather to only evaluate the reliability of the proposed experimental data processing. Knowing the finite element size of the numerical model (8 mm) and the size of the crack band localization zone (two times the element size), it is possible to determine the numerical fracture energy from the numerical model applying the standard averaging approach:

$$G_f^{FE} = l_c \int_{\varepsilon(\sigma=\sigma_{max})}^{+\infty} \overline{\sigma_i(\varepsilon_i)} d\varepsilon \tag{5.4}$$

where in this case $l_c = 2l_{el}$ with l_{el} the size of the finite element and the overline symbol denotes the volume average response of all the elements constituting the localization zone obtained at integration points.

Test	Density (kg/m^3)	E_c (GPa)	ν	σ_t (MPa)	ω	A, B	E_t/E_c	Crack band (mm)
Tomo1	2290	35.5	0	8.5	1	1, 1	0.585	16

Table 5.5: Numerical parameters of the Mazars' model assigned to the crack band localization zone to simulate one distinct dynamic fracture.

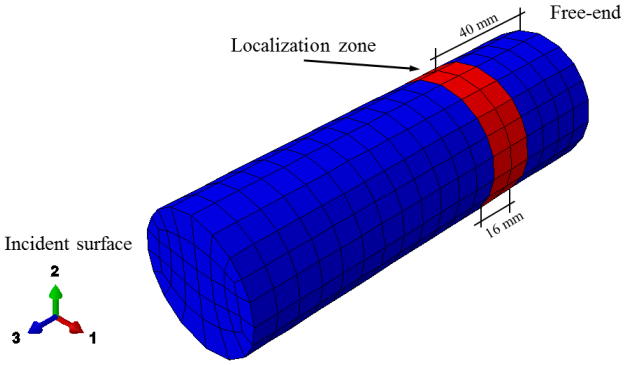

(a) FE mesh of 8 mm size with a pre-defined crack band at 40 mm from free-end ($l_c = 16mm$)

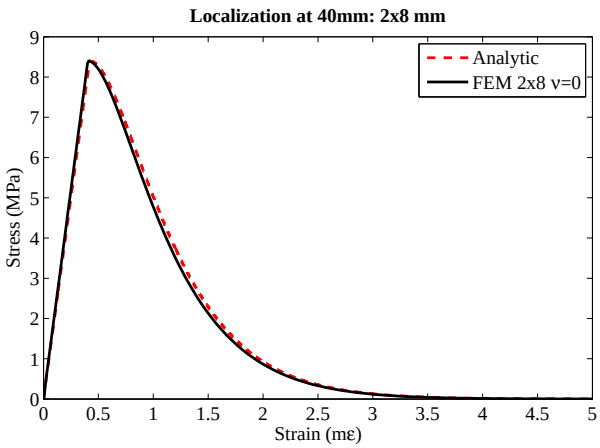

(b) Comparison of the average axial stress-strain response from the numerical crack band model and the analytical solution – Equation 3.4.2.2 ($\nu = 0$)

Figure 5.9: FEM modelling of one localisation zone.

5.3.2 Numerical results

To apply the same processing technique of the experimental data to the numerically simulated data, it is necessary to obtain the differential displacement at both sides of the numerically simulated localization zone that is located at 40 mm from the free end. This is obtained by computing the average axial nodal displacement through the cross-section for each of the two sets of nodes located in the first layer of elements on both sides of the numerically modelled localization zone. Then the same principle for subtracting the elastic material response is performed, utilizing the values of average axial stress response computed in the element volumes of all the elements constituting the modelled localized zone. Knowing the values of Young's modulus in compression and tension, a correction can be applied for both loading stages. Finally, the numerical Stress-FOD curve can be reconstructed in the same way as in the treatment of the real experimental data 5.2. Then, the dissipated specific fracture energy in the localization zone can be calculated as a direct integral of the reconstructed curve as:

$$G_f^{FOD} = \int_{u(\sigma=\sigma_{max})}^{+\infty} \sigma_i(u)du \tag{5.5}$$

Furthermore, the numerical model can be set to provide nodal velocity data at each node of the FE mesh with the same temporal discretization. This information can be used to investigate the already proposed experimental approach proposed by Schuler *et al.* [Schuler et al., 2006] to obtain the specific fracture energy, which is based on the moment transfer between spalling fragments. In the current numerical model it can be considered that there are only two principal fragments, one from each side of the localization zone. The momentum transfer processing method assumes homogeneous velocity field throughout the entire spall fragment after the cracking take place which can be regarded as a strong approximation since fracturing events can continue to take place within the formed fragment. However, it needs to be mentioned that in this work, since no physical discontinuities are modelled, the term spall fragment cannot be used within the same description. It is rather considered as the parts of the numerical sample from each side of the predetermined localization zone. Therefore, overall average axial velocity was calculated for two groups of nodes, belonging respectively to these two parts. The expression of the specific fracture energy needed to open one crack, in that case, is expressed as:

$$G_f^I = \Delta v m \dot{\delta} / A_s \tag{5.6}$$

where Δv is the change of velocity of the spall fragment between the moment when the cracking starts and the moment corresponding to complete separation of fragments. In current analysis, it is assumed that the first corresponds to the instant of peak tensile stress while the second corresponds to the moment when the post-peak stress values decrease to zero. $\dot{\delta}$ is the average fracture opening speed obtained as the difference of average fragment velocities after the fracture occurs. A_s is the crack surface, here taken to be equal to the cross-section of the numerical sample and m represents the spall fragment mass. Table 5.6 contains the results obtained when both processing methods are employed to treat the numerically simulated data from the same FE simulation by using Equations 5.3-5.6.

	Analytic Equation 5.3	Stress-Strain Equation 5.4	Stress-FOD Equation 5.5	Impulse transfer Equation 5.6
G_f $[J/m^2]$	112.9	109.3	122.1	281.3

Table 5.6: Numerical parameters of the Mazars' model assigned to the crack band localization zone to simulate one distinct dynamic fracture.

From the presented values it can be seen that the proposed processing method in this work, based on local data of the axial displacement around the localization zone, provides results quite close to the analytical values. The observed difference can be attributed to the fact that the numerical simulation does not account for any physical separation and formation of fragments but is modelled through the localized softening zone where the damaged elements stay present in the global matrix of stiffness (no erosion criteria). Furthermore, the numerical displacement gauge considered also the elements adjacent to the localization zone and also encodes the relaxation response occurring within those elements due to fracturing. For the above mentioned a slightly higher value was expected. This further suggests that the closer the measurement is to the fracture zone the more accurate the measurement of specific fracture energy is. On the other hand, it can be observed that the method based on the spall fragment velocity change – Impulse transfer method [Schuler et al., 2006], can provide higher results than the expected analytical values. This can be attributed to the fact that it relies on the assumption of uniform velocity fields for each of the observed spall fragment. Indeed, it has been suggested that the moment transfer method can provide inaccurate results, especially in the case when the notch is introduced in the sample [Schuler, 2007]. Finally, it could be concluded that the proposed experimental processing method that uses full-field measurements provides more realistic information on the concrete dynamic fracture energy. It is able to provide values of specific fracture energy dissipated per one dynamic fracture zone without any *a priori* assumptions on the material behaviour and applying a realistic correction for the material local elastic response.

5.4 Evaluation of the full-field measurement method used to identify the G_f on simulated experiments

5.4.1 Extended finite element modelling: XFEM

In this section the accent is on verifying the previously proposed experimental technique used to determine the concrete fracture energy directly from measured displacement maps through the use of *simulated experiments* (Chapter 4). Obtaining synthetic images that encode fracturing information in a controlled manner allow various external factors can be studied independently. Although, analytical solutions for the displacement field around stationary crack in an elastic media do exist [Williams, 1952], synthetic images created by displacement fields obtained within FE formulation represent a good alternative since any material law or loading conditions can be used [Barhli et al., 2017].

Here, the idea is to simulate one such fracturing process under dynamic loading conditions and to then embed this information into the synthetically generated grid images so that the same procedure, when real experimental images are treated, can be applied. The underlying motivation comes from the fact that, in case when conventional finite element modelling is used, strong discontinuities (such as a crack) cannot be truly taken into account as geometrical discontinuities without considerable mesh refinement around the neighbourhood of a crack tip. This arises from the fact that, as it is in all cases when local material description is defined within a formalism of a softening constitutive response, numerical localization will inevitably take place due to the mesh sensitivity; since the element size dictates the value of the dissipated specific fracture energy within the element. Non-local regularization schemes are then frequently used to circumvent this problem from the aspect of numerical modelling. However, introducing a regularisation technique in the light of maintaining a constant dissipated energy per surface unit in a single finite element regardless of its size, produces quasi-homogeneous displacement fields since a characteristic length is introduced in the model over which the meaningful constitutive quantities are computed, or not to say: smoothed. Some methods circumvent the problem of explicitly defining the material characteristic length by relying on the conservation of energy theory to define the damage localization such as phase field modelling [Miehe et al., 2010, Molnár and Gravouil, 2017]. However this technique requires small mesh size around the expected cracking domain. Often, in order to present the physical cracking patterns an erosion criterion can be used with in order to physically remove the damaged elements, but even in that case, the crack 'thickness' will always be equal to the smallest element size of damaged element. Although these numerical techniques can provide a good macroscopic numerical description of the various damage process, for example a truthfully represented damage field in the domain of continuum mechanics, the modelling of strong displacement jumps remains a challenge. For this reason the presented *Spall-simulator* can be tied with some other simulation strategies in order to account for presence of a strong displacement discontinuity.

The eXtended Finite Element Method (XFEM) presents one such possible strategy that alleviates the shortcomings of the conventional FE modelling when strong local displacement discontinuities are in question [Belytschko and Black, 1999]. It is a method based on the partition of unity concept [Babuška and Melenk, 1997], that allows the crack to 'cut-through' the finite element and as such it is particularly suitable for numerical modelling of crack inception and propagation phenomena not imposing the crack path *a priori*. When compared to the standard FEM, XFEM has several advantages in aspect of mesh independence. The most important feature of XFEM is that it can simulate an extending crack without any re-meshing by treating the cracks at element level. The basic concept relies on the use of conventional finite element method with added enrichment degrees of freedom through special displacement functions. Usually, the Heaviside function (that describes the displacement jump) and the asymptotic functions (that describes the crack tip), are all used to deal with the discontinuity. The approximation function of the XFEM element displacement vector is in general written as:

$$\mathbf{u}(\mathbf{x}) = \sum_{i=1}^{N} N_i(\mathbf{x})[u_i(\mathbf{x}) + H(\mathbf{x})a_i(\mathbf{x}) + \sum_{\alpha=1}^{4} F_\alpha(\mathbf{x})b_i^\alpha(\mathbf{x})] \tag{5.7}$$

where the $H(\mathbf{x})$ is the jump function and the $a_i(\mathbf{x})$ are the new degrees of freedom assigned to the nodes where the crack passed through the element interior, $F_\alpha(\mathbf{x})$ is the asymptotic crack-tip function and the $b_i^\alpha(\mathbf{x})$ are the nodal enriched degrees of freedom assigned to the nodes consisting the element that contains the crack tip.

Owing to these advantages, XFEM has found the numerical implementation in some stand-alone FEA software packages that have been aimed for commercial use, such as Abaqus^{TM}, where it was first introduced in 2009. Abaqus uses the Level Set Method that permits representing the crack position, as well as the location of crack tip [Osher and Sethian, 1988]. It is a numerical technique that represents discontinuities by two signed distance functions, one for the crack surface and another for the crack front. Current implementation in the Abaqus environment is based on also using the phantom nodes which are superimposed over and tied to the nodes of the original mesh

of the enrichment element. Once the element is cut through by the crack it is divided into two parts where each contains real or phantom nodes. Since its introduction XFEM was used to study various problems ranging from modeling crack growth [Stolarska et al., 2001], to the dynamic crack propagation [Réthoré et al., 2007, Song et al., 2008].

The aim of this study is not to perform a benchmark of the XFEM capabilities in the Abaqus environment, as for example it is done in [Gigliotti, 2012]; however, it is necessary to mention the main limitations of its numerical implementation from an end-user point of view (since it is used in that manner in this work) to which the following simulation work is being limited. These are as follows:

- It can be used within the Abaqus/Implicit Dynamic work environment or General Static.
- Only one propagating crack can exist within a domain of one element and its inception point has to be pre-defined.
- Only non-interacting cracks can be contained in the model domain
- The crack cannot branch nor turn for 90°.

Another limitation that is worth mentioning is that for the case when propagating cracks are modelled (such will be the case here) it is a pre-defined requirement that the crack itself, completely cuts an element. Therefore, the crack tip can only be located along an element edge. This means once a crack starts to propagate it will cut each element entirely, hence, the crack tip cannot be stopped within one element.

In the following section, the eXtended finite element method that is implemented in the Abaqus FE software package, is used to simulate the inception and growth of one distinct numerical macro-crack in concrete material considering a spalling experiment. The material behaviour outside of the crack is considered to be perfectly elastic and all the given fracture energy is assumed to be dissipated by one crack formation through a bi-linear traction separation law. The numerically simulated time-resolved displacement fields are extracted at nodal points to obtain the displacement fields which contain the fracturing information. These fields are then used in two stages. First, the numerical displacement fields are directly treated as the experimental ones. The acceleration fields are numerically computed through the numerical differentiation scheme and then the Equation 2.22 is used to obtain the axial cross-sectional stress. Then, the processing of the so called differential displacement gauge is applied and the obtained fracture energy is compared to that of the XFEM numerical simulation. Secondly, the same displacement fields are used to generate sequences of synthetically deformed grid images (assuming a perfect UHS camera) encoding the fracturing information directly through the change of gray level. Then, these images are treated as experimental data which allow validating the proposed methodology of evaluating a specific fracture energy from a spalling test.

5.4.2 Numerical model

A 2D numerical model is considered to simulate a spalling test with one predefined crack at the position of 40 mm from the sample free-end. It is used to model the initiation and growth of one distinct spall fracture whose predefined position is located on the outer top edge of the sample. The predefined crack length was taken to be 2 mm. A representation of the model is presented in Figure 5.10. The numerical model has been subjected to a pressure load assigned on the incident surface. The load amplitude history was obtained from a real experimental pulse recorder with the gauge glued on the sample at 20 mm from the bar-sample interface (Figure 3.14b). The mechanical response of this model was simulated using Abaqus/Standard to carry out the Dynamic-Implicit analysis of the problem. The FE simulation details are provided in Table 5.7. The boundary condition was set as a horizontal sliding pin of one node that lies in the horizontal axis on the left-hand side of the numerical sample. This boundary condition was chosen (as opposed to sliding pin condition of the top and bottom nodes) based on

a preliminary study, in order to maintain the uniformity of the axial pressure load applied during the compressive loading stage. As it has been done in previous numerical works presented in this Chapter 4, the mesh size was chosen to be 1x1 mm^2 resulting in 5400 elements consisting of 11132 nodes. The stated 2D problem was treated assuming plane stress conditions by assigning the CPS4 elements with full integration scheme to the generated FE mesh. Full integration scheme was chosen in order to obtain the crack path as accurate as possible since it was noticed that when reduced integration is used, the crack path tends to diverge from the expected vertical direction at the point of initiation (the crack tip).

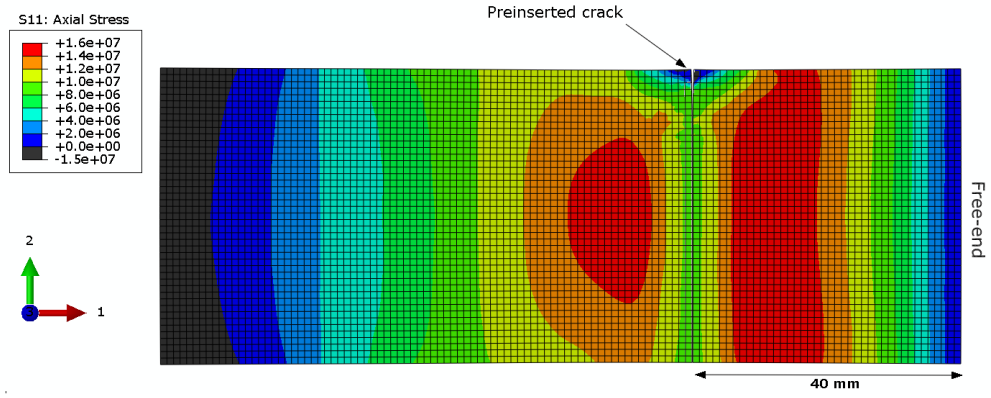

Figure 5.10: Representation of the 2d mesh used in simulating spalling test with XFEM.

Mesh size	1x1 mm
Element type	CPS4
Simulated time (μs)	92.5
Max. number of increments	10000
Increments size: initial (minimum)	5 μs (0.5 ns)
Inter-frame time (μs)	0.5
Length of pre-inserted crack	2 mm
Type of simulation	Dynamic/Implicit

Table 5.7: Details on the Abaqus/Standard model used for simulation of one spall fracture with XFEM.

The computations have been carried out using the general analysis step where non-linearities (geometrical and/or material) can occur and are involved in the solving of the kinematic relations with large-displacement formulation. The analysis of the presented problem involves solving a non-linear dynamic problem with a direct time integration scheme to calculate the transient response of the system. Abaqus/Standard provides the automatic time stepping scheme to resolve this problem, where the time step is determined (and if necessary updated) based on the half-increment equilibrium residuals. This will inevitably introduce slight high-frequency numerical noise in the simulated displacement fields. Furthermore, the numerical simulation is driven by a quasi-smooth loading pulse which was in fact experimentally designed in order to avoid high-frequency components to be introduced in the tested sample. Consequently, the accurate simulation of the high-frequency vibrations was considered not to be of interest. It is worth pointing out that any numerical high-frequency content present in the simulated displacement fields, that are later on used as inputs in the *spall-simulator*, will deteriorate the material identification procedure. In order to avoid any numerical noise to be introduced in the simulated displacement field, the simulated scenario was considered to fall into the range of moderate dissipation application, which is a sub-option offered within the solver. In this way, numerical damping through the implicit Hilber-Hughes-Taylor integrator was added, where the default values (α =-0.4142, β =0.5, γ =0.9142) were found sufficient. The detailed study on the effects of

the damping coefficients was not carried out and presents a task for future works, here, the simulations were run with the aim of showing the proof-of-concept. The acceleration fields were not computed in the first step in order to stabilize the numerical convergence, this was considered appropriate since the applied loading pulse does not significantly change within first several micro-seconds. The desired simulated time was initially set to be 100 μs with recording data outputs at 0.5 μs in order to simulate the acquisition speed of a 2 Mfps UHS camera. However, the full fracturing occurs before the full simulation time is reached, hence the desired time was not possible to reach since after the fracturing, the computation does not converge due to the flying ejecta. For that reason, the simulated time was reduced and set at 92.5 μs which was just enough to capture full stress-crack opening curve, yielding a total of 185 simulated camera frames.

The XFEM works within the Linear Elastic Fracture Mechanics (LEFM) formalism and as such requires the presence of a crack. Here, one pre-existing crack has been inserted at the distance of 40 mm from free-end. The spalling test is by its nature a uniaxial indirect tensile test, hence, only Mode I failure (pure tension) was considered. The formulation that governs the behaviour of crack propagation of the XFEM-based model is defined to follow the traction-separation law. The law assumes the linear-elastic behaviour upto the point of initiation followed by the evolution of damage. In this work a bi-linear traction separation law is considered with a linear softening response. The crack initiation criterion which marks the onset of degradation of the cohesive response at the predetermined enrichment location was chosen to be based on the maximal principal stress criterion which simply reads as follows:

$$f = \{\frac{\langle \sigma_1 \rangle}{\sigma^0_{max}}\} \tag{5.8}$$

where f is the dimensionless coefficient, σ_1 is the principal stress and the σ^0_{max} is the maximum allowed principal stress. Once the limit of maximum allowed principal stress at the pre-defined crack tip is reached, with a certain tolerance f_{tol} the crack inception takes place and continues to grow following the same procedure in the next step:

$$1 \leq f \leq 1 + f_{tol} \tag{5.9}$$

The tolerance here was taken to be 5% and therefore it can be expected that the simulated stress at the crack tip can be slightly elevated than the defined maximum. The damage evolution law was considered to follow a linear softening description based on the maximum allowed displacement at failure (U_{max}). The parameters of the damage law used in the simulation work have been obtained from the previously presented experimental works (Section 3.4.1) from the test named Tomo1. It is worth mentioning at this point, that the aim of this work is not to simulate the mentioned spalling test but to validate the methodology of the measurement of specific fracture energy assuming one unitary crack propagating in a linear elastic medium. Therefore, the material outside the enriched zone is considered to be linear elastic and the material parameters used in the simulations are given in Table 5.8.

Young's modulus (GPa)	35.5
Poisson ratio	0.2
Density (kg/m^3)	2290
Maximal principal stress - σ^0_{max} (MPa)	8.5
Displacement at failure - U_{max} (μm)	80
Damage evolution	Linear
Fracture energy - $G_f = \frac{1}{2}\sigma^0_{max}U_{max}$ (J/m^2)	340

Table 5.8: Details on the material parameters used for simulation of inception and growth of one spall fracture with XFEM.

5.4.3 Identification from simulated displacement fields

Full-field displacement maps have been output from the above described numerical model. These fields can then be used as the input in the VFM data processing so the validity of using the integration of acceleration fields to define the load cell in the post-peak regime can be directly examined. This concern typically arises from the fact that after the fracturing occurs, the mean amplitude of the axial acceleration drops drastically (Figure 5.11). In order to get the time resolved acceleration fields, numerical differentiation of the displacement data was performed. Since the simulations were carried out with Abaqus/Standard, that uses an implicit numerical scheme, it is expected that no numerical noise is present in the simulated data and some more straightforward derivation techniques can be used. For that reason the numerical derivation of the simulated displacement fields was carried using the simple finite differences method. However, as it has been mentioned earlier, it is not possible to simulate the total desired time of 100 μs since the fracturing happens earlier and can induce non convergence in the simulation of subsequent frames. This means that the final zero displacement is to be reached in the last simulated frame. On the other hand, when performing numerical derivation over a certain time window, several first and last frames that correspond to the half-widow size stay out of reach. This means that if the numerical derivation is performed on the extracted data the last two frames can be lost not allowing the full reconstruction of the desired Stress-COD curve. For this reason, the displacement data were extrapolated using the cubic spline data fitting, in order to recreate additional two time frames that simulate free motion of the spall fragment after the fracturing. Figure 5.12 presents simulated displacement and derived acceleration maps at three specific times corresponding to peak stress, half of the softening response and at total fracturing. The derived axial acceleration data were used to describe the average cross-sectional axial stress.

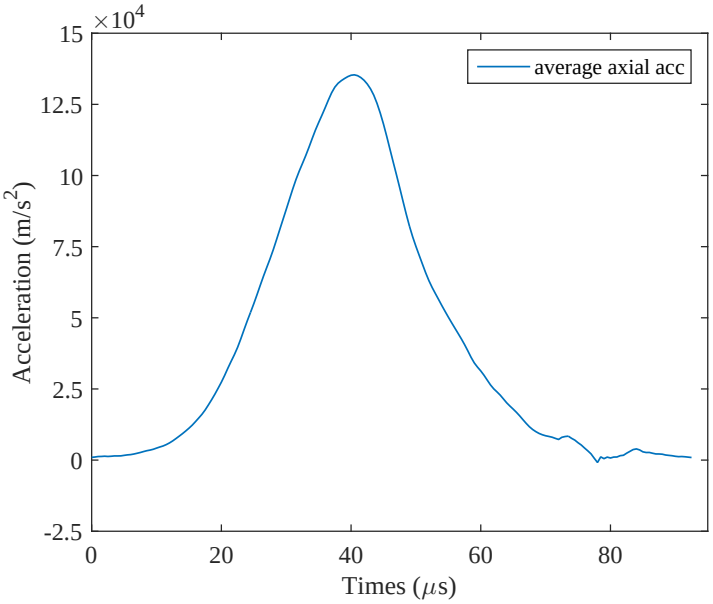

Figure 5.11: Average axial acceleration derived from simulated displacement fields using XFEM numerical modelling.(finite differences scheme)

Once the displacement and stress are obtained, the processing of the differential displacement gauges can be applied as in real experiments to obtain the specific fracture energy for one crack (Section 5.2). The correction for the elastic response of the differential displacement can be performed as in the Equation 5.1. The identification of the specific fracture energy requires the reconstruction of the local stress-fracture opening displacement curves. One advantage of having simulated displacement fields that contain the modelled fracturing information, is that the position of the differential gauges can be located exactly in the closest vicinity of the displacement discontinuity. The reconstructed Stress-FOD curves obtained directly from the results of the numerical model are presented in

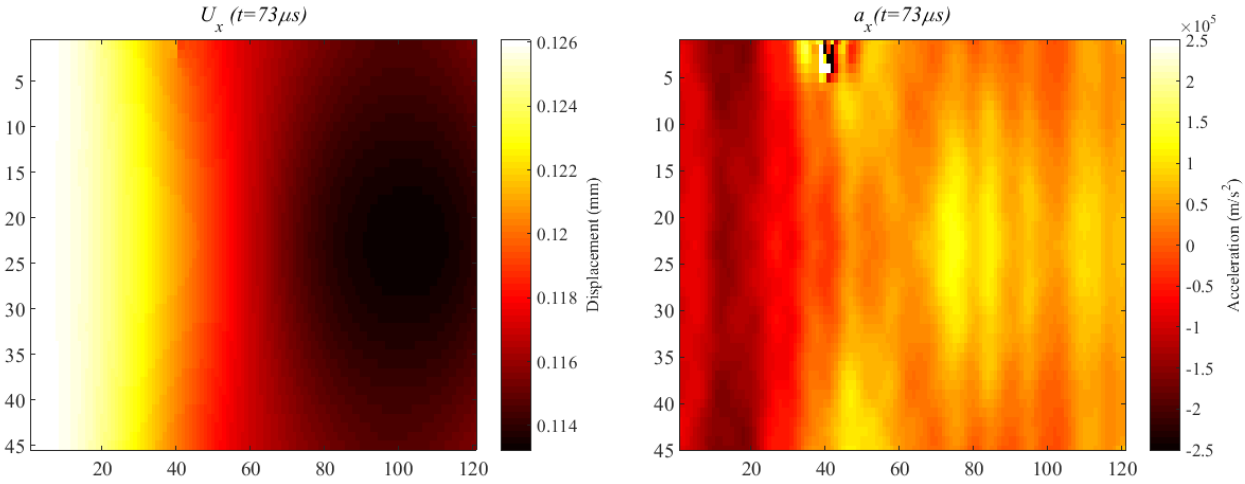

Figure 5.12: Maps of axial displacement and axial acceleration corresponding to times of maximal tensile stress ((a) and (b)), half the softening response ((c) and (d)) and full crack formation ((e) and (f)) (the vertical and horizontal direction correspond to the sample surface in millimetres where zero horizontal coordinate corresponds to the sample's free-end.)

Figure 5.13a. The average axial displacement measurements are taken in the first elements from the left and right hand-side of the simulated crack. Also, the comparison of the fracture opening velocity (FOV), obtained as time derivation of fracture opening displacement, is given in Figure 5.13b. A relatively good agreement between numerical curves and the ones identified from the VFM processing can be observed. The slight non-linear softening obtained from the VFM could be attributed to the way the acceleration fields are being integrated since the same deviation was obtained when simulated acceleration data was directly processed. The values of the identified specific fracture energy obtained by integrating the presented Stress-FOD curves are given in Table 5.9.

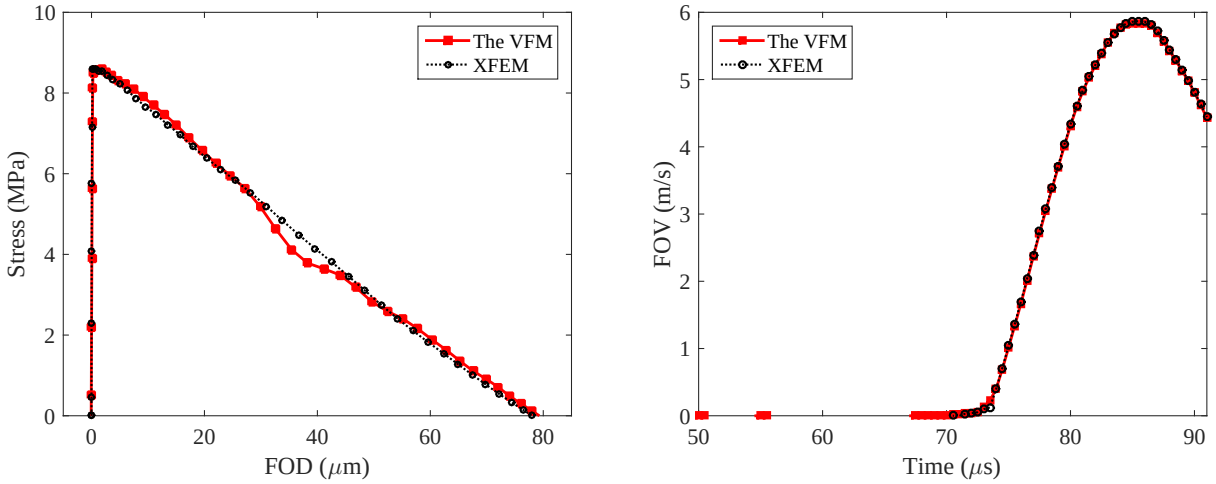

(a) Stress vs. Fracture opening displacement (FOD).

(b) Fracture opening velocity (FOV).

Figure 5.13: Comparison of the numerical results between XFEM simulation of one distinct crack and identification obtained by processing the simulated displacement data with the VFM.

Method	G_f $[J/m^2]$
Pre-defined	340
XFEM	331.55
The VFM	330.77

Table 5.9: Results of the identified specific fracture energy obtained from the integration of the curves in Figure 5.13a.

Interestingly, the results from the numerical simulations are about 5.1% lower than the energy defined within the used material damage criterion. This could be due to the applied averaging of the fields within the entire column of finite elements from both sides of the simulated crack. On the other hand, the value of specific fracture energy obtained by processing the simulated displacement maps with the VFM seems very close to the one from the numerical simulations, differing only for about 0.3%, which already indicates a fairly good result that validates the proposed VFM processing based on using the acceleration load cell and the differential displacement gauge for retrieving the value of specific fracture energy.

5.4.3.1 Effect of the virtual gauge processing

As previously mentioned, the accuracy of the measured specific fracture energy also depends where the fracture opening displacement is measured with respect to the fracture. Therefore, it is necessary to investigate how the size and the position of the used differential displacement gauges influence the reconstructed Stress-FOD curve (Figure 5.14). The results regarding the chosen size of differential displacement gauge, located in the close vicinity

(first set of data points) around the crack, are presented in Figure 5.15a. The values of specific fracture energy are summarized in Table 5.10b. It can be seen that the influence of the gauge size has a small impact of the determined specific fracture energy. Even if the displacement data are averaged on a length of 10 mm on both sides of the crack, the determined specific fracture energy is within 4% of the expected one. On the other hand, it seems that the impact of the gauge position has a slightly bigger impact (Figure 5.15b) with exhibiting an error of about 6% when the differential gauges are located 4 mm away from each side of the crack. It needs to be mentioned that, here, it is assumed that the material behaves perfectly elastic outside of the fracture. Which can be easily seen from the plot that represented the effect of the gauge position, since the peak stress keeps increasing with the distance away from the crack. This would not be realistic for a real material with a given limited strength. On the other hand, it could be anticipated that the fracture opening displacement would exhibit similar trend, meaning, the further the differential gauges are away from the fracture vicinity, the bigger the error would be on the FOD.

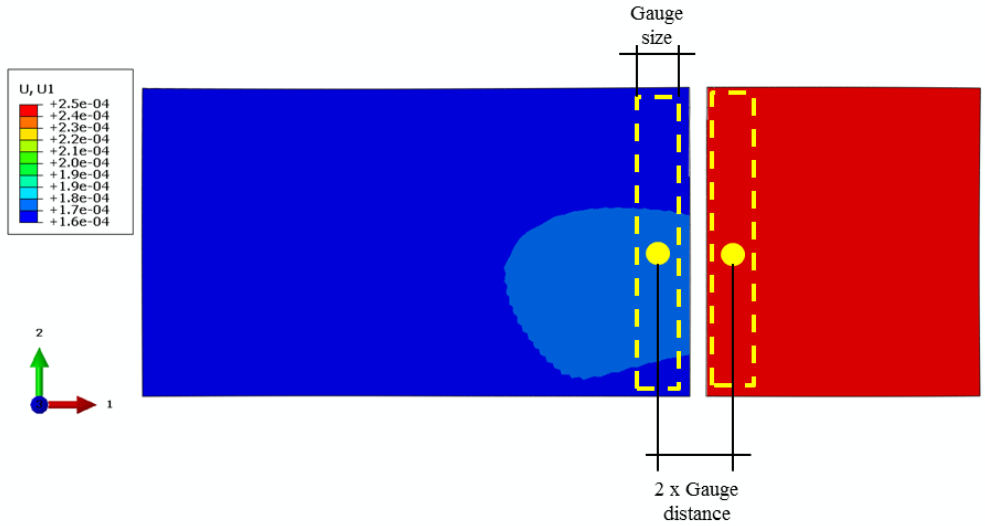

Figure 5.14: Schema on the investigated differental gauge size and distance in the 2d XFEM model used to simulating spalling test with one crack.

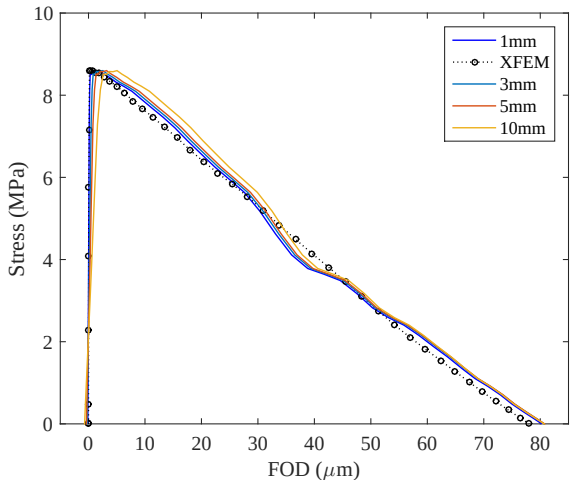

(a) Effect of the size of the virtual gages from each side of the crack.

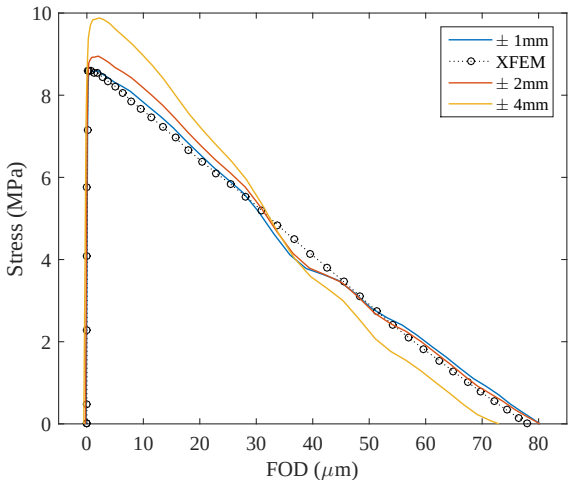

(b) Effect of the distance of the virtual gauges from the crack.

Figure 5.15: Effect of the differential displacement gauge size and positioning with respect to the simulated fracture.

Gauge size (mm)	G_f [J/m^2]
1	335.54 (1.2%)
3	338.74 (2.16%)
5	340.62 (2.73%)
10	344.74 (3.97%)

(a) Effect of the size of the differential gauges on the measured specific fracture energy. (distance ± 1mm from the crack)

Gauge distance (mm)	G_f [J/m^2]
1	342.67 (3.35%)
2	347.77 (4.89%)
4	352.06 (6.18%)

(b) Effect of distance from the crack of the differential gauges on the measured specific fracture energy. (size of the gauges 1x45 mm^2)

Table 5.10: Effect of size and position of the differential gauges on the measured specific fracture energy. (relative error given in brackets)

5.4.3.2 Effect of the camera acquisition rate

It is evident that the accuracy of the proposed methodology for measuring the specific fracture energy will also depend on the time discretization of both stress and displacement data since in quasi-brittle materials like concrete, capturing of the tensile failure under small deformation significantly relies on the high frame rate acquisition speed. For example it is suggested that the acquisition speed of 0.2 Mfps with 256x256 pixel count can suffice for observing a qualitative fracture characteristic of rock under dynamic compression through the analysis of strain and strain rate fields obtained by DIC [Xing et al., 2017a]. However, when it comes to extracting more significant quantities, higher acquisition speed is necessary. For instance, it has been shown through simulation of a perfect UHS camera, in the Section 4.1.2.3, that the acquisition of 1 Mfps and above is necessary for a reliable identification of elastic Young's modulus in a spalling test. Although this serves just as a guideline, it is interesting to see how the simulated acquisition speed affects the measurement of the specific fracture energy using the proposed identification methodology. The effect of the simulated frame rate on the relative error of the determined fracture energy is given in Figure 5.16. The relative error is computed as difference in percent of the energy obtained using the VFM to process the simulated displacement fields and the one directly obtained directly from the XFEM simulation. As expected, it can be seen that the error drastically decreased with the increased simulated frame rate, again indicating that the acquisition speed of 1 Mfps and above can be considered as an adequate one for measuring the specific fracture energy with a relative error of 6% and lower.

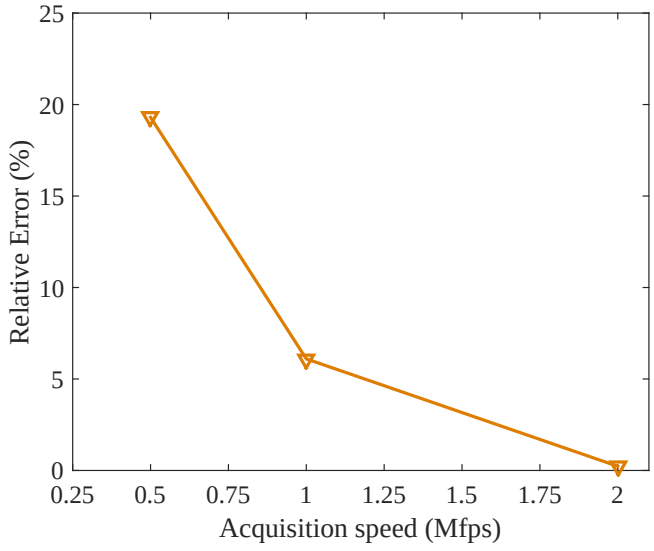

Figure 5.16: Effect of simulated camera acquisition speed on the identification of the specific fracture energy.

5.4.3.3 Measurement sensitivity to simulated displacement noise

In principle, the sources of uncertainty on the kinematic measurement are multiple and they can arise from various effects from the intrinsic sensor noise, the method used to recover displacements and the test conditions. All these effects get superimposed in real experimental conditions and introduce a final uncertainty in the measured displacement fields. It is a difficult task to identify a resulting noise model that takes into account all these potential sources of errors at once. One simple way of investigating the impact of noise on the desired measurement is to introduce standard deviation in the displacement maps directly as a zero mean random noise. Although, it worth noting that digital noise is more complicated than a mere random noise, it is still thought that it could be helpful to provide an idea on the measurement sensitivity to external noise influence. This assumption is known to be not realistic for raw data provided by digital imaging sensors and that it can be used only to provide first estimates of the measurement uncertainty [Grediac and Sur, 2014]. Assuming a non-correlated noise in time domain, each simulated displacement field can been corrupted with zero mean random noise field with a given standard deviation:

$$\widetilde{U}(x,y) = U(x,y) + \sigma.P(x,y) \tag{5.10}$$

where x, y are coordinates of each measurement point, $\widetilde{U}(x,y)$ is the new noise corrupted displacement field, $U(x,y)$ the numerically simulated displacement field considered to be ideal, σ is the standard deviation of the measured displacements and $P(x,y)$ is a zero-mean random field with a standard deviation equal to 1. The simulated displacement fields obtained from XFEM simulation simulating an acquisition speed of 2 Mfps were corrupted with random noise and then processed using the VFM. In this case, the acceleration fields were obtained by first performing a 2^{nd} order polynomial fit over 11 displacement points and then deriving it two times. The results regarding the reconstructed Stress-FOD curve for several levels of random noise are presented in Figure 5.17. As expected, no systematic errors are introduced in the identified specific fracture energy and a relative error for all cases was found not to be larger than 2%. However, from the presented plots the sensitivity of the measurement is quite obvious to observe. The quality of the identified material fracture response is highly affected by noise and with the increasing noise variance the post-peak region becomes more and more difficult to identify especially for the case when σ=4 μm which is a standard deviation close to the one obtained for the Shimadzu HPV-1 camera (Section 3.3.2).

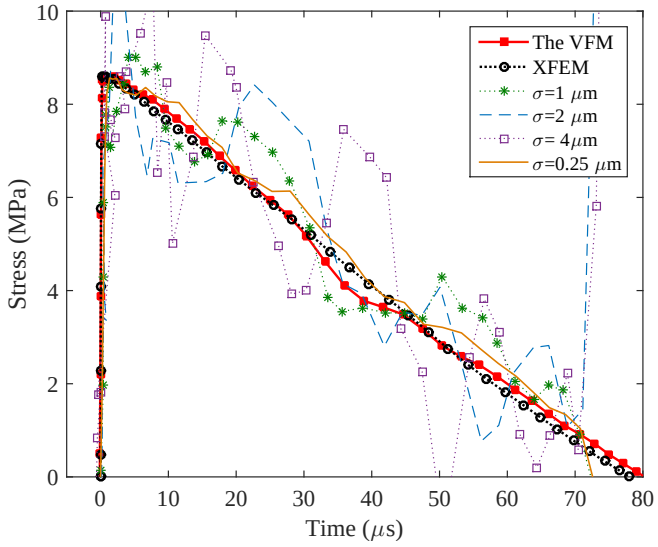

Figure 5.17: Effect of simulated displacement noise on the reconstruction of the Stress-FOD response. (zero-mean random noise with standard variation σ)

5.4.4 Identification from simulated image acquisition

In order to investigate possible effects that may arise during the recording of a grid image sequence with an UHS camera, synthetically deformed images were generated with the procedure described in Chapter 4 using the displacement fields output from XFEM simulations.

This procedure requires several interpolation steps so that the simulated fracturing information can be embedded into fictive pixel positions through their grey level change. In principle, two interpolation procedures are needed before image deformation, one to obtain the displacement maps on a regular mesh-grid and second to interpolate the obtained displacement maps onto fictive pixel positions. Here, the first step is skipped by already generating a regular mesh of finite elements in the numerical model which corresponds to the grid pitch of the desired synthetic grid image (1mm).

A first step is to interpolate the displacement maps onto the mesh-grid which represents fictive pixels $U(u_i, v_j)$, given a fixed grid pitch pixel sampling. Already here, some interpolation problems can be experienced at the edges which can be approximated by expanding the fictive mesh for one row of fictive pixels and then cutting it back down to the desired frame size. Next, a reference grid image needs to be generated based on the pixel count. In order to simulate the camera image digitisation of a single pixel, a super-sampling technique is used assuming a fictive area size of one photosensitive pixel region and allows taking into account the fact that a camera pixel only captures an average of the grey level over a certain physical domain. It is necessary to mention here that the choice of the super-samples can be beneficial for reducing the systematic errors caused by interpolation, as indicated in [Rossi et al., 2015], but can also increase the time needed to generate one sequence. For example, considering that a surface of 45x120 mm with 1 mm pitch grid is framed with 9 pixels per period for an image sequence consisting of 180 frames with 16 bit dynamic encoding: using 5x5 pix super-samples, the sequence will be generated within 120s, on the other hand using the 10x10 super-samples the sequence will be generated within 1980s (machine: Intel i7-3630 QM 2.40GHz, not – parallelized). As in previous simulation works, it was considered that the pixel photosensitive area covers the full pixel size, effectively simulating a fill factor of 100%, although ultra-high speed imaging sensors with on board memory suffer from much lower fill factor. After down-sampling the expanded image, a reference grid image $P(i, j)$ is obtained where i, j correspond to fictive pixel coordinates. Finally, the reference image is interpolated at each simulated frame at new pixel locations $P'(i+u_i, j+u_j)$ providing a sequence of deformed images.

Simulated frame rate	2 Mfps
Total sequence	186 frames (93 μs)
Grid pitch	1 mm
Grid pixel sampling	9 pix/pitch
Framed surface	45x120 mm
Pixel count	405x1089 pix
Super-sampling	10x10
Dynamic range	16bit
Fourier blur	1pix
Average illumination	47.8% dynamic range
Acceleration	2^{nd} order (11 points)

Table 5.11: Information on the generated synthetic image sequences.

So, it is obvious that the described procedure will, inevitably, introduce a systematic error in the measurement due to multiple interpolation stages and as such it is not perfect. Furthermore, it is expected that due to the

convolution window used in the grid method (which is 2N-1, N being equal to the grid sampling) the differential displacement gauges cannot be positioned exactly on the simulated fracture location but rather one measurement point away from both sides, which would, as showed in Figure 5.15b, provide slightly elevated measurement due to the numerical modelling assumptions. However, this procedure can still be used to provide global information on the possible effects regarding image quality, image illumination and effects regarding image grey level noise.

Here, the objective is to investigate how a grey level camera noise would impact the sought measurement of the specific fracture energy by adding simulated noise to the synthetic image sequence. One way to do so, is to define an overall standard deviation regarding the individual pixel mean grey level [Seghir and Pierron, 2017]. For that purpose, grey level zero-mean random temporal noise of standard deviation σ_g which represents a percentage of an average pixel grey level was added to simulated grid images to each pixel separately. An example of one corrupted synthetic pixel with 1% zero-mean random temporal noise is shown in Figure 5.18a. The information regarding the simulated grid image sequence and the acceleration derivation is provided in Table 5.11 Higher dynamic range was chosen here in order not to introduce additional errors due to quantization. The reconstructed Stress-FOD curves obtained after treating the synthetic images, for the case of perfect image sequence (no-noise) and the two cases of random temporal noise ($\sigma_g^1 = 1\%$, $\sigma_g^2 = 2\%$) are presented in Figure 5.18b. Values of the specific fracture energy calculated from the plotted curves are presented in Table 5.12. Although the determined fracture energy values are in the 10% error range, the figure clearly indicates the sensitivity of the measurement to the camera temporal noise and, as it can be anticipated, the noise mostly affects the stress level since it is its second derivative, present in the acceleration fields, that introduces substantial errors. Another remark is that, even though the noise model remains quite simple and not representative of a real camera, there is some similarity with the results reported in Figure 5.5. For this reason, a concluding remark can only focus on the prospective of the future work regarding the application of this technique. Once new advancements are made regarding the acquisition stability in the field of UHS imaging, the proposed identification methodology would experience nothing but benefit with regards to the accuracy of the identified results.

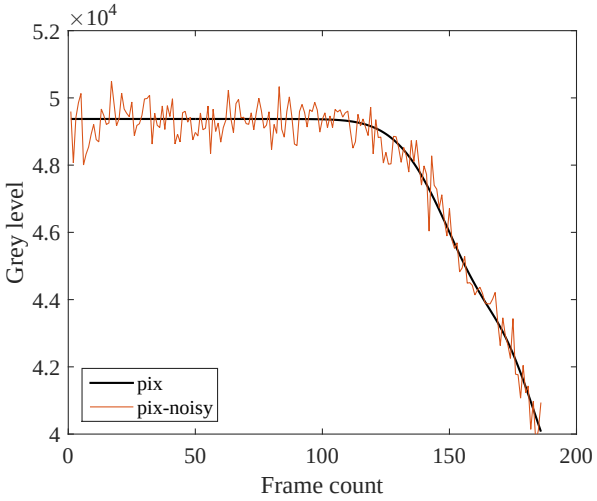

(a) Example of one simulated noisy pixel with 1% grey level zero-mean standard deviation.

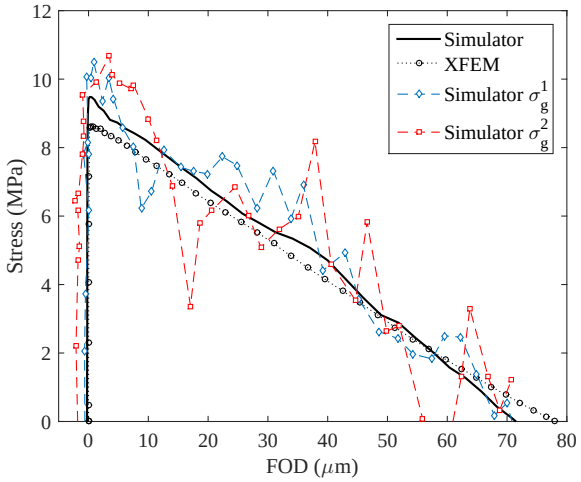

(b) Effect of two temporal noise levels: σ_g^1 is 1% and σ_g^2 is 2% of a individual pixel mean grey level.

Figure 5.18: Effect of the simulated zero-mean random temporal noise on the determination of the Stress-FOD curves.

Method	G_f [J/m^2]	Error (%)
XFEM	331.55	
Synthetic images (no-noise)	349.1	5.3
Synthetic images ($\sigma_g^1 = 1\%$)	361.1	8.9
Synthetic images ($\sigma_g^2 = 2\%$)	377.1	13.75

Table 5.12: Specific fracture energy determined from the Stress-FOD curves presented in Figure 5.18b.

5.5 Chapter summary

In this chapter, the identified results regarding the material constitutive response from two spalling tests presented in Chapter 3 have been extended towards obtaining values of specific fracture energy per each visualized dynamic tensile fracture. The motivation originates from the fact that very few works in the literature report such values and those that do, rely on methods that use indirect measurements adopting strong assumptions on the material behaviour. Additionally, current design standards [CEB, 1993] do not provide empirical formulations on the effect of strain rate on the specific fracture energy owing to the lack of experimental data, which makes this work even more interesting.

The first results showed that:

- Measuring full fields of axial displacement, the dynamic macro-cracks that are visualized can be analysed in a quantitative manner. The differential displacement gauges are used to provide differential displacement around the macro-crack showing that it is possible to conclude whether the observed fracture leads to sample complete failure (open fracture) or if it is a secondary fracture that is obscured by the adjacent dominant one (closed fracture) following their evolution in time.
- Thanks to having access to local measurements of stresses and strains it is possible to reconstruct the constitutive response of the material on the same points used to describe the fracture opening around the analyzed fracture. This further allows identifying the local elastic response around the macro-crack which is used to correct the differential displacement, providing the realistic measurement of the fracture opening displacement – FOD. Finally, the method allows reconstructing full stress-fracture opening displacement curves for each visualized dynamic fracture and therefore provides direct information on the concrete specific fracture energy.
- First results obtained for normal concrete indicated a markedly lower values of specific fracture energy G_f compared to the results present in the literature.

In order to assess the validity of the proposed experimental processing method for obtaining G_f, numerically simulated experiments were performed considering inception of growth of one distinct fracture through the use of XFEM method. The displacement fields were then extracted and processed with standard tools and the retrieved values of G_f were compared to those that have been given to the model. The first results show that the proposed method can provide values within about 5% confidence interval, which can be regarded as a good result since the data currently present in the literature exhibit a scatter of several hundred percent. The qualitative sensitivity of the proposed method was investigated through performing simulation of the entire chain of measurements involved in the photomechanical test using the methodology presented in Chapter 4. Synthetic grid image sequences that encode the fracturing information were generated. In order to model a noise coming from an acquisition system, as a first approximation, the images were polluted with zero-mean non-correlated grey level noise. It was noticed that with noise levels of just a few percent of mean image grey level can substantially disrupt the identification procedure

and requires strong low pass filtering to be applied in order to retrieve any meaningful information regarding the specific fracture energy. It is worth mentioning that currently available UHS imaging system exhibit higher noise levels. Nevertheless, the chapter presents a first application of such experimental method in light of providing quantitative fracturing information of concrete material under dynamic tension. The measurement refinement can benefit from the future technological advancements in the field UHS imaging regarding the increased stability of the images. For this reason, two latest UHS imaging sensors were considered and are presented in the following Chapter 6.

Chapter 6

Application of ultra-high speed CMOS-based image sensors in identification of dynamic tensile material response

Previously, in Chapters 4 and 5, it was shown how meaningful information on the dynamic fracturing can be obtained from a spalling test by simply taking use of its inertial component. Thanks to the VFM, the acceleration fields are directly tied to the axial stress description within the sample cross-section. However, obtaining the kinematic measurements with the means of full-field techniques is not an easy task, since their accuracy is directly dependant on the acquisition performance of the UHS imaging system in question. For example, the camera capabilities such as frame rate, can directly impact the identified result even in the case when no external noise is present. Moreover, the camera pixel count directly impacts the measurement resolution and the number of available data points. The camera used in previous sections, Shimadzu HPV-1, suffers from both these limitations. Nevertheless, the area of ultra-high speed imaging is a rapidly evolving domain and new technological sensor developments allowing to reach lower inter-frame times at larger pixel counts.

6.1 Chapter outline

In this chapter, two types of newly developed UHS imaging systems and their applicability to a spalling test will be investigated. The systems incorporate novel acquisition technologies that contain CMOS-based image sensors. For this reason, the chapter is devided into two parts:

- First part 6.2 is devoted to exploring the use of the Kirana camera in performing full-field measurement kinematics of dynamic tensile test. The camera sensor presents a hybrid technology between CCD and CMOS which resulted in a sensor a relatively large pixel count 926x768 pix able to reach inter-frame time down to 200 ns. The sensor technology is introduced and some results regarding acquisition stability are shown. Then the imaging system was employed in a spalling aluminium test to evaluate its performance. It is necessary to mention that during this work the sensor was under development, having the latest version installed in 2018.
- Second part 6.3 is devoted to using a purely CMOS based UHS imaging sensor for obtaining kinematic full field measurements. The camera used is Shimadzu HPV-X2 which provides 128 frames with 400x250 pixel count upto 5 Mfps. The sensor technology is presented together with some acquisition characteristics. Then, the imaging system was used in spalling test on both aluminium and concrete samples to evaluate its performance.

6.2 The Kirana camera experimental campaign

In this section the applicability of a Kirana sensor in identifying material response during dynamic tension is explored. The Kirana camera, from Specialised imaging [Crooks et al., 2013a], is a newly developed acquisition system based on a hybrid chip technology that merges the CMOS and the CCD together into what is called the uCMOS. It allows reaching the extremely short inter frame times (200 ns) providing constant pixel count of 0.7 Mpix (924 by 768 pix) over 180 captured frames. As such, it is currently the only acquisition system that provides

such a pixel output quantity of 1.5 Tpix/s in burst mode which has made it suitable for various applications. However, the aim of this section is to investigate and provide first (to the knowledge of the author) information on it metrological performance in measuring full field kinematic data such as displacements and accelerations of the observed sample surface. To this end, several spalling experiments were performed in the Laboratory-3SR in Grenoble. The grid-instrumented sample surface was recorded during the test to extract the time resolved displacement fields which are then processed using the VFM as to finally obtain the material constitutive response.

First, some principal information regarding the sensor architecture are introduced. Second, the camera noise is investigated from imaging a blank scene, mainly focusing on the temporal noise component. Possible effects of high frequency noise that propagates from the camera to the measured displacement fields and how it can affect the computation of accelerations is shown in Annex C.2. Finally, first results of applying the Kirana sensor in spalling test on aluminium material is presented. Possible perspectives regarding application of such sensor in measurement of full field kinematics for material identification are also discussed.

6.2.1 On the characteristics and performance of the uCMOS sensor

It is until recently that the CCD cameras were consider superior in the domain of ultra-high speed photography. In order to achieve high frame rates, it is necessary to temporary store a number of images in the device for subsequent readout. This influenced the development ISIS family of burst CCD cameras. But the demand for higher pixel count as well as larger number of continuously recorded frames has been found as requirement of scientist ranging across numerous fields [Etoh and Nguyen, 2018], and consequently influenced the camera developers' attention to be focused in finding alternative ways of dealing with these shortcomings. On the other hand, from the development of the CMOS sensors [Fossum, 1997], significant advancements have been made with respect to both image quality and size, when dealing with photographic of fast changing phenomena. However, the cameras based on purely CMOS technology that use out-of-the-chip memory enforce trade-off between the spatial resolution and the frame rate, resulting in significantly reduced pixel count per acquired frame which is often of little use to most users dealing with full-field meteorology.

In order to tackle both these challenges, the Specialized Imaging company has decided to take the best from both CCD and CMOS architectures and to combine them into a new technology that is named uCMOS, where u stands for ultra-high speed. The so-called Kirana imaging sensor is based on this architecture and is equipped with 924x768 pixels with an in-pixel memory of a CCD and with CMOS transistors for image readout. This unique hybrid chip allows reaching frame rates of 5 Mfps and provides 180 output frames of 10 bit grey level encoding with an overall relatively low power consumption and constant pixel count of 0.7 Mpix. In the following the sensor architecture and design will be briefly introduced. Then, some of the characteristics on the camera image quality and noise will be shown with mainly focusing on the camera temporal noise since it is the main source of uncertainty that impacts the measurement of field kinematics such as accelerations.

6.2.1.1 The Kirana sensor

Designing the CCD array in a CMOS image sensor is a challenge, one of which is the charge transfer efficiency (CTE) [Crooks et al., 2013a]. In the Kirana sensor, this was to some extent tackled by constructing closely packed gates that reduce the diffusion of the charge and buried channels as to avoid charge traps in the silicon oxide interface that can result in image ghosting. In order to reach frame rates up-to 5 Mfps, the exposure of the photosensitive area has to be as low as 200 ns. This means that the transfer time from the diode to the memory bank has to be very short. Due to adopting a photo-diode design that ensures full charge transfer in less than 100 ns, the diode space is very limited with respect to the total pixels size. The pixel domain size, including the memory, is of 30 μm and the diode occupies an area of 28 μm in the horizontal direction and 5 μm in the vertical direction.

This means that the fill factor in the horizontal direction is more than 90% but only 16% in vertical direction. The Kirana sensor is a front illuminated sensor. The layout of one pixel domain and a photograph of a sensor mounted on the printed circuit board is shown in Figure 6.1. It can be seen that the pixel diodes are very closely packed which results in an overlap between the memory bank area of one pixel domain (PD_i) with the area occupied by the photo-diode of the adjacent pixel (PD_{i+1}). A detailed representation of the entire Kirana sensor with its operation can be found in [Crooks et al., 2013a].

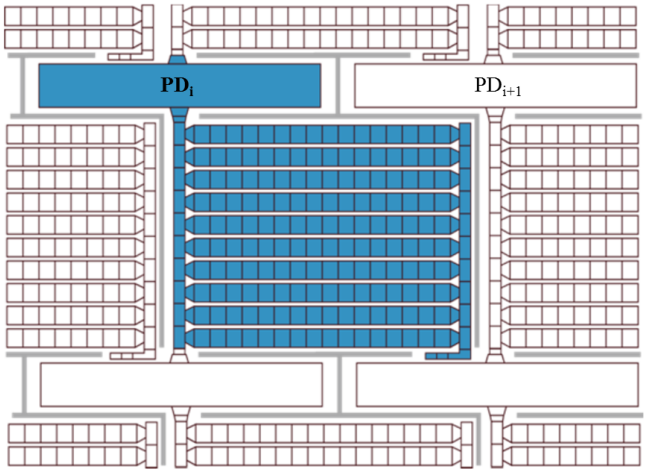

(a) Layout of a single Kirana pixel (highlighted) within a regular pixel array [Crooks et al., 2013b].

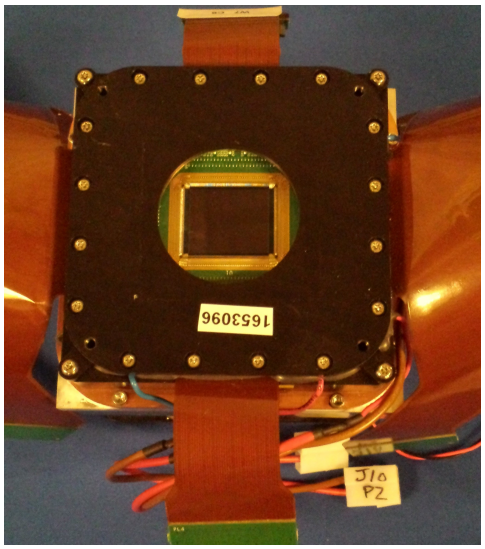

(b) Photograph of the Kirana sensor mounted on the circuit board with the read out connections and CCD drives.

Figure 6.1: Layout of the Kirana sensor and picture of the mounted sensor on the circuit board.

Pixel architecture A single pixel block diagram is presented in Figure 6.2 where the numbering schematic of frame storing is presented. As detailed in [Crooks et al., 2013a], one pixel domain consists of i) a fully pinned diode (PD), ii) the PD to CCD memory bank (MB) transfer structure (vertical entry), iii) the two dimensional MB, iv) the MB to pixel readout structure (vertical exit) and v) the pixel read out. The memory is organised in a two dimensional array with a serial-parallel-serial operating stage, a concept first proposed in [Kosonocky et al., 1996], but for a CCD based UHS camera. The CCD MB is composed of 180 memories divided into one sequence of 10 vertical entry (VEN) cells, 16 lateral registers (LAT) and one vertical exit register(VEX) consisting of 10 cells, in total constructing an array of 18x10. The MB works in three stages. First, the integrated charge is read through a single electrode and distributed in VEN bank. Once it is filled, a lateral buffer electrode (BUF_EN) shifts the charge into the LAT registers. Similarly one (BUF_EX) is connecting the lateral registered with the vertical exit bank (VEX). Once all the cells are filled, the sequence is read out through a single electrode (PGEX) into the pixel read out circuit (FD).

Pinned Photodiode and light shielding As mentioned the photodiode is 28x5 μm in size and constructed in a graded way as to enhance the charge collection. The diode is also surrounded with a guard ring which intends to prevent the excessive electronic charge, which is not collected by the PD, to be collected by the MB. Furthermore, a perforated light shield is constructed to protect the entire pixel domain exposing only the photo sensitive area to the incoming illumination (Figure 6.3). Another, recent innovation is the use of specific micro lens that minimises light scattering and concentrates all the light only on the photosensitive area resulting in minimization of the light that arrives at falls on the shielded MB and increases the effective fill factor [Taylor et al., 2017]. However, the microlense technology is still in prototype stage and the sensor used in the following does not contain this enhancement.

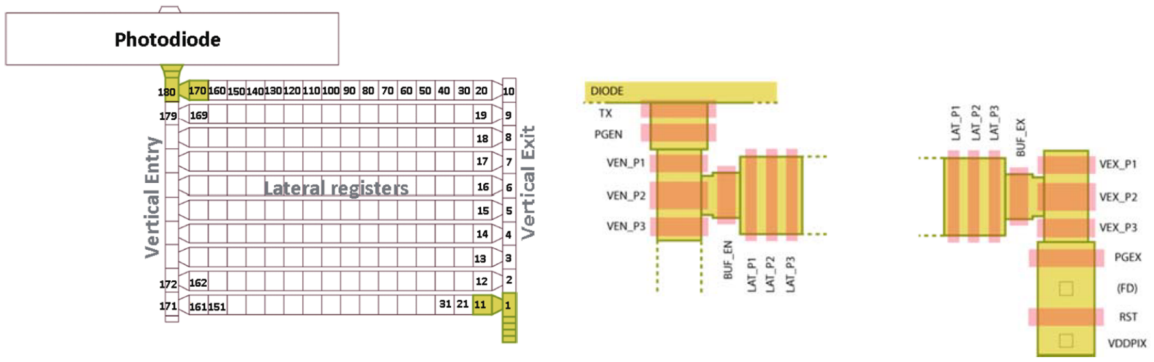

(a) Layout of a pixel with numering schema of the frame acqusition [Taylor et al., 2017].

(b) The layouts of the VEN to LAT and LAT to VEX transfer structures in a Kirana memory bank [Crooks et al., 2013a].

Figure 6.2: Three phase acquisition and operation of the Kirana memory bank for a single pixel domain.

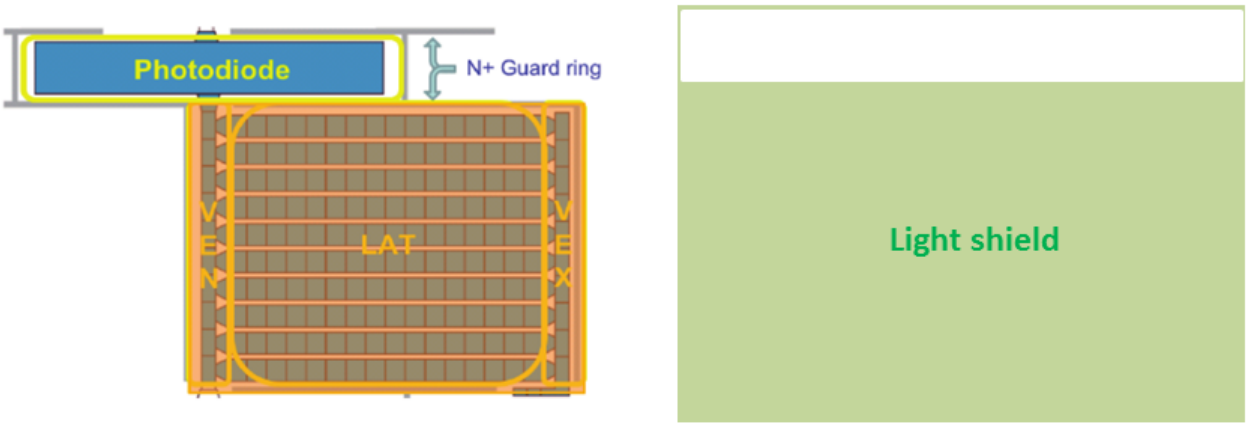

Figure 6.3: Design of the diode with the details of the light shielding and the guard ring.

6.2.1.2 Black image acquisition

Even in the absence of light arriving to the photo-detector, thermally generated electrons can be collected in the sensor producing a measured signal which is usually referred to as the dark current noise. Dark current can be, in principle, reduced by properly cooling the device down, but often there exists a certain amount of this type of noise even at the optimal working temperature and as such cannot be completely avoided. Furthermore, the dark current can vary from pixel to pixel, producing also a fixed pattern spatial noise or the dark signal non-uniformity. This noise depends on the sensor architecture and technology, being mainly induced by the way how pixel charge is red out from the pixel array.

Therefore first tests were conducted in order to investigate the presence of the black current noise, since as previously shown in Section 6.3.2, it can provide some first estimates on the sensor behaviour. This was conducted by completely covering the camera objective. In that case, during the acquisition sequence, the camera diaphragm opens for a given exposure time but no light source is present that may trigger the photo sensitive fill dedicated to the pixel space. Several acquisitions have been made at various recording speeds (5 Mfps,2 Mfps,1 Mfps,0.5 Mfps).

Furthermore, several exposure times have been used per acquisition set. The average frame grey level over acquired image sequence, for different frame rates and exposure times are presented in Figure 6.4a. The first observation is that the dark current noise is very small compared to the camera dynamic range (being just about several grey levels). However, a typical fluctuation can be observed regardless of the used frame rate. Temporal black noise, which manifests as a constant decrease of charge over a span of ten frames can be influenced by the fact that each acquired frame is consequently pushed down in the vertical entry, loosing some charge during the process. This could be caused by the charge traps. Once the vertical array is filled, the charges are then shifted and the jump is noted which inherits the same trend in the following frames. For acquisition speed up to 2 Mfps, the tendency is fairly similar while for 5 Mfps a higher deviation is observed during first 21 frames of the sequence. The exact reason for this is unknown. Finally, it should be noted that the dedicated software supplied with the acquisition system allows automatic correction of the back current noise through the option *session black* and the result is shown in Figure 6.4b.

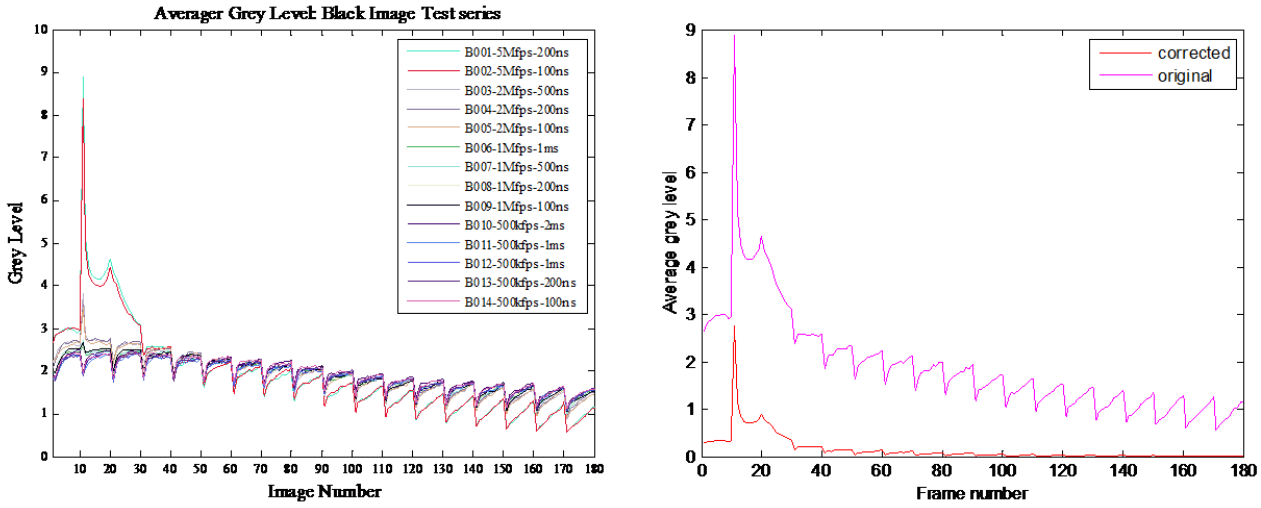

(a) Dark current noise over various range of rame rate and exposure time.

(b) Example of a corrected black scene acquisition at 5 Mfps.

Figure 6.4: Results of the black acquisition test over various frame rates of the Kirana camera.

6.2.1.3 Parasitic light effect (PLS)

The parasitic light effect can be defined as a fraction of signal that is measured in the memory bank other than the associated photo-diode. There are two main reasons that influence the appearance of PLS. First one is the optical cross-talk which comes from excessive light being absorbed by the memory bank. Second one is the electrical cross-talk where excessive charge is being trapped in the silicon and then collected by the memory [Taylor et al., 2017].

Evidence of optical cross-talk As already shown in the Figure 6.1 the pixel domains are tightly packed on the Kirana chip and memory area of one pixel domain overlaps with the area of a photo-diode of its adjacent neighbours. Ideally, the memory bank should not be sensitive to the light charge coming from another pixel once the shutter is closed due to the light shielding. However, this is not always the case and the memory banks, especially those close to the vertical entry (VEN) and vertical exit (VEX), are influenced by the parasitic charge. An example is provided in Figure 6.5. It represents an average frame grey level for several acquisitions sequences of a blank scene filmed using a Kirana camera. The scene was illuminated under constant illumination source. It can be easily observed that the PLS is affecting the first and the last 60 frames of the acquisition sequence which exhibit a peculiar over exposure. It was observed that this over exposure can be of more than 50% than the expected mean grey level in cases when more light is reaching the sensor, such for instance when a prime lens is used.

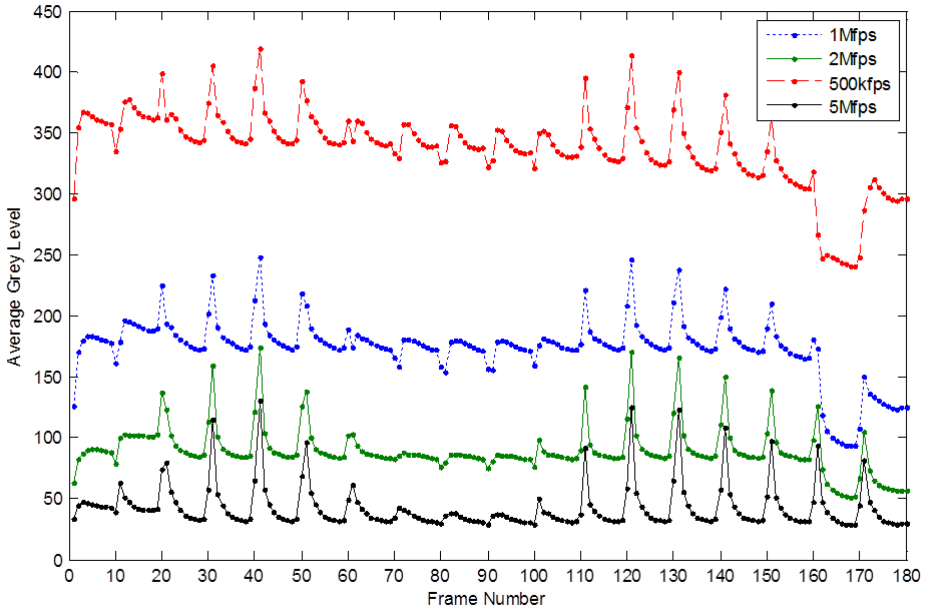

Figure 6.5: Effect of the Parasitic Light Effect (PLS) affecting the first and last 50 frames of the Kirana sequence. (case of mechanical shutter)

In order to reduce this effect the later version of the sensor was equipped with a improved metal shielding system with protective barriers located below the shield (orange structure in Figure 6.3). Additionally, a blue filter was added over the memory to provide additional prevention.

Evidence of temperature influence Even with the enhanced shielding system, some additional parasitic effects can be experienced. It was noticed that when continuous illumination sources that generate excessive heating are used, the sensor again exhibits the over exposure effect but without a global evidence of optical cross-talk. The Figure 6.6a shows average frame grey level obtained from two acquisition sequences captured at 2 Mfps. A blank scene was illuminated with two Dedo-Lights (DLH400DT 400/575W) set to spot focus and boost mode. It can be seen that the each 10 frames there is a strong over exposure and that the entire sequence does not stabilise throughout the acquisition process. This problem was addressed in 2016 Kirana edition by introducing a fast LCD shutter. However, the fast shutter reduces the light sensitivity for 2.5 stops. This can be solved by using instantaneous flash lamps to illuminate the scene (SI-AD 500 from Specialised Imaging) (Figure 6.6b). Further refinement regarding increased light detection was suggested in 2017 through the use of microlenses as a perspective [Taylor et al., 2017].

6.2.1.4 Evidence of temporal noise

In the previous subsection it was shown that the Kirana camera is based on a complex hybrid sensor technology that merges the CCD and the CMOS architecture into one single operating system. As such, it exhibits various unique noise structures that result in acquisition sequence instability and which are not easily tackled. One of the main issues appears to be the temporal grey level frequency content of the acquired sequence which seems to be higher than in other UHS systems. A comparison of average sequence grey level between two UHS systems that are based on different chip technologies, namely HPV-X2 and the Kirana camera, is shown if Figure 6.7. The average frame grey level is normalised to the camera bit depth. It can be observed that the temporal fluctuation

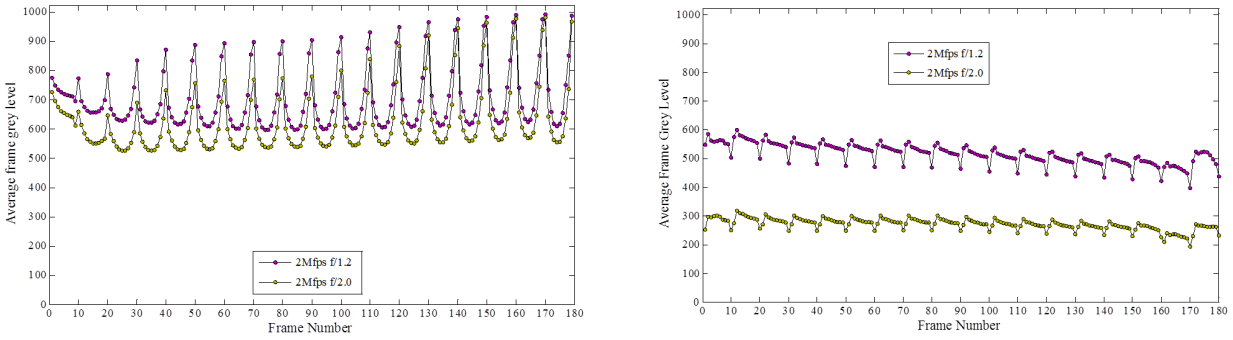

(a) Acquisitions with continuous illumination.

(b) Acquisition with instantaneous Flash illumination.

Figure 6.6: Effect of continuous hot light source on the Kirana sensor.

in case of the Kirana camera is substantially higher than in HPV-X2. The dips and peaks that can be observed seem to depend on the frame register location in the memory bank. The frames that correspond to the top two rows registers exhibit an over exposure while the frames on the bottom two rows registers, which are close to the pixel drain, exhibit an under exposure (see Figure 6.2a).

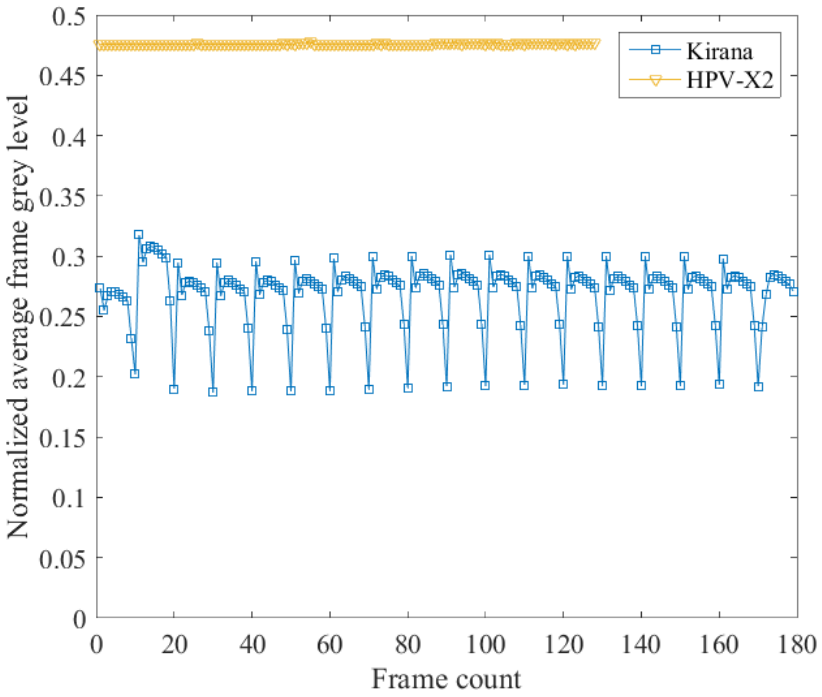

Figure 6.7: Comparison between two UHS cameras: The Shimadzu HPV-X2 and the Kirana camera. (Blank scene test filmed with 2 Mfps speed)

Despite the enhancements made on the shielding system, on a pixel level it was still observed that one pixel was affected by its surrounding neighbours. Therefore, it was decided to correct the affected frames by introducing a global linear interpolation between the non-affected frames to recreate the frames affected by the temporal noise. An example of the correction is presented for filming a heterogeneous speckle surface in Figure 6.8. Although the affected frames seem to be removed, it can be still observed that there exists a certain frequency content in the

treated image sequence. The frames which are located in the middle of each captured vertical entry in the memory bank, seem to continuously loose in mean gray level. This could be influenced by the sequenced three-stage operation of the two dimensional memory array. Indeed, it seems that the registered frames loose illumination until the vertical array is filled. Then, a shift is performed towards the lateral memory cells and the cycle starts again. This effect could be influenced by the fact that some charge diffusion occurs between the cell-to-cell transfer.

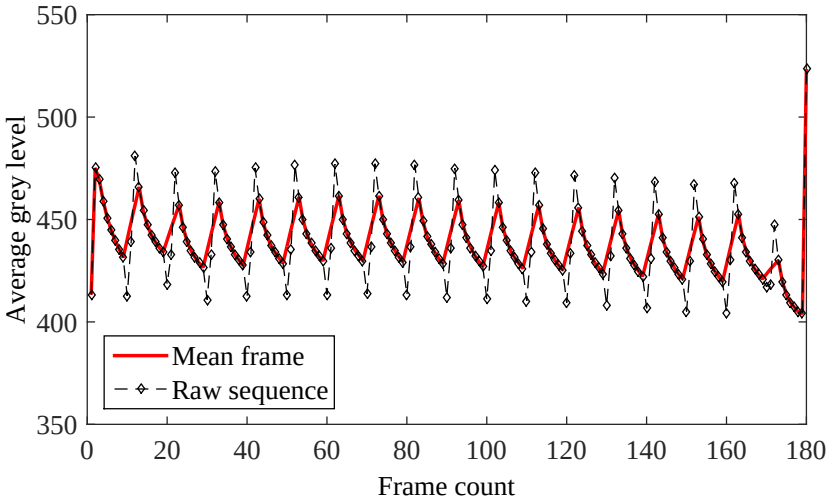

Figure 6.8: Example of correction of the frames affected by the temporal flickering effect.

A simple numerical demonstration of the effect of the high frequency noise on the derivation of the acceleration fields is shown in Annex C.2. The bottom line is to show that when image sequence is affected by such temporal noise, it is the noise frequency that pollutes the acceleration fields and not the amplitude. Finally, a simple approximative technique of smoothing the noise polluted acceleration fields by utilizing penalised least square method, also frequently referred to as smoothing spline method, is demonstrated in Annex C.

6.2.2 Spalling test with an aluminium sample – Preliminary study

6.2.2.1 Experimental set-up

In order to investigate the metrological performance of the Kirana camera in obtaining the full-field kinematic measurements such as displacement and acceleration maps, a spalling test was carried out on an aluminium alloy. The aluminium sample and the experimental set-up alongside all the measurement systems is the same as the one presented in Section 6.3.2.1. The only difference is that the sample surface had to be illuminated with two flash sources with high illumination power since the Kirana camera used contained the LCD shutter which reduced the amount of light that is reaching the sensor. This was done in order to reduce the parasitic light effects as low as possible which originate from the sensor architecture as detailed in Section 6.2.1. The flash lights were positioned to the observed gridded surface of the specimen. The flash light sources used consisted of two SI-AD500 from Specilised Imaging. In order to avoid occasional local image saturations that may occur when framing the girded surface as well as to obtain as homogeneous lightning as possible a translucent low-opacity paper can be added in front of the flash lights (Figure 6.9). The flash light duration is 2 milliseconds with about 50 microseconds rising time. In order to acquire high quality images and to make use of the entire acquired image sequence of the camera, the images need to be garbed during the full flash intensity and the camera should be triggered at the instant when this is satisfied. Therefore, it was necessary to trigger the flash with a secondary independent triggering system. The triggering of the flash lights was chosen to be during the impact of the projectile against the Hopkinson bar. In that way, when the incident wave reaches the sample, the light capacity would be at full power. For this, two pieces of thin copper film were bonded on the impact surface of the Hopkinson bar and connected to the wiring

system that leads to the flash power supply. When the launched projectile impacts the bar surface, it contacts both pieces of glued film which creating a short circuit that eventually triggers the flash lights.

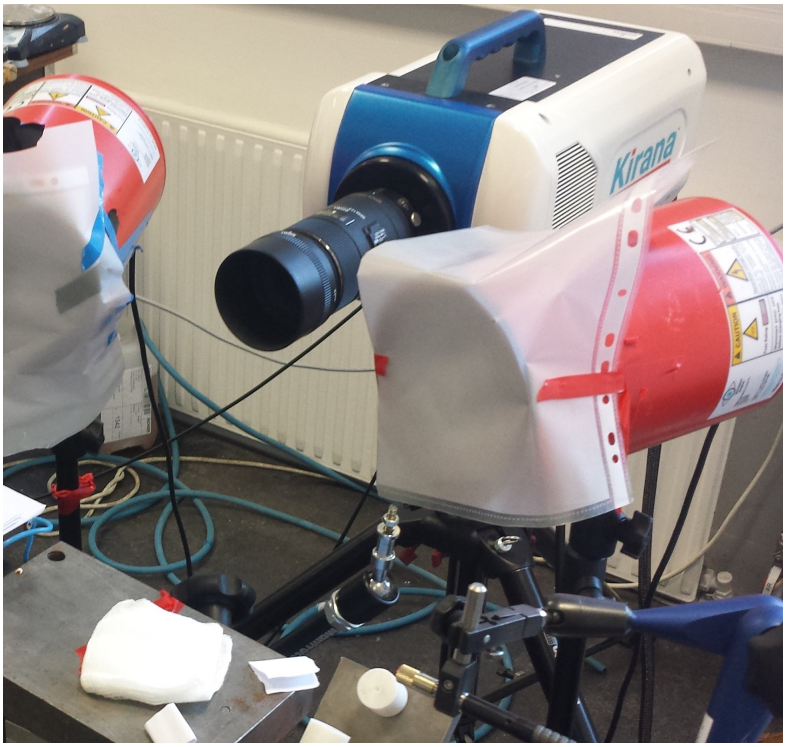

Figure 6.9: The Kirana camera and the flash lights used for spalling aluminium set-up.

6.2.2.2 Identification of the linear elastic response

Here, one reference test conducted on the aluminium sample will be shortly presented, SPF-ALU04. Thanks to the camera high pixel count, the 1 mm pitch grid on the sample surface was sampled with 15 pixels per grid period. It is necessary to mention that thanks to very large pixel count of the Kirana camera such large grid pitch sampling is possible. The acquisition speed was set to 2 Mfps since it is considered as an optimal speed for capturing both the compressive and tensile loading stage. The camera was mounted with a 105 mm Sigma Macro lens. The acquired sequence consisted of 180 images of 10 bit dynamic range. Before processing the acquired image sequence the frames that exhibit the peculiar over and under exposure were removed by performing direct image interpolation. Then the corrected sequence was processed with the grid method to obtain full field displacement data. As it has been already mentioned, even after removing the faulty frames from the image sequence, the entire image grey level exhibits a certain frequency oscillation which will propagate to the displacement maps and then corrupt the derived acceleration fields. This problem is difficult to tackle and filtering techniques need to be used in order to obtain exploitable values of accelerations. As noted by some authors, one posible way is to perform a Butterworth filter directly on the obtained displacement fields with a certain frequency cut-off [Davis et al., 2017, Dreuilhe et al., 2017]. In this way, the high frequency content is largely removed from the measured displacements. While this procedure can be considered applicable when the expected mechanical response is to be perfectly elastic, when dealing with brittle materials, the fracturing information can also be included in the high frequency content of the displacement fields and any such signal filtering approach may remove this information from the measured signal. For this reason a simple smoothing technique, presented in Annex C, that is based on fitting the smoothing spline onto the entire data set of the displacement maps, was adopted. When the fitting is performed, the derivation is straightforward from the coefficients of the fitted polynomials. What needs to be mentioned is that since it approximates the entire range of data, the spline fitting is much faster than the local SG filter since it does not require nested loops.

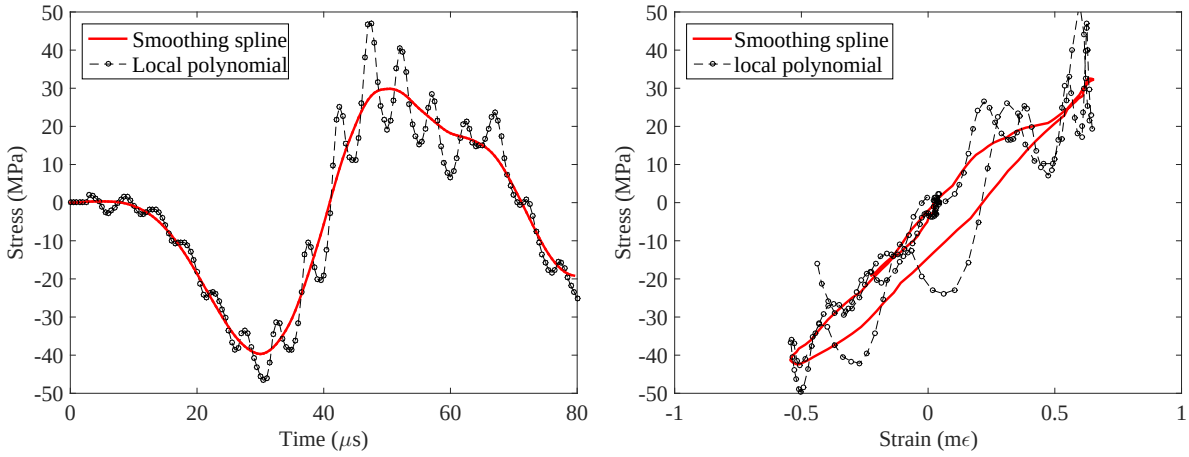

(a) Results of derived stress response at 40 mm from free-end.

(b) Reconstructed stress-strain response at 40 mm from free-end.

Figure 6.10: Results on the identified material response in case of using a the Kirana camera to retrieve elastic response of an aluminium alloy during a spalling experiment (SPF ALU04).

The obtained displacement fields were treated with both filtering techniques used to derive the acceleration fields for comparisons. Diffuse approach was used with 8 point displacement span for obtaining the strain fields differentiation. In one case, a local 2^{nd} degree polynomial reconstruction of acceleration over 13 temporal displacement points was used. In the second case, global smoothing spline filtering was applied using the previously identified smoothing coefficient. Results of the identified material response are presented in terms of virtual gauge at 40 mm from sample free end with 20 point spatial smoothing in Figure 6.10. The plots clearly demonstrate the benefit of using the smoothing spline as a tool for deriving acceleration fields as opposed to standard low-degree polynomial fitting. For the case when the latter is used, as depicted in Figure 6.10a, the high frequency content does not get filtered out and the standard deviation in measured stress can go as high as few tens of MPa. The identified Young's modulus obtained from performing linear regression on the reconstructed stress-strain curves is 66.04 GPa for the case of smoothing spline and 68.19 GPa for the case of the local polynomial fit which is reasonable close to the reference 72 GPa. According to this preliminary study, as it can be seen in the Figure 6.10a, the identified stress response can vary for several tens of MPa in case when polynomial fit is used to derive the acceleration measurements. This result can be regarded as severely impacted by camera temporal noise especially when compared to previous camera results obtained with similar processing settings (*e.g.* Figure 3.5b). For this reason, the sensor was not (yet) applied to testing concrete material as the anticipated material strength lies too close to the camera noise floor.

6.2.3 Perspectives

As it can be concluded from the previous two subsections, the Kirana camera is a imaging system which is based on a merger between the CCD and the CMOS technology and has been under development throughout this work. Due to its technology, it suffers from complex noise sources that need specific processing developments to limit these effects. One distinct draw back of the sensor is the high frequency content that is present in the acquired sequences and seems to be influenced by how the pixel memory bank operates. On one hand, this high frequency noise is barely observable in the measured displacement fields, and together with the large pixel count, this makes the sensor useful for situations when displacement data are needed, for example in case of propagating dynamic cracks in concrete material [Chen and Osovski, 2018]. On the other hand, in case of acceleration measurements, the noise is augmented by the double temporal derivation, often to such extent that the acceleration fields cannot be exploited for material identification unless specific smoothing techniques are employed.

For this reason, the investigation of the general metrological performance of the latest version of the sensor, is a strong perspective. A detailed experimental benchmark should be conducted by performing both controlled tests such as rigid body and uniaxial strain tests as well as dynamic tensile test such as spalling of aluminium alloy, in order to investigate the sensor metrological performance over wide range of frame rates. Only when the noise sources that are intrinsic for this sensor are well understood, a correction procedure can be proposed to reduce the image high frequency content and correct the affected frames in a more meaningful manner.

6.3 The Shimadzu HPV-X2 experimental campaign

In this section several spalling experiments that were performed with the second generation of a FTCMOS2 ultra-high speed camera, the Shimadzu HPV-X2, will be presented. The experimental campaign has been performed in the Laboratory-3SR in Grenoble in the period between 30 June and 05 July 2017 and the acquisition system used was provided by LMT Laboratory, ENS Paris-Saclay. The grid-instrumented sample surface was recorded during the test to extract the time resolved displacement fields which are then processed using the VFM as to finally obtain the material constitutive response. However, first, some information on the characteristics of the acquisition system and intrinsic noise will be given. The aim of the section is to provide first results regarding the application of such CMOS based UHS sensor in identifying material constitutive response in the spalling test and measuring the acceleration data.

The structure of this section is organised into three parts:

- First part 6.3.1 provides some principal information regarding the sensor architecture and some first attempts to investigate its intrinsic noise structures such as spatial and temporal noise.
- Second part 6.3.2 summarizes a short series of tests conducted on an aluminium alloy in light of identifying an elastic material response. The test were performed on the same benchmark sample as in Section 3.3, but at elevated frame rate and grid pixel sampling, having higher number of useful frames.
- Third part 6.3.3 shows first result regarding the spalling of ordinary concrete material using the acceleration fields derived from the squired images. The data have been compared with the point-wise measurements and the effect of the processing parameters has been explored.

6.3.1 On the sensor characteristics and performance of the FTCMOS sensor

The CCD cameras based on the *in situ* storage technology (ISIS-CCD) have shown a great ability of reaching ultra-high acquisition speed (*e.g.* Shimadzu HPV-1 maximum frame rate is 1 Mfps). However, there are certain technological limitations inherit to these types of systems which present major obstacles for their further advancement in the domain of acquisition speed and increased pixel count.

First, the main shortcoming of these sensors is in fact the use of the on board memory. On one hand, the on board memory allows the pixel charge to be transferred and stored in the vicinity of the photo-diode, reducing the storage time together with any possible charge drainage that results in an increased acquisition stability. On the other hand, it occupies a lot of physical space dedicated to one pixel, enforcing a reduced photo-active pixel area which leads to low fill factor. Moreover, the low fill factor is often different in horizontal and vertical direction (e.g Shimadzu HPV-1 14% horizontal and 76% in vertical direction [Reu, 2011a]), and depends on the arrangement of the memory bank and wiring. This altogether can produce image aliasing especially in cases of high frequency grey level content (such is when framing a grid image) [Rossi et al., 2014]. An adaptation based on merging two such sensors has been proposed in the 4^{th} generation of this camera, which aside of providing an increased pixel and frame count, also proposed the use of an on-chip micro lens which increases the fill factor upto 50% [Etoh et al.,

2003]. However, the maximum frame rate remained unchanged and the sensor did not reach a wide commercial use. This leads to the second disadvantage, which is a limited frame rate influenced by the high power consumption. The power used to drive the CCD can be considered proportional to the recording speed and induces great amount of heat which can potentially damage the sensor and pollute the image sequence. Finally, in the ISIS-CCD sensor technology, the exposure times depend on the imaging speed and it does not allow setting a short exposure time [Kondo et al., 2013], which potentially blurs the image and can introduce uncertainty in the measured displacement fields [Zappa et al., 2014].

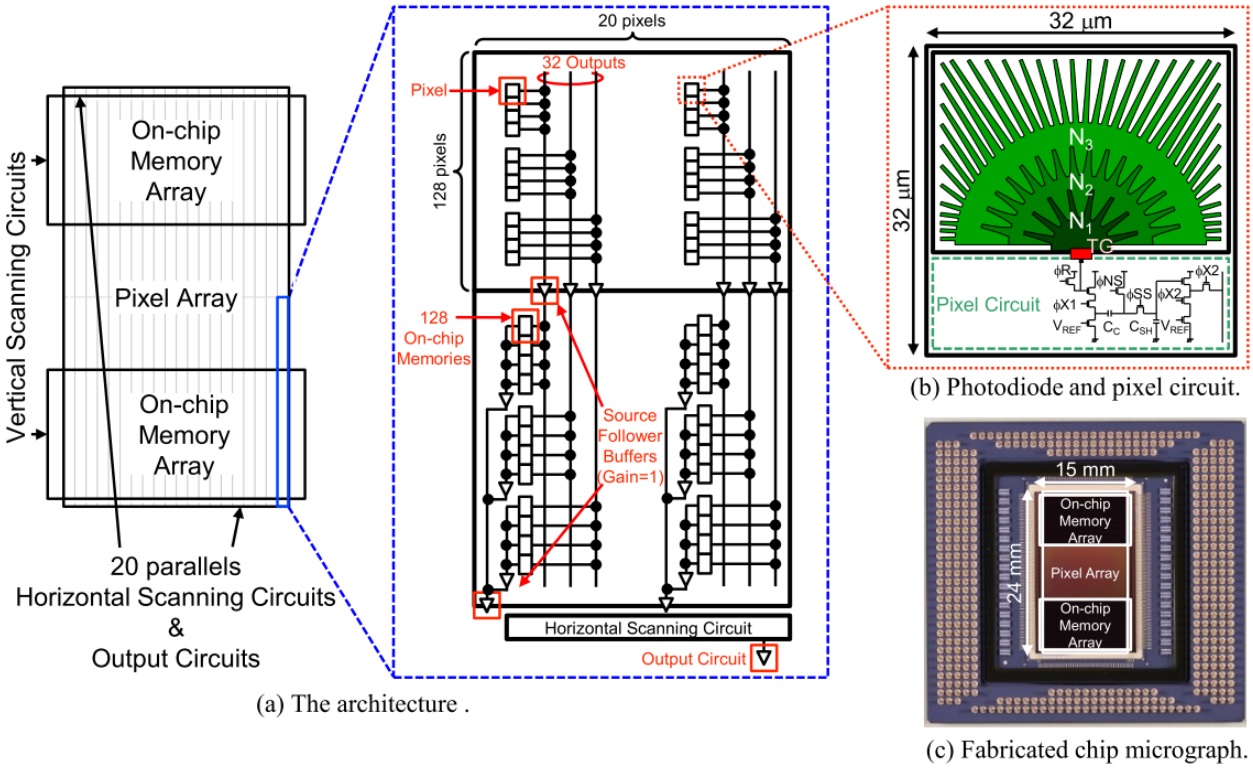

(a) The architecture .

(b) Photodiode and pixel circuit.

(c) Fabricated chip micrograph.

Figure 6.11: Block diagram and schematic representation of the FTCMOS2 image sensor and one parallel unit from pixel to output [Sugawa et al., 2016].

6.3.1.1 The Shimadzu HPV-X2 sensor

In order to overcomeabove mentioned limitations, an alternative burst type sensor was proposed which is based on CMOS image sensor technology – FTCMOS [Tochigi et al., 2013]. The main motivation for turning to CMOS was the low power consumption. The Shimadzu HPV-X is the representative of this technology [Kondo et al., 2013], later on followed by its successor, the Shimadzu HPV-X2 based the FTCMOS2 second generation. Although the sensor architecture is the same, the main difference between the two is an eight times higher light sensitivity of the latter due to increased fill factor and incresed signal readout gain [Sugawa et al., 2016]. A typical sensor arrangement of the FTCMOS2 is shown through a block diagram in Figure 6.11. The sensor arrangement consists of two memory arrays that are separated by the pixel domain with total 400x256 pixel count (Figure 6.11a). This unique design allows shielding each memory region completely with one unique cover which substantially reduces signal leakage (Figure 6.12). Each pixel has **128** on-chip memories that are connected with a wire in a one-to-one manner. In order to reach high read-out speeds, a parallel unit with 32 outputs is introduced to achieve a fast parallel transfer. In each output wire 4 pixel signals are read at the same time which allows reading 128 pixels per unit. In this way, a group of 20x128 pixels are read through the output circuit simultaneously over a horizontal range of 20 outputs, assembling a total of 400x128 pixels per one memory bank. Having the formed image being read in two halves, the two memories result in a 400x256 pixel outputs of for each frame and provide a final image

of **400x250** effective pixels, since the extra pixels are used as dark ones. The fabricated sensor size is 24x15 mm (Figure 6.11c). The entire dedicated pixel area is 32 μm^2 with a pinned photodiode size of 30x21.34 μm^2 which leads to an improved effective fill factor than in its predecessor HPV-X (reported fill factor for HPV-X is 37% [Tochigi et al., 2013]). Thanks to the use of the CMOS technology, it is possible to set any exposure time starting from 20 ns in frame rates upto 2 Mfps, however, for 5 Mfps the exposure times are fixed to 110 ns. This short exposure times allow reducing the image blur to a minimum. It is worth mentioning that the camera provides two types of recording modes. One is the full pixel mode (FP) with 100 kpix frame size and the maximum frame rate of 5 Mfps. The second is the half-pixel mode (HP) where due to speed priority the number of signal outputs is reduced by half, storing only two pixels per output wire, resulting in a checkerboard pattern readout. Although only half pixels are physically read out, the registered frame outputs are interpolated to full size during the post-processing. This mode allows reaching a maximum of 10 Mfps with a 256 frame outputs under a fixed exposure time of 50 ns. For both modes, the images encode a **10bit** grey level dynamic range. However, the outputs are rescaled to either 8 bit or 16 bit tagged image file (.tif), depending on the user choice.

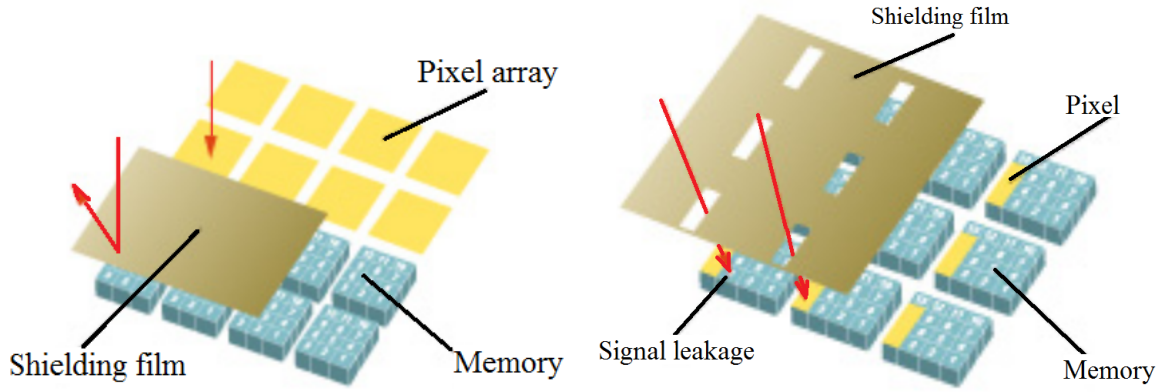

(a) FTCMOS burst image sensor memory shielding. (b) Conventional CCD image sensor memory shielding.

Figure 6.12: Shielding strategies of UHS imaging sensors [Shimadzu CO., 2017].

However, there exists no study dealing with the investigation of the detailed metrological performance of this sensor, such is for example provided for the ISIS-CCD Shimadzu HPV-1 in [Rossi et al., 2014]. It is obvious that the FTCMOS represents one new and complex ultra-high speed imaging systems, whit a specific sensor architecture on which the quality of the output data is dependant. For this reason, it is necessary to investigate how the imaging sensor would metrologically perform in real experimental conditions prior to performing quantitative photographic measurements. Moreover, limited information is available on the measurement resolution and measurement noise for given experimental conditions. Some information can be found for the HPV-X camera suggesting that standard deviation of measured displacement was about 0.17% of grid pitch (resulting in about 1 μm displacement) when the grid method is used, which was provided in [Zhu, 2015]. However, information is also needed for the HPV-X2 since it is reaching a much wider commercial use thanks to its better light sensitivity which allows the use of conventional continuous light sources (as opposed to instantaneous flash lights which are difficult to synchronize). In order to provide first information on the noise characteristics of the sensor used in this work (HPV-X2), several acquisitions have been performed prior the application to a material identification in a spalling test. First, black images were taken completely covering the lens in order to investigate the presence of the dark current noise. Second, the blank scene was filmed at 1 Mfps and 2 Mfps in order to provide first estimates of the spatial and temporal grey level pixel noise.

6.3.1.2 Black image acquisition

In order to inspect the level of dark current noise in the camera sensor, several acquisitions have been made having the camera lens completely covered. In that case, during the acquisition sequence, the camera diaphragm opens

for a given exposure time but no light reaches the photo sensitive fill. In an ideal camera, the recorded grey level value would be equal to zero at each pixel, but due to both spatial and temporal dark noise that is produced by image sensor this is not the case. The average frame grey level of the image sequences obtained from the black image acquisitions at 1 Mfps and 2 Mfps recording speed are presented in Figure 6.13a. From the presented plot it can be observed that the temporal evolution of the average frame dark noise changes for two acquisition speeds and is about 10% of the dynamic range. Map of standard deviation in grey levels is illustrated in Figure 6.13b. It can be noted that pixels closer to the left side of the sensor exhibit a slightly higher standard deviation compared to those on the right-hand side. Finally, from the presented results it can be concluded that the standard deviation of the dark noise is quite low (about 0.9% of the dynamic range) which can considered acceptable.

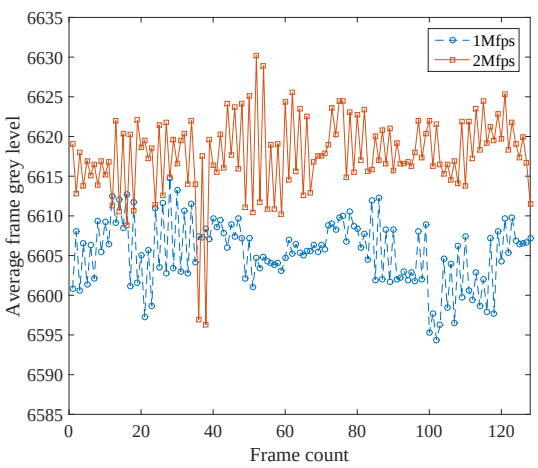

(a) Average frame grey level during the black image acquisition (dark current noise).

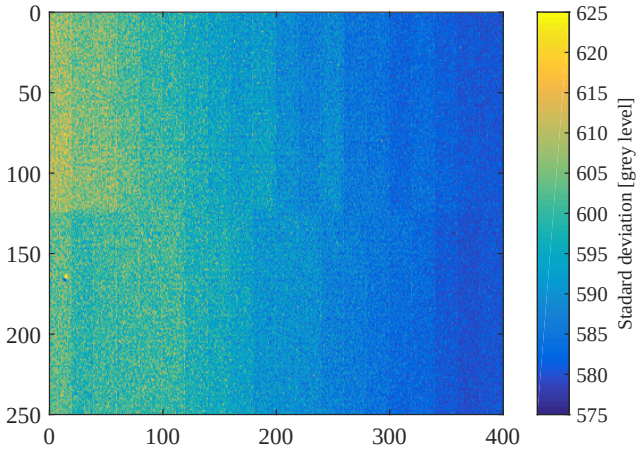

(b) Standard deviation map of grey levels for the black image acquisition at 2 Mfps.(dark current non-uniformity)

Figure 6.13: Inspection of the dark current noise in the Shimadzu HPV-X2 sensor (analysis of 16 bit image outputs).

6.3.1.3 Blank scene acquisition

In order to investigate the performance of the camera in recording images at different frame rates, several acquisitions have been made using a blank target. The exposure time was set to the value of 200 ns and 1 Mfps and 2 Mfps camera speeds were used to film a white paper illuminated with two DedoCool light sources, keeping the illumination conditions the same in both situations. The average frame grey level of the two acquisitions is given in the Figure 6.14a. Although the acquisitions were performed at the same illumination conditions, already it can be seen that the time fluctuation does not exhibit the same trend for the two recorded sequences. Figure 6.14c presents the percentual variation of average grey level with the respect to the overall mean grey level of the entire sequence for each recorded frame, this can be regarded as the global temporal noise of the sensor. It can be observed from the two plots that the temporal noise appears to be random which could be due to the fact that 4 pixel signals are read through the same wire which later on places each signal in a separate pixel memory domain. Once the pixel signals are in the parallel unit, it is difficult to say whether charge will be (or not) mixed in between them. On the other hand the temporal variation of the overall mean frame grey level seems to be in the limits of $\pm 0.3\%$. Moreover, contrary to the Shimadzu HPV-1 (see for example: Figure 3.9c), there appears to be no extreme frames exhibiting peculiar exposure effects, suggesting that all frames can be used from one recorded sequence (as opposed to HPV1 where only frames between 13th and 90th image can be used). The Figure 6.14b presents the pixel standard deviation given as percentage of average grey level for each pixel. From the plot it can be seen that the noise appears to be fairly constant and linear, exhibiting a value of about 9% with respect to the mean pixel grey level which is a few percent larger than in the post-treated image sequence of a HPV-1 camera (Figure 3.3c). Furthermore, all pixels seem to exhibit the same trend indicating no presence of defective pixels in the sensor.

It is necessary to mention that the presented treatment graphs concern the 16 bit image outputs, however the same trends are obtained when the 8 bit outputs are treated. Since simulated experiments and synthetic imaging have shown that higher dynamic range can provide slight improvement of the identification of the material elastic response, from now on, only 16 bit outputs have been considered (keeping in mind that they are just upscale from 10 bit encoded data). On the other hand, it is interesting to mention that the noise level value obtained in the same way regarding the Shimadzu HPV-X is reported to be 3.5% [Seghir and Pierron, 2017].

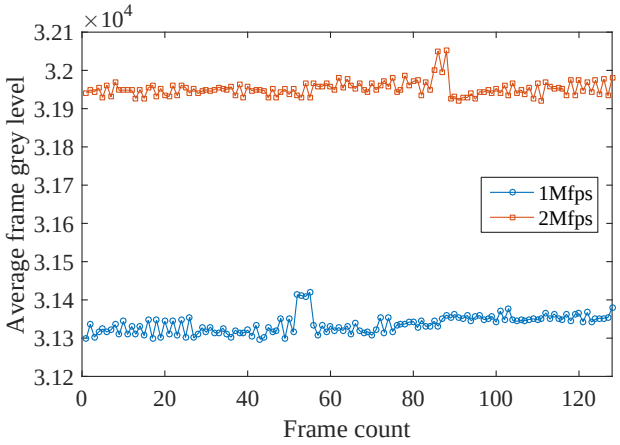

(a) Average frame grey level during recording of a blank scene with 1 Mfps and 2 Mfps acquisition speed.

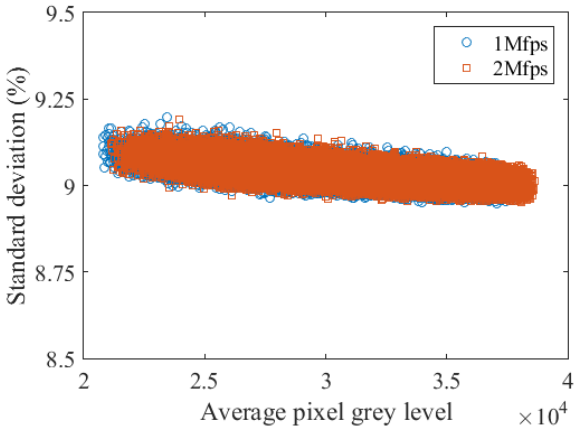

(b) Standard deviation of grey level computed for each pixel over entire image sequences with same levels of light and two frame rates.

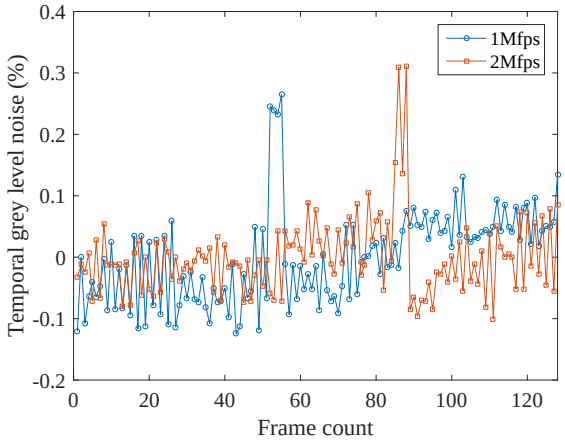

(c) Temporal grey level noise during recording of a blank scene with 1 Mfps and 2 Mfps acquisition speed.

Figure 6.14: Results from imaging a blank screen with Shimadzu HPV-X2 (analysis of 16 bit image outputs).

6.3.2 Spalling Aluminium – Experimental benchmark

In the following, the focus is on investigating the metrological performance of the Shimadzu HPV-X2 acquisition system in real experimental conditions applied to a spalling test. This is investigated through preforming several spalling aluminium test. The aluminium sample is instrumented both with point-wise measurements (*i.e.* strain gauges, laser interferometer) and a 1 mm pitch grid for measuring full-field in plane displacement maps. Comparing the measurements obtained from these two, allows validating the processing of full-field measurements given a set of processing parameters.

The outline of the following section is as follows:

- First, the experimental rig is introduced with details on the data acquisition systems and sample instrumentation.
- Second, still sample acquisitions have been made in order to investigate the uncertainty measurement of the displacement fields.
- Finally, two reference tests are chosen to present the results on the identification of the material elastic response where the full-field measurement are compared to the point-wise ones.

6.3.2.1 Experimental set-up and instrumentation

Several spalling experiments have been performed on aluminium alloy with the spalling experimental set-up. As already mentioned, the geometry of the sample was optimized in order to contain a flatten surface (140x24 mm) which will be recorded with the ultra-high speed camera. Due to limit pixel count of the camera, only a part of the surface can be visualized depending on the desired grid pitch pixel sampling. The specimen surface is instrumented with a 1 mm pitch grid in order to obtain full-field displacement measurements at each recorded instance by the camera. The grid sampling was set to 7 pixels per pitch, providing a region of interest of 24x57 mm from the sample free-end.

One of the things that requires paying considerable attention to, is the camera positioning and proper grid pixel sampling with respect to camera pixel count. The camera needs to be positioned in such a way that its sensor is completely parallel to the recorded surface in order for the image to encode equispaced grid pitch pixel sampling. If not properly placed, the camera will record a spatially non-equal grid sampling which introduces parasitic fringe effect in the measured quanitities [Grédiac et al., 2016]. One way for ensuring the camera perpendicularity is by placing a small mirror onto the observed surface. Once the camera can 'sees itself' in the mirror and its reflection is positioned in the mirror center, it can be considered that it is parallel to the observed surface.

The camera is equipped with Nikon F-mount to which a fast 105 mm macro lens was mounted (Sigma 105mm f/2.8 EX DG). Obtaining proper grid pixel sampling, is an iterative process. It is of prime importance for the quality of the measurements to adjust the location of the camera in such a way that the imaged specimen grid is precisely encoded by the sensor. Since the signal from the laser interferometer was used as the triggering input, the trigger position was set to 58th image in case of the 2 Mfps recording speed. This was chosen since, when testing concrete material, the aim was not only to film as long as possible in the tensile stage capturing the post-peak response but also to capture the compressive stage so the eventual bi-linear material stiffness can be quantified. However, this point is where the limiting frame count presents a challenge. In the simulated experiments it was observed that a optimal recording length is about 90 μs which at speed of 2 Mfps corresponds to 180 frames while the Shimadzu HPV-X2 allows only 128 recording frames. For this reason the test that were performed on concrete material (shown later in Chapter 7) where divided into two groups according to recording speed. One, performed at 1 Mfps in order to record as long as possible in the post peak material response and 2 Mfps where the focus was on obtaining peak strength with a sufficient time discretization.

6.3.2.2 Displacement measurement uncertainty

Here, the emphasis is on providing first information on the uncertainty measurement of the displacement fields using the Shimadzu HPV-X2 acquisition system and the grid method. Due to limiting frame count and trigger positioning, as previously mentioned, it was not possible to use the first several frames of an actual image sequence to provide information on the displacement uncertainty (as it has been done in Section 3.3.2) since they contain meaningful mechanical content encoding the sample movement. For this reason, the uncertainty (and hence resolution) of the measured kinematic fields was qualified by capturing images of a stationary sample using the same imaging conditions as in the spalling experiment. This simple procedure consists of filming a sample that does not move and is not under any loading conditions. In the case of an ideal camera and measurement algorithm, the

measured displacement fields should be uniformly null, but in practice this is not the case and is mainly induced by the camera digital noise. Figure 6.15 shows the average axial and vertical displacement component obtained for each frame through filming a grid-instrumented sample surface at 2 Mfps and using the first image of the sequence as the reference one. The values of displacement uncertainty for several analysed still sample sequences are given in the Table 6.1. The standard deviation reported represented a mean deviation obtained on each frame over the entire sequence. It can be noted that the standard deviation of the measured displacement is, once again, higher in the vertical direction which might be due to lower fill factor (Figure 6.11b). It is also worth noting that the same sample (*i.e.* the same grid) was filmed with both cameras. An overall mean resolution of the axial displacement component seems to be 0.21% of the grid pitch (0.014 pix) which is lower than what is obtained for the Shimadzu HPV-1 in Section 3.3.2. On the other hand it is still higher than the values reported for the Shimadzu HPV-X camera which is about 0.15% of the grid pitch (0.0075 pix) of the grid pitch or 0.6 μm [Seghir and Pierron, 2017]. Therefore, utilizing the HPV-X sensor presents an interesting future perspective of this work. Finally, it can be concluded that the true benefit of the using the Shimadzu HPV-X2 applied to a spalling test, as opposed to Shimadzu HPV-1, is the ability of performing acquisitions with the inter-frame time as low as 500ns and exposure time of 200 ns. Furthermore, the HPV-X2 acquisition system provides 128 frames that all can be used for performing the full-field displacement measurements.

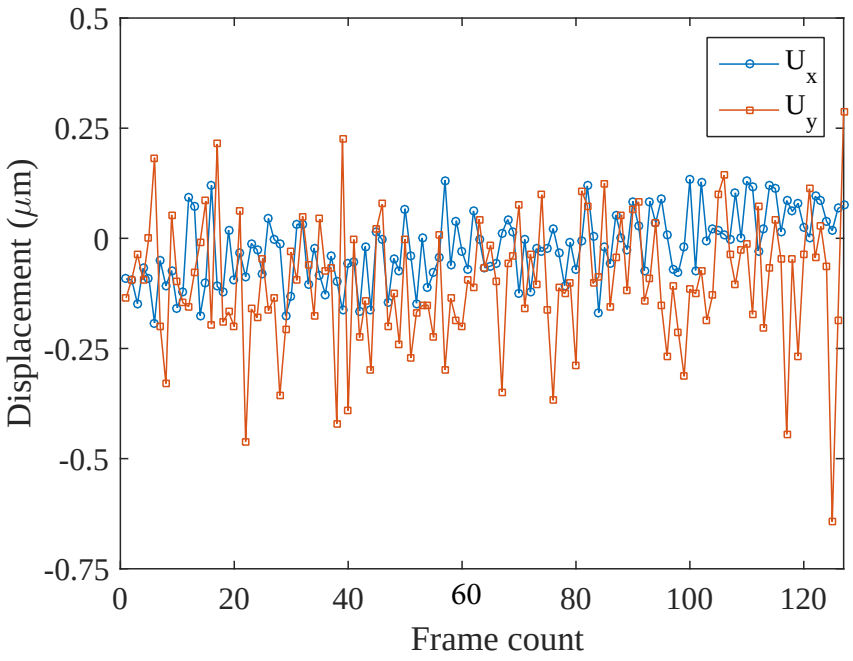

Figure 6.15: Average measured displacement of a stationary grid-instrumented sample filmed at 2 Mfps with ultra-high speed camera the Shimadzu HPV-X2.

Test	$\sigma^{eq}_{(X)}$ (μm)	$\lvert\overline{U_X}\rvert$ (μm)	$\sigma^{eq}_{(X)}$ (μm)	$\lvert\overline{U_Y}\rvert$ (μm)
AQ1	2.05	0.03	6.63	0.1
SPAG02fix	1.89	0.082	2.05	0.16
SPAG03fix2	2.26	0.08	3.46	0.09
SPAG04fix1	2.17	0.11	4.13	0.04

Table 6.1: Estimates of displacement uncertainty by performing the analysis on stationary sample image sequences framing the aluminium sample (2 Mfps and 7 pix/pitch/mm sampling).

6.3.2.3 Identification of the linear elastic material response

A series of spalling tests were carried out on the aluminium sample with the previously described experimental set-up concerning the Shimadzu HPV-X2 camera. A projectile was launched at about through the gas tube in order to reach a impact speed of about 10 m/s for these tests. In that case tested sample is loaded within the elastic limit of the material response and the identified elastic material stiffness can be compared to the expected one. The identified material parameters of one reference test (SPAG1702) recorded with 2 Mfps acquisition speed are presented in the following. The material identification is performed using the VFM as described in previous sections. The reconstructed stress-strain response concerning the reference test are provided in Figure 6.16 using the results from a 10 mm long virtual gauge at 30 mm and 40 mm from sample free end. The information of the processing parameters are provided in Table 6.2. Values of Young's modulus recovered from performing a regression of the two curves are given in Table 6.3. In principle, the identified material stiffness values are within 1.5% of the expected material stiffness with a lower standard error compared to that obtained for a reference spalling aluminium test utilizing the Shimadzu HPV-1 camera (Table 3.2).

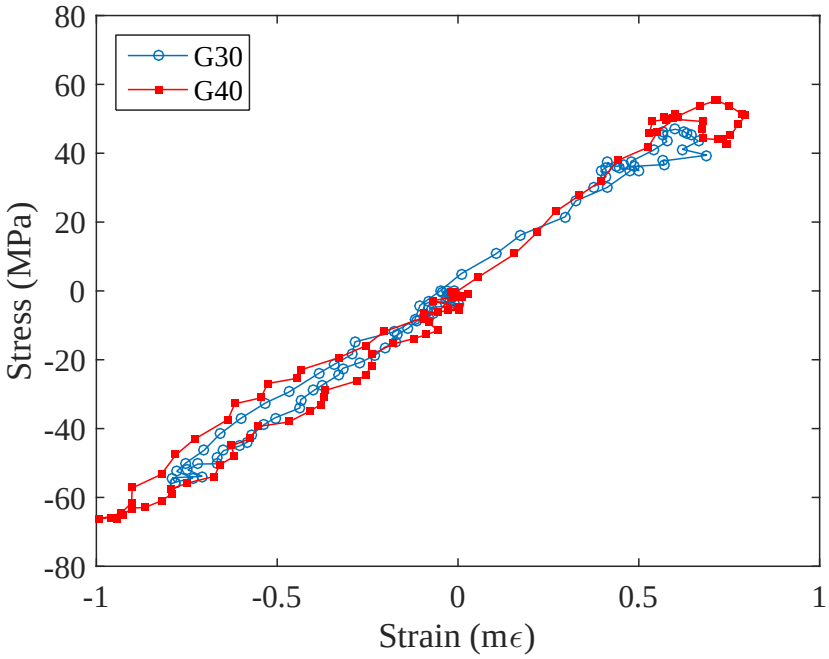

Figure 6.16: Reconstructed stress-strain curves at 30 mm and 40 mm from sample free end using a 10 mm long virtual gauge (recording 2 Mfps with the Shimadzu HPV-X2).

As previously mentioned, the aluminium sample used was also instrumented with point-wise measurement systems. Figure 6.17 shows a comparison of axial strain between a virtual gauge and a real strain gauge glued at 40 mm from free-end. A good agreement between the two measurements can be observed as expected, since the the HPV-X2 camera exhibits significantly lower spatial noise variation compared to the Shimadzu HPV-1. Furthermore, this validates that the uniaxiality of the spalling test since the gauge is located diametrically opposite of the grid surface. On the other hand, the limiting number of acquired frames can be clearly observed, as not the entire tensile stage seems to be completely recorded. In order to further investigate eventual effect of high frequency noise in the measured displacement fields, the derived axial velocity at the free end as well as the axial acceleration can be compared to the data recorded by the laser interferometer. This is shown in Figure 6.18 where the data from the laser were derived with simple finite differences method. The rear face velocity profile from the laser measurement and from the grid method show good agreement validating that the zero boundary condition (free-end) was well captured. A good agreement can be also observed with respect to the level of recorded free-end acceleration, however, due

	Shimadzu HPV-X2
Pixel count	400x250
Frame rate	2 Mfps
Exposure time	200 ns
Number of images	128
Reference image	1^{st}
Region of interest	392x161 pix (56x23 mm)
Grid pitch	1 mm
Grid sampling	7 pix/mm
Raw displacement uncertainty	0.21% grid pitch
	0.014 pix (2.1 μm)
Strain derivation	diffuse approximation (2nd order, 8 points)
Strain rate	2^{nd} order polynomial over 9 images (4.5 μs)
Acceleration computation	2^{nd} order polynomial over 15 images (7.5 μs)

Table 6.2: Information on the processing of the reference spalling aluminium test with the Shimadzu HPV-X2 (SPAG1702).

Virtual gauge	Young's modulus (GPa)	Standard error (GPa)
G30	71.14	1.23
G40	72.34	0.48

Table 6.3: Identified values of the Young's modulus for the test SPAG1702 by performing the linear regression of the stress-strain curves at 30 mm and 40 mm from free surface.

to double differentiation of the acceleration fields noise content starts to be visible, exhibiting a time variability. Finally, the measurements of kinematic fields seem refined with this acquisition system than when compared to the previous used Shimadzu HPV-1 as reported in [Saletti and Forquin, 2015]. However, one needs to keep in mind that the level of stress (*i.e.* axial acceleration) is quite high regarding the spalling alluminium test and it results in the low signal to noise ratio. When concrete material is tested, the expected measurement of tensile stress is of one order of magnitude lower and the signal to noise ratio drastically decreases.

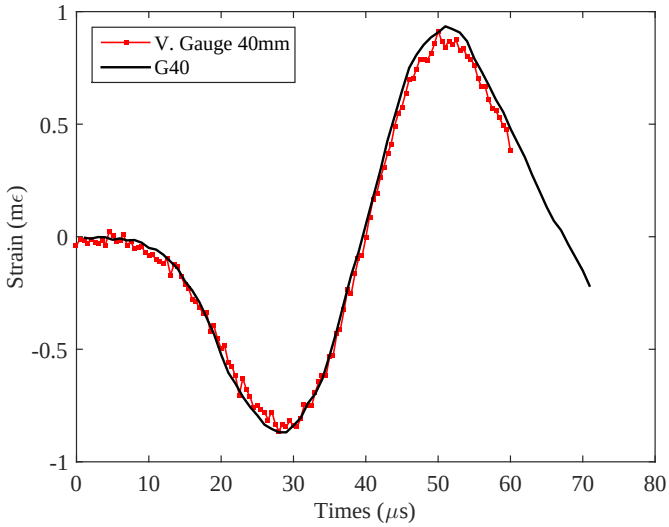

Figure 6.17: Comparison between a virtual gauge (L=10 mm) and real strain gauge glued at 40 mm from sample-free end for the case of 2 Mfps acquisition speed with the Shimadzu HPV-X2 (test: SPAG1703).

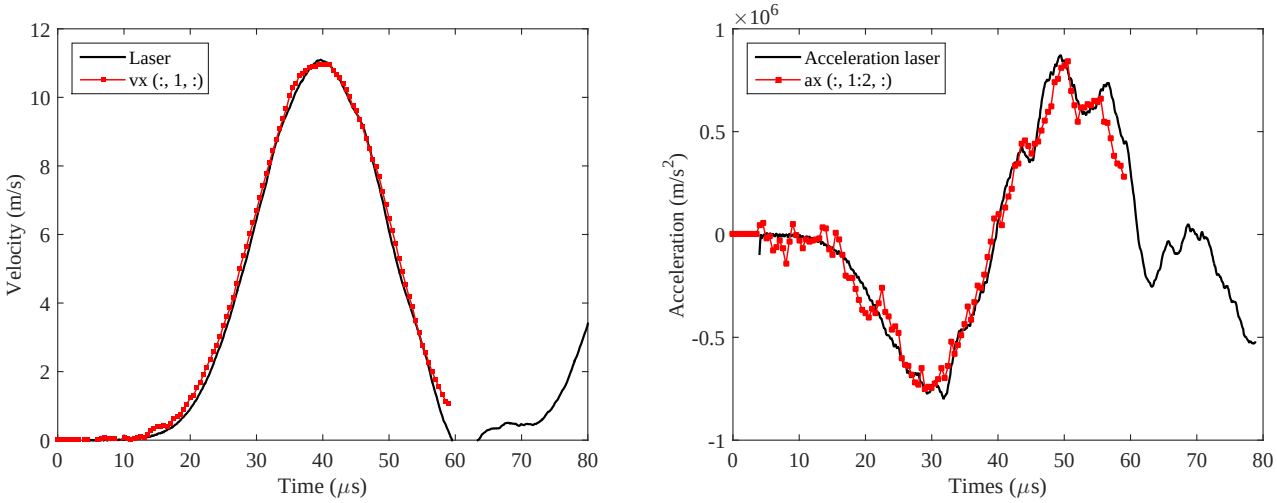

(a) Comparison between rear face axial velocity.

(b) Comparison between rear face axial acceleration.

Figure 6.18: Comparison between Laser measurements and kinetic measurements obtained from the grid method at the sample free-end and filming from sample with 2 Mfps acquisition speed with the Shimadzu HPV-X2 (test: SPAG1703).

6.3.2.4 Identification results and errors

Although, the current number of conducted test with the HPV-X2 acquisition system does not allow drawing any firm conclusion on its accuracy regarding the identification of the material stiffness, it is worth analysing the identified stiffness results and comparing them to the expected one. The linear regression results obtained for two virtual

gauge locations in the performed spalling aluminium tests, that have been conducted with 7 pixels/pitch/mm grid sampling, are gathered in the Table 6.4. From the presented results it can be observed that some tests show a systematically lower value than expected within a limit of about 7%. On the other hand, the standard error appears to be within a range of 2.5%. It is difficult to directly compare these results to the ones obtained with Shimadzu HPV-1 (Section 3.3.6) since the tests were performed at different frame rates and processing parameters. Nevertheless, as a general remark, a reduced standard error can be noted from the regression results obtained with HPV-X2 when comparing the two acquisition systems (see Table 3.6) which seems to be consistent and repeatable from one test to another.

Test	FPS	Virtual gauge	Young's modulus(GPa)	Standard error(GPa)	Strain rate (s^{-1})
SPAG1702	2 Mfps	G30	72.35	1.226	150.8
		G40	71.14	0.481	163.1
SPAG1703	2 Mfps	G30	66.44	1.58	94.7
		G40	65.37	1.038	118.2
SPAG1704	1 Mfps	G30	67.43	0.148	119.8
		G40	67.47	0.741	133.5

Table 6.4: Linear regression results for the spalling tests performed on aluminium alloy using the stress-strain curves at 30 mm and 40 mm from free surface (HPV-X2 camera and 7pix/pitch/mm sampling).

6.3.3 Spalling of ordinary concrete

In the following spalling test conducted on ordinary concrete will be presented with accompanied full-field identification results. The aim is to investigate the applicability of the Shimadzu HPV-X2 camera in the identification of the concrete dynamic fracturing response. The experimental configuration of the sample is similar to the one used for conducting spalling aluminium tests that is presented in Section 6.3.2.1 and shown in Figure 7.2. The concrete sample is instrumented with three axial strain gauges (L=10 mm) and a bi-directional grid of 1 mm pitch. The strain gauges were positioned at 40 mm, 60 mm and 120 mm distance from sample free end. The sampling of the visualised grid surface is 5 pixels per grid period. In that way, due to limit camera pixel count, a surface of 75 mm in length can be recorded and the measured data can be compared with both gauges close to free end. A laser interferometer is pointed to the sample free-end to measure the material particle velocity. As mentioned in the tests conducted on aluminium alloy, the limiting frame count of the camera presents a challenge and as a first test the recording speed was set to 1 Mfps (inter-fame time of 1 μs). The exposure time was set to 200 ns in order to reduce the sample movement blur. The camera was triggered by the laser interferometer pointed towards the sample free-end and was set to provide 58 images before the received triggering signal. The recorded exit velocity of the projectile was 7.65 m/s, generating a incident pulse within the Hopkinson bar of about 50 MPa. In order to well measure the incident pulse, the Hopkinson bar is also instrumented with strain gauges at 20 mm from the bar-specimen contact. An example of stress recordings obtained on the Hopkinson bar ($\sigma_{bar} = E.\varepsilon_{bar}$) are presented in Figure 6.19. Strain gauges were glued on three different positions on the concrete sample which allow measuring the material wave speed ($C_0 = 3970$ m/s) and compressive stiffness ($E_{comp} = 35$ GPa).

The axial displacement maps have been obtained using the grid method which has been introduced in Section 2.3.2. The displacements at a given point are related to the spatial phase change obtained using a spatial phase shifting algorithm. The algorithm used here is called WDFT (Windowed Discrete Fourier transform). It has been shown that when this algorithm is combined with a triangular windowing of 2N-1 size (N being the grid pixel sampling) it is robust enough and provides accurate phase detection even in the case when the grid is not exactly sampled at

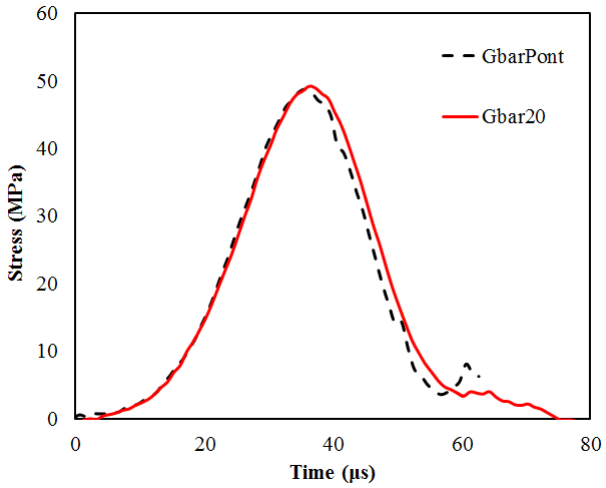

Figure 6.19: Typical shifted stress wave recordings from the gauges on the Hopkinson bar from one spalling test. (test SR30G05)

a pixel integer number [Surrel, 2000]. In order to perform this field measurement technique, a spatial carrier needs to be deposited on the surface with a special gluing procedure (Section 7.1.2.2) and as such, presents delicate step where some defects can be introduced. One of such defects is the missing information of the deposited carrier, caused by an insufficient bond strength between the glue and the coating. At these locations, the missing data occurs in the measured displacement fields since no phase detection is possible. This is particularly a challenge for concrete material because even after the rectification, the sample surface remains not-perfectly flat due to the presence of strong siliceous aggregates. The missing data, often occurs and is observed within the displacement maps. Some techniques do exist where this problem can be treated by approximating the displacement fields with 2D polynomial functions in a least-squares seance [Lira et al., 2004]. However, here this issue has been treated manually by performing local linear interpolation of the displacement information. This was considered as a preferable method due to the presence of strong discontinuities (*i.e.* cracks) in the displacement fields. An example of missing data in the displacement fields at 20 mm from sample free-end due to grid imperfections is shown in Figure 6.20, which represents the last recorder frame of the test.

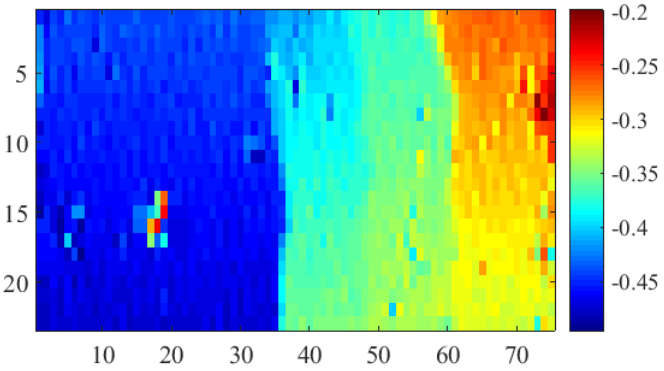

Figure 6.20: Example of missing data in the displacement fields due to grid imperfections. (test SR30G05, recording at 1 Mfps)

6.3.3.1 Identified material response

The axial strains were computed with a window of 8 displacement points and a 2^{nd} order polinomial was used to compute the strain fields. The time resolved kinematic fields are obtained by performing a 2^{nd} order polynomial fit

over a span of 13 time frames for each measurement point. The reconstructed space-time maps of strain and stress are shown in Figure 6.21a,b respectively. From the strain map it is clear that multiple cracks are formed by the end of the test. Some instabilities in the identified strain map can be observed at a distance of about 15 mm from free-end that are introduced by the missing data points. Three strain localization zones can be observed at 35 mm, 50 mm and 65 mm although the one located at the about 55 mm from free end seems to be less pronounced. The principal strain localization appears at the distance of 35 mm from free-end. This becomes clear when observing the stress map since the stress seems to be close to zero at the location of the more pronounced strain localization. The same observation can be made on the global Young's modulus in Figure 6.22 and axial virtual fields expanded from 8^{th} degree polynomials. The mean value obtained in the compressive stage (between 30 μs and the 45 μs) is about 29.2 GPa which is lower than what was obtained from performing wave shift of strain gauges. The maximal value in the tensile loading stage is 9.2 GPa. The lower identified values of the material response could be influenced by the presence of pre-damage introduced during the compressive loading stage due to elevated incident loading pulse. More precise values of tensile strength and material stiffness can be obtained from the reconstructed local stress-strain response. However, first it is necessary to validate the deformation measurements by comparing the measurements obtained from point-wise systems and full-field kinematic data.

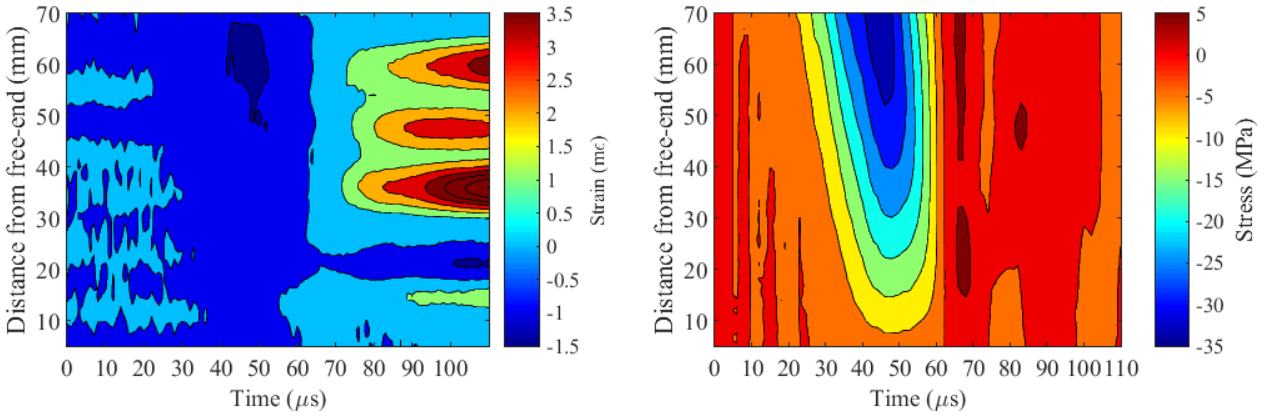

(a) Space-time map of axial strain.

(b) Space-time map of axial stress.

Figure 6.21: Space time maps of axial strain and stress identified using the Shimadzu HPV-X2 and 1 Mfps acquisition speed (test SR30G05, recording at 1 Mfps).

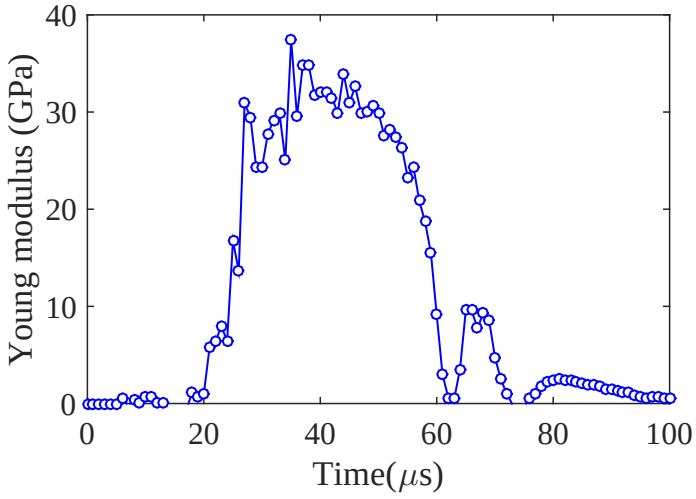

Figure 6.22: Identified global material Young's modulus. (test SR30G05, recording at 1 Mfps)

6.3.3.2 Comparison to point-wise measurements and validation

Thanks to also having the recordings of strain gauges glued on the sample surface, the recorded axial strain values can be compared to those derived from the virtual gauges and the grid method at the same position along the visualized portion of sample. Figure 6.23 presents comparison of axial strain measurement obtained from real strain gauges and the virtual strain gauge data from the grid method for two location on the sample length. From the presented plots it can be noted that during the compression stage the two measurement techniques show a very good agreement in measured axial strain values. On the other hand, in the tensile stage especially after the peak material tensile strength is reached (Figure 6.24), a discrepancy between gauge measurements and the ones obtained from field data can be noted. The origin of the observed discrepancy between the measurements provided by strain gauge and the virtual gauges is unknown. However, it can indicate a formation of fracture planes that are not planar with respect to the axis of the sample.

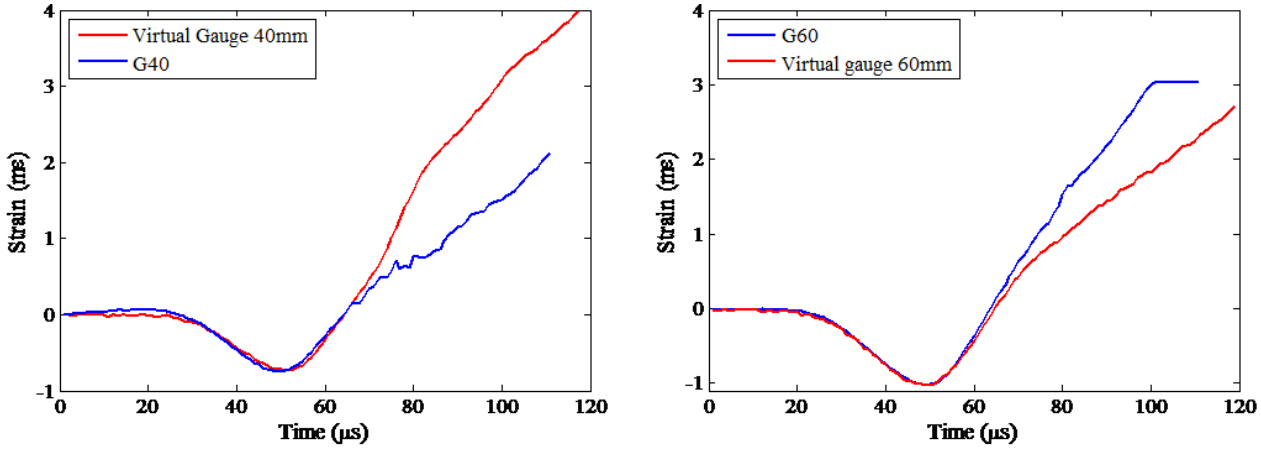

(a) Gauge at 40 mm distance from free-end.

(b) Gauge at 60 mm distance from free-end.

Figure 6.23: Comparison between strain gauge measurements and virtual gauge data (L=10 mm). (test: SR30G05).

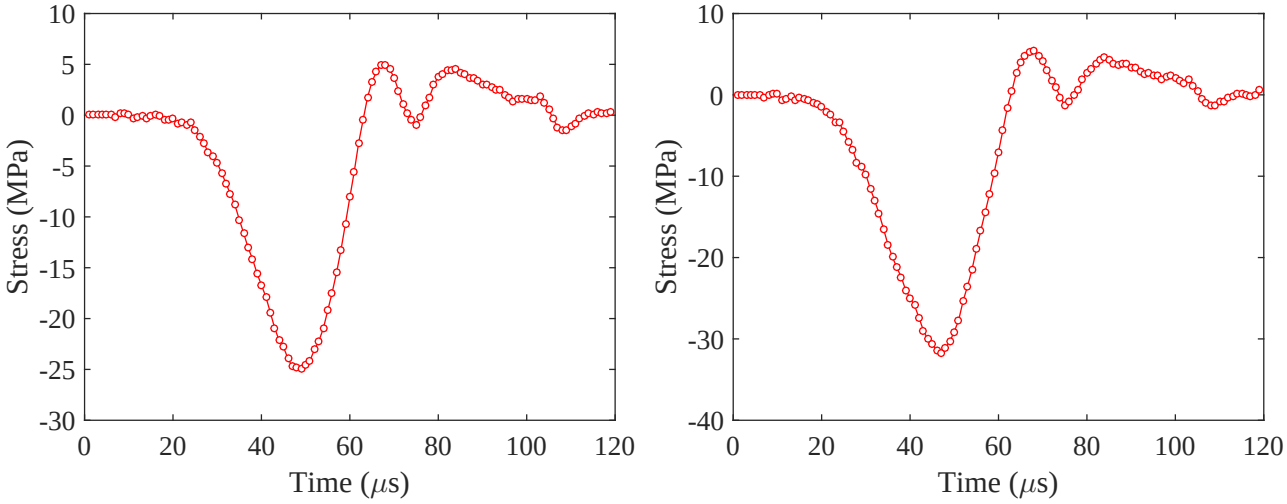

(a) Gauge at 40 mm distance from free-end.

(b) Gauge at 60 mm distance from free-end.

Figure 6.24: Stress measurement from virtual gauge data (L=10 mm). (test: SR30G05).

6.3.3.3 Reconstructed local stress-strain response

From the above presented measurement data it is possible to reconstruct local stress-strain response at any visualised cross-section of the sample. Two pronounced strain localization zones can be observed from the reconstructed strain space-time map, one at 35 mm and another at 55 mm from sample free end (Figure 6.21). Figure 6.25 show stress-strain response reconstructed on these two locations. From the plots, it can be observed that the maximal tensile strength does not exceed 5 MPa, while the value obtained with classical Novikov formula (Equation 3.3) is about 9.71 MPa. Furthermore, from the response at 55 mm from free end already some non-linearities can be observed during the compression stage which could indicated a presence of damage during the compressive loading. The VFM processing does not rely on any assumption on the material behaviour and allows the direct measurement of axial stress thanks to the image embedded load cell, which acts through the acceleration fields. However, the uniaxiality of the stress state is the assumption on which the load cell theory is derived and as such is pre-requisite for any successful spalling test. Here, this assumption is compromised due to the possible damage introduced in the compressive stage. The results presented here-in serves as example of practice that even when the measurements are in order the test may not be successful.

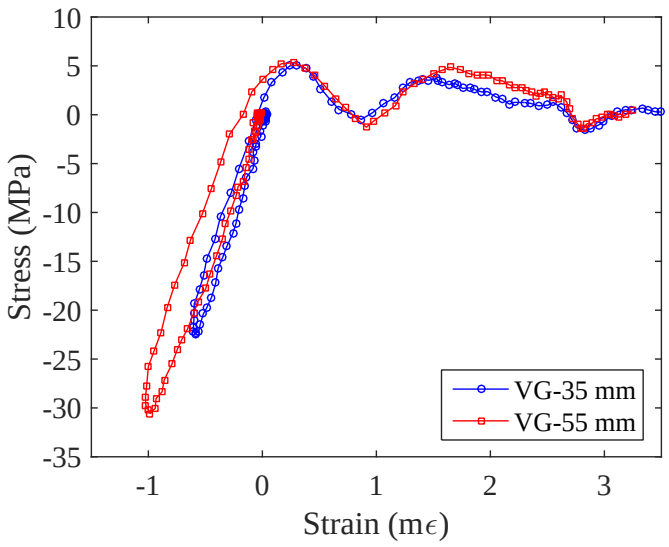

Figure 6.25: Identified local Stress-Strain material response at two locations from sample free-end using virtual gauge measurement. (test SR30G05, recording at 1 Mfps)

6.4 Chapter summary

In this chapter the metrological performance of two UHS imaging systems, the Kirana camera and the Shimadzu HPV-X2, was explored through performing dynamic spalling experiments. Both systems use CMOS-based sensor technology for reaching exposure times as low as 200 ns. The study was performed in light of determining which acquisition system would be more adequate for conducing an experimental testing of concrete material in dynamic tension. The accent was to determine which system provides more reliable (and stable) measurements of acceleration fields in terms of full-field measurements.

In case of the Kirana camera several image effects were observed which can be mainly contributed the sensor technology. Being a front illuminated sensor, the Kirana camera requires powerful light source (preferably two flash lights). However, due to the architecture of one pixel domain and its corresponding memory bank, it can suffer from parasitic light effects and optical cross-talk. These were to some extent removed thanks to the latest updates implemented in 2017, that include enhanced shielding of the pixel domain and fast LCD shutter. Nevertheless, the sensor still exhibits a high frequency fluctuation of grey levels within one acquire image sequence which manifests as a constant loss and recovery of charge (see Figure 6.8). Although it was found that such flickering effects are not visible by unaided eye and barely noticeable in the measured displacement fields, when acceleration fields are derived, the noise influence severely increases which makes this sensor less adequate (for the time being) for the proposed experimental procedure. On the other hand, it is worth mentioning that thanks to large pixel count (0.7 Mpix) and number of acquired frames (180), the sensor seems more adequate to situations when only displacement content is of interest or in situations where visual inspections are conducted such as those performed in ballistic and aerodynamics applications. Also, it is worth mentioning that throughout this entire PhD work the Kirana sensor was under development and thanks to close communication with Specialised Imaging, more throughout understanding of sensor noise sources was acquired.

In case of the Shimadzu HPV-X2 imaging system it was noticed that a more stable measurements of the acceleration data was obtained. The sensor exibits a low temporal fluctuation that appears to be random (see Figure 6.14a). Compared to previous camera versions provided by the same manufacturer, the HPV-X2 provides larger bit depth and more acquired frames with a clear advantage that all frames from the sequence can be used for performing field measurements. Although, considering current application the sensor pixel count remains low (0.1 Mpix) and the number of frames (128) does not allow capturing the entire post-peak response at desired acquisition speed (2 Mfps). Thanks to the stability of the image sequence it was chosen as the measurement system for the experimental application presented in the following Chapter 7.

Chapter 7

Experimental application

The following chapter presents an experimental work conducted on three types of concrete material using the previously described photomechanical dynamic spalling test. Traditional measurements were performed complementary to full field measurements and the processed results regarding material tensile strength at high strain rate were extracted and compared. The chapter presents an attempt of using such photomechanical procedure in studying the effects of concrete composition on the increase of material tensile strength at high strain rates which has been an open area of research over several decades. The chapter is organised into two principal parts. First, the types of tested materials are rapidly introduced together with the procedure of sample preparation and instrumentation. Second, the results obtained from processing the point-wise measurements and the full field measurements are presented and compared. Finally, all the results are synthesised and compared with the results from the literature.

7.1 Experimental procedure and materials

7.1.1 Tested materials

The experimental campaign was performed on three types of concrete in order to examine the effect of concrete composition on the dynamic tensile strength at elevated strain rates that reach up-to 200 s^{-1}. The effects in question concern the influence of the type of coarse aggregates and the influence of the cement matrix used in the concrete mixture. To this end, ordinary concrete was tested alongside two alternated mixtures. The compositions that were considered in this work are following and their mix proportions are given in Table 7.1:

- Ordinary concrete (OC) also known as R30A7 [Gabet, 2006].
- Limestone concrete (LC) composed of crushed aggregates obtained from limestone rock [Piotrowska, 2013].
- High performance concrete (HPC) containing added silica fume and low water-cement ratio [Zingg et al., 2016].

Concrete	OC	LC	HPC
Aggregates D 0.5/8 [kg/m^3]	1008	891	1008
Sand $D_{max} = 1800$ μm [kg/m^3]	838	838	795.4
Cement CEM I 52.5 N PM ES CP2 (Vicat) [kg/m^3]	263	263	420
Superplasticizer (Sikafluid) [kg/m^3]	/	1.8	/
Silica fumes (Condensil S95 DS) [kg/m^3]	/	/	46.7
Water [kg/m^3]	169	169	140

Table 7.1: Composition of three types of concrete mixtures used in dynamic tensile tests.

7.1.1.1 The R30A7 concrete – (OC)

The R30A7 concrete (OC) is considered as an adaptation of a standard concrete which is commonly used in civil engineering construction applications. Its mixture was designed with the aim of creating a composition with characteristics of standard concrete which can be studied on a laboratory scale [Gabet, 2006]. Alongside cement paste,

sand and water it contains rolled siliceous aggregates (d_{max} = 8 mm) and has an expected compressive strength of 30 MPa after 28 days with a slump of 7 cm measured by Abrams cone test. This type of concrete has been extensively studied under various stress states and in both quasi-static and dynamic loading regimes (*e.g.* [Vu, 2007, Gabet et al., 2008, Erzar, 2010, Piotrowska, 2013, Abdul Rahman, 2018]). Regarding dynamic tensile response, this type of concrete was tested under a wide range of strain rates (up-to about 150 s^{-1}) considering dry and wet sample conditions [Erzar and Forquin, 2011]. High speed hydraulic press and the spalling technique were used to load the samples upto failure. The processing of the spalling experiments, that relies on classical point-wise measurements as detailed in [Erzar and Forquin, 2010], had shown compelling results regarding the influence of the moisture content on the dynamic tensile strength. While almost no difference was noted at low strain rates (upto 1 s^{-1}) a notable difference between wet and dry concrete was observed at high strain rates (50-150 s^{-1}). Furthermore, the post-mortem observation clearly showed higher crack density with increasing strain rate, indicating the presence of cracks mostly within the concrete matrix and around the aggregates, while a few cracks cut through strong siliceous aggregate inclusions. These observations motivated the current study by testing a concrete with different mesoscopic content and matrix strength.

7.1.1.2 The Limestone concrete – (LC)

The limestone concrete (LC) used in this work is characterised by a relatively low aggregate strength. Its composition was designed in order to study the effect of coarse aggregate shape and nature on the confined behavior of concrete [Piotrowska, 2013]. When compared to R30A7, the LC is characterized by the same composition of the cement matrix, volume content and type of sand, alongside with the volume content and granulometric distribution of used aggregates. However, the aggregates are of different physical and mechanical properties which results in having different mesostructural content. The material was previously tested under both quasi-static and dynamic loading regimes in quasi-oedometric compression test [Piotrowska et al., 2016]. The obtained results showed that the nature of coarse aggregates affects the volumetric response at high confinement and that under dynamic loading conditions the deviatoric strength of LC considerably increased. It was concluded that the concrete mesostructure plays an important role in the behaviour of concrete under both high confining pressure and strain rates. Under dynamic tensile loading the effect of aggregates type in concrete composition has not been extensively studied. This can be mainly owing to the fact that no reference formulation of concrete has been proposed for studying such effects. On the other hand, the effect of aggregate size on dynamic tensile strength has been investigated by some authors and the evidence that enhancement of the mechanical properties in dynamic tension is influenced by this parameter was reported by [Cadoni et al., 2013].

7.1.1.3 The High Performance concrete – (HPC)

High performance concrete (HPC) used in this work is characterized by strong cement matrix and lower capillary porosity when compared to ordinary concrete. The mixture was designed with the aim of investigating the effect of cement matrix porosity on concrete confined response [Zingg et al., 2016]. Reduced porosity is achieved by adding silica fumes and decreasing the water-cement ratio. Having this ratio set to 0.3, the expected uniaxial compressive strength after 28 days is 80 MPa. The quantity of sand was adjusted compared to the ordinary concrete for workability reasons. The mixture is also characterized by the same coarse aggregate (rolled siliceous aggregates d_{max} = 8 mm) in both volume and size distribution. This concrete has been previously tested under very high confinements in both quasi-static and dynamic loadings conditions [Piotrowska and Forquin, 2015]. When compared to ordinary concrete, the results showed that HPC exhibits larger deviatoric strength under both low and high strain rates. Even though this particular mixture was not tested in dynamic tension, some other works in the literature investigated the effect of cement matrix and lower porosity content on the strength increase. One type of high performance concrete mixture was tested by [Schuler and Hansson, 2006] at elevated strain rates using the spalling technique. Although a higher ultimate strength was observed at high strain rates with respect to ordinary

concrete, tested by the same author [Schuler et al., 2006], the increase ratio of dynamic strength with respect to quasi-static strength was not significantly different than in ordinary concrete.

7.1.2 Sample preparation, instrumentation and conditions

Manufacturing procedure was established in order to obtain spalling samples with representative mechanical properties for each tested concrete composition. It consists of two stages: the fabrication and the instrumentation of the samples. The final geometry of instrumented cylindrical samples is 45 mm in diameter, 140 mm in length that contains a flatten surface of 24 mm on which the grid pattern is deposited.

7.1.2.1 Casting and fabrication

The concrete is first cast in plywood moulds with dimensions of 27x27x17 cm^3. Before pouring the freshly mixed concrete, oil is applied inside the mould to reduce friction and facilitate the removal of the block. The fresh concrete mixture is then poured, vibrated and sealed with plastic cover to prevent loss of any moisture content during the initial phase of hydration. The block is removed from the mould after $24h$ and is sealed within waterproof plastic bag which is submerged in a water container where it is conserved for 28 days. After this period, the cylindrical concrete samples are cored out from the block leaving a space of at least 20 mm from the block edges to avoid possible wall-effect. The coring is performed with a drilling machine (Diamant Evolution DK17) with the use a diamond instrumented core bit (Length 240 mm, interior diameter 46 mm) and with help of water. The coring of the samples is a delicate procedure which has to be performed patiently having the concrete block well fixed (Figure 7.1), since the resulting lateral surface of the cylinder represents the only reference for rectification of the sample geometry.

Figure 7.1: Sample manufacturing: example of the use of the coring machine.

After the coring, the cylindrical samples are cut down to the desired length (140 mm) leaving an additional +

1 mm margin. Then, the turning machine is used to perform the rectification of the cylindrical sample surfaces (i.e incident and free-end surface) in order to obtain a good parallelism between the two, considering a tolerance of $\pm 0.2mm$. To this end, a non rotary tool-bit is used (Diprotex PCD CPMB 120412) optimised for concrete material. The turning speed is set to about 300 turns per minute which in case of high strength concrete has to be reduced. The process is repeated on the other surface and in total, until the desired tolerance is met. After this step, a precision cut is performed to obtain the flatten surface used to deposit the grid. This surface is then polished with a rectification machine (grindstone granulometry 252 μm) in order to obtain a perfectly flat (*i.e.* as close as possible) surface which is parallel to the sample axis. In between all rectification steps, the samples were stored in lime saturated water.

7.1.2.2 Instrumentation

After obtaining the desired geometry the samples were instrumented with measurement systems. Before starting the instrumentation of the sample with the grid, the surface porosity present on the flatten part has to be filled. This is done by depositing a thin layer of a quick-hardening glue (Pleximon) and by filling the surface pores. After the glue is dried, the sample surface is polished to remove excessive layer of the glue.

Depositing the grid pattern The grid pattern is deposited on the flatten part following the procedure proposed in [Piro and Grediac, 2004, Badulescu, 2010]. The steps are as follows:

- The surface of the sample is first cleaned with using a clean cotton pad and degreaser. Then, the surface is de-oxidised using a fine abrasive paper and several drops of neutraliser. After that, the surface is once again cleaned using a few drops of a conditioner product and dried using a new clean pad. (All surface cleaning products are the same when strain gauges are used – *e.g.* supplier VPG Micro measurements). Finally, the paper scotch tape is used to protect the sample shaft surface from spilling of the excessive glue.

- A grid piece which is about 2 mm longer than the observational surface of the sample is cut from the printed grid deposit sheet. The grid piece is placed on the sample surface towards the free-end, centred with respect to sample axis and fixed with paper scotch on the opposite end. A small part of the grid is left to pass over the sample free-edge which will later facilitate the peal-off.

- Then, the bi-component (Part A and Part B) epoxy glue E504 supplied by Epotecny is prepared. The mixing is performed in a clean glass cup. The ratio between the two parts is: A/B=5/1. This ratio needs to be well respected and the use of a milligram precision balance is advised. A quantity of 3 g in total is prepared for a surface of 24x70 mm. The mixing is performed slowly for about 15 minutes.

- After mixing, a thin layer of glue is applied both on the sample surface and the grid deposit. The grid is then slowly pressed using a plastic roller in order to avoid air traps. Then a pressure is applied to push out the excessive glue and for an equally distribution of the quantity below the substrate. However, since the presence of strong siliceous aggregates does not allow obtaining perfectly flat surface, a relatively small pressure is applied (about 20 Pa). This results in slightly larger thickness of the glue (of about 0.2 mm).

- The grid instrumented sample is left within an oven for 40 hours at 40 degrees Celsius required for curing the epoxy glue. After this time, the substrate is removed starting from the free-end since the cured glue is much stronger than the bond between the photosensitive film and the grid coating. The left-over part of the substrate is used to start the peal-off. The substrate is slowly removed following an angle of 30 with respect to grid lines.

Now, it is necessary to mention that glueing of the grid is a delicate procedure and that uncertainties such as missing data can occur. The reason can be twofold: either the peal stress is not sufficient and the grid pattern is not locally transferred or the entrapped air bubbles do not allow glue distribution. In the first case, the missing

line parts might be corrected by re-tracing them with a thin black pen. In the second case, severe defects can be experienced that are often non-correctable and occasionally produce non exploitable result.

Strain gauge instrumentation Three polyester strain gauges (PFl-20-11 TML length 20 mm) are glued on the already grid instrumented samples. The gauges placed at 40 mm and 60 mm from the free-end are used to determine the strain rate at failure while the gauge at 120 mm from free end (*i.e.* 20 mm from bar-specimen contact) is used to determine the material wave speed so that the compressive Young's modulus is deduced. The gauge is secured with the paper scotch tape. Cyanoacrylate single component strain gauge adhesive (CN-E TML) is used to glue the gauges and the cable connector on the sample surface. After the gluing the gauge cables are soldered onto the connector. All gauges were soldered with thinned copper wiring and are connected to a high frequency acquisition system. The signal from the gauge measurements are processed with the following expression used to obtain the axial strain measurement in ($m\varepsilon$) on the sample surface:

$$\epsilon_{gauge} = \frac{4U_g}{kGU_{exc}} * 1000 \tag{7.1}$$

where U_g is the measured signal from the gauge in (V), U_{exc} is the gauge excitation in (V), G is the signal gain, k is the gauge resistance factor. In the present case the following parameters were used: k=2.13, G=1000, U_{exc}=5 V. Finally, an optical reflector of a few millimetres in size, used for laser measurement, is positioned on the sample free-end within half radius from the center of the cross section [Erzar and Forquin, 2010].

7.1.3 Experimental investigation and spalling set-up

Two experimental campaigns have been carried out in order to perform dynamic tensile testing of three grades of concrete using the spalling technique. All the samples were instrumented with measurement systems as described in previous section and were tested within a one weak period which favours the reduction of the variability of mechanical properties due to concrete ageing. The campaigns were performed in:

- June 2016 – The campaign was focused on testing ordinary concrete (OC)
- June 2017 – The campaign was focused on testing the other two mixtures, namely limestone concrete (LC) and high performance concrete (HPC).

The experimental setup used for testing several concrete samples of the three concrete mixtures is identical to the one used Section 6.3.2 and is shown in Figure 7.2.

The spalling setup in Laboratory 3SR consists of a single input Hopkinson bar which is in contact with a cylindrical sample on one end that is and impacted by a cylindrical projectile on the other end. The material used for the bar, projectile and the sample is an aluminium alloy of the following characteristics: density 2810 kg/m^3, expected elastic Young's modulus 72 GPa, material wave speed C_0=5090 m/s and high yielding strength of 450 MPa. The input bar is 1.4 m in length and 45 mm in diameter. It is instrumented with two crossed-element standard foil strain gauges (4 x FCA-1-23 120Ω L=1 mm *TML*) connected into a full bridge circuit, the Wheatstone bridge, and located in the mid-length. A 50 mm long projectile and 45 mm in diameter is launched through a launcher tube with the aid of a pressure gas tank of 100 bars maximal capacity. The launcher tube has an effective length of 1.85 m and is 65 mm in diameter with thickness of 7 mm. The tube is instrumented with three photodiods located at 150 mm, 100 mm and 50 mm from its end exit respectively, and are used to measure the projectile impact speed. The projectile's impact surface has been machined into a spherical-cap end, as to apply an adequate pulse shaping of the incident wave which increases the pulse rising time [Erzar and Forquin, 2010]. The pressure in the tank is controlled thanks to a digital barometer installed on a control-release unit witch allows fine tuning of the pressure with ±0.01 bar. All gauges, including those glued on the tested specimen, are connected to a high

resolution data acquisition control apparatus (ADwin-Pro II) with a 1 Mhz registration frequency. The signal from the gauge measurement positioned on the Hopkinson bar are processed with the following expression used to obtain the compensated strain measurement in mε of the wave propagating within the aluminium bar:

$$\epsilon_{gauge} = \frac{2U_g}{kGU_{exc}(1+\nu)} * 1000 \tag{7.2}$$

where U_g is the measured signal from the gauge in (V), U_{exc} is the gauge excitation in (V), G is the signal gain, k is the gauge resistance factor and $\nu = 0.33$ is the Poisson ration of the aluminium bar. In the present case the following parameters were used: k=2.1, G=5000, U_{exc}=1V. A laser interferometer from Polytech was pointed towards the sample free-end with having a bandwidth of 1.5 MHz, a registration sensitivity set to 2 m/s/V and being able to measure particle speed upto 20 m/s (10 V to signal saturation).

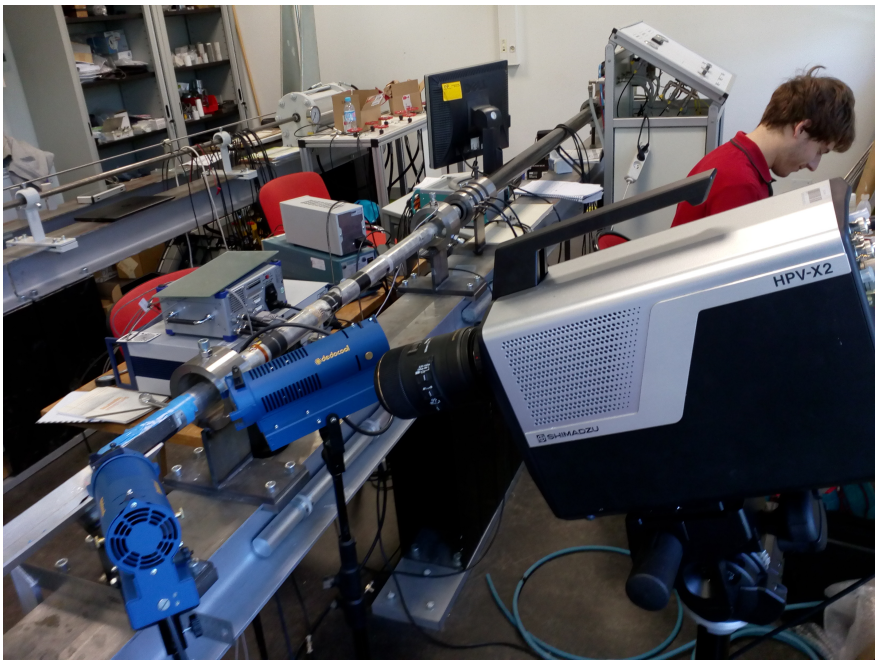

Figure 7.2: The experimental set-up at 3SR used to conduct spalling experiments with the ultra-high speed camera the Shimadzu HPV-X2.

The ultra high speed camera used to film the grid bonded on the tested sample surface is the Shimadzu HPV-X2 (Section 6.3.1.1). A macro lens was mounted on the the camera head that provides 1:1 magnification ratio (Sigma 105 f/2.8 EX DG Macro). The camera is triggered with the signal that is received from the laser interferometer. Acquisition speeds of both 1 Mfps and 2 Mfps were used depending on the test. For acquisitions of 2 Mfps it was crucial that a sufficient amount of images are devoted to recording the tensile loading stage, for that reason, the trigger position was set at the 68^{th} image. In that case 68 images are dedicated to recording the compressive stage of the test while the rest is used to record the reflection of the wave into the tensile stage. Due to the insufficient amount of recorded frames (128 frames), the main interest was focused on well capturing the material peak tensile strength. For the case of 1 Mfps acquisition speeds the trigger was set to the 54^{th} image.

The sample surface was illuminated with two DedoCool tungsten light sources, operating on boost mode with 250 W. The DedoCool lights, thanks to the use of low voltage lamps in combination with a special optical-reflector system, produce substantially reduced heating of the subject. The choice of the light source plays an important role since it can, in case of some sensors, cause additional noise effects as shown in Section 6.2.1.3. Furthermore, any flickering noise, for example caused by LED gas discharge lamps, would add additional component of temporal noise which pollutes the recorded sequence. Indeed, this was observed from an example of bad practice. In the first

experimental campaign dealing with testing ordinary concrete (OC), two high power LED lights with DC power sources provided by Specialised Imaging were used to illuminate the sample. The results from the first campaign were found to be inexploitable and it was only after that it was discovered that effects such as flicker noise to fast gas discharge was present within the recorded sequences. An example regarding average frame grey level of the two acquisitions made at 2 Mfps with different illumination sources is presented in Figure 7.3. For that reason, full-field measurement results presented herein will only concern the HPC and LC tested samples.

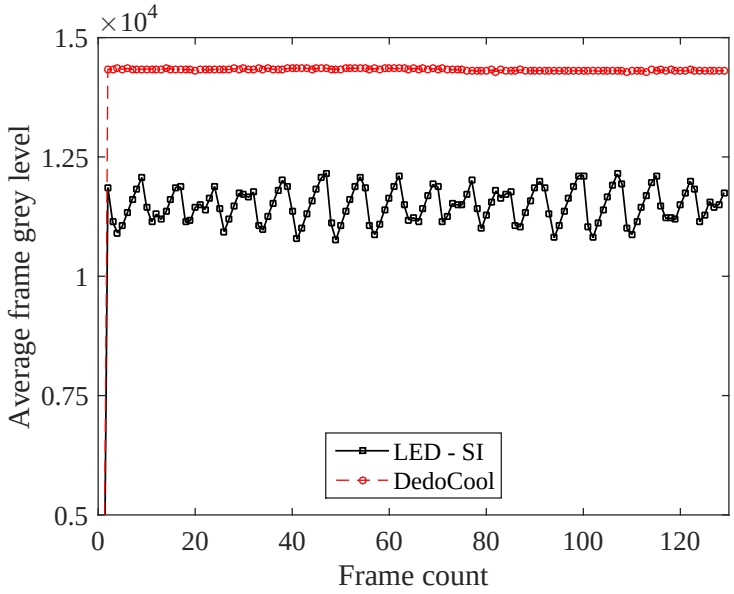

Figure 7.3: An example of bad illumination conditions due to flickering of the light source. Acquisitions are made with Shimadzu HPV-X2 at 2 Mfps.

7.1.4 Processing parameters and identification uncertainty

When dealing with full-field measurements it is necessary to assess the accuracy of the proposed identification methodology. This is often closely related to the displacement measurement uncertainty which can be evaluated as a standard deviation of displacement fields obtained from stationary image sequences. This procedure was employed in Section 6.3.2.2 to evaluate the displacement uncertainty of the Shimadzu HPV-X2 camera. However, as demonstrated throughout this manuscript, it is difficult to predict how the measurement uncertainties propagate through the entire identification chain and how they would affect the final result. The reason for this is that, although dominant, the camera noise is not the only possible source of errors. All these sources add up and cause the measurement uncertainty which requires some sort of smoothing algorithms to be applied that act as low pass filters both in case of spatial and temporal derivatives. Therefore, the identification result also depends on the set of processing parameters chosen to compute the sought kinematic and deformation fields (*i.e.* strains, strain rates and accelerations). Here, an approximative global approach of providing robust estimate of the uncertainty of the identified results is provided by passing stationary image sequences acquired before a test through the entire identification chain taking a set of processing parameters that are later used to process the real experimental data. Since in this work, the main goal is the reconstruction of the material stress-strain response due to the applied loading the treated stationary images can be used to provide such data. Theoretically, the reconstructed stress-strain curve should be equal to zero, however this is not the case. Therefore, by tracing the reconstructed fictive stress-strain response one can get an insight on both the error bounds and eventual systematic error that result from the identification chain given a set of processing parameters. This can be done by simply observing the bounding box of the fictive stress-strain plot. As previously mentioned, two acquisition speeds were used to record the spalling test on concrete specimens, namely 1 Mfps and 2 Mfps. The processing technique used to treat the

spalling tests is identical to the one used in previous works [Pierron and Forquin, 2012b] and in Section 4.4.1.2. The set of processing parameters is summarized in Table 7.2. Due to the temporal noise of the system the temporal window used to compute the acceleration data through the double derivation of displacement data was taken to be 15 (7.5 μs) time points for the case of 2 Mfps and 9 points (9 μs) for the case of 1 Mfps. It was observed that for the case of identified axial stress the bound values are ± 2.1 MPa while for the case of axial strain it is within ± 0.075 $m\epsilon$. These values could be considered as confidence intervals of the results presented in the following sections that already passed through low-pass filtering.

Camera - Shimadzu HPV-X2	
Pixel array size	400x250
Frame rate	2 Mfps (1 Mfps)
Exposure time	200 ns
Field of view	23x60 mm
Number of frame	128
Strain	
Smoothing method	Diffuse approximation, 8 pixel radius
Temporal resolution	0.5 μs (1 μs)
Strain rate	
Smoothing method	Second-order polynomial fit over 7 temporal strain points
Temporal resolution	3.5 μs (7 μs)
Acceleration	
Smoothing method	Second-order polynomial fit over 15 (9) temporal displacement points
Temporal resolution	7.5 μs (9 μs)

Table 7.2: Imaging measurement performance and processing information for the spalling tests performed with the Shimadzu HPV-X2 camera at 2 Mfps and 1 Mfps.

7.2 Experimental results

In the following the experimental results obtained from conducting dynamic tensile testing of three types of concrete mixtures will be presented. First, the results from classical processing are shown regarding the peak tensile stress and corresponding strain rate. Second, the results from full field identification are presented in terms of reconstructed local stress-strain curves. Finally, the results from two techniques are compared and plotted together with results from the literature.

7.2.1 Results from point wise measurements

The results obtained from performed spalling tests on three types of concrete and by treating the point-wise measurements are presented in the following. The processing of the data from strain gauges and laser interferometer has been detailed in Section 4.4.1.1. The failure stress deduced from the rear face velocity profile is depicted as a function of strain rate at failure obtained by deriving the strain gauge data in Figure 7.4. The small number of tested samples from the current study does not allow drawing any firm conclusions regarding the effect of concrete composition on the increase of tensile strength with strain rate. However, some qualitative observations can be made first hand. From the Figure 7.4a, it is observed that the HPC shows a higher dynamic tensile strength compared to ordinary concrete of about 5 MPa at approximately same level of strain rate. This was to some extent expected due to higher mechanical properties of HPC. On the other hand, no significant difference can be observed when results obtained from LC are compared to those of ordinary concrete; indicating (for the time being) no

notable influence of coarse aggregate shape and nature for the case of siliceous and crushed limestone aggregates. The obtained results are plotted together with the data from previous studies regarding ordinary concrete and micro-concrete [Erzar and Forquin, 2010, Erzar and Forquin, 2014] as in Figure 7.4b. It can be observed that the data obtained regarding ordinary concrete and LC in this study fit well with the previous results obtained for concrete in dry conditions. This is not surprising since all the samples have passed through a temperature treatment. This stage is necessary for curing the epoxy adhesive that is used to glue the grid onto the sample surface, as mentioned in previous Section 7.1.2.2. This is furthermore confirmed by observing the typical rear-face velocity profile for the tree types of concrete presented in Figure 7.5 that are tested at approximately the same loading rate. In all three cases, the post-rebound curve that is related to the tensile post-peak response exhibits a plateau after the rebound. This was observed as a characteristic post-rebound response for dry concrete which is related to the possibility of energy loss due to multiple micro-cracking [Erzar and Forquin, 2014]. In contrast, the presence of free water causes several sharp rebounds to appear as observed by the same authors. This occurrence can be related to the free-water viscosity effect acting in favour of closure of developing micro-cracks [Erzar and Forquin, 2014, Vegt, 2016]. All the results are gathered in Table 7.3.

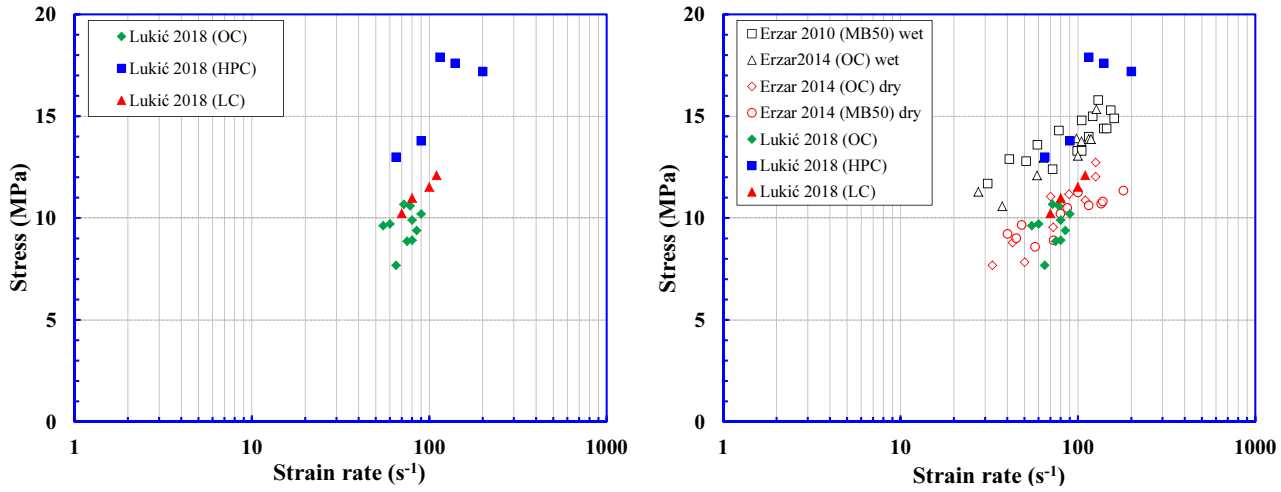

(a) Results from spalling tests conducted on: ordinary concrete (OC), high performance concrete (HPC) and Limestone aggregate concrete(LC).

(b) Comparisson with results obtained on R30A7 in [Erzar and Forquin, 2010] and MB50 [Erzar and Forquin, 2014].

Figure 7.4: Results from spalling tests on three types of concrete obtained by treating standard point-wise measurments as in [Erzar and Forquin, 2010].

7.2.2 Results from full field identification

It has been shown throughout Chapter 3 how a rich amount of information can be obtained regarding material dynamic response by performing photomoechanical identification from full field displacement measurements using the VFM and the load cell principle. Here the same methodology was applied to extract the material parameters from experimental spalling tests. Sequences of grey level images were acquired with the Shimadzu HPV-X2 ultra-high speed camera filming the grid instrumented concrete samples with acquisition speeds of 2 Mfps and 1 Mfps. The corresponding displacement fields were obtained by using the grid method. Since the material response can be assumed to stay within the domain of infinitesimal strain theory [1], the measured quantities of deformation are small strains. Owing to this, it was observed that spatial phase maps did not exhibit phase jumps and hence spatial unwraping was not used. However, in certain cases of lengthy recordings, such as when the 1 Mfps camera acquisition speed was used (resulting recording length of 128 μs), temporal jumps were occasionally observed in the evolution of axial displacement maps since the final value of the averaged axial displacement was above the grid

[1] characteristic for concrete-like materials

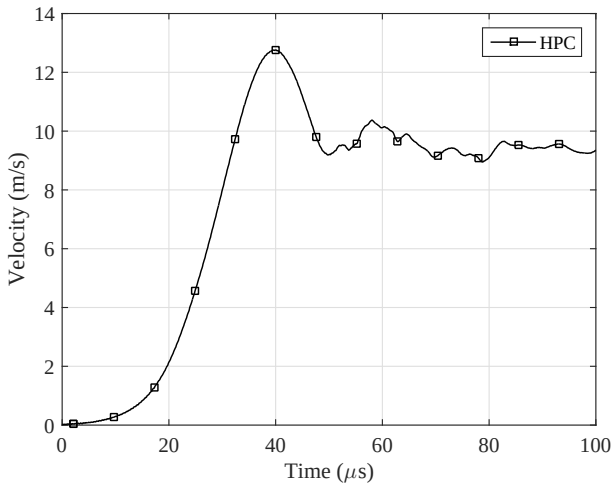

(a) (HPC)–High performance concrete.

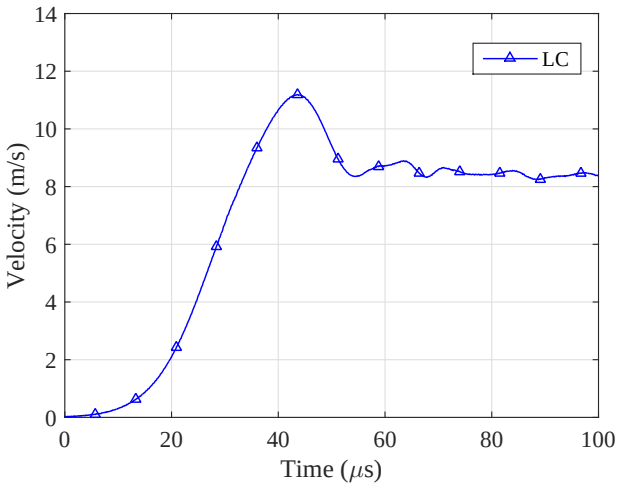

(b) (LC)–Limestone aggregate concrete.

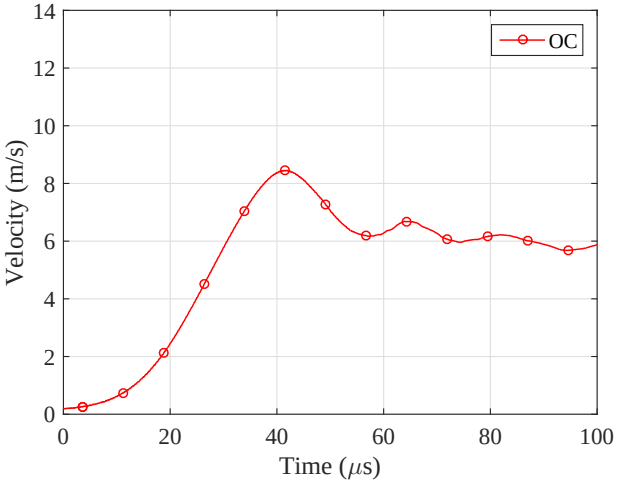

(c) (OC)–Ordinary concrete R30A7.

Figure 7.5: Typical rear-face velocity curves for three tested types of concrete. (Note: markers do not present measurement points)

Concrete	Name	C_0 (m/s)	ρ (kg/m^3)	E_c (GPa)	$\sigma_t^{Novikov}$ (MPa)	$\dot{\varepsilon}$ (1/s)
(OC)						
	SR30G05	3785	2286	32.75	9.71	60
	SR30G0DIC	3890	2275	34.44	7.68	66
	SR30G0DIC	3870	2296	34.39	9.62	55
	SR30D01	4060	2305	38.37	9.91	80
	SR30G02	3740	2341	32.74	10.2	90
	SR30G03	3780	2372	33.8	9.39	85
	SR30G04	3920	2360	36.3	8.86	75
	SR30G05	3880	2350	35.3	10.67	72
	SR30G06	3980	2368	37.52	8.91	80
		3873	2328	35.1		
		±101	±38	±2		
(HPC)						
	SBHP03	4135	2365	40.45	17.6	140
	SBHP01	4190	2426	42.60	13.8	90
	SBHP04	4125	2339	39.79	17.21	200
	SBHP05	4210	2365	41.92	17.89	115
	SBHP06	4120	2435	41.32	12.99	65
		4156	2386	41.3		
		±41	±42	±1.2		
(LC)						
	SLCG01	3995	2362	37.7	10.99	80
	SLCG02	3775	2257	32.2	11.51	100
	SLCG03	3890	2243	33.9	10.23	70
	SLCG04	3870	2252	33.7	12.1	110

Table 7.3: Results from spalling tests conducted on three types of concrete: Ordinary concrete R30A7–(OC), High performance concrete–(HPC), Limestone aggregate concrete–(LC) obtained from point-wise measurements.

pitch (1 mm grid pitch taken in all the tests). In those cases a temporal unwraping had to be used to correct the jumps in displacement evolution [Saldner and Huntley, 1997]. The unwrapping was performed here by computing the incremental phase between consecutive capture frames rather than relative to a reference image. The phase at the analysed frame is then simply obtained by summing the phase increments. In the following, the results obtained on high performance concrete(HPC) and Limestone aggregate concrete (LC) will be presented in terms of reconstructed local stress-strain response. Then, the identified fracture parameters such as specific fracture energy extracted per each macro-fracture visualized within the axial displacement maps, will be presented and compared to some previously obtained results. The experimental details regarding the performed spalling test on (LC) and (HPC) are detaild in Annex D.

7.2.2.1 Identified stress-strain response

The stress-strain response of the tested samples has been obtained following the procedure already shown in Section 3.4.1.3. The average cross-sectional axial stress at an observed location is derived from the axial acceleration component averaged from the free-end to the observed location. The strain maps have been obtained directly from the measured displacement fields using the diffuse approximation approach [Avril et al., 2008b]. All the processing parameters are listed in Table 7.2. The reconstructed stress-strain curves are obtained for several positions along the sample longitudinal axis introducing virtual gauges of 10 mm in length. The positions of the virtual gauges were chosen based on the position of the strain localizations present in the derived axial strain maps. These zones have been associated to the presence of mechanical damage within the sample and it is considered that the material exhibits the maximal bearing capacity (ultimate tensile strength) at the given position. The stress-strain curves presented herein have been obtained by using 1 Mfps recording speed since it allowed obtaining longer recordings within the tensile post-peak material response.

High performance concrete (HPC) The reconstructed stress-strain curves obtained from spalling tests conducted on (HPC) are plotted considering several positions of virtual gauges along the sample length in Figure 7.6. Firstly, a linear elastic material response can be noted in the compressive material response (*i.e.* in the 3^{rd} quadrant) for all plotted curves, confirming the validity of the spalling test. A linear regression was performed on the data in the compressive loading stage and the material compressive Young's modulus was retrieved which was in close agreement to the values identified from point-wise measurements and wave shifting (Table 7.3). Secondly, for all the tested samples it was noticed that the response of the virtual gauge at 30 mm from free-end was quasi-elastic in the tensile loading stage, which indicated that the principal fracture planes were located further from this zone. Therefore, the virtual gauges at 40, 50 and 60 mm from free end were analysed.

Next, the peak tensile stress was observed in between 64 and 67 μs for all test results, which corresponded to an average time of 5 - 6 μs from $\sigma = 0$ up to tensile stress peak after which the material softening response due to damage can be observed. Furthermore, pre-peak non linear response can been observed in the reconstructed stress-strain plots. The non-linear response starts approximately 2 - 3 μs prior to the peak tensile stress which indicates that the non-linear response can be expected at values of about 60% of peak tensile material strength. However, this should be further investigated once a higher temporal resolution is available which would enable to well capture pre-peak non-linear response. Moreover, the observed pre-peak non-linear response confirms that the assumption of the linear elastic material response up to the peak tensile strength is a strong approximation. Performing linear regression on the linear parts of the curve in tensile and compressive loading stage, the retrieved tensile stiffness was found to be in an average 50% lower than the one identified in the compressive loading stage. Finally, for all tested samples the identified peak tensile strength was found to be lower than the one derived from the rear-face velocity pull-back using the Novikov approximation. All the identification results are summarised in Table 7.4.

In the post-peak material response all tested samples exhibited a distinct multiple rebound response. One possible explanation of the observed post-peak rebounds can be tied to the multiple micro-cracking phenomena. The curves presented in Figure 7.6 have been traced until the time point indicated on the graphs. This time corresponded to low axial stress levels and large axial deformation levels, after which the rebounds were less pronounced and were below the signal-to-noise limit ($\leq$ 2 MPa) therefore considered insignificant.

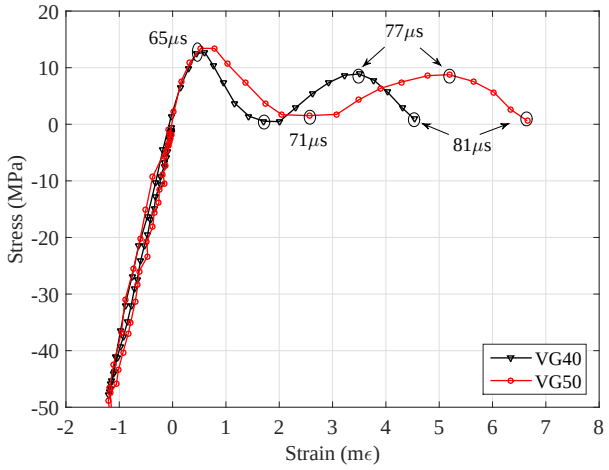

(a) SBHP03.

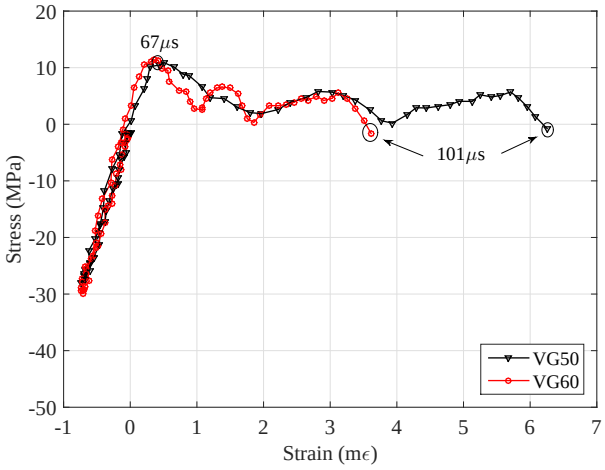

(b) SBHP01.

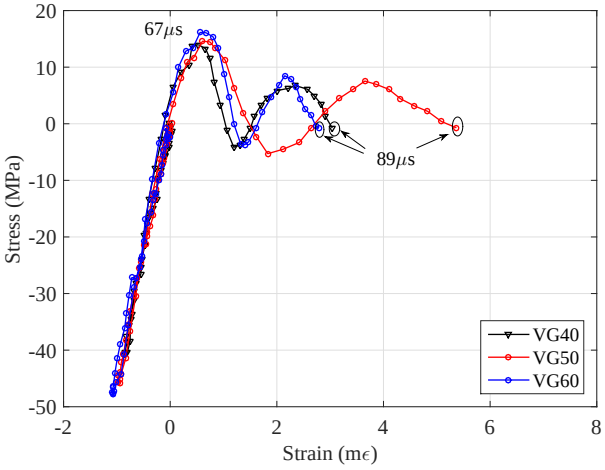

(c) SBHP05.

Figure 7.6: Typical rear-face velocity curves for three tested types of concrete.

When referring to the test SBHP03, one post-peak rebound is observed in stress-strain plots for both virtual gauge at 40 and 50 mm from free-end. The peak tensile stress is reached at 64 μs, then the stress level drops reaching a lowest value at 71 μs after which another increase is observed reaching a local maxima of 8.89 MPa at 77 μs and then finally dropping to zero value at 81 μs. The characteristic axial strain maps of this test are presented in Figure 7.7. Figure 7.7a represents axial strain map at 67 μs after the peak tensile stress is reached while Figure7.7b-d corresponds to the characteristic times indicated in the stress-strain curve Figure 7.6a. Following the evolution of axial strain maps strain, from the very beginning of the post-peak response it can be observed that two principal localization zones form at about 40 and 50 mm from free end. However, another localization is present at 25 mm from the free-end. This zone appears to be obscured by the adjacent macro-fracture at 40 mm by the end of the test. Such situations, where multiple micro-fractures occur simultaneously but one becomes dominant and enforces the closure of the secondary zones can cause relaxation of strain energy which in turn may be tied to the

bumps observed in the post-peak part of the stress strain curves. Although, the temporal and spatial measurement resolution do not allow for more throughout analysis of such phenomena, the clear presence of multiple cracking and possible obscuration phenomena can be noted from the presented strain maps.

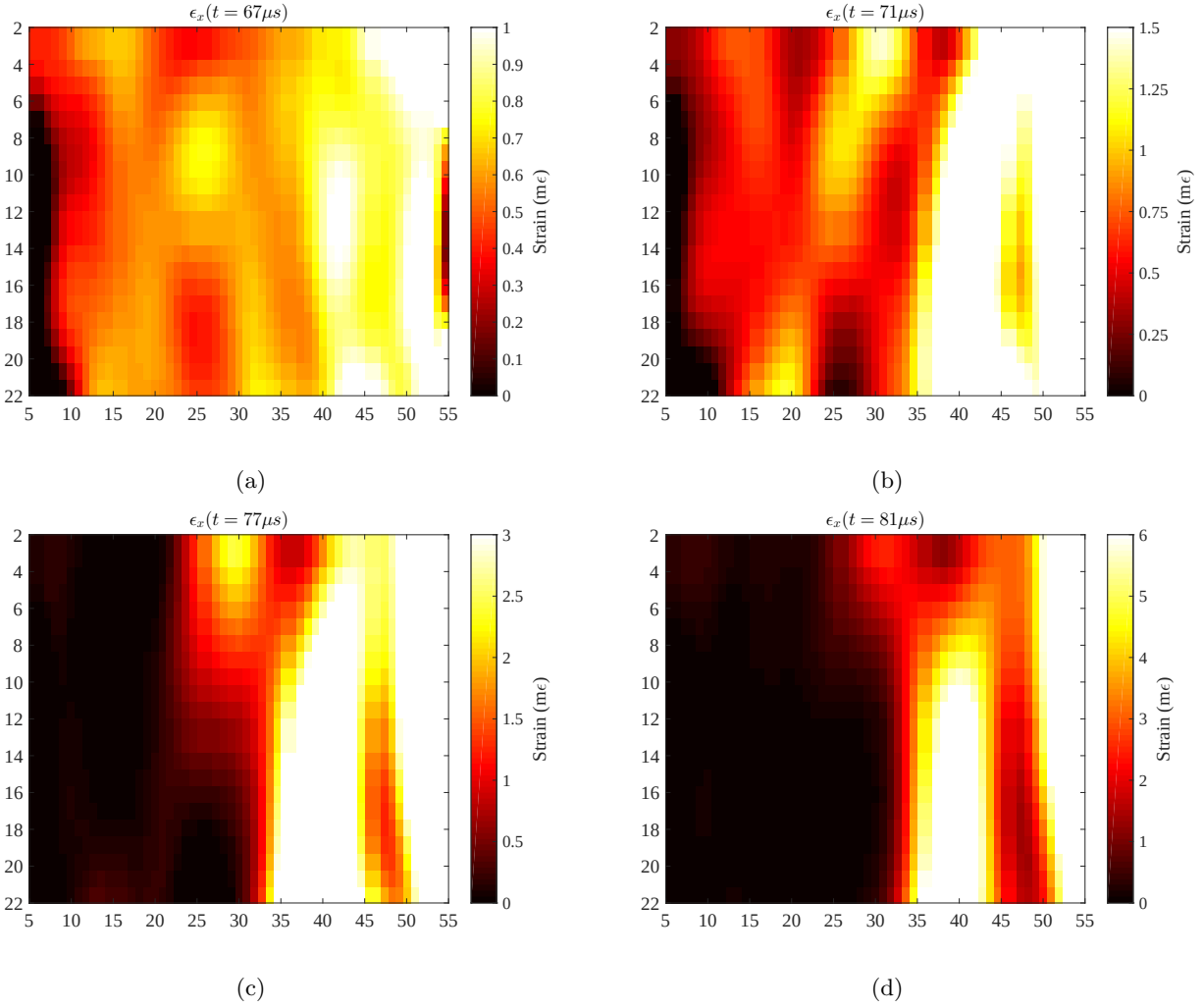

Figure 7.7: Characteristic axial strain maps of the test SBHP03. (Field maps are in (mm) where zero value corresponds to the free-end) Note the change of the colorbar range.

Concrete	V.G. (mm)	E_c^{lin} (GPa)	E_t^{lin} (GPa)	E_t^{lin}/E_c^{lin} (%)	t_{peak} (μs)	$\dot{\varepsilon}$ (1/s)	σ_t (MPa)
SBHP03	40	38.97	18.28	46.9	4	175	12.68
	50	40.28	18.76	46.6	4	205	13.42
SBHP01	50	37.98	18.89	49.9	5	100	10.26
	60	39.11	22.24	56.8	6	75	10.77
SBHP04	30	42.92	30.71	71.5	5	130	15.38
	40	42.84	24.53	57.3	4	170	13.96
SBHP05	40	46.02	19.71	42.8	5	115	13.98
	50	46.19	22.48	42.7	6	139	14.58
SBHP06	30	34.2	24.03	70.3	6	74	11.29

Table 7.4: Identification results using full-field measurements from spalling tests conducted on High performance concrete (HPC). (V.G stand for chosen virtual gauge distance from free-end)

Limestone aggregate concrete (LC) The reconstructed stress-strain response for two spalling tests conducted on Limestone aggregate concrete (LC) are presented in Figure 7.8. The distinctive bumps in the post-peak material response can be observed only for the case of SLCG04. The identified peak tensile strength (Table 7.5) was found to be 60% lower in average than the one obtained with the Novikov approach (Table 7.3), which was unexpected. Looking closely at the stress-strain plots, a hypothesis can be made on a presence of a non-linear response in the compressive loading stage. This could then allude to a situation where the material could be pre-damaged in the compressive stage before the tensile loading starts. The global Young's modulus can be used as a good indicator for checking if any loss of stiffness is present in the overall material response. The global Young's modulus is obtained by using the VFM identification and 8^{th} degree polynomial expansion of the virtual fields is presented in Figure 7.9. It appears that the identified value of global stiffness is not constant in compression but rather monotonically decreases. This might further explain the discrepancies between the obtained peak tensile strength using the two methods.

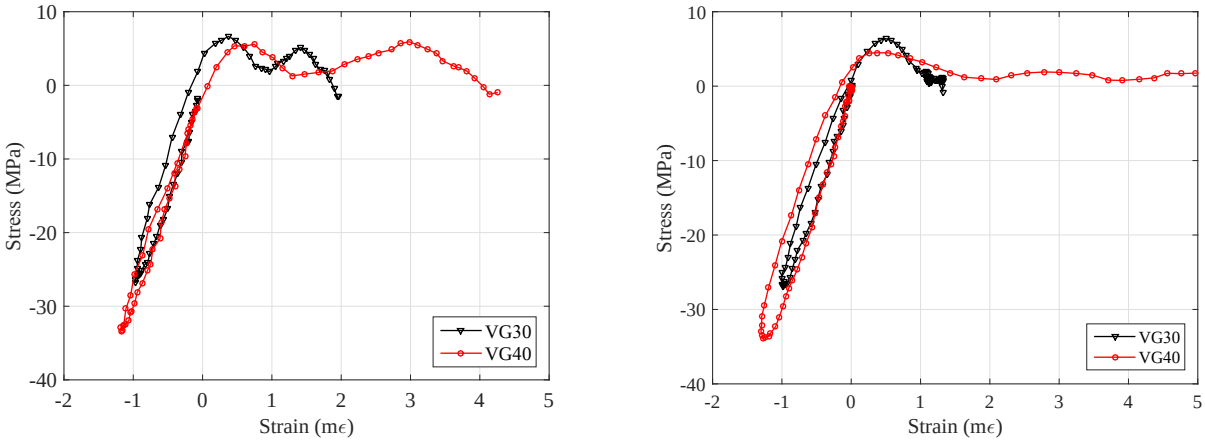

(a) SLCG02. (b) SLCG04.

Figure 7.8: Identified stress-strain curves from two spalling tests conducted on Limestone aggregate concrete (LC) at approximately same strain rate.

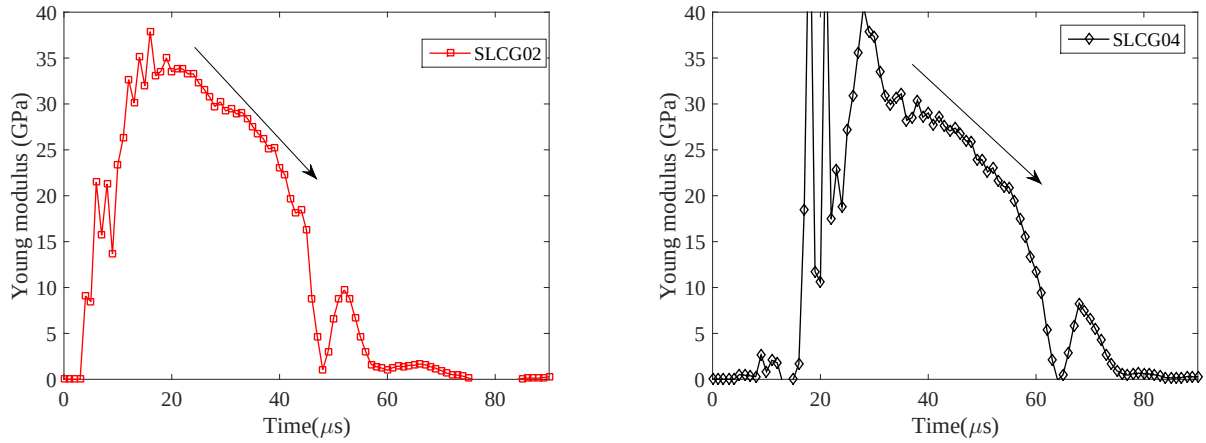

(a) SLCG02. (b) SLCG04.

Figure 7.9: Identified global Young's modulus from the spalling tests conducted on Limestone aggregate concrete (LC).

Concrete	V.G. (mm)	E_c^{lin} (GPa)	E_t^{lin} (GPa)	E_t^{lin}/E_c^{lin} (%)	t_{peak} (μs)	$\dot{\varepsilon}$ (1/s)	σ_t (MPa)
SLCG02	30	37.68	9.89	26.24	5	107	6.45
	40	37.77	10.27	27.19	5	137	5.71
SLCG03	30	35.03	23.23	66.1	5	72	8.22
	40	34.6	18.27	52.8	4.5	102	7.2
SLCG04	30	33.03	10.96	33.18	6	78	5.95
	40	33.39	15.96	47.79	6	140	6.09

Table 7.5: Identification results using full-field measurements from spalling tests conducted on Limestone aggregate concrete (LC). (V.G stand for chosen virtual gauge distance from the free-end). (Note samples have possibly experienced pre-damage during compressive loading stage)

7.2.2.2 Comparison of the results between two measurement methods

The results regarding the peak tensile stress identified directly from the reconstructed stress-strain curves and the corresponding strain rate can be compared to the values obtained from the classical processing of point-wise measurements. In the Section 3.4.1.4 three methods were proposed for obtaining the strain rate at peak tensile stress. Here, the method which uses the time to peak stress is used. The value of strain rate is obtained from the same time frame at which the peak tensile stress is observed, using the same virtual gauge position and size (length 10 mm). The comparison between the values obtained using two measurement methods for two types of concrete are presented in Figure 7.10.

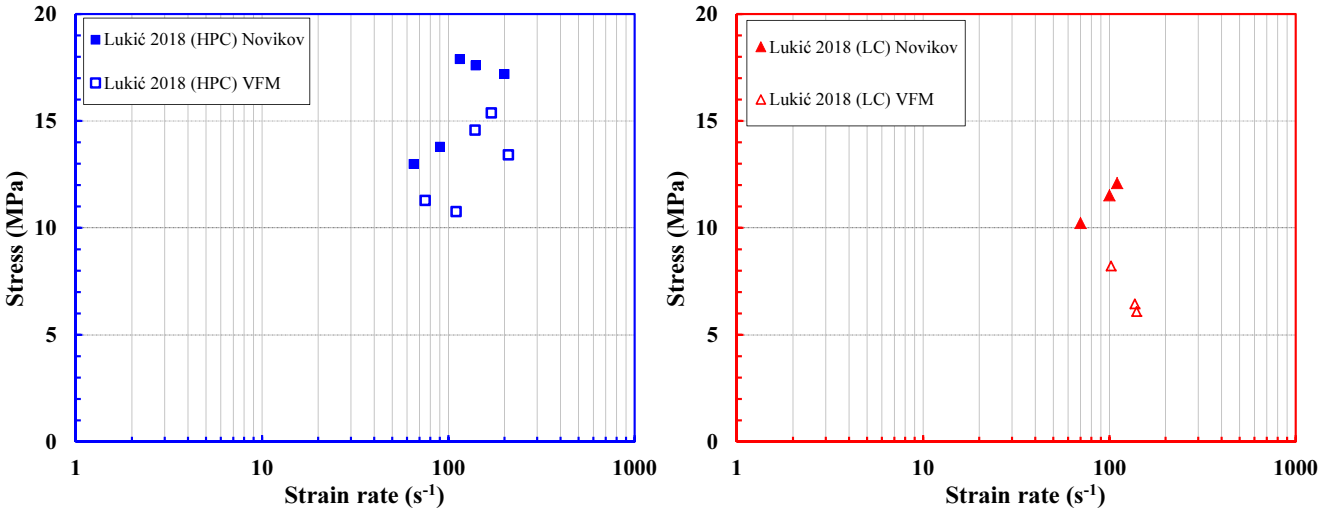

Figure 7.10: Comparison between the results regarding dynamic tensile strength obtained with Novikov approach and using the identification from full fields.

From the presented plot it can be observed that, in case of (HPC), the classical method shows higher dynamic tensile strength of about 20% when compared to the values identified from full field measurements. The main reasons for this over-estimate, as discussed in Section 3.4.2, are the assumption of perfect elasticity upto the peak and the unitary value of Young's modulus in tension and compression. While on the other hand from presented-stress curves in Figure 7.6 and the results reported in Table 7.4 the material stiffness response is not the same in compression and tension and for (HPC) the ratio between the tensile and compressive stiffness is about 54%.

7.2.3 Identified specific fracture energy G_f

In this section the methodology of extracting specific fracture energy per each visualized fracture observed within measured displacement fields that has been detailed in Chapter 5 is applied to spalling tests performed on (HPC). The fracture opening displacements (FOD) are first obtained by introducing a differential displacement gauge around each observable fracture zone. Thanks to a local measurement of axial stress around each visualized fracture, meaningful correction for the elastic response in compression can be applied to the differential displacement measurement. Finally, local Stress-FOD curves can be reconstructed and the specific fracture energy G_F be obtained. The results will be presented and compared to previous works.

7.2.3.1 Fracture opening displacements

As presented in Section 5.2.1 the measured full field displacement maps allow direct visualization of dynamic fracturing which occurs under the dynamic tensile loading. Meaningful descriptors, such as opening of one visualized fracture–fracture opening displacement (FOD) can be obtained from each fracture. These quantities then provide an insight into the phenomena associated to dynamic tensile failure of quasi-brittle materials induced by multiple fracturing phenomena. An example was shown in Section 5.2.1 where two fractures originate but one becomes a dominant one while the secondary one closes. Here, the FOD curves obtained from spalling tests conducted on (HPC) are presented in Figure 7.11 accompanied with last recorded axial displacement map of each test. Only the tests where multiple fracture were captured within the field of view are presented. The FOD curves clearly indicate the complexity of the multiple fracturing phenomena which can be associated to interaction between already initiated fractures and newly created ones. For example, in Figure7.11b, the dominant fracture is the one located at 46 mm. The fracture at 68 mm although arguably initiated with a delay propagates faster than the fracture at 56 mm for the first 10 μs from its insertion and then reaches a plateau after which it starts to close. Another case to fracture interaction can be observed in Figure 7.11d. The fracture at 38 mm appears to be initiated before the fracture at 56 mm. However, it reaches again a plateau and closes while the fracture at 56 mm becomes a dominant fracture. Indeed, in this case, only the macro-crack at 56 mm was observable by naked eye in the post-mortem overview.

7.2.3.2 Reconstructed Stress-FOD curves

The reconstructed Stress-FOD curves and the coresponding fracture opening velocity (FOD) plots are presented in Figure 7.12 concerning several spall tests conducted on (HPC). In the case of test named SBHPG01 only one macro-fracture was observed. When the data regarding the reported strain rate are examined in Table 7.3 regarding point wise or Table 7.4 regarding full field measurements, the value appears to be lower than in the rest of the tests. On the other hand, the two other tests reported in Figure 7.12 were conducted at higher strain rate and clearly exhibited more macro-fracture planes. This observation of increasing number of fracture planes with increasing strain rate has been well observed in the literature by numerous authors (*e.g.* [Klepaczko and Brara, 2001, Weerheijm and Van Doormaal, 2007, Schuler et al., 2006, Erzar and Forquin, 2014]).

When referring to the reconstructed Stress-FOD curves, it can be noticed that in cases of multiple adjacent macro-fractures, the stress values occasionally drop below zero indicating a negative (*i.e.* compressive stress). On the other hand, in the case of SBHPG01 where only one macro-fracture is observed that was not the case. The origin of the negative stress values is currently not understood. Another interesting observation is that in case of multiple fractures (which corresponds to test conducted at higher level of strain rate), the tensile strength is higher; however not all fractures exhibit the same fracture opening capacity. After a certain time period, one fracture exhibits a larger fracture opening and becomes a dominant macro crack that consumes larger amount of fracture energy while the secondary cracks tend to close and consume less energy. It is worth pointing out that these are currently just qualitative observations and that more experimental results are needed to confirm the above hypothesised statements. Finally, all the results regarding the specific fracture energy and the fracture opening velocity for the

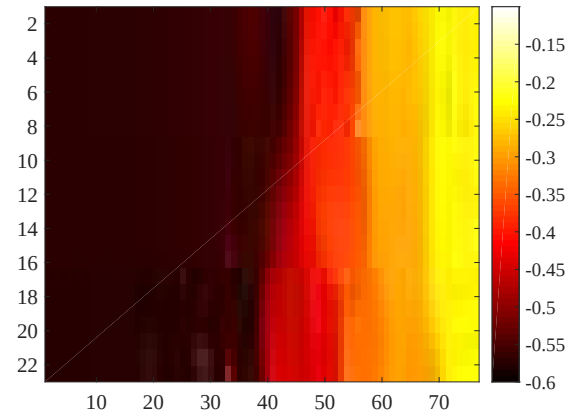

(a) SBHPG05: Final recorded displacement map.

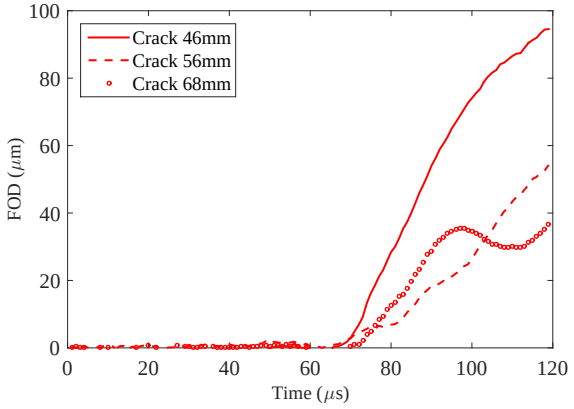

(b) SBHPG05: FOD.

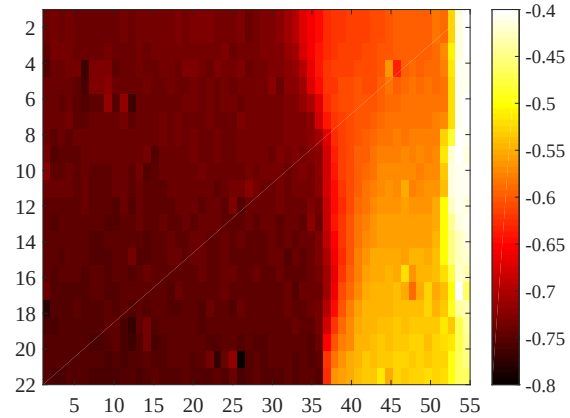

(c) SBHPG03: Final recorded displacement map.

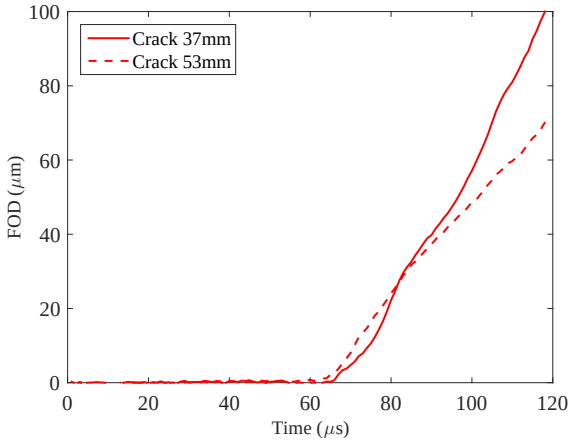

(d) SBHPG03: FOD.

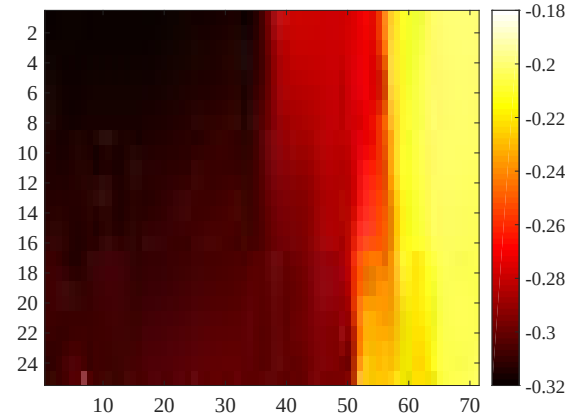

(e) SBHPG06: Final recorded displacement map.

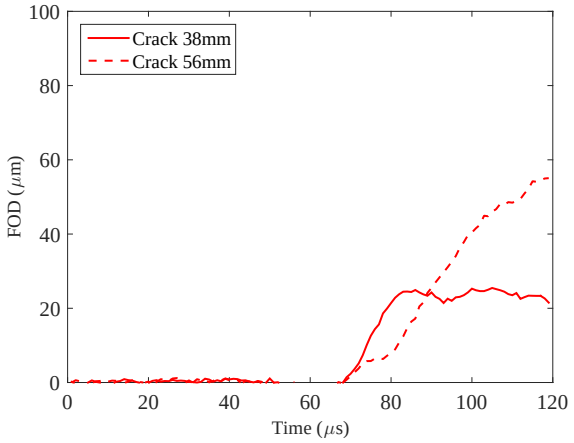

(f) SBHPG06: FOD.

Figure 7.11: Fracture opening displacement (FOD) for several spalling tests conducted on (HPC). (Note: colorbars represent displacement in (mm). Field maps are in (mm) where zero value corresponds to the free-end)

performed spalling tests on (HPC) are synthesised in Table 7.6.

Test	Fracture location (mm)	G_f (J/m^2)	FOV (m/s)
SBHPG03	37	174	2.63
	53	150	1.69
SBHPG01	56	361	2.64
SBHPG05	46	217	2.85
	57	102	1.69
	68	124	1.44
SBHPG06	38	213	2.26
	56	160	1.94

Table 7.6: Identified values of specific fracture energy (G_f) and fracture opening velocity (FOV) per each vizualized dynamic macro-fracture from the spalling tests conducted on (HPC).

7.2.3.3 Comparison with results from the literature regarding G_f

The results regarding specific fracture energy obtained from performing several spalling tests on (HPC) and by using the photomechanical identification procedure (Chapter 5) are presented in Figure 7.13. The results are also compared to the data present in the literature regarding ordinary concrete [Schuler et al., 2006] and high performance concrete [Schuler and Hansson, 2006] as well as with the data of (OC) previously presented in Section 5.2.4. As for further comparison the model prediction according to the preliminary synthesis report regarding the design regulations given by CEB [CEB (Comité Euro-International du Béton), 1988] are traced depending on several levels of quasi-static fracture energy.

From the presented results, it is interesting to note that the experimental values regarding the range of the fracture opening velocity obtained for (HPC) are in the same range as those obtained for (OC) as well as the results reported in the literature for both types of concrete mixtures. However, the values of specific fracture energy obtained for (HPC) is markedly lower compared to the values reported in the literature for similar type of concrete mixture. Furthermore, the range of values obtained on (HPC) in the present study do not significantly differ from the results obtained on (OC). Although the level of identified specific fracture energy in this work differs from the one reported by Schuler *et al.*, it is interesting to note that the cited authors reported the same observation when comparing the values of (HPC) and (OC) (*i.e.* no notable difference). Finally, a clear benefit of the present methodology is that it provides more realistic results and more importantly, since the measurement of G_f is obtained per each visualized fracture, several values may be extracted from just one test in cases where more than one macro fracture occurs.

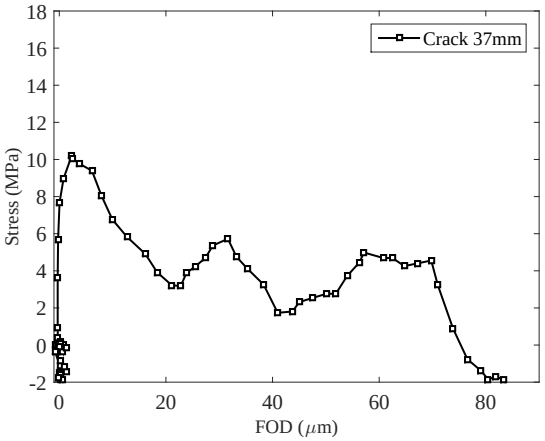

(a) SBHPG01: Stress-FOD.

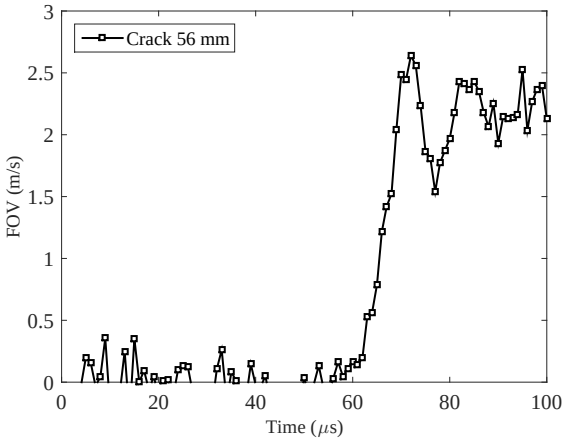

(b) SBHPG01: Fracture opening velocity.

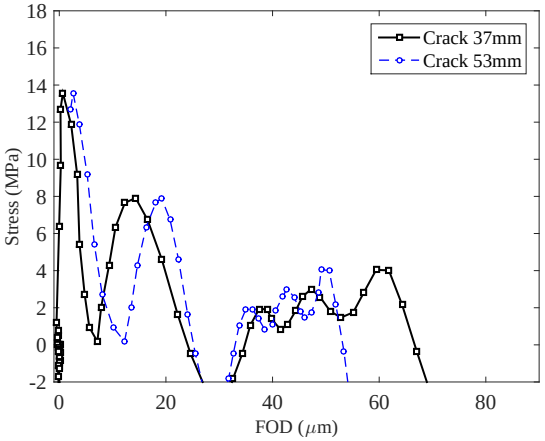

(c) SBHPG03: Stress-FOD.

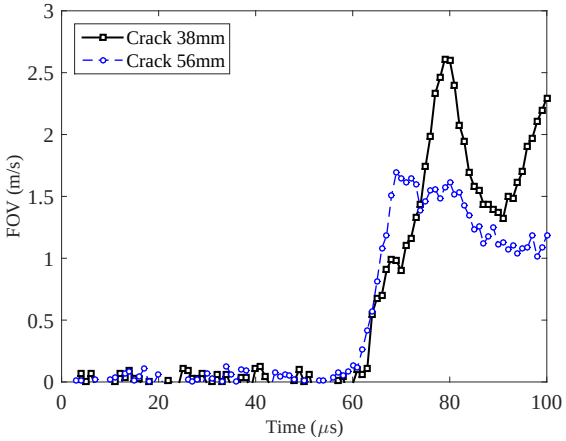

(d) SBHPG03: Fracture opening velocity.

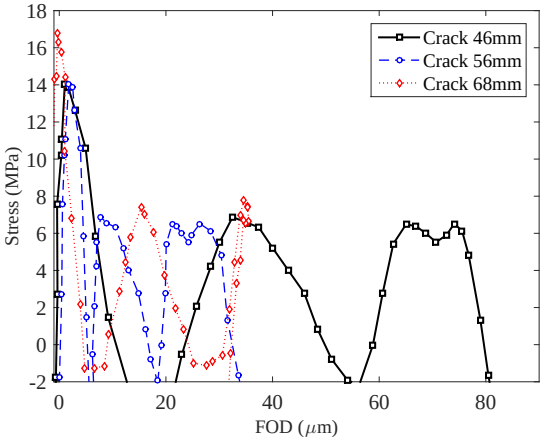

(e) SBHPG05: Stress-FOD.

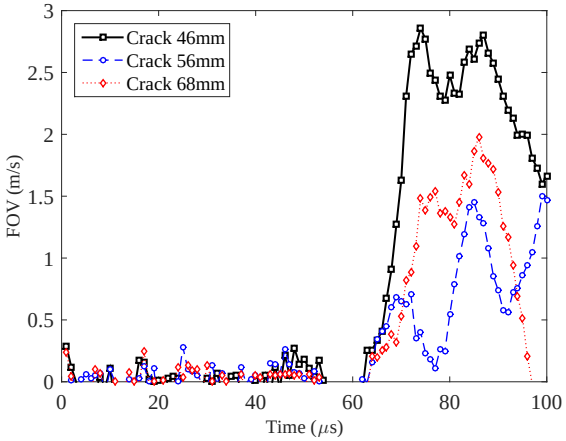

(f) SBHPG05: Fracture opening velocity.

Figure 7.12: Stress-FOD curves for several spalling tests conducted on (HPC) used to extract specific fracture energy per one observed macro-fracture. (SBHPG01: one macro-fracture; SBHPG03: two macro-fractures, SBHPG05: three macro-fractures).

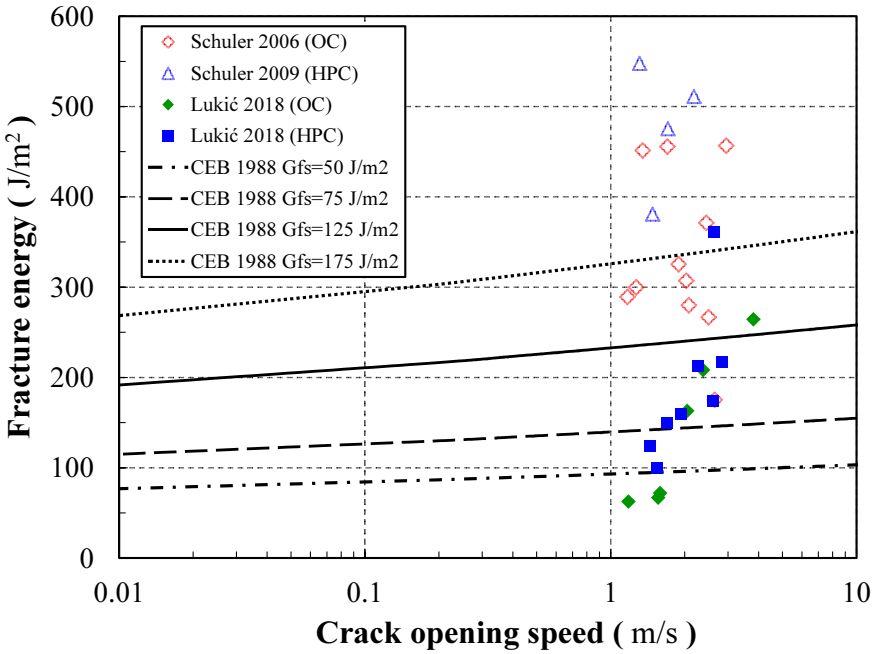

Figure 7.13: Comparison between the results regarding specific fracture energy obtained for each observable macro-fracture in HPC with the data in the literature and data from previous works.

7.3 Chapter summary

In this chapter, spalling experiments have been performed on three different types of concrete compositions namely, ordinary concrete (OC), limestone aggregate concrete (LC) and high performance concrete (HPC). The Shimadzu HPV-X2 camera was used to film a 1 mm grid deposited on the sample surface in order to obtain the time resolved displacement fields which were then processed with the VFM, as detailed in previous chapters. The experimental investigation was aimed at examining the effect of concrete composition and type of granulometric content on the dynamic tensile strength and the specific fracture energy. Alongside full field measurements, conventional point-wise measurements were also taken. This enabled the comparison between the results obtained from the full field identification method and those obtained with the classical processing of spalling tests. It was found that in case of (HPC) the tensile strength identified with the VFM processing was in average 20% lower than the values obtained when the Novikov processing of the rear face velocity pull-back is used. When comparing different concrete grades, (HPC) exhibited higher tensile strength than (OC) and (LC). It is necessary to mention that all tested samples went through a temperature treatment in order to apply proper curing of the glued grid substrate which implies that the samples can be considered to be in dry conditions. The specific fracture energy and the fracture opening velocity was determined for in case of (HPC) samples. Full stress-FOD curves were reconstructed per each visualized fracture in the displacement fields. The results obtained are markedly lower than the results found in the literature being on the average 187.6 $\pm$ 80 J/m^2 for a fracture opening velocity of 2.14 $\pm$ 0.53 m/s. It is worth mentioning that distinct bumps were observed in the post peak regime in the reconstructed stress-FOD curves. Although, in case when only one fracture was observed these were less pronounced than in cases when multiple adjacent fractures were present, the true origin of such behaviour is not known. Therefore as a perspective it remains that additional experiments have to be performed preferably with another full field measurement technique. So that the possible influence of the measurement methodology can be excluded.

Chapter 8

General Summary and Perspectives

8.1 General Summary

This thesis work focused on investigating a photomechanical dynamic tensile testing method and applying it to test several grades of concrete material. The experimental method consists of the so-called spalling test set-up, based on a use of a single Hopkinson bar placed in contact with a concrete sample on one end and impacted by a cylindrical projectile on the other end. Ultra-high speed imaging was used to film the sample surface and the grid method was used to obtain the time resolved full field displacement maps during the test. Thanks to the sample non-equilibrium state, the acceleration fields, that are derived from the obtained displacement maps, can be directly related to the average axial stress in the each cross-section, visualised by the camera, by using the virtual fields method. In this way, local constitutive response in terms of stress-strain curves can be identified. Alongside full field, point-wise measurements were performed as well, comparing back-to-back the identified results regarding the material tensile strength and corresponding strain rate. However, before the direct application of the method on investigating concrete material behaviour at high strain rates, its application was explored through several experimental campaigns. Although, the work performed is of experimental nature some simple numerical investigations were performed along the way to explore further the observed effects. A general summary of work presented in relevant chapters follows:

- In Chapter 3: several tests performed outside of this thesis have been analysed. These were performed using the Shimadzu HPV-1 camera. The first group consisted of the test performed on an aluminium alloy of known characteristics. These were treated in light of retrieving expected linear elastic material parameters as to perform benchmark of experimental settings that were later used for testing concrete material which consisted the second groupe of analysed data. The results obtained on ordinary concrete were compared with the results from classical processing of point wise measurements [Erzar and Forquin, 2010] using the rear face velocity profile and the Novikov formula (Equation 3.3). The discrepancy was noticed in terms of deduced material tensile strength. The results from the VFM identification were found to be lower than the ones provided by the Novikov processing. Furthermore, a non-symmetric response as well as pre-peak non-linear response was observed in the reconstructed stress-strain curves. The effect of these observations was then investigated through simple numerical simulations that incorporated the Mazars' damage model and the ability to account for both non-symmetric response and pre-peak non-linear response. It was found that both effects can influence the rear face velocity profile questioning the use of the Novikov formula for obtaining tensile strength of quasi-brittle materials at high strain rates.

- In Chapter 4: a numerical procedure was devised in order to validate the VFM processing. It consists of simulating the spalling experiment with the linear elastic FE explicit computations which provided time resolved displacement fields. These were treated within the VFM, successfully validating the procedure. Although this was the main purpose (and the main result), the method was extended to simulating the entire chain of measurements involved in the photomechanical spalling experiment. This includes simulation of synthetically deformed grid images based on FE formulation and image interpolation. This method proved to be a useful tool to investigate some of the often encountered experimental uncertainties as well as to place guidelines on what can be an optimal acquisition system.

- In Chapter 5: the rich amount of data embedded in the displacement fields of the tests performed on concrete

samples (presented in Chapter 3) were further analysed in order to extract the information on the concrete specific fracture energy per each visualized fracture in the displacement maps. The first results retrieved on concrete material were found to be lower than the results presented in the literature obtained with an indirect measurement techniques based on impulse transfer method [Schuler et al., 2006]. Numerical simulations employing a crack-band approach and the Mazars' damage model were performed to test the two techniques and it was found that having a local measurement kinematic content (such as the one provided by full field displacement maps) allows more reliable extraction of the values of specific fracture energy. Furthermore, the method was also explored using the photomechanical simulation procedure presented in Chapter 4 which successfully validated the entire chain of measurement suggesting (for the time being) that the accuracy of the method lies within 5% confidence interval.

- In Chapter 6: two ultra-high speed cameras were tested in light of investigating the possible refinement of the measurement brought by the latest CMOS based sensor technology. The Kirana camera and the Shimadzu HPV-X2 camera were tested performing spalling experiments on an aluminium allow. Although highly superior in pixel count and number of stored frames, the Kirana camera was found to be less suitable for the measurement of the acceleration field and the Shimadzu HPV-X2 was chosen to conduct the experiments on concrete. Furthermore, this chapter also shows that the spalling set-up can present one good candidate for evaluating the application of UHS imaging systems as well as their metrological performance regarding full field measurement under dynamic conditions.

- In Chapter 7: the photomechanical spalling test was used on several grades of concrete materials, namely high performance concrete (HPC), limestone aggregate concrete (LC) and ordinary concrete (LC). The results regarding material tensile strength were compared to the results of the Novikov formula confirming the systematically lower values of tensile strength provided by the VFM processing. Although, the number of tests performed are low and not all photographical content was exploitable, two principal observations were made. First, it was found that the VFM processing provides results of tensile strength of about 20% lower than the Novikov formula. Finally, the results regarding the fracture energy of (HPC) were found to be lower than the results presented in the literature [Schuler and Hansson, 2006].

The work presented in this thesis leaves many open questions. Consequently, drawing out conclusions (*i.e.* writing the section named: *Conclusions*) seems currently inconceivable. On the other hand, the work leaves ample room for future improvements as well as experimental investigations. Therefore writing a section named: *Perspectives* rather than *Conclusions* seems more appropriate. Some of these perspectives will be presented in the following section.

8.2 Perspectives

This section tries to wrap up some of the prominent perspectives of the work performed in this thesis. It contains principal ideas and suggestions on how to address future improvements as well as suggestions regarding future experimental works.

8.2.1 Improvements of the simulated photomechanical experiments

In this thesis a method of simulating the entire experimental chain has been developed. It is based on recreating synthetic grid image sequences using image interpolation techniques that can encode a simulated linear (or non-linear) material response assuming a ultra-high speed hypothetical camera.

Some of the perspectives for the improvement of this simple tool can be focused on:

- Improving the interpolation scheme used to deform the synthetic images.
  Currently, this is done by using cubic-spline formulation native for the Matlab environmental. Using higher

order splines as well as possibility of introducing additional spline knots in the zones (for example close to the simulated non-linearity) of interest, could improve the method by reducing the interpolation bias that is currently a limiting factor. Therefore this perspective can be considered as an imperative in order to reduce (as much as possible) the numerical bias present in the synthetic images.

- Considering more realistic photographical situations.
  More realistic situations concerning illumination content should be adopted in order to account for more realistic representation of an experimental enviornement [Badaloni et al., 2015]. Additional sugestion is aimed at accounting for realistic lens deformation and investigating how it can impact the entire identification method [Lava et al., 2013].

- Considering more realistic representation of an acquisition system.
  Presently, the simulation procedure adopts a perfect camera assumption with 100% fill factor. Obviously, these are not close to a realistic imaging sensor and the work aimed towards accounting for realistic properties remains a strong perspective. UHS imaging systems with on board memory suffer from low fill factor dedicated to the photosensitive region of one pixel. Often the fill factor is not the same with respect to horizontal and vertical axis of the the camera sensor. Simulating such effects would provide more insight on possible parasitic effects that could affect the deformation content. This can be performed in the current procedure by introducing non-equal kernel that down-samples the synthetic image. However, attention needs to be paid towards remaining on true pixel positions. Some instructions can be found in [Rossi and Pierron, 2012].

- Simulating other possible sources of errors that can affect the grid method.
  These include simulating missing data due to the non perfect grid pattern. Two cases can be considered: complete loss of data (Nan) or having the substrate not well transferred on the surface (discontinuous lines). Another effect that should be considered and that can often be experienced when performing real experiments is a continuously varying grid pitch through non-integer grid sampling.

- Scripting optimisation and compilation into an integrated automatized procedure.
  In its current form, the tool presents a set of scripts performing communication between several different software packages. An optimisation of this procedure is clearly needed as well as making it more user independent. Finally, performing a passage towards open-source platforms is highly encouraged.

Another prominent perspective, that requires special attention, is focused on accounting for realistic camera noise effects of an particular camera. In UHS imaging systems two principal types of noise affect the acquisition: one in spatial and the other one in temporal domain. Attempts should be made on numerically modelling these two noise components by analysing images captured with real acquisition systems. One more approach is to directly deform the true images captured by the UHS system. For example, taking an acquisition sequence of a still sample and then embedding simulated elastic response into those images. However, one should anticipate elevated interpolation bias since images provided by current UHS cameras are of low pixel count. The underlining idea of the above two mentioned approaches is to test and to provide information if one specific acquisition system fits to the desired purpose or not and to attempt to exploit the intrinsic noise content in the identification.

8.2.2 Further investigation with the current version of the image simulator

The above mentioned perspectives, can be regarded as a part of a long term development. However, some studies can be performed with the simulation procedure in its current form (short term), which either have not be performed in this work or have been only started. These include:

- Investigation of the eccentricity of the loading on the spalling sample.
  Due to the fabrication of the flattened surface on the concrete samples it is often difficult to exactly position the sample so that its axis well coincides with the axis of the bar. Although it could be suspected that

this effects have low impact on the identification of the true material stiffness, numerical work should be performed to confirm this assumption.

- Investigating the effects of camera tilt and sample parallelism.
  Some of these questions have been raised in Section 4.4.2.1, however the work should be extended towards accounting for possible camera tilt and sample tilt due to non-perfect parallelism between the impact and the free-end surface of the sample.

- Numerically simulating the effect of glue used to deposit the grid.
  Although some work is presented in the Annex A it still remains as an open question: to which extent the methodology of glueing the grid disrupts (or not) the measurement of the material response especially in the post peak region. To do so, a more realistic numerical modelling of the used adhesive should be considered. The parameters, for example regarding the tensile strength, can be obtained by performing spalling test on a aluminium sample that consisted of two glued parts. Aside from that, the method can be coupled with the VFM processing and used for a general investigation of the strength of adhesives at high strain rates.

8.2.3 Creating non-biased images for investigating accuracy performance

The primary function of the image simulation tool from this work, remains: *it is just a tool* for an experimentator to know and understand how to perform an experiment more effectively. As such, it can be used to provide *estimates* on how some error sources present in the experimental environment could eventually disrupt the measurement. Although, it can be used to provide basic understanding on the sensitivity of the measurement in a qualitative manner, in its current form, it cannot be used to provide quantitative analysis of the accuracy of the identification method. To do so, one needs non-biased realistic images that encode ground truth information [Bornert et al., 2012]. Unlike to speckle images, the synthetic grid images can be generated so that they are completely non-biased by simply hard-encoding the spatial modulation of the phase in the analytical description of the numerical grid image [Badulescu et al., 2013] (Equation 7 in the cited work). A possible adaptation to this work would be that simulated FE displacement fields are interpolated to fictive pixel super-samples and that at each such position the phase modulation is performed.

Digression:

Another very prominent perspective concerning the image simulation procedure can be, in fact, summarized in one figure (Figure 8.1).

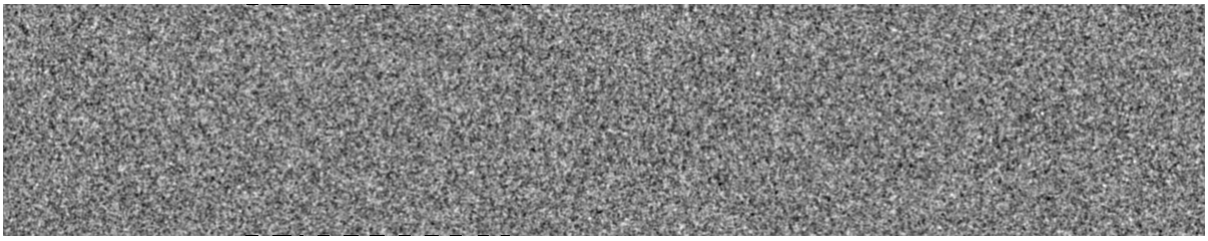

Figure 8.1: Synthetic speckle image that encodes linear elastic response of a simulated spalling test, obtained assuming a hypothetical UHS camera with 2 Mfps acquisition speed, 16 bit encoding and 1200x231 pixel count. (Speckle generated based on purely random pattern and FFT blur.) (The image alludes to possible perspectives of numerically investigating the use of Digital Image Correlation in a spalling test.)

8.2.4 Perspectives regarding experimental testing of concrete

In this work several concrete grades were tested; however, the number of tests appears scarce to draw any firm conclusions on the effect of concrete composition on its strain rate sensitivity in dynamic tension, since not all photographical data was exploitable. Therefore, as a strong perspectives it remains to perform additional testing considering same concrete compositions.

However, before doing so, an experimental campaign should be devoted to performing spalling test with another full-field measurement method, such as Digital Image Correlation (DIC) (see Figure 8.2). The main reason for this is to investigate the occurrence of the post-peak bumps that were observed in all the identified stress-strain curves. Aside from the fact that using DIC would exclude the possible effect of the measurement methodology on the identified results, it also would open the possibility of using some of recently proposed spatio-temporal regularisation methods which can have a positive effect on the reducing the measurement uncertainty [Besnard et al., 2012, Hild et al., 2018]. One very recently proposed method explores the possibility of using space-time regularisation method in order to use lower acquisition speeds [Passieux et al., 2018]. These methods together with the use of an UHS system with a large pixel count (such as the Kirana camera), may be considered as a prominent perspective. Finally, the use of DIC would alleviate the shortcomings of gluing the grid and add more experimental liberty with setting up one experiment as well as testing samples in wet conditions. Indeed, this would allow using the experimental methodology to investigate the well observed effects of free-water content in the sample on the increased tensile strength at high strain rates [Rossi et al., 1992, Ross et al., 1996, Erzar and Forquin, 2011].

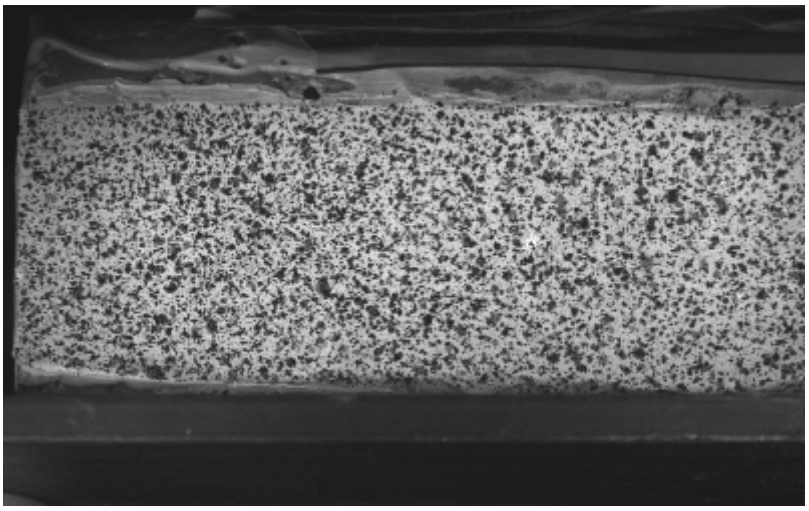

Figure 8.2: Synthetic speckle image of a concrete spall sample capture with the Shimadzu HPV-X2 with 1 Mfps acquisition speed.

Bibliography

[CEB, 1993] (1993). *Ceb-Fip Model Code 1990*.

[Abdul Rahman, 2018] Abdul Rahman, R. (2018). *Experimental Analysis of the confined behavior of concrete under static and dynamic shear loading*. PhD thesis, Univerity Grenoble Alpes.

[Albertini and Montagnani, 1994] Albertini, C. and Montagnani, M. (1994). Study of the true tensile stress-strain diagram of plain concrete with real size aggregate ; need for and design of a large Hopkinson bar bundle. *Le Journal de Physique IV*, 04(C8):C8–113–C8–118.

[Antoun et al., 2002] Antoun, T., Seaman, L., Curran, D. R., Kanel, G. I., Razorenov, S. V., and Utkin, A. V. (2002). *Spall Fracture*.

[Asprone et al., 2009] Asprone, D., Cadoni, E., and Prota, A. (2009). Experimental Analysis on Tensile Dynamic Behavior of Existing Concrete under High Strain Rates. *ACI Structural Journal*, (106).

[Avril et al., 2008a] Avril, S., Bonnet, M., Bretelle, A.-S. S., Grédiac, M., Hild, F., Ienny, P., Latourte, F., Lemosse, D., Pagano, S., Pagnacco, E., and Pierron, F. (2008a). Overview of Identification Methods of Mechanical Parameters Based on Full-field Measurements. *Experimental Mechanics*, 48(4):381–402.

[Avril et al., 2008b] Avril, S., Feissel, P., Pierron, F., and Villon, P. (2008b). Estimation of the strain field from full-field displacement noisy data. Comparing finite elements global least squares and polynomial diffuse approximation. *European Journal of Computational Mechanics*, 17(5-6-7):857–868.

[Avril et al., 2012] Avril, S., Feissel, P., Pierron, F., and Villon, P. (2012). Estimation of the strain field from full-field displacement noisy data. *European Journal of Computational Mechanics/Revue Européenne de Mécanique Numérique*.

[Avril et al., 2004a] Avril, S., Ferrier, E., Vautrin, A., Hamelin, P., and Surrel, Y. (2004a). A full-field optical method for the experimental analysis of reinforced concrete beams repaired with composites. *Composites Part A: Applied Science and Manufacturing*, 35(7-8):873–884.

[Avril et al., 2004b] Avril, S., Grédiac, M., and Pierron, F. (2004b). Sensitivity of the virtual fields method to noisy data. *Computational Mechanics*, 34(6):439–452.

[Babuška and Melenk, 1997] Babuška, I. and Melenk, J. M. (1997). The Partition of unity method. *International Journal for Numerical Methods in Engineering*, 40(4):727–758.

[Badaloni et al., 2015] Badaloni, M., Rossi, M., Chiappini, G., Lava, P., and Debruyne, D. (2015). Impact of Experimental Uncertainties on the Identification of Mechanical Material Properties using DIC. *Experimental Mechanics*, pages 1411–1426.

[Badulescu, 2010] Badulescu, C. (2010). *Calcul précis des déformations planes par la méthode de la grille. Application à l'étude d'un multicristal d'aluminium*. PhD thesis.

[Badulescu et al., 2013] Badulescu, C., Bornert, M., Dupré, J.-C., Equis, S., Grédiac, M., Molimard, J., Picart, P., Rotinat, R., and Valle, V. (2013). Demodulation of Spatial Carrier Images: Performance Analysis of Several Algorithms Using a Single Image. *Experimental Mechanics*, 53(8):1357–1370.

[Badulescu et al., 2009a] Badulescu, C., Grediac, M., and Mathias, J. D. (2009a). Investigation of the Grid Method for Accurate In-Plane Strain Measurement. *Measurement Science and Technology*, 20(9).

[Badulescu et al., 2009b] Badulescu, C., Grédiac, M., Mathias, J. D., and Roux, D. (2009b). A procedure for accurate one-dimensional strain measurement using the grid method. *Experimental Mechanics*, 49(6):841–854.

[Balcaen et al., 2017a] Balcaen, R., Reu, P. L., Lava, P., and Debruyne, D. (2017a). Experimental Mechanics Stereo-DIC uncertainty quantification based on simulated images Stereo-DIC uncertainty quantification based on simulated images.

[Balcaen et al., 2018] Balcaen, R., Reu, P. L., Lava, P., and Debruyne, D. (2018). Influence of Camera Rotation on Stereo-DIC and Compensation Methods. *Experimental Mechanics*.

[Balcaen et al., 2017b] Balcaen, R., Wittevrongel, L., Reu, P. L., Lava, P., and Debruyne, D. (2017b). Stereo-DIC Calibration and Speckle Image Generator Based on FE Formulations. *Experimental Mechanics*.

[Barhli et al., 2017] Barhli, S. M., Mostafavi, M., Cinar, A. F., Hollis, D., and Marrow, T. J. (2017). J-Integral Calculation by Finite Element Processing of Measured Full-Field Surface Displacements. *Experimental Mechanics*, pages 1–13.

[Bazant, 1991] Bazant, Z. P. (1991). *Current Trends in Concrete Fracture Research*. Springer Netherlands, Dordrecht.

[Bažant, 2001] Bažant, Z. P. (2001). Concrete fracture models: Testing and practice. *Engineering Fracture Mechanics*, 69(2):165–205.

[Bažant and Oh, 1983] Bažant, Z. P. and Oh, B. H. (1983). Crack band theory for fracture of concrete. *Matériaux et Constructions*, 16(3):155–177.

[Bažant et al., 1994] Bažant, Z. P., Ožbolt, J., and Eligehausen, R. (1994). Fracture Size Effect: Review of Evidence for Concrete Structures. *Journal of Structural Engineering*, 120(8):2377–2398.

[Belytschko and Black, 1999] Belytschko, T. and Black, T. (1999). Elastic crack growth in finite elements with minimal remeshing. *International Journal for Numerical Methods in Engineering*, 45(5):601–620.

[Berghaus and Cannon, 1973] Berghaus, D. G. and Cannon, J. P. (1973). Obtaining derivatives from experimental data using smoothed-spline functions. *Experimental Mechanics*, 13(1):38–42.

[Besnard et al., 2012] Besnard, G., Leclerc, H., Hild, F., Roux, S., and Swiergiel, N. (2012). Analysis of image series through global digital image correlation. *The Journal of Strain Analysis for Engineering Design*, 47(4):214–228.

[Bischoff and Perry, 1991] Bischoff, P. and Perry, S. (1991). Compressive behaviour of concrete at high strain rates. *Materials and Structures*, 24:425–450.

[Bomarito et al., 2017] Bomarito, G. F., Hochhalter, J. D., and Ruggles, T. J. (2017). Development of Optimal Multiscale Patterns for Digital Image Correlation via Local Grayscale Variation. *Experimental Mechanics*, pages 1–12.

[Bornert et al., 2009] Bornert, M., Brémand, F., Doumalin, P., Dupré, J. C., Fazzini, M., Grédiac, M., Hild, F., Mistou, S., Molimard, J., Orteu, J. J., Robert, L., Surrel, Y., Vacher, P., and Wattrisse, B. (2009). Assessment of digital image correlation measurement errors: Methodology and results. *Experimental Mechanics*, 49(3):353–370.

[Bornert et al., 2012] Bornert, M., Doumalin, P., Dupré, J., Poilane, C., Robert, L., Toussaint, E., and Wattrisse, B. (2012). Short Remarks About Synthetic Image Generation in the Context of the Assessment of Sub-Pixel Accuracy of DIC. *15th International Conference on Experimental Mechanics*, (July 2012):1–10.

[Brara et al., 2001] Brara, A., Camborde, F., Klepaczko, J. R., and Mariotti, C. (2001). Experimental and numerical study of concrete at high strain rates in tension. *Mechanics of Materials*, 33(1):33–45.

[Brara and Klepaczko, 2006] Brara, a. and Klepaczko, J. R. (2006). Experimental characterization of concrete in dynamic tension. *Mechanics of Materials*, 38(3):253–267.

[Brara and Klepaczko, 2007] Brara, A. and Klepaczko, J. R. (2007). Fracture energy of concrete at high loading rates in tension. *International Journal of Impact Engineering*, 34(3):424–435.

[Cadoni et al., 2001a] Cadoni, E., Labibes, K., Albertini, C., Berra, M., and Giangrasso, M. (2001a). Strain-rate effect on the tensile behaviour of concrete at different relative humidity levels. *Materials and Structures*, 34(February):21–26.

[Cadoni et al., 2001b] Cadoni, E., Labibes, K., Berra, M., Giangrasso, M., and Albertini, C. (2001b). Influence of aggregate size on strain-rate tensile behavior of concrete. *ACI Materials Journal*, 98(3):220–223.

[Cadoni et al., 2006] Cadoni, E., Solomos, G., and Albertini, C. (2006). Mechanical Characterization of Concrete at High Strain-Rate by a Modified Hopkinson Bar : a Tool in Blast and Impact Structural Assessment and Design. *Federation Internationale du Beton Proceedings of the 2nd International Congress June 5-8, 2006 - Naples, Italy*, 11.

[Cadoni et al., 2009] Cadoni, E., Solomos, G., and Albertini, C. (2009). Mechanical characterisation of concrete in tension and compression at high strain rate using a modified Hopkinson bar. *Magazine of Concrete Research*, 61(3):221–230.

[Cadoni et al., 2013] Cadoni, E., Solomos, G., and Albertini, C. (2013). Concrete behaviour in direct tension tests at high strain rates. *Magazine of Concrete Research*, 65(11):660–672.

[CEB (Comité Euro-International du Béton), 1988] CEB (Comité Euro-International du Béton) (1988). Concrete Structures under Impact and Impulsive Loading.

[Chalal et al., 2006] Chalal, H., Avril, S., Pierron, F., and Meraghni, F. (2006). Experimental identification of a nonlinear model for composites using the grid technique coupled to the virtual fields method. *Composites Part A: Applied Science and Manufacturing*, 37(2):315–325.

[Chalal et al., 2004] Chalal, H., Meraghni, F., Pierron, F., and Grédiac, M. (2004). Direct identification of the damage behaviour of composite materials using the virtual fields method. *Composites Part A: Applied Science and Manufacturing*, 35(7-8):841–848.

[Chen and Osovski, 2018] Chen, S. and Osovski, S. (2018). A new specimen for growing dynamic cracks along a well defined path using stress wave loading. *Engineering Fracture Mechanics*, 191(January):102–110.

[Chrysochoos and Surrel, 2012] Chrysochoos, A. and Surrel, Y. (2012). *Basics of Metrology and Introduction to Techniques*, pages 1–30. John Wiley & Sons, Inc., Hoboken, NJ USA.

[Cifuentes et al., 2013] Cifuentes, H., Alcalde, M., and Medina, F. (2013). Measuring the size-independent fracture energy of concrete. *Strain*, 49(1):54–59.

[Claire et al., 2004] Claire, D., Hild, F., and Roux, S. (2004). A finite element formulation to identify damage fields: The equilibrium gap method. *International Journal for Numerical Methods in Engineering*, 61(2):189–208.

[Conneely et al., 2011] Conneely, M., Rolfsnes, H. O., Main, C., McGloin, D., and Campbell, P. A. (2011). On the accuracy of framing-rate measurements in ultra-high speed rotating mirror cameras. *Optics Express*, 19(17):16432.

[Considine et al., 2017] Considine, J., Pierron, F., Turner, K., Lava, P., and Tang, X. (2017). Smoothly varying in-plane stiffness heterogeneity evaluated under uniaxial tensile stress. *Strain*, (January):e12237.

[Considine et al., 2016] Considine, J., Pierron, F., and Turner, K. T. (2016). Use of VFM for Heterogeneity Evaluation of Materials Under Uniaxial Tensile Stress. volume 4 of *Conference Proceedings of the Society for Experimental Mechanics Series*, pages 61–66. Springer International Publishing, Cham.

[Cooreman et al., 2007] Cooreman, S., Lecompte, D., Sol, H., Vantomme, J., and Debruyne, D. (2007). Elasto-plastic material parameter identification by inverse methods: Calculation of the sensitivity matrix. *International Journal of Solids and Structures*, 44(13):4329–4341.

[Courtney-Pratt, 1957] Courtney-Pratt, J. S. (1957). A review of the methods of high-speed photography. *Reports on Progress in Physics*, 20(1):379.

[Crammond et al., 2013] Crammond, G., Boyd, S., and Dulieu-Barton, J. (2013). Speckle pattern quality assessment for digital image correlation. *Optics and Lasers in Engineering*, 51(12):1368–1378.

[Crooks et al., 2013a] Crooks, J., Marsh, B., Turchetta, R., Taylor, K., Chan, W., Lahav, A., and Fenigstein, A. (2013a). Kirana: a solid-state megapixel uCMOS image sensor for ultrahigh speed imaging. In Widenhorn, R. and Dupret, A., editors, *Sensors, Cameras, and Systems for Industrial and Scientific Applications XIV*, volume 8659, page 865903.

[Crooks et al., 2013b] Crooks, J., Marsha, B., Turchettaa, R., and J. Crooks R. Turchetta, K. Taylor, W. Chan, A. Lahav, A. Fenigstein, B. M. (2013b). Ultra-high speed imaging at megaframes per second with a megapixel CMOS image sensor. *International Image Sensor Workshop*, pages 4–7.

[Curbach and Eibl, 1990] Curbach, M. and Eibl, J. (1990). Crack velocity in concrete. *Engineering Fracture Mechanics*, 35(1-3):321–326.

[Daudeville and Malecot, 2011] Daudeville, L. and Malecot, Y. (2011). Concrete structures under impact. *European Journal of Environmental and Civil Engineering*, 15(sup1):101–140.

[Davis et al., 2017] Davis, F., Pierron, F., and Siviour, C. R. (2017). *Inertial Impact Tests on Polymers for Inverse Parameter Identification*, pages 187–190. Springer International Publishing, Cham.

[de Boor, 1978] de Boor, C. (1978). *A Practical Guide to Splines*, volume 27. Springer-Verlag New York.

[Denoual and Hild, 2000] Denoual, C. and Hild, F. (2000). A damage model for the dynamic fragmentation of brittle solids. *Computer Methods in Applied Mechanics and Engineering*, 183(3-4):247–258.

[Diamaruya et al., 1997] Diamaruya, M., Kobayashi, H., and Nonaka, T. (1997). Impact Tensile Strength and Fracture of Concrete. *Le Journal de Physique IV*, 07(C3):C3–253–C3–258.

[Ditkowski et al., 2008] Ditkowski, A., Bhandari, A., and Sheldon, B. W. (2008). Computing derivatives of noisy signals using orthogonal functions expansions. *Journal of Scientific Computing*, 36(3):333–349.

[Dong and Pan, 2017] Dong, Y. and Pan, B. (2017). A Review of Speckle Pattern Fabrication and Assessment for Digital Image Correlation. *Experimental Mechanics*.

[Doormaal et al., 1994] Doormaal, J. V., Weerheijm, J., and Sluys, L. (1994). Experimental and Numerical Determination of the Dynamic Fracture Energy of Concrete. *Journal de Physique IV*, 04(C8):501–506.

[Dreuilhe et al., 2017] Dreuilhe, S., Davis, F., Siviour, C. R., and Pierron, F. (2017). *Image-Based Inertial Impact Tests on an Aluminum Alloy*, pages 219–223. Springer International Publishing, Cham.

[Dreuilhe et al., 2018] Dreuilhe, S., Davis, F., Sivour, C., and Pierron, F. (2018). Latest Results for Elasto-Plastic Identification at High Rates Using Inertial Impact. In Kimberley, J., Lamberson, L., and Mates, S., editors, *Dynamic Behavior of Materials, Volume 1*, pages 93–95, Cham. Springer International Publishing.

[Edgerton and Killian, 1954] Edgerton, H. E. and Killian, J. R. (1954). *Flash!: Seeing the unseen by ultra high-speed photography*. CT Branford Co.

[Erzar, 2010] Erzar, B. (2010). *Ecaillage, cratérisation et comportement en traction dynamique de bétons sous impact : approches expérimentales et modélisation*. PhD thesis, l'Université Paul Verlaine – Metz.

[Erzar and Forquin, 2010] Erzar, B. and Forquin, P. (2010). An Experimental Method to Determine the Tensile Strength of Concrete at High Rates of Strain. *Experimental Mechanics*, 50(7):941–955.

[Erzar and Forquin, 2011] Erzar, B. and Forquin, P. (2011). Experiments and mesoscopic modelling of dynamic testing of concrete. *Mechanics of Materials*, 43(9):505–527.

[Erzar and Forquin, 2014] Erzar, B. and Forquin, P. (2014). Analysis and modelling of the cohesion strength of concrete at high strain-rates. *International Journal of Solids and Structures*, 51(14):2559–2574.

[Etoh et al., 2005] Etoh, T. G., Hatsuki, Y., Okinaka, T., Ohtake, H., Maruyama, H., Hayashida, T., Yamada, M., Kitamura, K., Arai, T., Tanioka, K., Poggemann, D., Ruckelshausen, A., van Kuijk, H., Bosiers, J. T., and Theuwissen, A. J. (2005). An image sensor of 1,000,000 fps, 300,000 pixels, and 144 consecutive frames. In Paisley, D. L., Kleinfelder, S., Snyder, D. R., and Thompson, B. J., editors, *IEEE Transactions on Electron Devices*, volume 50, page 796.

[Etoh et al., 1999] Etoh, T. G., Mutoh, H., Takehara, K., and Okinaka, T. (1999). Improved design of an ISIS for a video camera of 1,000,000 pps. In Frank, A. M. and Walton, J. S., editors, *Proceedings SPIE, High-Speed Imaging and Sequence Analysis*, pages 127–132.

[Etoh and Nguyen, 2018] Etoh, T. G. and Nguyen, Q. A. (2018). *Evolution of High-Speed Image Sensors*, pages 81–101. Springer International Publishing, Cham.

[Etoh et al., 2003] Etoh, T. G., Poggemann, D., Kreider, G., Mutoh, H., Theuwissen, A. J. P., Ruckelshausen, A., Kondo, Y., Maruno, H., Takubo, K., Soya, H., Takehara, K., Okinaka, T., and Takano, Y. (2003). An image sensor which captures 100 consecutive frames at 1000 000 frames/s. *IEEE Transactions on Electron Devices*, 50(1):144–151.

[Fällström et al., 1989] Fällström, K. E., Gustavsson, H., Molin, N. E., and Wåhlin, A. (1989). Transient bending waves in plates studied by hologram interferometry. *Experimental Mechanics*, 29(4):378–387.

[Field, 1982] Field, J. E. (1982). High Speed Photography: Techniques And Applications. *Optical Engineering*, 21(4).

[Field et al., 2004] Field, J. E., Walley, S. M., Proud, W. G., Goldrein, H. T., and Siviour, C. R. (2004). Review of experimental techniques for high rate deformation and shock studies. *International Journal of Impact Engineering*, 30(7):725–775.

[Fletcher et al., 2018] Fletcher, L., Lamberson, L., and Pierron, F. (2018). Inertial Impact Method for the Tensile Strength of Tungsten Carbide at High Strain Rates. In *Proceedings of the annual conference and exposition on experimental and applied mechanics.*

[Forquin, 2012] Forquin, P. (2012). An optical correlation technique for characterizing the crack velocity in concrete. *The European Physical Journal Special Topics*, 206(1):89–95.

[Forquin, 2013] Forquin, P. (2013). A new processing of spalling-tests to characterize the dynamic strength of geomaterials. *SEM Annual Conference.*

[Forquin, 2017] Forquin, P. (2017). Brittle materials at high-loading rates: an open area of research. *Philosophical Transactions of the Royal Society A: Mathematical, Physical and Engineering Sciences*, 375(2085).

[Forquin and Erzar, 2009] Forquin, P. and Erzar, B. (2009). Dynamic fragmentation process in concrete under impact and spalling tests. *International Journal of Fracture*, 163(1-2):193–215.

[Forquin and Hild, 2010] Forquin, P. and Hild, F. (2010). A probabilistic damage model of the dynamic fragmentation process in brittle materials. *Advances in Applied Mechanics*, 44(June):1–72.

[Forquin et al., 2013] Forquin, P., Sallier, L., and Pierron, F. (2013). On the use of the Virtual Fields Method to characterize the dynamic response of geomaterials in spalling tests. In *DYMAT Technical Meeting*, London, UK.

[Forquin et al., 2015] Forquin, P., Sallier, L., and Pontiroli, C. (2015). A numerical study on the influence of free water content on the ballistic performances of plain concrete targets. *Mechanics of Materials*, 89:176–189.

[Fossum, 1997] Fossum, E. R. (1997). CMOS Active Pixel Sensor (APS) Technology for Multimedia Image Capture. *Multimedia Technology & Applications Conference*, pages 1–5.

[Fuller, 2013] Fuller, P. (2013). High-speed cinematography. In Peres, M., editor, *Focal encyclopedia of photography*, pages 539–544. Taylor & Francis, Oxford, United Kingdom, 4 edition.

[Gabet, 2006] Gabet, T. (2006). *Comportement triaxial du béton sous fortes contraintes: Influence du trajet de chargement*. PhD thesis, Université Joseph-Fourier - Grenoble I.

[Gabet et al., 2008] Gabet, T., Malecot, Y., and Daudeville, L. (2008). Triaxial behaviour of concrete under high stresses: Influence of the loading path on compaction and limit states. *Cement and Concrete Research*, 38(3):403–412.

[Geymonat and Pagano, 2003] Geymonat, G. and Pagano, S. (2003). Identification of Mechanical Properties by Displacement Field Measurement: A Variational Approach. *Meccanica*, 38(5):535–545.

[Gigliotti, 2012] Gigliotti, L. (2012). Assessment of the applicability of XFEM in Abaqus for modeling crack growth in rubber Luigi Gigliotti. page 76.

[Giraudeau et al., 2006] Giraudeau, A., Guo, B., and Pierron, F. (2006). Stiffness and damping identification from full field measurements on vibrating plates. *Experimental Mechanics*, 46(6):777–787.

[Giraudeau and Pierron, 2005] Giraudeau, A. and Pierron, F. (2005). Identification of stiffness and damping properties of thin isotropic vibrating plates using the virtual fields method: Theory and simulations. *Journal of Sound and Vibration*, 284(3-5):757–781.

[Gorry, 1990] Gorry, P. A. (1990). General Least-Squares Smoothing and Differentiation by the Convolution (Savitzky-Golay) Method. *Analytical Chemistry*, 62(6):570–573.

[Grédiac, 1989] Grédiac, M. (1989). Principe des travaux virtuels et identification. *Comptes rendus de l'Académie des sciences. Série 2, Mécanique, Physique, Chimie, Sciences de l'univers, Sciences de la Terre*, 309(1):1–5.

[Grédiac, 2004] Grédiac, M. (2004). The use of full-field measurement methods in composite material characterization: interest and limitations. *Composites Part A: Applied Science and Manufacturing*, 35(7-8):751–761.

[Grédiac et al., 2017] Grédiac, M., Blaysat, B., and Sur, F. (2017). A Critical Comparison of Some Metrological Parameters Characterizing Local Digital Image Correlation and Grid Method. *Experimental Mechanics*.

[Grédiac and Hild, 2012] Grédiac, M. and Hild, F. (2012). *Full-Field Measurements and Identification in Solid Mechanics*. ISTE/Wiley, London.

[Grédiac et al., 2008] Grédiac, M., Pierron, F., Avril, S., and Toussaint, E. (2008). The Virtual Fields Method for Extracting Constitutive Parameters From Full-Field Measurements: a Review. *Strain*, 42(4):233–253.

[Grediac and Sur, 2014] Grediac, M. and Sur, F. (2014). 50th anniversary article: Effect of sensor noise on the resolution and spatial resolution of displacement and strain maps estimated with the grid method. *Strain*, 50(1):1–27.

[Grédiac et al., 2013] Grédiac, M., Sur, F., Badulescu, C., and Mathias, J. D. (2013). Using deconvolution to improve the metrological performance of the grid method. *Optics and Lasers in Engineering*, 51(6):716–734.

[Grédiac et al., 2015] Grédiac, M., Sur, F., and Blaysat, B. (2015). Removing Quasi-Periodic Noise in Strain Maps by Filtering in the Fourier Domain. *Experimental Techniques*, (2015):n/a–n/a.

[Grédiac et al., 2016] Grédiac, M., Sur, F., and Blaysat, B. (2016). The Grid Method for In-plane Displacement and Strain Measurement: A Review and Analysis. *Strain*, 52(3):205–243.

[Gu and Pierron, 2016] Gu, X. and Pierron, F. (2016). Towards the design of a new standard for composite stiffness identification. *Composites Part A: Applied Science and Manufacturing*.

[Healey and Kondepudy, 1994] Healey, G. and Kondepudy, R. (1994). Radiometric CCD camera calibration and noise estimation. *IEEE Transactions on Pattern Analysis and Machine Intelligence*, 16(3).

[Heard et al., 2018] Heard, W., Song, B., Williams, B., Martin, B., Sparks, P., and Nie, X. (2018). Dynamic Tensile Experimental Techniques for Geomaterials: A Comprehensive Review. *Journal of Dynamic Behavior of Materials*.

[Hild, 2015] Hild, F. (2015). On characteristic parameters involved in dynamic fragmentation processes. *Mechanics of Materials*, 80(PB):340–350.

[Hild et al., 2018] Hild, F., Bouterf, A., Forquin, P., and Roux, S. (2018). On the Use of Digital Image Correlation for the Analysis of the Dynamic Behavior of Materials. In *The Micro-World Observed by Ultra High-Speed Cameras*, pages 185–206. Springer International Publishing, Cham.

[Hild et al., 2015] Hild, F., Bouterf, A., and Roux, S. (2015). Damage measurements via DIC. *International Journal of Fracture*, 191(1-2):77–105.

[Hild et al., 2003] Hild, F., Denoual, C., Forquin, P., and Brajer, X. (2003). On the probabilistic–deterministic transition involved in a fragmentation process of brittle materials. *Computers & Structures*, 81(12):1241–1253.

[Hild and Roux, 2006] Hild, F. and Roux, S. (2006). Digital image correlation: From displacement measurement to identification of elastic properties - A review. *Strain*, 42(2):69–80.

[Hild and Roux, 2012] Hild, F. and Roux, S. (2012). Comparison of Local and Global Approaches to Digital Image Correlation. *Experimental Mechanics*, 52(9):1503–1519.

[Hillerborg, 1985a] Hillerborg, A. (1985a). Results of three comparative test series for determining the fracture energyG F of concrete. *Materials and Structures*, 18(5):407–413.

[Hillerborg, 1985b] Hillerborg, A. (1985b). The theoretical basis of a method to determine the fracture energy Gf of concrete. *Materials and Structures*, 18(4):291–296.

[Hillerborg, 1985c] Hillerborg, A. (1985c). The theoretical basis of a method to determine the fracture energyG F of concrete. *Materials and Structures*, 18(4):291–296.

[Hillerborg, 1991] Hillerborg, A. (1991). Application of the fictitious crack model to different types of materials. *International Journal of Fracture*, 51(2):95–102.

[Hillerborg et al., 1976] Hillerborg, A., Modéer, M., and Petersson, P.-E. (1976). Analysis of crack formation and crack growth in concrete by means of fracture mechanics and finite elements. *Cement and Concrete Research*, 6(6):773–781.

[Holst, 1998] Holst, G. C. (1998). *CCD arrays, cameras, and displays*. SPIE Optical Engineering Press, Bellingham, Washington USA, 2nd ed. edition.

[Honour, 2009] Honour, J. (2009). A brief history of principles used in high speed cameras. *The Imaging Science Journal*, 57(6):303–316.

[Hopkinson, 1914] Hopkinson, B. (1914). A Method of Measuring the Pressure Produced in the Detonation of High Explosives or by the Impact of Bullets. *Philosophical Transactions of the Royal Society A: Mathematical, Physical and Engineering Sciences*, 213(497-508):437–456.

[Jacquot, 2008] Jacquot, P. (2008). Speckle Interferometry : A Review of the Principal Methods in Use for Experimental Mechanics Applications. *Strain*, pages 57–69.

[Kajberg et al., 2004] Kajberg, J., Sundin, K. G., Melin, L. G., and Ståhle, P. (2004). High strain-rate tensile testing and viscoplastic parameter identification using microscopic high-speed photography. *International Journal of Plasticity*, 20(4-5):561–575.

[Kanel, 2010] Kanel, G. I. (2010). Spall fracture: methodological aspects, mechanisms and governing factors. *International Journal of Fracture*, 163(1-2):173–191.

[Kim, 2008] Kim, J.-H. (2008). *Identification of the local stiffness reduction of a damaged composite plate using the virtual fields method.* PhD thesis, L'École Nationale Supérieure d'Arts et Métiers.

[Kim et al., 2017] Kim, J.-H., Park, J.-S., Barlat, F., and Pierron, F. (2017). Characterization of dynamic hardening behavior using acceleration information. *Procedia Engineering*, 207(September):245–250.

[Kleine and Settles, 2008] Kleine, H. and Settles, G. S. (2008). The art of shock waves and their flowfields. *Shock Waves*, 17(5):291–307.

[Klepaczko and Brara, 2001] Klepaczko, J. R. and Brara, A. (2001). An experimental method for dynamic tensile testing of concrete by spalling. *International Journal of Impact Engineering*, 25(4):387–409.

[Kolsky, 1964] Kolsky, H. (1964). Stress waves in solids. *Journal of Sound and Vibration*, 1(1):88–110.

[Kondo et al., 2003] Kondo, Y., Maruno, H., Tominaga, H., Soya, H., and Etohb, T. G. (2003). An ultra high-speed video camera and its applications. 4948:53–58.

[Kondo et al., 2013] Kondo, Y., Takubo, K., Tominaga, H., Hirose, R., Tokuoka, N., Kawaguchi, Y., Takaie, Y., and Ozaki, A. (2013). Development of " HyperVision HPV-X " High-speed Video Camera. Technical report.

[Koohbor et al., 2017] Koohbor, B., Kidane, A., Sutton, M. A., Zhao, X., and Mallon, S. (2017). Analysis of dynamic bending test using ultra high speed DIC and the virtual fields method. *International Journal of Impact Engineering*, 110:299–310.

[Kosonocky et al., 1996] Kosonocky, W., Guang Yang, Chao Ye, Kabra, R., Liansheng Xie, Lawrence, J., Mastrocolla, V., Shallcross, F., and Patel, V. (1996). 360 by 360-element very-high-frame-rate burst image sensor. In *1996 IEEE International Solid-State Circuits Conference. Digest of TEchnical Papers, ISSCC*, pages 182–183. IEEE.

[Labibes et al., 2000] Labibes, K., Berra, M., Cadoni, E., Giangrasso, M., and Albertini, C. (2000). High-strain-rate tensile behaviour of concrete. *Magazine of Concrete Research*, 52(5):365–370.

[Lambert and Ross, 2000] Lambert, D. E. and Ross, C. A. (2000). Strain Rate Effects on Dynamic Fracture and Strength. *International Journal of Impact Engineering*, 24:985–998.

[Landon and Quinney, 1923] Landon, J. W. and Quinney, H. (1923). Experiments with the Hopkinson Pressure Bar. *Proceedings of the Royal Society A: Mathematical, Physical and Engineering Sciences*, 103(723):622–643.

[Latourte et al., 2008] Latourte, F., Chrysochoos, A., Pagano, S., and Wattrisse, B. (2008). Elastoplastic Behavior Identification for Heterogeneous Loadings and Materials. *Experimental Mechanics*, 48(4):435–449.

[Lauterborn and Kurz, 2018] Lauterborn, W. and Kurz, T. (2018). The Bubble Challenge for High-Speed Photography. In *The Micro-World Observed by Ultra High-Speed Cameras*, pages 19–47. Springer International Publishing, Cham.

[Lava et al., 2009] Lava, P., Cooreman, S., Coppieters, S., De Strycker, M., and Debruyne, D. (2009). Assessment of measuring errors in DIC using deformation fields generated by plastic FEA. *Optics and Lasers in Engineering*, 47(7-8):747–753.

[Lava et al., 2010] Lava, P., Cooreman, S., and Debruyne, D. (2010). Study of systematic errors in strain fields obtained via DIC using heterogeneous deformation generated by plastic FEA. *Optics and Lasers in Engineering*.

[Lava et al., 2013] Lava, P., Van Paepegem, W., Coppieters, S., De Baere, I., Wang, Y., and Debruyne, D. (2013). Impact of lens distortions on strain measurements obtained with 2D digital image correlation. *Optics and Lasers in Engineering*, 51(5):576–584.

[Lecompte et al., 2006] Lecompte, D., Smits, A., Bossuyt, S., Sol, H., Vantomme, J., Van Hemelrijck, D., and Habraken, A. (2006). Quality assessment of speckle patterns for digital image correlation. *Optics and Lasers in Engineering*, 44(11):1132–1145.

[Lecompte et al., 2007] Lecompte, D., Smits, A., Sol, H., Vantomme, J., and Van Hemelrijck, D. (2007). Mixed numerical-experimental technique for orthotropic parameter identification using biaxial tensile tests on cruciform specimens. *International Journal of Solids and Structures*, 44(5):1643–1656.

[Lemaitre, 1996] Lemaitre, J. (1996). *A Course on Damage Mechanics*. Springer Berlin Heidelberg, Berlin, Heidelberg.

[Levi-Hevroni et al., 2017] Levi-Hevroni, D., Kochavi, E., Kofman, B., Gruntman, S., and Sadot, O. (2017). Experimental and numerical investigation on the dynamic increase factor of tensile strength in concrete. *International Journal of Impact Engineering*, 32(1-4):605–617.

[Li et al., 2005] Li, Q., Reid, S., Wen, H., and Telford, A. (2005). Local impact effects of hard missiles on concrete targets. *International Journal of Impact Engineering*, 32(1-4):224–284.

[Lira et al., 2004] Lira, I., Cordero, R. R., François, M., and Vial-Edwards, C. (2004). The uncertainty of experimental derivatives: application to strain measurement. *Measurement Science and Technology*, 15(12):2381–2388.

[Lu et al., 2017] Lu, D., Wang, G., Du, X., and Wang, Y. (2017). A nonlinear dynamic uniaxial strength criterion that considers the ultimate dynamic strength of concrete. *International Journal of Impact Engineering*, 103:124–137.

[Lu and Liu, 1997] Lu, F. K. and Liu, X. J. (1997). Optical design of Cranz-Schardin cameras. *Optical Engineering*, 36(7):1935–1941.

[Lu et al., 2013] Lu, Y., Xu, J., and Weerheijm, J. (2013). A mesoscale modeling perspective of cracking process and fracture energy under high strain rate tension. In Van Mier, J., Ruiz, G., Andrade, C., Yu, R., and Zhang, X., editors, *8th International Conference on Fracture Mechanics of Concrete and Concrete Structures - FraMCoS-8*, pages 942–952, Toledo.

[Lukić et al., 2017] Lukić, B., Saletti, D., and Forquin, P. (2017). Use of simulated experiments for material characterization of brittle materials subjected to high strain rate dynamic tension. *Philosophical Transactions of the Royal Society A: Mathematical, Physical and Engineering Sciences*, 375(2085):20160168.

[Malvar and Crawford, 1998] Malvar, L. J. and Crawford, J. E. (1998). Dynamic Increase Factors. In *28th Department of defense Explosives Safety Seminar*, pages 1–17, Orlando.

[Marek et al., 2017] Marek, A., Davis, F. M., and Pierron, F. (2017). Sensitivity-based virtual fields for the non-linear virtual fields method. *Computational Mechanics*, 60(3):409–431.

[Mathieu et al., 2014] Mathieu, F., Leclerc, H., Hild, F., and Roux, S. (2014). Estimation of Elastoplastic Parameters via Weighted FEMU and Integrated-DIC. *Experimental Mechanics*, pages 105–119.

[Mazars, 1986] Mazars, J. (1986). A description of micro- and macroscale damage of concrete structures. *Engineering Fracture Mechanics*, 25(5-6):729–737.

[Meyers, 1994] Meyers, M. A. (1994). *Dynamic behaviour of materials*. John Wiley & Sons, Inc., New York, NY.

[Miehe et al., 2010] Miehe, C., Hofacker, M., and Welschinger, F. (2010). A phase field model for rate-independent crack propagation: Robust algorithmic implementation based on operator splits. *Computer Methods in Applied Mechanics and Engineering*, 199(45):2765 – 2778.

[Millon et al., 2009] Millon, O., Riedel, W., Thoma, K., Fehling, E., and Nöldgen, M. (2009). Fiber-reinforced ultra-high performance concrete under tensile loads. *DYMAT 2009 - 9th International Conferences on the Mechanical and Physical Behaviour of Materials under Dynamic Loading*, 1:671–677.

[Molimard and Surrel, 2012] Molimard, J. and Surrel, Y. (2012). *Grid Method, Moiré and Deflectometry*, pages 61–92. John Wiley & Sons, Inc., Hoboken, NJ USA.

[Molnár and Gravouil, 2017] Molnár, G. and Gravouil, A. (2017). 2D and 3D Abaqus implementation of a robust staggered phase-field solution for modeling brittle fracture. *Finite Elements in Analysis and Design*, 130(February):27–38.

[Moulart et al., 2011] Moulart, R., Pierron, F., Hallett, S. R., and Wisnom, M. R. (2011). Full-Field Strain Measurement and Identification of Composites Moduli at High Strain Rate with the Virtual Fields Method. *Experimental Mechanics*, 51(4):509–536.

[Muybridge, 1878] Muybridge, E. (1878). The horse in motions. *Library of Congress Prints and Photographs Division*.

[Novikov and Ivanov, 1966] Novikov, S. A. and Ivanov, A. G. (1966). Failure of steel, aluminium and copper under explosive shock loading. *Fizika Metallov i Metallovedenie*, 21(4):608–615.

[Orteu et al., 2006] Orteu, J.-J., Garcia, D., Robert, L., and Bugarin, F. (2006). A speckle texture image generator. page 63410H.

[Osher and Sethian, 1988] Osher, S. and Sethian, J. A. (1988). Fronts propagating with curvature-dependent speed: Algorithms based on Hamilton-Jacobi formulations. *Journal of Computational Physics*, 79(1):12–49.

[Ozbolt and Eligehausen, 1991] Ozbolt, J. and Eligehausen, R. (1991). Analysis of reinforced concrete beams without shear reinforcement using non-local microplane model. In *Fracture processes in concrete, rock and ceramics. 2: Macroscopic modelling and structural engineering. (RILEM proceedings 13)*, Noordwijk; The Nederlands.

[Ožbolt et al., 2014] Ožbolt, J., Sharma, A., İrhan, B., and Sola, E. (2014). Tensile behavior of concrete under high loading rates. *International Journal of Impact Engineering*, 69:55–68.

[Ožbolt et al., 2013] Ožbolt, J., Weerheijm, J., and Sharma, A. (2013). Dynamic Tensile Resistance of Concrete - Split Hopkinson Bar. *FraMCoS-8*, pages 205–216.

[Pan et al., 2015] Pan, B., Wang, B., Lubineau, G., and Moussawi, A. (2015). Comparison of Subset-Based Local and Finite Element-Based Global Digital Image Correlation. *Experimental Mechanics*, 55(5):887–901.

[Passieux et al., 2018] Passieux, J., Bouclier, R., and Périé, J.-N. (2018). A Space-Time PGD-DIC Algorithm : Application to 3D Mode Shapes Measurements. *Experimental Mechanics*.

[Périé et al., 2009] Périé, J. N., Leclerc, H., Roux, S., and Hild, F. (2009). Digital image correlation and biaxial test on composite material for anisotropic damage law identification. *International Journal of Solids and Structures*, 46(11-12):2388–2396.

[Pierron, 2016] Pierron, F. (2016). Addendum to 'Characterising the Strain and Temperature Fields in a Surrogate Bone Material Subject to Power Ultrasonic Excitation'. *Strain*, 52(3):186–190.

[Pierron et al., 2011a] Pierron, F., Cheriguene, R., Forquin, P., Moulart, R., Rossi, M., and Sutton, M. (2011a). Performances and Limitations of Three Ultra High-Speed Imaging Cameras for Full-Field Deformation Measurements. *Applied Mechanics and Materials*, 70:81–86.

[Pierron and Forquin, 2012a] Pierron, F. and Forquin, P. (2012a). The virtual fields method applied to spalling tests on concrete. *EPJ Web of Conferences*, 26:01054.

[Pierron and Forquin, 2012b] Pierron, F. and Forquin, P. (2012b). Ultra-High-Speed Full-Field Deformation Measurements on Concrete Spalling Specimens and Stiffness Identification with the Virtual Fields Method. *Strain*, 48(5):388–405.

[Pierron and Grédiac, 2000] Pierron, F. and Grédiac, M. (2000). Identification of the through-thickness moduli of thick composites from whole-field measurements using the Iosipescu fixture: theory and simulations. 31:309–318.

[Pierron and Grédiac, 2012] Pierron, F. and Grédiac, M. (2012). *The Virtual Fields Method*. Springer New York, New York, NY, 1 edition.

[Pierron et al., 2011b] Pierron, F., Sutton, M. A., and Tiwari, V. (2011b). Ultra High Speed DIC and Virtual Fields Method Analysis of a Three Point Bending Impact Test on an Aluminium Bar. *Experimental Mechanics*, 51(4):537–563.

[Pierron et al., 2014] Pierron, F., Zhu, H., and Siviour, C. (2014). Beyond Hopkinson's bar. *Philosophical transactions. Series A, Mathematical, physical, and engineering sciences*, 372(2023):20130195.

[Piotrowska, 2013] Piotrowska, E. (2013). *Role of coarse aggregates in the triaxial behavior of concrete : experimental and numerical*. PhD thesis, L'Universite de Grenoble.

[Piotrowska and Forquin, 2015] Piotrowska, E. and Forquin, P. (2015). Experimental Investigation of the Confined Behavior of Dry and Wet High-Strength Concrete: Quasi Static Versus Dynamic Loading. *Journal of Dynamic Behavior of Materials*, 1(2):191–200.

[Piotrowska et al., 2016] Piotrowska, E., Forquin, P., and Malecot, Y. (2016). Experimental study of static and dynamic behavior of concrete under high confinement: Effect of coarse aggregate strength. *Mechanics of Materials*, 92(2016):164–174.

[Piro and Grediac, 2004] Piro, J. and Grediac, M. (2004). Producing and Transferring Low-Spatial-Frequency Grids for Measuring Displacement Fields With Moire and Grid Methods. *Experimental Techniques*, 28(4):23–26.

[Post and Han, 2008] Post, D. and Han, B. (2008). Moiré Interferometry. In *Springer Handbook of Experimental Solid Mechanics*, pages 627–654. Springer US, Boston, MA.

[Rastogy, 2000] Rastogy, P. K. (2000). *Photomechanics*, volume 77 of *Topics in Applied Physics*. Springer Berlin Heidelberg, Berlin, Heidelberg.

[Régal and Hanus, 2016] Régal, X. and Hanus, J.-L. (2016). Experimental Study of the Dynamic Flexural Strength of Concrete. *Experimental Mechanics*.

[Reinhardt et al., 1986] Reinhardt, H. W., Körmeling, H. A., and Zielinski, A. J. (1986). The split Hopkinson bar, a versatile tool for the impact testing of concrete. *Materials and Structures*, 19(1):55–63.

[Reinhardt and Weerheijm, 1991] Reinhardt, H. W. and Weerheijm, J. (1991). Tensile fracture of concrete at high loading rates taking account of inertia and crack velocity effects. *International Journal of Fracture*, 51(1):31–42.

[Réthoré et al., 2007] Réthoré, J., Gravouil, A., and Combescure, A. (2007). Prise en compte de discontinuités en espace et en temps par la méthode des elements finis étendus. *European Journal of Computational Mechanics*, 16(6-7):827–843.

[Reu, 2011a] Reu, P. (2011a). High/Ultra-high speed imaging as a diagnostic tool. *Applied Mechanics and Materials*, 70:69–74.

[Reu, 2011b] Reu, P. L. (2011b). Experimental and Numerical Methods for Exact Subpixel Shifting. *Experimental Mechanics*, 51(4):443–452.

[Reu and Miller, 2008] Reu, P. L. and Miller, T. J. (2008). The application of high-speed digital image correlation. *The Journal of Strain Analysis for Engineering Design*, 43(8):673–688.

[Reu et al., 2017] Reu, P. L., Toussaint, E., Jones, E., Bruck, H. A., Iadicola, M., Balcaen, R., Turner, D. Z., Siebert, T., Lava, P., and Simonsen, M. (2017). DIC Challenge: Developing Images and Guidelines for Evaluating Accuracy and Resolution of 2D Analyses. *Experimental Mechanics*.

[Rey-De-Pedraza et al., 2016] Rey-De-Pedraza, V., Cendón, D. A., Sánchez-Gálvez, V., and Gálvez, F. (2016). Measurement of fracture properties of concrete at high strain rates. *Philosophical Transactions of the Royal Society A: Mathematical, Physical and Engineering Sciences*, 375(2085).

[Riley and Dally, 1969] Riley, W. and Dally, J. (1969). Recording Dynamic Fringe Patterns with a Cranz-Schardin Camera camera with these requirements. *Experimental Mechanics*, 9(8):27–33.

[Ross et al., 1996] Ross, C. A., Jerome, M. D., Tedesco, W. J., and Hughes, L. M. (1996). Moisture and Strain Rate Effects on Concrete Strength. *ACI Materials Journal*, 93(3).

[Rossi et al., 2015] Rossi, M., Lava, P., Pierron, F., Debruyne, D., and Sasso, M. (2015). Effect of DIC Spatial Resolution, Noise and Interpolation Error on Identification Results with the VFM. *Strain*, 51(3):206–222.

[Rossi and Pierron, 2012] Rossi, M. and Pierron, F. (2012). On the use of simulated experiments in designing tests for material characterization from full-field measurements. *International Journal of Solids and Structures*, 49(3-4):420–435.

[Rossi et al., 2014] Rossi, M., Pierron, F., and Forquin, P. (2014). Assessment of the metrological performance of an in situ storage image sensor ultra-high speed camera for full-field deformation measurements. *Measurement Science and Technology*, 25(2):025401.

[Rossi et al., 1992] Rossi, P., Mier, J. G. M., Boulay, C., and Maou, F. (1992). The dynamic behaviour of concrete: influence of free water. *Materials and Structures*, 25(9):509–514.

[Rots and De Brost, 1989] Rots, J. and De Brost, R. (1989). Analysis of Concrete Fracture in 'Direct' Tension. *International Journal of Solids and Structures*, 25(12):1381–1394.

[Rouquand et al., 2007] Rouquand, A., Pontiroli, C., and Mazars, J. (2007). Concrete structures under severe loading : a strategy to model the response for a large range of dynamic loads. In *Fracture Mechanics of Concrete and Concrete Structures: Proceedings of FraMCoS-6*, Catania.

[Roux and Hild, 2006] Roux, S. and Hild, F. (2006). Stress intensity factor measurements from digital image correlation: post-processing and integrated approaches. *International Journal of Fracture*, 140:141–157.

[Roux et al., 2009] Roux, S., Réthoré, J., and Hild, F. (2009). Digital image correlation and fracture: an advanced technique for estimating stress intensity factors of 2D and 3D cracks. *Journal of Physics D: Applied Physics*, 42(21):214004.

[Rowlands et al., 1973] Rowlands, R. E., Liber, T., Daniel, I. M., and Rose, P. G. (1973). Higher-order numerical differentiation of experimental information. *Experimental Mechanics*, 13(3):105–112.

[Saadati et al., 2016] Saadati, M., Forquin, P., Weddfelt, K., and Larsson, P. L. (2016). On the tensile strength of granite at high strain rates considering the influence from preexisting cracks. *Advances in Materials Science and Engineering*, 2016.

[Saldner and Huntley, 1997] Saldner, H. O. and Huntley, J. M. (1997). Temporal phase unwrapping: application to surface profiling of discontinuous objects. *Applied optics*, 36(13):2770–2775.

[Saletti, 2011] Saletti, D. (2011). *Mesures de champs hétérogènes dans un alliage à mémoire de forme de Nickel - Titane sous sollicitations dynamiques*. PhD thesis, L'Ecole Normale Supérieure de Cachan.

[Saletti and Forquin, 2015] Saletti, D. and Forquin, P. (2015). A comparison of DIC and grid measurements for processing spalling tests with the VFM and an 80-kpixel ultra-high speed camera. *The European Physical Journal Special Topics*, 225(2):311–323.

[Sallier and Forquin, 2012] Sallier, L. and Forquin, P. (2012). On the use of Hillerborg regularization method to model the softening behaviour of concrete subjected to dynamic tensile loading. *The European Physical Journal Special Topics*, 206(1):97–105.

[Savitzky and Golay, 1964] Savitzky, A. and Golay, M. J. E. (1964). Smoothing and Differentiation of Data by Simplified Least Squares Procedures. *Analytical Chemistry*, 36(8):1627–1639.

[Schardin, 1942] Schardin, H. (1942). *Die Schlierenverfahren und ihre Anwendungen*, pages 303–439. Springer Berlin Heidelberg, Berlin, Heidelberg.

[Schardin, 1959] Schardin, H. (1959). Velocity effects in Fracture. In *International Conference on Fracture, ICF0*, Swampscott, USA.

[Schreier and Sutton, 2002] Schreier, H. and Sutton, M. (2002). Systematic Errors in Digital Image Correlation Due to Undermatched Subset Shape Functions. *Experimental Mechanics*, 42(3):303–310.

[Schuler, 2007] Schuler, H. (2007). Evaluation of an experimental method via numerical simulations. In *Fracture Mechanics of Concrete and Concrete Structures: Proceedings of FraMCoS-6*, volume 1, Catania.

[Schuler and Hansson, 2006] Schuler, H. and Hansson, H. (2006). Fracture behaviour of High Performance Concrete (HPC) investigated with a Hopkinson-Bar. *J. Phys. IV France*, 134(June):1145–1151.

[Schuler et al., 2006] Schuler, H., Mayrhofer, C., and Thoma, K. (2006). Spall experiments for the measurement of the tensile strength and fracture energy of concrete at high strain rates. *International Journal of Impact Engineering*, 32(10):1635–1650.

[Seghir and Pierron, 2017] Seghir, R. and Pierron, F. (2017). A Novel Image-based Ultrasonic Test to Map Material Mechanical Properties at High Strain-rates. *Experimental Mechanics*.

[Shimadzu CO., 2017] Shimadzu CO. (2017). Hyper Vision HPV-X2: FTCMOS2 Advanced, Next-Generation Burst Image Sensor.

[Sluys, 1992] Sluys, L. (1992). Wave Propagation, Localisation and Dispersion in Softening Solids.

[Song et al., 2008] Song, J.-H., Wang, H., and Belytschko, T. (2008). A comparative study on finite element methods for dynamic fracture. *Computational Mechanics*, 42(2):239–250.

[Stolarska et al., 2001] Stolarska, M., Chopp, D. L., Moës, N., and Belytschko, T. (2001). Modelling crack growth by level sets in the extended finite element method. *International Journal for Numerical Methods in Engineering*, 51(8):943–960.

[Sugawa et al., 2016] Sugawa, S., Kuroda, R., Takeda, T., Shao, F., Miyauchi, K., and Tochigi, Y. (2016). A 20Mfps Global Shutter CMOS Image Sensor with Improved Sensitivity and Power Consumption. *ITE Transactions on Media Technology and Applications*.

[Sur et al., 2016] Sur, F., Blaysat, B., and Grediac, M. (2016). Determining displacement and strain maps immune from aliasing effect with the grid method. *Optics and Lasers in Engineering*, 86:317–328.

[Sur and Grédiac, 2014] Sur, F. and Grédiac, M. (2014). Towards deconvolution to enhance the grid method for in-plane strain measurement. *Inverse Problems and Imaging*, 8(1):259–291.

[Sur and Grédiac, 2015] Sur, F. and Grédiac, M. (2015). On noise reduction in strain maps obtained with the grid method by averaging images affected by vibrations. *Optics and Lasers in Engineering*, 66:210–222.

[Sur and Grédiac, 2017] Sur, F. and Grédiac, M. (2017). Towards Computational Photomechanics. *ERCIM News, ERCIM,*, 108:30–31.

[Surrel, 1994] Surrel, Y. (1994). Moire and Grid Methods: A 'Signal Processing' approach. *Photomechanics*, 2342:118–127.

[Surrel, 1996] Surrel, Y. (1996). Design of algorithms for phase measurements by the use of phase stepping. *Applied optics*, 35(1):51–60.

[Surrel, 2000] Surrel, Y. (2000). Fringe Analysis. In Rastogi, P. K., editor, *Photomechanics. Topics in applied physics,*, volume 77 of *Topics in Applied Physics*, pages 55–102. Springer Berlin Heidelberg, Berlin, Heidelberg.

[Sutton et al., 2009] Sutton, M. A., Orteu, J.-J., and Schreier, H. (2009). *Image Correlation for Shape, Motion and Deformation Measurements*. Springer US, Boston, MA.

[Sutton et al., 1983] Sutton, M. A., Wolters, W. J., Peters, W. H., Ranson, W. F., and McNeill, S. R. (1983). Determination of displacements using an improved digital correlation method. *Image and Vision Computing*, 1(3):133–139.

[Taylor et al., 2017] Taylor, K., Chan, W., Birman, A., Lahav, A., Fenigstein, A., Marsh, B., Benhammadi, S., and Turchetta, R. (2017). A 5 Million fps Global Shutter Megapixel Sensor with Shutter Efficiency in Excess of 120 dB. In *2017 International Image Sensor Workshop*, pages 195–198.

[Tiwari et al., 2007] Tiwari, V., Sutton, M. a., and McNeill, S. R. (2007). Assessment of High Speed Imaging Systems for 2D and 3D Deformation Measurements: Methodology Development and Validation. *Experimental Mechanics*, 47(4):561–579.

[Tochigi et al., 2013] Tochigi, Y., Hanzawa, K., Kato, Y., Kuroda, R., Mutoh, H., Hirose, R., Tominaga, H., Takubo, K., Kondo, Y., and Sugawa, S. (2013). A Global-Shutter CMOS Image Sensor With Readout Speed of 1-Tpixel/s Burst and 780-Mpixel/s Continuous. *IEEE Journal of Solid-State Circuits*, 48(1):329–338.

[Toussaint et al., 2006] Toussaint, E., Grédiac, M., and Pierron, F. (2006). The virtual fields method with piecewise virtual fields. *International Journal of Mechanical Sciences*, 48(3):256–264.

[Toutlemonde, 1994] Toutlemonde, F. (1994). *Resistance au choc des structures en béton: du comportement du materiau au calcule des ouvrages*. PhD thesis, l'Ecole Nationale des Pont et Chaussées.

[Vegt, 2016] Vegt, I. (2016). *Concrete in dynamic tension : The fracture process*. PhD thesis, TU Delft.

[Vegt and Weerheijm, 2015] Vegt, I. and Weerheijm, J. (2015). The post peak responce of concrete for dynamic tensile loading. In Stewart, M. and Netherton, M., editors, *Third International Conferance on Protective Structures (ICPS3)*, number February, pages 3–6, Newcastle.

[Vegt and Weerheijm, 2016] Vegt, I. and Weerheijm, J. (2016). Influence of moister on the fracture behaviour of concrete loaded in dynamic tension. *FraMCos-9*, (October).

[Velten et al., 2013] Velten, A., Raskar, R., Wu, D., Jarabo, A., Masia, B., Barsi, C., Joshi, C., Lawson, E., Bawendi, M., and Gutierrez, D. (2013). Femto-photography: capturing and visualizing the propagation of light. *ACM Transactions on Graphics*, 32(4):1.

[Versluis, 2013] Versluis, M. (2013). High-speed imaging in fluids. *Experiments in Fluids*, 54(2).

[Volkov et al., 2017] Volkov, G. A., Petrov, Y. V., and Utkin, A. A. (2017). On some principal features of data processing of spall fracture tests. *Physics of the Solid State*, 59(2):310–315.

[Vu, 2007] Vu, X. H. (2007). *Caractérisation expérimentale du béton sous fort confinement: influences du degr de saturation et du rapport eau/ciment. Doctoral dissertation*. PhD thesis, Université Joseph-Fourier - Grenoble I.

[Wang et al., 2013a] Wang, D., Lucas, M., and Tanner, K. E. (2013a). Characterising the strain and temperature fields in a surrogate bone material subject to power ultrasonic excitation. *Strain*, 49(5):409–419.

[Wang et al., 2016] Wang, P., Pierron, F., Rossi, M., Lava, P., and Thomsen, O. (2016). Optimised Experimental Characterisation of Polymeric Foam Material Using DIC and the Virtual Fields Method. *Strain*, 52(1):59–79.

[Wang et al., 2013b] Wang, P., Pierron, F., and Thomsen, O. T. (2013b). Identification of Material Parameters of PVC Foams using Digital Image Correlation and the Virtual Fields Method. *Experimental Mechanics*, 53(6):1001–1015.

[Wang et al., 2015] Wang, Y., Lava, P., and Debruyne, D. (2015). Using super-resolution images to improve the measurement accuracy of DIC. In *Optical measurement techniques for systems and structures III*, pages 353–361, Antwerp, Belgium.

[Wang et al., 2007] Wang, Z. Y., Li, H. Q., Tong, J. W., and Ruan, J. T. (2007). Statistical Analysis of the Effect of Intensity Pattern Noise on the Displacement Measurement Precision of Digital Image Correlation Using Self-correlated Images. *Experimental Mechanics*, 47(5):701–707.

[Weerheijm, 1992] Weerheijm, J. (1992). *Concrete under Impact Tensile Loading and Lateral Compression*. Doctoral thesis, Delft University of Technology.

[Weerheijm, 2013] Weerheijm, J. (2013). *Understanding the Tensile Properties of Concrete*. Woodhead Publishing Limited.

[Weerheijm and Forquin, 2013] Weerheijm, J. and Forquin, P. (2013). Response mechanisms of concrete under impulsive tensile loading. In *Understanding the Tensile Properties of Concrete*, pages 181–217. Elsevier.

[Weerheijm and Van Doormaal, 2007] Weerheijm, J. and Van Doormaal, J. (2007). Tensile failure of concrete at high loading rates: New test data on strength and fracture energy from instrumented spalling tests. *International Journal of Impact Engineering*, 34(3):609–626.

[Weerheijm and Vegt, 2010] Weerheijm, J. and Vegt, I. (2010). The dynamic fracture energy of concrete: Review of test methods and data comparison. In Oh, B., editor, *FraMCos-7: Proceedings of the 7th International Conference on Fracture Mechanics of Concrete and Concrete Structures*, Seoul.

[Weerheijm and Vegt, 2011] Weerheijm, J. and Vegt, I. (2011). How to Determine the Dynamic Fracture Energy of Concrete. Theoretical Considerations and Experimental Evidence. *Applied Mechanics and Materials*, 82:51–56.

[Wen and Xian, 2015] Wen, H. M. and Xian, Y. X. (2015). A unified approach for concrete impact. *International Journal of Impact Engineering*, 77:84–96.

[Williams, 1952] Williams, M. L. (1952). Stress Singularities Resulting From Various Boundary Conditions in Angular Corners of Plates in Extension. *Journal of applied mechanics*, 19(4):526–528.

[Wittmann et al., 1987] Wittmann, F. H., Roelfstra, P. E., Mihashi, H., Huang, Y. Y., Zhang, X. H., and Nomura, N. (1987). Influence of age of loading, water-cement ratio and rate of loading on fracture energy of concrete. *Materials and Structures*, 20(2):103–110.

[Wu et al., 2005] Wu, H., Zhang, Q., Huang, F., and Jin, Q. (2005). Experimental and numerical investigation on the dynamic tensile strength of concrete. *International Journal of Impact Engineering*, 32(1-4):605–617.

[Wu et al., 2012] Wu, S., Chen, X., and Zhou, J. (2012). Tensile strength of concrete under static and intermediate strain rates: Correlated results from different testing methods. *Nuclear Engineering and Design*, 250:173–183.

[Xing et al., 2017a] Xing, H., Zhang, Q., Ruan, D., Dehkhoda, S., Lu, G., and Zhao, J. (2017a). Full-field measurement and fracture characterisations of rocks under dynamic loads using high-speed three-dimensional digital image correlation. *International Journal of Impact Engineering*, (2017).

[Xing et al., 2017b] Xing, H. Z., Zhang, Q. B., Braithwaite, C. H., Pan, B., and Zhao, J. (2017b). High-Speed Photography and Digital Optical Measurement Techniques for Geomaterials: Fundamentals and Applications. *Rock Mechanics and Rock Engineering*, 50(6):1611–1659.

[Yan and Lin, 2006] Yan, D. and Lin, G. (2006). Dynamic properties of concrete in direct tension. *Cement and Concrete Research*, 36(7):1371–1378.

[Yasmeen et al., 2018] Yasmeen, F., Balcaen, R., Sutton, M., Debruyne, D., Rajan, S., and Schreier, H. (2018). Sensitivity of in-Plane Strain Measurement to Calibration Parameter for out-of-Plane Specimen Rotations. *Experimental Mechanics*.

[Yoon et al., 2015] Yoon, S.-h., Giannakopoulos, I., and Siviour, C. R. (2015). Application of the Virtual Fields Method to the uniaxial behavior of rubbers at medium strain rates. *International Journal of Solids and Structures*, 69-70:553–568.

[Yoon and Siviour, 2017] Yoon, S.-H. and Siviour, C. R. (2017). Application of the Virtual Fields Method to Rubbers Under Medium Strain Rate Deformation Using Both Acceleration and Traction Force Data. *Journal of Dynamic Behavior of Materials*, 3(1):12–22.

[Zappa et al., 2014] Zappa, E., Mazzoleni, P., and Matinmanesh, A. (2014). Uncertainty assessment of digital image correlation method in dynamic applications. *Optics and Lasers in Engineering*, 56:140–151.

[Zhang et al., 2008] Zhang, L., Hu, S.-S., Chen, D.-X., Yu, Z.-Q., and Liu, F. (2008). An Experimental Technique for Spalling of Concrete. *Experimental Mechanics*, 49(4):523–532.

[Zhang et al., 2016] Zhang, L., Thakku, S. G., Beotra, M. R., Baskaran, M., Aung, T., Goh, J. C. H., Strouthidis, N. G., and Girard, M. J. A. (2016). Verification of a virtual fields method to extract the mechanical properties of human optic nerve head tissues in vivo. *Biomechanics and Modeling in Mechanobiology*.

[Zhang and Zhao, 2014] Zhang, Q. B. and Zhao, J. (2014). A review of dynamic experimental techniques and mechanical behaviour of rock materials. *Rock Mechanics and Rock Engineering*, 47(4):1411–1478.

[Zhu, 2015] Zhu, H. (2015). *A Novel Methodology for High Strain Rate Testing using Full-field Measurements and the Virtual Fields Methods*. PhD thesis, Université de Technologie de Troyes.

[Zhu and Pierron, 2016] Zhu, H. and Pierron, F. (2016). Exploration of Saint-Venant's Principle in Inertial High Strain Rate Testing of Materials. *Experimental Mechanics*, 56(1):3–23.

[Zielinski, 1980] Zielinski, A. J. (1980). Experiments on mortar under single and repeated uniaxial tensile loading. Technical report, TU Delft.

[Zielinski et al., 1981] Zielinski, A. J., Reinhard, H. W., and Körmeling, H. a. (1981). Experiments on concrete under uniaxial impact tensile loading. *Matériaux et Constructions*, 14(3):163–169.

[Zingg et al., 2016] Zingg, L., Briffaut, M., Baroth, J., and Malecot, Y. (2016). Influence of cement matrix porosity on the triaxial behaviour of concrete. *Cement and Concrete Research*, 80:52–59.

Appendices

Appendix A

Effect of epoxy glue on the use of grid method for damage measurements

In the following, a possibility of a locally induced stiffening of epoxy adhesive used to glue the grid on the concrete sample is numerically investigated. The study investigates effects of the presence of the thin layer of glue (0.3 mm) on the damage measurements of concrete in dynamic tension. The properties of the glue are considered linear elastic while a uniaxial local damage model is adopted for concrete material. A spalling test is simulated and the time resolved displacement fields are extracted from the nodes that constitute the glue surface on top of that of concrete. Then, they the displacement maps are processed within the VFM to obtain the local axial stress-strain softening response. The comparison is made with results of the numerical simulation when no glue is used. A small effect on the failure strain is noticed while no notable effects on the failure stress as well as measured concrete Young's modulus have been noted. This work presents a first effort towards investigating to which extent the presence of glued grid can disrupt the dynamic damage measurement of concrete.

A.1 Introduction

The basic principle of the grid method is to analyse the phase change of the grid that is glued, deposited or even engraved onto a specimen surface in order to get the the displacements at each grid point. Although there are several ways of instrumenting a sample with a grid pattern [Post and Han, 2008], one of the most common ways is to first print the grid on a photosensitive coating and then to use epoxy-based adhesive to glue or transfer the grid on the specimen surface [Piro and Grediac, 2004, Badulescu, 2010]. It is generally advised to perform the grid transferring rather than glueing the entire film carrier, in order to avoid any additional surface stiffening. The assumption of a good kinematic transfer between the substrate and the grid along with the assumption that the grid does not change the global material response, are the fundamental prerequisites of the grid method [Molimard and Surrel, 2012].

In principle, one can relate this assumptions to those made when strain gauges are used. However, one cannot help but noticing that in case of strain gauges the glued surface is much smaller. Furthermore, strain gauge adhesives, such as cyanoacrility glue, are in principle an older technology, which has gone through optimizations that resulted in glue characteristics which assure good bond between the gauge and the sample without altering the measured response. On the other hand, the epoxy adhesive (*e.g.* used in this work a bi-component E504 from Epotecny) is an initially viscose adhesive which requires specific curing stages and in principle is not optimised for all kind of materials in question. Although the resulting thickness of the glue is often around 0.1-0.2 mm and (in this work) small strains are measured, it is still difficult to say that the epoxy glued grid would not modify or disturb the measures.

In the following an attempt is made to numerically investigate a possible effect of local stiffening due to the applied glue over the sample surface with explicit finite element computations. The principle relies on simulating a spalling experiment with a thin layer of element on the sample surface. Then, the simulated displacement fields are extracted and treated with the VFM to obtain the simulated softening stress-strain response. Generally, numerical simulation of thin films is a challenging task especially in case of expected viscosity effects. However, as a first

step, a purely elastic response of the glue layer is adopted while the concrete specimen is simulated with a uniaxial damage model as in (Section 3.4.2.2).

A.2 Numerical model

The 3D Numerical model (Section 3.2.1) has been used for this purpose. A thin layer of finite elements (C3D8R) with a total thickness of 0.3 mm has been crated on top of the elements that constitute the region of interest by the simple use of offset command. Reduced integration elements are used as a first attempt and the investigation of the possible effects of hourglassing and shear locking remain a perspective. The adhesive layer was approximated with 3 sub-layers that have a thickness of 0.1 mm (Figure A.1).

As mentioned an uiaxial damage model is used to simulated the concrete failure in tension while a perfectly elastic response is considered in compression (Table A.1). The layer of elements that represent the glue are considered perfectly elastic. The mechanical characteristics of the glue after curing are not provided by the manufacturer and the measurement of thin film stiffness is a complicated matter. The only available information is that after the curing, the glue exhibits a durometer hardness between 80-90 (Shore D scale), which according to empirical formulation in the literature (*e.g.* ASTME 2240) corresponds to an Young's modulus of about 1 - 4 GPa (Figure A.2). Final elastic parameters adopted for the glue are given in Table A.2.

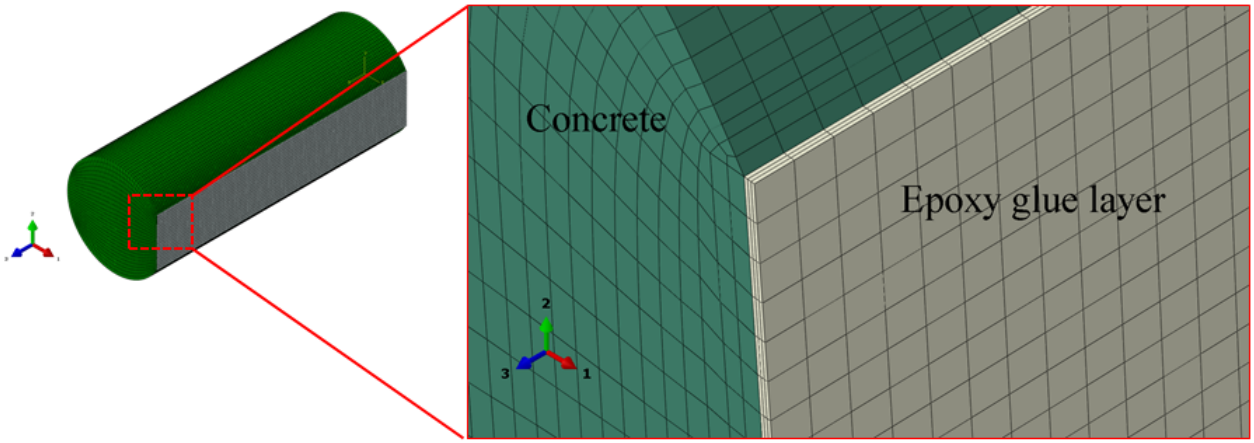

Figure A.1: FE mesh use to simulate a thin layer of epoxy glue on the concrete sample surface.

Density (kg/m^3)	E (GPa)	ν	σ_u (MPa)	E_t	E_t/E_c
2200	40	0.2	8	20	0.5

Table A.1: Parameters used to simulate softening response of concrete in dynamic tension using a local uniaxial damage model.

Density (kg/m^3)	E (GPa)	ν
1500	4	0.2

Table A.2: Parameters used to simulate elastic response of thin layer of epoxy gluel.

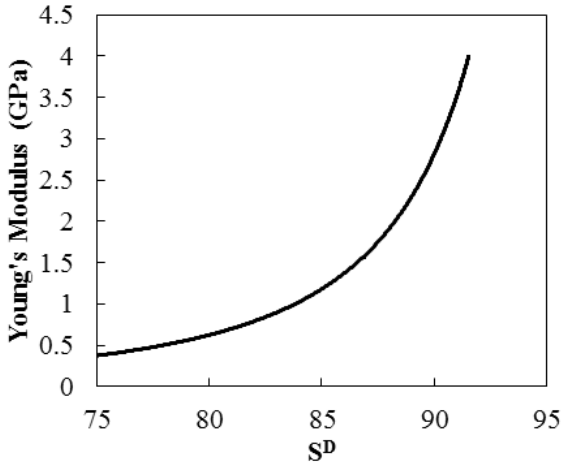

Figure A.2: Relation between durometer hardness (Shore D scale) and elastic Young's modulus of an epoxy adhesive.

A.3 Numerical results

The above described numerical model has been used to investigate possible effects of local stiffening due to the presence of epoxy glue on the sample surface. The numerical model has been used to obtain time resolved displacements fields on the sample surface with and without the considered thin layer of elastic adhesive material. The simulated displacement fields are processed within the VFM using the load cell principle in order to obtain the axial stress-strain response averaged within each transversal cross-section. The parameters used in the processing are provided in Table 3.12 (note that here synthetic images are not generated). In case when purely elastic material response is considered for both materials no effects were noted on the determined Young's modulus of concrete an the identified stiffness was within 0.5% confidence interval. Then, a softening response was assigned to concrete sample and the results from the VFM processing regarding the stress-strain response were analysed. The identified stress-strain response at 30 mm and 40 mm from the sample free end for the case when 0.3 mm layer of glue is present and when there is no glue on the sample surface are shown in Figure A.3. From a first qualitative observation, slight differences can be spotted in the softening part of the reconstructed stress-strain curves especially regarding the failure strain (*i.e.* axial strain at zero stress). This was expected since the strain on the sample surface is expected to be slightly larger than the one measured on the surface of the glue. Interestingly, no effect on the measured failure stress (*i.e.* peak axial stress determining the onset of damage) is noted. On the other hand, the limitations of the current numerical modelling do not allow drawing any firm conclusions since strong hypotheses are made by adopting purely elastic behaviour of the epoxy glue. A strong prospect is the consideration of a limit strength criterion and a viscosity component for the simulated glue material which would allow to better describe the behaviour of the simulated adhesive, especially focusing on the post peak regime.

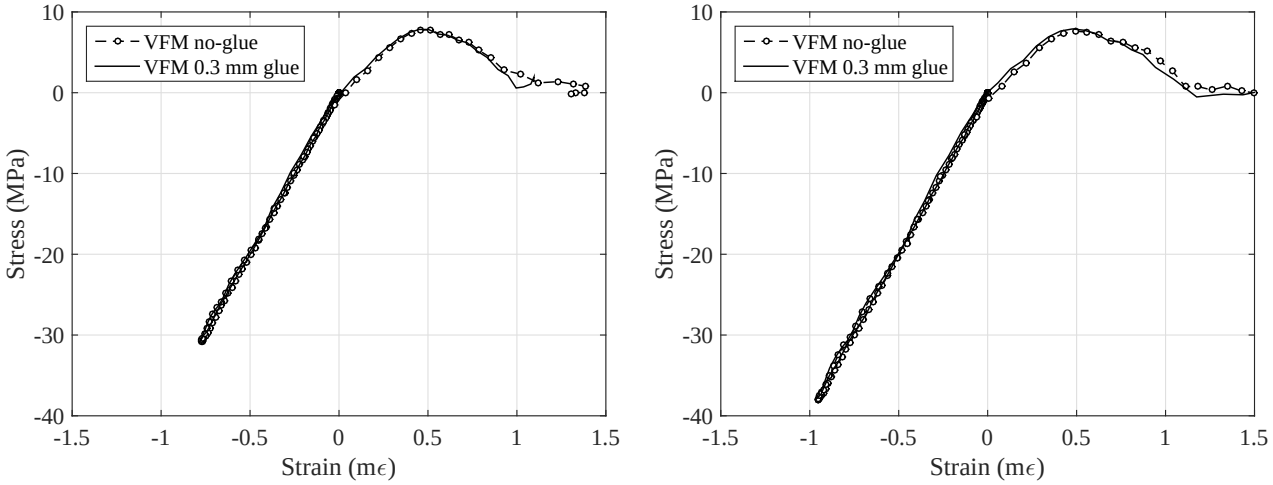

(a) Axial stress-stress response at 30 mm from free end. (b) Axial stress-strain response at 40 mm from free end.

Figure A.3: Effect of 0.3 mm layer of elastic epoxy glue on the identification of concrete dynamic tensile damage response.

Appendix B

Validation of the acceleration magnitude

It is reasonable to question the use of the load cell principle at lower levels of acceleration magnitudes. Such as for example when conducting tests at intermediate strain rate levels with the use of a SHPB bar [Kim et al., 2017]. In such tests often low magnitude of acceleration is experienced which is argued not to be high enough for the VFM identification. However, it is true that the dynamic equilibrium equation is valid at all times. It is just the inability of a measurement system to accurately detects such small acceleration magnitudes. Therefore, a more precise explanation in such situations could be that the lowest measurement resolution of the used full-field measurement technique which does not allow the detection of such small acceleration magnitudes for a reliable material identification using the VFM and the load cell principle. This can be simply demonstrated with the above described simulation procedure by reducing the input load magnitudes. The initially assigned load pulse, in previous simulations, is 50 MPa in magnitude inducing an average axial acceleration of 1.5 x10^5m/s^2. Figure B.1 presents overall average identified global Young's modulus for the same case of load amplitude but with lower pulse magnitude (namely 10 MPa, 10 Pa and 1 Pa). As expected the reference value is identified even in cases of simulated acceleration levels of 10^{-7}m/s^2 although numerical sensitivity of the identified stiffness is increased, which is again expected.

Although the made observation remains quite trivial, it is still useful to show that the load cell principle can be used even in cases when extremely low levels of accelerations are experienced. Currently, it seems a bit far-fetched to measure such low levels of displacements using a full field measurement technique and ultra-high speed imaging. However, the principle can be used if any other measurement system is employed, providing that the measurement resolution is good enough to accurately obtain exploitable acceleration data.

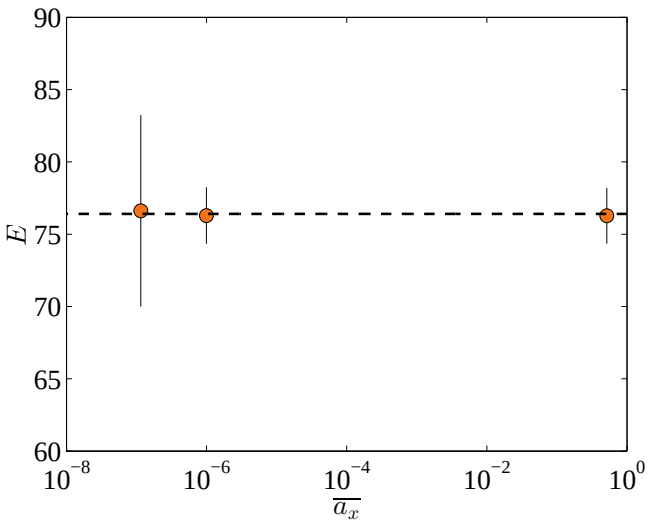

Figure B.1: Effect of low acceleration levels on the identification of global Young's modulus ($\overline{a_x}$ is mean acceleration in mm/s^2 and E is identified stiffness in GPa).

Appendix C

Computing acceleration fields from noisy displacements

C.1 Introduction

As shown previously in Section 6.2, the Kirana imaging systems can suffer from intrinsic sensor temporal noise. This type of high frequency temporal fluctuation of pixel grey levels can propagate from the registered camera images to the measured displacement fields. Numerical differentiation of the time polluted displacement signals amplifies the noise magnitude often to extent that it becomes difficult to distinguish between real material response and the background effect. This particularly becomes an issue when the measured mechanical response of the material is in the low range of signal-to-noise ratio such is, for instance, the acceleration levels tied to dynamic tensile failure of concrete materials. In that case numerical filtering techniques need to be used as an intermediate step prior the differentiation, as to smooth out the recorded displacement signals and allow identification of some part of the *clean* signal that carries the meaningful information of the pure physical phenomena. Derivation of noisy signals has been a frequently addressed

Another strategy of filtering severely corrupted noisy data, prior to the numerical derivation, consists in either interpolating or approximating the entire data sets using smooth functions [Ditkowski et al., 2008]. Then, the differentiation is simply achieved by knowing the coefficients of the fitted functions, which is also more computationally effective especially in case where velocity fields also need to be evaluated as an intermediate derivation step. This can be performed by approximating a set of experimental data with the so-called smoothing cubic-spline polynomials [Berghaus and Cannon, 1973, Rowlands et al., 1973], where the demand to replace the strict interpolation by adding a certain level of smoothing is met through the introduction of a smoothing coefficient.

In the following, the problem of deriving the meaningful acceleration fields from the noisy displacement maps obtained with ultra-high speed imaging systems is addressed. Smoothing of a high-frequency noise is attempted through the application of the global approximation strategy, using the smoothing spline approximation. Since the level of smoothing is controlled through a specific coefficient a methodology of providing the first estimate of this coefficient is presented. It consists in numerically simulating the elastic displacement maps of a spalling test which are then corrupted with a periodical noise component. The smoothing spline approximation is then applied on the noisy displacement fields to compute the acceleration data which is then compared to the exact solution to estimate the value of the smoothing coefficient.

Then, the applicability of this specific smoothing strategy, in case of a completely random time alternating noise, was investigated. The processing is performed with both the smoothing spline method (the global method) and the low order polynomial fit over a moving span of data (the local method). The identified results of both methods are compared to the exact solution in terms of both the derived acceleration response and the identified axial stress response for a given case of noise magnitude.

C.2 Effect of periodical noise

The major problem in time derivation is the amplification of the high frequency noise on the derived signal. The attempt to using standard finite difference method often fails, especially where the magnitude of the derivative represents a large portion the *clean* signal. The problem obviously magnifies in cases of second order derivation.

This can be easily demonstrated through a simple example. Here, the term signal is defined as the measurement data (*i.e.* measured surface displacement during a spalling test) and the *clean* signal is the one that describes a pure physical phenomenon (or real mechanical response) whose exact form can be obtained from a theoretical description (*i.e.* theory of perfect-elastic material response). Let the sampled signal be the measured average surface displacement in an elastic case of a spalling test, denoted as:

$$f(t) = u(t) + \epsilon sin(\omega t) \tag{C.1}$$

Where, $u(t)$ is the *clean* displacement signal measured in millimetres (or the true elastic response of the material) and the $\epsilon\ sin(\omega t)$ is the noise with the amplitude ϵ and angular frequency ω. If it is assumed that the $u(t)$ is of order 1, as well as $\epsilon << 1$ and $\omega >> 1$, then the second derivative with respect to time (*i.e.* the sought acceleration response signal) is denoted as:

$$f''(t) = u''(t) - \epsilon\omega^2 sin(\omega t) \tag{C.2}$$

It is often that the term $\epsilon\omega^2 >> 1$ and therefore $u''(t)$ is strongly perturbed due to the magnitude amplification of the noise derivative to such an extent that it cannot be accurately measured.

C.2.1 Numerical demonstration

A simple numerical interpretation of the above mentioned example is provided in Figure C.1. The figure summarizes results of an elastic 3D numerical simulation of a spalling test, obtained with an explicit FE solver (Abaqus/Explicit) mimicking an acquisition speed of 2 Mfps. A plot of the global axial displacement, obtained as an average elastic response of all surface nodes, is presented in Figure C.1a and considered as the *clean* signal. The sampled displacement signal, which is a superposition of the assumed periodical high-frequency noise and the *clean* signal, is shown in Figure C.1b. The noise magnitude is assumed to be 0.05% of the final displacement reached in a spalling test in mm ($\epsilon = 0.12\ \mu$m). This can be regarded as of a relatively small order compared to measured magnitude of the displacement. However, it is chosen deliberately. The noise temporally frequency is assumed to be 200 kHz. This was chosen as it is close to the high frequency noise present in a treated acquisition sequence of the Kirana camera at the given acquisition speed of 2 Mfps (Figure 6.8). The second derivative of both the sampled signal and the *clean* signal, computed with standard finite differences are presented in Figure C.1c.

From this trivial example it is easily concluded that a high frequency oscillating noise of a relatively small magnitude can disturb the computation of the signal second derivative as the noise magnification is influenced by its angular frequency to the second exponent. Moreover, this noise does not appear to be at all obvious in the sampled measurement signal and it seems not clear how to distinguish between the noise polluted and the *clean* signal when the data is already registered. For example, just looking at the acquisition sequence of the UHS camera, even after it is slowed down numerous times, it is difficult to observe these fluctuations visually, simply because human eyes have difficulties following an intensity change faster than 20 Hz.

C.2.2 Derivation of smoothed displacement signals

Smoothing spline is a special case of spline function [de Boor, 1978]. It can be used as a procedure of fitting a smooth cubic spline function to a set of data where the values on the ordinate are given by an approximation (*i.e.* a large set of experimental data) or in case of noisy data [Berghaus and Cannon, 1973]. In these cases

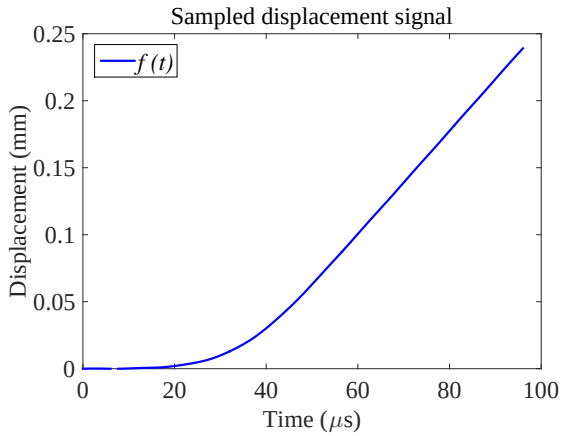

(a) The sampled signal - as an average elastic axial displacement of all surface nodes in an explicit FE simulation of a spalling test.

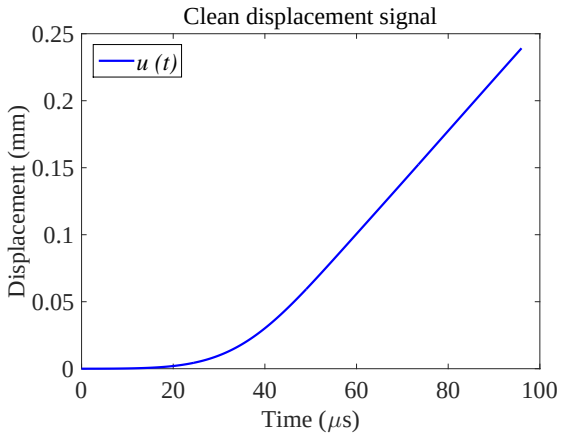

(b) The clean signal – as the clean signal with the contribution of $\epsilon sin(\omega t)$ periodical noise.

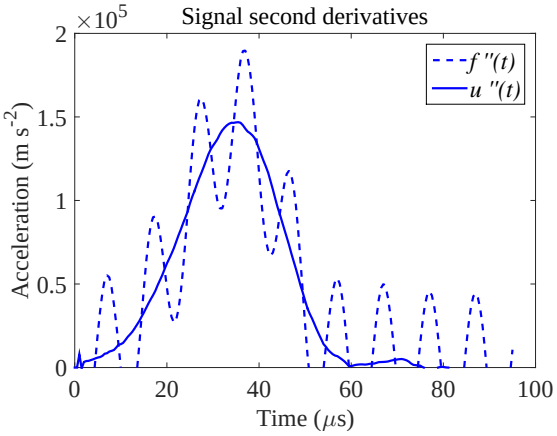

(c) The second derivative of both clean (u'') and sampled signal (f'') with the use of the classical finite differences method.

Figure C.1: Effect periodical noise on measured displacement signal – A numerical example.

the strict interpolation can be loosen by adding a degree of smoothness through specific smooth coefficient. It provides a balance between the deviation of the reconstructed data from the true response and the smoothness of the reconstructed data. The choice of the smoothing parameter can be regarded as compromise between how precise the newly obtained function will represent the given data and the tendency to obtain the smooth function. Therefore, this coefficient needs to be determined beforehand. The smoothing spline fitting is integrated in the Matlab environment through the command *csaps*.

The difficulty of spline filtering lies in controlling this smoothing parameter. In general, the most reliable practice seems to be to determine the smoothing coefficient for each experimental testing individually. It is suggested to perform preceding tests on specimens where the results of material response are known, so the smoothing parameter can be associated to the particular experimental setting [Berghaus and Cannon, 1973]. In the following case, this procedure is adopted. However, by treating numerically generated test data obtained from elastic FE simulations of a spalling test. This procedure is used in order to provide first estimate of this coefficient. To determine the smoothing coefficient a fairly simple iterative approach was employed by back-identifying the primary elastic response of the clean displacement signal obtained from numerically simulated test. This was done by subsequently fitting the smoothing spline to the noisy displacement signal (shown in Figure C.1a) with different values of smoothing coefficient until the retrieved response matched the expected one with a sufficient degree of confidentiality. After fitting the smoothing spline to the sampled displacement signal, the retrieved function was derived two times in order to obtain the average acceleration response which was then compared to the exact one (the one from the FE simulation). The overall error defined as absolute mean difference between the exact acceleration response and the response derived by the smoothing spline function. The iterations were arrested when the overall error was close to 1%. The obtained result is presented in the Figure C.2a.

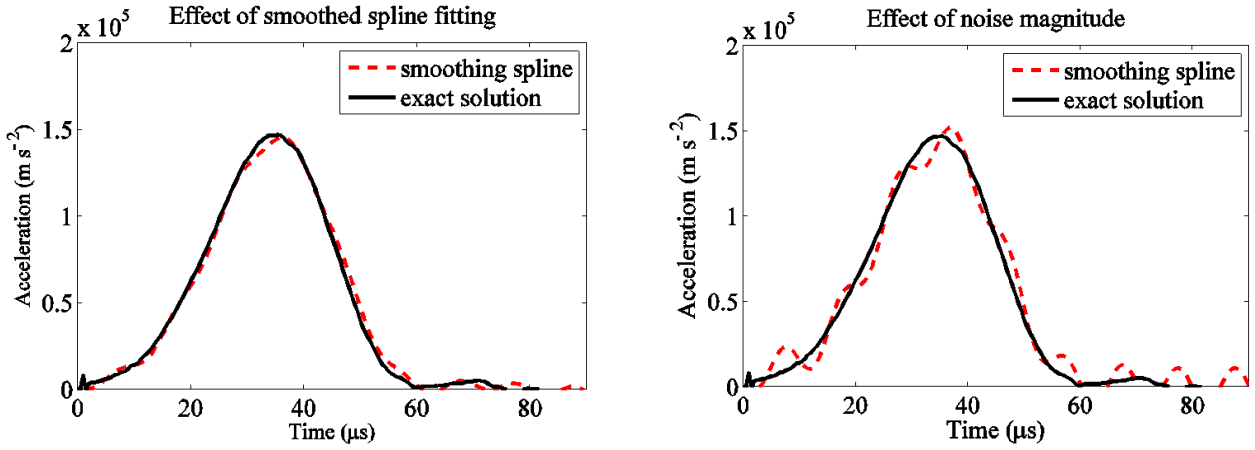

(a) $\epsilon = 0.12$ μm, 200 kHz

(b) $\epsilon = 0.48$ μm, 200 kHz

Figure C.2: Effect of using smoothing spline to derive average acceleration from the displacement data with it corrupted with periodical high frequency noise $\epsilon sin(\omega t)$.

It is obvious that a proper selection of the smoothing coefficient is a prerequisite to obtain a accurate derivative from the approximated smooth function. On one hand, the smoothing parameter should ultimately give a sufficiently smooth second derivative function with a sufficiently small deviation from the *clean* signal. On the other hand, the smoothing coefficient has to be chosen in such a way not to provide a case of over-smoothing of results. The above presented simple numerical method of obtaining initial estimate of the smoothing coefficient from numerically generated data for an assumed periodical noise can be a useful guideline for the initial processing experimental results. Interestingly, the chosen smoothing spline family seems robust enough to filter out the designed noise frequency regardless of the phase and in a wide angular frequency range. The same result was retrieved when on the top of

the noisy signal already used, an additional component of an out-of-phase noise was added as $-\epsilon cos(\omega t)$. The same can be said when the noise frequency was varied from 200 kHz to 800 kHz. However, the amplitude of the added noise seems to affect the filtering constraint of the smoothing spline. An example is provided on the following Figure C.2b, where the noise amplitude was increased to 0.2% of the final displacement in mm (ϵ=0.48 μm).

C.2.3 Numerical validation

It was shown that the smoothing spline can represent a useful tool for obtaining smooth second order derivatives compared to other conventional methods. However, in some cases an effect of over-smoothing can occur which causes deviation from the expected theoretical response. In order to this, an analysis was conducted with the aim of validating the processing procedure and identified smoothing coefficient. An experimental test was simulated with FE computation in order to obtain reliable displacement fields for the identification as explained in Section 4.1.1, and will not be detailed here. The reference material stiffness entered in the numerical simulation serve as a perfect reference validation values (E=78 GPa). The simulated elastic displacement fields were extracted at nodal points of a 3D elastic model which constitute a flattened sample surface. Time resolved FE data was obtained by simulated acquisition speed of 2 Mfps. Then these fields (no added noise) have been processed using the VFM processing. The chosen virtual fields are obtained from 8th degree polynomials. The strain fields are derived utilizing the diffuse approximation algorithm on a span of 8 displacement points with second order polynomials. The acceleration fields were derived with both a 2nd order polynomial fitting on a temporal sliding of 7 points (SG filtering) and the smoothing spline with the previously identified coefficient. The identified elastic Young's modulus and reconstructed stress-strain curve of a virtual gauge at 40 mm from sample's free end (20 point spatial smoothing) are shown in Figure C.3.

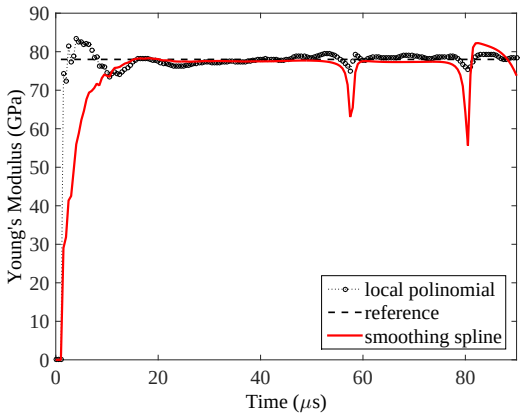

(a) Identified Young's modulus. Evidence of spline over smoothing.

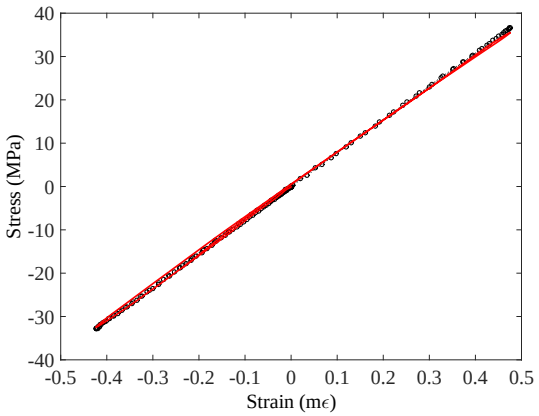

(b) Identified Stress-strain response.

Figure C.3: (A)Validation of the of the identified smoothing spline coefficient on perfect simulated displacement fields without added noise. (B)Comparison between: 2nd degree polynomial fit over 7 temporal displacement points and the smoothing spline fitting for reconstruction of acceleration.

The results of the smoothing spline qualitatively exhibit a good agreement with the reconstructed results from local polynomial fit, and seem to be sufficiently close to the reference values. The values of identified Young's modulus obtained as linear regression of the reconstructed stress-strain response at several location along the numerical sample axis are summarized in in Table C.1.

Method	Virtual gauge 50 mm	Virtual gauge 40 mm	Virtual gauge 30 mm
Local Polynomial	77.34	77.26	77.25
Smoothing spline	76.33	76.15	76.01

Table C.1: Results of linear regression and identified Young's modulus from reconstructed stress-strain response for two smoothing methods for obtaining acceleration data with the expected reference $E = 78$ GPa.

C.3 Numerical testing

Besides being affected by periodical high-frequency noise, displacement maps can be also affected by other types of camera noise artefacts such the photon noise, dark current noise, readout, and digitization noise [Holst, 1998]. All this increases the randomness of the overall artefacts in the measured displacement maps. In order to further investigate the proposed filtering method, the smoothing spline fit was also tested in the case of a completely random noise present in the measured signal. Here, the supposed random camera noise is simulated by adding standard white noise to the numerically computed elastic maps. In the present case, numerically simulated displacement fields were corrupted frame by frame at each measurement point, with non-correlated zero mean random noise multiplied with a positive value γ, also referred to as displacement uncertainty measurement. The magnitude of the random zero-mean input noise does not affect the average value of the identified elastic stiffness parameter but only increases the standard deviation [Avril et al., 2004b]. The numerical procedure of simulated fields of a spalling experiment follows the methodology used to validate the experimental procedure that is presented in Section 4.1. Two cases of the added random noise are analysed with the magnitude of 1% and 10% of axial displacement reached at the end of the simulated test (see Figure C.4).

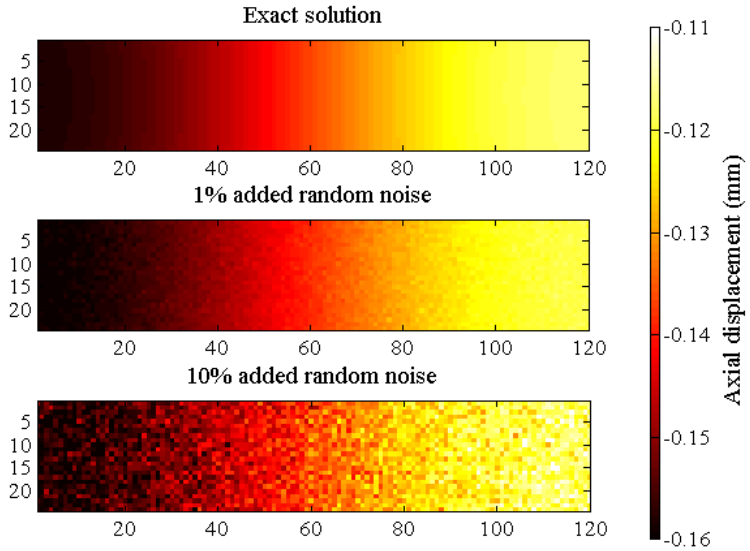

Figure C.4: Example of numerically simulated axial displacement maps, obtained from a 3D elastic FEM simulation of a spalling test, corrupted with alternating zero-mean random noise. Maps correspond to 70 μs from the beginning of loading. Top: Exact elastic response from numerical simulation; Middle: 1% of added noise (γ=2.4 μm); Bottom: 10% of added noise (γ=24 μm).

The noise magnitude is of one order higher than the previously simulated high-frequency noise component as in this case it is an example of an alternating random spatial noise that changes at each frame which does not have any specific frequency. The corrupted displacement fields were processed in order to obtain the derived acceleration fields by utilizing two methods, a local second order polynomial fit over moving 7 temporal data points and a

global smoothing spline fit with the coefficient identified previously. The results are presented in Figure C.5. It can be observed that the proposed global filtering method with smoothing spline approximation that utilizes the previously identified smoothing coefficient can also be successfully used to filter out alternating zero-mean random noise from the displacement fields.

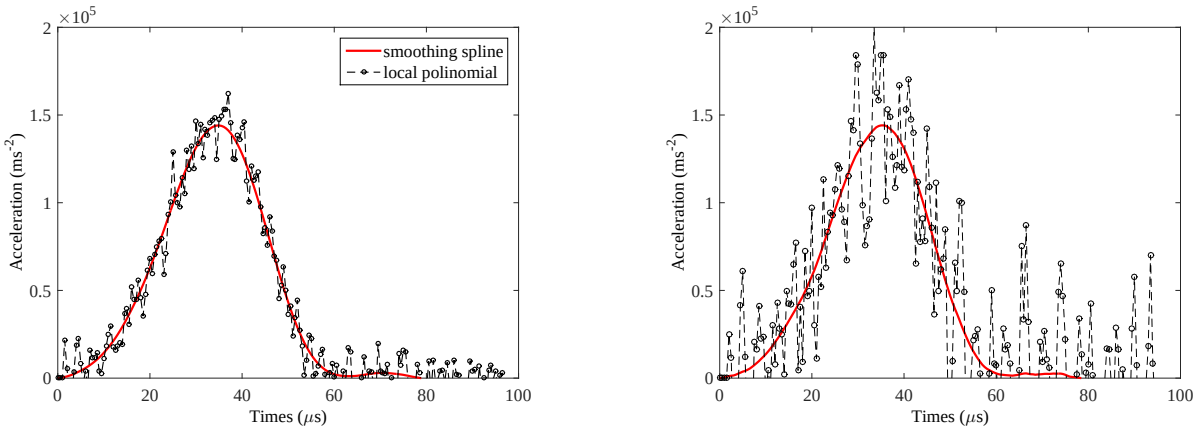

(a) $\gamma = 2.4$ μm. (b) $\gamma = 24$ μm.

Figure C.5: Effect of deriving acceleration from corrupted displacement data. Comparison of a local 2nd degree polynomial fit over moving 7 data points and the global smoothing spline fit by comparing the overall average acceleration response.

Finally, it is also interesting to perform full identification of the material response on the numerically simulated data, in the same way as when the real experimental data obtained from a spalling test are processed. It has to be mentioned that simulated noise also propagates to the strain fields. However, the effect of time alternating noise on temporal strain measurement is out of the scope of this work. Here the only focus is on obtaining accurate (or as accurate as possible) stress description. The identified elastic Young's modulus and reconstructed stress-strain curve averaged on the entire sample surface obtained with VFM and the proposed global smoothing for noisy displacement data are shown in Figure C.6. The plots illustrate a possible benefit of using smoothing spline to filter out highly corrupted displacement data and to identify the linear elastic response of material. While the identification stress-strain response is considerably ameliorated, some fluctuations are still present in the identified Young's modulus. This is expected, due to the fact that the choice of virtual fields depends on the displacement data. This is clear when first 20 μs of the test are observed, where is a low signal-to noise ratio. However, during the principal part of the loading: compressive pulse (35 - 55 μs) and reflected tensile pulse (60 - 80 μs) the reference value is relatively reproduced with low fluctuation. On the other hand, the processing with the local polynomial filtering indicates large deviation from the reference value of Young's modulus.

C.4 Experimental testing

Spalling experiments were performed on ordinary concrete material using the experimental set-up described in Section 7.1.3. The Shimadzu HPV-X2 camera was used to film grid instrumented concrete samples at 1 Mfps. Due to the illumination difficulties that manifested as high-frequency flickering of the continuous light source provided by LED lights, the images were corrupted with additional high frequency content due to this temporal noise (see Figure 7.3). Although it was found that the sequences can not be used to provide reliable information on the material tensile strength and specific fracture energy, they can be used to test the above introduced method for computing the acceleration data from noisy images. Figure C.7 results in terms of reconstructed stress-strain curve at the 40 mm from the sample free-end using a virtual gauge of 10 mm in size. Two types of processing were used, the above mentioned global smoothing spline method with the identified coefficient and the 2^{nd} degree polynomial

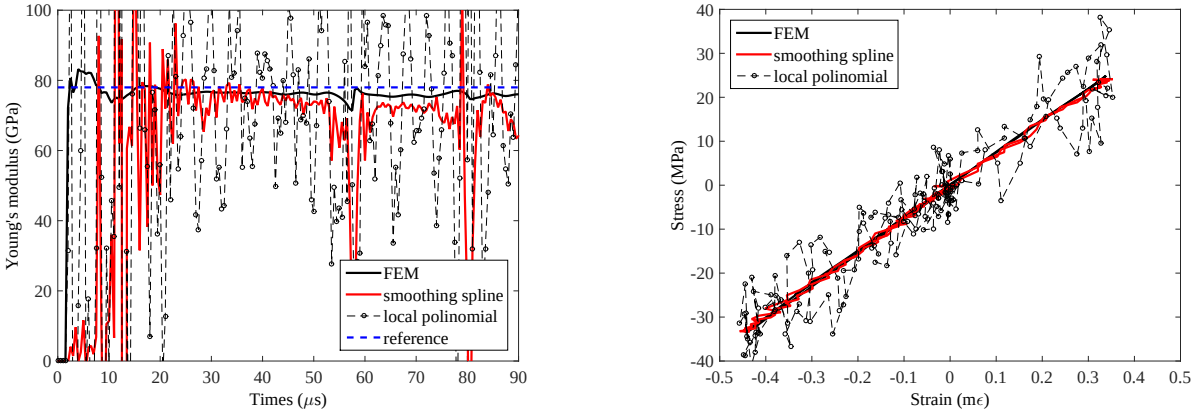

(a) Identified Young's modulus.

(b) Reconstructed stress-strain response..

Figure C.6: Identified material response for the case of 10% of time alternating zero-mean random noise are processed. Diffuse approach was used with 8 point displacement span for obtaining the strain fields differentiation. The virtual fields used are of a 8^{th} degree polynomial fit over displacement maps averaged in vertical direction. The results are shown in case of 2^{nd} degree polynomial reconstruction of acceleration over 7 temporal displacement points and global smoothing spline filtering.

fit over 17 temporal displacement points. From the presented curves it can be seen that the two curves, although coinciding well in the compressive stage, exhibit large difference in the tensile stage. The reason for this is currently not known which influenced that fact that the smoothing spline method was not used in the treating experimental results presented in Chapter 7. One could suspect a strong over smoothing of the results in case when the smoothing spline method is used to retrieve material non-linear response. A possible perspective would be to use also the data from the results point-wise measurements (*i.e.* Laser interferometer) and perform the error minimisation with respect to data obtained from corrupted full field displacement measurements in order to optimise the smoothing spline coefficient.

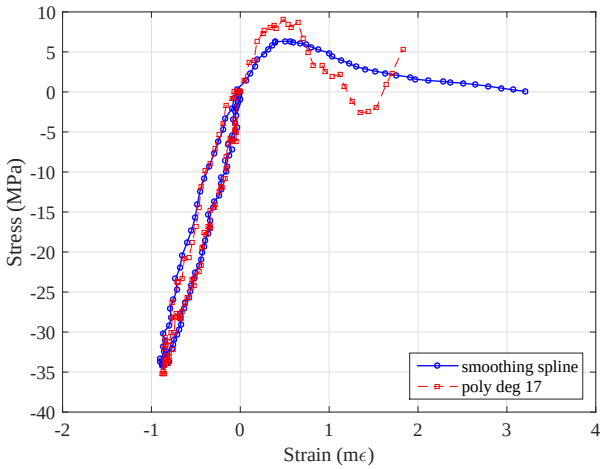

Figure C.7: Identified material stress-strain response for the case of an noise polluted spalling experiment on ordinary concrete. Diffuse approach was used with 8 point displacement span for obtaining the strain fields differentiation. The virtual fields used are of a 8^{th} degree polynomial fit over displacement maps averaged in vertical direction. The results are shown in case of 2^{nd} degree polynomial reconstruction of acceleration over 17 temporal displacement points and global smoothing spline filtering.

Appendix D

Photographical details regarding the spalling test conducted on (LC) and (HPC)

Concrete	Name	Camera speed	Post.Trig Img.	Tank pressure (bar)	Projectile speed (m/s)	Grid sampling (pix/pitch/mm)
(HPC)						
	SBHP03	1 Mfps	54	0.45	10.8	7
	SBHP01	1 Mfps	58	0.24	6.1	5
	SBHP04	2 Mfps	64	0.51	11.4	7
	SBHP05	1 Mfps	58	0.38	9.2	5
	SBHP06	1 Mfps	56	0.21	5.94	5
(LC)						
	SLCG01	1 Mfps	58	0.24	6.2	5
	SLCG02	1 Mfps	40	0.48	11.3	7
	SLCG03	2 Mfps	58	0.43	10.2	7
	SLCG04	1 Mfps	54	0.5	11.5	7

Table D.1: Experimental details regarding spalling test performed on (LC) and (HPC) recorded with Shimadzu HPV-X2 ultra-high speed camera. (All test were performed with projectile having 50 mm length and were instrumented with a grid of 1 mm pitch).